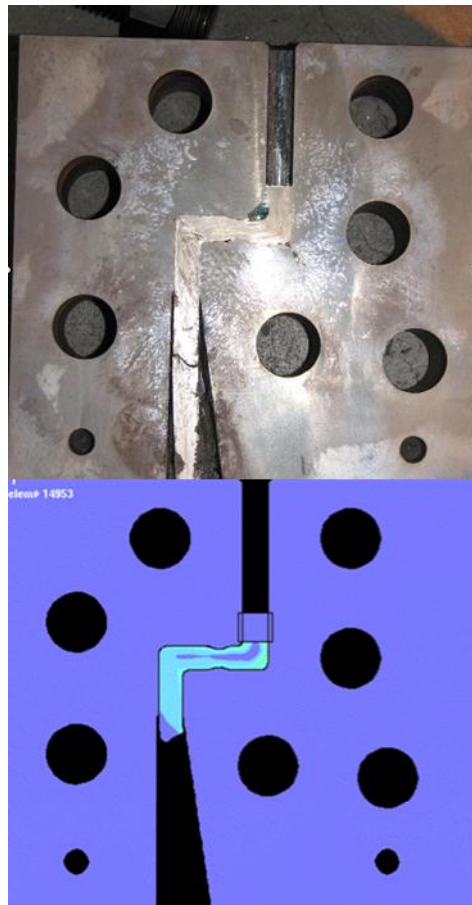# MIVA

Mikrorakenteisten metallituotteiden joustava valmistus

TEKES, diaarionro 1097/31/08, päätösnro 40186/08

2008-2011

Loppuraportti

toim. Jari Larkiola, VTT

TEKES diaarionro 1097/31/08, päätösnro 40186/08	
Projektin nimi **Mikrorakenteisten metallituotteiden joustava valmistus**	Projektin numero/lyhytnimi 29985/MIVA
Raportin laatija(t) Koonnut Jari Larkiola	Sivujen/liitesivujen lukumäärä 9/317
Avainsanat UFG metals, SPD, severe plastic deformation, ECAP	Raportin numero VTT-R-06863-11

Tiivistelmä

Tuotteiden kestävyys ja kuormitettavuus pohjautuvat tuotteen materiaaliominaisuuksiin ja muotoon. Yksi uusi ja tehokas tapa parantaa tuotteen ominaisuuksia valmistusvaiheessa on SPD-menetelmä (Severe Plastic Deformation). SPD -menetelmissä voimakas valmistuksen aikana tapahtuva muokkaus - samalla kun se antaa tuotteelle muodon - pienentää materiaalin raekokoa mikroluokkaan. Mikrorakenteisessa materiaalissa raekoko on alle 1 µm (normaalisti raekoko on luokkaa 20 - 100 µm). Raekoon pienentäminen parantaa merkittävästi mm. mekaanisia ominaisuuksia.

Teollisuus ei vielä ole alkanut valmistaa mikrorakenteisia raaka-aineita ja aihioita. Tämä johtuu pääosin siitä, että ei ole olemassa hyvin toimivaa jatkuvaan prosessiin sopivaa SPD-menetelmää. Tämä luo mahdollisuuden saavuttaa kilpailuetua valmistamalla SPD-komponentteja. Tämän hankkeen tavoitteena oli kehittää ja hyödyntää SDP -tekniikkaa, ko. prosessiin sopivia materiaaleja sekä hyödyntää menetelmää valmistavassa kappaletavara-teollisuudessa.

Projektissa kartoitettiin laajasti ufg–materiaalien valmistustekniikoita, ominaisuuksia ja käyttömahdollisuuksia. Yritysesimerkkien kohdalla tavoitteita ei täysin saavutettu. Kuitenkin yritykset jatkavat kokeita tuotannon sopivasti salliessa. Tällöin mahdollisuus tavoitteissa määritettyihin ratkaisuihin on edelleen olemassa ja hankkeen vaikutus yritysten uusiin tuotteisiin ja liikevaihtoon nähdään myöhemmin. *Yksi yritys jatkaa SPD-valmistusprosessin kehitystä ja tavoitteena heillä on uuden SPD-materiaalien tuominen markkinoille 2012.*

Raportissa esitetään hankkeen tuloksia yksityiskohtaisemmin sekä projektin aikana tehdyt julkaisut.

Luottamuksellisuus	julkinen		
Espoossa 31.8.2011 Laatija		Tarkastaja	Hyväksyjä
Jari Larkiola, Asiakaspäällikkö		Hannu Martikainen, Erikoistutkija	Riikka Virkkunen, Teknologiapäällikkö
VTT:n yhteystiedot VTT, PL 1000, FI-0204 VTT			
VTT:n nimen käyttäminen mainonnassa tai tämän raportin osittainen julkaiseminen *on sallittu vain VTT:ltä saadun kirjallisen luvan perusteella.*			

Sisällysluettelo

1. Taustaa

Tuotteiden kestävyys ja kuormitettavuus pohjautuvat tuotteen materiaaliominaisuuksiin ja muotoon. Yksi uusi ja tehokas tapa parantaa tuotteen ominaisuuksia valmistusvaiheessa on SPD-menetelmä (Severe Plastic Deformation). SPD -menetelmissä voimakas valmistuksen aikana tapahtuva muokkaus - samalla kun se antaa tuotteelle muodon - pienentää materiaalin raekokoa mikroluokkaan. Mikrorakenteisessa materiaalissa raekoko on alle 1 µm (normaalisti raekoko on luokkaa 20 - 100 µm). Raekoon pienentäminen parantaa merkittävästi mm. mekaanisia ominaisuuksia.

2. Tavoitteet

Raekoon pienentäminen parantaa merkittävästi materiaalin ominaisuuksia. Mikrorakenteisilla tuotteilla on poikkeavat ominaisuudet ja ominaisuusyhdistelmät: esimerkiksi korkea lujuus, hyvä väsymiskestävyys, sitkeys ja korroosionkestävyys sekä hyvä jatkovalmistettavuus (työstettävyys, superplastiset ominaisuudet). Mikrorakenteisten tuotteiden käyttöalue on laaja, kuten avaruustekniikka, kuljetustekniikka, terveydenhoitoon liittyvät laitteet ja komponentit, urheiluvälineet, elintarvike ja kemianteollisuus, elektroniikka ja puolustussektori.

SPD-menetelmiä voidaan hyödyntää joko raaka-aineen tai aihion valmistusvaiheessa tai lopullisen tuotteen valmistuksen yhteydessä. Konepaja voi räätälöidä tuotteen vastaamaan paremmin käyttövaatimuksia. Menetelmillä voidaan esimerkiksi parantaa perusmateriaalin lujuutta, komponentin pinnan väsymisominaisuuksia ja korroosionkestävyyttä. Mikrorakenteisen tuotteen ominaisuuksia voidaan vielä lopuksi muuttaa lämpökäsittelyllä: raekoko ja ominaisuudet voidaan muuttaa kappaleessa paikkakohtaisesti!

Teollisuus ei vielä ole alkanut valmistaa mikrorakenteisia raaka-aineita ja aihioita. Tämä johtuu pääosin siitä, että ei ole olemassa hyvin toimivaa jatkuvaan prosessiin sopivaa SPD-menetelmää. Tämä luo mahdollisuuden saavuttaa kilpailuetua valmistamalla SPD-komponentteja. Konepajaan sopivia koko kappaleen rakennetta muokkaavia menetelmiä ovat mm. ECAP (Equal Channel Angular Pressing) ja MAC (Multiaxial Compression). Kappaleen pinnan käsittelyyn sopivia menetelmiä ovat mm CRPD (Circulation Rolling Plastic Deformation) ja HESP (High Energy Shot Peening).

Hankkeen tavoitteena oli kehittää SDP–tekniikkaa ja sopivaa menetelmää valmistavan kappaletavarateollisuuden käyttöön.

3. Toteutus

Hankkeessa kehitettiin menetelmiä ja lähtömateriaaleja mikrorakenteisten tuotteiden valmistukseen. Lisäksi tutkittiin ECAP-prosessin toimintaa omilla laitteistoilla ja työkaluilla.
Sovelluksia testattiin osallistuvien yritysten esimerkeissä. Pääsääntöisesti TTY keskittyi tutkimukseen, joka liittyi dynaamisten ilmiöiden hyödyntämiseen ko. materiaaleilla ja valmistettujen materiaalien analysointiin. TKK:lla tutkittiin lämpökäsittelyn ja pinnoituksen vaikutusta SPD-prosessissa. VTT:llä tehtiin menetelmäkehityksestä sekä kokeita yritysten sovelluksiin liittyen.

4. Tulokset

MIVA-hankkeessa tehtiin suuri määrä kirjallisuuskatsauksia ja selvitettiin SPD-teknologian nykytilaa.

4.1 Kirjallisuusselvitykset

Hanke aloitettiin kattavilla kirjallisuusselvityksillä. Mikro/nanorakenteisten metallituotteiden valmistusta sekä prosessointia on käsitelty useissa tutkimuksen aikana kirjoitetussa selvityksessä, Liitteet 1-10. Hankkeessa ja selvitysten tekemisessä oli mukana myös ulkomaisia alan asiantuntijoita: Professori Leijun Li (Utah University) ja Dr A. Rosochowski (Strahclyde University, Glasgow). Projektiin liittynyt tutkimusvierailu The Ohio State Universityyn, USA, (TkT Mikko Hokka) on lisännyt kansainvälistä yhteistyötä ja on jo johtanut jatkoyhteistyöhön toisen Tekesin rahoittaman tutkimusprojektin yhteydessä (Fimecc/Demanding Applications).

4.2 ECAPE

Hankkeessa rakennettiin ECAPE-työkalut, joilla tarkoituksena oli tuottaa hyvin hienorakeista alumiinia, Kuva 1. Ko. kappaleiden analysointi tehtiin TTY:llä sekä vaihtotutkijan TkT Mikko Hokan (TTY) toimesta Ohio State Universityssa.
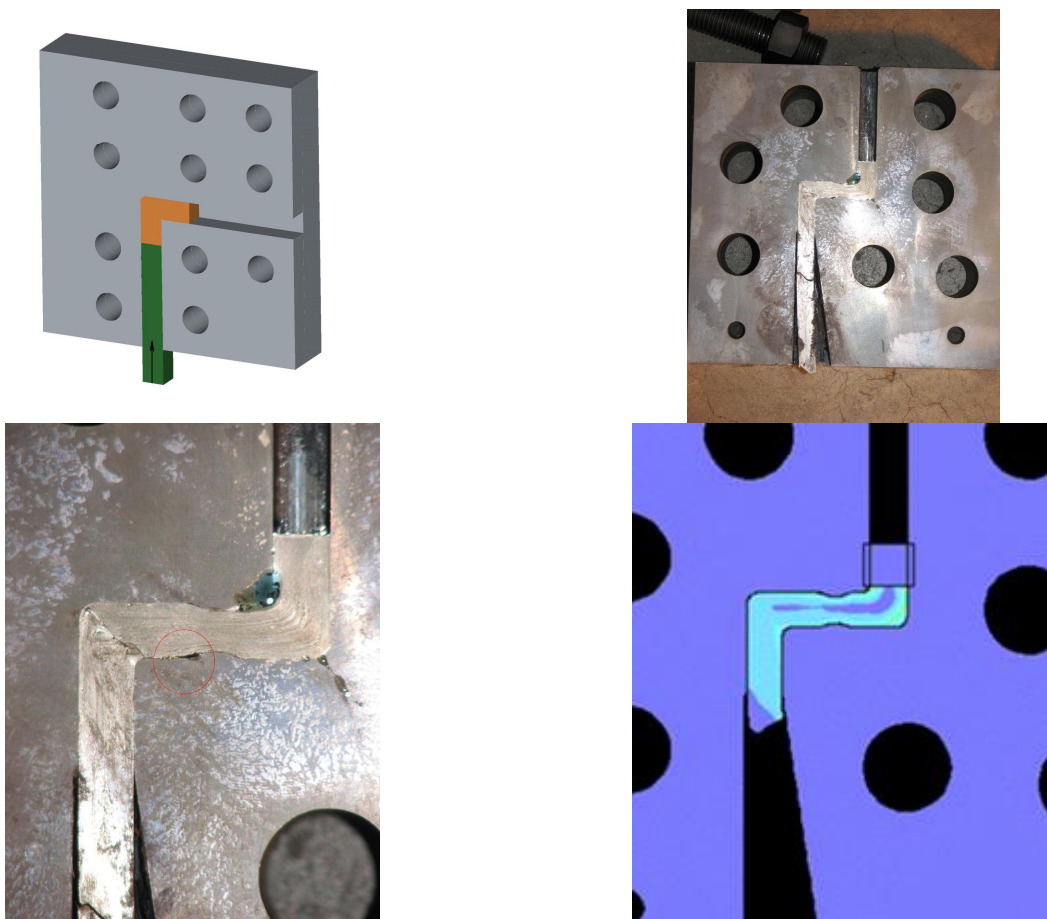
Kuva 1. Esimerkki ECAPE-pursotuksesta ja alumiinin virtauksesta prosessin aikana.

SPD-materiaalin raekoko hienontui ECAPE-muottia käytettäessä. Hienontumista ei kuitenkaan tapahtunut siinä määrin kuin oli arvioitu. Raekoon hienontumiseen vaikuttaa kuitenkin muotin lisäksi mm voitelu ja prosessin nopeus. Tästä johtuen saavutettuja tuloksia on vaikea vertailla

kirjallisuusarvoihin kun pyritään selvittämään ECAPE-muotin geometrian vaikutusta raekoon hienontumiseen.

Tietyissä tutkimuksissa on osoitettu kappaleen poikkipinnasta mitatun "raekoon" (dislocation cell size) kasvavan siirryttäessä kappaleen keskeltä pinnalle (mm. Baik et al). ECAPE-menetelmän pitäisi johtaa tasaisempaan rakenteeseen. Selkeää paranemista ei kuitenkaan pystytty mittauksilla todentamaan. Tarkemmat tulokset esitetään Liitteessä 2.

ECAPE-osavaiheeseen liittyen tutkimus jatkuu yrityshankkeena Protoshop Oy:n toimesta. Heillä on tavoitteena aloittaa SPD-materiaalin valmistaminen jatkuvatoimisella tuotantokoneella.

4.3 Austeniittinen piippumateriaali

Kiväärin piipun tulee olla lujaa ja sitkeää. Tällä hetkellä käytetään paljon ruostumattomia seoksia piippumateriaalina. Piippujen useat kalibeerit vaikeuttavat valmistusohjelmaa, sillä usein jokainen reikäkoko pitää esiporata omaan mittaansa. Sopivasti muokkautuva teräs ja yksi reikäkoko voisi olla vaihtoehto keventämään valmistuskustannuksia. Samalla materiaalin tulisi olla taottavissa myös patruunapesän alueelta, jolloin voitaisiin vähentää kalvamista.

Selvitysten perusteella tavoitteeksi tuli asuteniittisen ruostumattoman teräksen hyödyntäminen piippumateriaalina. Kyseinen teräs on muokattunakin sitkeää ja lujaa. Valmiiksi porattuja ja ennen testaamattomia koeaihioita löytyi ja ne taottiin piipuiksi. Iskusitkeyskokeissa todettiin kuitenkin, että kyseiset aihiot eivät ole nykyisten käytössä olevien materiaalien vertaisia. Iskusitkeys oli heikompi. Analyysin perusteella huomattiin, että materiaalit eivät olleet austeniittisia ruostumattomia teräksiä. Tuotannossa tehtävät takomiset vaativat aina aikaa ja valitettavasti uusia aihioita (EN 1.4301) ei ehditty testaamaan projektin aikana. Yritys tekee kuitenkin testit kun tuotantoaikataulu antaa myöten. Tarkempi selvitys esitetään Liitteessä 3.

4.4 UFG ja valssaus

Epäsymmetrisellä valssauksella on kirjallisuuden perusteella vaikutusta muokattuun raerakenteeseen. Sopivasti valituilla valssausparametreilla voidaan aihion ylä- ja alapinnan välille saada selkeää mikrorakenteellista eroa. Epäsymmetrisellä valssauksella pyritään saamaan aikaan leikkautumista aihioon valssikidassa. Osahankkeen tavoitteena oli selvittää, voidaanko kitkamuutoksilla saada aikaan mikrorakenteellista eroa nauhan ylä- ja alapintaan.

Kokeet suoritettiin Oulun yliopistolla ja näytteiden analysointi TTY:llä. Mikrorakennekuvien perusteella eroa saatiin aikaan mutta vähän. Selkeämpään leikkautumiseen olisi päästy luultavammin paremmin, jos työvalsseille olisi saatu nopeuseroa suoraan moottorista. Tarkemmat tulokset esitetään Liitteessä 4.

4.5 Ultraluja lanka ja korkeahiilinen teräs

Lujin massatuotannolla valmistettu teräs on langaksi kylmävedetty korkeahiilinen perliittinen teräs. Laboratorio-olosuhteissa on päästy n. 5000 MPa:n lujuuteen. Lujia teräslankoja käytetään tyypillisesti betonirakenteissa, vaijereissa (sillat, hissit, nostimet) ja autonrenkaissa.

Teräslankojen lujuustasoa voidaan nostaa lisäämällä hiilipitoisuutta ja käyttämällä seosaineita. Hiilipitoisuuden nostaminen ja seostuksen lisääminen lisäävät valanteiden/teelmien huokoisuutta, suotautumista ja ei toivottuja erkaumia. Tällöin valaminen, valssaus ja muut loppukäsittelyprosessit vaikeutuvat.

Osahankkeen tavoitteena oli valmistaa hyvin korkeahiilistä erittäin lujaa teräslankaa. Vastaavaa tuotetta ei ole maailmassa markkinoilla. Hankkeessa selvitettiin seosaineet, valettiin aihiot, liitettiin koeaihiot tehtaan teelmiin ja suoritettiin valssaus. Valitettavsti ensimmäiset aihiot repesivät hitsiliitoksistaan ja valssauksen aikana ja koelankaa ei päästy vetämään. Hanke kuitenkin jatkuu FN-Steelillä ja tuotannon salliessa valssataan uusi koeteelmä. Osahankkeeseen liittyvät selvitykset esitetään Liitteessä 5.

4.6 UFG materiaalit ja menetelmäkehitys SPD ominaisuuksien tutkimiseen

Osahankkeessa on selvitetty laajasti raekoon pienentämisen ns. ufg (ultra fine-grained) -alueelle vaikutuksia erilaisten metallien ja metalliseosten ominaisuuksiin ja käyttäytymiseen. Lisäksi on käytetty ja kehitetty useita uusia tutkimusmenetelmiä, joiden avulla tämän tyyppisten materiaalien ominaisuuksia ja käyttäytymistä voidaan paremmin tutkia. Digitaalinen kuvakorrelaatio, DIC, on osoittautunut toimivaksi menetelmäksi mm. suurilla muodonmuutosnopeuksilla. Projektiin liittynyt tutkimusvierailu The Ohio State Universityyn, USA, (TkT Mikko Hokka) on lisännyt kansainvälistä yhteistyötä, joka on jo johtanut jatkoyhteistyöhön toisen Tekesin rahoittaman tutkimusprojektin yhteydessä (Fimecc/Demanding Applications).

Liitteessä 6 esitetään osahankkeeseen liittyvät tarkemmat selvitykset ja raportit.

5. Yhteenveto

Projektissa on kartoitettu laajasti ufg–materiaalien valmistustekniikoita, ominaisuuksia ja käyttömahdollisuuksia. Projektista on valmistunut yhteensä 4 kandidaatintyötä, 1 review – tutkimusraportti, 3 kansainvälistä konferenssijulkaisua, 3 referoitua tieteellistä artikkelia, 2 tutkimusraporttia sekä useita projektin sisäisiä selvityksiä. Lisäksi projektissa on kehitetty ja otettu käyttöön tutkimusmenetelmiä, jotka mahdollistavat ufg–rakenteisten materiaalien ominaisuuksien ja käyttäytymisen yksityiskohtaisemman ja tarkemman tutkimisen.

Viimeisimmässä selvityksessä (Angelina Gianni, 29.8.2011, Severe Plastic Deformation) tulee ilmi kyseisen teknologian kiinnostavuuden kasvu tukittaessa julkaisujen määrää / julkaisuvuosi, Kuva 2.
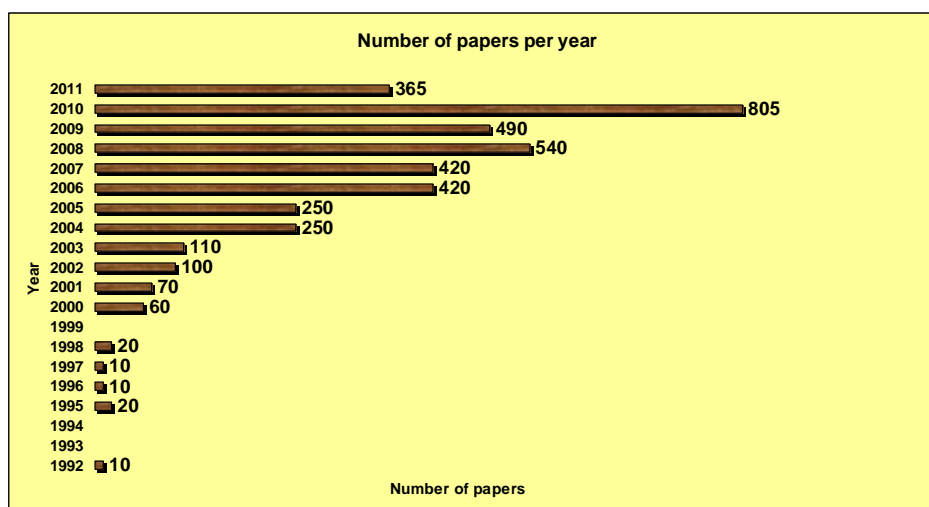
Kuva 2. SPD-menetelmään liittyvien julkaisujen määrä / julkaisuvuosi.

Yritysesimerkkien kohdalla tavoitteita ei täysin saavutettu. Kuitenkin yritykset jatkavat kokeita tuotannon sopivasti salliessa. Tällöin mahdollisuus tavoitteissa määritettyihin ratkaisuihin on edelleen olemassa ja hankkeen vaikutus yritysten uusiin tuotteisiin ja liikevaihtoon nähdään myöhemmin. Yksi yritys jatkaa SPD-valmistusprosessin kehitystä ja tavoitteena heillä on uuden SPD-materiaalien tuominen markkinoille 2012.

Tutkimus on tuottanut siihen osallistuneille yrityksille uutta tietoa, jonka hyödyntämiseen ja käyttöönottoon kuluu aikaa sovelluskohteesta riippuen. Perustietämys tutkimuksen kohteena olleista materiaaleista ja käsittelytekniikoista on merkittävästi lisääntynyt ja yhteistyö yritysten ja tutkimuslaitosten välillä tiivistynyt.

Projektiin ulkomaiset asiantuntijat sekä tutkijavierailu helpottavat jatkossa ko laitosten kanssa tehtävää yhteistyötä.

Ultra-high Strength Wire Rods and Wires Based on Severe Plastic Deformation (SPD) and Ultrafine-grained (UFG) Microstructure

Leijun Li* and Jouko Virta

VTT Technical Research Centre of Finland

leijun.li@vtt.fi

September 2009

Abstract

A comprehensive review of recent literature on high strength, fine grained steels has been conducted. While all relevant technologies in alloy design, processing, and heat treating are included in this review, the emphasis has been on high-carbon steel wire processing technology that can be achieved with "conventional" wire rolling and drawing facilities. The thermomechanical processing for a pearlitic microstructure, followed by cold drawing is recommended as the process of choice to efficiently produce an ultrafine grained ferrite-cementite microstructure for ultrahigh-strength, ultrahigh-carbon steel wires.

---

*Visiting Professor from Utah State University, Logan, Utah, USA; leijun.li@usu.edu

Contents

1   Introduction

The Hall-Petch relation predicts the yield strength σ_y of an alloy to be inversely proportional to the square root of grain size d by the equation $\sigma_y = \sigma_i + k_y d^{-1/2}$, where σ_i is friction stress and k_y is grain boundary resistance of the alloy. It is believed that the Hall-Petch relation holds valid for grain sizes as small as 20 nanometers [Bhadeshia 2008]. Therefore, there exists an opportunity for creating ultrahigh-strength alloys by simply reducing the grain sizes. A dramatic gain in the alloy strength is thus possible without significantly changing the alloy chemistry. The potential of using ultrahigh-strength alloy in new designs, and the associated impact on materials and energy savings, have attracted great interest from a wide range of researchers to focus on developing new alloys and processes.

Conventional steels generally have grain sizes of above 10 μm in diameter. Ultrafine grained (UFG) steels generally have grain sizes smaller than a couple of micrometers (1 to 2 μm) in diameter. Such UFG steels can be classified as bulk nanostructured materials, which are formally defined as ultrafine grained materials, existing in bulk form, where the average grain sizes are less than 1 μm and the microstructures are fairly homogeneous with a majority of the boundaries having high angles of misorientation [Langdon 2007]. The term ultrafine "grained structure" should be differentiated from the term ultrafine "substructure". Only ultrafine grained structures may have high strength and ductility, while ultrafine substructures may have high strength but not high ductility. Superplastic behavior depends on rotations and deformation of fine grains having high angle grain boundaries [Humphreys et al. 2001, Furuhara et al. 2005a].

The UFG steels represent a result of the intensified effort over the past two decades on exploiting the Hall-Petch relation. Shown in Figure 1 are the recent activities in steel design and processing to increase the yield strength according to the Hall-Petch relation. Cold drawn, severely deformed carbon steel wire with UFG microstructure is reported to have achieved the highest tensile strength of 3000 - 4000 MPa [Hono et al. 2001]. Steel wire with a tensile strength of 6000 MPa is expected in the near future.

This report is based on a comprehensive review of the openly published recent literature on the science and technology of ultra-fine grained high strength steels. A recommendation for new alloy design and processing is made based on the review and interpretation of the collected literature. An electronic archive that includes all the referenced papers, listed alphabetically according to author's last name, is also available for downloading.

2   Two Approaches for Ultrafine Grained (UFG) Steels

To achieve ultrafine grained steels, two approaches are generally used. The first approach is collectively referred to as severe plastic deformation (SPD). The second approach is collectively
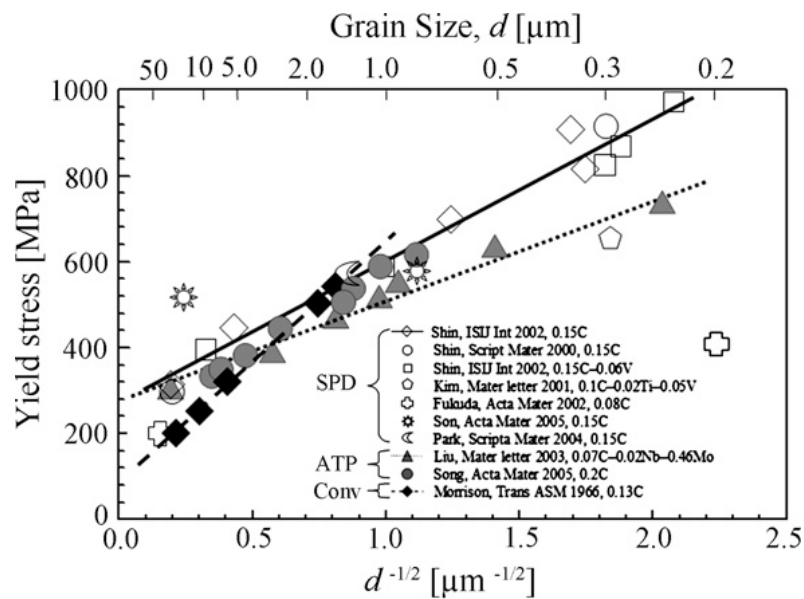
Figure 1: Hall-Petch relation in ultrafine grained BCC steels [Song et al. 2006]. The open symbols display the results from the severe plastic deformation methods; the full symbols in gray display the results from the advanced thermomechanical process methods; the full symbols in black display the results from the conventional deformation methods. The straight lines show the Hall-Petch relation for different steels.

referred to as advanced thermomechanical processing (ATP). SPD refers to deformation of a material to large accumulated plastic strains at room or warm temperatures that leads to a subdivision of the initial coarse grains into dislocation cell blocks and ultrafine grains with large-angle grain boundaries. There are many different variants of SPD, such as ball milling [Xu et al. 2002]. The few that have industrial potential includes equal channel angular extrusion, accumulative roll bonding, and high pressure torsion.

The advanced thermomechanical processing (ATP) approach for ultrafine grained steels exploits additional mechanisms for grain refinement. Besides plastic deformation, phase transformations from austenite to ferrite, dynamic recrystallization, or strain-induced ferritic transformation are involved during thermomechanical deformation and annealing. Conventional processes, including rolling, forging, drawing, and extrusion, are combined with controlled cooling and heat treatment to generate ultrafine grained steels. The greatest advantage of advanced thermomechanical processing is associated with the available conventional process facilities, and the continuous, up-scalable, manufacturing processes.

Depending on the chemical composition, a steel cooled from austenite temperature will transform into a combination of ferrite, pearlite, and martensite structures. The formation of new microstructure provides chances for grain refinement. Figure 2 shows schematically the three types of typical microstructure and the definitions of sizes of structural components. Superimposed with thermomechanical processing, the possible variations of microstructure and grain size control are numerous. Tsuji and Maki classified the procedural variations according
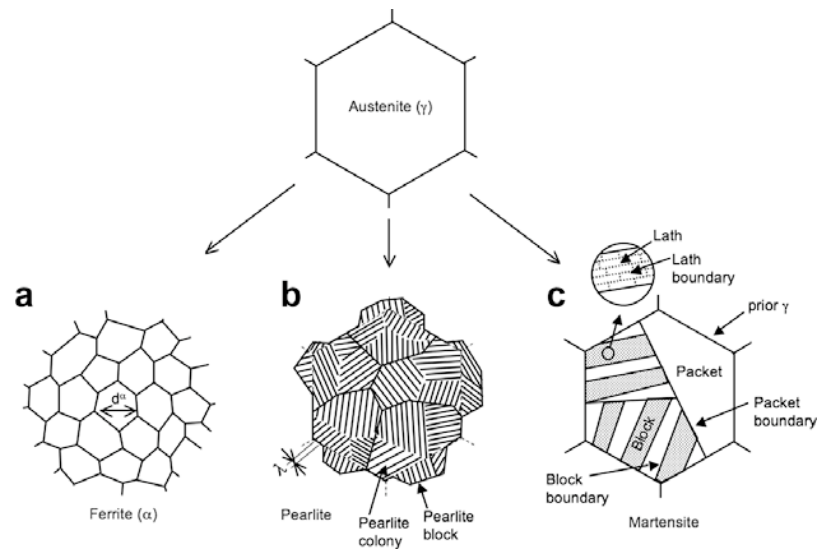
Figure 2: Schematic of austenite decomposition into typical microstructure on-cooling [Tsuji & Maki 2009].

to the sequences of phase transformation and plastic deformation (Figure 3) [Tsuji & Maki 2009]. With this classification, controlled hot rolling and ausforming can be seen as examples of Sequence i; most of the SPD methods, cold rolling, and wire-drawing can be seen as examples of Sequence ii; and repeated thermal cycling and multiaxial forging can be seen as examples of Sequence iii.
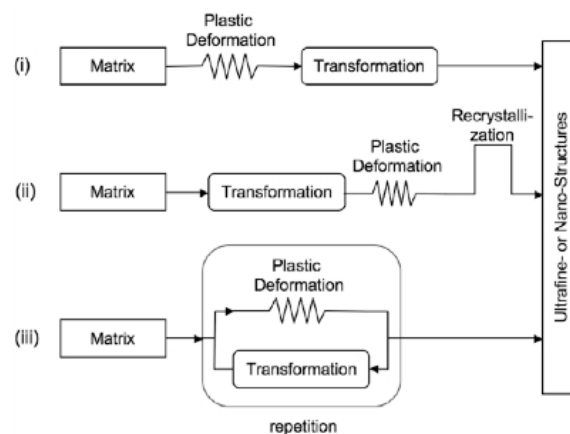
Figure 3: Three sequences combining phase transformation and plastic deformation for fabricating nanostructured metals. (i) Plastic deformation of the mother phase prior to phase transformation, (ii) Plastic deformation after phase transformation, (iii) Repetitive plastic deformation and phase transformation [Tsuji & Maki 2009].

2.1   SPD: Equal channel angular extrusion

Equal channel angular extrusion (ECAE), also known as equal channel angular pressing (ECAP), imposes large plastic strains on billets via pure shearing by pushing the billets through an angled channel of constant cross-section. A schematic of ECAE is shown in Figure 4a.
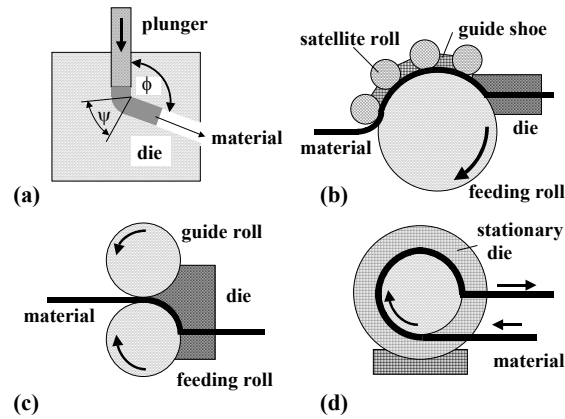
Figure 4: Schematic of equal-channel angular extrusion (ECAE) setup (a), conshearing process (b), continuous confined strip shearing (c), and ECAE-conform setup (d) [Verlinden 2005].

The equivalent plastic strain per pass depends on the angles ϕ and ψ:

$$\epsilon = \frac{1}{\sqrt{3}[2\cot(\psi/2 + \phi/2) + \psi\csc(\psi/2 + \phi/2)]}$$

For $\psi = 0$ and $\phi = 90°$, the equivalent strain ϵ is 1.55 per pass. With multiple passes, the total plastic strain applied to the billets can quickly be multiplied. Typically to obtain an ultrafine grained metal structure, the required equivalent strain ϵ is about 4-5, which requires three to four passes of ECAE. The limitations of ECAE method must be recognized. First, it has been mostly applied to non-ferrous alloys. Second, discontinuous billet feeding to ECAE has limited up-scaling capability. Third, only a portion of a billet (from 30 to 80%) is fully deformed as intended.

To overcome the limitations on the up-scaling of discontinuous billets, several variations of the original ECAE have been proposed (shown in Figures 4b, c, and d). A special feature of ECAE is that the cross section of the material remains constant during the processing. This feature makes it possible to apply high strains without causing failure in the materials.

2.2   SPD: Accumulative roll bonding

Repeated application of conventional rolling leads to a process referred to as the accumulative roll bonding (ARB) [Tsuji et al. 1999]. As the sheet gets thinner, it is cut and stacked to obtain

further reduction of thickness through rolling; at the same time, the stacked sheets are bonded together under deformation pressure through a solid-state bonding process (Figure 5).
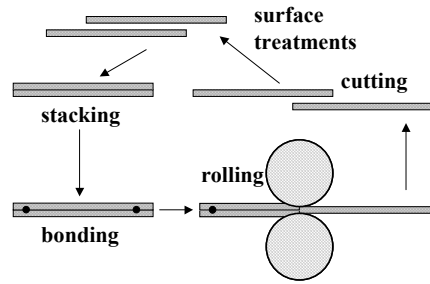
Figure 5: Schematic of accumulative roll bonding [Verlinden 2005].

The true plastic strain (or equivalent strain) defined for rolling is [Yanagimoto et al. 2009]

$$\epsilon = \frac{2}{\sqrt{3}} \ln(1 - r)$$

where r is the reduction of thickness. It was reported that conventional rolling and annealing of the microstructure processed with ϵ of 2-3 was found to achieve ultrafine grains in steels [Yanagimoto et al. 2009].

In the ARB process, de-greased and roughened sheets are stacked and rolled to an accumulative equivalent strain of approximately 4.0 at "warm" (i.e., about 500°C for steels and room to 200°C for aluminum and copper) temperatures. Unless used to decrease the rolling force, lubrication is usually not used. Friction between the rolls and the workpiece enhances shear strains and increases bonding of the sheets. After a couple of cutting and re-stacking sequences, the ARB processed sheet is homogeneous along the thickness direction [Lee et al. 2002, Li et al. 2006].

A typical ARB processed microstructure shows slightly elongated fine grains with the length to width ratio of about 2:1 (Figure 6). As the number of ARB cycles (or the effective plastic strain) increases, the average grain length in the rolling direction and grain width in the normal direction decrease. Typically 3 ARB cycles can produce ultrafine grain sizes with the width of the grains smaller than 1 μm.

2.3 SPD: High pressure torsion

In high pressure torsion (HPT) process, the disk-shaped samples are processed by torsional deformation under high pressure in an almost closed die. The shear strain applied during the processing generates significant refinement of substructures in the material (Figure 7).
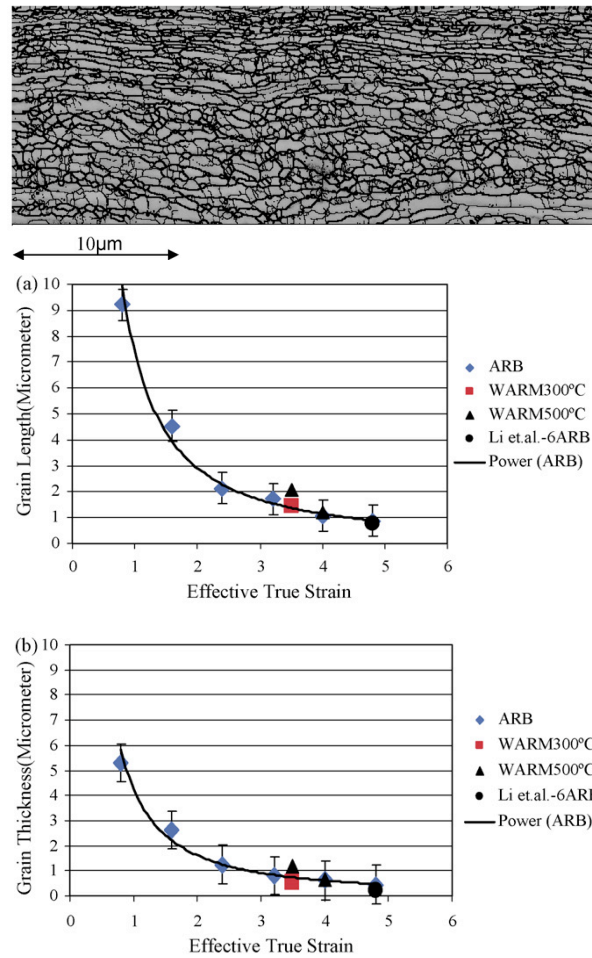
Figure 6: A typical EBSD microstructure in a low-carbon ferritic steel after 6 ARB cycles [Kolahi et al. 2009]. Curves represent effect of ARB cycles on the shape and sizes of ferrite.

In the classical torsion test, the torsional strain (γ) is defined by

$$\gamma = \frac{2\pi R N}{l}$$

where R is the distance from the axis, N is the number of rotations, and l is the sample length. The material close to the center would not be deformed as $R = 0$. However, numerous investigations have verified that after several rotations the HPT samples have uniform deformation across the diameter. This observation indicates the complexity of actual HPT vs. the classical torsion test [Yoon et al. 2008].

HPT is shown to produce ultrafine grained ferrite in low-carbon steels with the total equivalent strain of 1.5 [Kelly et al. 2002, Azevedo et al. 2005]. The strain-induced ferrite with low-angle boundaries during HPT is metastable and tends to coarsen during holding at the deformation temperature. With further deformation the ferrite refines to an ultrafine size with large-angle boundaries. The studies also outlined the use of martensite as a starting microstructure before the warm torsion to obtain ultrafine grained ferrite. An interesting observation in
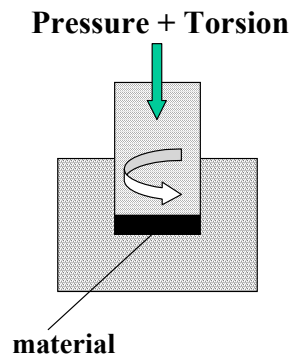
Figure 7: Schematic of high pressure torsion process [Verlinden 2005].

low-alloy steels of various chemical composition is the absence of a significant difference in the final microstructure, which indicates the predominant effect of the processing schedule and not a steel composition. The outstanding feature of HPT is that extremely refined (as small as 100 nm in diameter) grain sizes can be obtained.

2.4   ATP: Hot deformation and dynamic recrystallization

Recrystallization involves formation of new grains in a deformed alloy through grain boundary migration that is driven by the stored energy of deformation. The newly formed grains are "strain free", with high angle grain boundaries, thereby lowering the free energy of the alloy system. Discontinuous recrystallization occurs if a cold deformed alloy is heated in subsequent annealing to stimulate recrystallization. Dynamic recrystallization occurs if the deformation is applied at intermediate or high temperatures, when new grains form during the deformation. In steels, dynamic recrystallization of both austenite and ferrite can happen during, not after, hot deformation. The Zener-Hollomon parameter (Z) is usually used to describe dynamic recrystallization.

$$Z = \dot{\epsilon} \exp\left(\frac{Q}{RT}\right)$$

where $\dot{\epsilon}$ is the strain rate, T is the deformation temperature, Q is the activation energy, and R is the gas constant. Increasing Z produces smaller grain sizes following dynamic recrystallization. To increase the As Z parameter, the strain rate $\dot{\epsilon}$ needs to be increased and the temperature T needs to be decreased.

The dynamic recrystallization in aluminum alloys have been studied in great detail. To provide an understanding for the case of steels, the experimentally determined process window for producing an ultrafine grain structure in Al-2%Mg alloy is given in Figure 8. The smallest grains can be obtained through dynamic recrystallization in the temperature range between 200 and 400 °C and with a large strain rate. The Zener-Hollomon parameter for dynamic recrystallization imposes a limit (line A-B-C) that only to the right of this limit will there be
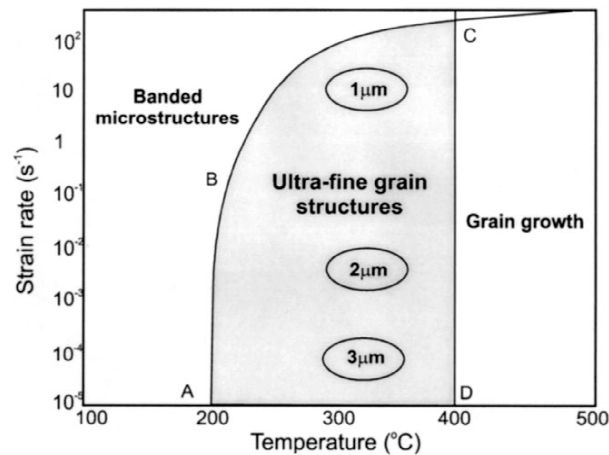
Figure 8: The process window for producing ultrafine grain structure in Al-2%Mg alloy by plane strain deformation to a strain of 3 [Humphreys et al. 2001].

a large enough Z for recrystallization. In addition, at higher temperatures, grain growth will happen because there are not enough second-phase particles to prevent grain growth (line C-D). Therefore, the process window that is able to give ultrafine grained microstructure is small.

To achieve grain refinement in steels, several factors will need to be controlled [Song et al. 2006]. First, the required driving force for dynamic recrystallization is provided by the hot deformation. Second, accelerated cooling rate through the transformation temperature zone is applied to suppress the phase transformation temperature for ferrite. A lowered transformation temperature will result in a greater number of ferrite grains with a slower growth rate. Third, alloying elements are added to the steel to increase the recrystallization temperature, such that deformation can be applied at below the recrystallization temperature to increase the sites for new grains. Alloying elements may also form fine precipitates that serve to restrict grain growth after deformation.

Hot deformation and dynamic recrystallization are reported to have achieved ferrite grain sizes of 2-5 μm through recrystallization-controlled rolling. Besides hot rolling, several hot deformation processes have also been used to provide the driving force for dynamic recrystallization. An interesting example is the multiaxial forging (Figure 9). Reported in [Valiev et al. 2000, Huang & Xu 2006], sub-micron grain sizes have been achieved in low-carbon steels with this method.

A hot deformation process referred to as "tempforming" has also been shown to produce ultrafine grained steels with exceptionally high impact toughness [Kimura et al. 2007]. A low-alloy, 0.57%-carbon, steel was hot rolled at 1473K to a squared bar with a cross-section area of 10 cm^2 and then solution treated at 1473K for 3.6 ks. The quenched bar was tempered at 773K for 5.4 ks and then multi-pass caliber-rolled to a square bar with a cross-section area of 2 cm^2, and air cooled. This process had an accumulative reduction in area of 80% in 10 passes,
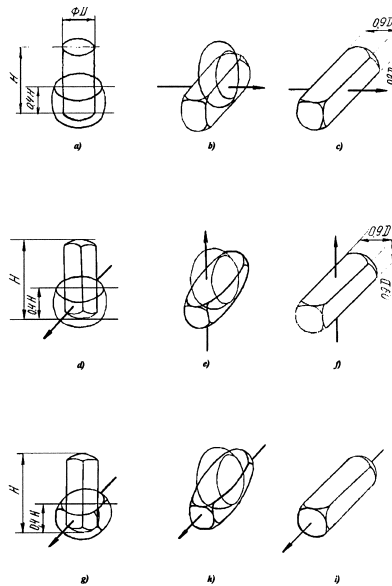
Figure 9: Schematic of multiaxial forging: setting and pull broaching along the first, second, and third axis [Valiev et al. 2000].

with an equivalent strain of 1.8. The sample was held in a furnace for 0.3 ks after every 3 passes during the rolling, and passed twice through the final groove to control the cross-sectional shape. With this process, the resulting microstructure is consisted of elongated fibrous ferrite with a transverse dimension of 0.33 μm, and fine cementite particles distributed homogeneously in the ferrite grains.

Severe plastic deformation of austenite is found to affect ferrite grain refinement during dynamic recrystallization [Suh et al. 2005]. In Figure 10, the ferrite grain size is shown to decrease as the compressive strain in the austenite increases. However, the ferrite grain size stabilizes after a certain level of strains in the austenite. The researchers believe the severe plastic deformation changes the grain boundary structures of the austenite which limits the further refinement of ferrite.

2.5   ATP: Cold rolling and annealing

Traditionally, cold rolling has been mostly limited to low-carbon mild steels. Since mid-1990s, Japanese researchers [Tsuji et al. 1992, Tsuji et al. 1993, Tsuji et al. 1994] have tested and developed a procedure to cold roll steels of martensite starting microstructure with 50% reduction. After a post-roll annealing, the final microstructure is reported to be ultrafine ferrite grains and uniformly distributed carbides [Tsuji et al. 2002]. Since the cold rolling uses a low plastic strain of 0.8, ultrafine grained microstructure is produced "without severe plastic deformation".
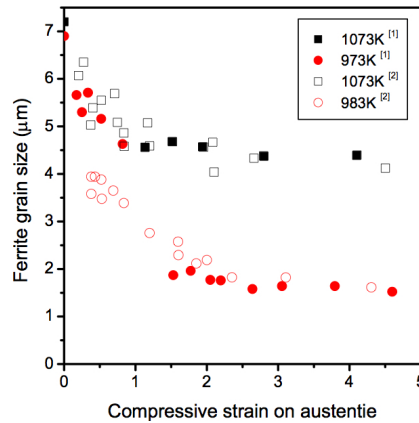
Figure 10: Changes of ferrite grain size according to the deformation of austenite at each deformation temperature. The initial grain size of austenite is 17 μm [Suh et al. 2005].

The capability to form ultrafine grained microstructure without severe plastic deformation is attributed to the characteristic martensite starting microstructure. For martensite starting microstructure, lamellar dislocation cells with 60 nm thickness form at a 50% cold roll reduction. These dislocation cells are similar to those obtained in SPD processed steels. Annealing of such cells gives ultrafine ferrite with mean grain size of 180 nm, nano-carbides, and fine tempered martensite blocks [Ueji et al. 2002, Nedjad et al. 2008]. It is believed the original fine grained, high dislocation density, structure of martensite contributes to the grain subdivision. Figure 11 shows TEM micrographs to outline the above sequence of transformation.
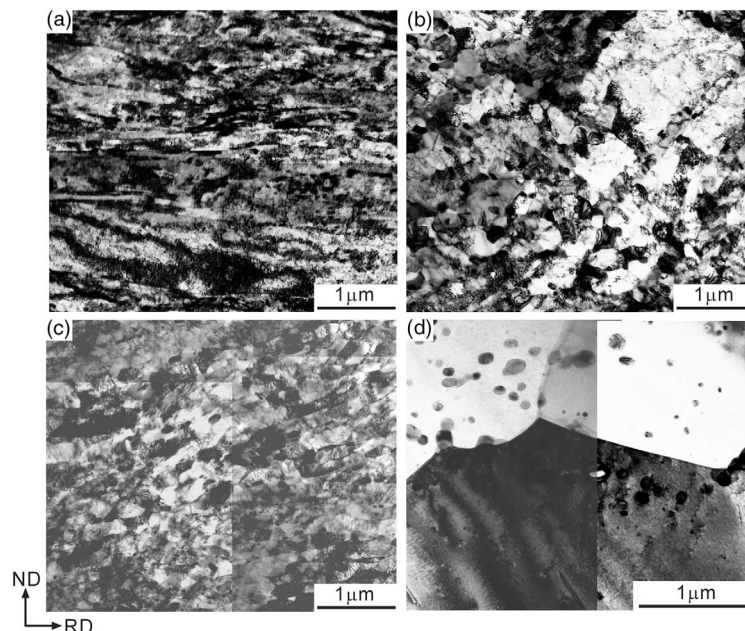
Figure 11: TEM micrographs of the 0.13%C steel 50% cold-rolled and subsequently annealed at 673K (a), 773K (b), 823K (c), and 873K (d) for 1.8 ks. The starting microstructure was martensite [Ueji et al. 2002]. Observed from transverse direction (TD).
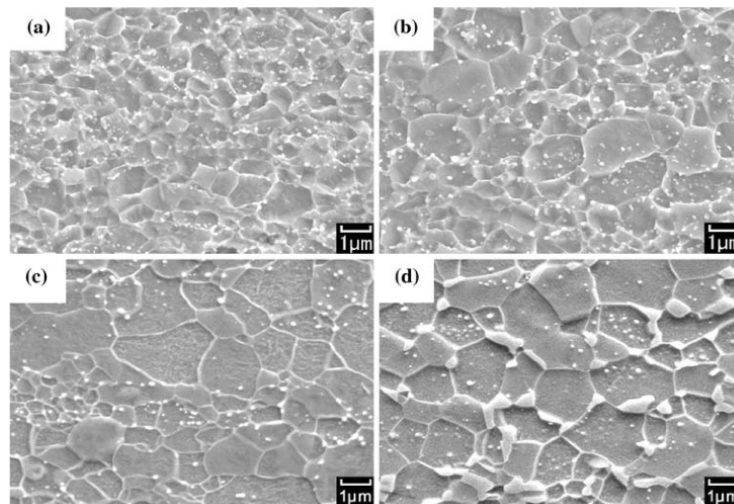
Figure 12: Effect of annealing temperature following rolling on grain size [Okitsu et al. 2008]. The low-carbon steel was cold-rolled by a 91% reduction, and annealed at (a) 620, (b) 635, (c) 655, and (d) 700 °C for 120 s and water cooled.

For ferrite starting microstructure in an interstitial-free (IF) steel, even small amount of cold rolling deformation results in the formation of cell blocks, with the extended planar dislocation boundaries forming the cell blocks lying at an angle of about 40° with the rolling direction (RD) [Li et al. 2004, Lan et al. 2007]. Increased plastic strain produces a lamellar structure with dislocation boundaries lying parallel to the rolling plane. Repeated shearing of these elongated cell blocks gives rise to ultrafine grained microstructure.

For a low carbon steel with a ferrite-martensite dual-phase structure, cold rolling and annealing treatment are reported to produce a bimodal grain size distribution [Azizi et al. 2007]. The difference in the recrystallization behavior of ferrite and martensite produces the distribution of coarse and fine grains. This type of microstructure provides opportunity to fine tune the balance of strength and uniform elongation in the ultrafine grained low carbon steel.

The microstructural evolution of steels upon annealing generally depends on the annealing temperature and the time held at the temperature. The effect of annealing temperature on the grain size of a cold-rolled low-carbon steel is shown in Figure 12. As the annealing temperature increases, larger ferrite grains and less number of cementite particles are seen in the microstructure. Recovery and recrystallization may occur depending on the temperature. The effect of time at annealing temperature on a warm-rolled low-carbon steel is shown in Figure 13. At a given anneal temperature, a longer hold time produces larger ferrite grains, and a greater degree of dissolution of cementite particles.
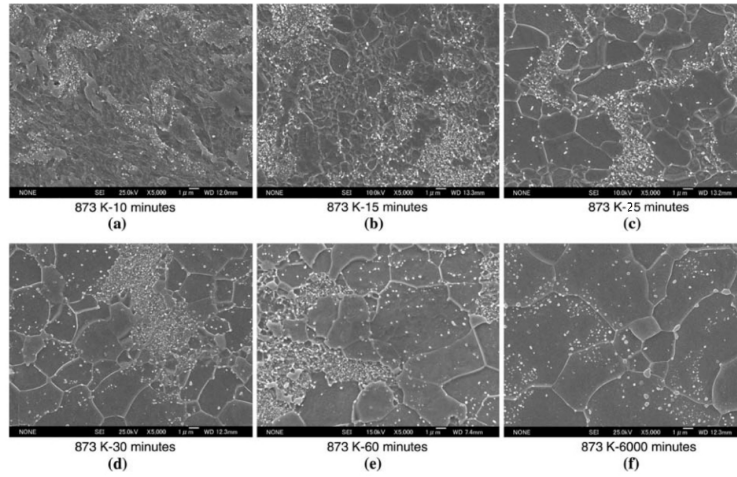
Figure 13: Effect of annealing time at 873 K for warm-rolled low-carbon steel [Zhao et al. 2008].

2.6 ATP: Extrusion and wire drawing

For extrusion or wire drawing, the extrusion or drawing ratio is defined as

$$\rho = \frac{A_1}{A_f} = \left(\frac{R_i}{R_f}\right)^2$$

where A_i is the initial cross-sectional area and A_f is the final cross-sectional area, and R_i and R_f are radii for round cross-sections. The equivalent plastic strain for extrusion and drawing is defined as [Yanagimoto et al. 2009]

$$\epsilon = \ln \rho = 2 \ln \frac{R_i}{R_f}$$

It has been found that wire drawing is able to produce ultrafine grained steels with an ϵ of 2.4.

Extrusion has the advantage that brittle materials can be processed without cracking defects, because the stress state during extrusion is always compressive. It also is capable of producing ultrafine grained microstructure with a single-pass deformation. For example, with an extrusion ratio of 11.6, a plastic strain of 2.5 is applied. That strain is corresponding to rolling with a 88% reduction ratio, which requires multiple rolling passes [Yanagimoto et al. 2009].

Figure 14 summarizes the common techniques to produce ultrafine grained steels and the ferrite grain sizes obtained. To obtain ultrafine grains using SPD methods, the accumulated plastic strains are required to be of the order of 3-4 for ECAP and be of the order of 5-6 for ARB process. To obtain ultrafine grains using ATP methods, the accumulated plastic strain is required to be of the order of 1-3.6. Compared with SPD methods, the ATP methods are generally less effective in producing ultrafine grains, but ATP methods are more adaptable to large scale production.

Techniques	Steels	Steels composition (wt.%)	Ferrite grain size achieved (μm)	Log. strain imposed [1]	Deformation temperature (K)	Heat treatment after deformation	Reference
ECAP	Plain low carbon steel	0.08C–0.42Mn–0.18Si	0.2	3.0	293	AC	[7]
	Plain low carbon steel	0.15C–1.1Mn–0.25Si	0.3 in thickness	4.0	623	AC	[22]
	Ti–V carbon steel	0.1C–1.59Mn–0.29Si–0.02Ti–0.05V	~0.3 in thickness	1.0	573	AC	[59]
	Ferrite–martensite dual phase steel	0.15C–1.06 Mn–0.25Si	0.8	4.0	773	1003 K × 10 min WQ	[46]
ARB	Ti added IF steel	0.003C–0.15Mn–<0.01Si–0.049Ti	0.4	5.6	773	WC	[14]
HPT	Plain low carbon steel	~0.7C–~1.0Mn–~0.3Si	0.01	Shear strain 300, log. strain 0.45	293	AC	[16,18]
DRX* during hot deformation	Microalloyed steel	0.11C–1.45Mn–0.34Si–0.068Nb	2–5	Final rolling 2.2–3.6	1153–1033	AC	[26]
Strain-induced ferrite transformation	Plain low carbon steel	0.06C–0.59Mn	1.0 (strip surface)	0.36	1053	AC	[27]
Deformation in the intercritical region	Plain low carbon steel	0.17C–1.32Mn–0.44Si–0.15Nb	2.1	2.3	973	WQ	[60]
Warm rolling in the ferrite region	Ti added IF steel	0.003C–0.15Mn–0.022Si–0.065Ti	1–3	Final rolling ~0.55 × 5	Below A_{r1}^*	WQ	[34]
DRX* of ferrite during warm deformation	Ultra-low carbon steel	0.0016C–0.1Si–0.3Mn	–	4.0	723–823 (lower than A_{c1}^*)	WQ	[36]
Pronounced recovery of ferrite during warm deformation and annealing	Plain medium carbon steel	0.22C–0.21Si–0.74Mn	1.3	1.6 at strain rate of 0.01 s^{-1}	823	823 K × 120 min	[39]
Cold deformation and annealing of martensitic steel	Martensitic steel	0.13C–0.37Mn–0.01Si	0.18	0.8	293	773 K × 30 min	[49]

Abbreviations: DRX*, dynamic recrystallization; A_{r1}^*, austenite to pearlite transformation temperature during cooling; A_{c1}^*, pearlite to austenite transformation temperature during heating; ECAP, equal channel angular pressing; ARB, accumulative roll bonding; HPT, high pressure torsion; AC, air cooling; WC, water cooling; WQ, water quench.

Figure 14: Summary of different techniques reported prior to 2006 to produce ultrafine grained steels [Song et al. 2006]. The reference numbers in the last column refer to those in [Song et al. 2006], not to this report.

3 Effect of Processing on Ultrafine Grained Microstructure and Properties

3.1 Effect of grain size and plastic strain on strength

Grain size effect on the yield strength was the original scope of the Hall-Petch relation. Numerous studies have produced results to confirm the Hall-Petch behavior. Figure 15 shows a typical set of results for low carbon steels in the as-rolled or annealed state. A roughly linear relationship exists between the inverse square root of the grain size and the yield strength for the grain size down to 0.5μm. At grain sizes close to 0.5μm (right end of the line), there seems to be a slight deviation of strength value from the straight line. This deviation has been the focus of many recent studies, although a commonly accepted explanation has not been provided. One popular theory is based on dislocation pile-up behavior [Song et al. 2006], in which the slope of the line is treated as a function of number of dislocations. As grain sizes decrease to lower than 0.79μm, the number of dislocations drops to below 20. The pile-up behavior for smaller number of dislocations is significantly different from large number of dislocations. Figure 16 shows the result of the above analysis.

3.2 Ductility and strain hardening

Conventional grain refinement of steels results in improved ductility (Figure 17), although the reported data tend to scatter over a wide range. Further reduction of grain sizes to below 1μm, however, consistently results in a significant decrease in ductility. The total elongation during
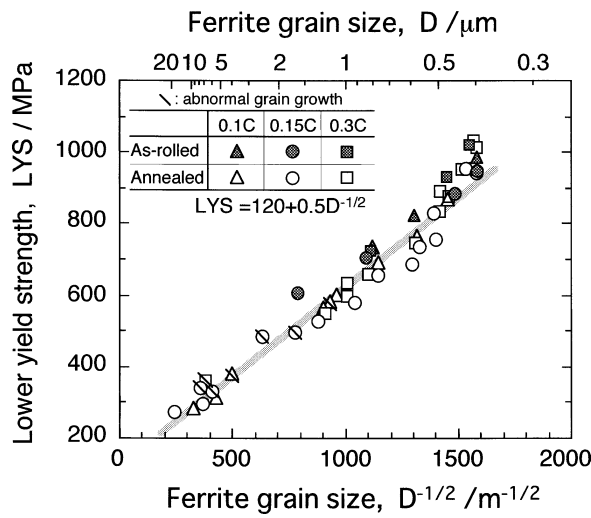
Figure 15: Relationship between ferrite grain size and lower yield point of low-carbon steels [Ohmori et al. 2004].
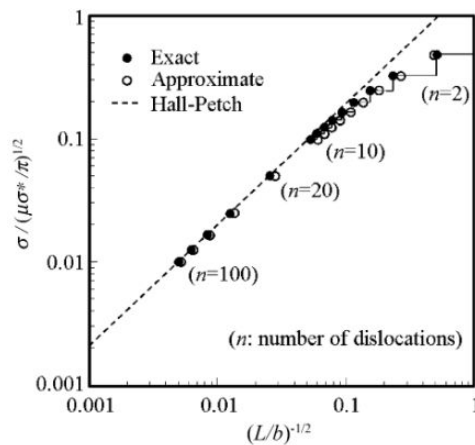
Figure 16: Effect of grain size and number of dislocations. L is the length of pile up (grain size), b is the magnitude of Burger's vector, σ is the applied stress, σ^* is the constant barrier stress, and μ is the shear modulus [Song et al. 2006].
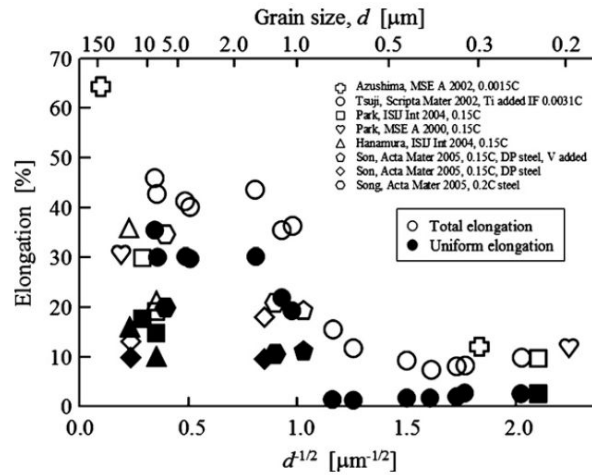
Figure 17: Effect of grain size on ductility for low-carbon steels [Song et al. 2006]. Open symbols represent total elongation (including elongation after necking); filled symbols represent uniform elongation in tension.
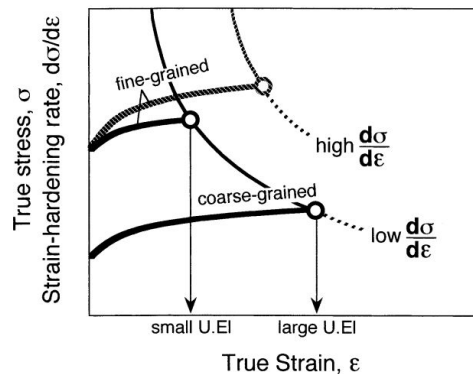
Figure 18: Schematic illustration of the uniform elongation (U. El) as influenced by the grain size and strain hardening rate [Ohmori et al. 2004].

tensile tests for ultrafine grained steels is approximately 10%. But the uniform elongation during tension drops to almost zero. This behavior indicates the loss of work (strain) hardening capability for ultrafine grained steels, with the yield strength becoming very close to the tensile strength.

The uniform elongation is a measurement of plasticity before the plastic instability (i.e., necking) starts during tension. The instability condition in tension is expressed by $\sigma > d\sigma/d\epsilon$, where σ is the flow stress and ϵ is the true strain. Since the flow stress σ increases with smaller grain sizes, the strain hardening rate $d\sigma/d\epsilon$ needs to increase accordingly to maintain a large uniform elongation (Figure 18).

It is believed that strain hardening requires dislocation multiplication and interactions. For ultrafine grained steels, the dislocation multiplication fails because the proximity of the closely spaced boundaries [Bhadeshia 2008]. This explanation is consistent with the dislocation "pile

up" theory for the ultrafine grained Hall-Petch behavior outlined in the previous section.

To compensate for the loss of ductility, several theories and practices have been put forward [Nishida et al. 1998, Ma 2006, Delince et al. 2007]. Among them, more feasible and popular methods are introduced here. Bhadeshia suggests introducing retained austenite into the microstructure. The argument is based on the belief that the stress- or strain-induced martensitic transformation of the retained austenite enhances the work-hardening coefficient. A volume of 10% retained austenite has been estimated to deliver such an effect [Bhadeshia 2008]. Using a similar logic, steels with a "bimodal" grain distribution are developed to obtain high strength by the fine grains and obtain high ductility from the coarser grains [Zhao et al. 2006, Zhao et al. 2007, Zhao et al. 2008, Wang et al. 2008]. The bimodal microstructure has demonstrated to have a good combination of strength and ductility.
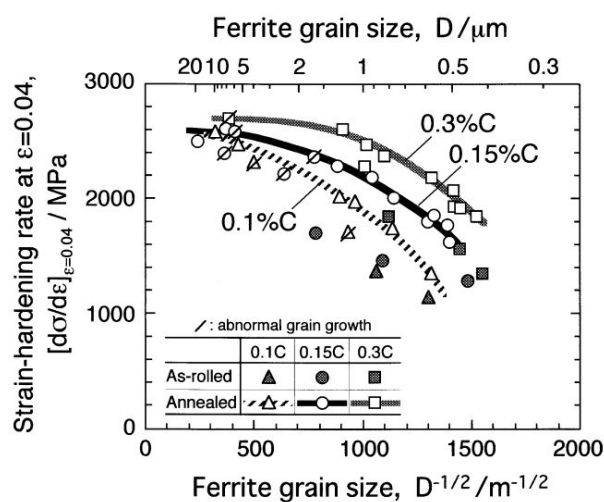
Figure 19: Effect of carbon content, thermomechanical treatment, and grain size on strain hardening rate at a strain of $\epsilon = 0.04$ [Ohmori et al. 2004].

Other researchers [Ohmori et al. 2004, Park et al. 2004, Song et al. 2005] suggest a solution with dispersed cementite or carbide for low carbon steels. The so-called "strain hardening design" is based on a theory that the strain hardening rate depends on the dispersion of hard second-phase particles and is proportional to a dispersion parameter $(f/d)^{1/2}$, where f is the volume fraction of the second-phase particles, and d is the mean diameter of the particles. Since the amount of particles is mostly determined by the carbon and alloy content, and the distribution of particles is mostly determined by the thermomechanical treatment, a technical solution based on this theory is readily achievable with alloy and process design. As shown in Figure 19, increasing the carbon content does have a positive effect on improving the strain hardening rate. Further, for the same carbon content, an annealed structure has a significantly higher strain hardening rate than that of the as-rolled structure.

Choo and Bae propose to use small additions of boron (B) in medium-carbon steels to increase ductility [Choo & Bae 2002]. Their results show that B increases the strain hardening

rate by reducing the amount of proeutectoid ferrite and stabilizing the carbide in the steel.

3.3   Effect of pearlitic lamella spacing and carbide particle size

Heavily cold-drawn pearlitic steels are currently the strongest steels in use. The pearlite derives its strength from a laminar, composite, structure of ductile ferrite and strong cementite. The interlamellar spacing of pearlite, which is dependent on the transformation temperature and carbon content, has been observed to affect pearlite strength. Figure 20 shows typical relations between the transformation temperature, interlamellar spacing, and hardness (strength) of pearlite. A linear increase of interlamellar spacing as a function of transformation temperature is observed in steels with various carbon and alloy contents. A higher carbon content generally results in a linearly finer pearlite interlamellar spacing, although the alloying elements may also change the slopes of the lines. Finer pearlite interlamellar spacings clearly lead to stronger steels as shown in Figure 20b. Additional data on carbon content, lamellar spacing, and tensile strength are shown in Figure 21. As carbon content increases from 0.2% to 1.2%, the lamellar spacing decreases almost linearly. Tensile strength of the steels increases linearly as the lamellar spacing is decreased.
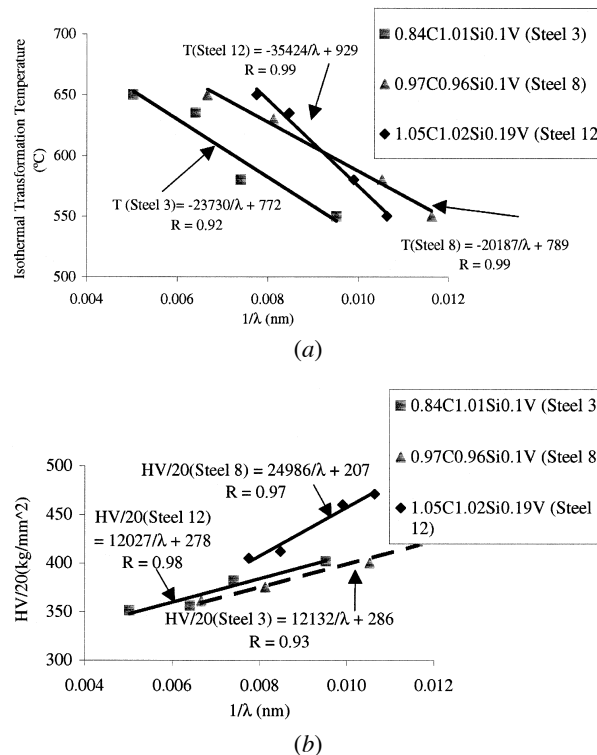
Figure 20: Heat treatment and microstructure on hardness of three steels that were austenitized at 1050 C for 10 min before isothermal transformation at various temperatures for 3 min. (a) isothermal transformation temperature vs. reciprocal interlamellar spacing, (b) hardness vs. reciprocal interlamellar spacing [Han et al. 2001].
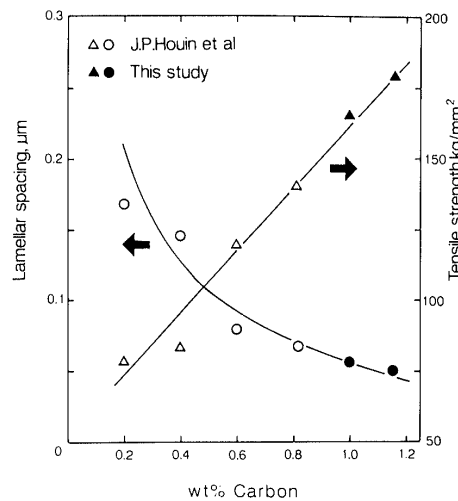
Figure 21: Effect of carbon content on pearlite interlamellar spacing and tensile strength of steels [Kanetsuki et al. 1991].

The yield strength of several pearlite-containing steels as a function of pearlite interlamellar spacing is shown in Figure 22. As can be seen, the slope of the line for hyper-eutectoid steels (with carbon content higher than 0.8%) is the same as the eutectoid steel (with 0.8% C), indicating the strengthening effect of pearlite. The distance between the two lines, however, can be attributed to the strengthening effect of the pro-eutectoid cementite.
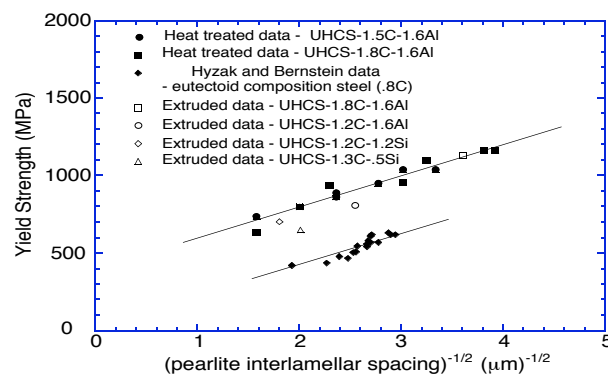
Figure 22: Effect of pearlite interlamellar spacing on the yield strength of several ultrahigh carbon steels. The data for eutectoid steel are included for comparison [Lesuer et al. 1997].

Cold deformation decreases the interlamellar spacing of pearlite, besides inducing microstructure changes such as nanocrystallization of cementite, dissolution of cementite into ferrite, and formation of nano-ferrite. Direct observation of deformed pearlite confirmed that the plastic deformation fractures the continuous cementite lamellae into fragments [Vedani et al. 2006]. A dramatic example is shown in Figure 23, in which lamellar cementite has been reduced to fine particles after severe torsional straining at room temperature.

The effect of cold deformation and annealing on pearlite strength and ductility is shown in
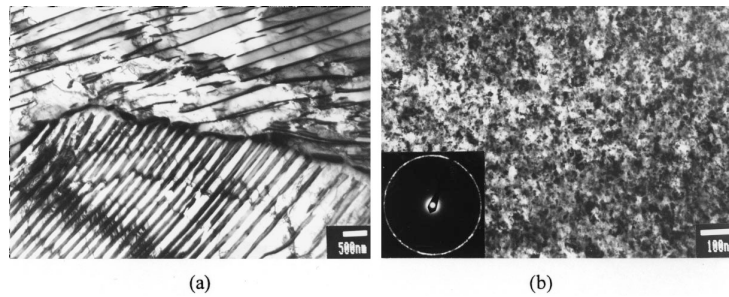
Figure 23: Structure of an ultrahigh-carbon (1.8%C) steel in the initial normalized state (a), and after severe torsion straining at room temperature [Valiev et al. 2000].

Figure 24 as a typical example. Cold rolling significantly increases the strength and decreases the ductility of pearlite. Annealing can restore the ductility while retaining some strengthening effect. During annealing, fine grained ferrite and cementite form with sizes less than 1μm.
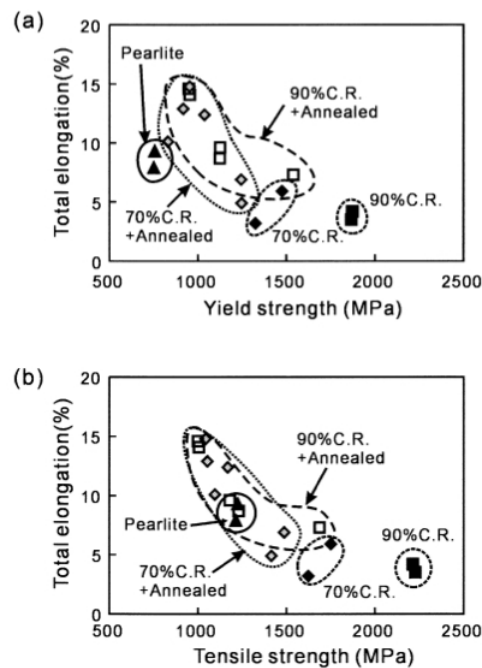
Figure 24: The effect of cold rolling and annealing on pearlite yield strength and ductility (a), and tensile strength and ductility (b). The as-transformed pearlite properties are indicated by solid triangular symbols [Furuhara et al. 2005].

It has been observed that the size and distribution of ferrite and cementite upon annealing are not uniform for a given piece of pearlitic steel [Furuhara et al. 2005, Furuhara et al. 2005a]. Furuhara et al. classified the deformed pearlite into three types: the irregular bend lamella (IBL), fine lamella (FL), and coarse lamella with shear band (CLS), as shown in Figure 25. Pearlite tends to deform into IBL at a lower degree of deformation, but with greater cold rolling deformation, more pearlite turns into fine lamella (FL). Therefore, greater degree of deformation results in a more uniform pearlitic structure.
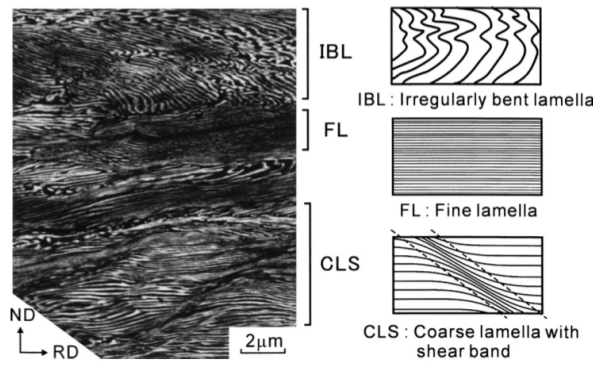
Figure 25: Observed deformation patterns in pearlite and their classification [Furuhara et al. 2005].

Upon annealing, however, most cementite lamella transform into particles, and the ferrite lamella transform into fine grains. As schematically shown in Figure 26, the fine lamella pearlite region tends to form ferrite with low-angle boundaries; while IBL region tends to form ferrite with high-angle boundaries. Through the control of time and temperature, a wide range of strength-ductility for the steels can be achieved.
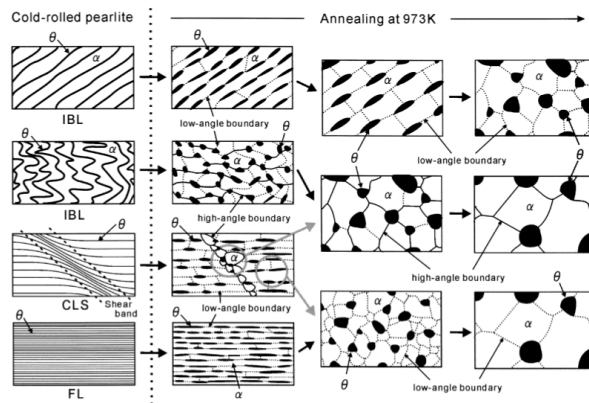
Figure 26: A proposed mechanism for deformed pearlite transformation during annealing at 973K [Furuhara et al. 2005].

Carbides in steels exist as pre-eutectoid cementite, lamellar cementite in pearlite, or precipitates as solubility changes with temperature. As for the case of ferritic grains, the carbide particle size also has a Hall-Petch type relationship with strength. Figure 27 compiles the fracture strength data as a function of average carbide particle size from several independent studies on hypereutectoid steels. The extrapolated fracture strength for steels with ultrafine carbide size of 0.017 μm is 5000 MPa.
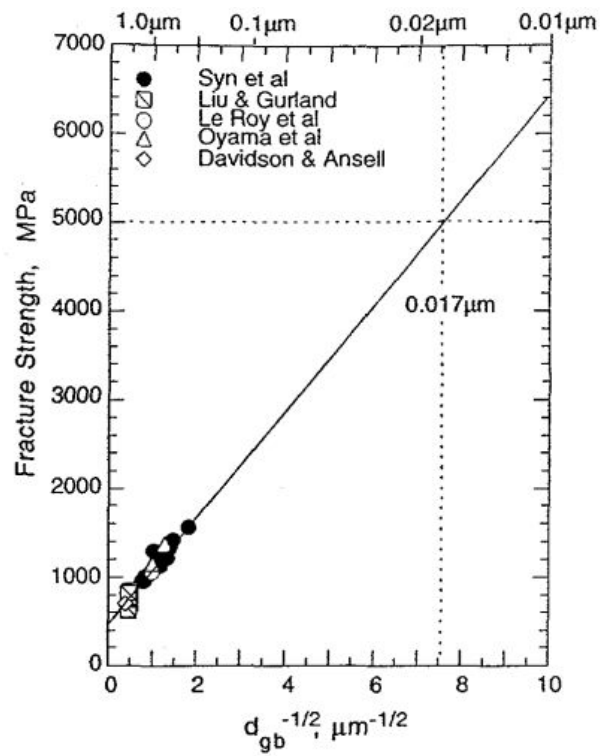
Figure 27: Fracture strength of spheroidized hypereutectoid steels as a function of average carbide size [Lesuer et al. 1996]. Extrapolation of data predicts high fracture strength at ultrafine carbide sizes.

3.4   Fracture and fatigue of UFG steels

For conventionally processed low carbon steels with ferrite grain sizes greater than 10 μm, Pickering's classical work indicated that the ductile-to-brittle transition temperature (DBTT) is a function of strengthening mechanism [Hanamura et al. 2004]. For a yield strength increase of 9.8 MPa, if the strengthening is by dislocation, the DBTT will increase by 6K; if by dispersion strengthening, the DBTT will increase by 4K; if by grain-size refinement, however, the DBTT will decrease by 10K. The effect of grain size on DBTT is characterized by Hall-Petch style formula:

$$DBTT = A - Kd^{-1/2}$$

and

$$DBTT = A - K \ln d^{-1/2}$$

where constants A and K depend on metallurgical factors other than the grain size, and d is grain size. With these relationships, it is expected that ultrafine grained steels would have improved impact toughness.

The reported impact toughness data from ultrafine grained steels are still limited, partly due to the difficulty in obtaining large enough specimens from the laboratory-scale SPD processed samples. Figure 28 shows a set of recent results, comparing the DBTT of two steels with ferrite sizes of 6.8 and 1.3 μm, respectively. The upper shelf energy of the ultrafine grained steel is lower, and the transition region occurs over a wider range of temperature, compared with the coarser grained steel. The DBTT for the ultrafine grained steel is lower than the coarser grained steel. A detailed explanation of the DBTT curves is provided in references [Song et al. 2005c, Song et al. 2006].
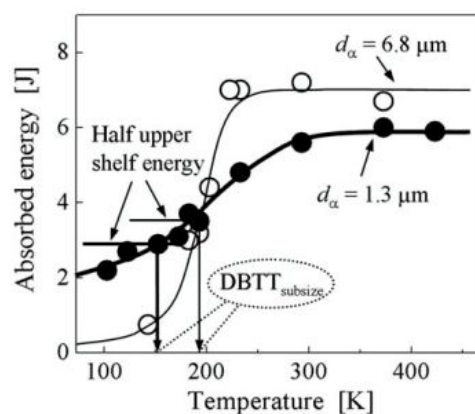
Figure 28: Effect of test temperature on Charpy impact energy of two steels with different ferrite grain sizes [Song et al. 2005c]. The symbol d_α indicates the average ferrite grain diameter. $DBTT_{subsize}$ refers to ductile-to-brittle transition temperature measured with subsized specimen (ligament size of $3 \times 4 \ mm^2$).

The DBTT results reported by Hanamura et al. also confirm that a low-carbon steel with ultrafine grained ferrite/cementite microstructure has a much lower DBTT than that of the conventional ferrite/pearlite, quench/tempered, or quenched microstructure [Hanamura et al. 2004]. Unlike Song et al's results, Hanamura et al's results show the upper shelf energy of the ultrafine grained microstructure is as high as that of the coarser grained ferrite/pearlite microstructure for the same steel (Figure 29).
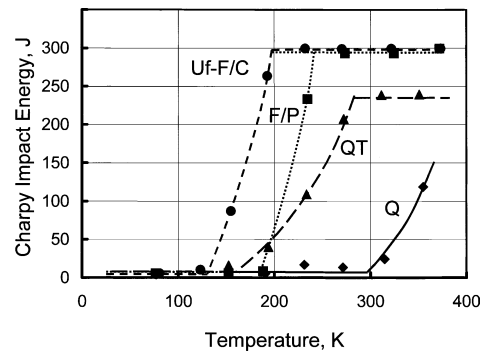
Figure 29: Charpy impact energy as a function of test temperature for ferrite/pearlite (F/P), ultrafine ferrite/cementite (Uf-F/C), as quenched (Q), and quench and tempered (Q/T) steels [Hanamura et al. 2004].

The effective grain size (d_{eff}) is a useful measurement to characterize the effect of grain size on impact toughness. Instead of using the directly measured grain size, Hanamura et al. have proposed to use the effective grain size as the variable to measure the impact toughness. The d_{eff} is defined as the unit crack path in which a cleavage crack goes through in a straight fashion to form a facet, corresponding to the microstructural unit having a specific crystallographic orientation and bounded by large-angle grain boundaries. The d_{eff} can be experimentally measured from the fractography. Using the d_{eff} concept, the four types of microstructure are ranked as $d_{eff} = 8$ μm for the ultrafine grained ferrite/cementite (Uf-F/C) microstructure, 20 μm for the ferrite/pearlite (F/P) microstructure, 25 μm for the quenched and tempered (Q/T) microstructure, and 100 μm for the as-quenched (Q) microstructure. This ranking is the same as the DBTT ranking, with smaller d_{eff} having a lower DBTT. Further, it is found that the d_{eff} number is determined by the ferrite grain size for F/P, by the prior austenite grain size for Q, by the martensite packet size for Q/T, and by the ferrite grain size for Uf-F/C microstructure. With such knowledge, the impact toughness can be tailored by the microstructure design.

Statistically, the impact toughness for low-alloy steels follows an inverse trend against the yield strength, as shown in Figure 30, in which the shaded region on the left side of figure indicates the data distribution. Conventional quench and tempering (QT) can significantly increase the yield strength, but greatly decreases the impact energy. Ultrafine grained steels, as processed with the "tempforming" (TF) process, however, can have 16 times higher impact toughness than the conventional quench and tempered steel.
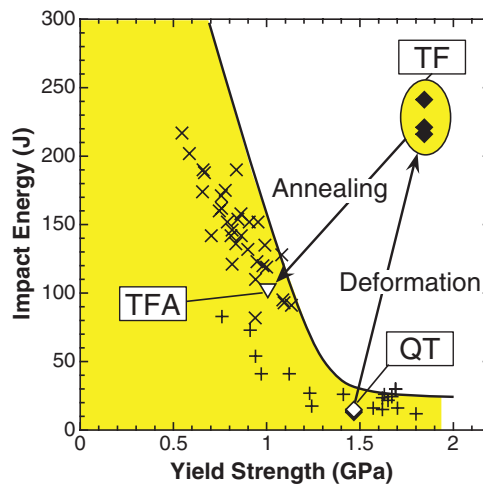
Figure 30: Charpy V-notch impact energy absorption of the low-alloy steel as a function of yield strength at room temperature [Kimura et al. 2008]. The steel that was "tempformed" at 500°C (TF) shows large impact energy as compared to that of the steel that was conventionally quenched and tempered (QT), also at 500°C. Annealing of TF steel at 700°C degraded the impact energy to conventionally processed steels.

The extremely high impact toughness for this "tempformed" steel is owing to the ultrafine, elongated, fibrous ferrite grains with <110> crystalline orientation along the rolling direction, interspersed with nanometer-sized carbides. With such a microstructure, the fractured specimens showed fibrous delamination that is thought to relax the triaxial stress conditions ahead of the advancing crack tip, thus leading to high impact energy [Kimura et al. 2008].

Similar to impact toughness, the fracture toughness of ultrafine grained steels are shown to improve with grain refinement. Figure 31 shows some fracture toughness data for a low-alloyed 1.3%C ultrahigh-carbon steel tested using the chevron-notched specimens. As the prior austenite grain size is decreased to below 25 μm, the fracture toughness increases significantly. There are insufficient data, however, on the fracture toughness of fully pearlitic steels using fatigue pre-
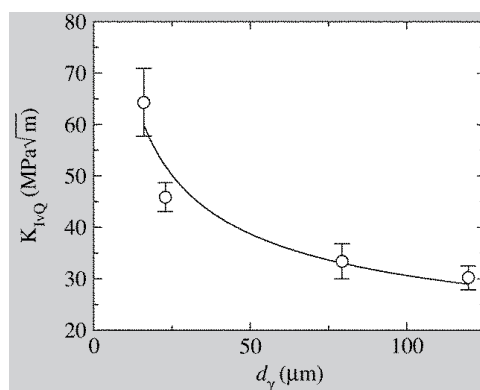
Figure 31: The fracture toughness of an ultrahigh-carbon steel containing 1.3 C, 0.5 Mn, 0.51 Mn and 0.22 Cr (wt.%) is shown as a function of prior austenite grain size [Taleff et al. 2002].

cracked specimens. Preliminary tests using fatigue pre-cracked specimens with sharp crack-tips seem to indicate the opposite trend – that more plastic deformation (thus smaller prior austenite grain sizes) decreases the fracture toughness [Taleff et al. 2002], as quoted below.

> A eutectoid steel (0.78 wt.%C) wire with a 1.83 mm diameter, a tensile strength of 2206 MPa, and a yield strength of 1792 MPa produced a fracture toughness of 64 MPa$\sqrt{m}$. A similar eutectoid steel (0.79 wt.%C) drawn to a diameter of 0.965 mm produced a tensile strength of 2280 MPa and a yield strength of 1996 MPa, but had a fracture toughness of 56 MPa$\sqrt{m}$. This indicates a reduction in fracture toughness with increasing yield strength from added drawing reduction. A hypereutectoid steel (1.02 wt.%C) drawn to the same diameter, 0.965 mm, achieved a tensile strength of 2767 MPa and a yield strength of 2478 MPa. The fracture toughness of the hypereutectoid steel was measured to be 51 MPa$\sqrt{m}$. These data indicate a gain in yield strength of approximately 26 MPa for every 1 MPa$\sqrt{m}$ lost in fracture toughness during drawing of eutectoid steel wire. This is compared with a gain in yield strength of 96 MPa for a 1 MPa$\sqrt{m}$ loss in fracture toughness from increasing carbon content beyond the eutectoid level.

Based on the fracture toughness results, it has been recommended that increasing carbon content is a better means for increasing the wire strength than is increasing drawing reduction.
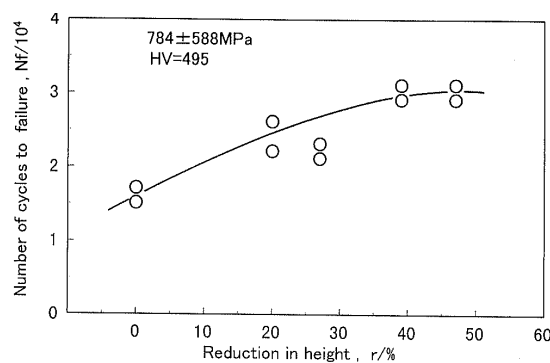
Figure 32: Number of cycles to failure vs. reduction in height for a medium-carbon spring steel [Ayada et al. 1998].

Reported fatigue properties as influenced by grain sizes are inconsistent. Ayada et al. identifies the positive effect of increasing the reduction ratio (i.e., decreasing the grain size) on the fatigue life of a medium-carbon steel (Figure 32). Other studies [Furuya et al. 2007] also confirmed that the ultrafine grained ferrite-cementite microstructure has higher fatigue limits than that of the conventional ferrite-pearlite microstructure (Figure 33). For ultrahigh-carbon steels, however, the very limited data (Figure 34) on fatigue of ultrafine grained microstructure indicate some opposite trends: compared with the 0.82% C steel, the 1.02% C steel has a lower

endurance limit; for the same carbon content, a slight increase of drawing strain from 4.12 to 4.32 significantly lowers the fatigue life for both steels, with the 1.02% C steel showing more reduction in fatigue life.
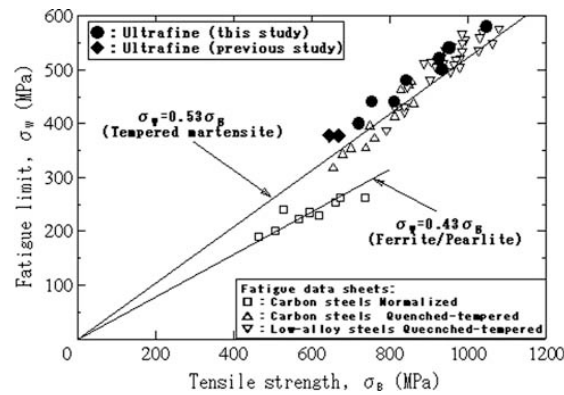
Figure 33: Fatigue limits of the ultrafine ferrite-cementite steels plotted against tensile strength, together with other reported results [Furuya et al. 2007].
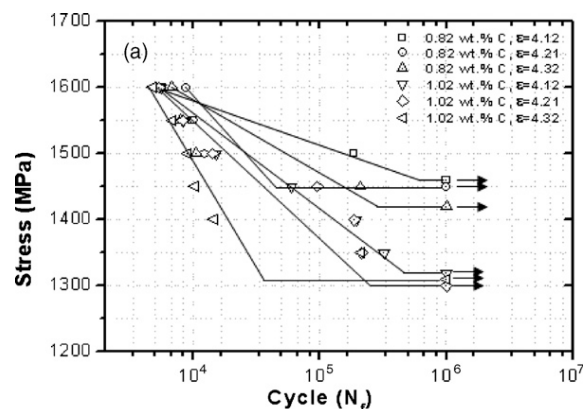
Figure 34: S-N curves of steel wires with two carbon contents tested using a Hunter-type rotating beam fatigue tester under a bending stress [Yang et al. 2009].

Assuming both sets of fatigue data are valid, then there should be a carbon content below which grain refinement improves the fatigue properties, and above which grain refinement deteriorates the fatigue properties. Based on the carbon-contents of the test steels, that deflection point seems to be the eutectoid (0.77% C) concentration. A study of fatigue properties that involves steels with carbon contents from medium to ultrahigh levels that bracket the assumed deflection point of 0.77% C is needed to prove or disprove this hypothesis.

In an attempt to characterize the thermal stability of fatigue behavior of ultrafine grained steel, Niendorf et al. tested an equal channel angular extruded interstitial-free steel at different homologous temperatures [Niendorf et al. 2009]. The steel shows significant shortened fatigue life when the temperature exceeds 200°C (or 0.26 homologous temperature), due to localized

grain growth. Therefore, the thermal stability of ultrafine grained steels will need further studies should the steels be put in a higher temperature environment.

3.5 Effect of alloying elements

3.5.1 Effect of carbon and boron

For steels, the most important alloying element is carbon, to the extent that steels are classified based on the carbon content. As for the low-carbon steels, there is a linear relation between the carbon content and the tensile strength for high-carbon cold drawn wire steels (Figure 35). Projected ultrahigh-carbon steel wires with 1.8%C can have the strength close to 6000 MPa.
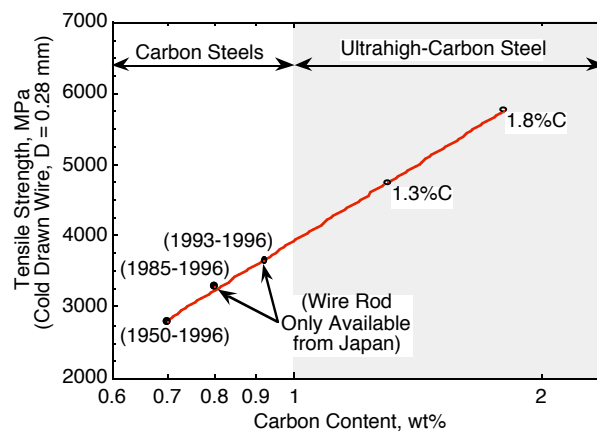
Figure 35: Effect of carbon content on the strength of cold drawn steel wire. The projected strength for ultrahigh carbon steels containing 1.3 and 1.8% C are shown by the open circle symbols [Lesuer et al. 1997].

The strengthening effect of carbon in steels stems from the increased amount of cementite, decreased interlamellar spacing in the pearlite, and refined grain sizes [Furuya et al. 2005]. For quenched steels, a higher carbon content also increases the hardenability of the steels by increasing the amount and hardness of martensite. During thermomechanical processing, the dynamic recrystallization in steels is also dependent on the carbon content. Figure 36 clearly shows that the higher carbon containing steels have finer grain sizes after undergoing the same deformation process. As the carbon content of the steels increases, the degree of recrystallization is higher, and the recrystallized ferrite grain sizes are smaller. It is believed that higher carbon has decreased the lath martensite width and increased the fraction of cementite, which suppresses the growth of recrystallized ferrite grains [Poorganji et al. 2008].

While the equilibrium amount of cementite in steels is governed by the carbon content, the actual amount of cementite in continuously cooled steels is also affected by the cooling rate. For hypereutectoid steels, the grain boundary networked cementite significantly decreases the ductility, thus deteriorates drawability of wires. Therefore, network carbide on the grain
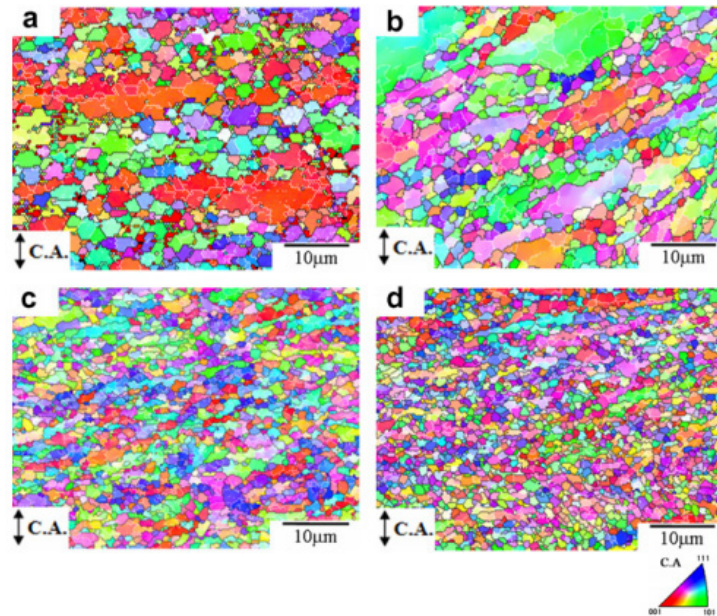
Figure 36: Orientation map of (a) 0.1, (b) 0.2, (c) 0.35, and (d) 0.8 C alloys deformed at 923K and a strain rate of $10^{-3}s^{-1}$. Black and white lines represent high and low angle boundaries, respectively [Poorganji et al. 2008].

boundaries should be avoided. Controlling the cooling rate provides an effective way to obtain pearlite structure for hypereutectoid steels. In Figure 37, it is shown that for a given carbon content, increasing the cooling rate can change the pearlite plus proeutectoid carbide structure into pure pearlite structure. Lesuer et al. believe that "hypereutectoid steels with carbon content up to 1.10% could be 'patented' to obtain a network-free microstructure using commercially-available cooling equipment which can achieve cooling rates of 10-15°C/s" [Lesuer et al. 1997]. *Patenting* is a special heat treatment for medium carbon, high carbon and alloy steel wire rod, in which a fully austenitized steel is quenched in a bath maintained at a constant temperature in the vicinity of the nose of the TTT curve for the given steel. This treatment results in transformation of austenite to pearlite with fine interlamellar spacings that provides heavier drafting during wire drawing.

Boron (B) is an interstitial solid-solution strengthener and forms borides in steels. Boron can substitute for carbon in cementite by up to 80 atomic percent to form boron-cementite, which is more stable than cementite in plain carbon steels. A small amount of B is known to reduce the volume fraction of proeutectoid ferrite, especially when the carbon content of the steel is low. It has the effect of accelerating the transformation rate of austenite to pearlite. So the basic behavior of B in steels is similar to that of C, in that it promotes pearlite formation and carbide stability [Choo & Bae 2002, Saha & Ray 2007].

To eliminate the slow, costly patenting heat treatment in wire drawing, Choo and Bae used small addition of B (0.0013 to 0.0022 wt.%) to a medium-carbon steel. It is shown B is able to
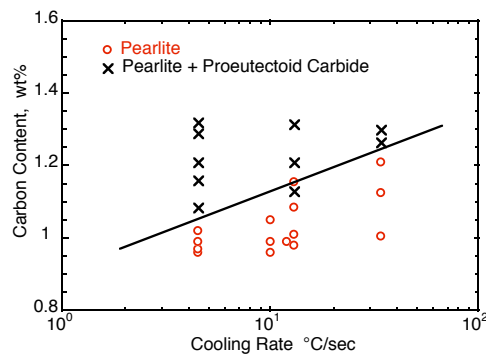
Figure 37: Effect of cooling rate on the formation of a proeutectoid carbide network in hypereutectoid steels [Lesuer et al. 1997].
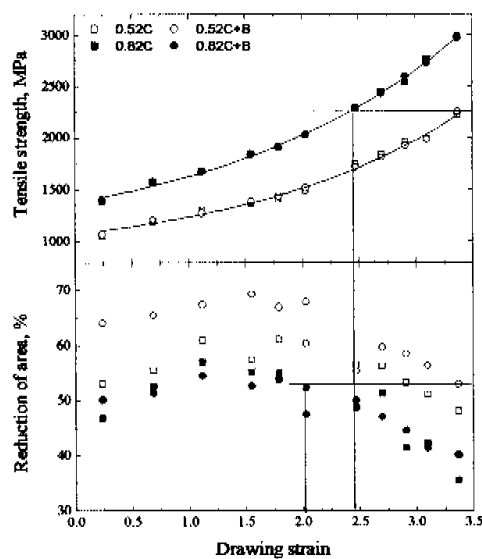
Figure 38: Variation of mechanical properties of wire with drawing strain for steels with different B contents [Choo & Bae 2002].

improve the ductility, especially in severely deformed wire after bluing. Figure 38 shows that while the tensile strength does not seem to be affected by B addition, the reduction of area is significantly increased.

3.5.2   Effect of Al, Si, Co, and P

Solid-solution elements such as Si and P strengthen pearlite mainly by solid-solution hardening of the ferrite phase [Han et al. 2001, Furuya et al. 2005]. They also have functions on controlling the morphology of phases in steels. In high-carbon steels, the carbon can form two detrimental constituents, one being the above-mentioned grain boundary networked cementite, and the other being the graphitization of carbon. Added in hypereutectoid steels, aluminum (Al), silicon (Si), and cobalt (Co) are effective in controlling these two detrimental constituents.

Figure 39 summarizes the effect of Al and Si on network carbide formation and graphitization. The horizontal axis represents the degree of graphitization, with lower numbers indicating more desired conditions. The vertical axis represents the degree of carbide network formation, with lower numbers indicating more desired conditions. To avoid carbide network formation, Si seems to be more effective than Al. To avoid graphitization, Al seems to be more effective than Si. These general trends are also influenced by the deformation temperature.
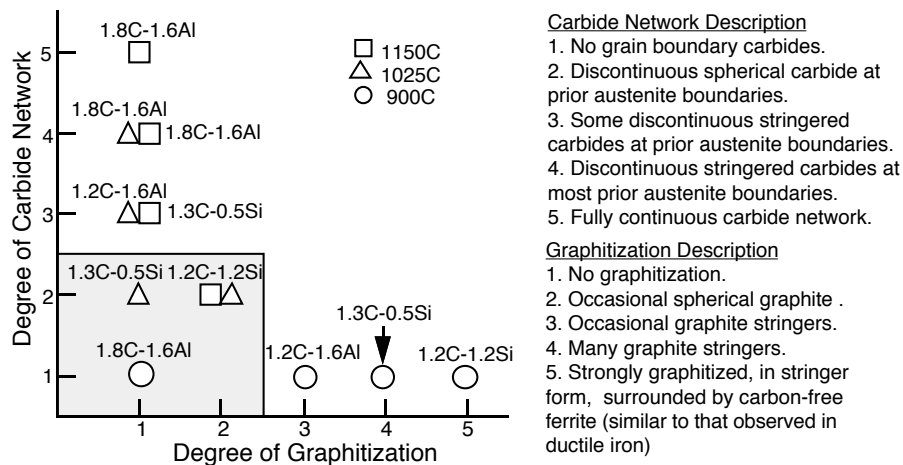
Figure 39: Relative degree of carbide network formation and degree of graphitization as influenced by Al and Si in high-carbon steels [Lesuer et al. 1997]. The compositions and extrusion temperatures that fall into the shaded box in the lower-left corner the figure are considered favorable in preventing carbide network and graphitization.

The effect of Co on grain boundary carbide network formation is shown in Figure 40. For steels with carbon content up to 1.2 wt.%, addition of Co with less than 1:1 Co to C ratio is sufficient to prevent carbide network formation. For steels with carbon content higher than 1.2 wt.%, an increased Co to C ratio of 2:1 is required to prevent carbide network formation. Although adding Co is more costly, compared with Si, Co is known not to reduce the ductility of ferrite [Kanetsuki et al. 1991, Tashiro & Sato 1991]. On the other hand, there are reports to indicate that Si improves strength but does not decrease ductility. Si is effective in improving ductility of cold-rolled and annealed pearlite, especially when the strength is at a higher level [Fu et al. 2004].

3.5.3 Effect of carbide-forming elements

Carbide forming elements are frequently used in low-carbon and low-alloy steels to form fine carbides and nitrides for strengthening [Han et al. 2001] and microstructure stability (inhibit recrystallization) during hot-rolling. For these purposes, Cr, Ti, Nb, and V are often used. In medium-carbon steels, the effect of V and Nb on recovery and recrystallization has been studied [Ayada et al. 1998]. According to Figure 41, V is found to be effective in inhibiting

Table 1. Chemical compositions of steels. (wt%)

Steel	C	Si	Mn	P	S	Cu	Co
A	1.01	0.20	0.48	0.004	0.002	<0.01	0.49
B	1.15	0.23	0.52	0.008	0.003	<0.01	0.98
C	1.15	0.21	0.49	0.005	0.002	<0.01	0.51
D	1.14	0.22	0.52	0.005	0.002	<0.01	1.96
E	1.28	0.19	0.50	0.004	0.005	<0.01	3.05
F	1.48	0.19	0.49	0.001	0.004	<0.01	2.98

A–F: Steel codes shown in Table 1
○: Grain boundary precipitation free
●: Grain boundary precipitation observed
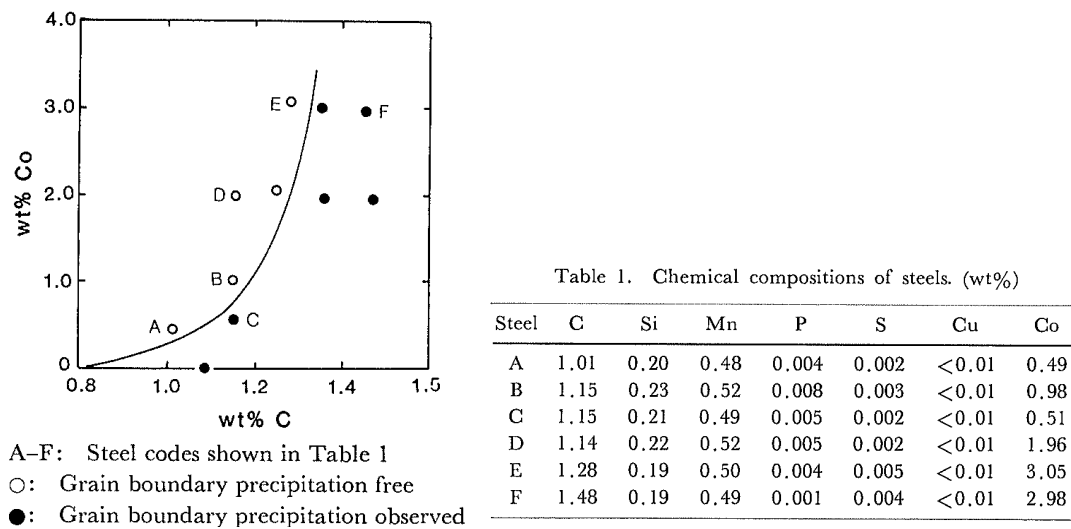
Figure 40: Effect of carbon and cobalt on grain boundary precipitation [Kanetsuki et al. 1991].

the static recovery and recrystallization after hot deformation of medium-carbon spring steels. Fine V carbide precipitation during and after hot deformation is attributed to suppress recovery, thereby producing finer austenite grain sizes. A heat treatment designed for V carbide to precipitate during severe plastic deformation and subsequent annealing has been effective in improving thermal stability and overall tensile properties of the steel [Park et al. 2004]. The improvement is due to the uniform distribution of nano-vanadium carbide that provides extensive interactions with the lattice dislocations inside the ultrafine grained ferrite.

The effect of Nb is small, because Nb forms coarse carbides before hot deformation to have an influence on inhibiting grain boundary migration. Cr has the effect of decreasing the interlamellar spacing of pearlite, and therefore increases the strength and work hardening rate of steels [Tashiro & Sato 1991, Song et al. 2007]. Another work has identified Cr to not only increase the tensile strength but also increase the ductility [Park et al. 2007]. This effect of Cr has been effective in decreasing the delamination of hypereutectoid steel wire during cold drawing. Additionally, it has been found that Cr, when added with Si to high-carbon steels, can inhibit the softening of cold drawn steel wire during the hot-dip galvanizing [Tarui et al. 2005, Lv et al. 2008a].

3.5.4 Effect of Mn and Ni

Mn influences the segregation of substitutional alloying elements during solidification of low-alloy steels, and lowers the ductility of steels [Tashiro & Sato 1991] The effect of Mn on grain refinement, however, has been positive [Song et al. 2005b]. In a low-carbon steel, increased Mn contents lead to a decrease in the average ferrite grain size. The mechanism for this beneficial effect of Mn on grain refinement is suggested as the enrichment of Mn in the cementite particles,
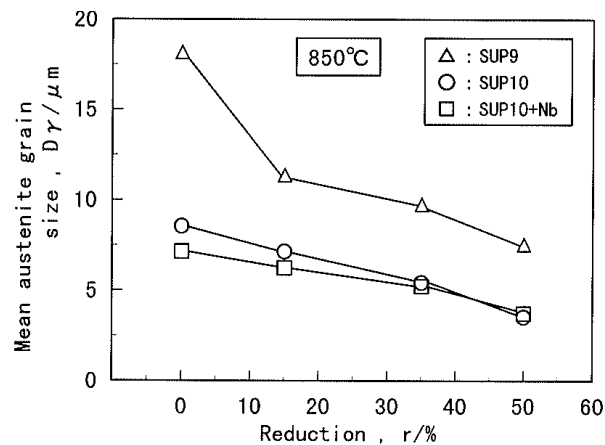
Figure 41: Effect of plastic deformation on mean austenite grain size [Ayada et al. 1998] for steels with different V and Nb concentrations. Steel SUP9 does not contain V or Nb; steel SUP10 contains 0.16% V; steel SUP10+Nb contains 0.16% V and 0.12% Nb.

which become finer with a higher Mn content. Song et al. reported an increase of strength at an equal ductility and toughness with more Mn in the C-Mn ultrafine grained steels. Mn also is found to improve the ductility of a pearlitic steel in the cold-rolled and annealed state [Fu et al. 2004].

Ni has been known to have a beneficial effect of resisting the delamination by decreasing the decomposition rate of lamellar cementite during wire drawing. However, the Ni addition up to 0.8% has not caused any change in strength, work hardening rate and Hall-Petch parameters for cold drawn hypereutectoid steel wire [Song et al. 2007].

3.5.5 Effect of Alloying Elements on Castability

Besides achieving strengthening effects, some of the above alloying elements also influence the steel castability, which is related with fluidity, chilling tendency, and shrinkage characteristics of liquid steels during casting. Possible cast defects can occur in various forms, but they can be broadly classified into either due to uncastable melts, or due to cast product not meeting the specifications. It is generally believed that for continuous casting of steels, the following list of elements need to be controlled in the melts before casting [Matschullat et al. 2007]: C, Si, Mn, S, Al, N, Zn, and O. Among these elements, C, Si, Mn, Al, and N are known to be added as alloying elements for mechanical strengthening reasons, as outlined earlier.

Uncastable melts interact with the casting machines, leading to disruptive casting processes. A common problem of such uncastable melts is the clogging of casting channels and nozzles by oxide deposits in Al-killed (deoxidized) continuous casting steel melts. This problem arises due to the desire to control the oxygen content in the steel. Aluminum, as a potent de-oxidizer, is added to reduce O by forming Al-containing oxides (alumina) in liquid steel. Alumina has a

high melting point, and tends to cluster and clog the casting nozzles [Janke et al. 2000].

Efforts to prevent nozzle clogging have lead to calcium (Ca) treatment of Al-killed steel melts before casting. Calcium oxide (CaO) forms a low melting-point eutectic with alumina (Al_2O_3), effectively transforming solid alumina into a liquid phase. The delicate balance between Ca, Al, Si, and O through slag reactions can be found in references [Janke et al. 2000, Yuan et al. 2006, Alekseenko et al. 2007].

Formation of low-melting liquid films during the last stage of solidification along with shrinkage strains often produces hot cracking in some castings. Some alloying elements have a tendency to widen the liquid-solid two-phase zone that leads to a higher tendency for segregation and thus, hot cracking. A general theory, initially developed in early 1960s [Borland 1960], is still proved to be valid today. The theory relates the behavior of alloy segregation and shrinkage strain to hot cracking (hot-shortness) in welds and castings. Due to the complexity of interactions of various alloying elements, designed experiments on castability, such as hot ductility testing, will usually be conducted for specific alloy systems.

4 Ultrahigh Strength Steel Wire

4.1 Applications of ultrahigh strength wire

Ultrahigh strength wire can have many applications that demand exceptional tensile strength. In terms of quantity, two most important applications for ultrahigh strength steel wire are in the automotive tire reinforcement [Lesuer et al. 1996] and in the cable wire for suspension bridges [Elices 2004]. Figure 42 provides a historical view of the development of wire strength as applied in these two industrial fields. With stronger cable wire, the suspension bridges have become slender, stronger, with longer spans. With increased tire reinforcement, automobiles have lighter and more reliable tires that give improved gas millage. The strength of ultrahigh-carbon steel wire is compared favorably with other reinforcing fibers such as S-glass, Kevlar-49, and carbon fiber. More important, the ultrahigh-carbon steel wire is significantly less expensive than other reinforcing fibers [Lesuer et al. 1996].
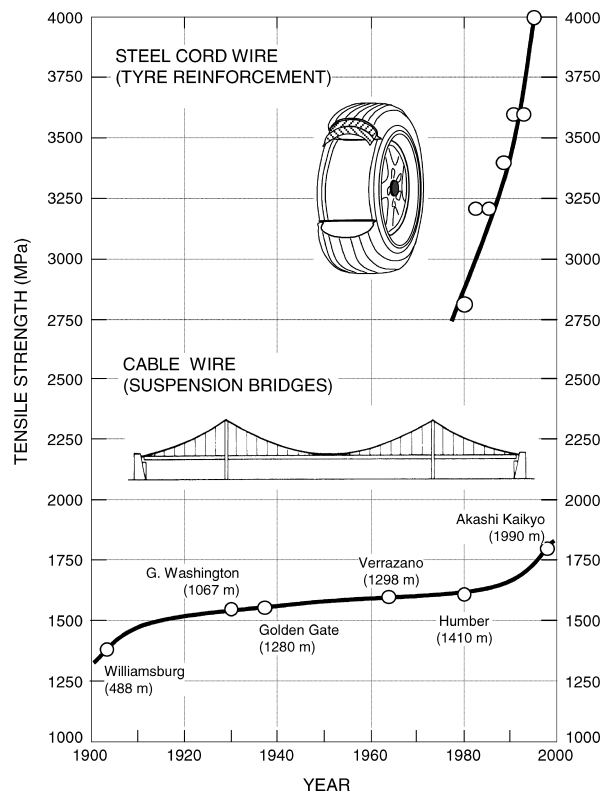
Figure 42: Historical development of the tensile strength of cold-drawn wires. The lower curve corresponds to steel wires for bridge cables. The upper figure is for steel cord for tire reinforcement [Elices 2004].

In addition to the application in tires and bridges, ultrahigh strength wire can serve as springs, wire rope, and reinforcement in a wide range of composite structures, such as prestressed concrete structures. The application of ultrahigh strength wire in the composite industry is

largely un-explored because the wire was not available before, but the application potential is expected to be enormous. It is highly recommended to conduct exploratory studies to verify the physical-mechanical properties, manufacturing procedural, and cost-saving advantages of ultrahigh strength wire reinforced composites.

4.2   Eutectoid and hypereutectoid carbon steels

These refer to steels with a carbon content from eutectoid (0.77 wt.%) up to 1.0 wt.%. The earliest openly reported ultrahigh-strength steel wire, however, is not strictly eutectoid in carbon composition. The so called *Scifer* wire developed by Kobe Steel in the early 1990s has a composition of 0.2%C-1.2%Si-1.5%Mn with a 5 GPa strength, "although the wire is drawn as for conventional piano wire, the heat-treatment is radically different from that involved in the patenting process [Bhadeshia & Harada 1993]." During the heat-treatment, the quenched steel is inter-critically annealed in the $\alpha + \gamma$ phase field between Ac_1 and Ac_3 temperatures, which produces a small quantity of austenite between the original martensite. The original martensite tempers during the annealing, while the newly formed austenite decomposes into high carbon martensite, due to carbon migration. The extremely high strength of the thin wire has been attributed to the ultrafine dislocation cell structure and solid solution of carbon, both enhanced by the severe plastic deformation.

The heavily drawn pearlitic steel wires are typically produced by drawing wire to an intermediate diameter, patenting to produce a fine pearlite microstructure, and then cold drawing to strains between 1.5 to 5.0. It is reported [Hono et al. 2001] that a cold drawn 0.97C-0.30Mn-0.21Si-0.21Cr steel wire, provided by Nippon Steel, to have a tensile strength of 3841 MPa after drawing with a true strain $\epsilon = \ln(A_i/A_f)$ of 3.6, and a strength of 5170 MPa after drawing with a true strain of 5.1. The patenting is consisted of austenitizing at 950°C for 80 s followed by isothermal transformation for 20 s in a lead bath at 575°C. The mechanism for strengthening is the nanoscale ferrite fibers supersaturated with carbon. The researchers believe all cementite lamellae that existed in the as-patented condition have been decomposed after heavy cold drawing, leading a dissolution of carbon into the ferrite to 4.4 at.%. Although there has been a dispute about the cementite decomposition [Gavriljuk 2002], nanoscaled ferrite fibers seem to be the apparent microstructure that has provided the ultrahigh strength.

Figure 43 shows the TEM micrographs and selected area electron diffraction patterns for heavily cold drawn pearlitic steel wire with $\epsilon = 5.1$. Lamellar ferrite structures are observed from the longitudinal image of the wire. The cross-sectional image shows a typical curled ferrite morphology. There are no diffraction rings from cementite, indicating the cementite decomposition during heavy cold drawing.

Subsequent research seems to support the dissolution and refinement of cementite mechanism for strengthening of the nanoscale ferrite [Tarui et al. 2005, Lv et al. 2008]. At lower drawing
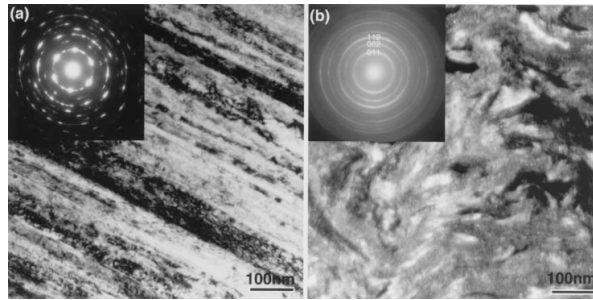
Figure 43: Longitudinal (a) and cross-sectional (b) TEM micrographs and selected area electron diffraction patterns from a pearlitic steel wire cold drawn with $\epsilon = 5.1$ [Hono et al. 2001].

deformation, the steels always show a decreased grain size with finer interlamellar spacings in the pearlite, and the cementite becoming fragmented, especially in warm deformation [Han et al. 2001, Sun et al. 2005, Park et al. 2007]. The change of cementite fraction as a function of drawing strain is shown in Figure 44. With an increased drawing strain, the cementite fraction decreases, indicating a partial dissolution of cementite during the cold work. The dissolution of cementite starts at a lower strain level for fine pearlite steels (Steel A and Steel C), and it starts at a higher strain level for the coarser pearlite steel (Steel B). Further, the cementite fraction seems to stabilize to a level about 8 to 9% as the drawing strain is increased.
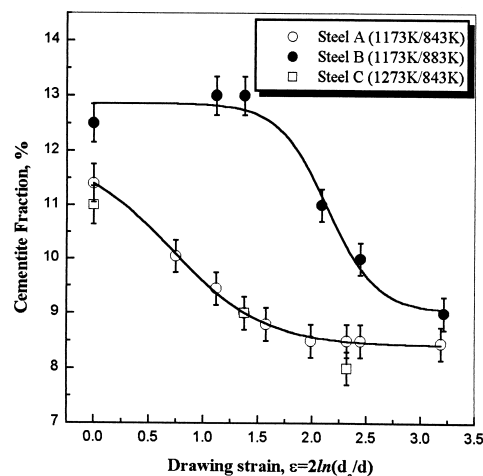
Figure 44: Changes of cementite fraction as a function of drawing strain for pearlitic steels of different pearlite spacings. Steels A and C have fine pearlite, and Steel B has coarse pearlite [Nam et al. 2000].

At higher cold drawn deformation, the steel microstructure is lamellar ferrite grains with a 10 nm lamella spacing (Figure 45). The selected area diffraction patterns from regions of different contrasts indicate these regions are all ferrite with the same orientation. Again, cementite is not detected. Three-dimensional mapping of carbon using the atom probe shows a distribution of carbon in ferrite, with carbon most likely segregated to dislocations.
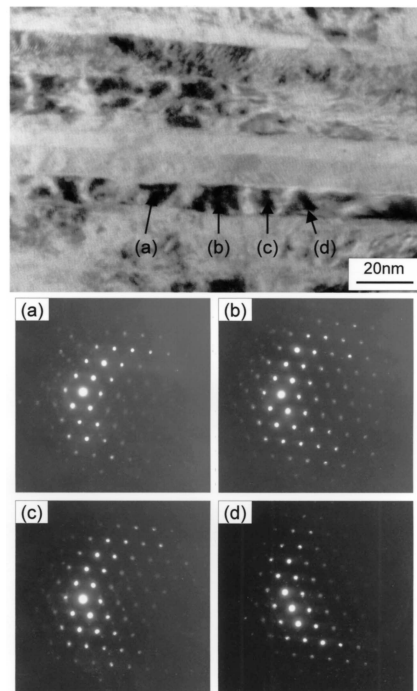
Figure 45: TEM micrograph and selected area electron diffraction patterns of a high-carbon steel wire cold drawn with $\epsilon = 4.2$ [Tarui et al. 2005].
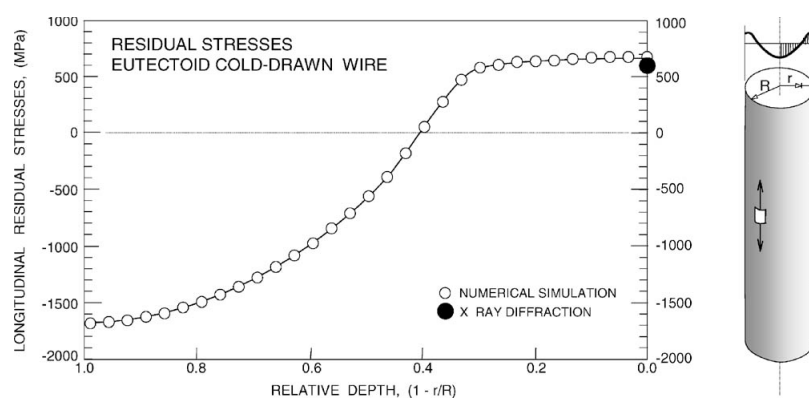
Figure 46: Computed longitudinal residual stresses in cold drawn eutectoid steel wire. A data point of residual stress in the ferrite phase measured by X-ray diffraction is also shown [Elices 2004].

There are studies of residual stresses in cold-drawn pearlitic steel wires [Elices 2004]. The residual stresses due to cold drawing are tensile on the surface, which will favor the onset of yielding. Figure 46 shows an axisymmetric distribution of the longitudinal residual stress across the radius of a cold drawn pearlitic steel wire. Other performance factors of the cold drawn wire, including stress relaxation, environmental assisted cracking, fatigue, and delamination, are also affected by the residual stresses.

4.3   Ultrahigh carbon steels

These refer to steels with a carbon content higher than 1.0 wt.%, but lesser than 2.1 wt.%, the minimum carbon content for cast irons. Slowly cooled ultrahigh carbon steels will have a proeutectoid cementite network along the pearlitic grain boundaries, with limited ductility. Higher cooling rate generates martensite structure in the steel [Jiewu et al. 2004]. Therefore, most of the thermomechanical processing is done in the austenitizing temperature. Controlled cooling, patenting, and addition of alloying elements are generally used to obtain network cementite-free, fine pearlite for cold drawing. Typical controlled microstructure for ultrahigh carbon steels is shown in Figure 47.
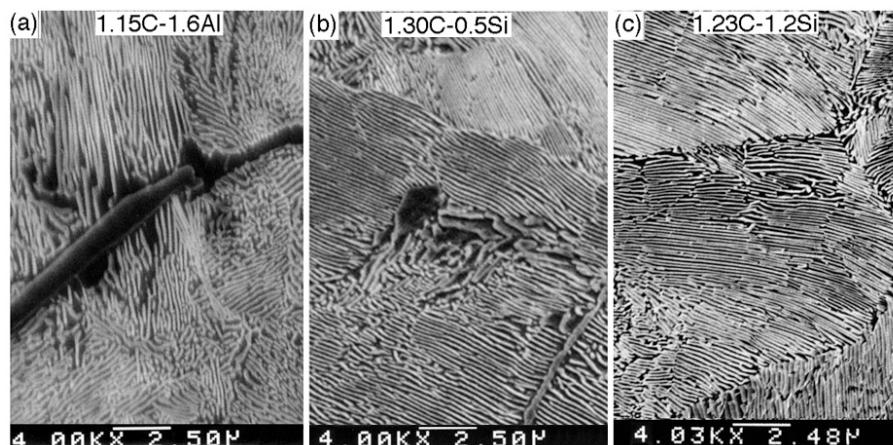
Figure 47: SEM micrographs showing the effect of composition on the microstructure of ultrahigh carbon steels after extrusion at 1150°C [Lesuer et al. 1997].

Steels with carbon content between 1.0 and 1.45 wt.% are hot forged to process the ingots into rough cylindrical rods. The rods are austenitized in Ar at 1000C, then patented by quenching in a tin bath of 550°C for 3 min. Cold drawing is done on the patented rods at 15% reduction of area per pass, with a lubricant, and at a drawing speed of 8 m/min [Kanetsuki et al. 1991]. Cold drawing is shown to significantly increase tensile strength of hypereutectoid and ultrahigh carbon steels. Figure 48 shows the strength increment as a function of wire drawing strain in hypereutectoid steels. The strength increment is defined as the strength after cold drawing minus the as-patented strength. A approximately linear relationship can be seen between the drawing
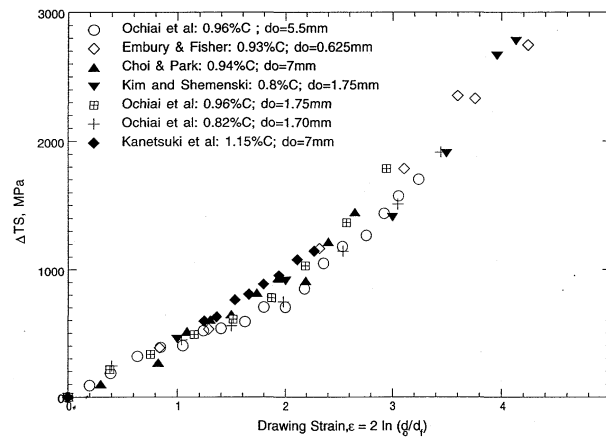
Figure 48: Strength increment as a function of wire drawing strain for the eutectoid and hypereutectoid steels [Lesuer et al. 1997].

strain and strength increment.

Besides conventional ingot casting as the first stage of ultrahigh carbon steel processing, rapid casting through wheel spinning [Cooper & Jones 2002] and spray forming [Luo et al. 2004]. A more refined starting microstructure are resulted from such processes. Nippon Steel has also developed a direct in-line patenting (DLP) for wire rods to eliminate the lead (Pb) patenting [Ohba et al. 2007]. There is direct energy saving in addition to the environmental benefits by reducing lead pollution.

The basic strengthening mechanisms for ultrafine grained ultrahigh carbon steels are identical with those for the eutectoid steels, especially for those steels with network carbides eliminated to obtain a homogeneous pearlitic microstructure. The adiabatic shearing bands can sometimes be observed in ultrahigh carbon steels [Zelin 2002, Lesuer et al. 2005]. These bands are localized severe plastic deformation zones observed under higher strain rates. Adiabatic heating leads to transformation to austenite and subsequent rapid cooling produced a divorced eutectoid transformation. A much higher hardness is obtained in the shearing bands, which contain ultrafine ferrite grains with nano-size carbides. Zelin points out that the shearing bands can form at a relatively smaller drawing stains, explaining the observed decrease in total elongation in small degrees of deformation. The adiabatic shearing bands are also observed in low-alloy steels [Odeshi et al. 2006].

5 Summary

Ultrafine grained steels can be obtained by either severe plastic deformation (SPD) or advanced thermomechanical processing (ATP). Both SPD and ATP as methods for producing nanocrystalline structures in bulk quantity of steels have attracted significant interest from researchers world wide. Generally speaking, there is still a large gap between laboratory-scale fundamental studies and industrial-scale production of steels using SPD. Advanced thermomechanical processing methods, on the other hand, have been successfully developed to produce large quantities of ultrahigh strength steel wires for current engineering projects, such as the longest suspension bridges under construction, or the next-generation tires for automobiles.

For low-carbon alloy steels, cold or warm rolling and annealing of a martensitic starting microstructure have been proved to produce ultrafine grained microstructure with excellent strength, ductility, and toughness.

For hypereutectoid steels with carbon content higher than 1.0%, ultrafine grained microstructure can be obtained by cold drawing. The starting microstructure needs to be controlled as fine pearlite, in order to provide enough draft for wire drawing. The fine pearlite can be resulted from controlling the cooling rate, modifying the alloy concentration, patenting heat treatment, and thermomechanical processing such as forging and extrusion. Ultrahigh carbon steel wires with 4000 to 5000 MPa tensile strength have been produced in quantity by Japanese steel makers.

Much is known about ultrahigh carbon, ultrafine grained, ultrahigh strength steels. Detailed description of mechanical properties for these ultrahigh strength steels is available in the literature, as are the strengthening mechanisms for various alloys under various process conditions. The detailed information on alloying composition and processing procedures, however, is much sketchier and not as public knowledge. Studies will therefore have to be conducted to investigate the unknown issues from design, processing, testing, and application of specific steels.

6 Recommendations

It is recommended to design an ultrahigh carbon steel with 1.3 % C with Co, Si, Cr additions for wire application. To ensure good drawability (or ductility), patenting or direct in-line patenting should be developed for the steel with special cooling system designs. Cold drawing is recommended for producing the ultrafine grained ferrite with nanoscaled carbide dispersion for strengthening.

References

[Alekseenko et al. 2007] Alekseenko, A., Baibekova, E., Kuznetsov, S., Baldaev, B., Pono-marenko A., and Ponomarenko, D., Effect of some technological factors on the casta-bility of an aluminum-killed steel in a continuous billet caster, Russian Met. (Metally), (2007) 7, pp. 611-616

[Ayada et al. 1998] Ayada, M., Yuga, M., Tsuji, N., Saito, Y. and Yoneguti, A., Effect of vanadium and niobium on restoration behavior after hot deformation in medium carbon spring steels, ISIJ International, 38 (1998) 9, pp. 1022-1031

[Azevedo et al. 2005] Azevedo, G., Barbosa, R., Pereloma, E., and Santos, D., Development of an ultrafine grained ferrite in a low C-Mn and Nb-Ti microalloyed steels after warm torsion and intercritical annealing, Mater Sci & Eng A, 402 (2005) pp. 98-108

[Azizi et al. 2007] Azizi-Alizamini, H., Militzer, M., and Poole, W.J., A novel technique for developing bimodal grain size distributions in low carbon steels, Scripta Mater, 57 (2007) pp. 1065-1068

[Barani et al. 2007] Barani, A.A., Li, F., Romano, P., Ponge, D., and Raabe, Design of high-strength steels by microalloying and thermomechanical treatment, Mater Sci & Eng A, 463 (2007) pp. 138-146

[Beladi et al. 2009] Beladi, H., Adachi, Y., Timokhina, I., Hodgson, P.D., Crystallographic analysis of nanobainitic steels, Scripta Mater, 60 (2009) pp. 455-458.

[Bhadeshia & Harada 1993] Bhadeshia, H.K.D.H., and Harada, H., High-strength (5 GPa) steel wire: an atom-prove study, Applied Surface Sci, 67 (1993), pp. 328-333

[Bhadeshia 2008] Bhadeshia, H.K.D.H., Properties of fine-grained steels generated by dis-placive transformation, Mater Sci & Eng A,481-482 (2008), pp.36-39

[Borland 1960] Borland, J.C., Generalized Theory of Super- Solidus Cracking in Welds (and Castings). Brit Weld J, 7 (1960), H. 8, pp. 508/512

[Caballero et al. 2008] Caballero, E.G., Miller, M.K., Carcia-Mateo, C., Capdevila, C., and Garcia de Andres, C., Phase transformation theory: A powerful tool for the design of advanced steels, JOM, 60 (2008) 12, pp. 16-21

[Cetlin et al. 1993] Cetlin, P.R., Yue, S., and Jonas, J.J., Simulated rod rolling of interstitial free steels, ISIJ International, 33 (1993) 4, pp. 488-497

[Chen et al. 2008] Chen, W., Li, L., Yang, W., and Sun, Z, Ultra-refinement of hypereutectoid steel during deformation of uldercooled austenite, Chinese J Mater Res, 22 (2008) 4, pp. 374-378 (in Chinese)

[Choo & Bae 2002] Choo, W.Y., and Bae, C.M., Drawing behavior of pearlitic steel wire rods controlled by boron addition in medium carbon steel, ISIJ International, 42 (2002) Supplement, pp. S47-S51

[Cooper & Jones 2002] Cooper, K.P, and Jones, III, H.N., Phase transformation-induced grain refinement in rapidly solidified ultra-high-carbon steels, Met & Mater Trans A, 33A (2002) pp. 2789-2799

[Delince et al. 2007] Delince, M., Brechet, Y., Embury, J.D., Geers, M., Jacques, P., and Pardoen, T., Structure-property optimization of ultrafine-grained dual-phase steels using a microstructure-based strain hardening model, Acta Mater, 55 (2007) pp. 2337-2350.

[Dupuy & Rauch 2002] Dupuy, L., Rauch, E.F., Deformation paths related to equal channel angular extrusion, Mater Sci & Eng A, 337 (2002) pp. 241-247.

[Eghbali 2005] Eghbali, B., and Abdollah-zaleh, A., Influence of thermomechanical parameters in ferrite grain refinement in a low carbon Nb-microalloyed steel, Scripta Mater, 53 (2005) pp. 41-45

[Eghbali 2007] Eghbali, B., EBSD study on formation of fine ferrite grains in plain carbon steel during warm deformation, Mater Letters, 61 (2007), pp. 4006-4010

[Elices 2004] Elices, M., Influence of residual stresses in the performance of cold-drawn pearlitic wires, J Mater Sci, 39 (2004), pp. 3889-3899

[El-Shabasy & Lewandowski 2004] El-Shabasy, A., Lewandowski, J.J., Effects of load ratio, R, and test temperature on fatigue crack growth of fully pearlitic eutectoid steel (fatigue crack growth of pearlitic steel), Intl J Fatigue, 26 (2004), pp. 305-309

[Figueiredo et al. 2006] Figueiredo, R., Pinheiro, I., Aguilar, M., Modenesi, P., and Cetlin, P., Finite element analysis of equal channel angular processing (ECAP) considering the strain path dependence of work hardening of metals, J Mater Proc Tech, 180 (2006), pp. 30-36

[Fu et al. 2004] Fu, W., Furuhara, T., and Maki, T., Effect of Mn and Si addition on microstructure and tensile properties of cold-rolled and annealed pearlite in eutectoid Fe-C alloys, ISIJ International, 44 (2004) 1, pp. 171-18

[Furuhara et al. 2005] Furuhara, T., Mizoguchi, T., and Maki, T., Ultrafine $(\alpha + \theta)$ duplex structure formed by cold rolling and annealing of pearlite, ISIJ International, 45 (2005) pp. 392-398

[Furuhara et al. 2005a] Furuhara, T., and Maki, T., Grain boundary engineering of superplasticity in steels, J Mater Sci, 40 (2005) pp. 919-926

[Furuya et al. 2005] Furuya, Y., Matsuoka, S., Shimakura, S., Hanamura, T., Torizuka, S., Effect of carbon and phosphorus addition on the fatigue properties of ultrafine-grained steels, Scripta Mater, 52 (2005) pp. 1163-1167

[Furuya et al. 2007] Furuya, Y., Matsuoka, S., Shimakura, S., Hanamura, T., Torizuka, S., Fatigue strength of ultrafine ferrite-cementite steels and effects of strengthening mechanisms, Met & Mater Trans A, 38A (2007) pp. 2984-2991

[Gavriljuk 2002] Gavriljuk, V., Comment on "cementite decomposition in heavily drawn pearlite steel wire", Scripta Mater, 46 (2002) 00. 175-177

[Gonzalez et al. 2003] Gonzalez, B.M., Marchi, L.A., Fonseca, E., Modenesi, P., and Buono, V., Measurement of dynamic strain aging in pearlitic steels by tensile test, ISIJ International, 43 (2003) 3, pp. 428-432

[Groche et al. 2007] Groche, P., Fritsche, D., Tekkaya, E., Allwood, J., Hirt, G., Neugebauer, R., Incremental bulk metal forming, Annals CIRP, 56 (2007) 2, pp. 635-656

[Han et al. 2001] Han, K., Edmonds, D.V. and Smith, G.D.W., Optimization of mechanical properties of high-carbon pearlitic steels with Si and V additions, Met & Mater Trans A, 32 (2001) 6, pp. 1313-1324

[Han & Yue 2003] Han, B., Yue, S., Processing of ultrafine ferrite steels, J Mater Proc Tech, 136 (2003) pp. 100-104

[Hanamura et al. 2004] Hanamura T., Yin, F., and Nagai, K., Ductile-brittle transition temperature of ultrafine ferrite/cementite microstructure in a low carbon steel controlled by effective grain size, ISIJ International, 44 (2004) 3, pp. 610-617

[Hidaka et al. 2001] Hidaka, H., Tsuchiyama, T. and Takaki, S., Relation between microstructure and hardness in Fe-C alloys with ultra fine grained structure, Scripta Mater, 44 (2001) pp. 1503-1506

[Hono et al. 2001] Hono, K., Ohnuma, M., Murayama, M., Nishida, S., Yoshie, A. and Takahashi, T., Cementite decomposition in heavily drawn pearlite steel wire. Scripta Mater, 44 (2001), pp. 977-983

[Hu et al. 2008] Hu, Q., Zhao, Y., Zhao, M., and Hanamura, T., Difference in grain growth between the submicron-sized and micron-sized ferrite in C-Mn steels, Chinese J Mater Research, 22 (2008) 4, pp. 152-156.

[Hua 2003] Hua, T., High-carbon steel products made with continuous cast billets, Southern Iron & Steel, April 30, 2003

[Huang & Xu 2006] Huang, J., and Xu, Z., Evolution mechanism of grain refinement based on dynamic recrystallization in multiaxially forged austenite, Mater Letters, 60 (2006), pp. 1854-1858

[Huang et al. 2007] Huang, Q., Yang, W., and Sun, Z., Influence of undercooling on dynamic transformation and microstructure evolution in eutectoid steel, Chinese J Mater Res, 21 (2007) 6, pp. 593-598 (in Chinese)

[Humphreys et al. 2001] Humphreys, F.J., Prangnell, P.B., and Prestner, R., Fine-grained alloys by thermomechanical processing, Current Opinion in Solid State & Mater Sci, 5 (2001), pp. 15-21

[Janke et al. 2000] Janke, D., Ma, Z., Valentin, P., Heinen, A., Improvement of castability and quality of continuously cast steel, ISIJ International, 40 (2000) 1, pp. 31-39

[Jiewu et al. 2004] Jiewu, Z., Yan, X., and Liu, Y., Lath martensite in 1.4%C ultra-high carbon steel and grain size effect, Mater Sci & Eng A, 385 (2004), pp. 440-444

[Kanetsuki et al. 1991] Kanetsuki, Y., Ibaraki, N., and Ashida, S., Effect of cobalt addition on transformation behavior and drawability of hypereutectoid steel wire, ISIJ International, 31 (1991) 3, pp. 304-311

[Kazemineshad & Taheri 2003] Kazeminezhad, M. and Taheri, A. K., The effect of controlled cooling after hot rolling on the mechanical properties of a commercial high carbon steel wire rod, Mater & Design, 24 (2003), pp. 415-421

[Kelly et al. 2002] Kelly, G., Baladi, H., and Hodgson, P., Ultrafine grained ferrite formed by interrupted hot torsion deformation of plain carbon steel, ISIJ International, 42 (2002) 12, pp. 1585-1590

[Kimura et al. 2008] Kimura, Y., Inoue, T., Yin, F., and Tsuzaki, K., Inverse temperature dependence of toughness in an ultrafine grain-structure steel, Science, 320 (2008), pp. 1057-1059

[Kimura et al. 2007] Kimura, Y., Inoue, T., Yin, F., Sitdikov, O., and Tsuzaki, K., Toughening of an 1500 MPA class steel through formation of an ultrafine fibrous grain structure, Scripta Mater, 57 (2007), pp. 465-468

[Kitahara et al. 2006] Kitahara, H., Ueji, R., Tsuji, N., Manamino, Y., Crystallographic features of lath martensite in low-carbon steel, Acta Mater, 54 (2006), pp. 1279-1288

[Kolahi et al. 2009] Kolahi, A., Akbarzadeh, A., Barnett, M., Electron back scattered diffraction (EBSD) characterization of warm rolled and accumulative roll bonding (ARB) processed ferrite, J Mater Proc Tech, 209 (2009), pp. 1436-1444

[Lan et al. 2007] Lan, H., Liu, W., and Liu X., Ultrafine ferrite grains produced by tempering cold-rolled martensite in low carbon and microalloyed steel, ISIJ International, 47 (2007) 11, pp. 1652-1657

[Langdon 2007] Langdon, T.G., Research on bulk nanostructured materials in Ufa: Twenty years of scientific achievements, Mater Sci & Eng A, 503 (2009) pp. 6-9.

[Lee et al. 2002] Lee, S., Saito, Y., Tsuji, N., Utzunomiya, H., and Sakai, T., Role of shear strain in ultragrain refinement by accumulative roll-bonding (ARB) process, Scripta Mater, 46 (2002), pp. 281-285

[Lesuer et al. 1996] Lesuer, D.R., Syn, C.K., Sherby, O.D., Ultrahigh carbon steel for automotive applications, 1996 SAE International Congress & Exposition, Detroit, MI, Feb. 26-29, 1996

[Lesuer et al. 1997] Lesuer, D.R., Syn, C.K., Sherby, O.D., and Whittenberger, W.D., Mechanical behavior of ultrahigh strength ultrahigh carbon steel wire and rod, Thermomechanical Processing and Mechanical Properties of Hypereutectoid steels, TMS Symposium, Indianapolis, IN, Sept. 15-18, 1997

[Lesuer et al. 1999] Lesuer, D.R., Syn, C.K. and Sherby, O.D., Influence of severe plastic deformation on the structure and properties of ultrahigh-carbon steel wire. NATO Advanced Research Workshop on Investigations and Applications of Severe Plastic Deformation August 2 - 7, 1999 Moscow, Russia. pp. 11

[Lesuer et al. 2005] Lesuer, D.R., Syn, C.K., and Sherby, O.D., Severe plastic deformation through adiabatic shear banding in Fe-C steels, Mater Sci & Eng A, 410-411 (2005), pp. 222-225

[Li et al. 2005] Li, S., Beyerlein, I., Alexander, D., and Vogel, S., Texture evolution during multi-pass equal channel angular extrusion of copper: neutron diffraction characterization and polycrystal modeling, Acta Mater, 53 (2005), pp. 2111-2125

[Li et al. 2004] Li, B., Godfrey, A., Meng, Q., Liu, Q., and Hansen, N., Microstructure evolution of IF-steel during cold rolling, Acta Mater, 52 (2004), pp. 1069-1081

[Li et al. 2006] Li, B., Tsuji, N., and Kamikawa, N., Microstructure homogeneity in various metallic materials heavily deformed by accumulative roll-bonding, Mater Sci & Eng A, 423 (2006), pp. 331-342

[Li et al. 2008] Li, L., Yang, W., and Sun, Z., Microstructure evolution of a pearlitic steel during hot deformation of undercooled austenite and subsequent annealing, Met & Mater Trans A, 39A (2008), pp.624-635

[Li et al. 2009] Li, Q., Wang, T., Jing, T., Gao, Y., Zhou, J., and Li, H., Warm deformation behavior of quenched medium carbon steel and its effect on microstructure and mechanical properties, Mater Sci & Eng A, 515 (2009), pp. 38-42

[Liu et al. 2003] Liu, M., Shi, B., Wang, C., Ji, S., Cai, X., and Song, H., Normal Hall-Petch behavior of mild steel with submicron grains, Mater Letters, 57 (2003), pp. 2798-2802

[Liu et al. 2003a] Liu, M., Shi, B., Guo, J., Cai, X., and Song, H., Lattice constant dependence of elastic modulus for ultrafine grained mild steel, Scripta Mater, 49 (2003), pp. 167-171

[Luo et al. 2004] Luo, G., Wu, J., Fan, J., Shi, H., Lin, Y. and Zhang, J., Deformation behavior of an ultrahigh carbon steel (UHCS-3.0Si) at elevated temperature, Mater Sci & Eng A, A379 (2004) 1-2, pp. 302-307

[Lv et al. 2008] Lv, Z, Jiang, P., Wang, Z., Zhang, W., Sun, S., and Fu, W., XRD analyses of dissolution behavior of cementite in eutectoid pearlitic steel during cold rolling, Mater Letters, 62 (2008), pp. 2825-2827.

[Lv et al. 2008a] Lv, Z., Sun, S., Wang, Z., Qv, M., Jiang, P., and Fu, W., Effect of alloying elements addition on coarsening behavior of cementite particles after severe cold rolling and annealing, Mater Sci & Eng A, 489 (2008) pp. 107-112

[Ma 2006] Ma, E., Eight routes to improve the tensile ductility of bulk nanostructured metals and alloys, JOM, (2006) 4, pp. 49-53

[Matschullat et al. 2007] Method for predicting and controlling the castability of liquid steel, US Patent Application Publication, US2007/0000578 A1

[Morales et al. 1990] Morales, D., Lopez, A., Olivares, I., Heat transfer analysis during water spray cooling of steel rods, ISIJ International, 30 (1990) 1, pp. 48-57

[Murty et al. 2005] Murty, S., Torizuka, S., and Nagai, K., Microstructural and micro-textural evolution during single pass high Z large strain deformation of a 0.15C steel, ISIJ International, 45 (2005) 11, pp. 1651-1657

[Murty et al. 2005a] Murty, S., Torizuka, S., Nagai, K., Koseki, N., and Kogo, Y., Classification of microstructural evolution during large strain high Z deformation of a 0.15 carbon steel, Scripta Mater, 52 (2005), pp. 713-718

[Muszka et al. 2006] Muszka, K., Hodgson, P., and Majta, J., A physical based modeling approach for the dynamic behavior of ultrafine grained structures, J Mater Proc Tech, 177 (2006), pp. 456-460

[Muszka et al. 2007] Muszka, K., Majta, J., and Hodgson, P., Modeling of mechanical behavior of nanastructured HSLA steels, ISIJ International, 47 (2007) 8, pp. 1221-1227

[Nagato et al. 2008] Nagato, K., Sigiyama, S., Yanagida, A., and Yanagimoto, J., Single-pass severe plastic forming of ultrafine-grained plain carbon steel, Mater Sci & Eng A, 478 (2008), pp. 376-383

[Nam et al. 2000] Nam, W., Bae, C., Oh, S., and Kwon, S., Effect of interlamellar spacing on cementite dissolution during wire drawing of pearlitic steel wires, Scripta Mater, 42 (2000), pp. 457-463

[Nedjad et al. 2008] Nedjad, S., Ahmadabadi, M., Furuhara, T., Extend and mechanism of nanostructure formation during cold rolling and aging of lath martensite in alloy steel, Mater Sci & Eng A, 485 (2008), pp 544-549

[Nedjad et al. 2009] Nedjad, S., Ahmadabadi, M., Furuhara, T., Annealing behavior of an ultrafine-grained Fe-Ni-Mn steel during isothermal aging, Mater Sci & Eng A, 503 (2009), pp. 156-159

[Niendorf et al. 2009] Niendorf, T., Maier, H., Canadinc, D., and Karaman, I., Cyclic stability of ultrafine-grained interstitial-free steel at elevated temperatures, Mater Sci & Eng A, 503 (2009), pp. 160-162

[Nishida et al. 1998] Nishida, S., Yoshie, A, and Imagumbai, M., Work hardening of hypereutectoid and eutectoid steels during drawing, ISIJ International, 38 (1998) 2, pp. 177-186

[Odeshi et al. 2006] Odeshi, A., Bassim, M, and Al-Ameeri, S., Effect of heat treatment on adiabatic shear bands in a high-strength low alloy steel, Mater Sci & Eng A, 419 92006), pp. 69-75

[Ohba et al. 2007] Ohba, H., Nishida, S., Tarui, T., Yoshimua, K., Sugimoto, M., Matsuoka, K., Hikita, N., and Toda, M., High performance wire rods produced with DLP, Nippon Steel Tech Rep, No. 96 (2007), pp. 50-56

[Oh-ishi et al. 2007] Oh-ishi, K., Zhang, H. Ohkubo, T., and Hono, K., Microstructure characterization of bulk nanocrystalline Fe-0.8C alloy produced by mechanical milling and spark plasma sintering, Mater Sci & Eng A, 456 (2007), pp. 20-27

[Ohmori et al. 2004] Ohmori A., Torizuka, S., and Nagai, K., Strain-hardening due to dispersed cementite for low carbon ultrafine-grained steels, ISIJ International, 44 (2004) 6, pp. 1063-1071

[Okitsu et al. 2008] Okitsu, Y., Takata, N., and Tsuji, N., Mechanical properties of ultrafine grained ferritic steel sheets fabricated by rolling and annealing of duplex microstructure, J Mater Sci, 43 (2008) pp. 7391-7396

[Okitsu et al. 2009] Okitsu, Y., Takata, N., and Tsuji, N., A new route to fabricate ultrafine-grained structures in carbon steels without severe plastic deformation, Scripta Mater, 60 (2009), pp.76-79

[Pan et al. 2003] Pan, L.X., Karjalainen, L.P., and Somani, M.C., Observations on the formation of ultrafine ferrite grain size in steels by physical simulation routes, J Mater Sci Tech, 19 (2003) Suppl 1, pp. 112-114.

[Park et al. 2004] Park, K., Han, S., Shin, D., Lee, Y., Lee, K., and Lee, K., Effect of heat treatment on microstructures and tensile properties of ultrafine grained C-Mn steel containing 0.34mass% V, ISIJ International, 44 (2004) 6, pp. 1054-1062

[Park et al. 2007] Park, D.B., Kang, E.G., and Nam, W.J., Prediction of occurrence of delamination in cold drawn hyper-eutectoid steel wires, J Mater Proc Tech, 187-188 (2007) pp. 178-181

[Poorganji et al. 2008] Poorganji, B., Miyamoto, G., Maki, T., Furuhara, T., Formation of ultrafine grained ferrite by warm deformation of lath martensite in low-alloy steels with different carbon content, Scripta Mater, 59 (2008), pp. 279-281

[Saha & Ray 2007] Saha, R., and Ray, R., Microstructural and textural changes in a severely cold rolled boron-added interstitial-free steel, Scripta Mater, 57 (2007), pp. 841-844

[Sakai et al. 2008] Sakai, T., Belyakov, A., and Miura, H., Ultrafine grain formation in ferritic stainless steel during severe plastic deformation, Met & Mater Trans A, 39A (2008) 9, pp. 2206-2214

[Somani et al. 2009] Somani, M., Juntunen, P., Karjalainen, L., Misra, R., and Kyrolainen, A., Enhanced mechanical properties through reversion in metastable austenite stainless steels, Met & Mater Trans A, 40A (2009), pp.729-744

[Song et al. 2005] Song, R., Ponge, D., and Raabe, D., Improvement of work hardening rate of ultrafine grained steels through second phase particles, Scripta Mater, 52 (2005), pp. 1075-1080

[Song et al. 2005a] Song, R., Ponge, D., Raabe, D., and Kaspar, R., Microstructure and crystallographic texture of an ultrafine grained C-Mn steel and their evolution during warm deformation and annealing, Acta Mater, 53 (2005), pp. 845-858

[Song et al. 2005b] Song, R., Ponge, D., and Raabe, D., Influence of Mn content on microstructure and mechanical properties of ultrafine grained C-Mn steels, ISIJ International, 45 (2005) 11, pp. 1721-1726

[Song et al. 2005c] Song, R., Ponge, D., and Raabe, D., Mechanical properties of an ultrafine grained C-Mn steel processed by warm deformation and annealing, Acta Mater, 53 (2005), pp. 4881-4892

[Song et al. 2006] Song, R., Ponge, D., Raabe, D., Speer, J.G., and Matlock, D.K., Overview of processing, microstructure and mechanical properties of ultrafine grained bcc steels, Mater Sci & Eng A, 441 (2006), pp. 1-17

[Song et al. 2007] Song, H.R., Kang, E.G.and Nam, W.J., Effect of alloying elements on work hardening behavior in cold drawn hyper-eutectoid steel wires. Mater Sci & Eng A, 449-451 (2007), pp. 1147-1150

[Suh et al. 2005] Suh, D., Oh, C., and Kim, S., Limit of ferrite grain refinement by severe plastic deformation of austenite, Met & Mater Trans A, 36A (2005) 1057-1059

[Sun et al. 2005] Sun, S., Xiong, Y., Zhao, J., Lv, Z., Li, Y., Zhao, D., and Fu, W., Microstructure characteristics in high carbon steel rod after warm cross-wedge rolling, Scripta Mater, 53 (2005), pp. 137-140

[Takaki et al. 2004] Takaki, S., Tsuchiyama, T., Nakashima, K., Hidaka, H., Kawasaki, K., and Futamura, Y, Microstructure development of steel during severe plastic deformation, Metals & Mater International, 10 (2004) 6, pp. 533-539

[Takaki 2006] Takaki, S., Nano-structure control technology in steel materials, J Japan Inst of Light Metals, 56 (2006) 11, pp. 609-614 (in Japanese)

[Taleff et al. 2002] Taleff, E.M., Lewandowski, J.J. and Pourladian, B., Microstructure-property relationships in pearlitic eutectoid and hypereutectoid carbon steels. JOM, 54 (2002) 7, pp. 25-30

[Tarui et al. 2005] Tarui, T, Maruyama, N., Takahashi, J., Nishida, S. and Tashiro, H., Microstructure Control and Strengthening of High-carbon Steel Wires. Nippon Steel technical report No. 91, January 2005, pp. 56-61

[Todaka et al. 2007] Todaka, Y., Umemoto, M., Yin, J., Liu, Z., and Tsuchiya, K., Role of strain gradient on grain refinement by severe plastic deformation, Mater Sci & Eng A, 462 (2007), pp. 264-268

[Tashiro & Sato 1991] Tashiro, H. and Sato, H., Effect of alloying elements on the drawability of eutectoid steel wires. J Japan Inst of Metals, 55 (1991) 11, pp. 1232-1239

[Torizuka et al. 2006] Torizuka, S., Ohmori, A., Murty, S., Nagai, K., Effect of strain on microstructure and mechanical properties of multi-pass warm caliber rolled low carbon steel, Scripta Mater, 54 (2006) pp. 563-568

[Tsuji et al. 1992] Tsuji, N., Tsuzaki, K., and Maki, T., Effect of initial orientation on the cold rolling behavior of solidified columnar crystals in a 19% Cr ferritic stainless steel, ISIJ International, 32 (1992) 12, pp. 1319-1328

[Tsuji et al. 1993] Tsuji, N., Tsuzaki, K., and Maki, T., Effect of initial orientation on the recrystallization behavior of solidified columnar crystals in a 19% Cr ferritic stainless steel, ISIJ International, 33 (1993) 7, pp. 783-792

[Tsuji et al. 1994] Tsuji, N., Tsuzaki, K., and Maki, T., Effect of rolling reduction and annealing temperature on recrystallization structure of solidified columnar crystals in a 19% Cr ferritic stainless steel, ISIJ International, 34 (1994) 12, pp. 1008-1017

[Tsuji et al. 1999] Tsuji, N., Saito, Y., Utsunomiya, H., Tanigawa, S., Ultra-fine grained bulk steel produced by accumulative roll-bonding (ARB) process, Scripta Mater, 40 (1999) 7, pp. 795-800

[Tsuji et al. 2002] Tsuji, N., Ueji, R., Minamino, Y., and Saito, Y., A new and simple process to obtain nano-structured bulk low-carbon steel with superior mechanical property, Scripta Mater, 46 (2002), pp. 305-310

[Tsuji & Maki 2009] Tsuji, N. and Maki, T., Enhanced structural refinement by combining phase transformation and plastic deformation in steels, Scripta Mater, 60 (2009), pp. 1044-1049

[Tsuchida et al. 2008] Tsuchida, N., Masuda, H., Harada, Y., Fukaura, K., Tomota, Y., Nagai, K., Effect of ferrite grain size on tensile deformation behavior of a ferrite-cementite low carbon steel, Mater Sci & Eng A, 488 (2008), pp. 446-452

[Ueji et al. 2002] Ueji, R., Tsuji, N., Minamino, Y., and Koizumi, Y., Ultra grain refinement of plain low carbon steel by cold-rolling and annealing of martensite, Acta Mater, 50 (2002), pp. 4177-4189

[Umemoto 2003] Umemoto, M., Nanocrystallization of steels by severe plastic deformation, Mater Trans, 44 (2003) 10, pp.1900-1911

[US Pat 7462250] US Patent 7462250 - High strength, high toughness, high carbon steel wire rod and method of production of same. US Patent Issued on December 9, 2008

[Verlinden 2005] Verlinden, B., Severe plastic deformation of metals, Metalurgija - J of Metallurgy, 11 (2005) 3, pp. 165-182.

[Valiev et al. 2000] Valiev, R.Z., Islamgaliev, R.K., and Alexandrov, I.V., Bulk nanostructured materials from severe plastic deformation, Progress in Mater Sci, 45 (2000), pp. 103-189

[Vedani et al. 2006] Vedani, M., Angella, G., Bassani, P., and Tuissi, A., Metalli a struttura ultrafine ottenuti mediante deformazione plastica severa, la Metallurgia Italiana, (2006) 5, pp. 17-26 (in Italian)

[Wang et al. 2008] Wang, T., Zhang, F., Zhang, M., Lv, B., A novel process to obtain ultrafine-grained low carbon steel with bimodal grain size distribution for potentially improving ductility, Mater Sci & Eng A, 485 (2008), pp. 456-460

[Wang et al. 2009] Wang, T., Yang, J., Shang, C., Li, X., Zhang, B., and Zhang, F., Microstructure and impact toughness of low-alloy high-carbon steel austempered at low temperature, Scripta Mater, 61 (2009), pp. 434-437

[Xiao et al. 2006] Xiao, F., Liao, B., Qiao, G., Guan, S., Effect of hot deformation on phase transformation kinetics of 86CrMoV7 steel, Mater Charact, 57 (2006), pp. 306-313

[Xiong et al. 2007] Xiong, Y., Zhao, W., Sun, S., Lu, Z, and Fu, W., Evolution of pearlite microstructure during warm cross wedge rolling, Chinese J Mater Research, 21 (2007) 2, pp. 183-188 (in Chinese)

[Xu et al. 2002] Xu, Y., Umemoto, M., Tsuchiya, K., Comparison of characteristics of nanocrystalline ferrite in Fe-0.89C steels with pearlite and spheroidite structure produced by ball milling, Mater Trans, 43 (2002) 9, pp. 2205-2212

[Yan et al. 2009] Yan, H., Bi, H., Li, X., and Xu, Z., Microstructure, texture and grain boundaries character distribution evolution of ferritic stainless steel during rolling process, J Mater Proc Tech, 209 (2009), pp. 2627-2631

[Yanagimoto et al. 2009] Yanagimoto, J., Sugiyama, S., Yanagida, A., Iwamura, N., and Ishizuka, M., Control of ultrafine microstructure by single-pass heavy deformation and cold forging of metal, J Mater Proc Tech, 209 (2009), pp. 679-685

[Yang et al. 2009] Yang, Y., Bae, J., and Park, C., Nanostructure and mechanical properties of heavily cold-drawn steel wires, Mater Sci & Eng A, 508 (2009) pp. 148-155.

[Yokota et al. 2004] Yokota, T., Mateo, C., Bhadeshia, H., Formation of nanostructured steels by phase transformation, Scripta Mater, 51 (2004), pp.767-770

[Yoo et al. 2008] Yoo, C., Park, Y., Jung, Y., and Lee, Y., Effect of grain size on transformation-induced plasticity in an ultrafine-grained metastable austenitic steel, Scripta Mater, 59 (2008), pp. 71-74

[Yoon et al. 2008] Yoon, S., Horita, Z., and Kim, H., Finite element analysis of plastic deformation behavior during high pressure torsion processing, J Mater Proc Tech, 201 (2008), pp.32-36

[Yuan et al. 2006] Yuan, F., Wang, X., and Yang, X., Influence of calcium content on solid ratio of inclusions in Ca-treated liquid steel, J Univ Sci & Tech Beijing, 13 (2006) 6, pp. 486-489

[Zelin 2002] Zelin, M., Microstructure evolution in pearlitic steels during wire drawing, Acta Mater, 50 (2002) pp. 4431-4447

[Zhao et al. 2006] Zhao, M., Hanamura, T., Qiu, H., Nagai, K., and Yang, K., Dependence of strength and strength-elongation balance on the volume fraction of cementite particles in ultrafine grained ferrite/cementite steels, Scripta Mater, 54 (2006), pp. 1385-1389

[Zhao et al. 2007] Zhao, M., Yin, F., Hanamura, T., Nagai, and Atrens, A., Relationship between yield strength and grain size for a bimodal structural ultrafine-grained ferrite/cementite steel, Scripta Mater, 57 (2007), pp. 857-860

[Zhao et al. 2008] Zhao, M., Hanamura, T., Yin, F., Qiu, H., and Nagai, K., Formation of bimodal-sized structure and its tensile properties in a warm-rolled and annealed ultrafine-grained ferrite/cementite steel, Met & Mater Trans A, 39A (2008), pp. 1690-1701

[Zheng et al. 2008] Zheng, C., Li, D., Lu, S., and Li, Y., On ferrite refinement during the dynamic strain-induced transformation: A cellular automaton modeling, Scripta Mater, 58 (2008), pp. 838-841

Severe plastic deformation SPD

Angelina Gianni /Aalto University

29.08.2011

Abstract

This report consists of a literature review on severe plastic deformation processes.

Introduction

Severe plastic deformation (SPD) is one of the methods of obtaining very fine crystalline structure in different bulk metals and alloys which possess different crystallographic structure. SPD causes the formation of micrometer and sub-micrometer sized subgrains in the initially coarse grain materials. As a result of that enhanced mechanical performance is observed. It is believed that short and long-range intersecting shear bands produced by plastic deformation play major role at grain subdivision and local dynamic recovery and recrystallization processes contribute to grain refinement. Sufficiently large deformation leads to a distinct structure of dislocation-free and highly misoriented fine grains. The structural changes caused by SPD are reflected in improved mechanical properties of metals. These effects include increased hardness and yield stress, both featuring tendency to saturation.

Nanocrystalline and ultra-fine grain size metals have been found to have many excellent properties compared to their large grained counterparts. For example most metals with grain sizes in the nanocrystalline range show excellent strength, hardness and fatigue properties and improved friction, wear and corrosion properties combined with increased toughness even at low temperatures.

The development of severe plastic deformation (SPD) processing for grain size refinement of metals begun already in early 80's according to the literature.

SPD experimental processes

Obtaining large plastic deformation is a difficult task since in most metal forming processes it is limited by either material or tool failure. Few processes such as accumulative rolling and multi-pass drawing enable large plastic deformation to be achieved. However, metal foils or micro wires produced by these processes are not necessary the billet forms required. Therefore, special metal

forming processes capable for producing SPD without a major change in the billet are following processes:

$$\varepsilon = n\frac{2}{\sqrt{3}}\cot\varphi \qquad \varepsilon = n4\ln\left(\frac{D}{d}\right) \qquad \varepsilon = \frac{tg\gamma}{\sqrt{3}}$$

$$\varepsilon = n\frac{2}{\sqrt{3}}\ln\left(\frac{H}{W}\right) \qquad \varepsilon = n\frac{2}{\sqrt{3}}\ln\left(\frac{T}{t}\right) \qquad \varepsilon = n\frac{4}{\sqrt{3}}\ln\left(\frac{r+t}{r+0.5t}\right)$$
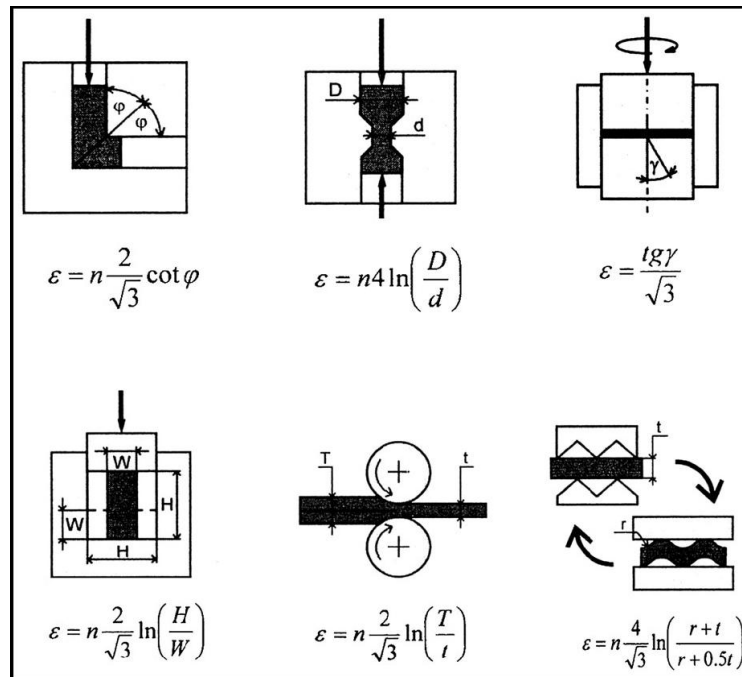
- **Equal channel angular pressing (ECAP, Segal 1977)**

ECAP is based on simple shear taking place in athin layer at the crossing plane of the equal channels. Has become the most frequently used SPD process. This is due to its low force requirement and the resulting low tool pressure. Also, the laboratory tooling is easy because of the simple tool geometry.

- **High pressure torsion (HPT, Valiev at al.,1989)**

Erbel seems to be the first who carried out HPT experiments for copper.
For this method a coin-shape sample is pressed between two anvils under hydrostatic pressure. During the build-up of the pressure the sample is pressed into the cavities in the anvil and a burr is formed at the edge of the sample. Then one anvil is rotated with respect to the other one and the rotation speed can be varied over a large range. This leads to a deformation of the sample by almost simple shear.

- **Accumulative roll bonding (ARB, Saito, Tsuji, Utsonomiya, Sakai, 1998)**

ARB is the only SPD process applicable to continuous production of bulky materials. In the process, 50% rolled material is cut into two, stacked to be the initial dimension and then rolled again. In order to obtain one-body solid material, the rolling in ARB is not only a deformation process but also a bonding process (roll-bonding).

- **Reciprocating extrusion-compression (REC, J and M.Richert, Zasadzinski, Korbel, 1979)**

RE involves the cyclic flow of metal between the alternating extrusion and compression chambers. The formation effect could obviously be achieved with the frame/die fixed and the movable punches or vice versa.

- **Cyclic close die forging (CCDF, Ghosh, 1988)**

- **Repetitive corrugation and straightening (RCS, Zhu, Lowe, Jiang, Huang 2001)**

This method involves bending a straight slab with corrugated tools and then restoring the straight shape of the slab with flat tool.

Literature review

Various aspects of structural changes caused by SPD have been the research goals in laboratories worldwide. Hundreds of papers are published each year in distinguished journals and conference proceeding. Also, the potential of SPD processing for the production of bulk nanostructure materials with special mechanical and physical properties has been highlighted at several international meetings known as the NanoSPD conferences. The International NanoSPD Steering Committee organizes this conference series and has also established formal definitions for the various terms associated with SPD processing.

General view of the number of papers during the last years

Number of papers per year

Year	Number of papers
2011	365
2010	805
2009	490
2008	540
2007	420
2006	420
2005	250
2004	250
2003	110
2002	100
2001	70
2000	60
1999	
1998	20
1997	10
1996	10
1995	20
1994	
1993	
1992	10
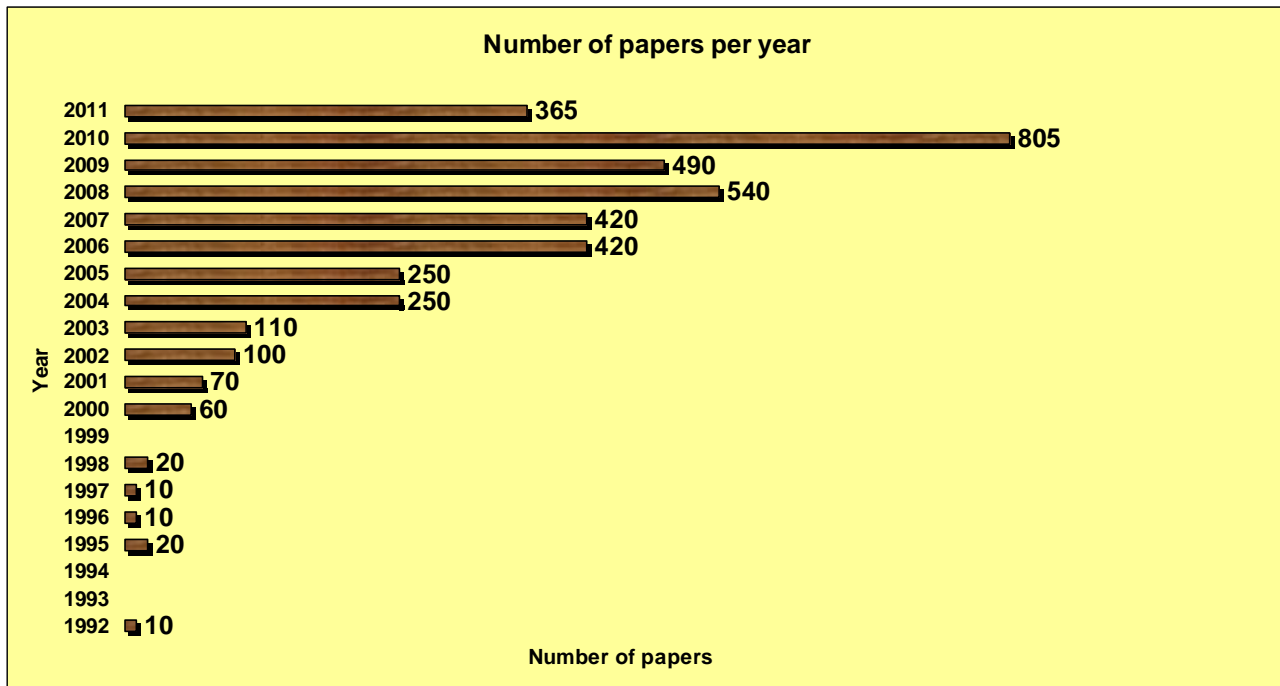
As we can noticed from the above diagram that the survey activity during last yeas has been increased with the pick in 2010. This is really expected due to the equipment and methods development.

In the next pages we are going to have a summary of some papers after the year 2008.

2011

❖ *Comparison of microstructures and mechanical properties of a Cu-Ag alloy processed using different severe plastic deformation modes (Y.Z Tian,Sd Wu, Z.F Zhang, RB Fihueiredo, N Gao, TG Langdon)*

This article is dealing with the investigation of the mechanical properties of a Cu-wt8% Ag alloy after was processed by ECAP, DPD and HPT at room temperature.
 The smallest grains produced by HPT. Also, the yield strength and micro hardness are inter-related over a wide range of values.

Results:

Using ECAP method gives large billets 20mm in diameter for 8 passes.

Gives banded grains and tensile strength of 720 MPa.

Using DPD method in room temperature led to properties and microstructure similar to those processing by ECAP fro 8 passes.

Deforming to a lighter strain by DPD at liquid nitrogen temperature may lead to a significantly higher tensile strength.

By using HPT method for 5 revolutions banded structure is observed on the transverse section and the tensile strength increases to about 1.1 GPa.

❖ *Strain hardening and softening in a nanocrystalline Ni-Fe alloy induced by severe plastic deformation (S. Ni, YB Wang, XZ Liao, SN Alhajeri, HQ Li, YH Zhao, EJ Lavernia, SP Ringer, TG Langdom, YT Zhu)*

In this article was investigated a high-pressure torsion (HPT) process by monitoring changes in hardness. First in the early stage o HPT strain was observed next followed by strain softening and finally a second strain hardening stage followed.

With the two hardening stages happened an increase in the dislocation density whereas the strain softening stage was accompanied by a reduction in the dislocation and twin densities. In such way is it predicted the dependence of hardness on the dislocation density in this material.

Conclusions:

The hardness evolution of the material is primarily controlled by the evolution of the dislocation density.

The effect on the hardness of HPT- induced grain growth the twinning is outweighed by the stronger role of the dislocations.

2010

❖ *Fatigue behaviour of light alloys with ultrafine grain structure prouced by severe plastic deformation: An overview (Yuri Estrin, Alexei Vinogradov)*

Abstract

In this article is being investigated the fatigue behaviour of light alloys with grain sizes reduced to the micron or submicron scale by SPD.

While the tensile strength is being enhanced the fatigue strength is usually not improved in the same extent. This observation is common to Al, Mg and Ti alloys.

Also are reviewed some effects that may influence that behaviour and the role of the alloying effects as the main contributors to fatigue strength.

The direct contribution of solutes to fatigue strength is usually stronger than their indirect effect through the influence of solutes on the grain refinement.

Results

Extreme grain refinement by SPD generally improves the fatigue performance of Al, Mg and Ti based light alloys.

However, the full potential of achieving favorable combinations of grain refinement and texture has not been explored.

Also, it has been concluded that complex interplay of the effects of grain refinement texture and alloy composition makes it difficult to assess the role of individual effects in the overall change of the fatigue behaviour after SPD processing.

Another factor is that the effect of residual macro-stresses which are 'locked-in' within a material after manufacturing. SPD gives rise to high residual stresses across the samples.

Also, it is sure that chemical composition plays a principal role in the fatigue properties of light alloys.

Finally, the authors maintained that SPD processes are overestimated since the properties may well be achieved with chemical composition more economically.

2009

❖ *Achieving high strength and high ductility in magnesium alloys using severe plastic deformation combined with low temperature aging. (WJ Kim, HG Jeong and HT Jeong)*

Abstract

At this paper was investigated a method of fabricating age-hardenable magnesium alloys with high strength and high ductility using high ratio differential speed rolling combined with low-temperature aging.

Procedure

One effective way to improve the strength of Mg alloys in bulk form is through grain refinement. This is because the grain size strengthening effect in Mg alloys high compared with other metals with bcc and fcc crystal structures, since Mg has a large Taylor factor.

Using equal channel angular pressing (ECAP), accumulative roll bonding (ARB) or equal channel angular rolling (ECAR) it is hard to simultaneously obtain high strength and high ductility in M alloys. So this paper propose the high ratio differential speed rolling (HRDSR) technique combined with low-temperature aging as a means to produce ultrafine-grained Mg alloy sheets with controlled texture which exhibit a superb combination of high strength and high ductility.

The processes AZ91 alloy sheet with a very small grain size, $< 0,3$ µm and weakened basal texture exhibited a high yield strength of over 12-14%. This technique can be readily applied to other Mg alloy systems with high age-hardening ability.

2008

❖ *Severe plastic deformation of metals by high-pressure tube twisting*. (*LS Toth, M Arzaghi, JJ Fundenberger, B Beausir, O Bouaziz and R Arruffat-Massion*)

Abstarct

This article is dealing with a new severe plastic deformation process that is suitable for deforming cylindrical tubes to extremely large strains without changing their dimensions. Thin-walled tubes being deforming to very high strains in a single operation.

Procedure

 The tube is twisted by an external torque with the help of the friction force generated by hydrostatic pressure.

Severe plastic deformation processes for steel (SPD)

❖ *Ultra-high Strength Wire Rods and Wires Based on Severe Plastic Deformation (SPD) and Ultrafine-grained (UFG) Microstructure (Leijun Li and Jouko Virta, VTT Technical Research Center of Finland, September 2009)*

Ultrafine grained steels can be obtained by either severe plastic deformation (SPD) or advanced thermo mechanical processing (ATP). Both are methods for producing nanocrystalline structures in bulk quantity of steels. Production of steel using SPD processes is less developed in laboratories than advanced thermomechanical processing method which has been successfully developed to produce large quantities of ultrahigh strength steel wires for current engineering projects.

For low-carbon alloy steels, cold or warm rolling and annealing of a martensitic starting microstructure have been produce ultrafine grained microstructure with excellent strength, ductility and toughness.

For hypereutectoid steel with carbon content higher than 1 % ultrafine grained microstructure can be obtained by cold drawing.

Ultrahigh carbon steel wires with 4000 to 5000 MPa tensile strength have been produced in quantity by Japanese steel makers.

❖ *Nanocrystalline and Ultrafine Grain Size Steels by Severe Plastic Deformation – Sheet Steels and Surface Nanocrystallization (Dr. Mikko Hokka, Tampere University of Technology - Department of Materials Science, The Ohio State University – Department of Mechanical Engineering)*

In the case of steel the most interesting properties that are improved compared to the coarse grained steels include strength, fatigue corrosion wear and toughness.

Grain refinement is the only strengthening method which increases the strength without drastic embrittlement of the steel. In practice small grain sizes can be achieved by advanced thermomechanical treatments or by severe plastic deformation. Good results can be achieved by both methods; however the advanced thermomechanical treatments can only reach grain sizes

around 1μm, whereas the severe plastic deformation processing can refine the grain size to the nanometre range.

The price of the SPD processed metals is still very high due to the lack of continuous mass production. Scaling up the capabilities is the key to lowering the costs for more competitive prices. The benefits of grain refinement by SPD include reduce need for expensive alloying and heat treatments such as quenching and tempering.

It is proved that equal channel angular pressing (ECAP) is so far the most effective method to produce nanocrystalline and ultrafine grained steels the applicability of this method to continuous production is somewhat limited.

References:

- Processing of metals by severe plastic deformation (SPD)-structure and mechanical properties respond. (J.Zrink, S.V. Dobatkin, I.Mamuzic)
- Severe plastic deformation (SPD) processes for metals (A.Azushima, R.Kopp, A.Korhonen, D.Y Yang, F.Micari, G.D Lahoti, P.Groche, J.Yanagimoto, N.Tsuji, A.Rosochowski, A.Yanagida)
- Severe plastic deformation of metals by high-pressure tube twisting. (LS Toth, M Arzaghi, JJ Fundenberger, B Beausir, O Bouaziz and R Arruffat-Massion)
- Nanocrystalline and Ultrafine Grain Size Steels by Severe Plastic Deformation – Sheet Steels and Surface Nanocrystallization (Dr. Mikko Hokka, Tampere University of Technology - Department of Materials Science, The Ohio State University – Department of Mechanical Engineering)
- Ultra-high Strength Wire Rods and Wires Based on Severe Plastic Deformation (SPD) and Ultrafine-grained (UFG) Microstructure (Leijun Li and Jouko Virta, VTT Technical Research Center of Finland, September 2009)
- Achieving high strength and high ductility in magnesium alloys using severe plastic deformation combined with low temperature aging. (WJ Kim, HG Jeong and HT Jeong)
- Fatigue behaviour of light alloys with ultrafine grain structure prouced by severe plastic deformation: An overview (Yuri Estrin, Alexei Vinogradov)
- Strain hardening and softening in a nanocrystalline Ni-Fe alloy induced by severe plastic deformation (S. Ni, YB Wang, XZ Liao, SN Alhajeri, HQ Li, YH Zhao, EJ Lavernia, SP Ringer, TG Langdom, YT Zhu)

- Comparison of microstructures and mechanical properties of a Cu-Ag alloy processed using different severe plastic deformation modes (Y.Z Tian,Sd Wu, Z.F Zhang, RB Fihueiredo, N Gao, TG Langdon)
- Science direct
- Google Scholar

UFG ferrous metals produced by SPD

Andrzej Rosochowski, University of Strathclyde, Glasgow UK

Introduction

Severe plastic deformation (SPD) is a new metal forming discipline, with the scope of refining grain structure of ordinary metals and alloys so their average grain size is reduced to the level below 1 micron (so called ultrafine grained (UFG) metals). An additional characteristic of the SPD processes is their ability to retain the shape and dimensions of the processed billets. This is what differentiates SPD from other metal forming techniques, in which such dimensions are substantially reduced like in rolling or drawing. The main purpose of grain size reduction is to achieve unique strength properties which allow using less alloyed metals and/or designing lighter structures. The SPD technology has been developed over the last 30 years, with the last 10 years resulting in the vast majority of more than 3000 publications in this field so far. This large number of publications reflects the multithreaded character of research, which involves structural investigations, properties testing and process developments for different metals. The vast majority of the SPD research has been done for aluminium and copper alloys. However, there is also an interest in other materials such as titanium, magnesium and ferrous metals. This report is based on two batches of selected literature on UFG ferrous metals published before 2005 and recently.

Research on UFG ferrous metals before 2005

The research on UFG ferrous metals was initially carried out for pure iron and eventually also for iron alloys. The following tables and figures show the main results of this research as reported in [1-7]. Equal channel angular pressing (ECAP) and high pressure torsion (HPT) are the two most popular SPD processes used in these researches. HV indicates the micro-hardness measured on Vickers scale, YS is the yield strength of the material, UTS its ultimate tensile strength and El is the total elongation at fracture.

Table 1

Material	Process	HV	YS MPa	UTS MPa	El. %	Comments
α-Fe		90	200	350	21	[1]
	ECAP	300	850	980	6	
Armco iron	HPT	470				Disks 10×0.5 mm; maximum strain 9 revolutions; maximum grain size after HPT 100-200 nm; hardness retained till 400°C [2].
Armco iron 0.035C, 0.2Si, 0.2Mn, 0.0012P, 0.008S	HPT		1000	2200		Annealing in the temperature range of 200-400°C for 1 hour does not lead to a notable grain growth [3].
	Anneal 200°C		1170	1600		
	Anneal 400°C		840			
	Anneal 500°C		500	1000	10	

As can be seen in Table 1 for α-Fe, refining its grain structure by ECAP results in much increased YS and substantially increased UTS. El is reduced, which although not universal is quite common for many metals strengthened by SPD. It is also common that HPT produces better results than ECAP as illustrated by HV=470 rather than HV=300 (because of higher pressure). Another characteristic feature of UFG metals is that UTS is only slightly higher than YS, which means low uniform elongation. The 2200 MPa UTS claimed in [3] is unusually high (?), however, the interesting fact illustrated in Fig. 1, is the relative stability of the UFG structure subjected to annealing for 1 hour at up to 500°C. This is reassuring since early research suggested a possibility of rapid grain growth at elevated temperatures because of the large energy stored in

non-equilibrium grain boundaries of UFG metals. Apparently, small addition of alloying elements (C, Si, Mn, etc.) increases thermal stability of ferrous alloys.
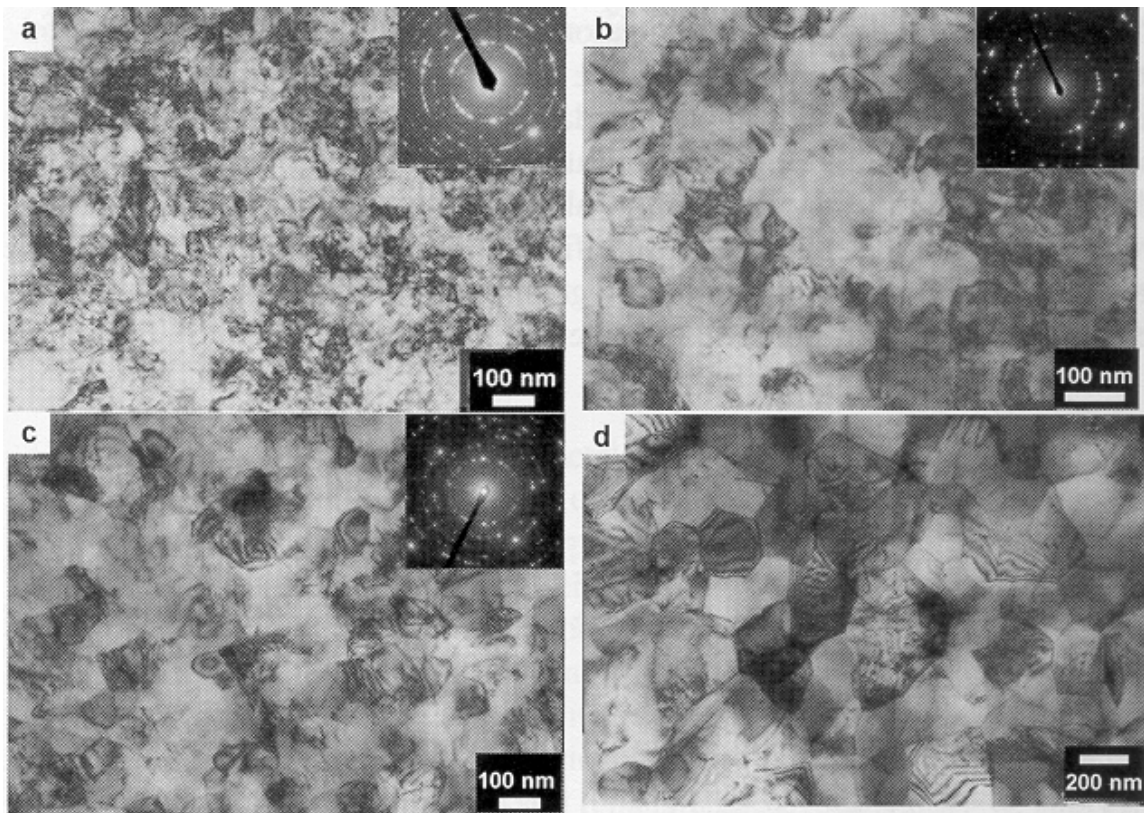

Fig. 1 Armco iron after HPT (a) and annealing for 1 hour at 200°C (b), 400°C (c) and 500°C (d) [3]

Table 2 [2]

Material	Process	HV	Comments
0.08C-18Cr-0.6Ti ferritic steel	Compression to ε=0.5	320	Disks 10×0.5 mm.
	HPT	580	Maximum strain 9 revolutions.
0.08C-18Cr-10Ni-0.6Ti austenitic steel	Compression to ε=0.5	320	Maximum grain size after HPT 50-100 nm. For austenitic steels α→γ and α→ε→γ transformations observed.
	HPT	580	
0.05C-15Cr-10Ni-V-N austenitic steel	Compression to ε=0.5	250	Hardness retained till 400°C.
	HPT	580	

For ferritic and austenitic steels subjected to HPT at room temperature, the hardness doubles and remains unchanged till 400°C (Table 2). The minimum grain size in the austenitic steels reaches 50nm, which means that alloyed metals, which have a more complex structure, are more susceptible to grain refinement by SPD. Interestingly, SPD is also responsible for the martensitic α→γ and α→ε→γ transformations.

Ferritic/pearlitic steel was subjected to a thermo-mechanical treatment, which resulted in different structures and properties (Table 3) [4]. Fig. 2 compares the original ferrite/pearlite (F/P) structure with one featuring a nearly UFG structure of ferrite (average grain size 2.7µm) and finely dispersed cementite (Uf-F/C structure). The main emphasis was put on toughness measured in the Charpy impact test (Fig. 3); the Uf-P/C material exhibited improved toughness, which manifested itself as a substantial reduction in the ductile-brittle transition temperature.

Table 3 [4]

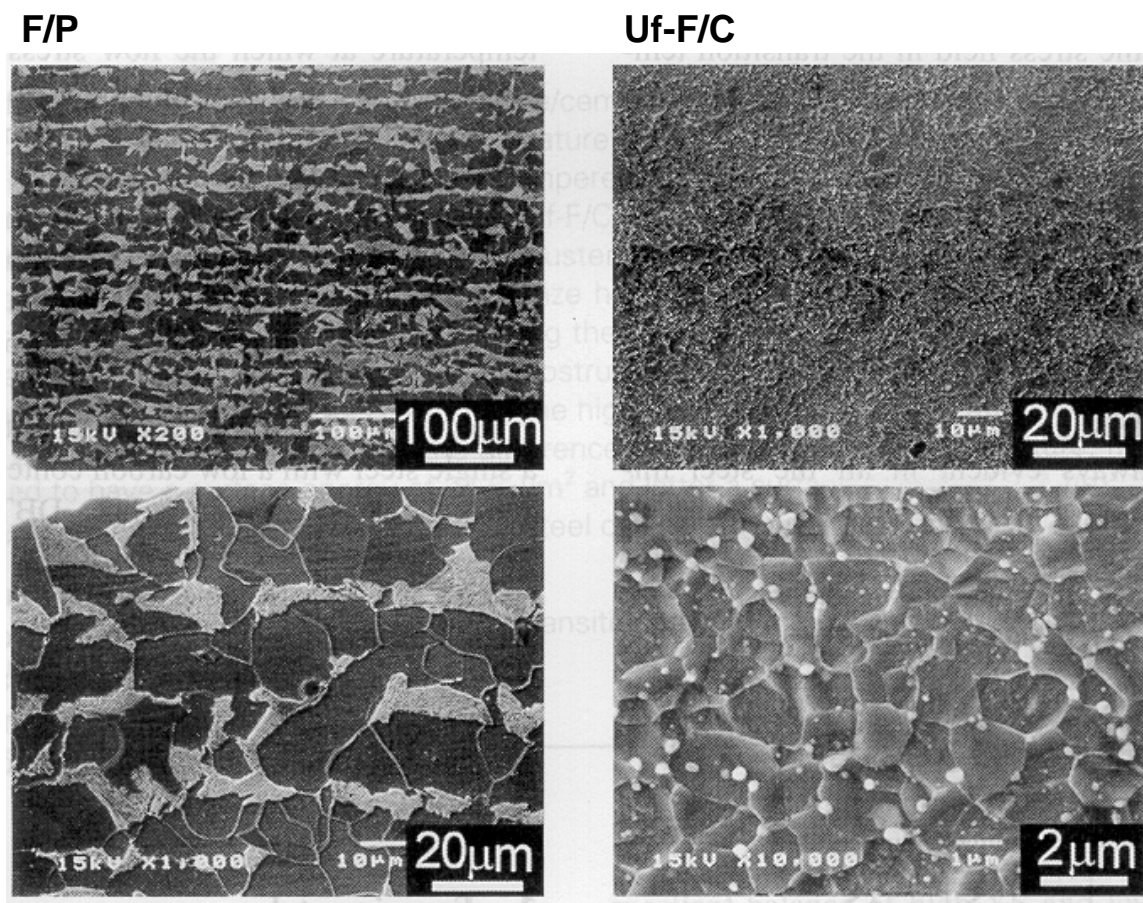| Material	Process	HV	YS MPa	UTS MPa	El. %	Charpy impact energy at 230 K, J	Comments
0.15C ferritic pearlitic steel 0.148C, 0.33Si, 1.41Mn, 0.001P, 0.001S, 0.003T-Al, 0.0012T-N	F/P		261	463	35	230	Homogenized for 1800 s at 1473 K and hot rolled to 23 mm plate (F/P samples). Hot rolled plate heated for 1800 s at 1173 K, water quenched and caliber-warm-rolled into 12 mm square rods with accumulated area reduction of 85% (Uf-F/C samples). Uf-F/C samples annealed for 3600 s at 1373 K and water quenched (Q samples). Q samples tempered at 723 K (QT samples).
	Uf-F/C		536	612	21	300	
	Q		619	1027	4	15	
	QT		548	676	17	110	

F/P   **Uf-F/C**

Fig. 2 Initial and ultrafine structure of a 0.15C ferritic/pearlitic steel [4]
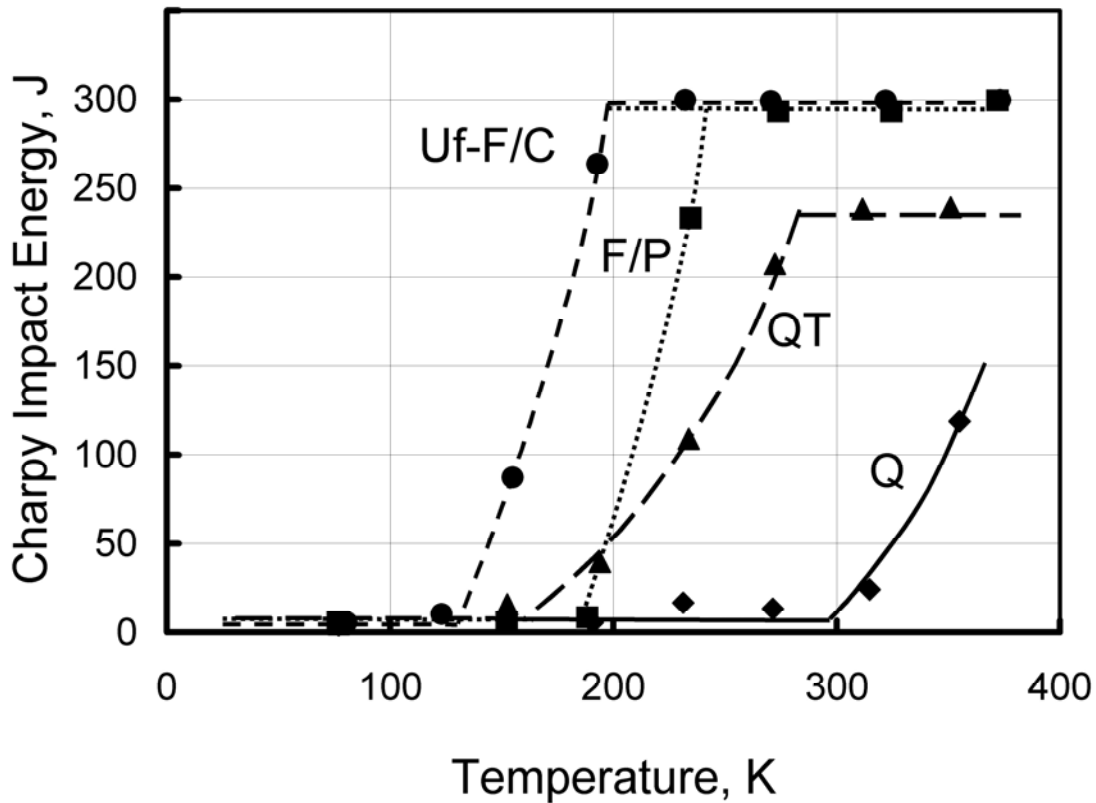
Fig. 3 Charpy impact absorbed energy as a function of test temperature for steel structures identified in Table 3 [4]

Table 4 [5]

Material	Process	HV	YS MPa	UTS MPa	El. %	Comments
0.15C ferritic			310	480	30	Austenitised at 1200°C for 1 hour and air cooled (80% ferrite + 20% pearlite; ferrite grain size 30µm).
pearlitic CS steel 0.15C, 0.25Si, 1.1Mn	ECAP		930	940	11	4 passes of ECAP at 350°C, with rotation of sample by 180° between consecutive passes; ferrite grain structure 200-300 nm; carbon from cementite partially dissolved; after-ECAP annealing for 1 hour.
	Anneal 420°C		900	910	13	
	Anneal 480°C		810	820	12	
	Anneal 540°C		690	710	21	

Similar 0.15C ferritic/pearlitic steel called CS, as well as steel CS with a small addition of vanadium and nitrogen called CSV, was investigated in [5]. The results for steel CS are presented in Table 4. A relatively good resistance to annealing is attributed to partially dissolved carbon from pearlitic cementite, which increases the carbon content in ferrite above the equilibrium level, which in turn leads to nano-particles of cementite precipitating at grain boundaries during annealing; such precipitates have a stabilising effect on grain growth. This effect was found to be higher for 8 passes of ECAP compared to 4 passes, which confirms the fact that the dissolution of carbon is higher for severely worked material. Microalloying with
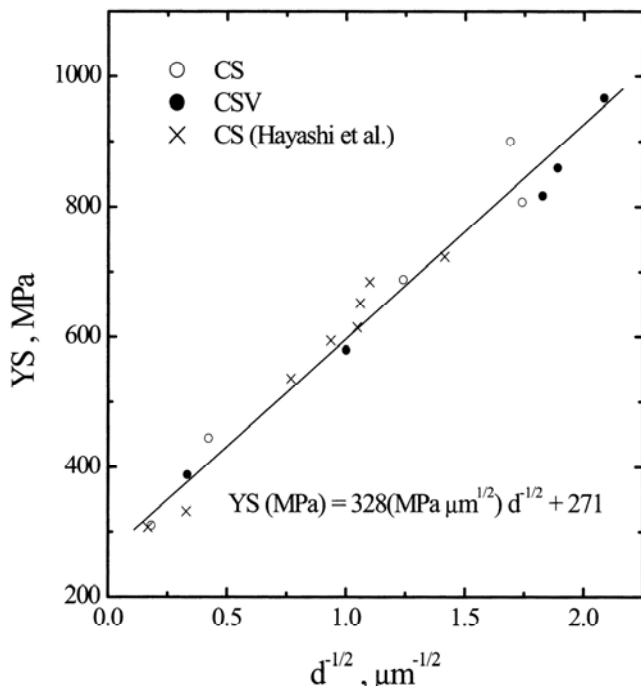
Fig. 4 The Hall-Petch plot for the yield strength of
the UFG CS and CSV steels [5]

carbide and/or nitride forming elements has also proved to be beneficial as indicated by the results obtained for steel CSV (not quoted here). The numerous results of yield strength obtained for CS and CSV steels enabled the yield strength vs. grain size relationship to be established. As can be seen in Fig. 4, this relationship follows the well known Hall-Petch linear equation relating the yield strength (YS) and the inverse of square root of the grain size (d).

$$YS\,(MPa) = 328(MPa\,\mu m^{1/2})\,d^{-1/2} + 271$$

Table 5 presents mechanical properties for 0.17C steel [2, 6]. As usual, the UFG structure obtained by ECAP at 500°C (Fig. 5) resulted in higher strength and reduced ductility. Unfortunately, the impact toughness was very low (0.39 MJm^{-2}). The remedy was reheating the material after ECAP for 30 minutes at 550°C, which resulted in the average grain size increased to 4 µm and toughness increased fivefold, to 1.98.

0.5 µm   0.3 µm
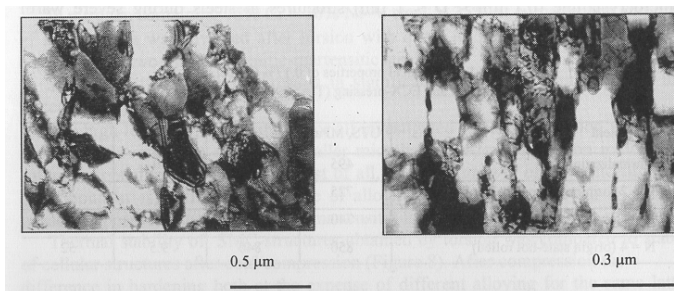
Fig. 5 Structure of 0.17C steel after 4 passes of
ECAP at 500°C [6]

Table 5 [2, 6]

Material	Process		YS MPa	UTS MPa	El. %	Area red. %	Impact toughness KCV MJ/m2	Comments
0.17C ferritic pearlitic steel 0.17C, 0.18Si, 0.32Mn, <0.04P, <0.05S	Normalised		295	495	30	75		Mixed microstructure with low and high-angle grain boundaries and average grain size of 0.35 µm; after-ECAP heating to 550 °C for 30 min produced a mixture of recrystallised grains (0.4-5 µm) and subgrains (0.26-0.65 µm).
	Norm	4 passes of 90° ECAP at 500°C	715	740	13	53		
	Hot rolled		840	850	10	52	0.39 at 20°C	

A similar effect of increased impact toughness has been obtained for 0.2C steel subjected to hot ECAP at 750°C; compared to warm ECAP at 550°C, impact toughness at 20°C increased from 0.55 MJm^{-2} to 2 MJm^{-2} (Table 6).

Table 6 [6]

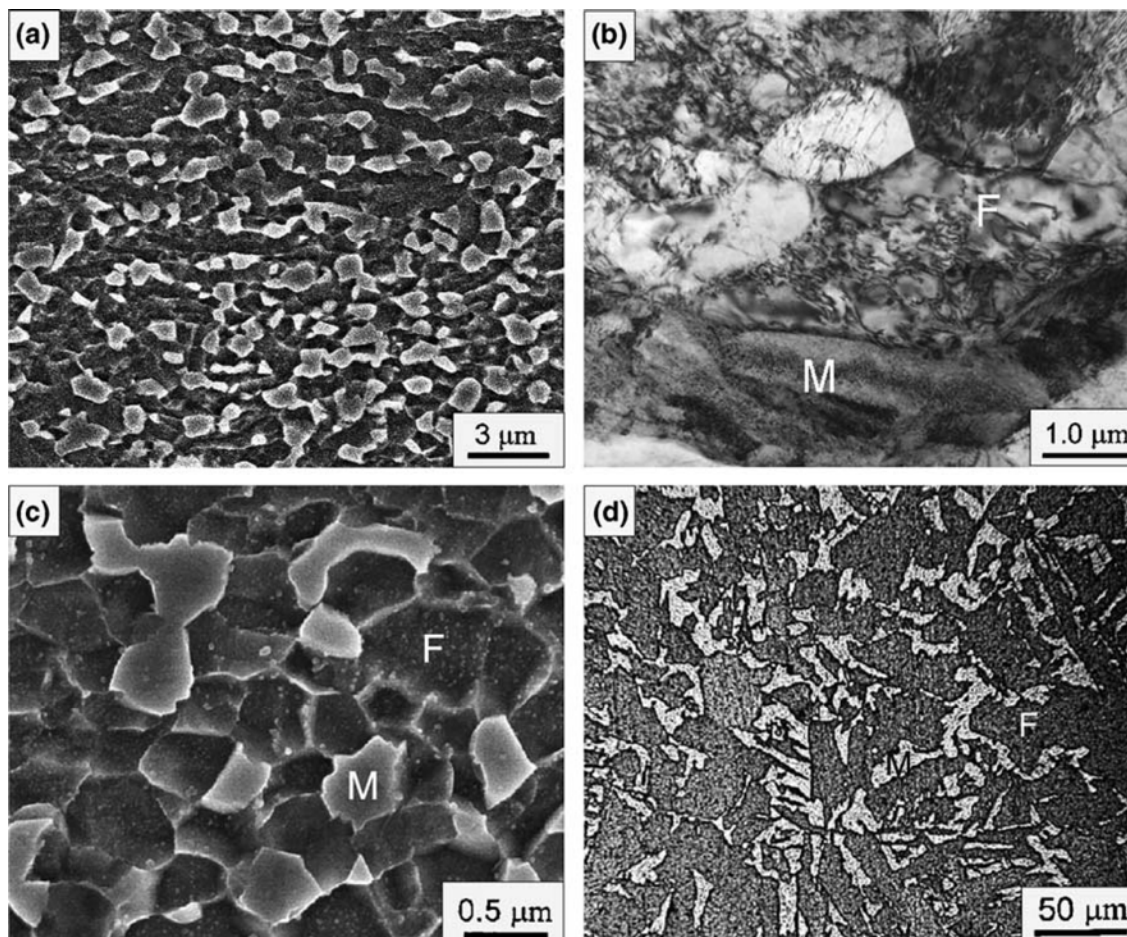| Material	Process	HV	YS MPa	UTS MPa	El. %	Area red. %	Impact toughness KCV MJ/m2	Comments
0.2CMnSiV 0.21C, 0.78Si, 0.89Mn, 0.16V, <0.03P, <0.025S	4 passes of 90° ECAP at 550°C		1110	1120	8	40	0.55 at 20°C; 0.15 at -40°C	Average grain size 0.3-0.5 µm
	4 passes of 90° ECAP at 750°C		905	975	13	36	2 at 20°C; 1.2 at -40°C	
	8 passes of 110° ECAP at 750°C		820	850	15	45	2.52 at 20°C	Recrystallised grains 0.3-6 µm and subgrains 0.5 µm

Fig. 6. Structure of low-carbon manganese dual-phase steel; SEM of UFG-DP (a, b, c) and OM of CG-DP (d) [7]

To deal with low ductility and especially low uniform elongation, the low carbon - manganese CS steel with ferritic/pearlitic structure (investigated earlier in [5]) was subjected to intercritical annealing after ECAP [7]. The ECAP temperature was increased to 500°C in order to minimize grain growth of retained ferrite during subsequent intercritical annealing. Intercritical annealing requires heating up the material above the A_{c1} temperature that is in a ferrite/austenite two phase region. That temperature was chosen to be 740°C over 10 minutes. As a result of subsequent water quenching, a dual phase ferrite/martensite structure was created with uniformly distributed martensite islands (Fig. 6 a, b, c). This structure differs from less regular ferrite/martensite structure obtained by intercritical annealing without ECAP (Fig. 6 d). This is attributed to the specific ECAPed structure and also dissolved cementite, which promote creation of the regular ferrite/martensite structure. The mechanical properties are listed in Table 7 and also illustrated in Fig. 7. The properties of UFG-DP steel are superior to CG-DP steel in terms of both UTS and elongation. The lower yield strength, compared to the ECAPed material, results in much improved uniform deformation. It seems that the ability of the material to strain harden has been restored.

Table 7 [7]

| Material	Process	YS MPa	UTS MPa	El. tot. %	El.uni. %	Comments
0.15C ferritic pearlitic CS steel 0.15C, 0.25Si, 1.1Mn		310	480	30	18	Austenitised at 1200°C for 1 hour and air cooled (80% ferrite + 20% pearlite; grain size 30µm).
	ECAP at 500°C	600	610	22	10	4 passes of ECAP, with billet rotation by 180°.
	ECAP at 500°C + intercritical annealing	581	978	17.6	9.3	Intercritical annealing at 740°C for 10 min and water quenched; DP structure with 28.2% martensite; dm=1.3µm; df=1.4µm.
	Intercritical annealing	510	843	13.5	9.8	Itercritical annealing at 740°C for 10 min. and water quenched; DP structure with 22.1% martensite; dm=9.8µm; df=19.4µm.
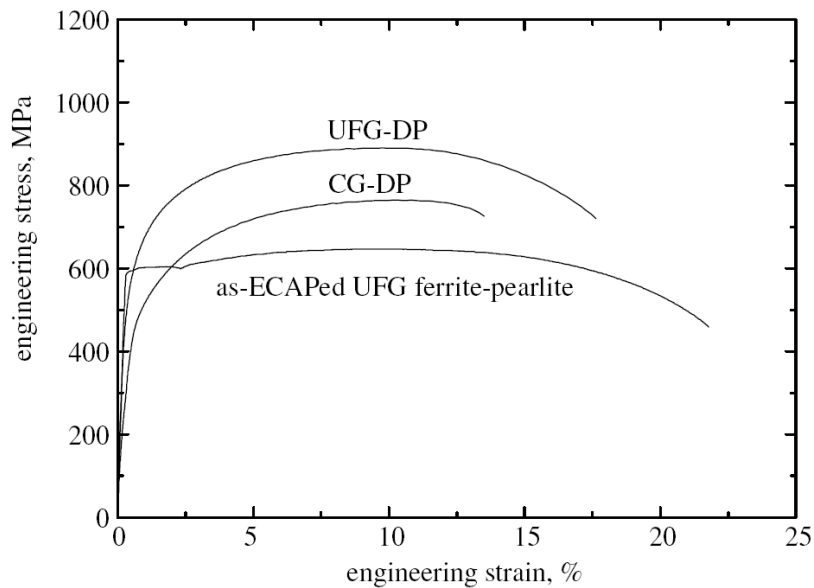
Fig. 7 Engineering stress-strain curves for the materials investigated in [7]

Recent research on UFG ferrous metals
The yield strength vs. total elongation results for different UFG steels reported above can be mapped on a graph illustrating these properties for the conventional and advanced steels currently in use. As indicated by red squares in Fig. 8, the UFG steels do not break the known pattern for the current materials, where higher strength can only be achieved by sacrificing ductility. The only benefit of UFG materials is that they all fall into the category of ultra high strength steels, irrespective of their simple metallurgical origin. However, in the recent years, new evidence has been published, which suggests that the strength vs. ductility trend can be overcome.
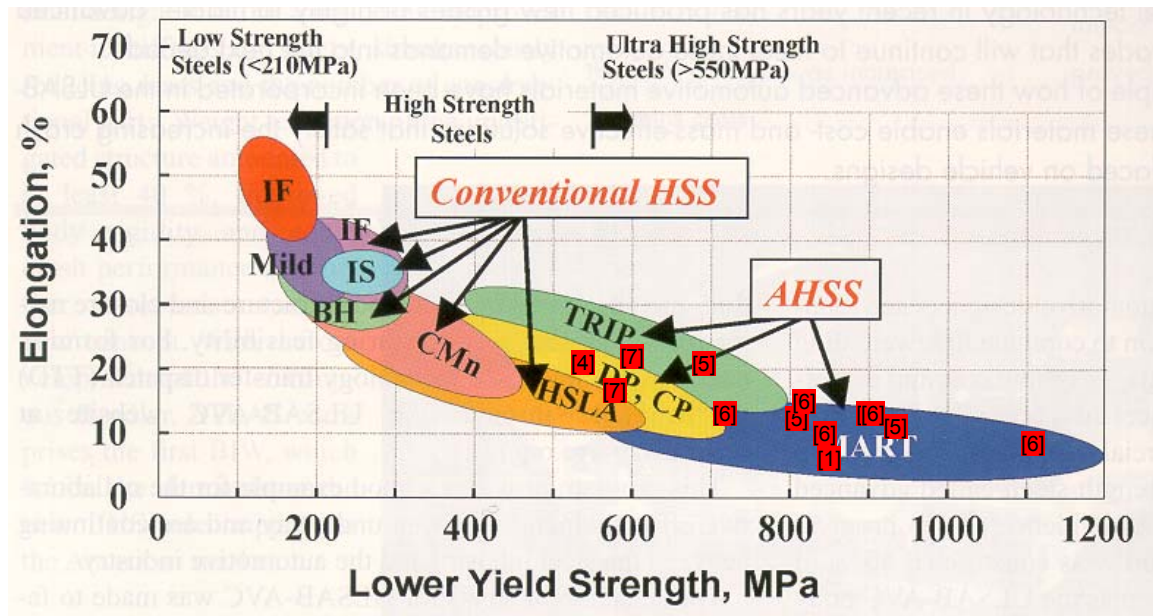

Fig. 8 Total elongation vs. yield strength for conventional/advanced steels and UFG low carbon steels.

In [8], for example, an ingot of low carbon steel (0.1C, 0.01Si, 1.98Mn, 0.002P, 0.001S, 0.018Al, 0.018Nb, 0.015B, 0.0011N) was hot rolled to the thickness of 6.8 mm in the austenite region followed by air-cooling to 540°C and substantial cooling by water spray to room temperature to obtain a duplex microstructure of ferrite and martensite. The hot rolled sheets were cold-rolled in multi-passes at room temperature using a four-high rolling mill with lubricant. The total reduction in thickness through the cold-rolling was 91%, corresponding to an equivalent plastic strain of 2.8. In order to obtain UFG microstructures, the cold-rolled sheets 150 mm wide and 0.6 mm thick were annealed over 120 seconds at 625°C and at 655°C in a salt bath followed by water cooling.
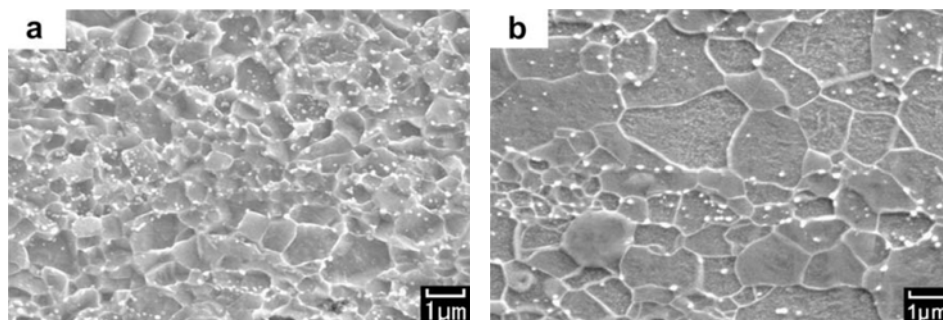

Fig. 9 SEM images of UFG steel obtained by annealing at 625°C (a) and 655°C (b) [8]

The microstructure obtained via this process was fully annealed ultrafine grains of ferrite including homogenously dispersed cementite particles. The mean ferrite grain size obtained was 0.49 μm (Fig. 9 a) and 0.85 μm (Fig. 9 b). The resulting properties are listed in Table 8. The UFG structure has led to high strength and low ductility, which follows the trend in Fig. 8. Annealing at 650°C over 57.6 ks has increased the average grain size to 2.6 μm and halved the yield strength compared to the best result for the UFG material. However, it also increased the total elongation to 35.1%. Despite much lower strength, this combination of strength and ductility is promising, as indicated by a green square in Fig. 10.

Table 8 [8]

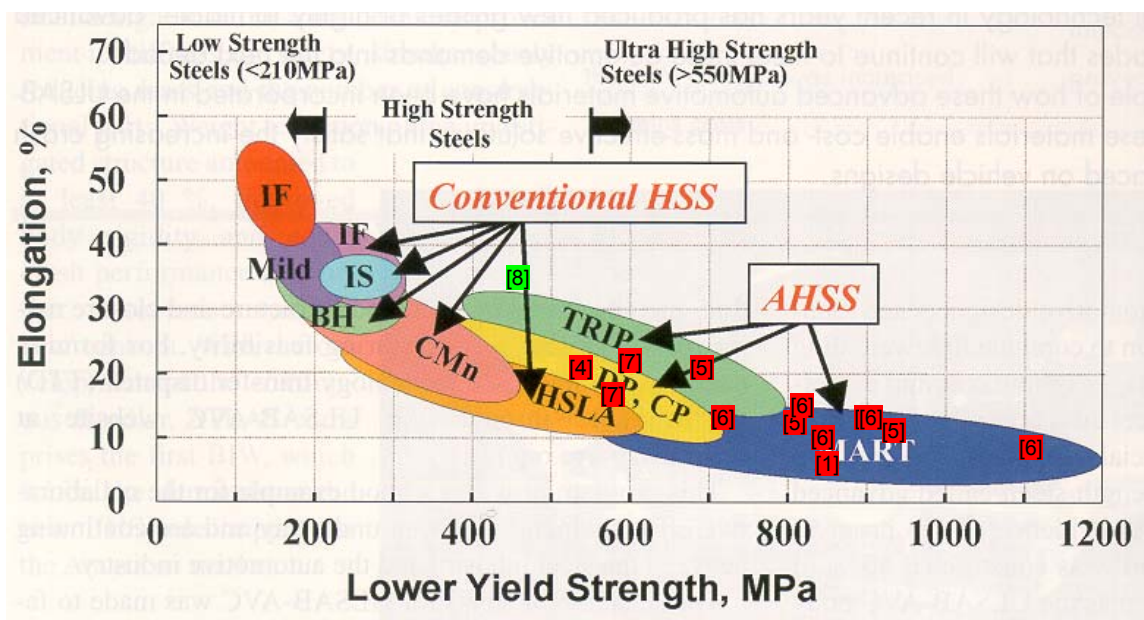| Annealing temperature and time	Mean ferrite grain size (μm)	0.2% offset stress (MPa)	Tensile strength (MPa)	Uniform elongation (%)	Total elongation (%)
625 °C, 120 s	0.49	966	966	0.6	8.4
655 °C, 120 s	0.85	658	672	4.1	16.7
650 °C, 57.6 ks [8]	2.6	457	476	19.6	35.1

Fig. 10 Total elongation vs. yield strength for an annealed low carbon steel indicated by a green square [8]

Another attempt to obtain a favourable combination of strength and ductility dealt with 0.17C-Mn steel (0.17C, 0.28.Si, 1.63Mn, 0,0021P, 0.0038S, 0.036Al, 0.0025N) [9]. After 3 min austenitisation at 100°C above Ae3, a one-step deformation pass was imposed at 870°C in order to obtain fully recrystallized austenite. This was followed by a controlled cooling procedure down to the pearlite finish temperature at moderate cooling rates to obtain a bainite free ferrite-pearlite microstructure. The large strain warm deformation was performed by exerting a four-step flat compression series with an inter-pass time of 0.5 s. Each of the four subsequent deformation steps imposed a logarithmic strain of ε=0.4 at a strain rate of 10 s-1. Subsequently, an annealing treatment of 2 h at 550°C was applied. The resulting microstructure was an ultrafine grained ferrite matrix with homogeneously distributed spheroidized cementite particles which make up 2-3 vol.% (UFG F/C steel). After the intercritical annealing, the microstructure consisted of 25% martensite and had an average ferrite and martensite grain size of 1-2 μm (UFG F/M DP steel). The whole procedure is schematically illustrated in Fig. 11, while mechanical properties in Fig. 12

and Table 9. While the UFG F/M DP steel exhibits very good strain hardening and tensile strength, the UFG F/C steel gives a better combination of yield strength and elongation (Fig. 13).
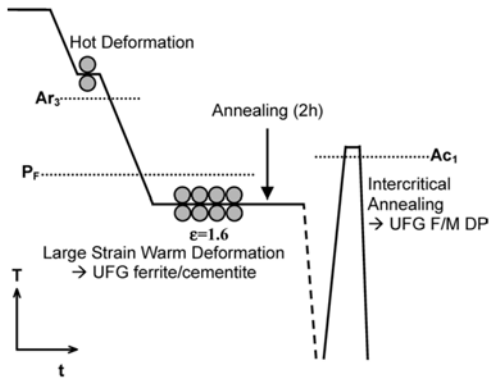
Fig. 11 Thermo-mechanical treatment for 0.17C-Mn steel [9]
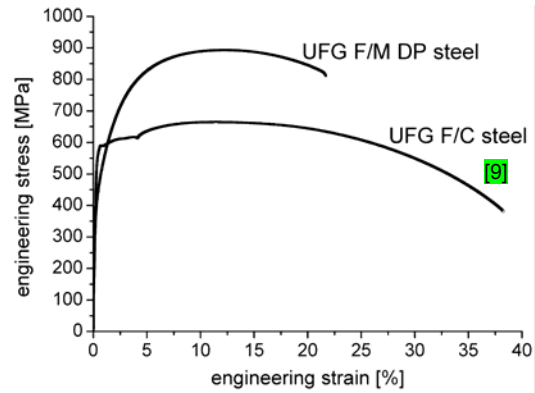
Fig. 12 Stress-strain curves for 17C-Mn steel [9]

Table 9 [9]

Steel	σ_y [MPa]	UTS [MPa]	yield ratio	ε_u [%]	ε_{tot} [%]	RA [%]
UFG F/C [9]	589	665	0.89	10.6	38	65
UFG F/M DP	452	893	0.51	11.3	22	31
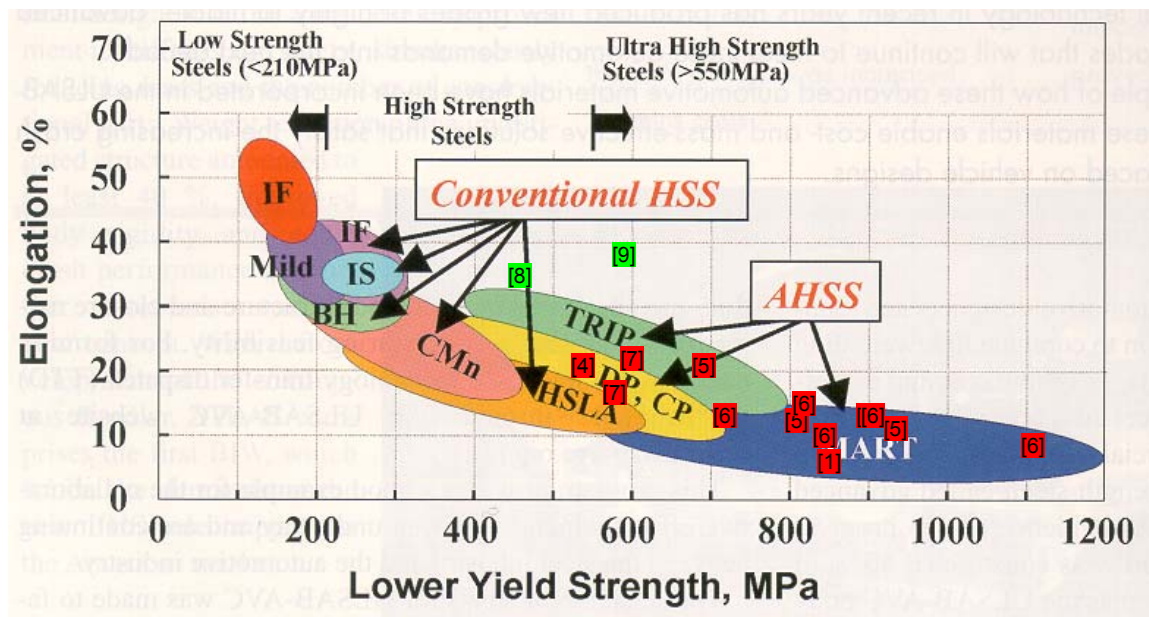
Fig. 13 Total elongation vs. yield strength for a UFG F/C 0.17C-Mn steel indicated by a green square [9]

The material selected to study in [10] was an Fe–Cr–Ni–Mn austenitic steel with a nominal composition in wt % of 10Cr, 5Ni, 8Mn, 0.1C, and balance Fe. The ingot was hot rolled to a 10-mm-thick plate and was solution treated at 1473 K for 30 min. The solution-treated plate was cold rolled with about 75% thickness reduction, and most of the γ (fcc) austenite phase was transformed into the α (bcc) martensite phase. Then, the plate was annealed at 913 K for 10 min to induce the reverse transformation of the mechanically induced α back to γ. After the reverse transformation, the UFG austenite (γ) was obtained, with the average grain size o 0.35 µm (Fig. 14). The macroscopic tensile stress-strain curve recorded during the *in situ* neutron diffraction measurements is presented in Fig. 15. The same figure shows the stress - strain curve for the CG material obtained after solution treatment, which resulted in the average grain size of 50 µm. While UTS for both materials remains the same, yield strength has been increased 3.5 times for the UFG material. Uniform elongation has reached nearly 20% while total elongation 36%. The improved ductility is contributed to the martensitic transformation during cold deformation. Fig. 16 illustrates the unusual combination of yield strength and total elongation obtained in the UFG TRIP steel.
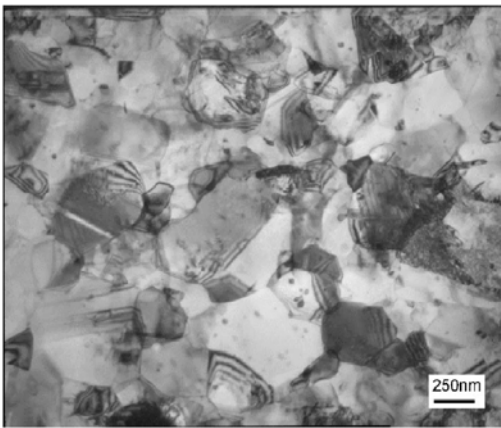
Fig. 14 TEM image of UFG TRIP steel [10]
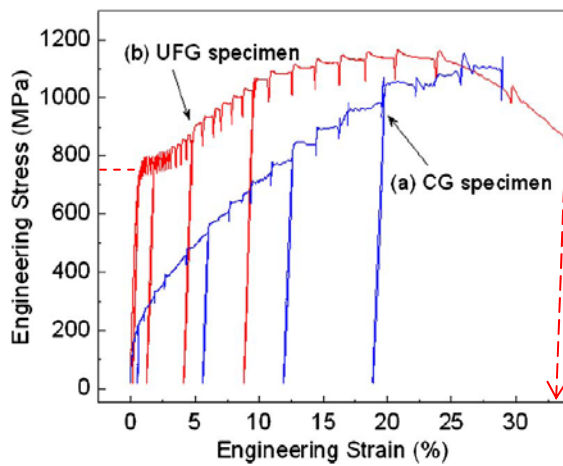
Fig. 15 Tensile stress - strain curves [10]
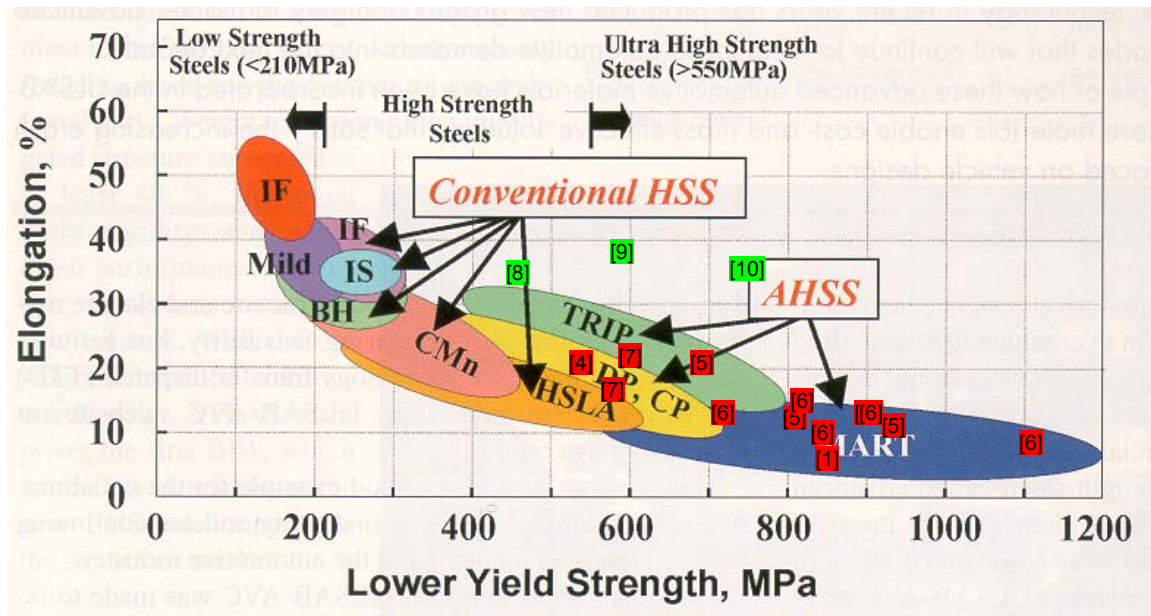
Fig. 16 Total elongation vs. yield strength for a UFG TRIP steel indicated by a green square[10]

A similar material, whose composition was 0.0013C, 8.14Ni, 10.3Cr, 7.47Mn in mass per cent, was investigated in [11]. It was homogenized at 1200°C for 12 h and hot-rolled at around 1000°C to a plate 10 mm thick. The austenite plate was cold-rolled with a thickness reduction of 75% to make it fully martensite and annealed at three different temperatures (Af + 35, 65 and 125°C) for 2.5 min in a salt bath. This conventional cold rolling and annealing process generated three different austenite grain sizes: 0.3, 0.6 and 2.0 µm on average. The resulting stress -strain curves, together with that for a conventional 316 stainless steel, are presented in Fig. 17. Fig. 18 confirms an extraordinary combination of yield strength and total elongation for the UFG TRIP steel.

Fig. 17 Stress - strain curves for UFG stainless steels with different grain size (a, b, c) and for conventional 316 stainless steel (d) [11]

Fig. 18 Total elongation vs. yield strength for a UFG TRIP steel with grain size 0.3 µm and 0.6 µm indicated by green squares [11]

Conclusions

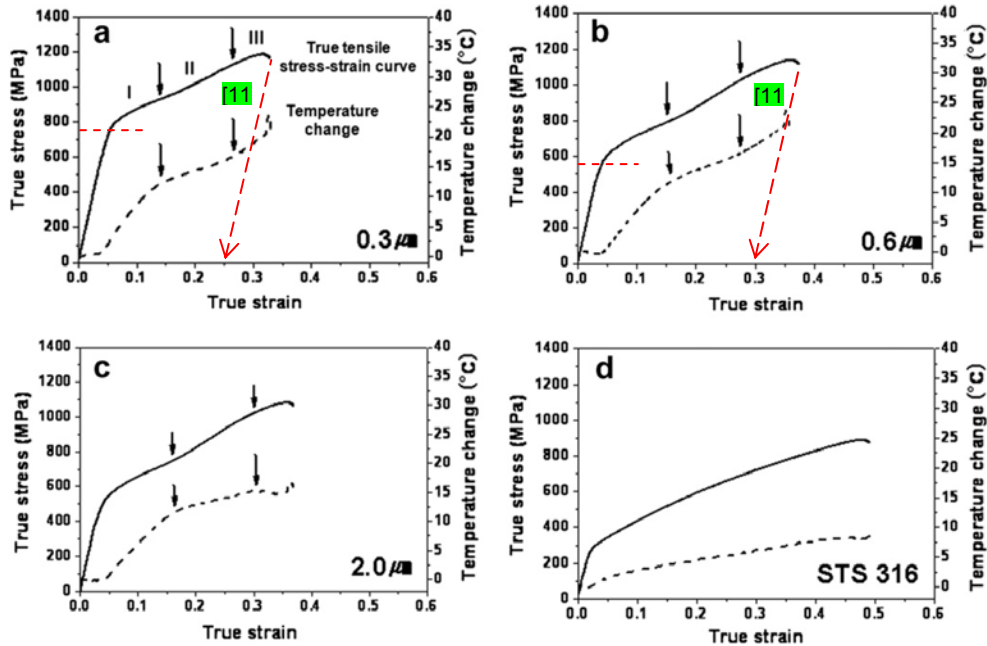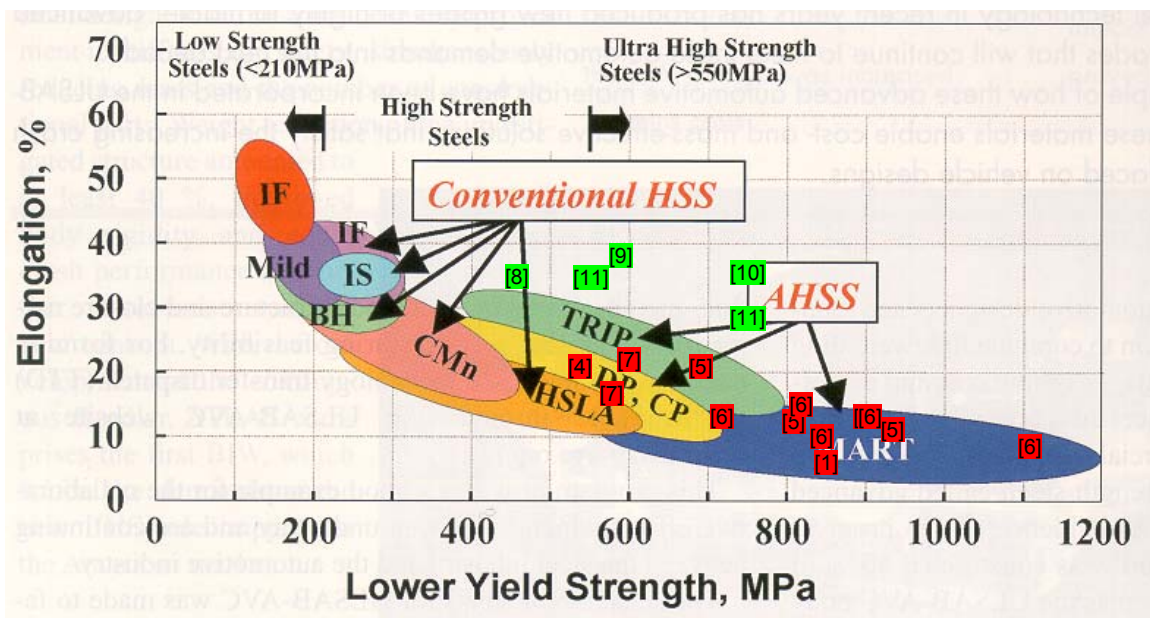There are more publications on UFG steels, for example [12-19], but the overall trend can be already captured based on the research described in this report.

Among the different strengthening mechanisms, grain refinement is the only method to improve both strength and toughness simultaneously. Therefore, ultrafine grained steels with relatively simple chemical compositions, strengthened primarily by grain refinement, have great potential for replacing some conventional low alloyed high strength steels. The main benefits behind such an approach are to avoid additional alloying elements; to avoid additional heat treatments like soft annealing, quenching and tempering; and to improve weldability owing to lower required carbon contents and other alloying elements when compared with other high strength steels.

Recently, advanced thermo-mechanical treatment (rather than classical severe plastic deformation) of higher alloyed steels has resulted in a promising combination of yield strength and total elongation for UFG steels, which breaks out of the known envelope relating strength and ductility. Especially useful might be the retention of the strain hardening capability for UFG steels, which results in highly increased uniform elongation.

References

[1] V.I. Kopylov, Application of ECAP technology for producing nano and microcrystalline materials, in T. C. Lowe and R. Z. Valiev (Eds), Investigations and Applications of Severe Plastic Deformation, Kluwer, Dordrecht, 2000, p. 23/27.

[2] S.V. Dobatkin, Severe plastic deformation of steels: structure, properties and techniques, in T. C. Lowe and R. Z. Valiev (Eds), Investigations and Applications of Severe Plastic Deformation, Kluwer, Dordrecht, 2000, p. 13/22.

[3] Yu. Ivanisenko, A.V. Sergueeva, A. Minkov, R.Z. Valiev, H.-J. Fecht, Mechanical properties and thermal stability of nano-structured Armco iron produced by high pressure torsion, in M. Zehetbauer and R. Z. Valiev (Eds), Nanomaterials by Severe Plastic Deformation, Wiley-VCH 2004, p. 453/458.

[4] T. Hanamura, F. Yin, K. Nagai, Ductile-brittle transition temperature of ultrafine ferrite/cementite microstructure in a low carbon steel controlled by effective grain size, ISIJ Int. 44 (2004) 610-617.

[5] D.H. Shin, K.-T. Park, Microstructural stability and tensile properties of nanostructured low carbon steels processed by ECAP, in M. Zehetbauer and R. Z. Valiev (Eds), Nanomaterials by Severe Plastic Deformation, Wiley-VCH 2004, p. 616/22.

[6] S.V. Dobatkin, P.D. Odessky, R. Pippan, G.I. Raab, N.A. Krasilnikov, A.M. Arsenkin, Developing of structure and properties in low-carbon steels during warm and hot equal channel angular pressing, in M. Zehetbauer and R. Z. Valiev (Eds), Nanomaterials by Severe Plastic Deformation, Wiley-VCH 2004, p. 804/809.

[7] K.-T. Park, S.Y. Han, B.D. Ahn, D.H. Shin, Y.K. Lee, K.K. Um, Ultrafine grained dual phase steel fabricated by equal channel angular pressing and subsequent intercritical annealing, Scripta Mater. 51 (2004) 909-913.

[8] Y. Okitsu, N. Takata, N. Tsuji, A new route to fabricate ultrafine-grained structures in carbon steels without severe plastic deformation, Scripta Mater. 60 (2009) 76–79.

[9] M. Calgagnotto, D. Ponge, D. Raabe, Ultrafine grained ferrite/martensite dual phase steel fabricated by large strain warm deformation and subsequent intercritical annealing, ISIJ Int. 48 (2008) 1096-1101.

[10] K. Tao, H. Choo, H. Li, Transformation-induced plasticity in an ultrafine-grained steel: An *in situ* neutron diffraction study, Applied Physics Letters 90, 101911, 2007.

[11] C.-S. Yoo, Y.-M. Park, Y.-S. Jung, Y.-K. Lee, Effect of grain size on transformation-induced plasticity in an ultrafine-grained metastable austenitic steel, Scripta Mater. 59 (2008) 71–74.

[12] K.-T. Park, Y.-S. Kim, D.-H. Shin, Microstructural stability of ultrafine grained low-carbon steel containing vanadium fabricated by intense plastic straining, Metallurgical and Materials Transactions A 32 (2001) 2373-2381.

[13] R. Ueji, N. Tsuji, Y. Minamino, Y. Koizumi, Effect of rolling reduction on ultrafine grained structure and mechanical properties of low-carbon thermomechanically processed from martensite starting structure, Science and Technology of Advanced Materials 5 (2004) 153-162.

[14] K.-T. Park, Y.K. Lee , D.H. Shin, Fabrication of ultrafine grained ferrite/martensite dual phase steel by severe plastic deformation, ISIJ Int. 45 (2005) 750-755.

[15] K.-T. Park, C.S. Lee, D.H. Shin, Strain hardenability of ultrafine grained low carbon steels processed by ECAP, Rev. Adv. Mater. Sci. 10 (2005) 133-137.

[16] R. Song, D. Ponge, D. Raabe, Mechanical properties of ultrafine grained C-Mn steel processed by warm deformation and annealing, Acta Meter. 53 (2005) 4881-4892.

[17] Y. Ma, J.-E. Jin, Y.-K. Lee, A repetitive thermomechanical process to produce nano-crystalline in a metastable austenitic steel, Scripta Mater. 52 (2005) 1311-1315.

[18] Y.K. Lee, J.E. Jin, Y.Q. Ma, Transformation-induced extraordinary ductility in an ultrafine-grained alloy with nanosized precipitates, Scripta Mater. 57 (2007) 707-710.

[19] S.V. Dobatkin, J. Zrnik, I. Mamuzic, Ultrafine-grained low carbon steels by severe plastic deformation, Metallurgija 47 (2008), p. 181-186.

ECAPE-hanke

Hannu Martikainen   VTT

1. ECAPE-muotti

Muottina käytettiin projektissa kehitettyä ECAPE-muottia (Equal Channel Angular Pressing Extrusion), Kuva 1. Siinä on yhdistetty perinteinen ECAP-muotti ja pursotusmuotti. Muotin suunnittelussa käytettiin apuna kirjallisuudessa esitettyjä ohjeita (mm lähteet Maciejewski et al, Vedani et al). Suunnitellulla muotilla toivottiin saatavan mikrorakenne hienonemaan entistä nopeammin ja tasaisemmin kuin perinteistä ECAP-muottia käytettäessä.
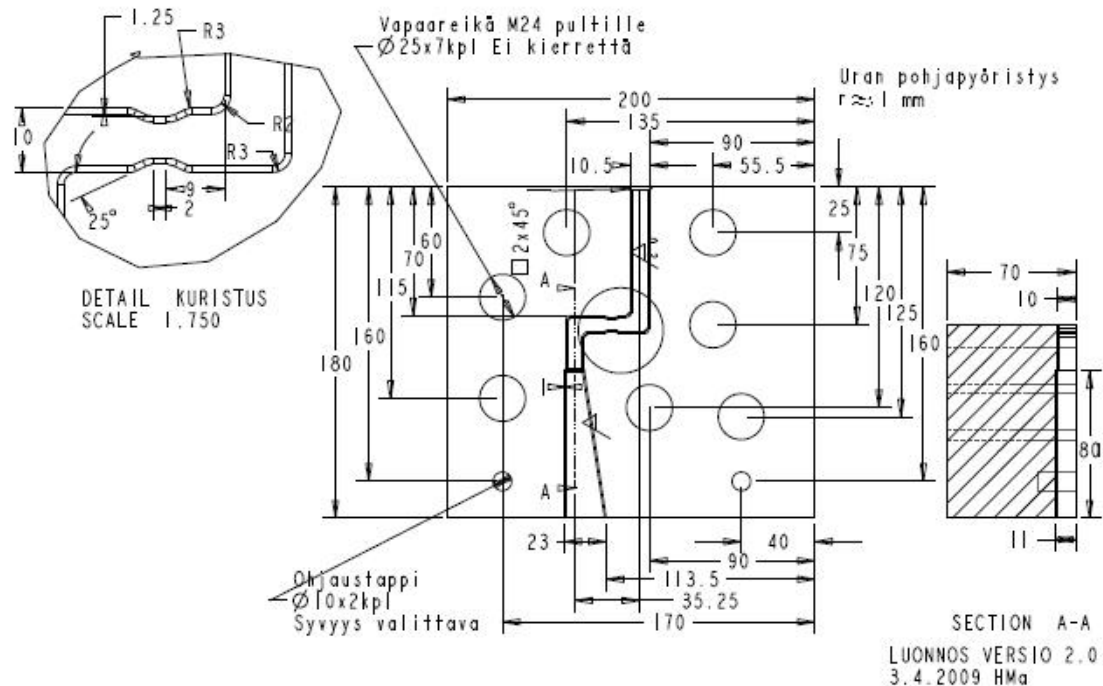
Kuva 1. ECAPE-muotin kanavapuolisko.

Muotti valmistettiin Uddeholmin Unimax-teräksestä. Se lämpökäsiteltiin kovuuteen 58HRC. Kokeiden aikana muotti vaurioitui. Epäiltiin, että muotin kovuus saattoi olla liian suuri ja korjauksen jälkeen työkalut lämpökäsiteltiin kovuuteen 48 HRC.

Kokeissa käytetty pistin on esitetty kuvassa 2.

Kuva 2. Pistin.

1.1 Koesarja 1

Alkuperäisellä muotilla tehdyt kokeet tehtiin kahdessa osiossa, koska pistin jäi kiinni muottiin ja muotti jouduttiin välillä aukaisemaan sen irrottamiseksi.

Aihion materiaalina käytettiin puhdasta alumiinia (Goodfellow AL007915: Aluminium 99.999 %) ja hieman enemmän epäpuhtauksia sisältävää alumiinia Al 1050 (Al 99,5%,). Aihion poikkipinnan mitat olivat 10x10 mm (AL007915-aihiot työstettiin pyörötangosta ja Al 1050 -aihiot leikattiin levystä). Analysoidun aihion alkuperäinen pituus oli n. 65mm. Koesarjassa tehdyt kokeet on esitetty taulukossa 1.

Prosessin kuvaus
-Muotin voitelu: muotti ruiskutettiin MoS_2-spräyllä. Tämän lisäksi voiteluaineena käytettiin vaseliinin ja Molykoten seosta (ProtoShop Oy).
-Pistonopeus n. **0,17**…0,25 mm/s. Aihion päät suoristettiin ennen toista työkiertoa.

Taulukko 1. Alkuperäisellä muotilla tehdyt kokeet.

Aihio	Vaiheita	Koe-osio	Materiaali
1	1	1	AL007915
2	1+ kierto 90°	1	AL007915
3	1+ kierto 90°	1	AL007915
P	1	1	AL007915
4x	1, kesken	2	Al l050

Taulukossa esitettyjen aihioiden lisäksi muottiin sijoitettiin lyhyt 20 mm:n pala (kuristuksen jälkeen). Tämän toivottiin muodostavan tarvittavan vastapaineen ensimmäiselle varsinaiselle aihiolle.

Aihiot 1, 2, 3 ja P käsiteltiin ensimmäisessä koe-osiossa. Kokeen loppuvaiheessa pistin jäi muottiin: pistimen kiinnitys ei kestänyt ulosvetovoimaa. Muotti avattiin ja pistin irrotettiin. Koetta jatkettiin toisessa koeosiossa lisäämällä muottiin aihio 4x, Kuva 3. Koe keskeytettiin siinä vaiheessa, kun muottiin muodostui säröjä, Kuva 4

2 x pure_Al and Al 1050

Kuva 3. Avattu muotti.

Fracture...

Fracture 2

Kuva 4. Yksi muotin säröistä.

Valmistettuja SPD-kappaleita on esitetty kuvissa 5 ja 6.

Kuva 5. Valmistettuja SPD-kappaleita.
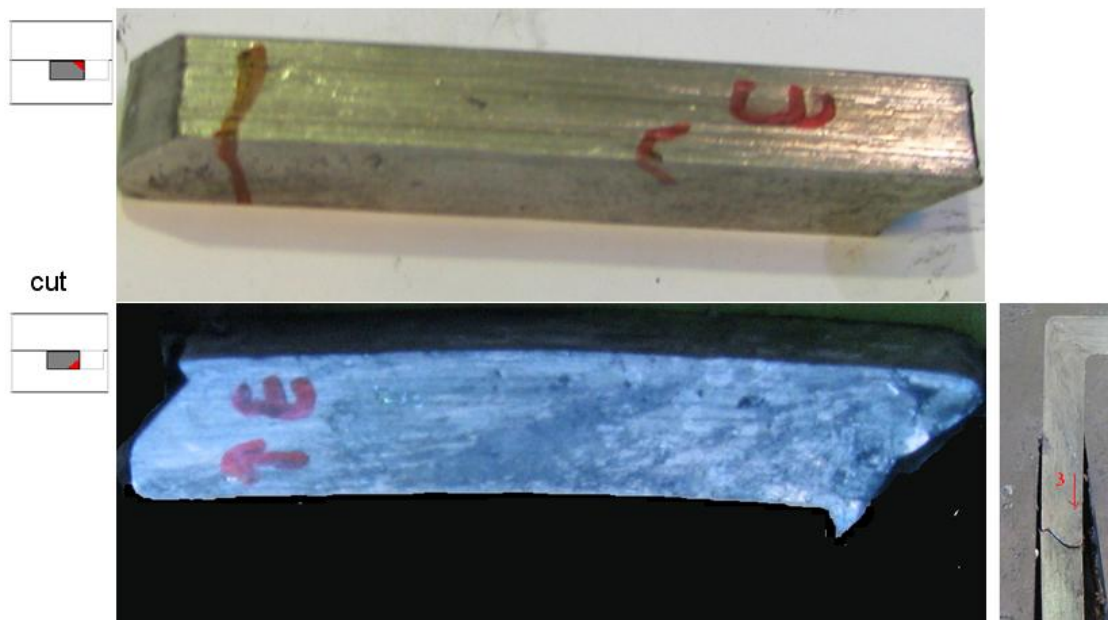
Kuva 6. Kahteen kertaan pursotettu SPD-kappale (välillä 90 asteen kierto)

Kokeiden simuloinneista on esitetty kuvassa 7 puhtaalle alumiinille tehdyistä simuloinnista plastinen venymä (ensimmäinen pursotus).
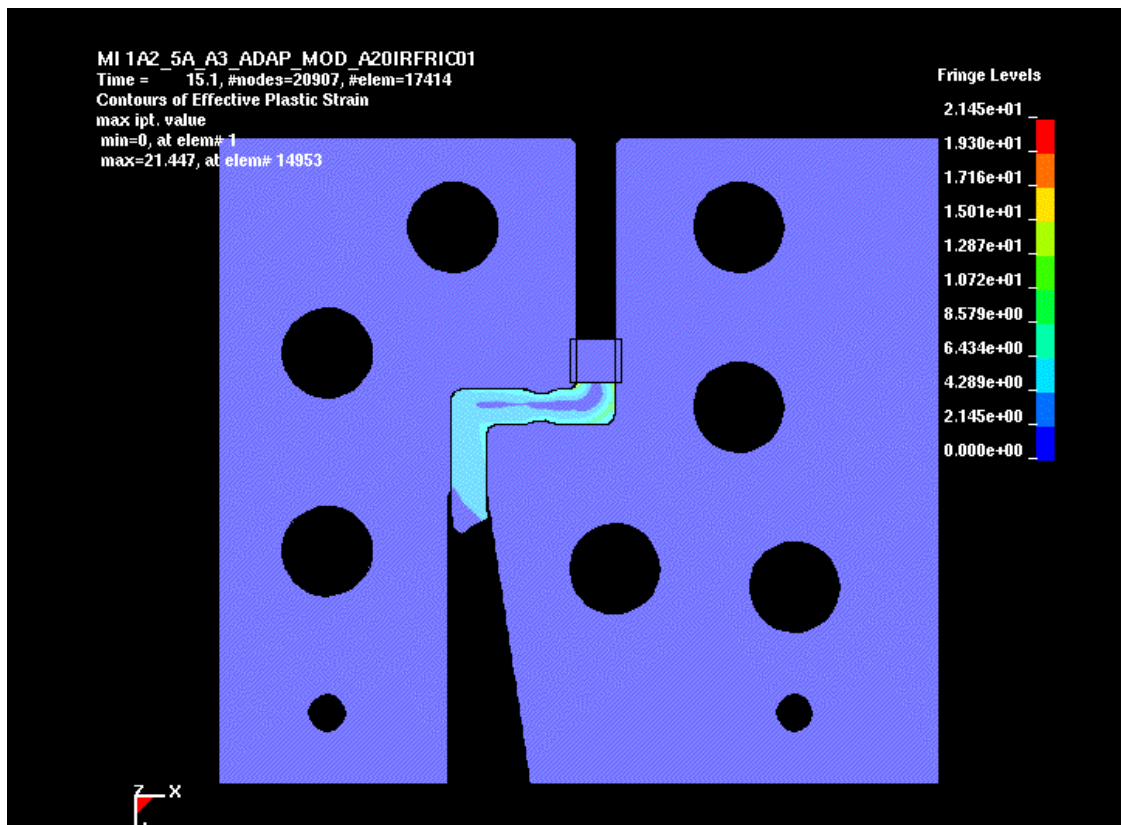
Kuva 7. ECAPE-simulointi: pursotuksen loppuvaihe (aihion materiaalina puhdas alumiini).

1.2 Koesarja 2

Koesarjassa 2 käytettiin korjattua muottia. Vaurioitunut muotti korjattiin jyrsimällä uusi kanava ja lämpökäsittelemällä ko. muottipuolisko kovuuteen **48 HRC.** Kokeet tehtiin materiaaleille Al 1050 ja AL007915.

Al 1050 –materiaaliaihiot leikattiin levystä. Aihion kovuus oli 33 HV. Aihion poikkipinnan mitat olivat 10x10 mm ja mitatun kappaleen alkuperäinen pituus n. 75 mm.

Prosessin kuvaus
- Voiteluaineena käytettiin vaseliinin ja Molykoten seosta (ProtoShop Oy).
- Pistonopeus n. **0.17**… 0.25 mm/s. Aihion päät suoristettiin (leikattiin) ennen toista työkiertoa.

Valitut aihiot puristettiin kerran (muottia koottaessa kanavaan ei laitettu aloituspalaa). Koe keskeytettiin, kun alumiini pursui muottipintojen väliin. Muotti aukaistiin ja puhdistettiin.

Muottia koottaessa vaakasuoraan kanavaan laitettiin aihiopala (L= n. 20 mm). Edellisen kokeen ensimmäiseksi prosessoidun koekappaleen päät leikattiin suoriksi ja käytettiin tässä kokeessa. Aihio kierrettiin 90 astetta myötäpäivään tulosuunnasta katsottuna ja pursotettiin.

Koekappaleelle tehdyt kovuusmittaukset on esitetty kuvassa 8. Mittaustuloksissa oli hajontaa yhden pinnan sisällä ja vastaavien pintojen välillä (tulokset suuntaa-antavia).

Puristus 1

Etupinta: 1 kerta -> 58 HV   2 kertaa ->59HV
Sivupinta: 1 kerta -> 63 HV   2 kertaa -> 68 HV
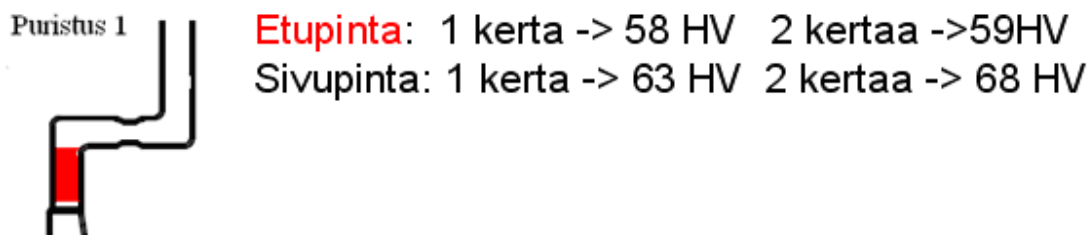
Kuva 8. Koekappaleen kovuusmittaukset. Kovuus mitattu keskiarvona eri pinnoilta.

Puhtaalle alumiinille tehdyissä kokeissa materiaalina oli Goodfellow AL007915

Aihion poikkipinna mitat olivat n. 10,3 x 9,7 mm. Aihion alkuperäinen pituus oli 65 mm.

Prosessin kuvaus
- Voiteluaineena käytettiin vaseliinin ja Molokyten seosta (uusi sekoituserä)
- Pistonopeus= n. **0.5** mm/s
Muottia koottaessa vaakasuoraan kanavaan kuristuksen jälkeen laitettiin alumiinipala (pituus n. 20mm)

Kokeessa alumiini pääsi pursuamaan muottipintojen väliin ja koe keskeytettiin. Kertaalleen kanavan läpi pursotettu aihio on esitetty kuvassa 9.

Kuva 9. Keskeytetyn muokkauksen aihio.

2. Johtopäätökset

SPD-materiaalin raekoko hienontui ECAPE-muottia käytettäessä. Hienontumista ei kuitenkaan tapahtunut siinä määrin kuin oli arvioitu. Raekoon hienontumiseen vaikuttaa kuitenkin muotin lisäksi mm voitelu ja prosessin nopeus. Tästä johtuen saavutettuja tuloksia on vaikea vertailla kirjallisuusarvoihin kun pyritään selvittämään ECAPE-muotin geometrian vaikutusta raekoon hienontumiseen. ECAPE-muotin hyvyyden selvittämiseksi olisi voitu tehdä koe muotilla, josta kanavan kuristus on poistettu (eli ECAP-muotti). Tällöin olisi kuitenkin jouduttu muuttamaan (tuhoamaan) toimiva muotti, mikä olisi estänyt mahdollisten lisäkokeiden tekemisen.

Tietyissä tutkimuksissa on osoitettu kappaleen poikkipinnasta mitatun solukoon (dislocation cell size) kasvavan siirryttäessä kappaleen keskeltä pinnalle (mm. Baik et al). ECAPE-menetelmän pitäisi johtaa tasaisempaan rakenteeseen. Tätä ei kuitenkaan pystyttä mittauksilla todentamaan.

UFG-materiaalia voidaan valmistaa hankkeessa kehitetyllä ECAPE-muotilla, mutta työkiertoja on oltava kokeiltuja enemmän.

Lähteet

Baik, S. C., Estrin, Y., Kim, H. S.,Hellmig, R. J., Dislocation density-based modeling of deformation behavior of aluminium under equal channel angular pressing, Materials Science and Engineering A, Volume 351, Issues 1-2, 25 June 2003, s. 86-97, ISSN 0921-5093

Maciejewski, J.,Kopeć, H., Petryk, H., Finite element analysis of strain non-uniformity in two processes of severe plastic deformation, Engineering Transactions ,2007, Vol. 55, No. 3, s.197-216,

Vedani, M., Bassani, P., Cabibbo, M. ,Evangelista, E. ,Experimental aspects related to equal channel angular pressing of a commercial AA6082 alloy, Metallurgical Science and Technology, Vol 21, No. 2, December 2003,s. 3-9.

Kiväärin piiput

Antti Korhonen, Teknillinen korkeakoulu

Jari Larkiola, VTT

Tavoitteet

- optimaalisen materiaalin löytäminen (lujuus/sitkeys ja kilpailuetu)
- reikäkokojen vähentäminen (ruostumattomalla 14 eri kokoa)
- sulkuolakkeiden kulumisen vähentäminen
- patruunapesän ja piipun taonta samalla (kalviminen aiheuttaa vaikeuksia)

Taustaa

Kiväärin piippujen valmistamisessa ensimmäinen vaihe on pitkän reiän poraaminen tankoon erikoisvalmisteisella poralla (kanuunapora). Tavallinen kierukkapora ei tehtävään sovi, sillä reiän pitää olla suora. Porauksen jälkeen reikä voidaan hioa tai kalvia. Varsinaisen rihlauksen tekemiseen on kolme yleisesti käytettyä menetelmää: lastuaminen, kovametallituurnan vetäminen reiän läpi tai pyörötaonta. Pyörötaonta kuitenkin edellyttää kalliita laiteinvestointeja eikä siihen pienillä asepajoilla ole varaa. Esim. U.S.A.:ssa toisin kuin Euroopassa on paljon pieniä asepajoja, jotka tekevät rihlauksen lastuamalla. Suomessakin aikoinaan myös Tikkakoski tiettävästi menetteli näin. Myös elektrolyyttisesti voidaan rihlaus tehdä.

Pyörötaonta on saksalainen keksintö. Sen ensimmäinen sovellus oli saksalaisen konekiväärin M42 piipun valmistus. Konekivääri ampui 7,92 x 57 mm patruunaa. Konekivääri oli ilmajäähdytteinen ja sen osat oli muovattu halvalla ohutlevystä. Merkittävää oli kuitenkin aseen suuri tulinopeus 1500 laukausta/min (25 laukausta/s), mikä oli yli kaksi kertaa sen mihin liittoutuneiden aseilla yllettiin[1,2,3]. Rihlauksen muovaus lujitti sitä, mutta suuri tulinopeus kulutti silti. Piippujen kestoikä oli tiettävästi 3500 - 4000 laukausta ja kovakromattuna 8000 laukausta. Ensimmäinen pyörötaontakone rakennettiin tiettävästi Erfurtissa 1939. Sodan loppuvaiheessa se siirrettiin kuitenkin etenevien venäläisten tieltä turvaan Itävaltaan, jossa laitteita valmistaa nykyään GFM yhtiö.

Rihlaus pyörötakomalla tuurnan päällä luo piippuun jäännösjännityksiä, jotka joudutaan poistamaan hehkuttamalla (jännitystenpoistohehkutus) n. 600 ^{o}C lämpötilassa ja jäähdyttämällä hitaasti hehkutuksen jälkeen. Piippumateriaalien lämpökäsittely on ongelmallista, sillä esim. käytetyillä martensiittisilla ruostumattomilla teräksillä esiintyy päästöhaurausalueita, joita lämpökäsittelyssä on vältettävä.

[1] D. Musgrave, Deutsche Maschinen Gewehre – Entwicklung, Technik, Typen, Motorbuch Verlag, Stuttgart, 361 s.

[2] http://de.wikipedia.org/wiki/MG42

[3] G. Kolbe, The making of a rifled barrel, http://www.firearmsid.com/Feature%20Articles/RifledBarrelManuf/BarrelManufacture.htm

Kiväärin piippujen materiaalit

Kiväärin piippua voidaan pitää paineastiana, johon kohdistuu toistuva väsyttävä kuormitus ja luodin aiheuttama sisäpuolinen kulutus. Aikojen kuluessa on etsitty yhä parempia materiaaleja. Nykyään käytetään piippujen valmistukseen yleisesti 0,4 – 0, 5 % C sisältäviä nuorrutusteräksiä (51CrV4, 42CrMo4) tai martensiittisia ruostumattomia teräksiä. Jälkimmäiset piiput ovat yleensä metallin värisiä eikä mustia. Mustan piipun etuna on, ettei se heijasta valoa, jonka kohde voisi havaita. Piippuja on Suomessakin mustattu ns. mustanitrausmenetelmällä[4], mutta murtumien takia menetelmästä on luovuttu[5]. Myös hydrauliikkaputkissa, kuten kuorma-autojen kipeissä on menetelmää käytetty, mutta niissäkin on ollut murtumisongelmia[6].
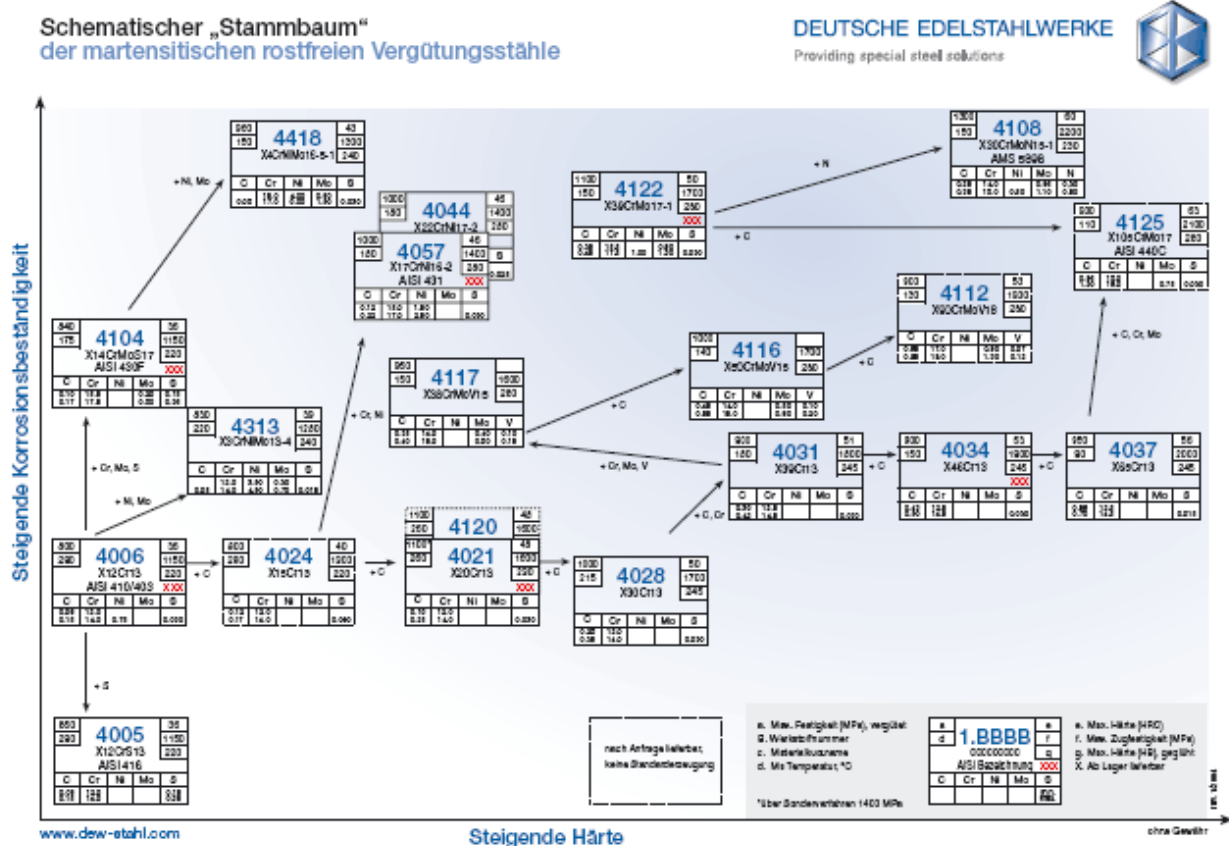
Ruostumattomat teräkset keksittiin lähes samanaikaisesti viime vuosisadan alussa Englannissa ja Saksassa. Englannissa Sheffieldissä Harry Brearley etsi uusia paremmin kulumista kestäviä piipputeräsmateriaaleja ja keksi martensiittisen ruostumattoman teräksen[7]. Saksassa Kruppin

---

[4] Hiilitypetys ja sitä seuraavaan hapettaminen, joka antaa korroosiota kestävän mustan pinnan.

[5] T. Hyytinen, Asesuunnitelua Suomessa, Arma Fennica, 2001, s. 125.

[6] Typetys luo tyypillisesti muutamia mm kymmenyksiä paksun kovan diffuusiokerroksen. Kuten yleensä, kovuuden kasvaessa sitkeys myös vähenee.

[7] Eräiden tietojen mukaan ensimmäinen kaupallinen sulatus tehtiin Ruotsissa. Vuonna 1913 ruotsalainen metsästys- ja kalastuslehti nimittäin kertoi aseen piippuun käytetystä teräksestä, joka muistutti ruostumatonta terästä. http://www.stainless-steel-world.net/basicfacts/ShowPage.aspx?pageID=463

tehtailla taas keksittiin austeniittinen ruostumaton teräs V2A, jonka tyypillisin edustaja nykyään on Cr-Ni-teräs 18/8 eli AISI 304.

Oheisessa kuvassa on esitetty martensiittisten ruostumattomien terästen sukupuu[8]. Saksankielisessä kuvassa teräksistä käytetään nimitystä "martensiittiset ruostumattomat nuorrutusteräkset", koska teräkset päästetään yleensä varsin korkeissa lämpötiloissa.

Tyypillisiä piipuissa käytettyjä martensiittisia teräksiä ovat 1.4021 (AISI 420), 1.4057 (AISI 431), 1.4313, 1.4006 (AISI 410) ja 1.4005 (AISI 416). Teräksillä esiintyy tyypillisesti päästöhaurautta ja alueita, joilla päästöhaurautta esiintyy tulee lämpökäsittelyssä välttää.
- 1.4021 päästöä alueella 400 – 600°C tulee välttää (hauraiden faasien erkautuminen)
- 1.4057 päästöä alueella 420 – 520°C tulee välttää(475°-hauraus ongelmana)

Martensiittisilla ruostumattomilla on raportoitu piippujen murtumisista. Esim. 1.4057 teräs on murtunut ammuttaessa. Kylmissä oloissa sanotaan murtumariskin kasvavan, mikä on ymmärrettävää iskusitkeyden laskiessa alemmissa lämpötiloissa. Todettakoon, että austeniittisilla ruostumattomilla ei erilaisesta kidemuodosta (pkk) johtuen vastaavaa ongelmaa ole ja niitä käytetään yleisesti myös kryoalueen sovelluksissa (esim. nestetypen kuljettamiseen tarkoitetuissa astioissa kuten dewareissa jne.)

VTT:n vetokokeissa 1.4057 murtui hauraasti, mutta 1.4021 sitkeästi (cup and cone, shear)[9]. Tehdyissä puristuskokeissa kuitenkin näitä sitkeämmäksi osoittautui 1.4313 (X3CrNiMo13-4). Koska sitkeyseroihin vaikuttaa myös kuormituksen luonne, on mahdollista, että staattista puristuskoetta paremmin eroja mittaisi esim. Charpy-vasaralla tehtävä iskukoe, jolla mitataan iskuenergiaa. Mittauksia voitaisiin tehdä esim. neliöpoikkipintaisilla loveamattomilla sauvoilla.

Martensiittisten ruostumattomien piippujen räjähdyksistä kerrotaan esim. www:n keskustelupalstoilla. Rikkiä pidetään yleisesti ongelmana. Piippusovelluksissa kehotetaan välttämään laatuja 410 tai 416, joihin on lisätty S lastuttavuuden parantamiseksi (1.4005, X12CrS13). Rikin lisäksi seleenin (Se) sanotaan haurastuttava aine. Esim. laadulla 416 nimellinen rikkipitoisuus on S < 0,35 % ja 1.4021 S = 0,030 %. Esim. laaduilla 1.4021 (X20Cr13) ja 1.4057 (X17CrNi16-2) on sama rikkipitoisuus, mutta jälkimmäisessä on nikkeliä. Rikin ja nikkelin sanotaan reagoivan muodostaen matalan sulamispisteen omaavan seoksen. Binäärisen Ni – S – tasapainopiirroksen mukaan alin sulamispiste näyttää olevan 640 ^{o}C koostumuksella n. 22 p-% S.. Esim. Miekk-ojan mukaan rikin haurastuttava vaikutus nikkelissä perustuu siihen, että rikin liukoisuus nikkeliin on huono, jolloin sulan nikkelin jähmettyessä S jää raerajoille haurastuttaen ne[10]. Binäärisestä tasapainopiirroksesta ei kuitenkaan pidemmälle meneviä johtopäätöksiä voi tehdä, kun teräksessä on nikkelin ja rikin lisäksi rautaa ja monia muitakin seosaineita. Monikomponenttiseosten tasapainopiirrosten tarkasteluun on nykyään käytettävissä tietokoneohjelmia kuten Calphad. Puhtaassa nikkelissäkin rikin haurastuttava vaikutus voidaan

[8] http://www.dew-stahl.de/index.php?id=1381
[9] Jari Larkiola, Alejandro Revuelta, Ruostumattoman teräspiipun takomisen simulointi ja sopivan teräslaadun valinta, VTT: n raportti, 28.10.2005, 23 s.
[10] Uudistettu Miekk-ojan metallioppi (Lindroos, Sulonen ja Veistinen), Otava, 1986, s. 642.

eliminoida sitomalla se Mn- tai Mg-lisäyksillä sulfideiksi. Toisaalta esim. rikin ja fosforin teräksiä haurastuttava vaikutus tunnetaan yleisesti. Esim. nesteytetyn maakaasun (LNG) kuljetukseen tarkoitettujen säiliöiden terästen rikin määrä pyritään pitämään alle 0,003 %, jotta taattaisiin mahdollisimman hyvät sitkeys- ja lujuusarvot[11]. Keskustelupalstoilla sanotaan myös rikkipitoisten lastuamisnesteiden voivan toimia rikin lähteinä haurastuttaen teräksen. Samasta varoitetaan myös puhtaan nikkelin tapauksessa em. Miekk-ojan kirjassa, jossa todetaan myös uuniatmosfäärin voivan toimia rikin lähteenä. Todettakoon, että em. VTT:n testeissä sitkeimmäksi osoittautui teräs 1.4313 (X3CrNiMo13-4), jonka S-pitoisuus on vain 0,015 %. Keskustelupalstoilla sanotaan piippulaatuisen 416-teräksen sisältävän vain noin puolet normaalin 416-teräksen rikkimäärästä. Teräksen merkinnäksi on ilmoitettu 416R tai 416RS[12].

Taotuissa piipuissa sanotaan käytettävän 410 terästä 416 sijasta[13]

Iskusitkeystestit loveamattomillakin sauvoilla Charpy-V vasaralla saattaisivat antaa tietoa sitkeydestä ja materiaalien sekä pintakäsittelyjen eroista. Iskusitkeysarvoiksi 25°C lämpötilassa on kirjallisuudessa annettu seuraavia lukuja:

1.4021 ISO-V > 20 J
1.4057 ISO-V > 15 – 20 J

Vertailun vuoksi perusausteniittiselle 1.4301 (AISI 304) laadulle on sitkeydeksi annettu KV = 60 J.

Selvitettävä peruskysymys on, riittääkö myötölujuus $R_{p0.2}$ austeniittisilla laaduilla piippumateriaaliksi. Kylmämuokkauksella voidaan austeniittisten laatujen lujuutta nostaa huomattavasti. Esim. laadulla 1.4318 (AISI 301LN) sanotaan päästävän arvoon R_p = 2000 MPa (laatu HyTens 2000) kylmämuokattuna[14].

Aseissa käytetään useita ruostumattomia teräksiä. Esim. amerikkalaisen haulikkokaliiberin sarjatuliaseessa AA12 sanotaan käytetyn seitsemää erilaista ruostumatonta terästä. Mitä ja missä osissa, siitä ei ole meillä tarkempaa tietoa kuten ei AISI 300-sarjan terästen soveltuvuudesta piippumateriaaliksikaan.

---

[11] K. Hickmann, A. Kern, U. Schriever and J. Stumpfe, Production and properties of high-strength nickel-alloy steel plates for low temperature applications, Raportti, ThyssenKrupp Stahl AG, 11 s.
http://www.msm.cam.ac.uk/phase-trans/2005/LINK/95.pdf
[12] Cruciblen tai Carpenterin nykyisiltä listoilta ei nimikkeitä löydy. Voivat olla vanhoja.
[13] G. Kolbe, The making of rifled barrel,
http://www.firearmsid.com/Feature%20Articles/RifledBarrelManuf/BarrelManufacture.htm
[14] http://www.avestapolarit.fi/upload/technology/Acom%203%20and%204%202002.pdf

Ruostumattomien martensiittisten terästen lämpökäsittelystä

Antti Korhonen, TKK
Jari Larkiola, VTT

Ruostumattomilla martensiittisilla teräksillä esiintyy päästöhaurausalueita, joita lämpökäsittelyssä on syytä välttää. VTT:n vetokeissa testatuista teräksistä 1.4057 murtui hauraasti, mutta 1.4021 sitkeästi[1]. Tehdyissä puristuskokeissa näitä sitkeämmäksi osoittautui 1.4313.

Teräs 1.4057 (X17CrNi16-2)

Teräksen 1.4057 pehmeäksihehkutus tehdään alueella 680 $^{\circ}$C – 800 $^{\circ}$C jäähdyttämällä hitaasti joko uunin mukana tai ilmassa[2]. Pehmeäksihehkutetulle teräkselle murtolujuus ja Brinell- kovuus ovat tyypillisesti $R_m \le$ 950 MPa ja HB $\le$ 295.

Teräs voidaan karkaista hehkuttamalla 950 – 1060 $^{\circ}$C lämpötilassa ja jäähdyttämällä sen jälkeen ilmassa tai öljyssä. Päästölämpötila riippuu halutusta lujuudesta. Koska teräksellä on taipumusta 475 $^{\circ}$C haurauteen, tulee päästöä alueella 420 – 520 $^{\circ}$C välttää. Yleisesti on käytössä kaksi päästötilaa QT800 ja QT900. Edellisessä (QT800) tehdään kaksivaiheinen päästö ensin alueella 750 – 800 $^{\circ}$C ja sen jälkeen toinen päästö lämpötilassa 650 – 700 $^{\circ}$C. (Mikäli Ni-pitoisuus on kuitenkin alarajalla, riittää yksinkertainen päästö alueella 620 – 720 $^{\circ}$C). Tilaa QT900 vastaa yksi päästö alueella 600 – 650 $^{\circ}$C. Tiloja vastaavat mekaaniset ominaisuudet on annettu alla olevassa taulukossa.

		QT800		Typische Werte (ca.)	
		1 – 80**	81 – 160	1 – 80**	81 – 160
Streckgrenze (MPa)	$R_{p0,2}$	$\ge$ 600	$\ge$ 600	620	620
Zugfestigkeit (MPa)	R_m	800 – 950	800 – 950	820	820
Bruchdehnung (%)	A_5	$\ge$ 14	$\ge$ 12	20	20
Kerbschlagarbeit (J)					
25 °C	ISO-V	$\ge$ 25	$\ge$ 20		
		QT900		Typische Werte (ca.)	
		1 – 80**	81 – 160	1 – 80**	81 – 160
Streckgrenze (MPa)	$R_{p0,2}$	$\ge$ 700	$\ge$ 700	710	710
Zugfestigkeit (MPa)	R_m	900 – 1050	900 –1050	920	920
Bruchdehnung (%)	A_5	$\ge$ 12	$\ge$ 10	16	16
Kerbschlagarbeit (J)					
25 °C	ISO-V	$\ge$ 20	$\ge$ 15		

**Angegebene Werte gelten nur für den nicht kaltverfestigten Zustand.

---

[1] Jari Larkiola, Alejandro Revuelta, Ruostumattoman teräspiipun takomisen simulointi ja sopivan teräslaadun valinta, VTT: n raportti, 28.10.2005, 23 s.

[2] http://dew.edelstahl-e.com/upload/binarydata_ewkinterd4cms/54/38/00/00/00/00/3854/1.4057.pdf

Eräiden mekaanisten ominaisuuksien muuttuminen eri päästölämpötiloissa on esitetty oheisessa kuvassa. Päästöhauraus näkyy erityisesti iskusitkeyden Av arvoissa (asteikko puuttuu kuvasta).
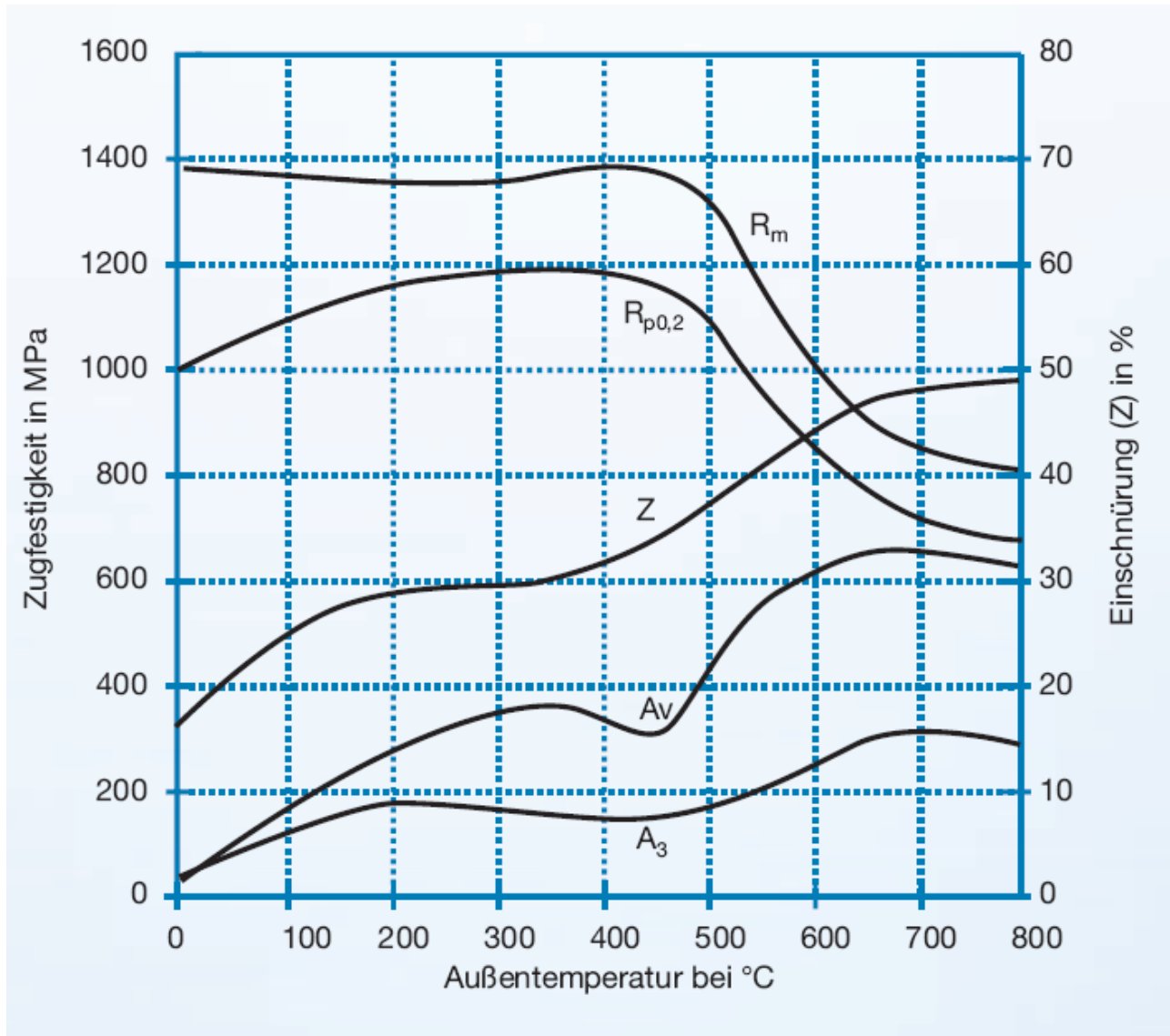
Teräs 1.4021 (X20Cr13)

Teräksen 1.4057 pehmeäksihehkutus tehdään alueella 745 ^{o}C – 825 ^{o}C jäähdyttämällä hitaasti joko uunin mukana tai ilmassa[3]. Pehmeäksihehkutetulle teräkselle murtolujuus ja Brinell- kovuus ovat tyypillisesti R_m ≤ 760 MPa ja HB ≤ 230.

Teräs voidaan karkaista hehkuttamalla 950 – 1050 ^{o}C lämpötilassa ja jäähdyttämällä sen jälkeen ilmassa tai polymeeri- tai öljykylvyssä. Päästölämpötila riippuu halutusta lujuudesta. Päästöä alueella 400 – 600 ^{o}C välttää, koska se johtaa haitallisten faasien erkautumiseen. Yleisesti on käytössä kaksi päästötilaa QT700 ja QT800. Edellisessä (QT700) tehdään päästö alueella 650 – 750

---

[3] http://dew.edelstahl-e.com/upload/binarydata_ewkinterd4cms/53/38/00/00/00/00/3853/1.4021.pdf

°C. Tilaa QT800 vastaa päästö alueella 600 – 700 °C. Tiloja vastaavat mekaaniset ominaisuudet on annettu alla olevassa taulukossa.

		QT700		Typische Werte (ca.)	
		1 – 80*	81 – 160	1 – 80*	81 – 160
Streckgrenze (MPa)	$R_{p0,2}$	≥ 500	≥ 500	680	680
Zugfestigkeit (MPa)	R_m	700 – 850	700 – 850	830	830
Bruchdehnung (%)	A_5	≥ 13	≥ 13	16	16
Kerbschlagarbeit (J) 25 °C	ISO-V	≥ 25	≥ 25		
		QT800		Typische Werte (ca.)	
		1 – 80*	81 – 160	1 – 80*	81 – 160
Streckgrenze (MPa)	$R_{p0,2}$	≥ 600	≥ 600	760	760
Zugfestigkeit (MPa)	R_m	800 – 950	800 –950	930	930
Bruchdehnung (%)	A_5	≥ 12	≥ 12	15	15
Kerbschlagarbeit (J) 25 °C	ISO-V	≥ 20	≥ 20		

*Angegebene Werte gelten nur für den nicht kaltverfestigten Zustand.
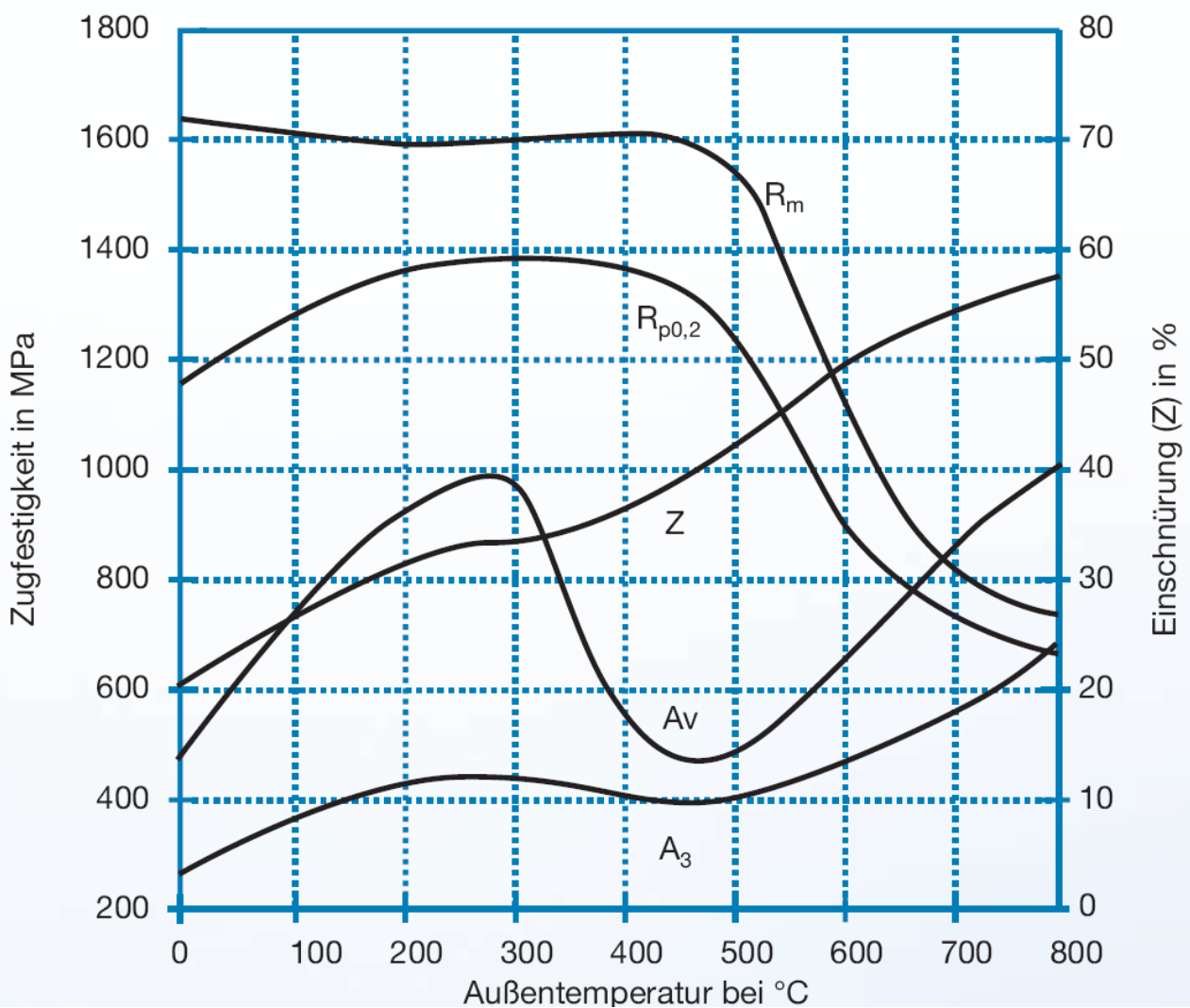
Eräiden mekaanisten ominaisuuksien muuttuminen eri päästölämpötiloissa on esitetty oheisessa kuvassa. Päästöhauraus näkyy erityisesti iskusitkeyden Av arvoissa (asteikko puuttuu kuvasta).

Teräs 1.4313 (X3CrNiMo13-4)

Teräs 1.4313 on pehmeämartensiittinen ruostumaton teräs. Hyvän sitkeytensä ansiosta se sopii nuorrutettuna käytettäväksi lämpötila-alueella -60 ^{o}C – +300 ^{o}C. Mo-lisäyksen ansiosta sen korroosionkestävyys vastaa terästä 1.4057[4].

Teräksen 1.4313 pehmeäksihehkutus tehdään alueella 600 ^{o}C – 650 ^{o}C jäähdyttämällä hitaasti joko uunin mukana tai ilmassa. Pehmeäksihehkutetulle teräkselle murtolujuus ja Brinell- kovuus ovat tyypillisesti R_m ≤ 1100 MPa ja HB ≤ 320.

Lämpökäsittelyssä tulee välttää 825 ^{o}C lämpötilan läheistä aluetta, koska teräs tällöin haurastuu.

Teräs voidaan karkaista hehkuttamalla 950 – 1050 ^{o}C lämpötilassa ja jäähdyttämällä sen jälkeen ilmassa tai öljy- tai polymeerikylvyssä. Päästölämpötila riippuu halutusta lujuudesta. Yleisesti on käytössä kolme päästötilaa QT650, QT780 ja QT900. Tilassa QT650 tehdään kaksivaiheinen päästö ensin alueella 650 – 700 ^{o}C ja sen jälkeen toinen päästö lämpötilassa 600 – 620 ^{o}C. Tilaa QT780 vastaa yksi päästö alueella 550 – 600 ^{o}C. Tilaa QT900 puolestaan päästö välillä 520 – 580 ^{o}C. Tiloja vastaavat mekaaniset ominaisuudet on annettu alla olevassa taulukossa.

Zustand	Anlasstemperatur °C	R_m N/mm²	$R_{p0,2}$ N/mm²	A_5 %	Av J
QT 650	650 °C – 700 °C und 600 °C – 620 °C Luft oder Wasser	650 – 830 (760)	≥ 520 (690)	≥ 15 (20)	≥ 70
QT780	550 °C – 600 °C Luft oder Wasser	780 – 980 (875)	≥ 620 (800)	≥ 15 (19)	≥ 70
QT900	520 °C – 580 °C Luft oder Wasser	900 – 1000 (990)	≥ 800 (940)	≥ 12 (17)	≥ 50

---

[4] http://dew.edelstahl-e.com/upload/binarydata_ewkinterd4cms/32/34/00/00/00/00/3432/Datenblatt_4313_GER.pdf

UFG ja valssaus

▪ Epäsymmetrinen valssaus

- kitka tai nopeusero ylä- ja alavalssin välillä

- leikkautuminen ⇒ hieno raekoko

Kokeet Oulussa, I

Näytteet pestiin (vesi ja etanoli) ja pinnat kiilotettiin (240 grid)/puhallettiin (hiekka AlO3, puhallus noin 45°) ennen jokaista pistoa.

Voiteluaineena käytettiin Piniferin Pini CF öljyä laimentamattomana.

Kitkavalssaus

Näytemateriaalit, joista tutkittiin: a, d, k ja n

Valssaussuuntaan		Kita/mm	3.75	2.81	2.1	laskettu 25% reduktion/ pisto mukaan
Pinnat ylä/ala(pistoittain)		h0	h1	h2	h3	r
0/0	a	4.95	4.10	3.27	2.58	47.87879
0/kiillotettu	b	4.95	4.14	3.29	2.66	46.26263
0/kiillotettu+öljytty	c	4.95	4.11	3.30	2.60	47.47475
hpuhallettu/kiillotettu+öljytty	d	4.94	4.13	3.31	2.66	46.15385

90° valssaussuuntaan		Kita/mm	3.75	2.81	2.1	laskettu 25% reduktion/ pisto mukaan
Pinnat ylä/ala(pistoittain)		h0	h1	h2	h3	r
0/0	k	4.98	4.14	3.28	2.62	47.38956
0/kiillotettu	l	4.97	4.14	3.30	2.65	46.68008
0/kiillotettu+öljytty	m	4.99	4.12	3.29	2.65	46.89379
hpuhallettu/kiillotettu+öljytty	n	4.99	4.14	3.30	2.65	46.89379

Makrokovuudet

Viisi mittausta näytesuikaleen poikki noin tasajaolla.

| Näyte	Puoli	1	2	3	4	5	ka.	menetelmä
a	ylä	183	182	199	188	186	188	HV2
	ala	179	180	181	176	177	179	HV3
d	ylä	170	189	188	184	179	182	HV2
	ala	176	181	176	166	181	176	HV2
k	ylä	170	176	182	182	180	178	HV2
	ala	178	183	178	184	180	181	HV2
n	ylä	171	182	185	194	182	183	HV2
	ala	168	175	175	171	170	172	HV2

Makrokovuudet

Yläpuoli näyttää pääsääntöisesti vähän kovemmalta.
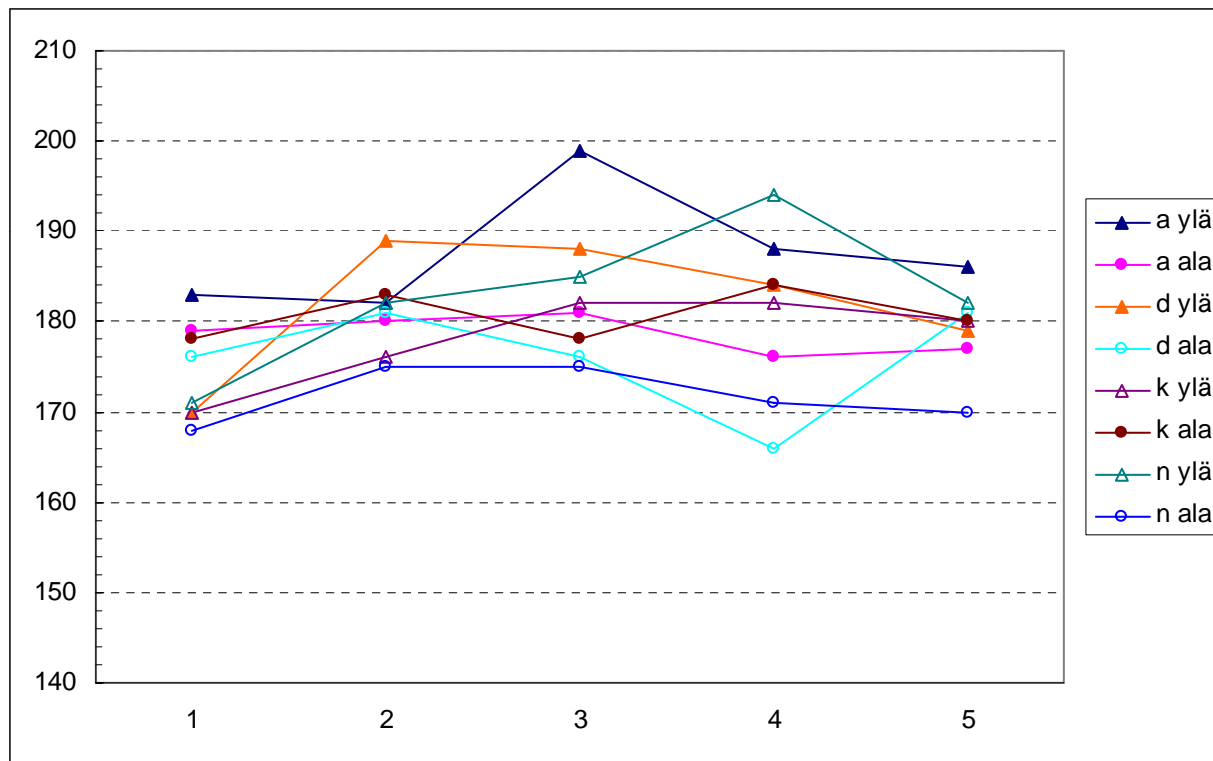
Mikrokovuudet

Poikkileikkaus mikrokovuuksien
ja mikrorakennekuvien suunnat

suunta y

suunta x
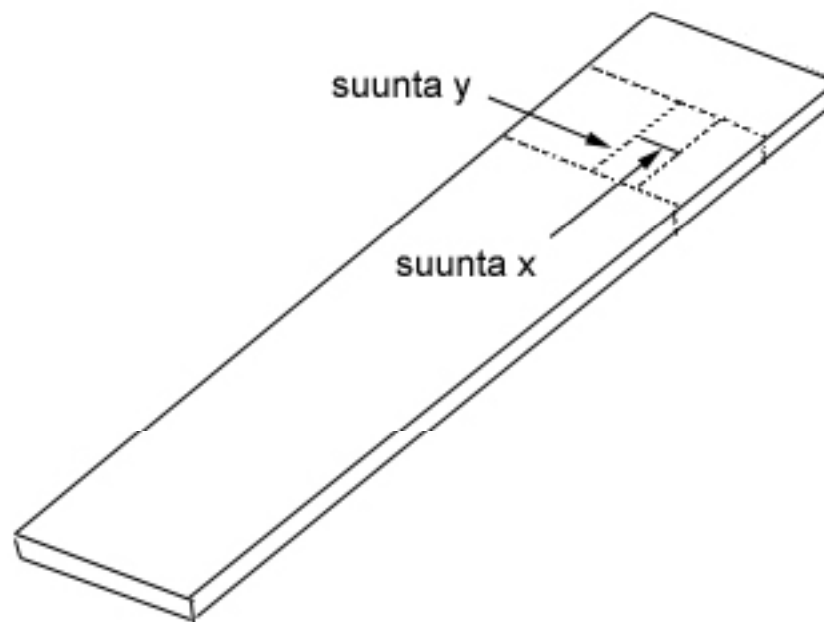
Mikrokovuus

NÄYTE	kovuus[HV 0,5]								ka.
a_x	196	195	195	198	194	194	200	197	196
a_y	204	203	203	199	220	213	203	192	205
d_x	207	208	200	205	203	198	202	206	204
d_y	205	198	212	212	200	209	210	203	206
k_x	205	202	205	212	200	207	205	205	205
k_y	191	200	209	202	204	212	201	208	203
n_x	207	195	199	208	205	202	209	201	203
n_y	196	205	196	208	207	202	202	197	202

Mikrokovuus
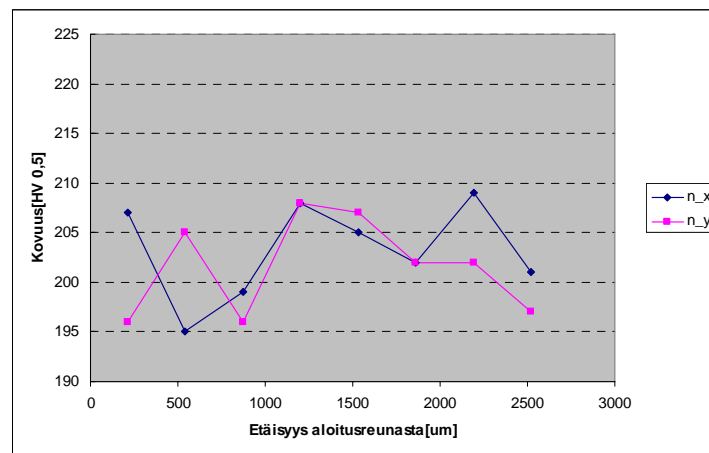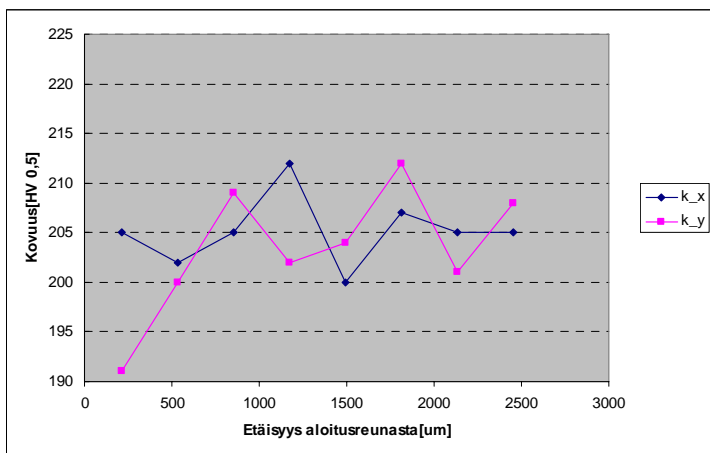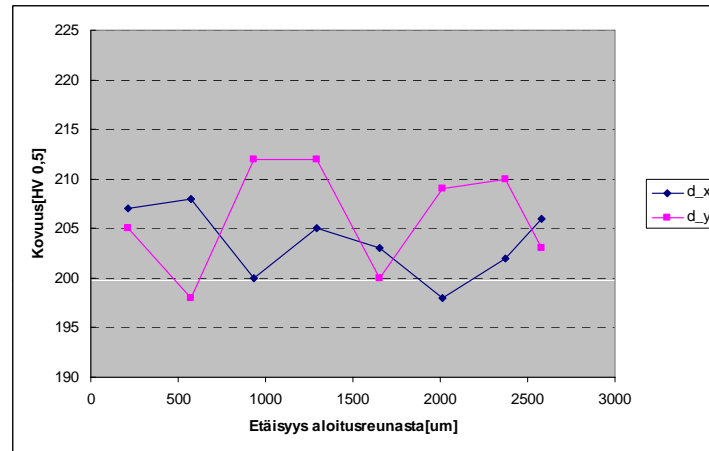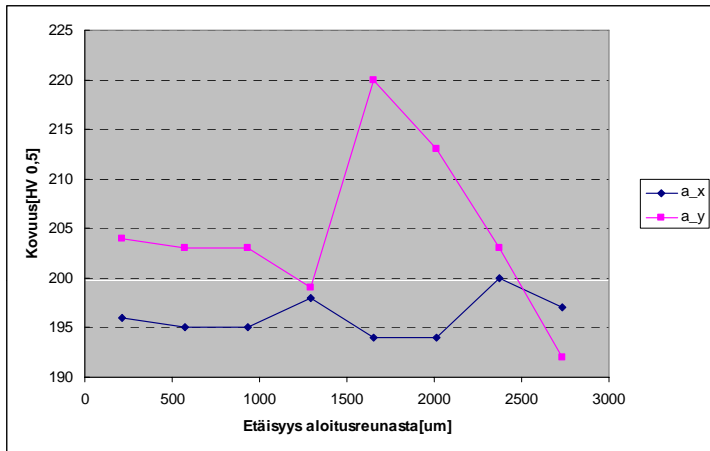
Mikrokovuus, tarkistusmittaus

näyte	alareuna	etäisyys alkaen alareunasta[um]								yläreuna
		210	550	890	1230	1570	1910	2250	2590	

		Kovuus[HV 0,5]								ka
d_x		214	199	201	202	195	207	202	202	203
d_y		201	200	202	211	201	204	213	203	204
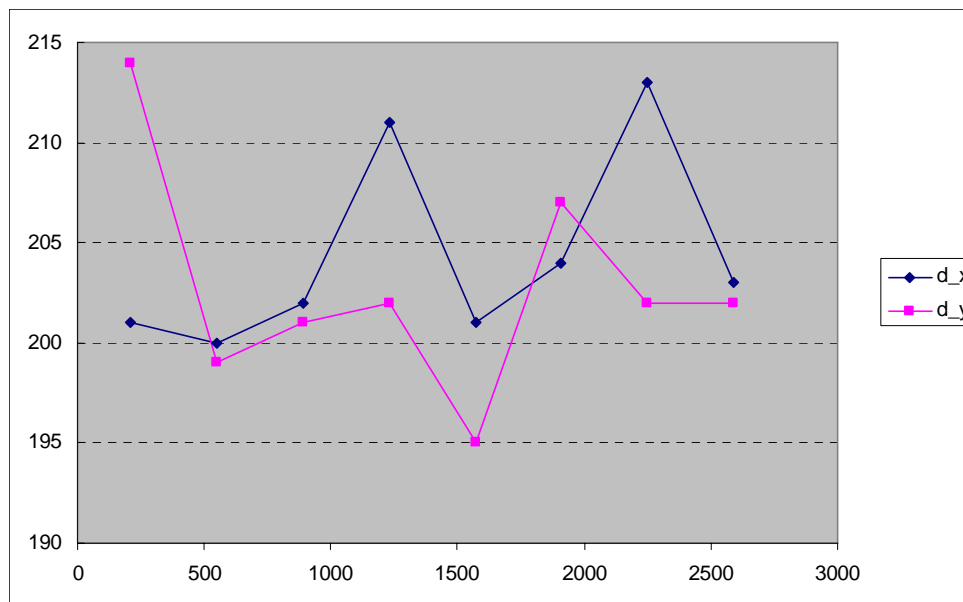
Mikrorakennekuvat

- Kuviin yhdistetty poikkileikkauksen molemmat reunat ja pala keskeltä

a_x
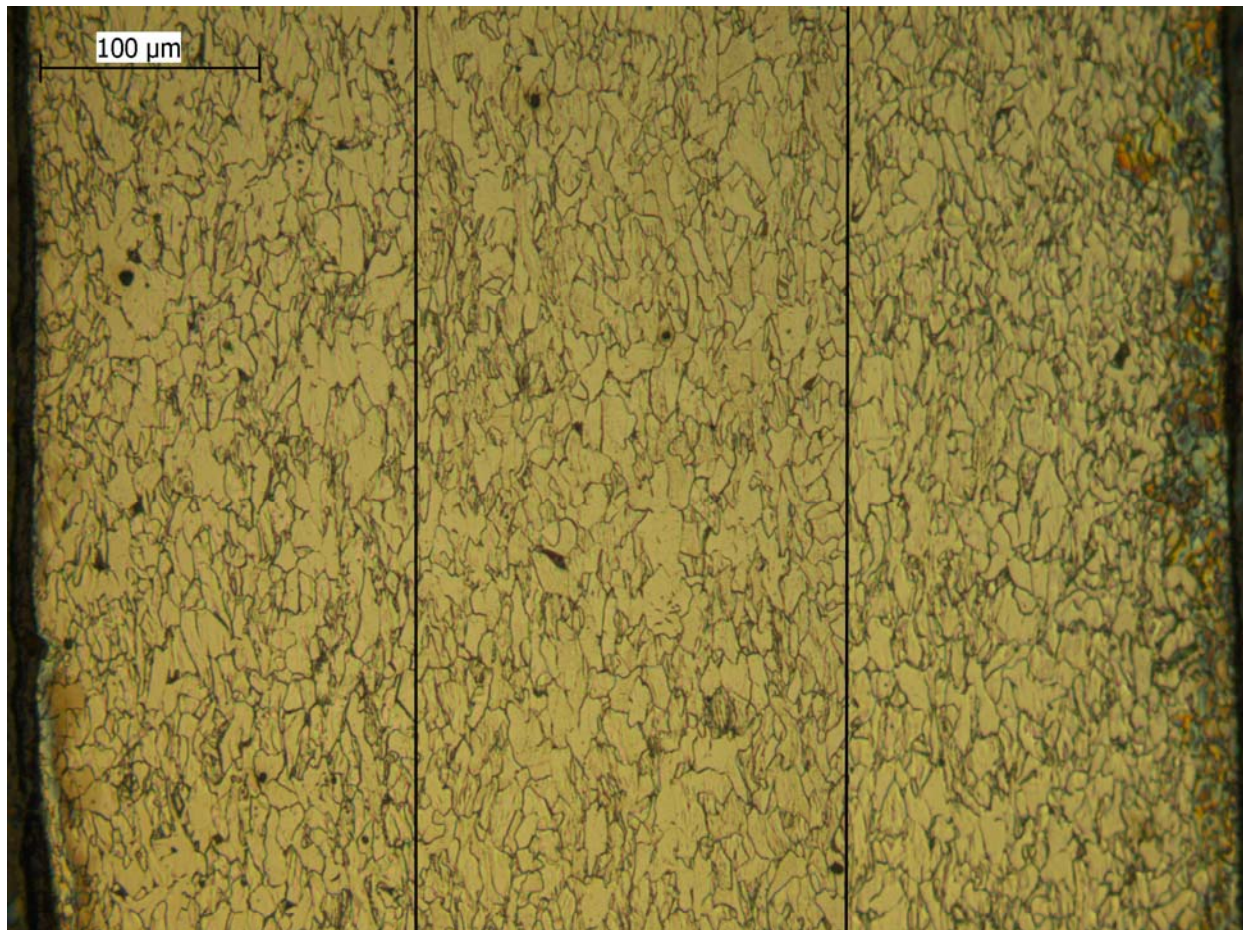
Mikrorakennekuvat

a_y
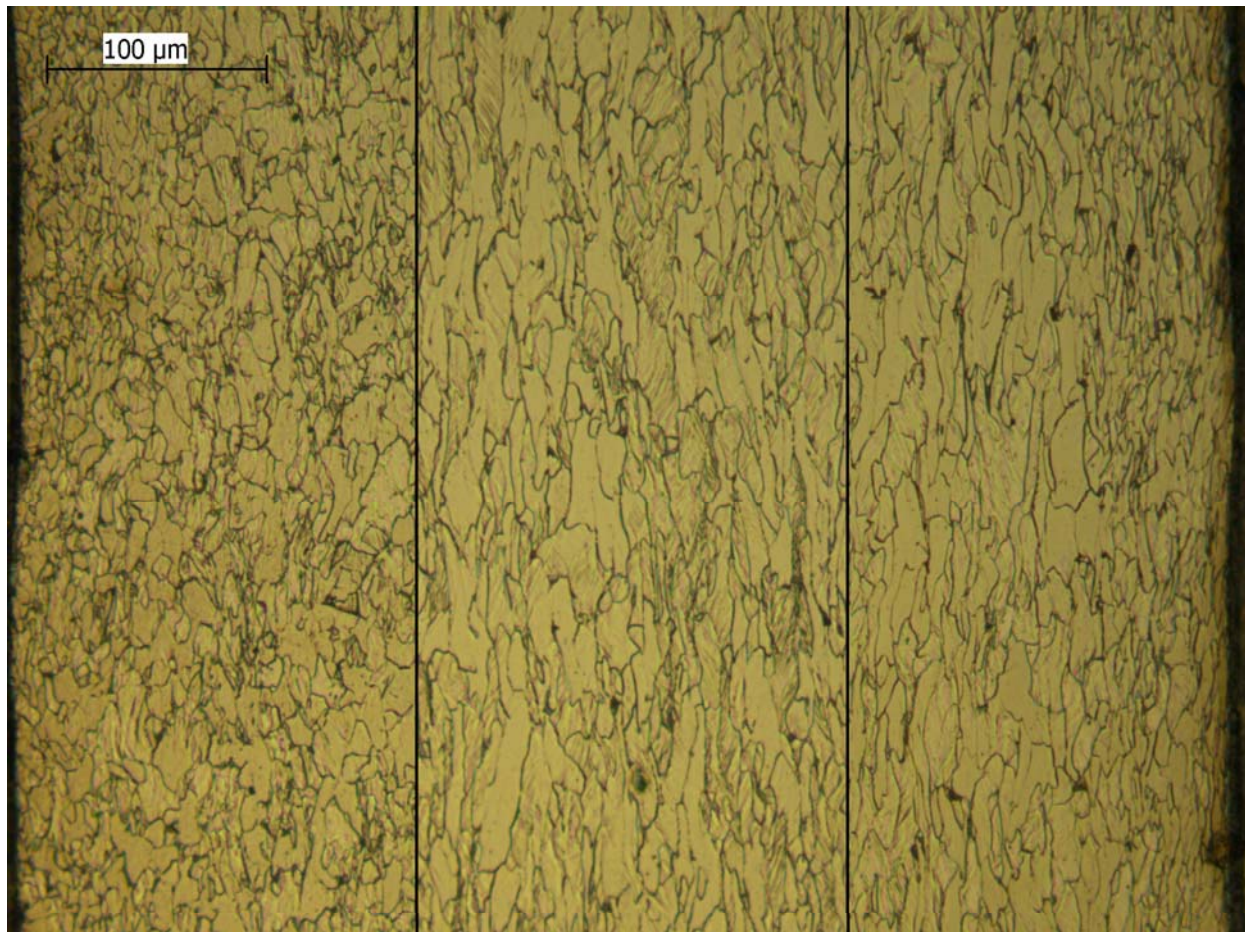
Mikrorakennekuvat

d_x
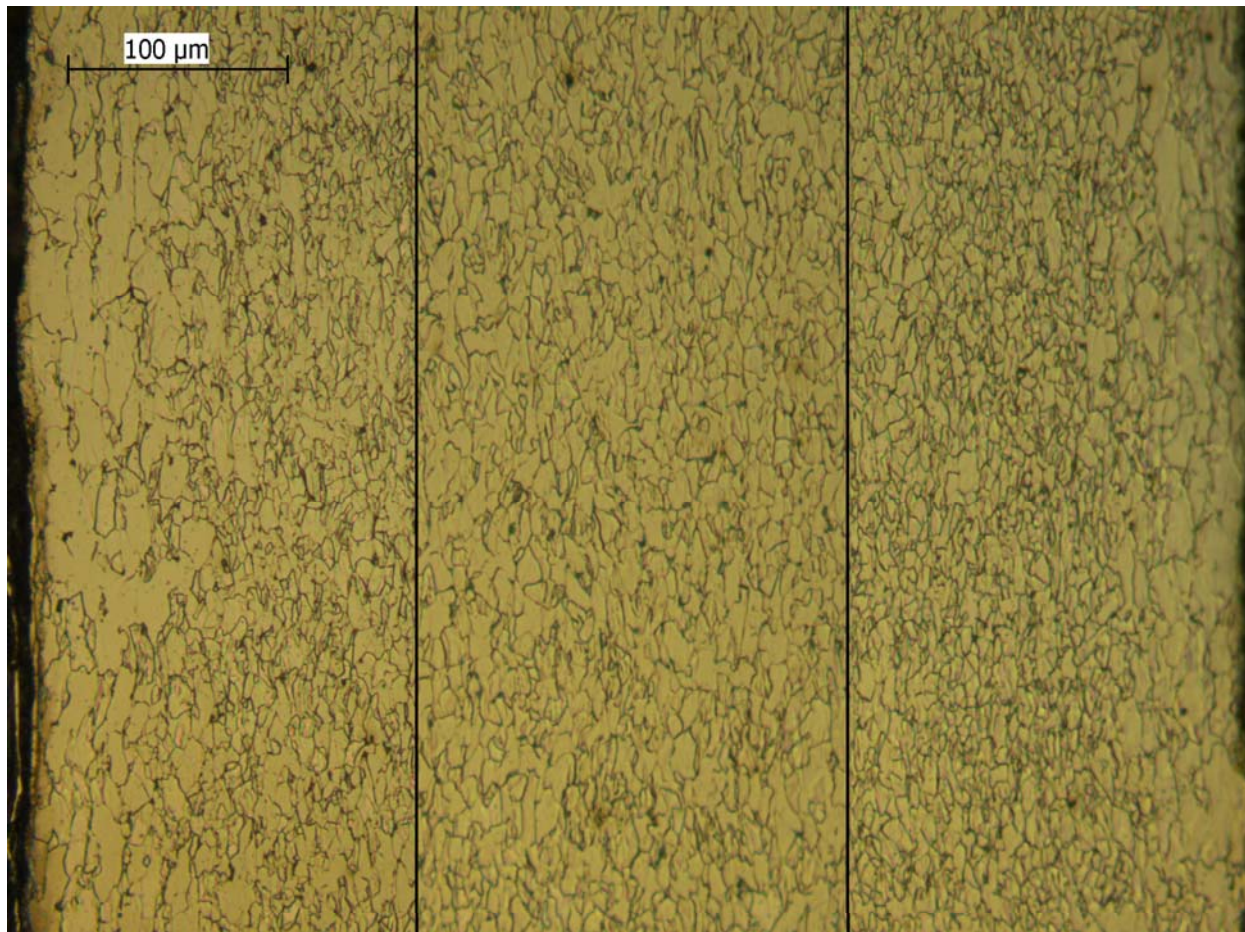
Mikrorakennekuvat

d_y
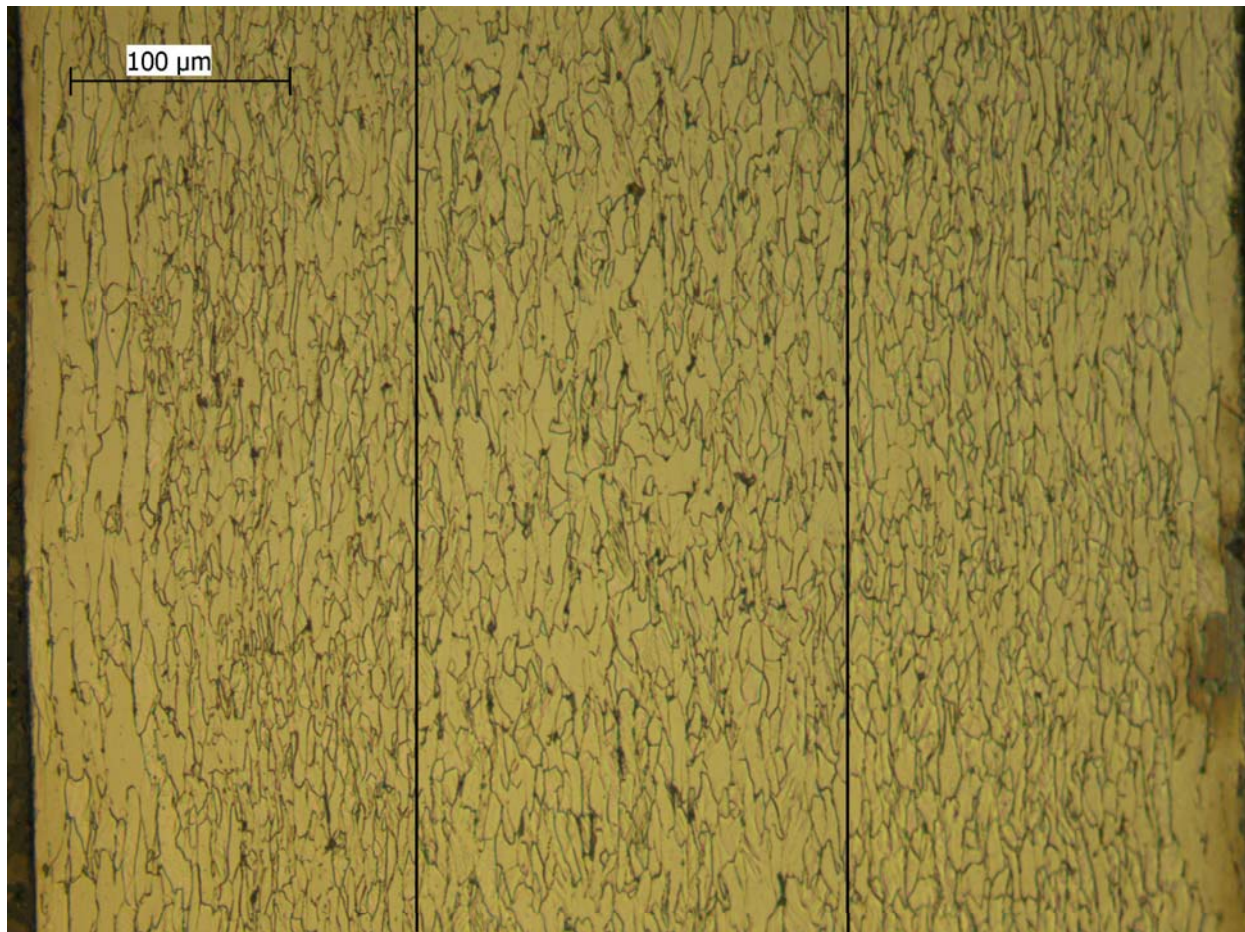
Mikrorakennekuvat

k_x
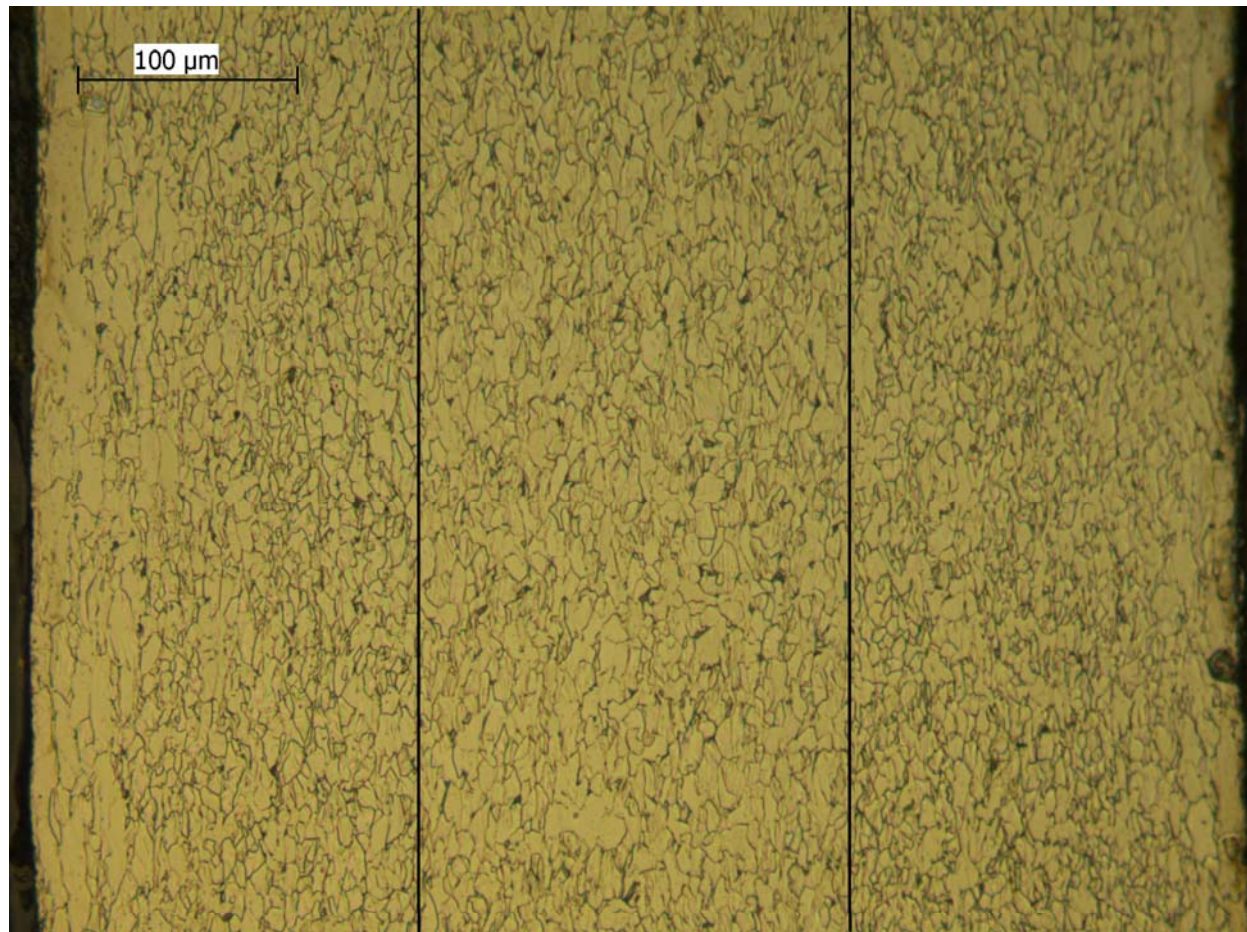
Mikrorakennekuvat

k_y
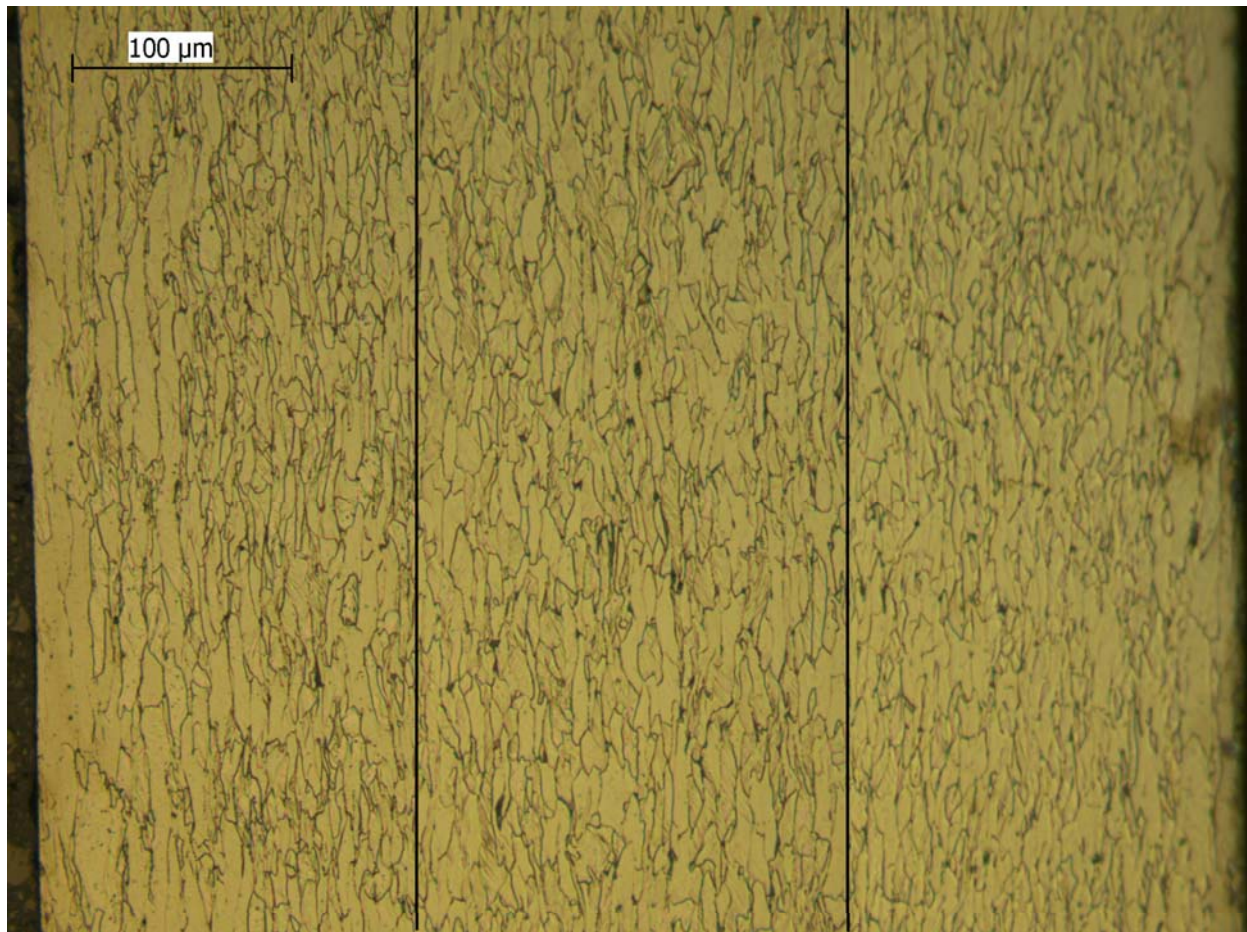
Mikrorakennekuvat

n_x
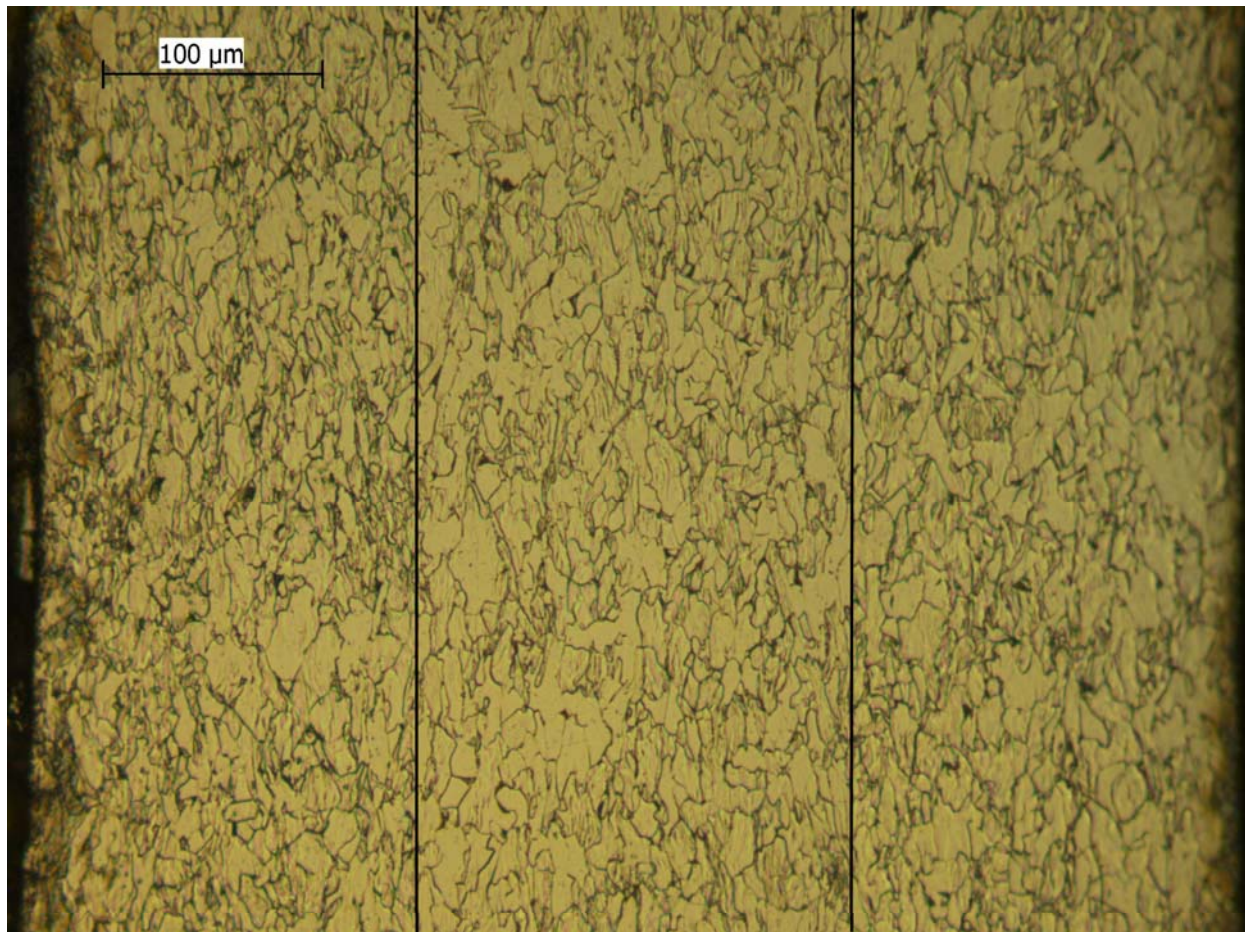
Mikrorakennekuvat

n_y
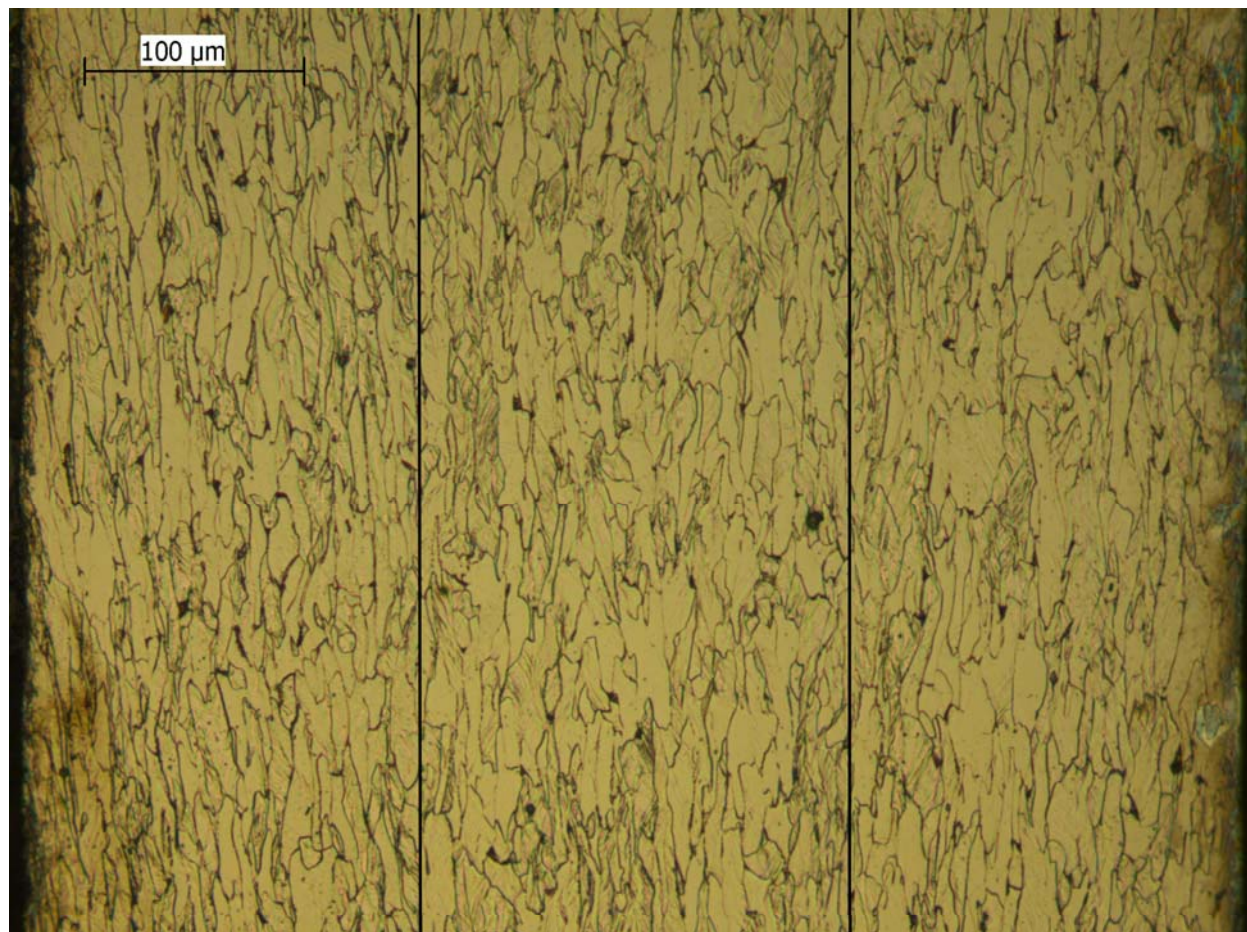
Mikrorakenteisten metallituotteiden joustava valmistus, MIVA
Ovako Wire

Johtoryhmän kokous 4
VTT Espoo 30.9.2009
Jouko Virta

VTT

Business from technology

VTT TECHNICAL RESEARCH CENTRE OF FINLAND

Ovako Wire - MIVA _ Luja hyvin vedettävä valssilanka

Erikoislujat valssilangat ja langat -tutkielma

- Vieraileva professori Leijun Li Utahin yliopistosta (Utah State University, Logan, Utah, USA) teki aiheesta kattavan kirjallisuustutkielman

- Tutkielmassa päädyttiin lopputulokseen, joka korostaa tavanomaisia valssaus- ja langanvetotekniikoita sekä korkeahiilistä hiiliterästä

VTT

2

Ovako Wire - MIVA _ Luja hyvin vedettävä valssilanka

Luja ja sitkeä teräs

- Vain hienorakeinen rakenne (UFG) voi olla sekä lujaa että sitkeää
- Hieno alirakenne (ilman hienorakeisuutta voi olla lujaa, mutta ei sitkeää
- Superplastisuus on seuraus hienojen rakeiden pyörimisestä ja muodonmuutoksesta
- Raekoon hienoneminen on ainoa lujittumismekanismeista, joka alentaa iskusitkeyden transitiolämpötilaa

3

Ovako Wire - MIVA _ Luja hyvin vedettävä valssilanka

UFG-terästä SPD ja ATP -tekniikoilla

- Hienorakeinen UFG rakenne saadaan joko voimakkaalla kylmä/lämminmuokkauksella (SPD severe plastic deformation) tai kehittyneellä termomekaanisella käsittelyllä (ATP)
- SPD on pelkkää kylmämuokkausta kokonaismuokkausasteen ollessa useita satoja prosentteja (3-5)
- ATP sisältää muokkauksen (kuuma, lämmin, kylmä) lisäksi hallitun lämpötilasyklin ja jopa erillisen lämpökäsittelyn
- ATP:n etuna on perinteisten tekniikoiden käyttö: valssaus, takominen, langanveto ja pursotus

4

Ovako Wire - MIVA _ Luja hyvin vedettävä valssilanka

ATP -tekniikka

- ATP pohjautuu muokkaukseen, Nb, Ti, V -mikroseostukseen ja hallittuun jäähtymiseen:
  - austeniitin dynaaminen rekristallisaatio kuumamuokkauksessa
  - austeniitti-ferriitti –faasimuutos
  - voimakkaan muodonmuutoksen aikaansaama ferriittimuutos SIF
  - kuumamuokkaus austeniitti-ferriittialueella,
  - rakeen kasvun estäminen: nopea jäähdytys, mikroseostus
  - ferriitin lämminmuokkaus ja rekristallisaatio / toipuminen

VTT

5

Ovako Wire - MIVA _ Luja hyvin vedettävä valssilanka

ATP -tekniikka

- Dynaamisessa rekristallisaatiossa syntyvät rakeet ovat sitä hienojakoisempia mitä suurempi on muodonmuutosnopeus ja matalampi kuumamuokkauslämpötila

- Rakeet eivät kasva nopean jäähdytyksen ja mikroseostuksen ansiosta, ferriitin raekoko on 1-2 μm

VTT

6

VTT TECHNICAL RESEARCH CENTRE OF FINLAND

Ovako Wire - MIVA _ Luja hyvin vedettävä valssilanka

TERMOMEKAANINEN KÄSITTELY

Austeniitin voimakas muokkaus pienentää ferriitin raekokoa tiettyyn muokkausasteeseen asti

Matala muokkauslämpötila johtaa pieneen raekokoon, nopea jäähtyminen siirtää ferriittialuetta matalampiin lämpötiloihin, seostus nostaa rekristallisoitumislämpötilaa sekä estää rakeenkasvua

Ylieutektoisilla teräksillä muokkaus austeniitti-sementiittialueella estää raerajakarbidien muodostumisen

7

VTT TECHNICAL RESEARCH CENTRE OF FINLAND
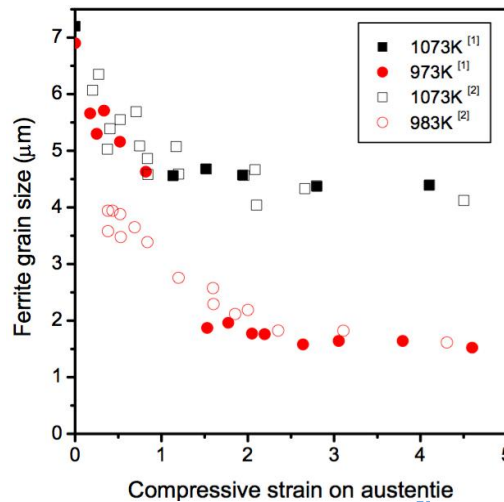
Ovako Wire - MIVA _ Luja hyvin vedettävä valssilanka

TERMOMEKAANINEN KÄSITTELY MARTENSIITTIALUEELLA

- Erikoisena ATP-tekniikkana on kylmämuokkaus Ms-lämpötilassa ja muokkauksen jälkeinen hehkutus
- Ferriitin raekoko 0,18 μm ja tasaisesti ferriittiin jakautuneet nanokarbidierkaumat
- Kylmämuokkaus 50 % Ms-lämpötilassa ja jälkihehkutus johtaa hienoon ferriittiseen rakenteeseen, jossa on hienoja nanoluokan karbidierkaumia
- Muokkauksessa syntynyt hienojakoinen dislokaatiosellirakenne muuttuu hehkutuksessa hienorakeiseksi ferriitiksi raekokoon 0,18 μm

8

Ovako Wire - MIVA _ Luja hyvin vedettävä valssilanka

ATP -tekniikan vertailua

• Muodonmuutos on pienempi kuin SPD:ssä
• Raekoko ei ole yhtä hieno
• Hyödyntää tunnettuja jatkuvia teollisia massatuotantomenetelmiä
• Prosessointi-ikkuna kapea ja vaativa kontrolloitavaksi

9

Ovako Wire - MIVA _ Luja hyvin vedettävä valssilanka

UFG-terästä SPD ja ATP -tekniikoilla

Menetelmä	Koostumus [%]	Ferriitin raekoko [μm]	Log. venymä	Muokkauslämpötila [°C]	Jäähtyminen ja jälkihehkutus
ECAP	0.08C–0.42Mn–0.18S	0,2	3,0	20	ilma
ECAP	0.15C–1.06 Mn–0.25Si	0,8	4,0	500	730 °C / 10 min, vesisammutus
ATP	0.11C–1.45Mn–0.34Si–0.068Nb	2,0 - 5,0	2,2 - 3,6	880 - 760	ilma
ATP	0.17C–1.32Mn–0.44Si–0.15Nb	2,1	2,3	700	vesi
ATP	0.22C–0.21Si–0.74Mn	1,3	1,6	550	550 °C / 120 min
ATP	0.13C–0.37Mn–0.01Si	0,18	0,8	293 (Ms)	500 °C / 30 min

10

Ovako Wire - MIVA _ Luja hyvin vedettävä valssilanka

Hienorakeinen UFG teräs termomekaanisesti

- Niukka ja matalahiilisillä teräksillä UFG-rakenne ja hyvät mekaaniset ominaisuudet saadaan kylmä- tai lämminvalssauksella Ms-lämpötilassa ja hehkutuksella
- Ylieutektoidisilla teräksillä (>1 %C) UFG-rakenne saadaan kylmämuokkaamalla (langanveto)
- Lähtörakenteen pitää olla homogeenista hienojakoista perliittiä ilman karbidiverkkoa.
- Kyseinen rakenne saadaan sopivalla jäähdytystekniikalla ja seostuksella, ja tarvittaessa termomekaanisesti takomalla tai pursottamalla.

11

Ovako Wire - MIVA _ Luja ja hyvin vedettävä valssilanka

YLIEUTEKTOIDISET HIILITERÄKSET

- Hiilipitoisuuden nostaminen on edullinen tapa lujittaa terästä: UHCS - teräkset (ultrahigh-carbon steel) 1,0 – 2,1 % C
- Suurin laboratorio-olosuhteissa saavutettu vedetyn langan lujuus on 5000 MPa
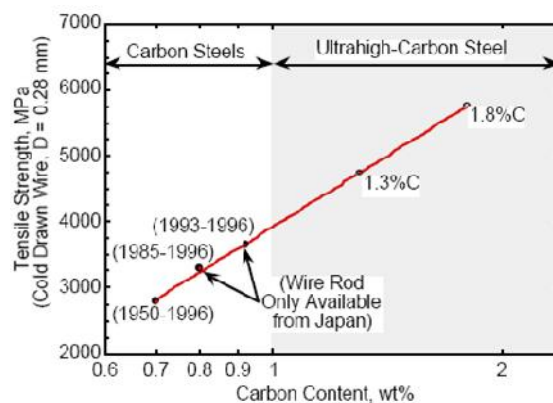
12

Ovako Wire - MIVA _ Luja hyvin vedettävä valssilanka

Ylieutektoidisen langan lujuuden kasvu langanvedossa
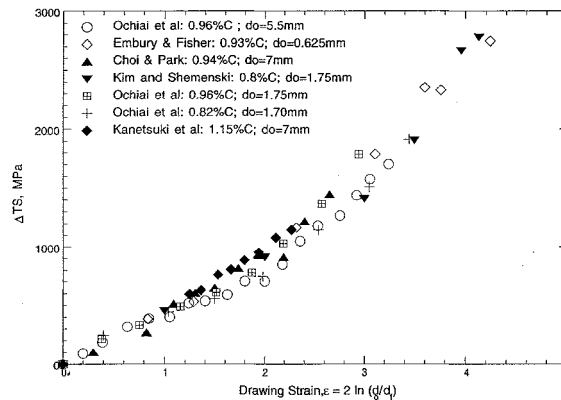
Fig. 13. Strength increment as a function of wire drawing strain for eutectoid and hypereutectoid steels with different compositions, initial wire diameters and initial strengths.

Ovako Wire - MIVA _ Luja hyvin vedettävä valssilanka

YLIEUTEKTOIDISET HIILITERÄKSET

- Raerajakarbideja ei saa esiintyä, sementiittilamellien tulisi olla mahdollisimman ohuita

- Raerajakarbidiverkko voidaan estää
  - nopealla jäähdyttämisellä valssauslämpötilasta (1,3 %C, 10 – 15 °C/s riittää hiilipitoisuudelle 1,1 %)
  - seostuksella Si, Al ja **Co**
  - termomekaanisella käsittelyllä

Ovako Wire - MIVA _ Luja hyvin vedettävä valssilanka

YLIEUTEKTOIDISET HIILITERÄKSET

- Seostus
  - C pienentää perliitin lamellietäisyyksiä, vedettävyys paranee, delaminoitumisvaara pienenee, muokkauslujittumisnopeus kasvaa
  - Mn hidastaa perlitoitumista
  - Cr pienentää lamellietäisyyksiä, estää grafitoitumista
  - Si ehkäisee karbidiverkkoa, lujittaa, nostaa perlitointilämpötilaa
  - Al estää karbidiverkon muodostumista
  - Co estää karbidiverkon muodostumista (1,3 %C)
  - Ni vähentää delaminoitumista
  - Seosaineiden haitat:
    - valu vaikeutuu
    - suotautuminen
    - perlitoitumisaika pitenee
    - oksidikerroksen poisto vaikeutuu

15

Ovako Wire - MIVA _ Luja hyvin vedettävä valssilanka

YLIEUTEKTOIDISET HIILITERÄKSET
Esimerkki valmistuksesta

- Aihiot valetaan tavanomaisesti
  - Parempi valurakenne saavutettaisiin nopealla jähmettymisellä (sulakerrostus)
- Valetut aihiot 1,0 - 1,45 %C kuumamuokataan
- Tangot austenitoidaan argonissa 1000 °C:ssa, patentoidaan lyijykylvyssä 550 °C / 3 min
- Kylmävedetään vaiheittain 15 % reduktioin nopeudella 8 m/min

16

Ovako Wire - MIVA _ Luja hyvin vedettävä valssilanka

YLIEUTEKTOIDISET HIILITERÄKSET

UHC terästen mikrorakenne pursotettuna

(a) 1.15C-1.6Al   (b) 1.30C-0.5Si   (c) 1.23C-1.2Si

4.00KX 2.50µ   4.00KX 2.50µ   4.03KX 2.48µ

17

Ovako Wire - MIVA _ Luja hyvin vedettävä valssilanka

Ylieutektoidinen teräslanka

Esieutektoidinen sementiitti lujittaa perliittistä rakennetta.

Ylieutektoidisen perliittisen hiiliteräksen lujuus kulkee selvästi ylempänä kuin eutektoidisen

Legend:
- ● Heat treated data - UHCS-1.5C-1.6Al
- ■ Heat treated data - UHCS-1.8C-1.6Al
- ◆ Hyzak and Bernstein data - eutectoid composition steel (.8C)
- □ Extruded data - UHCS-1.8C-1.6Al
- ○ Extruded data - UHCS-1.2C-1.6Al
- ◇ Extruded data - UHCS-1.2C-1.2Si
- △ Extruded data - UHCS-1.3C-.5Si

Y-axis: Yield Strength (MPa)

X-axis: (pearlite interlamellar spacing)$^{-1/2}$ $(\mu m)^{-1/2}$

18

Ovako Wire - MIVA _ Luja hyvin vedettävä valssilanka

Ylieutektoidinen teräslanka

Voimakkaasti vedetty lanka sisältää ferriittilamelleja. Sementiitin hiili on liuennut yikyllästeisenä
tai erkautunut dislokaatioihin. Ferriittilamellien paksuus on luokkaa 10 nm.
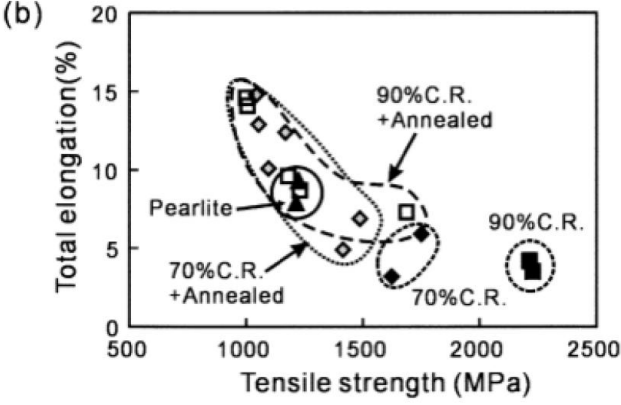
Ovako Wire - MIVA _ Luja hyvin vedettävä valssilanka

Ylieutektoidinen teräslanka

Hehkutus palauttaa kylmämuokatun perliitin sitkeyden ja jättää jäljelle jonkin verran lujittumista.
Hehkutuksessa perliitin sementiitti palloutuu ja ferriitti muuttuu hienorakeiseksi tasa-
aksiaaliseksi. Ferriitin ja sementiitin raekoko on <1 μm.

Ovako Wire - MIVA _ Luja hyvin vedettävä valssilanka

SUOSITELLAAN LUJAN LANGAN KEHITTÄMISTÄ

- Käytettävä tekniikka on ylieutektoidisen hiiliteräksen termomekaaninen valssaus ja kylmäveto
- Teräs on ylieutektoidista hiiliterästä 1,3 % C seosaineina Co, Si ja Cr
- Hyvä vedettävyys taataan laadukkaalla perlitoinnilla valssilinjassa tai erillisessä patentoinnissa (hienolamellaarinen perliitti)
- Valssilinjalla perlitointi vaatii erityisjärjestelyjä, mutta erillisessä patentoinnissa jäähtymiseen tulee myös kiinnittää huomiota
- Kylmäveto useissa vaiheissa nanomittakaavaisen hienojakoisen mikrorakenteen aikaansaamiseksi

21

Ovako Wire - MIVA _ Luja hyvin vedettävä valssilanka

JATKOTOIMENPITEET

- Valssilangan jäähdytyksen kehittäminen
  - Perlitoinnin laadun parantaminen
  - Nopea ja tasainen jäähdytys

- Patentointimahdollisuuksien ja vaatimusten tutkiminen
  - Jäähtymisen reunaehdot

- Menetelmät
  - Simulointi: kokeellinen, tietokoneavusteinen

22

Teknologiasta liiketoimintaa

Mikrorakenteisten metallituotteiden joustava valmistus, MIVA
Ovako Wire

Johtoryhmän kokous 6
Ovako Wire Taalintehdas 4.6.2010
Jouko Virta ja Mika Siren

8.7.2010   2

Ovako Wire - MIVA
Luja hyvin vedettävä valssilanka

KIRJALLISUUSSELVITYS 'ERIKOISLUJAT VALSSILANGAT JA LANGAT'

- Professori Leijun Li Utahin yliopistosta laatima review-artikkeli "Ultrahigh Strength Wire Rods and Wires Based on Severe Plastic Deformation (SPD) and Ultrafinegrained (UFG) Microstructure" ilmestyy Materials Science and Technology -lehdessä kesäkuussa

- Käyttölupa artikkelin lähteistä otettuihin kuviin hankittu ja osin ostettu

8.7.2010   3   VTT

Ovako Wire - MIVA
Luja hyvin vedettävä valssilanka

LUJAN LANGAN VALMISTUS
YLIEUTEKTOIDISESTA HIILITERÄKSESTÄ

- Taalintehtaalla on tarkoitus valssata 5,5 mm:n valssilankaa koeaihioista
- Kolme valssausaihiota 125 x 125 mm valettiin (Inst.)
- Valut pehmeäksihehkutettiin 200 °C/h lämpötilaan 1100 °C, pito 4 h ja jäähtyminen uunin mukana lämpötilaan <200 °C (Inst.)
- Jyrsintä mittaan 115 x 115 x n. 700 mm (Inst.)
- Jyrsittyihin pintoihin jäi näkyviin valupinnassa olleiden kuoppien pohjia
- Huonolaatuisin aihio halkaistiin: sisus ehjän näköistä

8.7.2010   4   VTT

Ovako Wire - MIVA
Luja hyvin vedettävä valssilanka

YLIEUTEKTOIDINEN HIILITERÄS

- Mikrorakenteessa ei saa olla karbidiverkkoa, perliitin ja muunkin mikrorakenteen tulee olla mahdollisimman hienojakoista ja epämetallisia sulkeumia on vältettävä
- Koostumuksen valintaperusteita:
  - 1,6 % C (korkea hiili on lujuuden perusta, hiili lisää lujuutta ja lujittumista langanvedossa)
  - 1,5 % Al (alumiini estää raerajakarbidien muodostumisen, nostaa A_1-lämpötilaa)
  - 1,3 % Cr (kromi estää grafitoitumista, pienentää lamellietäisyyksiä, lisää lujuutta ja lujittumista langanvedossa)
  - 0,2 % Si (pii ehkäisee karbidiverkkoa ja liuoslujittaa)
  - 0,3 % Mn (mangaani rikin ja fosforin sitomiseen, yhdessä kromin kanssa parantaa karkenevuutta)
  - Epäpuhtausrajat: <0,015 % S, <0,020 % P, <0,001 % As, <0,0001 % Pb ja <0,004 % Sn (lujan langan tulee olla mahdollisimman puhdasta)
  - Matala rikki on etu langanvedossa vähentäen katkeamista ja delaminoitumista: Tavanomainen rikkitaso 0,015 - 0,025 % takaa riittävän vetositkeyden. Lujilla langoilla tätä matalampi rikki antaa riittävän sitkeyden myös väännössä.

2

Ovako Wire - MIVA
Luja hyvin vedettävä valssilanka

YLIEUTEKTOIDISEN HIILITERÄKSEN TOTEUTUNUT KOOSTUMUS

Seos-aine	Tilattu (VTT)	Sula-analyysi (Instituutti)	Kanaviston pala (Instituutti)	Kappaleanalyysit (Ruukki)
C	1,45 - 1,75	1,66	1,71	1,68
Si	(0,2)	0,64	0,69	0,71
Mn	(0,3)	0,70	0,70	0,76
P	<0,010	0,01	<0,01	0,017
S	<0,020	0,01	<0,01	0,007
Al	1,35 - 1,75	1,36	1,36-1,8	1,8
Cr	1,10 - 1,45	1.36	1.30	1,37
Pb	-	-	<0,01	<0,002
Sn	-	-	<0,01	<0,002

Ovako Wire - MIVA
Luja hyvin vedettävä valssilanka

KUUMAPURISTUSTA VTT:SSA
- Valuista leikattuja palikoita 50 x 50 x 50 mm kuumapuristettiin
- Puristuslämpötila 1100 – n.850 °C
- Tavoite pinta-alareduktio 80 – 90 % (50 x 50 mm^2 → 22,36 – 15,81 mm^2):
  - luonnollinen venymä: $\ln(A_0/A_1) = 1,61 – 2,30$ → **2,00**
  - **1. venytys** $\ln(A_0/A_1) = 0,50$ → $A_1 = 1516$ mm^2 = **39 x 39 mm**
  - **1. tyssäys** $A_1(1516)$ → $A_0(2500)$; $\ln(A_1/A_0) = 0,50$
  - **2. venytys** $\ln(A_0/A_1) = 0,50$ → $A_1 = 1516 = 39$ x 39 mm
  - **2. tyssäys** $A_1(1516)$ → $A_0(2500)$; $\ln(A_1/A_0) = 0,50$
  - **Luonnollinen venymä yhteensä** 4 x 0,5 = **2,00** venytys-tyssäysohjelmalla:
    - 50 x 50 x 50 mm → 82 x 39 x 39 mm → 50 x 50 x 50 mm → 39 x 39 x 82 mm → 50 x 50 x 50 mm
- **Teelmän 115x115 mm valssauksessa valssilangaksi ⌀5,5 mm:**
  - **Pinta-alareduktio $(A_0-A_1)/A_0$ = 99,82 %**
  - **Luonnollinen venymä $\ln(A_0/A_1)$ = 6,322**
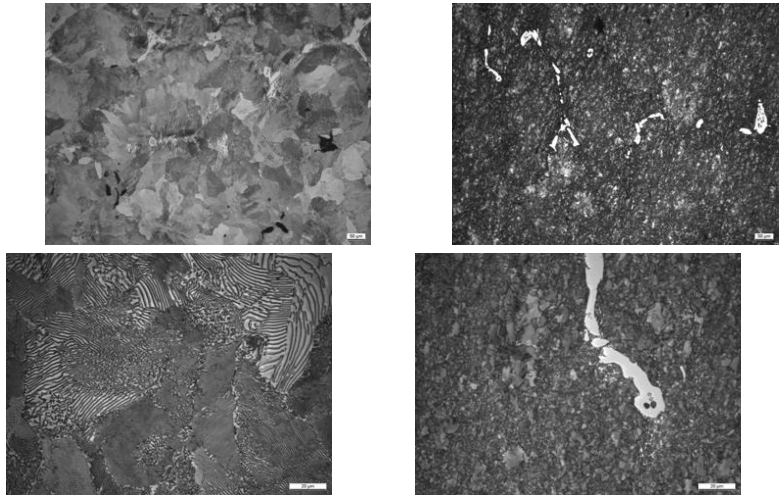
3
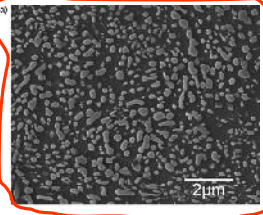
Ovako Wire - MIVA
Luja hyvin vedettävä valssilanka
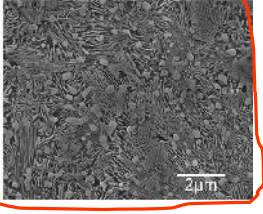
KUUMAPURISTETTUJEN JATKOKÄSITTELYT

Mikrorakennehaaveet:

- **Sementiitin palloutus:**
  - austenitointi 20 min lämpötilassa 815 °C (hieman A1:n yläpuolella)
  - hidas jäähtyminen lämpötilaan 750 °C nopeudella 1 °C/min
  - jäähtyminen vapaasti ilmassa

- **Perlitointi/patentointi:**
  - austenitointi 30 min lämpötilassa 860 °C (reilusti A1:n yläpuolella)
  - nopea jäähdytys lämpötilaan noin 575 °C leijupatjaan
  - pito 20 min lämpötilassa 575 °C leijupatjassa
  - jäähtyminen vapaasti ilmassa

Ovako Wire - MIVA
Luja hyvin vedettävä valssilanka

YLIEUTEKTOIDISEN VALSSILAGAN VALSSAUS TAALINTEHTAALLA

- Aihiot 115 x 115 x n.700 mm liitetään Taalintehtaan 650-parin aihion eteen ja valssataan 5,5 mm:n langaksi
- Liitoshitsaus:
  - valetun aihion kulmien pyöristys: näyteaihion särmät voidaan rälläköidä pyöreiksi
  - viisteytys 30° hitsausta varten, keskelle voi jättää 2-3 mm navan
  - hyvä esikuumennus aiemman kokemuksen mukaisesti
  - hitsaustarkastelu seuraavissa kalvoissa
- Valssauslämpötilat ja reduktiot sekä langan jäähdytys valssilinjassa
  - valssaus lievennetyllä 5,5 mm:n HC-ohjelmalla (?)
  - karbidiverkolta vältytään, kun valssaus riittävän matalaan lämpötilaan (valssauslämpötila ~1100 - 780 °C)
  - hidas jäähtyminen jäähdytyspedillä (valssilanka patentoitava erikseen)

Ovako Wire - MIVA
Luja hyvin vedettävä valssilanka

650-VARSIA TAALINTEHTAALLA

- 650-parilla valssatuista aihioista, 650-aihion mitat?
- Varsilla pyöreät särmät, jolloin näyteaihion särmät voidaan rälläköidä pyöreiksi
- Polttoleikatut päätypinnat viisteytetään 30° hitsausta varten, keskelle voi jättää 2-3 mm navan
- Esikuumennus aiempien kokemusten mukaan
- Hitsaustarkastelu seuraavissa kalvoissa
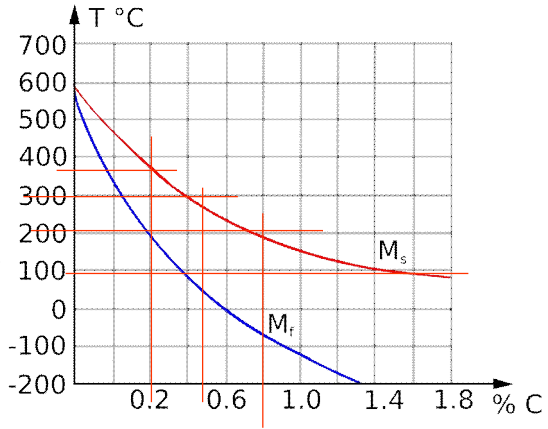
Ovako Wire - MIVA
Luja hyvin vedettävä valssilanka

HIILITERÄKSEN Ms-LÄMPÖTILA

- Ms-lämpötila: aihio <200 °C,
- varsi 200 - 350 °C (arvaus)

http://www.google.fi/imgres?imgurl=http://upload.wikimedia.org/wikipedia/commons/thumb/c/cd/Carbon_dependance_of_martensite.svg/265px-Carbon_dependance_of_martensite.svg.png&imgrefurl=http://commons.wikimedia.org/wiki/File:Carbon_dependance_of_martensite.svg&usg=__Oo4gtyxMZ6a7-P168rGXKF6Mo7I=&h=208&w=265&sz=11&hl=fi&start=41&um=1&itbs=1&tbnid=kGmutvYNRdSMBM:&tbnh=88&tbnw=112&prev=/images%3Fq%3D%2522martensite%2Bstart%2522%26start%3D36%26m%3D1%26hl%3Dfi%26sa%3DN%26rls%3DGGLG,GGLG:2006-03,GGLG:fi%26ndsp%3D18%26tbs%3Disch:1

UHCS-hitsaus

- SFS-EN 1011-2: Metallisten materiaalien hitsaussuositukset. Osa 2: Ferriittisten terästen kaarihitsaus
  - Ylihiilinen teräs ei mahdu SFS-EN1011-2 liite C kaavoihin
  - Esikuumennustarpeen määrittäminen vetyhalkeilun välttämiseksi
  - Tapa A graafinen: hiiliekvivalentti 0.3 < CE < 0.7

$$CE = C + \frac{Mn}{6} + \frac{Cr + Mo + V}{5} + \frac{Ni + Cu}{15} \,(\%)$$

   - **CE_{UHCS} = 2.08**

  - Tapa B laskennallinen: hiiliekvivalentti 0.2 < CET < 0.75

$$CET = C + \frac{Mn + Mo}{10} + \frac{Cr + Cu}{20} + \frac{Ni}{40} \,(\%)$$

   - **CET_{UHCS} = 1.82**

UHCS-hitsaus

- Musta-ruostumaton eripariliitosten hitsauksessa käytetään yleisesti Schaeffler-diagrammia (ja sen modifioituja versioita)
  - Ylihiilinen teräs ei mahdu myöskään näihinkään diagrammeihin
- ⇨ **Laskentakaavoista ei apua**
- ⇨ **Hitsausohjeet määritettävä kokeellisesti**
- **Yleisiä ohjeita kuitenkin valuraudan ja -terästen pohjalta:**
  - Käytetään mieluummin matalahiilistä vartta
    - Ei haeta lisäongelmia korkeahiilisellä
  - Esikuumenna aina kun se on mahdollista
  - Mitä korkeampi esikuumennus, sitä parempi (~ 200 – 250 °C?)
  - Käytä pehmeää austeniittista tai nikkelipohjaista lisäainetta
  - Esim. E 23 12 L R 3 2 ("67.60") tai E 23 12 2 L R 3 2 ("67.70") (puikot)
  - Tai vastaava MAG-umpi- tai rutiilitäytelanka (ns. asentolanka)

UHCS-hitsaus

Lisäainemäärä: hyvin karkea laskelma ("suuruusluokka")

- Railo: esim. 60° V-railo (eli 30° + 30°)
  - V_{railo} = 1900 cm^3/m (teoreettinen)
  - Hitsiainemäärä ~ 15 kg/m
  - Esim. 3.2 tai 4.0 mm "67.60" tai "67.70" puikko: hitsiainetta n. 0.6 kg/1 kg puikkoja
  - Puikkomenekki ~ 25 kg/m; railon kokonaispituus (4x0,5)x115=230 mm; puikkoja ~ 6 kg(?)
- Ilmarako ~ 2 mm
- Juuripinta ~ 2 – 3 mm/sivu
- Hitsausjärjestys suoruusvaatimusten mukaan (vetelyt ja taipumiset, varsi ja näyte linjaan)

Ovako Wire - MIVA
Luja hyvin vedettävä valssilanka

VALSSILANGAN TUTKIMINEN

- Valssilangasta tutkitaan
  - mikrorakenne
  - mitataan mekaaniset ominaisuudet, Re, Rm, A, Z,
- Valssilanka kylmämuokataan ja tutkitaan mahdollisuuksien mukaan
  - vedettävyys ja muokkauslujittuminen
  - kylmämuokatusta mikrorakenne ja mekaaniset ominaisuudet

VTT luo teknologiasta liiketoimintaa

TAMPEREEN TEKNILLINEN YLIOPISTO
Materiaalitenkiikan koulutusohjelma

Materiaalitekniikan laitos 14.4.2009

JUHO RAJAMÄKI

ECAP-PROSESSOITUJEN METALLIEN RAKENNNE JA MEKAANISET OMINAISUUDET.

STRUCTURE AND MECHANICAL PROPERTIES OF ECAP PROCESSED METALS.

Kandidaatin työ

Tarkastaja: Yliassistentti Mikko Hokka

TIIVISTELMÄ

Tämä työ on selvitys kirjallisuudessa julkaistusta aineistosta equal-channel angular pressing-prosessilla (ECAP) valmistetuista ultra-hienorakeisista (UHR) metalleista. ECAP-prosessointi on teollisesti lupaava menetelmä, koska sillä voidaan hienontaa metallien raekoko alle 1 µm ilman ylimääräisiä seosaineita. Tarkoitus oli selvittää millaisia mekaanisia ominaisuuksia ECAP-prosessoimalla metalleja on saavutettu, ja erityisesti miten lämpötila ja myötönopeus vaikuttavat näihin ominaisuuksiin. Kirjallisuusselvityksen tuloksena voidaan todeta, että UHR metallit ovat yleisesti erittäin lujia, mutta näiden murtositkeys on alhainen vedossa ja ne muokkauslujittuvat erittäin vähän. Erilaiset termomekaaniset ja mekaaniset käsittelyt voivat parantaa UHR metallien sitkeyttä, ilman että lujuus laskee merkittävästi. UHR metallit käyttäytyvät sitkeämmin sekä lujemmin, kun niitä kuormitetaan korkeilla myötönopeuksilla tai alle huoneen lämpötilassa. Riittävän matalilla myötönopeuksilla ja korkeissa lämpötiloissa useat UHR metallit käyttäytyvät superplastisesti, eli ovat pehmeitä ja erittäin hyvin muokkautuvia. UHR metalleissa tapahtuu toipumista ja rekristallaatio huomattavasti alhaisemmissa lämpötiloissa kuin tavallisilla menetelmillä valmistetuissa metalleissa, mikäli näitä ei ole erityisesti staboitu. UHR metallien myötönopeusherkkyys on suurempi kuin suurirakeiten metallien, mikäli näiden kiderakenne on pintakeskeinen kuutiollinen (PKK), ja pienempi, mikäli kiderakenne on tilakeskeinen kuutiollinen (TKK). Suurin osa julkaistuista tutkimuksista käsitteli PKK ja TKK metalleja, joten heksagonaalisen tiivispakkaus rakenteen UHR metalleista voidaan arvioida vain mekaanisten ominaisuuksien peruspiirteitä kohtuullisen luotettavasti. Näiden mekaanisten ominaisuuksien lämpötila- ja myötönopeusriippuvuuksista ei voida tehdä varmoja johtopäätöksiä.

ALKUSANAT

Tämä on Tampereen teknilliselle yliopistolle suoritettava tekniikan kandidaatin opin-
näytetyö. Se on laadittu materiaali- ja koneinsinööreille suunnatuksi selvitykseksi ultra-
hienorakeisten metallien mekaanisista ominaisuuksista.

Työ on tehty ensimmäinen kirjallinen selvitykseni, joten tarvitsin sen tekemiseen run-
saasti apua. Suurimman osan ohjeista sain ohjaajaltani Mikko Hokalta ja hän auttoi mi-
nua asiakysymysten jäsentelyssä sekä työssä esittämieni ajatusten selkeyttämisessä. Kii-
tos kuuluu myös vanhemmilleni Erkki Rajamäelle ja Leena Rajamäelle, heidän kärsiväl-
lisyydestään ja neuvoistaan. Lopuksi kiitän kihlattuani Anne-Mari Honkavaaraa loput-
tomasta kärsivällisyydestä, tuesta ja oikeinkirjoitusohjeista.

Sisällys

Lyhenteet ja merkinnät

CP	Commersial purity
ECAP	Equal-channel angular pressing
PKK	Pintakeskeinen kuutiollinen rakenne
TKK	Tilakeskeinen kuutiollinen rakenne
UHR	Ultra-hienorakeinen
φ	ECAP-muotin kulma
ψ	ECAP-muotin sisäkulman pyöristys
$\sigma_{0,2}$	Myötölujuus 0,2 % myötymän arvolla
σ_0	Hilakitka
α	Hall-Petch yhtälön materiaalivakio
d	Keskimääräinen raekoko
σ	Myötölujuus
α	Taylorin yhtälön materiaalivakio
M	Taylorin kerroin
G	Leikkausmoduuli
b	Burgersvektorin pituus
ρ	Dislokaatiotiheys
wt-%	Painoprosenttia
$\gamma`$	Alumiinin ja hopean välinen metastabiili faasi

1. Johdanto

Nykyisin yritykset tarvitsevat jatkuvasti lujempia ja halvempia materiaaleja. Lujuuden kasvaessa materiaalin sitkeys tavallisesti vähenee, mikä vähentää lujien materiaalien käyttökohteita. Raekokoa pienentämällä voidaan parantaa metallien lujuutta ja samalla säilyttää parempi sitkeys kuin tavallisilla lujittamismenetelmillä [1,2]. Tämä on kasvattanut kiinnostusta ultra-hienorakeisia (UHR) metalleja kohtaan. UHR metalleiksi luetaan metallit joiden raekoko on välillä 0,1-1 µm, ja joiden mikrorakenne on tasaakselinen sekä kohtuullisen homogeeninen. Lisäksi suurimmassa osassa raerajoista täytyy tapahtua suuri orientaation muutos, eli yli 50 % raerajoista täytyy olla korkean kulman rajoja (high angle boundary) [2].

Perinteisesti raekokoa on pyritty pienentämään termomekaanisten käsittelyjen avulla. Tällaisilla menetelmillä saavutetut raekoot ovat pienimmillään luokkaa ~1-10 µm [3]. Termomekaanisen prosessointi täytyy suunnitella erikseen jokaiselle seokselle, ja mikäli raekoko halutaan hyvin pieneksi, metalleihin täytyy seostaa aineita, jotka tekevät niistä kalliimpia sekä vaikeammin kierrätettäviä. Lisäksi lämpökäsittelyillä on vaikeata valmistaa metalleja, joiden raekoko on sama kappaleen sisustassa ja pinnassa. Pieni raekoko voidaan saavuttaa vaihtoehtoisesti erilaisilla voimakkaaseen plastiseen muodonmuutokseen perustuvilla prosesseilla [2,3]. Nämä prosessit ovat alkaneet kiinnostaa kansainvälistä tiedeyhteisöä, koska niiden avulla voidaan valmistaa bulkki UHR tai jopa nanorakeisia metalleja [3] ilman termomekaaniseen käsittelyyn liittyviä ongelmia [2,4].

Equal-channel angular pressing (ECAP) on prosessointimenetelmä, jolla voidaan aikaansaada voimakas plastinen muodonmuutos. Siinä aihio puristetaan suurella mekaanisella voimalla kanavan läpi, joka sisältää jyrkän kulman. Kulkiessaan kulman läpi aihio muuttaa muotoaan, mutta säilyttää saman poikkipinta-alan, jolloin prosessi voidaan toistaa niin monta kertaa, että aihioon on saavutettu haluttu määrä plastista muodonmuutosta. ECAP-prosessi on erityisen kiinnostava, koska sama prosessi käy lähes jokaiselle metalliseokselle, sillä saadaan aikaiseksi homogeeninen UHR mikrorakenne ja se on mahdollista laajentaa teolliseen mittakaavaan sopivaksi [2].

Tässä työssä kootaan tieteellisistä julkaisuissa esitettyä tietoa UHR metallien mekaanisista ominaisuuksista, sekä lämpötilan ja myötönopeuden vaikutusista niihin. Pääpaino on ECAP-prosessilla valmistettujen UHR metallien mekaanisissa ominaisuuksissa. Työ kuuluu osakokonaisuutena projektiin, jonka tarkoituksena on tutkia, onko ECAP-prosessi kehitettävissä teolliseen mittakaavaan sopivaksi, ja voidaanko sen avulla saavuttaa merkittävää kilpailuetua raaka-aine markkinoilla. Tämän työn tarkoitus on koota kirjallisuudessa esitettyä tietoa ECAP-prosessoiduista metalleista, ja siten auttaa ym-

märtämään menetelmän potentiaalista arvoa sekä helpottaa näiden raaka-aineiden posi-
tioimista oikealle markkinasegmentille sopivaksi.

2. ECAP-menetelmä

ECAP-prosessointi on tapa valmistaa ultra-hienorakeisia metalleja, jotka eivät sisällä huokosia ja ovat mikrorakenteeltaan homogeenisia. Tässä menetelmässä työstettävä aihio puristetaan muotin läpi, jonka sisällä kaksi samankokoista tasapaksua kanavaa, jotka kohtaavat toisensa kulmassa φ. Kuva 1 esittää poikkileikkauksen yksinkertaisesta ECAP-muotista. Aihio puristetaan muotin läpi mekaanisen voiman avulla, jolloin se muokkautuu voimakkaasti. Kun aihio puristetaan muotin, jonka kulma φ on 90°, läpi aihioon kohdistuu ~1 mm/mm myötymää vastaava plastinen muodonmuutos [2,3,5]. Raekoko pienenee voimakkaan plastisen muodonmuutoksen seurauksena [6-8].
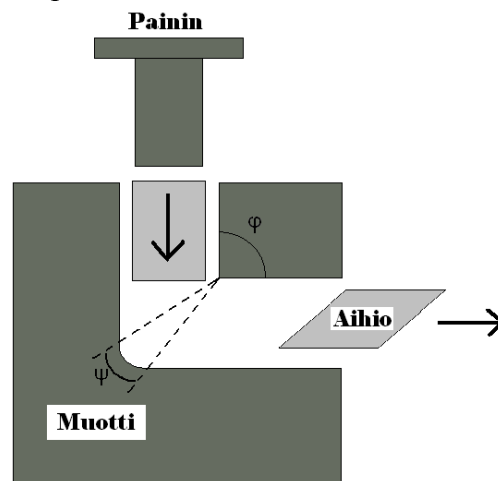
Kuva 1. ECAP-muotin poikkileikkaus

Kulma φ sekä sisäkulman pyöristys ψ vaikuttavat aihioon kohdistuvan plastisen myötymän määrään. Jotkin metallit eivät kestä puristusta 90° kulman läpi, joten näille käytetään muotteja, joiden φ kulma on suurempi. ECAP-prosessin helpottamiseksi ja nopeuttamiseksi muottia voidaan lämmittää ja muotissa voi olla samaan aikaan useampia kulmia, jolloin yhdellä puristuskerralla saavutetaan suurempi myötymä. ECAP-muoteista on myös kehitetty erilaisia valssausteloilla toimivia jatkuvatoimisia malleja, jotta prosessia voitaisiin nopeuttaa ja kasvattaa teollisuuden tarpeisiin sopivaksi. Tarkempi selvitys erilaisista ECAP-prosessointi mahdollisuuksista löytyy esimerkiksi lähteestä [2].

ECAP-prosessointi voidaan yhdistää muihin lujittamismenetelmiin helposti. ECAP-prosessointi voidaan suorittaa sellaisessa lämpötilassa, että rakenteeseen saadaan syntymään toivottuja erkaumia tai faasimuutoksia sekä mikrorakenteesta saadaan sellainen kuin halutaan. Prosessointi soveltuu suurimmalle osalle metalliseoksista, joten liuoslujittaminen on mahdollista. Lisäksi metalleihin jää prosessoinnin jälkeen jonkin verran sitkeyttä jäljelle, jolloin näitä voidaan lujittaa vielä kylmämuokkaamalla, mikäli se on

tarpeen. ECAP-prosessia voidaan käyttää myös erilaisten metallimatriisi komposiittien käsittelyyn [2].

ECAP-prosessoinnilla on monia etuja muihin voimakkaan plastisen muodonmuutoksen aikaansaaviin menetelmiin nähden. Sillä voidaan prosessoida materiaalia teollisessa mittakaavassa [2,9], eikä kappaleeseen pääse syntymään virheitä erilaisten tiivistysprosessien seurauksena [5]. Perinteisiin termomekaanisiin menetelmiin verrattuna ECAP-prosessi on hyödyllinen, koska voimakas plastinen muodonmuutos mahdollistaa huomattavasti pienemmän raekoon saavuttamisen, eikä prosessia tarvitse suunnitella erikseen eri metalliseoksille [3]. Voimakkaalla plastisella muodonmuutoksella voidaan tuottaa metalleille erittäin houkuttelevia ominaisuuksia, ilman seostusta, mikä parantaa materiaalien kierrätettävyyttä [4] sekä tuottaa materiaalisäästöjä.

3. ECAP-prosessoinnin aikaansaama mikrorakenne

ECAP-metallien mikrorakenne on ollut intensiivisen tutkimisen kohteena viimeisten vuosikymmenien aikana. Useita tutkimuksia on suoritettu erilliskiteillä sekä monikiteisillä metalleilla, ja ne kuvailevat kuinka metallin mikrorakenne muuttuu voimakkaan plastisen muodonmuutoksen seurauksena [10,11]. Keskimääräinen dislokaatiotiheys kasvaa ja raekoko pienenee puristuskertojen lisääntyessä, kunnes nämä saavuttavat kyllästetyn arvonsa. Saturaatiotila saavutetaan materiaalista riippuen, kun aihio puristetaan muotin läpi huoneen lämpötilassa 4-12 kertaa [12]. Mikäli aihiota käännetään 90 astetta samaan suuntaan pitkittäisen akselinsa ympäri ennen jokaista puristusta muotin läpi, kiderakenteesta tulee tasa-akselinen [3].

ECAP-prosessoitujen metallien mekaanista käyttäytymisen ymmärtämisen kannalta, näiden mikrorakenteen karakterisoiminen on välttämätöntä. UHR metallien mikrorakenteen erityispiirteitä ovat raerajoilla vallitseva jännitys sekä rakeiden orientaatiojakauma. Käytännön kannalta on välttämätöntä tietää, että raerajoilla vallitsee suuria mikrojännityksiä, silla ne vaikuttavat kaikkiin näiden metallien mekaanisiin ominaisuuksiin. Lisäksi prosessoinnista riippuen, raerajojen määrästä 10-75 % ovat korkeankulman raerajoja [13]. Näiden lukumäärän tietäminen on tärkeätä, sillä dislokaatioiden liikkumismekanismit riippuvat raerajojen orientaatiosta.

ECAP-prosessoitujen UHR metallien raekoko vaihtelee heterogeenisesti, siten että keskimääräinen raekoko on materiaalista riippuen tavallisesti välillä 0,07-1 μm [2,14,15]. Raekoon vaihtelu riippuu prosessoitavasta materiaalista siten, että suuren pinousvikaenergian omaavilla metalleilla mikrorakenne on homogeenisempi kuin alhaisen pinousvikaenergian metalleilla ECAP-prosessoinnin jälkeen. Monet muutkin tekijät, kuten erkaumat ja epäpuhtaudet vaikuttavat syntyvän rakenteen raekokojakaumaan, joten joissain metalliseoksissa rakenne saattaa olla hyvin kirjava, kun taas esimerkiksi puhtaan alumiinin rakenne on äärimmäisen homogeeninen [2].

Heterogeenisen rakenteen omaavien UHR metallien sisältämät rakeet voidaan jakaa kolmeen suuruusluokkaan, niiden sisältämän tekstuurin mukaan. Suurimmat rakeet ovat alle 1 μm kokoluokkaa ja pienimmät alle 100 nm [1,15]. Suurimmat rakeet sisältävät alirakeita ja omaavat korkean dislokaatiotiheyden. Keskikokoiset rakeet eivät sisällä alirakeita, mutta niissä on silti korkea dislokaatiotiheys. Pienimmät rakeet, jotka ovat nano kokoluokkaa, ovat lähes dislokaatiovapaita sisältä [1,15]. Rakenne sisältää suuria mikrojännityksiä ja raerajat ovat epätasapainossa [1,5,16], mikä tarkoittaa, että raerajoilla on enemmän dislokaatioita kuin vierekkäisten rakeiden yhteensopivuuden kannalta

olisi välttämätöntä. Suuret mikrojännitykset johtuvat korkeasta dislokaatiotiheydestä raerajojen tuntumassa ja rakeiden sisältämistä pienen kulman raerajoista [1].

Prosessointikertojen lisääntyessä suuren kulman rajojen määrä lisääntyy ja raerajat ohenevat ja samalla pienen kulman rajojen määrä vähenee [17-19]. Rakeiden sisällä olevat dislokaatiot pakkaantuvat sellien rajoille minimoidakseen jännitykseen sitoutuneen energian [12]. Riippumatta puristuskerroista, rakenteeseen jää kuitenkin suuri määrä pienen kulman rajoja [13], ja mikrotekstuuri koostuu eri leikkaus komponenteista [12].

4. Muodonmuutosmekanismit UHR metalleissa

Aktiiviset muodonmuutosmekanismit riippuvat ainakin mikrorakenteesta, koostumuksesta, lämpötilasta ja myötönopeudesta. Tavallisesti metalleilla dominoiva muodonmuutosmekanismi huoneen lämpötilassa on dislokaatioiden liukuminen. Raekoon pienentyessä alle 1 µm, myös raerajojen liukumisella ja kiertymisellä alkaa olla merkitystä.

ECAP-prosessoinnilla valmistetuilla metalleilla on hyvin pieni raekoko sekä erittäin korkea dislokaatiotiheys. Ultra-hienot rakeet muokkautuvat päätoimisesti samoilla mekanismeilla kuin suuremmat, joten näiden materiaalien kyky muokkauslujittua ei ole kovin suuri. Tämä merkitsee tavallisesti korkeaa lujuutta alhaista sitkeyttä vetokokeissa. UHR metallit eivät kuitenkaan ole hauraita, vaan ne murtuvat sitkeästi [20]. Vaikka UHR metallien dislokaatioiden generoimisnopeus on hyvin suuri, nämä eivät lujitu, sillä dynaaminen toipuminen on huomattavasti suurirakeisia metalleita voimakkaampaa [21]. Dislokaatiot törmäävät raerajoilla vastakkaismerkkisiin dislokaatioihin tai yhdistyvät näihin kiipeämällä ja annihiloituvat [22]. UHR metallia vedettäessä dislokaatiotiheys saavuttaa nopeasti kyllästetyn arvon, joten muokkauslujittuminen ei voi enää kompensoida poikkipinta-alan pienentymistä ja syntyy kurouma, joka johtaa lopulta murtumaan.

Dislokaatiotiheyden kyllästetty arvo riippuu dislokaatioiden syntymisnopeuden ja palautumisnopeuden välisestä tasapainosta. Kyllästetty tiheys on suurempi matalissa lämpötiloissa sekä suuremmilla myötönopeuksilla kuormitetussa metallissa, joten sitkeys paranee näissä kuomitusolosuhteissa [2,12,23]. Kyllästetyn tiheyden arvo kasvaa, koska dynaaminen palautuminen vähenee lämpötilan laskiessa ja myötönopeuden kasvaessa [13,23]. Dislokaatioita lukitsevat seosaineet, kuten magnesium alumiinissa, nostavat metalliseoksen myötölujuutta, koska ne sitovat dislokaatioita paikoilleen ja siten haittaavat dynaamista toipumista, mikä nostaa dislokaatiotiheyden kyllästettyä arvoa [12].

Yleensä UHR metallit myötävät vetokokeessa melko vähän ja lisäksi muokkauslujittuvat myötämisen alkaessa tavallisesti erittäin vähän tai eivät ollenkaan, jonka jälkeen ne alkavat muokkauspehmenemään [2,4,23,24]. Tämä on seurausta UHR metallien mikrorakenteesta. Voimakkaalla plastisella muodonmuutoksella käsitellyissä metalleissa on suuri määrä sekä matalan- että korkeankulman rajoja, jotka vaikeuttavat dislokaatioiden liukumista [18]. Pienestä raekoosta johtuen raerajat toimivat sekä dislokaatiolähteinä että dislokaatiokaivoina ultra-hienoissa rakeissa [1,4,22,24], jolloin dislokaatioiden vapaa matka jää vääjäämättä alle raekoon. Suuren dislokaatioitiheyden sekä rakeiden sisältämien matalan kulman raerajojen vuoksi dislokaatioiden liikkeen keskimääräinen vapaa matka jää UHR metalleilla alle tavallisilla tavoilla tuotettujen metallien vapaan matkan. Esimerkiksi Al–3.3Mg–0.2Sc–0.2Zr seoksella, jonka keskimääräinen raekoko

oli 200 nm, alirakeiden koko oli 140 nm ja nämä sisälsivät sekalaisia dislokaatioryhmittymiä, joten dislokaatioiden keskimääräinen vapaa matka tässä materiaalissa oli luultavasti alle 100 nm. Dislokaatiotiheyden arvo saturoituu UHR metalleilla tavallisesti valmistusprosessin aikana tai nopeasti UHR metallin myötäessä, jonka vuoksi kyky muokkauslujittua jää alhaiseksi [12,25].

Alle 100 nm koon rakeissa on havaittu nanokaksosia, jotka syntyvät osittaisdislokaatioiden emissiosta raerajoilta [22,26]. Näitä kaksosia on löydetty keskisuure ja suuren pinousvikaenergian omaavilla metalleilla, kuten alumiinilla, nikkelillä ja kuparilla. Alhaisen pinousvikaenergian omaavilla metalleilla tällaisia mikrokaksosia voi esiintyä myös yli 100 nm rakeiden sisällä [26]. Mikrokaksoset voivat pysäyttää dislokaatioita keskelle raetta, jolloin rakeen dislokaatioiden varastointikapasiteetti kasvaa. Tämä nostaa materiaalin myötölujuutta ja sitkeyttä sekä mahdollisesti kykyä muokkauslujittua [12,26]. Aiheesta ei ole vielä kuitenkaan saatavilla riittävästi tutkimustuloksia, jotta vaikutusta voitaisiin arvioida luotettavasti.

Raekoon pienentyessä rakeet voivat kuormitettaessa alkaa liukumaan ja kiertymään toistensa suhteen. Monissa tutkimuksissa on pyritty selvittämään eri ultrahienorakeisten metalliseosten superplastista käyttäytymistä [16,27,28]. Superplastisesta muokkauksesta pyritään kehittämään näiden materiaalien teollista muokkausta tukevaa tekniikkaa. Useissa tutkimuksissa [2,20,22,24,29,30] epäillään, että osa UHR metallien sitkeydestä koostuu raerajojen liukumisesta ja kiertymisestä. Tällaiset mekanismit riippuvat voimakkaasti lämpötilasta, ja tyypillisesti toimivat riittävän nopeasti vasta usean sadan Celsiusasteen lämpötiloissa aiheuttaakseen havaittavaa muodonmuutosta hienorakeisissa metalleissa. Kun metalleja kuormitetaan huoneenlämpötilassa, superplastiset muodonmuutosmekanismit vastaavan suurimmasta osasta metallin muodonmuutoksesta vasta raekoon laskiessa alle 10 nm. Raekoon ollessa ~100 nm luokkaa, rakeiden liikkumisella on kiistaton vaikutus metallien muodonmuutokseen huoneenlämpötilassa, mikäli myötönopeudet ovat erittäin pieniä [24]. Lämpötilan kasvaessa näiden mekanismien vaikutus kasvaa, siten että esimerkiksi Al–4Y–4Ni seoksen vetomurtositkeys myötönopeudella 10^{-3} s^{-1} kasvoi kymmenestä prosentista neljäänkymmeneen prosenttiin lämpötilan kasvaessa huoneenlämmöstä lämpötilaan 350 °C [23]. Rakeiden kiertymistä ja liukumista ei kuitenkaan vielä ymmärretä riittävän hyvin, että tätä mekanismia pystyttäisiin hallitsemaan, ja monissa tutkimuksissa vain todetaan että rakeet muokkautuvat näillä mekanismeilla, ottamatta kantaa miksi ja miten tarkkaan ottaen tämä tapahtuu.

Iso osa UHR metallien murtositkeydestä on tasamyötymän jälkeen tapahtuvaa kaulan kuroutumista. Ilman erityisiä käsittelyjä, ECAP-prosessoiduissa materiaaleissa on hyvin pieni tai ei ollenkaan tasamyötymää ennen muodonmuutoksen lokalisoitumista. Segal et al. tutkivat [20] ECAE prosessoidun [2] puhtaan Al0.5%Cu seoksen kuroutumista ja havaitsivat, että tämän metallin kuroutumisvaihe oli pidempi kuin saman materiaalin, jonka raekoko oli kasvatettu hehkuttamalla 12 µm: riin. Tähän arveltiin syyksi, että jännitys on riittävä mikromurtumien ydintämiseksi heti myötymän alkaessa lokalisoitua, mistä seurauksena on usean mikromurtuman homogeeninen ydintyminen ja kasvaminen. Esitetyn teorian mukaan yksittäinen mikromurtuma ei muodostu dominoivaksi, ku-

ten suurempirakeisissa metalleissa, jolloin murtuman kasvaminen lokalisoi jännityksen vasta myöhäisemmässä vaiheessa murtumisprosessia. Kyseisessä tutkimuksessa UHR Al0,5%Cu seoksen murtositkeydestä noin 90% oli kurouman myötämistä. Huomion arvoista on, että tutkimuksessa käytetty alumiiniseos sisälsi 0,1 μm erkaumia, jotka toimivat murtuman ydintäjinä. Mikäli näitä ei olisi, murtumisprosessi voisi olla toisenlainen.

UHR metallien muodonmuutosmekanismeja ei vielä täysin ymmärretä. Erilaisia matemaattisia malleja muodonmuutosmekanismeista on paljon, mutta monia näistä ei ole tutkittu riittävästi, jotta niitä voitaisiin pitää luotettavina [1]. Esimerkiksi matemaattisen mallin mukaan, raerajat voivat säilyttää yhtenevyyden muokkautumalla ryhmissä, ja tämänlaiseen käyttäytymiseen viittaavia havaintoja on tehty UHR titaanilla [1], mutta aiheesta ei ole vielä varsinaista tutkimusta joka vahvistaisi syyksi juuri tällaisen mekanismin. Voimakkaan plastisen muodonmuutoksen avulla saavutetut ultra-hienot rakeet voivat muokkautua myös eri diffuusioprosessien avulla [1], sillä näihin rajoihin on sitoutunut paljon energiaa ja rakenteessa on paljon raerajaa, joten diffuusion ajava voima on riittävän suuri [16,31], jotta tämän kaltainen mekanismi voisi saada aikaan makroskooppisesti merkittävän muodonmuutoksen alhaisissa lämpötiloissa. Ainakin UHR metalleilla on tutkitusti huomattavasti pienempi raerajadiffuusion aktivaatioenergia kuin suurirakeisilla metalleilla [26], joten esimerkiksi Coble-viruminen voisi olla merkittävää alhaisissa homologisissa lämpötiloissa [1]. Diffuusiopohjaisista mekanismeista ei ole tehty vielä riittävästi tutkimuksia, että niiden vaikutuksia voitaisiin käsitellä luotettavasti, joten niiden merkityksen arviointi kokonaismuodonmuutoksen kannalta on vielä spekulointia.

5. UHR metallien mekaaniset ominaisuudet

Tässä osiossa esitetään UHR metallien mekaaniset ominaisuudet peruspiirteittäin. Pääpaino on näiden metallien sitkeydellä, lujuudella sekä sillä, miten nämä ominaisuudet muuttuvat lämpötilan ja myötönopeuden muuttuessa.

UHR metalleilla on tyypillisesti korkea lujuus ja kovuus sekä alhainen tasamyötymä verrattaessa vastaaviin suurirakeisiin metalleihin. Toisaalta tasamyötymän loppua seuraava kurouma kestää suhteessa pidempään kuin suurirakeisilla metalleilla [14,20]. Vaikka UHR metallien sitkeys on alhainen, ne murtuvat sitkeästi eivätkä hauraasti. ECAP-prosessilla valmistetut UHR metallit ovat myös sitkeämpiä kuin tavallisilla lujittamismenetelmillä samalle lujuustasolle prosessoidut metallit [2,32], joskaan näiden sitkeys ei ole riittävä tavallisiin rakenteellisiin sovelluksiin ilman erityisiä sitkeyttä lisääviä käsittelyjä. Raekoon pienentäminen laskee sitkeä-hauras siirtymä lämpötilaa teräksissä [31], mikä puolestaan lisää UHR teräksien käyttökohteita. Raekoko ei vaikuta metallien jäykkyyteen eli näiden materiaalien eri kimmomoduuleihin.

5.1. Lujuus, kovuus ja sitkeys

Lujuutta voidaan arvioida raekoon perusteella, käyttämällä niin sanottua Hall-Petch yhtälöä. Se pitää paikkansa ainakin 0,2 µm raekokoon asti sekä PKK että TKK metalleilla [5,31], ja antoi luotettavan ennusteen Jia et al. [33] suorittamassa tutkimuksessa UHR titaanin, jonka raekoko oli noin 260 nm, lujuudeksi. Yhtälö 1 on niin sanottu Hall-Petch yhtälö ja siinä $\sigma_{0,2}$ on myötölujuus 0,2 % myötymän arvolla, σ_0 hilakitka, α materiaalivakio ja d keskimääräinen raekoko. Tässä yhtälössä α muuttuu dislokaatiotiheyden eli myötymän mukaan. Hall-Petch yhtälöä voidaan käyttää myös materiaalin kovuuden arvioimiseen, jolloin se antaa hyvän ennusteen ainakin teräksen kovuudeksi, aina 0,1 µm raekokoon asti [31].

$$\sigma_{0,2}(MPa) = \sigma_0 + \alpha d^{-\frac{1}{2}}$$

(1)

Lujuutta voidaan arvioida myös niin sanotun Taylorin yhtälön avulla [12,25]. Yhtälö 2 on Taylorin yhtälö ja se kuvaa dislokaatiotiheyden vaikutusta metallin lujuuteen. Siinä σ on myötölujuus, σ_0 hilakitka, α dislokaatiorakennetta kuvaava materiaalivakio, M Taylorin kerroin, G leikkausmoduuli, b burgesvektorin pituus ja ρ dislokaatiotiheys. α:n arvo muuttuu dislokaatiorakenteen mukaan. Metallin prosessointi vaikuttaa α arvoon [25], koska ECAP-prosessoinnilla saadaan aikaa erilaisia mikrorakenteita riippuen prosessointiparametreista [2].

$$\sigma(MPa) = \sigma_0 + \alpha MGb\rho^{\frac{1}{2}}$$

(2)

Hall-Petch yhtälö on lähinnä käyrän sovitus empiiriseen dataan, eikä se huomioi materiaalin muodonmuutosmekanismeja tai mikrorakennetta [1]. Mikäli UHR metallin mikrorakenne koostuu sekä erittäin pienistä rakeista että isommista, Hall-Petch yhtälö ei pysty ennustamaan metallin lujuutta kovin hyvin [2,15]. Taylorin yhtälö on puoliempiirinen yhtälö, joten se on sekä totuudenmukaisempi että kankeampi käyttää kuin Hall-Petch yhtälö. Se ei varsinaisesti huomioi materiaalin mikrorakennetta eikä sisäisiä jännityksiä, vaan ainoastaan kuvaa niitä sovitusparametrilla [15,25]. Molempien yhtälöiden käyttö UHR metalleiden lujuuden arvioimisessa on käytännöllistä, mikäli niiden tuloksia pidetään vain karkeina arvioina, sillä molemmat yhtälöt ovat pohjimmiltaan vain käyrän sovituksia mitattuun dataan. Tästä syystä yhtälöt eivät päde hyvin kaikille UHR metalleille, ja ne huomioivat myötönopeuden tai lämpötilan vaikutuksen vain, mikäli jokin yhtälön parametreista on riippuvainen näistä [24].

UHR metallien sitkeyden parantamiseen on kehitetty useita menetelmiä. ECAP-prosessoinnin jälkeen sitkeyttä voidaan parantaa sopivassa lämpötilassa hehkuttamalla, syklisellä kuormittamisella tai näiden yhdistelmällä [35]. Näin saadaan aikaan mikrorakenne, joka koostuu sekä ultra-hienorakeisesta matriisista että tämän seassa olevista isommista rekristalloituneista rakeista [2,35]. Tällaisen rakenteen omaavan metallin lujuus on samaa suuruusluokkaa kuin heti ECAP-prosessoinnin jälkeen, mutta sen sitkeys on huomattavasti parempi [2]. 8 kertaa ECAP-muotin läpi puristetun, 1000 sykliä väsytetyn ja huoneen lämpötilassa viisi kuukautta pidetyn puhtaan kuparin (99,97 %) myötölujuus oli noin 350 MPa ja murtovenymä 22 % [35]. Puhtaan kupari myötölujuus hehkutettuna on noin 33 MPa ja murtovenymä 60 % [36].

Toinen tapa parantaa näiden UHR metallien sitkeyttä on lisätä prosessoinnissa tuotetun plastisen muodonmuutoksen määrää. Esimerkiksi kuparin sitkeys alkaa palautua ECAP-puristuskertojen lisääntyessä [13]. Tämän katsotaan johtuvan korkean kulman raerajojen osuuden kasvamisesta [13], mikä puolestaan edistää raerajojen liukumista ja kiertymistä [2,37]. Erittäin puhdas kupari (99,98 %) omaa 400 MPa murtolujuuden ja 15 % murtovenymän 25 ECAP-muotin läpipurituksen jälkeen, mikä vastaa noin 29 mm/mm myötymää [2,25]. Vertailun vuoksi kylmämuokatun puhtaan kuparin murtolujuus on 340 MPa ja murtovenymä 14 % [35]. Raekoon pienentäminen edelleen alle 100 nm kokoluokkaan parantaa sitkeyttä ja saattaa nostaa lujuutta, sillä se edistää samoja raerajojen kiertymis- ja liukumismekanismeja kuin myötymän lisääminen [2].

Kolmas tapa lisätä UHR metalliseoksien sitkeyttä on seostaa niihin aineita, jotka muodostavat sopivan lämpökäsittelyn aikana metastabiileja erkaumia. Nämä faasit lisäävät UHR metalien sitkeyttä, minkä uskotaan johtuvan siitä, että ne haittaavat leikkausnauhojen (shear-band) etenemistä [2]. ECAP-prosessoitua Al10,8wt-%Ag seosta hehkutettiin 373 K lämpötilassa, jotta tähän saatiin erkautettua metastabiilia γ` faasia. Tä-

män seoksen murtolujuus oli 270 MPa, ja sitä vastasi 14 % tasamyötymä ja 40 % murtovenymä [37].

UHR metallien sitkeyttä voidaan parantaa myös ECAP-prosessoinnin jälkeisellä kryogeenisessä lämpötilassa tapahtuvalla kylmämuokkauksella. Puhdas kupari (99,99 %) prosessoitiin eräässä tutkimuksessa [36] ECAP-menetelmällä, jonka jälkeen se kylmävedettiin ja valssattiin nestetypen lämpötilassa, jonka jälkeen materiaalin murtolujuus oli noin 500 MPa ja murtovenymä 11,8 %. Parantuneet mekaaniset ominaisuudet selitettiin sillä, että muokkaus nestetypen lämpötilassa lisäsi rakenteeseen korkean kulman raerajoja sekä muodosti kaksosia (deformation twin).

UHR metallit kärsivät vedossa plastisesta epästabiilisuudesta alhaisilla myötymän arvoilla, koska näiden lujuus on korkea ja muokkauslujittuminen tavallisesti lähes olematonta. Tämä tarkoittaa että myötymä lokalisoituu helposti [23]. Myötymä lokalisoituu UHR metalleilla matalilla myötymillä, koska niiden muokkauslujittuminen on liian alhaista, jotta lujuuden kasvaminen pystyisi kompensoimaan poikkipinta-alan pienentymisen. Kun materiaaliin syntyy mikrokurouma, myötönopeus kuroutuneella alueella kasvaa, mikä lujittaa kuroumaa ja voi siten siirtää kuroutumisen toiseen paikkaan. Tämän vuoksi myötönopeusherkkyydellä voidaan katsoa olevan samanlainen vaikutus kurouman vastustamisessa kuin muokkauslujittumisellakin [23], millä on merkitystä etenkin superplastisessa muodonmuutoksessa. PKK rakenteiset UHR metallit vastustavat lokalisoitumista paremmin kuin TKK rakenteiset, koska näiden myötönopeusherkkyys on suurempi [38], mutta myös niillä havaitaan plastista epästabiilisuutta matalilla myötymillä [39]. Useilla TKK UHR metalleilla, kuten raudalla, tantaalilla ja volframilla, on havaittu plastista epästabiilisuutta suurilla myötönopeuksilla [38,40-43]. Jia et al. [33] tutkivat ECAP-prosessoitua puhdasta (CP) titaania ja havaitsivat, että myötymä lokalisoituu helposti tätä materiaalia vedettäessä. Tuloksesta voidaan päätellä, että ainakin jotkut HTP rakenteen omaavista UHR metalleista ovat plastisesti epästabiileja jo pienillä myötymillä.

Pelkkä myötölujuuden arvo on huono suure kuvaamaan UHR metallien käyttäytymistä, sillä nämä sallivat vain erittäin pieniä myötölujuuden ylityksiä ja ovat herkkiä esim. korkeille lämpötiloille. Monilla UHR metalleilla ja seoksilla esiintyy joissain kuormitusolosuhteissa erittäin alhaista sitkeyttä ja muokkauspehmenemistä [22,30,44,45]. Jännitys-myötymä käyrä on huomattavasti parempi työkalu suunnittelussa kuin pelkkä myötölujuus, sillä se antaa realistisemman kuvan materiaalin käyttäytymisestä, mutta tämän lisäksi tarvitaan myös ymmärrystä näiden materiaalien tavallisista reaktioista eri kuormituksiin.

5.2. Lämpötilan vaikutus mekaanisiin ominaisuuksiin

Yleisesti ottaen UHR metallit käyttäytyvät sekä sitkeämmin että ovat lujempia, kun näitä kuormitetaan alle huoneenlämpötiloissa [2,39,46]. Matalassa lämpötilassa muokattuun materiaaliin mahtuu enemmän dislokaatioita, sillä dislokaatiotiheyden kyllästetty arvo kasvaa lämpötilan laskiessa [12]. Dislokaatioiden annihiloituminen tapahtuu voi-

makkaammin korkeammissa lämpötiloissa, jolloin dynaaminen palautuminen voimistuu ja rakenteen kyllästetty dislokaatiotiheys laskee. Lujuus kasvaa lämpötilan laskiessa, koska termisen energian määrä vähenee ja muodonmuutoslujuuden (flow stress) terminen komponentti kasvaa. Mikäli lämpötila on riittävän korkea, rakenne palautuu erilaisten dynaamisten rekristallaatioprosessien avulla, mikä vähentävää dislokaatioiden liikettä rajoittavien esteiden määrä, eli laskee materiaalin lujuutta [16,23]. Dynaamiset rekristallaatioprosessit aiheuttavat UHR metalleissa myös muokkauspehmenemistä [22]. Samalla kun lujuus laskee lämpötilan kasvaessa, sitkeys paranee. Riittävän korkeissa lämpötiloissa ja riittävän alhaisilla myötönopeuksilla muokattaessa UHR metallit alkavat käyttäytyä superplastisesti, jolloin näiden sitkeys paranee huomattavasti ja lujuus laskee.

Farrokh et al. [47] valmistivat puristuskoenäytteitä pyörittämällä metallipulvereita kuulamyllyssä ja tiivistämällä ne paineistetun sintrausprosessin avulla. Näin saatiin aikaiseksi nanokiteisiä alumiini- ja kupari-näytteitä, joiden myötö- ja muodonmuutoslujuutta tutkittiin eri lämpötiloissa sekä eri myötönopeuksilla. Lämpötilan vaikutus näiden metallien lujuusominaisuuksiin oli suurempi kvasi-staattisilla myötönopeuksilla kuin dynaamisissa kokeissa. Samassa tutkimuksessa havaittiin, että puristusmyötäminen sisälsi muokkauslujittumista aina huoneenlämpötilaan asti, mutta korkeammissa lämpötiloissa muokkauslujittumista ei tapahtunut lainkaan. Nämä tulokset eivät ole aivan suoraa yleistettävissä UHR metalleihin, koska testattujen materiaalien raekoko on niin pieni, että se mahdollistaa eri muokkautumismekanismeja. Lisäksi metallipulverien tiivistyksen yhteydessä on voinut syntyä erilaisia sulkeumia ja huokosia, jotka vääristävät tuloksia. ECAP-prosessoiduilla kuparilla, nikkelillä ja alumiinilla [16,22,46,48] on havaittu, että lämpötilan noustessa huoneenlämpötilan yläpuolelle, nämä metallit muokkauslujittuvat aluksi hyvin vähän, jonka jälkeen niiden lujuus pysyy samana tai laskee. Tämä trendi ei kuitenkaan päde kaikille UHR metalleille, sillä esimerkiksi Al–4Y–4Ni muokkauslujittui vielä 150 ºC lämpötilassa suoritetussa vetokokeessa [23].

Lämpötilan kasvaessa yli huoneen lämpötilan UHR metallien lujuus laskee. Lujuuden laskeminen on PKK UHR metalleilla huomattavasti voimakkaampaa kuin suurirakeisilla PKK metalleilla [16,23,22,48]. Samalla kun lujuus laskee, näiden metallien sitkeys paranee. UHR metallien korkean lämpötilan käyttäytymiseen liittyy myös muokkauspehmenemistä. Lähellä korkeinta lämpötilaa, jossa rakeet ovat stabiileja, ECAP-prosessoidulla puhtaalla (99,99 %) kuparilla havaittiin pehmenemistä materiaalia kuormitettaessa [22]. Sama ilmiö on havaittu myös UHR puhtaalla alumiinilla ja muutamalla eri alumiiniseoksella [16,23,48]. Pehmeneminen liittyy läheisesti UHR metallien superplastiseen muodonmuutoskäyttäytymiseen korkeissa lämpötiloissa ja matalilla myötönopeuksilla. Tällaisissa olosuhteissa metalli pehmenee ja muuttuu sitkeämmäksi, minkä arvellaan johtuvan raekoon kasvamisesta, pienen kulman raerajojen vähenemisestä sekä raerajoilla sijaitsevien dislokaatioiden annihiloitumisesta kiipeämisen avulla [22].

Suuren dislokaatiotiheyden seurauksena ECAP-prosessilla valmistettuihin materiaaleihin on sitoutunut paljon myötymäenergiaa [5]. Wan et al. [49] osoittivat differentiaalisella pyyhkäisykalorimetrialla, että tämä energia vapautuu materiaalia lämmitettäessä.

Energia purkautuu, kun rakenteessa tapahtuu sisäisten jännitysten palautumista, rakeen kasvua tai rekristallaatio. Termisellä stabiilisuudella tarkoitetaan materiaalin kykyä säilyttää mikrorakennemuuttumattomana, eli vastustaa näitä palautumisprosesseja korotetussa lämpötilassa. Se on yksi tärkeimmistä UHR metallien käyttöä rajoittavista ominaisuuksista, koska rekristallaatio ja rakeenkasvu ovat suurimmat tekijät, jotka heikentävät näiden metallien ominaisuuksia korkeissa käyttölämpötiloissa, ja koska korkein käyttölämpötila on ainakin seostamattomilla UHR metalleilla hyvin alhainen. Kuvassa 2 on ECAP-prosessoidun puhtaan alumiinin mikrorakenne eri lämpötiloissa tapahtuneen tunnin pituisen hehkutuksen jälkeen. Kuvasta nähdään, että UHR alumiinin raekoko säilyy stabiilina aina 423 K lämpötilaan asti, mutta rakenne alkaa rekristalloitumaan lämpötilan ylittäessä tämän, ja jo 150 K lämpötilan nousu johtaa täydelliseen rekristalloitumiseen.
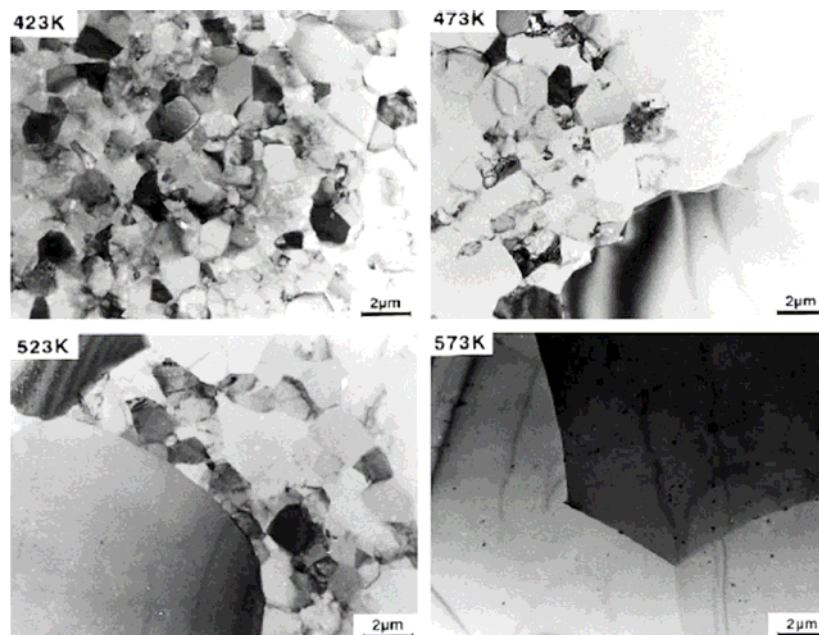
Kuva 2. Puhtaan alumiinin mikrorakenne ECAP-prosessoinnin ja 1 h hehkutuksen jälkeen lämpötiloissa 423 K, 473 K, 523 K ja 573 K [2].

ECAP-prosessoidun alumiiniseoksen rakeenkasvun aktivaatioenergia on Geng et al. [16] mukaan huomattavasti alhaisempi kuin puhtaan alumiinin itsediffuusion aktivaatioenergia, sekä alhaisempi kuin alumiiniseoksen epäpuhtauksien diffuusion aktivaatioenergia. Tämä tarkoittaa, että atomien diffuusio on helpompaa, koska mikrorakenne sisältää ylimääräistä jännityskenttiin sitoutunutta energiaa [16]. Seurauksena alhaisesta rakeenkasvun aktivaatio energiasta ja suuresta määrästä raerajaa, rakeenkasvua ajava voima on korkea ja UHR metallien terminen stabiilisuus alhainen. Mekaaniset ominaisuudet alkavat heikentyä hyvin voimakkaasti lämpötilan noustessa, koska dislokaatiotiheys laskee ja raekoko kasvaa, jolloin molempien lujittava vaikutus vähenee. ECAP-prosessoidulla Al1,5wt-%Mg seoksella havaittiin mikrorakenteen relaksoitumista jo huoneen lämpötilassa, kun näyteet puristettiin 0,2 mm/mm myötymään [48]. Kuormitusolosuhteet voivat edesauttaa mikrorakenteen palautumista, sillä UHR metalleissa tapahtuu myös plastisen myötymän aikaansaamaa rakeenkasvua [22,34].

Rakeenkasvua voidaan ehkäistä UHR metalleissa useilla eri tavoilla. UHR metallia voidaan stabiloida erkaumilla tai sopivalla seostuksella [32]. Hyvin pienet erkaumat ja seosaineet, jotka konsentroituvat raerajoille, parantavat termistä stabiilisuutta, koska ne hillitsevät rakeiden kasvua [50]. On kuitenkin syitä epäillä, että erkaumat ja seostus eivät ehkäise rakenteen relaksoitumista [48]. Hehkutusen rekristallisaatiolämpötilan alapuolella on havaittu myös parantavan termistä stabiilisuutta, koska tämä poistaa mikrojännityksiä ja tasapainottaa rakennetta [32]. UHR metallit, jotka eivät ole tyypiltään aaltoilevasti liukuvia (wavy slip), eli joiden pinousvikaenergia on alhainen, vaikuttavat kestävän korkeampia lämpötiloja [32]. Tämän tyyppisten metallien käyttäminen on suositeltavaa, mikäli UHR metallissa ei saa alkaa tapahtumaan rakeenkasvua käytön aikana.

Metallin terminen stabiilisuus vaikuttaa korkean lämpötilan murtumismekanismeihin, sillä osittain tai kokonaan rekristalloitunut rakenne murtuu eri tavalla kuin ultrahienorakeinen. Segal et al. [20] tekemässä, murtumismekaniikkaa käsittelevässä tutkimuksessa $Al0.5\%Cu$ seos homogenisoitiin, erkautushehkutettiin ja prosessoitiin ECAE menetelmällä. Tutkimuksessa havaittiin, että tällä UHR metallilla on oma tyypillinen murtumisjälkensä, joka poikkeaa hieman hienorakeisten metallien murtumisesta. Samassa tutkimuksessa havaittiin, että 448 K lämpötilassa tunnin ajan hehkutettu UHR $Al0.5\%Cu$ seos murtui samalla tavalla kuin hehkuttamaton. Kyseisessä metallissa ei tapahdu rakeenkasvua vielä hehkutuslämpötilassa, mutta hehkutus poistaa kuitenkin mikrojännityksiä, eli voidaan päätellä että toipumishehkutuksella ei ole ratkaisevaa vaikutusta murtumismekanismeihin.

5.3. Myötönopeuden vaikutus mekaanisiin ominaisuuksiin

UHR metallit käyttäytyvät yleisesti sekä lujemmin että sitkeämmin, kun niitä kuormitetaan suuremmilla myötönopeuksilla [2,24]. Dislokaatioiden generoitumisnopeus kilpailee dynaamisen palautumisen kanssa, ja kun nämä ovat tasapainossa, ei muokkauslujittumista enää tapahdu [21]. Mikäli dislokaatioiden generoituminen lisääntyy myötönopeuden kasvaessa, muokkauslujittuminen voimistuu ja sitkeys paranee, sillä muokkauslujittuminen viivyttää kurouman syntymistä, joka on metalleilla tavallisin murtumaan johtava syy [24]. Tällainen teoria selittäisi UHR metallien käyttäytymisen kohtuullisen hyvin. Lujuuden kasvaminen myötönopeuden kasvaessa voidaan selittää samalla tavalla kuin suurirakeisilla metalleilla, eli termisen aktivaation vähentymisen avulla [51]. Suuremmilla myötönopeuksilla termisestä energiasta ei saada yhtä paljon hyötyä, joten tarvitaan enemmän ulkoista työtä metallin muokkaamiseen, mikä näkyy lujuuden kasvamisena. Alhaisilla myötönopeuksilla lujuus ei kuitenkaan kasva täysin lineaarisesti suhteessa myötönopeuden logaritmiin. Epälineaarisuus johtuu raerajojen liukuminen ja kiertyminen sekä muista hitaasti aktivoituvista prosesseista, jotka tyypillisesti nostavat sitkeyttä ja laskevat lujuutta alhaisilla myötönopeuksilla [24].

Myötönopeusherkkyys kuvaa lujuuden muutosta myötönopeuden muuttuessa. Materiaali, jolla on suuri myötönopeusherkkyys, vastustaa myötönopeuden kasvamista voi-

makkaasti, jolloin sen lujuus kasvaa huomattavasti myötönopeuden lisääntyessä. Yhtälö 3 on myötönopeusherkkyyden suhteellinen määritelmä [24]. UHR metallien myötöno-peusherkkyys riippuu voimakkaasti kiderakenteesta. PKK rakenteen omaavilla UHR metalleilla on isorakeisiin vastineisiinsa verrattuna korkeampi myötönopeusherkkyys [38,52,53]. Kuva 3a esittää PKK metallien myötönopeusherkkyyden riippuvuutta rae-koosta. TKK rakenteen UHR metalleilla myötönopeusherkkyys puolestaan pienenee raekoon pienentyessä, mikä on esitetty kuvassa 3b. Näillä TKK rakenteisilla UHR me-talleilla on pieni myötönopeusherkkyyden arvo verrattuna isorakeisiin vastineisiin [38,40]. Yang et al. [7] havaitsivat, että AZ31B magnesiumseoksen myötönopeusherk-kyys kasvaa, kun sen raekoko hienonnetaan ABRC (alternate biaxial revese corrugati-on) prosessin [54] avulla luokkaan ~1 µm. Toisaalta Jia et al. [33] tutkivat puhdasta (CP) ECAP-prosessoitua titaania ja havaitsivat, että sillä oli alempi myötönopeusherk-kyys kuin suurirakeisella titaanilla. Heksagonaalisen tiivispakkauksellisen rakenteen UHR metalleista ei ole kuitenkaan saatavilla riittävästi tutkimustuloksia, jotta näiden myötönopeusherkkyydestä pystyttäisiin tekemään luotettavia arvioita.

$$m = \left\{ \frac{\partial \log \sigma}{\partial \log \dot{\varepsilon}} \right\}_{\varepsilon, T}$$

(3)
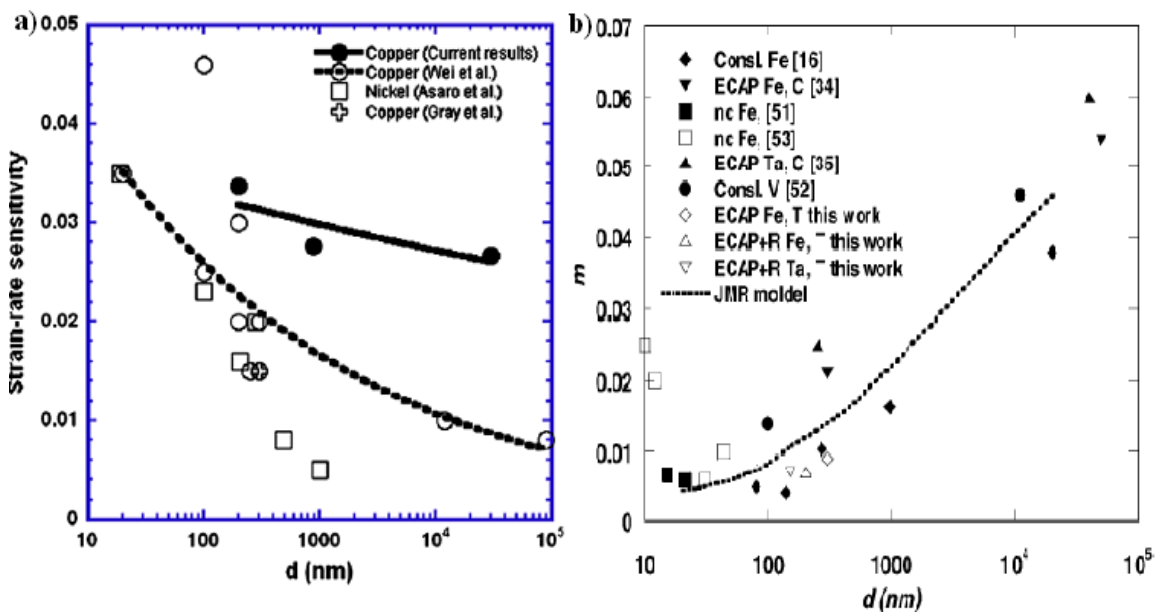
Kuva 3. Myötönopeusherkkyyden riippuvuus raekoosta a) PKK metalleilla [53] ja b) TKK metalleilla [38].

Wei et al. [38] sekä Kapoor et al. [48] esittävät, että PKK metallien myötönopeus-herkkyyden kasvaminen raekoon pienentyessä johtuu aktivaatiotilavuuden pienentymi-sestä. Aktivaatiotilavuus kuvaa dislokaatioiden keskimäärin liikkumaa matkaa, ennen esteeseen törmäämistä ja pysähtymistä, joten se vaikuttaa suoraan myötönopeuden riip-puvuuteen ulkoisesta jännityksestä. Wei et al. [48] mittasivat sekä vertailivat suurira-keisten sekä UHR metallien aktivaatiotilavuuksien arvoja ja havaitsivat, että UHR me-

talleilla on selkeästi pienempi aktivaatiotilavuus. Esteet, jotka rajoittavat dislokaatioiden liikettä pienentävät aktivaatiotilavuutta. Molemmissa aktivaatiotilavuuden pienentymistä selittävistä tutkimuksista uskottiin, että rearajat haittaavat dislokaatioiden liikettä, ja siten aiheuttavan aktivaatiotilavuuden pienentymisen [38,48], mutta tätä ei pystytty todistamaan. Luultavimmin raerajojen luonne muuttuu siten, että ne alkavat emittoida dislokaatioita, mikä tekee näistä termisesti aktivoituvia esteitä [24,38,53]. Voimakkaaseen plastiseen muodonmuutokseen perustuva valmistusprosessi lisää raerajojen määrä ja dislokaatiotiheyttä, samalla kun se pienentää raekokoa. Aktivaatiotilavuus laskee, koska PKK metalleissa suurimmat esteet ovat raerajat sekä metsädislokaatiot [38,48,53]. Myötönopeuden kasvattaminen vaikuttaa siis samalla tavalla PKK rakenteisiin UHR metalleihin kuin isompirakeisiin vastineisiin, mutta riittävän pienirakeisten metallien raerajat alkavat haitata dislokaatioden liikettä samalla tavoin kuin metsädislokaatiot, jolloin metallin lujuus riippuu voimakkaammin termisestä energiasta [38,48].

TKK rakenteen UHR metallien suurin terminen este on Peierlsin hilakitka [38]. Dislokaatiot eivät voi ylittää raerajoja termisen energian avulla, joten raerajat muodostavat atermisen esteen dislokaatioiden liikkeelle. Tämä poikkeaa PKK UHR metallien käyttäytymisestä, joissa raerajat toimivat luultavasti termisenä esteenä [24,38,53]. Raekoon pienentyessä atermisten esteiden määrä kasvaa suhteessa termisiin esteisiin, sillä raerajan määrä metallissa lisääntyy, mutta hilakitka pysyy jokseenkin vakiona. Dislokaatioiden liikkumiseen tarvittava kokonaisenergia kasvaa, koska lujuuden aterminen komponentti voimistuu raekoon pienentyessä. Lujuuden terminen komponentti ei kasva, joten sen osuus pienenee suhteessa kokonaisenergiaan. Siten termisen energian vaikutus dislokaatioiden liikkumisnopeuteen pienenee, kun raekoko pienenee. Matalilla myötönopeuksilla, myötönopeuden muuttaminen vaikuttaa ainoastaan termisen aktivaation määrään, jolloin lujuuden ja myötönopeuden suhde riippuu tärkeimmästä termisesti aktivoidusta prosessista. Pienirakeisilla TKK metalleilla, tärkeimmän termisesti aktivoidun prosessin vaikutus kokonaislujuuteen on pieni, jolloin myös myötönopeusherkkyys on pienempi kuin suurempirakeisilla metalleilla [38,40].

ECAP-prosessoidun puhtaan (99,6 %) alumiinin murtositkeys laski myötönopeuden pienentyessä, UHR metalleille tyypillisellä tavalla, mutta kasvoi huomattavasti myötönopeuden laskiessa arvosta 10^{-3} s^{-1} arvoon 10^{-4} s^{-1}. Myötönopeuden pienentyessä edelleen alle 10^{-4} s^{-1}, murtositkeys jatkoi kasvamistaan. Tämän uskottiin johtuvan eri muodonmuutosmekanismien aktivoitumisesta. Pienemmillä myötönopeuksilla rakeiden kiertyminen ja raerajojen liukuminen sekä muut diffuusiopohjaiset mekanismit ja rakenteen relaksoituminen, vaikuttavat myötämiseen enemmän. Hitaat mekanismit voivat olla estyneitä tai liian hitaita aiheuttaakseen havaittavaa eroa suuremmilla myötönopeuden arvoilla, mutta ne lisäävät sitkeyttä, mikäli kuormitusolosuhteet sallivat sen [24].

PKK rakenteen UHR metallien myötönopeusherkkyys kasvaa tavallisesti lämpötilan mukana [22,23,38,48]. Lämpötilan vaikutus myötönopeusherkkyyteen ei ole täysin lineaarinen, koska näiden myötönopeusherkkyys on monimutkainen, useasta eri ilmiöstä koostuva ominaisuus. TKK metalleilla myötönopeusherkkyys pienenee lämpötilan kasvaessa, kun absoluuttinen lämpötila on lähellä huoneen lämpötilaa [38]. Korkeammissa

lämpötiloissa myötönopeusherkkyys alkaa kasvaa samalla tavalla kuin PKK UHR metalleilla [38]. Kuva 4 esittää kahden eri alumiiniseoksen myötönopeusherkkyyden riippuvuutta lämpötilasta.
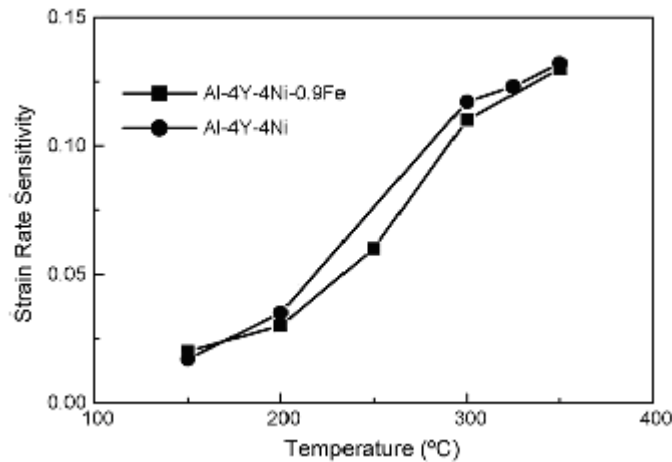
Kuva 4. Kahden eri alumiini seoksen myötönopeusherkkyyden riippuvuus lämpötilasta [23].

Mishra et al. [53] havaitsivat myötönopeudella 2500 s^{-1} testatuissa, 0,3 mm/mm myötymään puristetussa puhtaassa UHR kuparissa dynaamista rekristallisaatiota [53]. Tämä johtuu adiabaattisesta lämpenemisestä, eli metallien lämpenemisestä muokkauksen seurauksena. Samassa tutkimuksessa dynaaminen rekristalloituminen todettiin myös hatun muotoisilla veto Hopkinson Split Bar näytteillä ja Taylorin iskukoe-näytteillä. Mishra et al. [53] laskivat, että puristusnäytteissä 2500 s^{-1} myötönopeus ja 0,3 mm/mm myötymä saivat aikaan ~60 K lämpötilan nousun, mikä oli riittävä aiheuttamaan rekristallaatioita ECAP-prosessoidussa kuparissa. Adiabaattinen lämpeneminen riippuu voimakkaasti materiaalin lämmönjohtavuudesta, ominaislämpökapasiteetista sekä kuormitusolosuhteista. UHR metallit myötävät vetokuorman alla tavallisesti hyvin vähän ennen murtumista, joten adiabaattinen lämpeneminen aiheuttaa rekristalloitumista tällöin lähinnä kurouman alueelle, mikäli myötönopeus on riittävän suuri. UHR metallit ovat termisesti epästabiileja [2,53], joten ne ovat alttiita dynaamiselle rekristalloitumiselle puristettaessa.

5.4. UHR metallien syklinen käyttäytyminen

Väsymismurtuman syntyminen voidaan jakaa murtuman ydintymiseen ja sen etenemiseen. Lujat materiaalit vastustavat paremmin murtuman syntymistä, kun taas sitkeät materiaalit kestävät paremmin murtuman etenemistä. UHR metallit kestävät luontaisesti paremmin murtuman syntymistä kuin sen etenemistä korkean lujuutensa ja alhaisen sitkeytensä vuoksi. Näillä materiaaleilla on mahdollista saavuttaa korkea lujuus sekä paremmat sitkeysominaisuudet kuin tavallisilla lujittamismenetelmillä, joten UHR metallit vaikuttavat lupaavilta materiaaleilta poikkeuksellisia väsymisominaisuuksia vaativiin sovelluksiin [2].

UHR metalleilla on parempi pitkäkestoisen väsytyksen väsymislujuus (high cycle fatique) yksinkertaisissa väsytyskokeissa suurempirakeisiin metalleihin verrattuna [32,44,55]. Pitkäkestoisen väsytyksen väsymislujuuden on todettu seuraavan Hall-Petch yhtälöä [2], joten esimerkiksi ECAP-prosessoinnilla voidaan parantaa tätä osaa metallien väsymisestä huomattavasti. Jännityskontrolloiduissa testeissä on osoitettu, että esimerkiksi puhtaan (CP) titaanin sietoraja 10^7 syklin jälkeen on voitu nostaa 50 % ECAP-prosessoinnin ja kylmävedon avulla [55].

UHR metalleilla tehdyissä myötymäkontrolloiduissa väsytyskokeissa havaitaan syklistä pehmenemistä, rakeen kasvua ja myötymän lokalisoitumista, mitkä johtavat alhaiseen väsymisikään [2]. Väsymisikä saattaa olla UHR metalleilla jopa alhaisempi kuin tavallisen raekoon metalleilla, minkä katsotaan johtuvan UHR rakenteen alhaisesta termisestä ja mekaanisesta stabiilisuudesta sekä rakenteen voimakkaasta taipumuksesta palautumiseen [2]. Tämä ilmiö havaitaan voimakkaampana, kun plastisen myötymä-amplitudin arvoa kasvatetaan. UHR metallin sisältämä mikrotekstuuri vaikuttaa sykliseen pehmenemiseen siten, että tasa-akselinen rakenne on tavallisesti stabiilimpi kuin orientoitunut tai lamellimainen rakenne [2].

UHR metallien väsymislujuutta voidaan räätälöidä käyttötarkoitukseen sopivaksi joko parantamalla niiden sitkeyttä aikaisemmassa luvussa esitetyillä tavoilla tai parantamalla metallin myötölujuutta kylmämuokkauksen avulla. Esimerkiksi sopivalla jälkihehkutuksella voidaan nostaa kuparin lyhytkestoinen väsymisikä ~5-10 kertaiseksi [2]. Oikein suoritetulla erkaumakarkaisulla voidaan parantaa UHR metallien väsyttävän kuormituksen alaista käyttöikää, sillä erkaumat lisäävät sitkeyttä samalla kuin ne hidastavat rakenteen palautumista. Lisäksi oikein suunniteltu erkautushehkutus vähentää rakenteesta jäännösjännityksiä, mikä staboi rakennetta myötymän lokalisoitumista ja murtuman syntymistä vastaan [2].

6. Yhteenveto

Tässä työssä kerättiin tieteellisissä lähteissä julkaistua tietoa ECAP-prosessoitujen UHR metallien mekaanisista ominaisuuksista. Työ sisältää taustatiedon ECAP-prosessoinnista sekä selvityksen UHR metallien mekaanisista ominaisuuksista ja lämpötilan sekä myötönopeuden vaikutuksista niihin.

ECAP-prosessoinnilla voidaan pienentää metallien raekoko ~0,07-1 mikrometriin. Tällä tavalla prosessoitaessa metalleiden mikrorakenteesta saadaan tasa-akselinen ja homogeeninen ja se sisältää suuria jäännösjännityksiä sekä suuren määrän korkeankulman raerajoja. ECAP-prosessoitujen metallien dislokaatiotiheys on erittäin korkea ja raekoko vaihtelee heterogeenisesti, mikäli metallin pinousvikaenergia on alhainen.

ECAP-prosessoinnilla valmistetut UHR metallit ovat erittäin lujia, mutta ne eivät muokkauslujitu juuri lainkaan. Näitä metalleja vedettäessä myötymä lokalisoituu lähes heti plastisen muodonmuutoksen alkaessa ja murtositkeys jää alhaiseksi. Sitkeyttä voidaan parantaa sopivalla hehkutuksella, erkaumakarkaisulla ja menetelmillä, jotka lisäävät rakenteen suuren kulman raerajojen määrää, kuten ECAP-prosessoinnin aiheuttaman myötymän lisääminen ja kryogeenisessä lämpötilassa tapahtuva kylmämuokkaus.

ECAP-prosessoidut metallit eivät kestä korkeita käyttölämpötiloja, koska näiden mikrorakenne pyrkii toipumaan ja rekristalloitumaan. Mikrorakennetta voidaan stabiloida toipumishehkutuksen, liuoslujittamisen ja erkaumien avulla. Lämpötilan kasvaessa käsittelemättömät UHR metallit käyttäytyvät sitkeämmin, mutta muokkauslujittuvat vähemmän. Myötymä voi laukaista korkeissa lämpötiloissa rakenteen rekristalloitumisen. UHR metallit ovat sekä sitkeämpiä että lujempia, kun niitä kuormitetaan alle huoneen lämpötilassa.

Useimpien PKK UHR metallien myötönopeusherkkyys on korkeampi kuin suurirakeisilla metalleilla, kun taas TKK UHR metallien myötönopeusherkkyys on tyypillisesti alhaisempi. UHR metallit ovat sitkeämpiä ja samalla lujempia, kun niitä kuormitetaan suuremmilla myötönopeuksilla. Matalilla myötönopeuksilla ja korkeissa lämpötiloissa useat UHR metallit käyttäytyvät superplastisesti, eli näiden lujuus laskee ja sitkeys nousee huomattavasti.

ECAP-prosessoitujen metallien pitkäkestoinen syklinen väsymislujuus on huomattavasti korkeampi kuin suurirakeisilla metalleilla, mutta lyhytkestoinen syklinen väsymislujuus on heikompi. Väsymisominaisuuksia voidaan parantaa erityisillä termomekaanisilla ja mekaanisilla käsittelyillä ECAP-prosessoinnin jälkeen.

Lähteet

[1] Y. T. Zhu, T. G. Langdon. Influence of grain size on deformation mechanisms: An extension to nanocrystalline materials. Materials Science and Engineering A 409 (2005) 234–242.

[2] R. Z. Valiev, T. G. Langdon. Principles of equal-channel angular pressing as a processing tool for grain refinement. Progress in Materials Science 51 (2006) 881-981.

[3] T. G. Langdon. The principles of grain refinement in equal-channel angular pressing. Materials Science and Engineering A 462 (2007) 3–11.

[4] D. H. Shin, K. Park. Ultrafine grained steels processed by equal channel angular pressing. Materials Science and Engineering A 410–411 (2005) 299–302.

[5] M. Furukawa, Z. Horita, M. Nemoto, R. Z. Valiev, T. G. Langdon. Microstructural Characteristics of an Ultrafine Grain Metal Processed with Equal-Channel Angular Pressing. Materials Charcterization 37:277-283 (1996).

[6] J. Wang, Z. Horita, M. Furukawa, M. Nemoto, N.K. Tsenev, R.Z. Valiev, Y. Ma, T.G. Langdon. An investigation of ductility and microstructural evolution in an Al-3% Mg alloy with submicron grain size. Journal of. Materials. Reseach. 8 (1993) 2810.

[7] T.G. Langdon, M. Furukawa, M. Nemoto, Z. Horita. Using Equal-Channel Angular Pressing for Refining Grain Size. JOM 52 April (2000) 30.

[8] A.P. Zhilyaev, G.V. Nurislamova, B.-K. Kim, M.D. Bar´o, J.A. Szpunar, T.G. Langdon. Experimental parameters influencing grain refinement and microstructural evolution during high-pressure torsion. Acta Materialia. 51 (2003) 753.

[9] Z. Horita, T. Fujinami, T.G. Langdon. The potential for scaling ECAP: effect of sample size on grain refinement and mechanical properties Materials Science and Engineering A318 (2001) 34–41.

[10] M. Furukawa, Z. Horita, T. G. Langdon. Principles of deformation in single crystals of two different orientations processed by equal-channelangular pressing. Materials Science and Engineering A. (2008). doi:10.1016/j.msea.2008.03.053.

[11] G.M. Stoica, D.E. Fielden , R. McDaniels, Y. Liu, B. Huang, P.K. Liaw, C. Xu, T.G. Langdon. An analysis of the shear zone for metals deformed by equal-channel angular processing. Materials Science and Engineering A 410–411 (2005) 239–242.

[12] J. Gubicza, N.Q. Chinh, T. Csan´adi, T.G. Langdon, T. Ung´ar. Microstructure and strength of severely deformed fcc metals. Materials Science and Engineering A 462 (2007) 86–90.

[13] A.P. Zhilyaev, D.L. Swisher, K. Oh-ishi, T.G. Langdon, T.R. McNelley. Microtexture and microstructure evolution during processing of pure aluminum by repetitive ECAP. Materials Science and Engineering A 429 (2006) 137–148.

[14] Q. Yang, A.K. Ghosh. Deformation behavior of ultrafine-grain (UFG) AZ31B Mg alloy at room temperature. Acta Materialia 54 (2006) 5159–5170.

[15] E.V. Kozlov, A.N. Zhdanov, N.A. Popova, E.E. Pekarskaya, N.A. Koneva. Sub-grain structure and internal stress fields in UFG materials: problem of Hall–Petch relation. Materials Science and Engineering A 387–389 (2004) 789–794.

[16] Hong Bin Geng, Suk Bong Kang, Bok Ki Min. High temperature tensile behavior of ultra-fine grained Al–3.3Mg–0.2Sc–0.2Zr alloy by equal channel angular pressing. Materials Science and Engineering A 373 (2004) 229–238.

[17] F. Dalla Torre, R. Lapovok, J. Sandlin, P.F. Thomson, C.H.J. Davies, E.V. Pereloma. Microstructures and properties of copper processed by equal channel angular extrusion for 1–16 passes. Acta Materialia 52 (2004) 4819.

[18] D.A. Hughes, N. Hansen. Microstructure and strength of nickel at large strains. Acta Materialia 48 (2000) 2985.

[19] S.V. Bobylev, M.Yu. Gutkin, I.A. Ovidko. Transformations of grain boundaries in deformed nanocrystalline materials. Acta Materialia 52 (2004) 3793.

[20] V. M. Segal, S. Ferrasse, F. Alford. Tensile testing of ultra fine grained metals. Materials Science and Engineering A 422 (2006) 321–326.

[21] W. Blum, X.H. Zeng. A simple dislocation model of deformation resistance of ultrafine-grained materials explaining Hall–Petch strengthening and enhanced strain rate sensitivity. Acta Mater (2009), doi:10.1016/j.actamat.2008.12.041.

[22]] Y.J. Li, X.H. Zeng, W. Blum. Transition from strengthening to softening by grain boundaries in ultrafine-grained Cu. Acta Materialia 52 (2004) 5009–5018.

[23] X.L. Shi, R.S. Mishra, T.J.Watson. Effect of temperature and strain rate on tensile behavior of ultrafine-grained aluminum alloys. Materials Science and Engineering A 494 (2008) 247–252.

[24] M. Wang, A. Shan. Effect of strain rate on the tensile behavior of ultra-fine grained pure aluminum. Journal of Alloys and Compounds 455 (2008) L10–L14.

[25] J. Gubiczaa, N.Q. Chinh, J.L. Labar, S. Dobatkin, Z. Hegedüs, T.G. Langdon. Correlation between microstructure and mechanical properties of severely deformed metals. Journal of Alloys and Compounds (2008), doi:10.1016/j.jallcom.2008.07.200.

[26] Z. W. Wang, Y. B. Wang, X. Z. Liao, Y. H. Zhao, E. J. Lavernia, Y. T. Zhu, Z. Horita, T. G. Langdon. Influence of stacking fault energy on deformation mechanism and dislocation storage capacity in ultrafine-grained materials. Scripta Materialia 60 (2009) 52–55.

[27] D. W. Kum, W. J. Kim, G. Frommeyer. High strain rate superplasticity of an ultrafine grained Al-Ti-Fe alloy. Scripta Materialia 40 (1999). 223–228.

[28] H. Somekawa, T. Tanaka, H. Sasaki, K. Kita, A. Inoue, K. Higashi. Diffusion bonding in ultra fine-grained Al–Fe alloy indicating high-strain-rate superplasticity. Acta Materialia 52 (2004) 1051–1059.

[29] H. Kurishita, S. Matsuo, H. Arakawa, M. Narui, M. Yamazaki, T. Sakamoto, S. Kobayashi, K. Nakai, T. Takida, K. Takebe, M. Kawai, N. Yoshida, High Temperature Tensile Properties and Their Application to Toughness Enhancement in Ultra-Fine

Grained   W-(0-1.5)wt%TiC,   Journal   of   Nuclear   Materials   (2008),   doi: 10.1016/j.jnucmat.2008.12.181.

[30] Y.J. Li, R. Z. Valiev, W. Blum. Deformation kinetics of ultrafine-grained Cu and Ti. Materials Science and Engineering A 410–411 (2005) 451–456.

[31] S. Takaki, K. Kawasaki, Y. Kimura. Mechanical properties of ultra fine grained steels. Journal of Materials Processing Technology 117 (2001) 359- 363.

[32] A. Vinogradov, V. Patlan, Y. Suzuki, K. Kitagawa, V.I. Kopylov. Structure and properties of ultra-fine grain Cu–Cr–Zr alloy produced by equal-channel angular pressing. Acta Materialia 50 (2002) 1639–1651.

[33] D. Jia, Y. M. Wang, K. T. Ramesh, E. Ma, R. Z. Valiev , Y. T. Zhu. Deformation behavior and plastic instabilities of ultrafine-grained titanium. Applied Physics Letters 79 (2001).

[34] C.X. Huang, S.D. Wu, G.Y. Li, S.X. Li. Influences of cyclic deformation and subsequent aging treatment on the tensile properties of Cu processed by equal-channel angular pressing. Materials Science and Engineering A 483–484 (2008) 433–436.

[35] ASM handbook online Volume 2, Properties and Selection: Nonferrous Alloys and Special-Purpose Materials: Properties of Pure Metals: Copper (Cu). Saatavilla http://products.asminternational.org/hbk/index.jsp.

[36] Y. Zhao, J. F. Bingert, X. Liao, B. Cui, K. Han, A. V. Sergueeva, A. K. Mukherjee, R. Z. Valiev, T. G. Langdon, Y. T. Zhu. Simultaneously increasing the ductility and strength of ultra-fine- grained pure copper. Advanced materials 18 (2006) 2949–2953.

[37] Z. Horita, K. Ohashi, T. Fujita, K. Kaneko, T. G. Langdon. Achieving high strength and high ductility in precipitation- hardened alloys. Advanced materials 17 (2005) 1599.

[38] Q. Wei, S. Cheng, K. T. Ramesh, E. Ma. Effect of nanocrystalline and ultrafine grain sizes on the strain rate sensitivity and activation volume: fcc versus bcc metals. Materials Science and Engineering A 381 (2004) 71–79.

[39] K. Park, J. H. Park, Y. S. Lee, W. J. Nam. Microstructures developed by compressive deformation of coarse grained and ultrafine grained 5083 Al alloys at 77K and 298K. Materials Science and Engineering A 408 (2005) 102–109.

[40] Q. Wei, T. Jiao, K. T. Ramesh, E. Ma, L. J. Kecskes, L. Magness, R. Dowding, V. U. Kazykhanov, R. Z. Valiev. Mechanical behavior and dynamic failure of high-strength ultrafine grained tungsten under uniaxial compression. Acta Materialia 54 (2006) 77–87.

[41] D. Jia, K. T. Ramesh, E.Ma. Effects of nanocrystalline and ultrafine grain sizes on constitutive behavior and shear bands in iron. Acta Materialia 51 (2003) 3495–3509.

[42] Q. Wei, L. Kecskes, T. Jiao, K. T. Hartwig, K. T. Ramesh, E. Ma. Adiabatic shear banding in ultrafine-grained Fe processed by severe plastic deformation. Acta Materialia 52 (2004) 1859–1869.

[43] Q. Wei, T. Jiao, S. N. Mathaudhu, E. Ma, K. T. Hartwig, K. T. Ramesh. Microstructure and mechanical properties of tantalum after equal channel angular extrusion (ECAE). Materials Science and Engineering A358 (2003) 266–272.

[44] D. Canadinc, H. J. Maier, P. Gabor, J. May. On the cyclic deformation response of ultrafine-grained Al–Mg alloys at elevated temperatures. Materials Science and Engineering A 496 (2008) 114–120.

[45] W. Blum, Y. J. Li, F. Breutinger. Deformation kinetics of coarse-grained and ultrafine-grained commercially pure Ti. Materials Science and Engineering A 462 (2006) 275–278.

[46] G. T. Gray III, T. C. Lowe, C. M. Cady, R. Z. Valiev, I. V. Aleksandrov. Influence of strain rate & temperature on the mechanical response of ultrafine- grained Cu, Ni and Al- 4Cu- 0,5Zr. Nanostructured materials 9 (1997) 477-480.

[47] B. Farrokh, A.S. Khan. Grain size, strain rate, and temperature dependence of flow stress in ultra-fine grained and nanocrystalline Cu and Al: Synthesis, experiment, and constitutive modeling. International Journal of Plasticity (2008), doi:10.1016/j.ijplas.2008.08.001.

[48] R. Kapoor, J.K. Chakravartty. Deformation behavior of an ultrafine-grained Al–Mg alloy produced by equal-channel angular pressing. Acta Materialia 55 (2007) 5408–5418.

[49] J. Wang, Y. Iwahshi, Z. Horita, M. Furukawa, M. Nemoto, R. Z. Valiev, T. G. Langdon. An Investigation of microstructural stability in an Al-Mg alloy with submicrometer grain size. Acta materialia vol. 44 7 (1996) 2973-2982.

[50] D. H. Shin, J. Pak, Y. K. Kim, K. Park, Y. Kim. Effect of pressing temperature on microstructure and tensile behavior of low carbon steels processed by equal channel angular pressing. Materials Science and Engineering A325 (2002) 31–37.

[51] M. A. Meyers. Dynamic behavior of materials. New York 1994, Wiley. 668 s.

[52] Z. Horita, M. Furukawa, M. Nemoto, A. J. Barnes, T. G. Langdon. Superplastic forming at high strain rates after severe plastic deformation. Acta Mater. 48 (2000) 3633–3640.

[53] A. Mishra, M. Martin, N.N. Thadhani, B.K. Kad, E.A. Kenik, M.A. Meyers. High-strain-rate response of ultra-fine-grained copper. Acta Materialia 56 (2008) 2770–2783.

[54] Q. Yang, A. K. Ghosh. Production of ultrafine-grain microstructure in Mg alloy by alternate biaxial reverse corrugation. Acta Materialia 54 (2006) 5147.

[55] I. P. Semenova, G. Kh. Salimgareeva, V. V. Latysh, T. Lowe, R. Z. Valiev. Enhanced fatigue strength of commercially pure Ti processed by severe plastic deformation. Materials Science and Engineering A 503 (2009) 92–95.

Dynamic Torsion Properties of Ultrafine Grained Aluminum

Mikko Hokka[1,2], Jari Kokkonen[1], Jeremy Seidt[2], Thomas Matrka[2], Amos Gilat[2], Veli-Tapani Kuokkala[1]

[1]Tampere University of Technology, Department of Materials Science
P.O.B. 589, 33101 Tampere, Finland
mikko.hokka@tut.fi
[2]The Ohio State University, Department of Mechanical Engineering

ABSTRACT

Mechanical properties of most metallic materials can be improved by reducing their grain size. One of the methods used to reduce the grain size even to the nanometer level is the severe plastic deformation processing. Equal Channel Angular Pressing (ECAP) is one of the most promising severe plastic deformation processes for nanocrystallization of ductile metals. Nanocrystalline and ultrafine grained metals usually have significantly higher strength properties but lower tensile ductility compared to the coarse grained metals. In this work, the torsion properties of ECAP processed ultrafine grained pure 1070 aluminum were studied in a wide range of strain rates using both servohydraulic materials testing machines and Hopkinson Split Bar techniques. The material exhibits extremely high ductility in torsion and the specimens did not fail even after 300% of strain. Pronounced yield point behavior was observed at strain rates 500 s^{-1} and higher, whereas at lower strain rates the yielding was continuous. The material showed slight strain softening at the strain rate of 10^{-4} s^{-1}, almost ideally plastic behavior at strain rates between 10^{-3} s^{-1} and 500 s^{-1}, and slight but increasing strain hardening at strain rates higher than that. The tests were monitored using digital cameras, and the strain distributions on the surface of the specimens were calculated using digital image correlation. The strain in the specimen localized very rapidly after yielding at all strain rates, and the localization lead to the development of a shear band. At high strain rates the shear band developed faster than at low strain rates.

INTRODUCTION

Metallic materials can be distinguished into coarse grained, fine grained, ultrafine grained, and nanocrystalline depending on the average grain size. If the average grain size is larger than 1 µm, the material is either fine grained or coarse grained, the transition between these two being somewhere around 10 µm. Between 100 nm and 1 µm, the material is called ultrafine grained, and when the grain size is less than 100 nm, it is classified as a nanocrystalline material. Nanocrystalline and ultrafine grain size metals have many excellent properties compared to the coarse grained materials with the same chemical composition. For example, most metals with grain sizes in the nanocrystalline range show excellent strength, hardness, and fatigue properties as well as improved wear and corrosion resistance, in some cases combined with increased toughness even at low temperatures. Potential applicability of these materials is also wide, including aerospace applications, transportation, health care equipment and components, defense applications, and even implant technology due to the possible high purity of the materials (i.e., even pure metals can exhibit substantial strength values when the grain size is small enough).

There are basically two main techniques to produce metals with grain sizes less than one micrometer; consolidating and sintering of metal powders, and severe plastic deformation. Sintering of metal powders, however, often produces porous microstructures with higher impurity content. Severe plastic deformation, on the other hand, can be used to produce nanocrystalline or ultrafine grain size metals from virtually any metal by simply applying extreme plastic strains on the existing coarse grained bulk material. One of the severe plastic deformation processes that have been successfully used to produce nanocrystalline and ultrafine grained metals is the Equal Channel Angular Pressing (ECAP). In the traditional ECAP, the material billet is pressed several times through the channels in the ECAP die. The ECAP die consists of input and output channels, which meet at an angle usually close to 90°. The material undergoes simple shear as the billet is pushed through the die and the

strain accumulates during consecutive passes. Eventually, the high plastic shear strains will lead to refined microstructure and texture. Different kind of microstructures and textures can be manufactured by using different processing "routes", in which the billet is rotated between consecutive passes. In route C, the billet is rotated 180° between passes, whereas alternating 90° rotation between clockwise and counter-clockwise directions is called route B_a, and 90° rotation in the same direction route B_c. In route A, the billet is not rotated at all. Route B_c has been found to produce the most equiaxed grain structure with the highest ratio of high-angle boundaries [3]. For a good review of the ECAP processes, see for example ref. [10].

The mechanical properties and behavior of most materials are strongly affected by the applied strain rate, temperature, and type of loading. For coarse grained metals, the strength usually increases with increasing strain rate, especially at strain rates around 10^3 s^{-1}, where a rapid increase in strength is often observed. At quasi-static and intermediate strain rates ($<\sim 500$ s^{-1}), the deformation behavior of crystalline materials, such as coarse grained metals, is readily explained by the thermally activated dislocation motion. At higher strain rates ($>\sim 1000$ s^{-1}), the dislocation drag mechanisms start to control the deformation behavior, and usually the strength of the material increases dramatically as the mechanism changes. However, when the crystal size is decreased to nanometer scale, the movement of dislocations becomes increasingly difficult. At the moment, however, the strain rate dependent deformation and hardening mechanisms of nanocrystalline metals are not properly understood yet. May [1] et al. studied the strain rate sensitivity of coarse grained and ECAP processed ultrafine grained aluminum (AA1050) and found that the strain rate sensitivity in compression for the ultrafine grained aluminum is about 3.5 times higher than that for the coarse grained material. The effect was even more clear at elevated temperatures, where the strain rate sensitivity factor, $m=\log(\sigma)/\log(\dot{\varepsilon})$, was as high as 0.25, which is ten times higher than that for the same coarse grained material. Also the strain hardening rate, $\theta=d\sigma/d\varepsilon$, is different for the ultrafine grained metals when compared to large grained metals. Kokkonen et al. [4] performed tension and compression tests at various strain rates and temperatures for ECAP processed AA1070 and found that the strain softening observed at low strain rates changes to strain hardening at high strain rates and/or low temperatures. The strain softening in ECAP processed aluminum alloys at low strain rates has generally been attributed to dynamic recovery, which is reduced at low temperatures [2-3].

Some materials such as the ECAP processed metals can show fairly poor ductility in tension, which is due to the low strain hardening capability and plastic instability of the material that occurs rapidly after the yielding. However, the material can still flow significantly in tension after the necking and the fracture strains can be fairly high. Therefore, the formability of ultrafine grained materials can still be very good as was shown by Sirivaraman and Chakkingal [12], who studied the deformability of ultrafine grained commercial purity aluminum by upsetting tests. Also, the instability and fracture that is observed in tension does not necessarily occur in the same way in shear, and the torsion deformation can continue to much higher strains before the final fracture of the material. Therefore, the torsion behavior often describes the overall formability of the material better than the results of a simple tension test, which are influenced also by the structural response of the specimen. In this work, the torsion properties and behavior of ECAP processed 1070 aluminum were studied at a wide range of strain rates. The tests were also monitored by high speed digital cameras, and the strain distributions were calculated from the acquired images using digital image correlation.

MATERIALS AND EXPERIMENTS

The material studied in this work was pure AA1070 (99.7 wt-% Al) aluminum. The material was processed at the Warsaw University of Technology by forcing 25*25*115 mm^3 billets through a two-turn ECAP die four times and rotating the billet by 90° between the passes. The channels in the two-turn die make two 90° turns, so one pass effectively corresponds to two passes in a single turn die following the route C, and when the billets are rotated 90° between the passes, the route becomes C + B_c. The die design is shown in Fig. 1. The total accumulated strain after the ECAP processing was equivalent to about 9.4, leading to the average grain size around 750 nm. The grain size was determined from transmission electron micrographs in a previous study [4]. The die construction, numerical simulations used for the optimization of the design, and the actual ECAP processing are presented in more details in refs. [5,6]. In addition to the ultrafine grained AA1070 aluminum, some tests were also performed on a standard AA7075-T6 aluminum alloy for comparison.

Figure 1: Equal channel angular pressing die used for producing the ultrafine grained structure.

The behavior of this material at different strain rates and temperatures has been previously characterized in tension and in compression [4, 8-9]. In this study, the material properties were characterized in torsion using both a servohydraulic materials testing machine and a torsion Split Hopkinson Pressure Bar (SHPB) device with a pre-torque clamp-release system. The device used in this work is described in details in ref. [8].The SHPB device consists of 7/8 inch diameter aluminum alloy incident and transmitted bars, between which the thin walled tube specimen is glued. The incident torsion pulse is generated by releasing a pre-stored torsion load from the free end of the incident bar. The pre-torque is applied by a hydraulic pulley and stored by clamping the incident bar at a suitable distance from the pulley. The clamp is held by a brittle(ish) aluminum pin, which can be rapidly broken by a second hydraulic press. When the pin is broken, the torsion pulse is released to propagate in the bar towards both the specimen and the pre-torque pulley. As the wave reaches the pulley, it is reflected back as a torsion wave with equal magnitude but opposite sign, which cancels the original pulse creating an incident pulse with a length equal to twice the distance from the clamp to the hydraulic pulley. As the incident wave reaches the specimen, part of the wave is reflected back as a wave of torsion with a sign opposite to the incident wave, and part of the incident wave is transmitted through the specimen into the transmitted bar deforming the specimen at a high rate. The time resolved load and strain history of the specimen can be calculated from the incident, reflected, and transmitted shear stress pulses. In this study, however, the strains and strain rates were calculated from the image analysis results.

The high rate torsion tests were monitored using two Photron Fastcam SA1.1 high speed cameras, whereas two Point Gray Research Grasshopper cameras with 2 megapixel resolution were used to monitor the low rate experiments. The cameras were viewing the specimen at different angles and synchronized to take images at the same time. VIC 3D image correlation software was used to calculate the full field strain distributions on the surface of the specimens as well as the displacements of the grip sections of the specimen, from which the average shear strain can also be calculated. The cameras were acquiring images at the frame rate of 125.000 s^{-1} in the high rate experiments and at frame rates between 0.1..19 s^{-1} in the low rate experiments, yielding about 150 to 400 image pairs for each test.

The thin walled torsion specimens were machined from rectangular bars for the ultrafine grained aluminum and from a standard 0.5 inch diameter round bar for the 7075-T6 aluminum alloy. The gage length of the specimens was 5.08 mm (0.2 in), the outer diameter 9.65 mm (0.38 in), and the wall thickness 0.38 mm (0.015 in) for the 7075 alloy. The dimensions were the same for the ultrafine grained specimens except for the wall thickness that was increased to 0.76 mm (0.03 in). The specimens were further connected to adaptors, and the whole specimen adaptor assembly was glued to the ends of the stress bars of the Hopkinson Bar device or fixed to the hydraulic clamps of the servohydraulic materials testing machine. The contrast pattern for photography was first applied by painting the gage section of the specimens and the adaptors with black base color, over which white speckles were hand painted for maximum contrast. However, it was soon noticed that the hand painted dots were too thick and broke off from the surface at fairly low strains. Even though white base color and spray painted black contrast pattern were found to have better adhesion to the surface, it still broke off at shear strains around 60-90%. Therefore, the average strain on the specimen was at the end calculated from the 3D displacements of the ends of the bars using Equation 1.

$$\gamma = \frac{r_s \theta}{l_s} = \frac{r_s}{l_s} \arccos\left(\frac{\overline{a} \bullet \overline{b}}{\| a \| * \| b \|}\right) \tag{1}$$

where r_s and l_s are the average radius and gage length of the specimen, θ is the angle of twist between the opposite ends of the specimen, and $\overline{a}$ and $\overline{b}$ are vectors from the centerline to the surface of the specimen at the opposite ends of the gage section.

RESULTS AND DISCUSSION

Figure 2a shows the shear stress *vs.* shear strain curves at different strain rates for the ultrafine grained 1070 aluminum and Figure 2b the corresponding curves for the 7075-T6 aluminum alloy. The strength levels for the 7075 alloy are naturally significantly higher than those measured for the ultrafine grained 1070 pure aluminum. However, the maximum strains are rather low for the 7075 aluminum, whereas none of the ultrafine grained 1070 specimens failed in any of the tests, and shear strains of more than 300% were measured without fracture. At strain rate 10^{-4} s^{-1}, the ultrafine grained material clearly softens with increasing strain, but when the strain rate is increased by a factor of ten, the strain softening is already reduced significantly. At the strain rates of 10^{-3} s^{-1} to 10^{-2} s^{-1} the material softens in the beginning of the test, but above 20% of strain the material is almost ideally plastic. At the strain rate 0.5 s^{-1}, the behavior of the material is virtually ideally plastic without the previously seen softening in the beginning of the test. At higher strain rates, the yielding of the specimen is clearly different from that observed at low strain rates. At the strain rate of 500 s^{-1}, the yield point is clearly pronounced, and the at strain rate of 2000 s^{-1}, the peak is more than 10 MPa higher than the subsequent flow stress after a few percent of plastic strain. Also, the material slightly hardens with strain at the strain rate of 2000 s^{-1} and shows a maximum stress at around 80-100% of shear strain, after which the strength slightly decreases. The observed behavior resembles the behavior found for this material also in compression [4]. The strain softening at very low strain rates is most likely due to the dynamic recovery, which is significantly reduced at higher strain rates and lower temperatures [2,3], leading to slightly increasing strain hardening of the material. The pronounced yielding behavior, on the other hand, is most likely explained by the lack of sufficient mobile dislocations in the initially heavily deformed material, leading to the observed increasing yield peak with increasing strain rates.
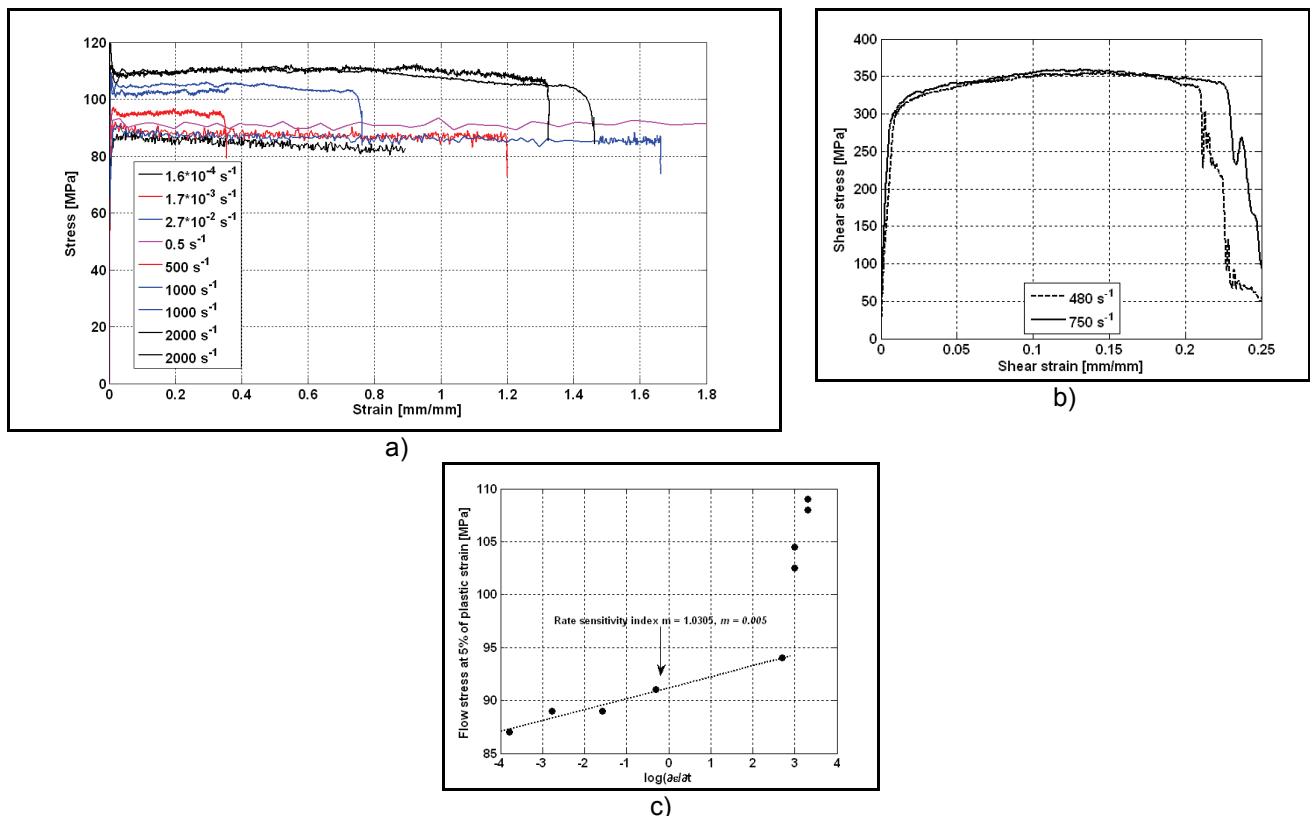
a)

b)

c)

Figure 2: Results from the torsion tests: a) stress strain curves for the ultrafine grained pure 1070 aluminum, b) stress strain curves for the 7075-T6 aluminum alloy, and c) flow stress at 5% of plastic strain for the ultrafine grained aluminum as a function of logarithmic strain rate.

Figure 2c shows the flow stress at 5% of plastic strain for the ultrafine grained 1070 aluminum. In the low strain rate region, the flow stress steadily increases from 87 MPa to 94 MPa, and the absolute strain rate sensitivity factor, $m=\Delta\sigma/\Delta\log(\dot{\varepsilon})$, and the relative strain rate sensitivity factor, $m = \Delta\log(\sigma)/\Delta\log(\dot{\varepsilon})$, have values of 1.0305 MPa and 0.005, respectively. The values measured in this study for torsion are somewhat lower than those presented by Kokkonen et al. [11] and Kuokkala et al. [9] in compression and tension for similar ultrafine grained 1070 aluminum. However, the differences are small and can most likely be explained by slight differences in the grain size refinement procedures and therefore slightly different microstructures.
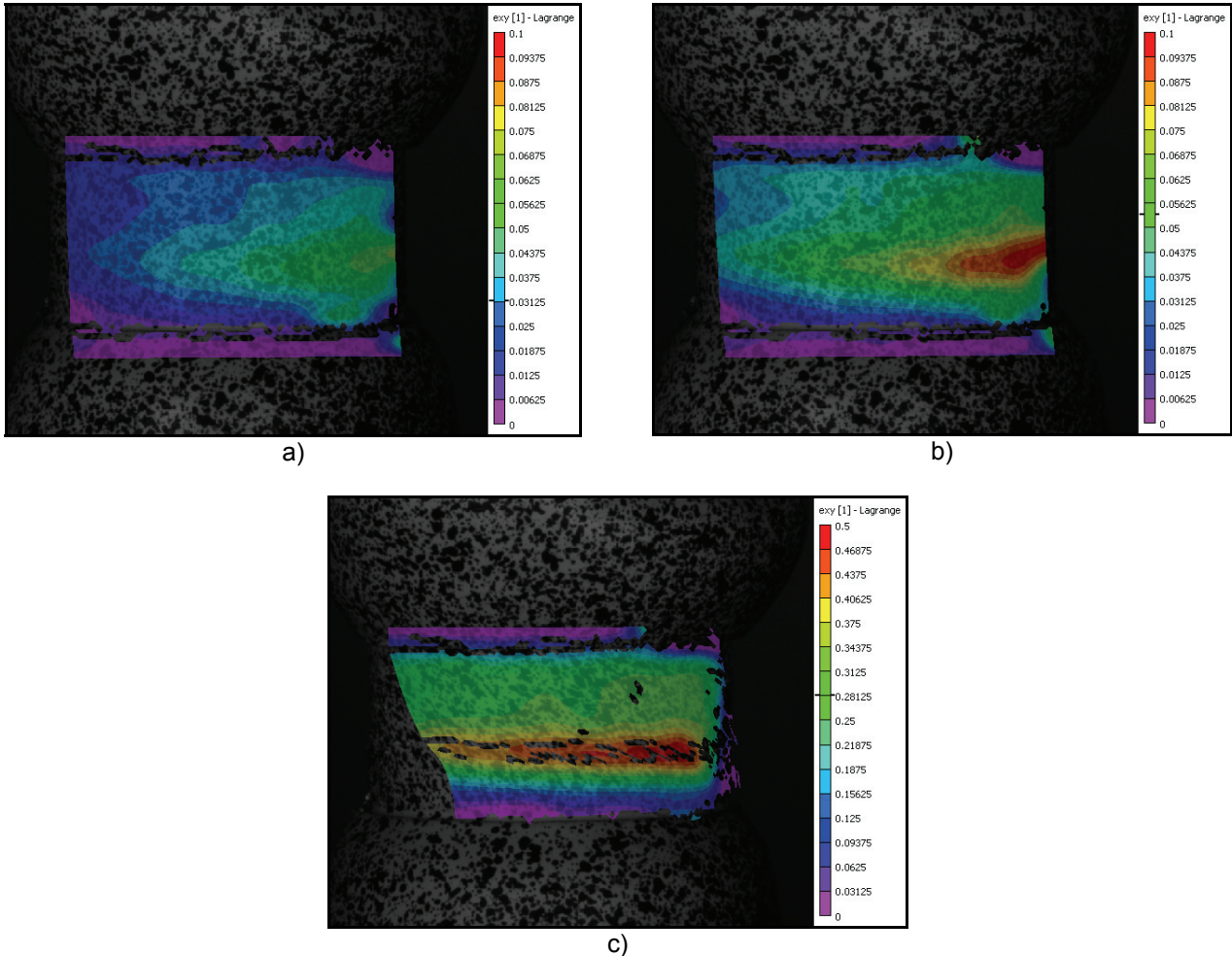

a)

b)

c)

Figure 3: Localization of strain in a torsion test at the strain rate of 1.6 10^{-4} s^{-1}: a) strains just after yielding, b) a developing shear band, and c) a fully developed shear band.

Figure 3 shows the image correlation results for the torsion test of an ultrafine grained 1070 aluminum sample at the strain rate of 1.6 10^{-4} s^{-1}. In the very early stages of the test (Figure 3a), both ends of the specimen are nearly undeformed and the yielding starts rather uniformly in the middle of the gage section, but then rapidly localizes to the right side of the gage section. The maximum strain is around 6% of Lagrange shear strain ($\varepsilon_{xy}=\frac{1}{2}*\gamma$), whereas most of the gage section is still at around 2-3% of Lagrange shear strain. In Figure 3b, the localization is more clearly visible, showing a maximum Lagrange shear strain of 10%, while the surrounding regions still remain at about 6-7% of Lagrange shear strain. However, the shear band does not extend over the whole gage section until at much higher strains. Figure 3c shows the fully developed shear band in the middle of the gage section with a maximum Lagrange shear strain around 50%, while the surrounding areas remain closer to 35%. The behavior does not change much in the low rate experiments, which can be seen in Figure 4, where similar pictures taken from a test performed at the strain rate of 0.5 s^{-1} are shown. The yielding starts this time from the left hand side

and localizes rapidly only after a few percent of strain. The shear band develops, and in Fig 4b it already extends across the whole gage section but still shows a clear maximum on the left hand side with strains up to 10%. The right hand side is still at only 5% of strain, and the regions outside the shear band at about 2-3 % of strain. At later stages, the shear band develops further and the strain increases more rapidly within the shear band, while other regions experience much less strain. Figure 4c shows a fully developed shear band with twice as much strain compared to the surrounding regions.
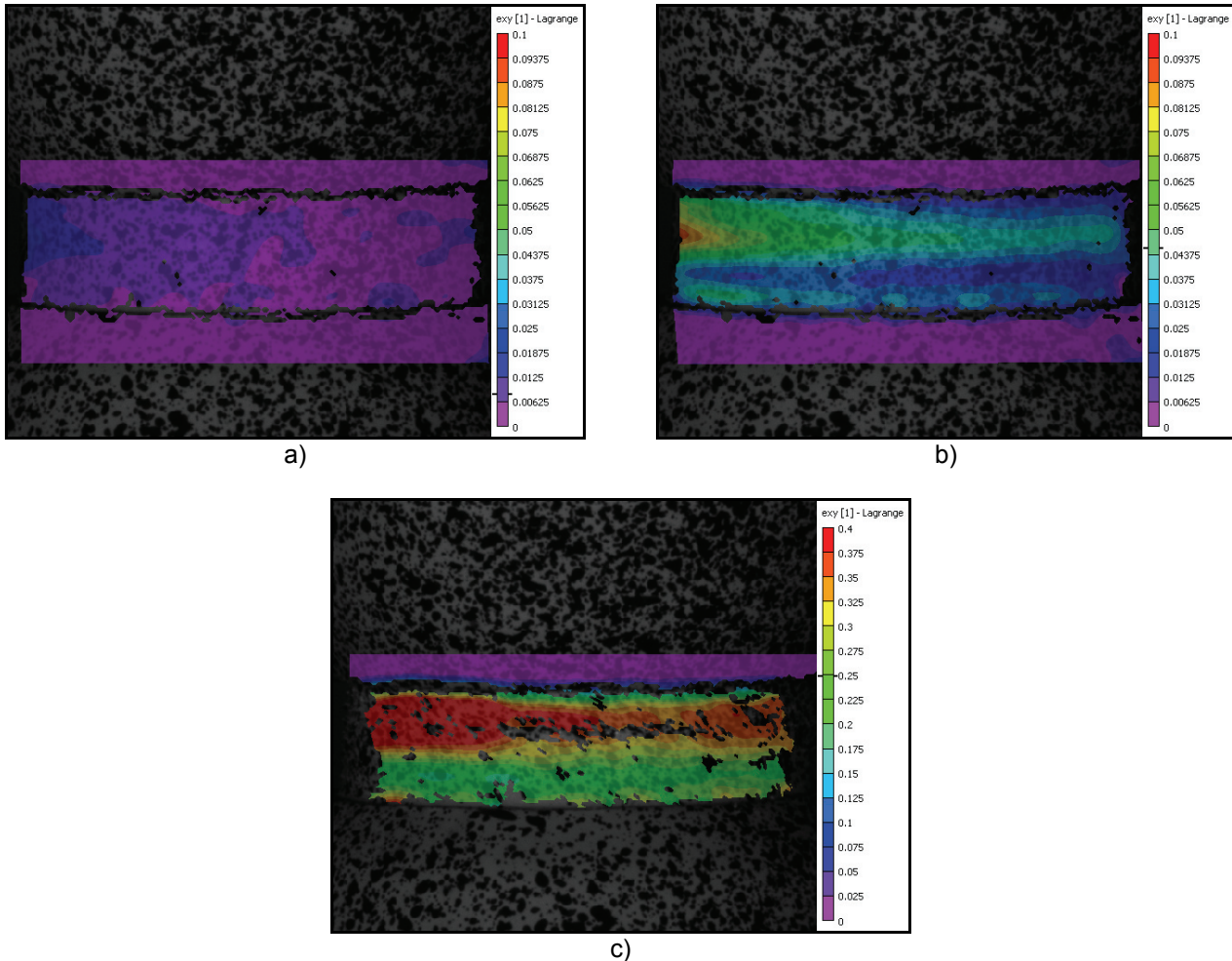

a)

b)

c)

Figure 4: Localization of strain in a torsion test at the strain rate of 0.5 s^{-1}: a) strains just after yielding, b) a developing shear band, and c) a fully developed shear band.

The development of the shear band clearly changes when the strain rate is further increased. Figure 5 shows the development of the shear band at the strain rate of 1000 s^{-1}. Also at high strain rates, the strain localizes already after the first few percents of Lagrange shear strain, but at this strain rate the localization zone is much narrower and extends through the gage section already at very low strains. Fig. 5a shows the early stages of the test, where the strain has already localized and the shear band extends through the entire gage section. The strain in the localized region is around 3-4%, whereas in the surrounding regions it is only 0-2%. The shear band develops fast and the localization continues throughout the test, as shown in Figures 5b and 5c.This type of behavior was observed in all high strain rate tests. It should be noted, however, that despite the localization of strain and the development of the shear band, the strain also increases in the surrounding regions throughout the test at all strain rates. This means that the material in the shear band must have a positive strain hardening rate at all strain rates and that it is high enough to compensate for the thermal softening taking place in the shear band, which at high strain rates and high strains can be quite significant.

The more rapid development of the shear band at high strain rates could simply be explained by the adiabatic heating and consequent thermal softening of the material. However, the shear band extends through the gage section almost immediately after yielding, and therefore the thermal softening alone cannot contribute enough to the development of the shear band. The faster development of the shear band is most likely related to the different yielding behavior of the material at higher strain rates. The pronounced yielding of utrafine grained metals is usually explained by the lack of mobile dislocations that causes the remaining free dislocation to move faster in the beginning of the test [1], thus requiring a higher stress. Therefore it is possible that the avalanche of gliding dislocations that follows the break-up of pinned dislocations causes faster localization of strain due to the very high local deformation rates and consequent thermal softening.
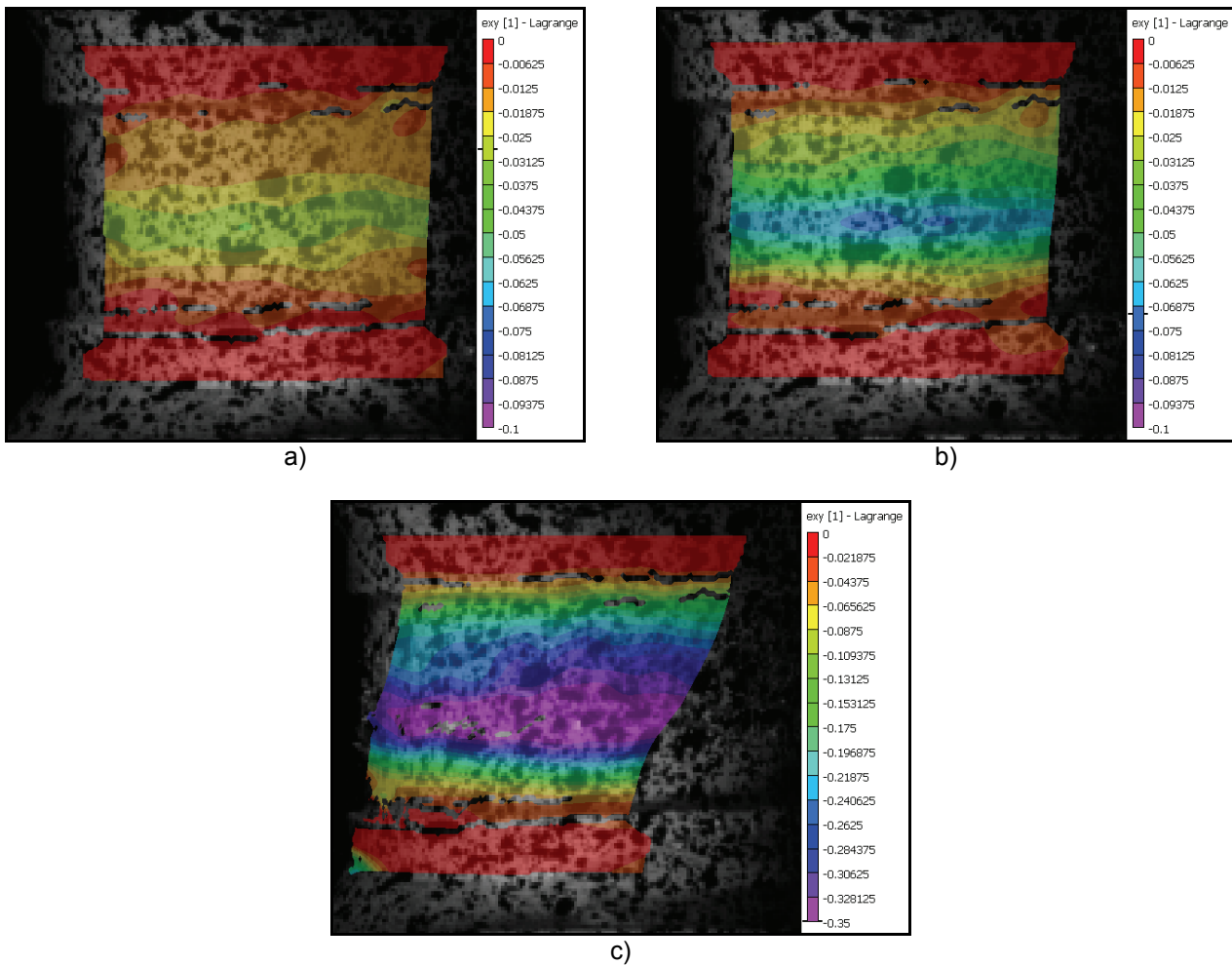

a)

b)

c)

Figure 5: Localization of strain in a torsion test at the strain rate of 1000 s^{-1}: a) strains just after yielding, b) a developing shear band, and c) a fully developed shear band.

From the digital image correlation results it is very clear that the average strain calculated from the displacements of the ends of the bars does not represent the behavior of the material very well. The strain localizes very rapidly during the first few percents of deformation. The maximum strain in the shear band can be more than twice as high as in the surrounding regions of the gage section. However, the problems with the adhesion of the contrast pattern currently limit the usable range of digital image correlation to about 60-100 % of shear strain.

SUMMARY

The behavior and properties of pure 1070 aluminum were characterized in a wide range of strain rates in torsion. Thin walled tube specimens were machined from ECAP processed 1070 aluminum and tested using a conventional servohydraulic materials testing machine at low strain rates and the Hopkinson Split Bar technique at high strain rates. A pronounced yielding behavior was observed at strain rates 500 s^{-1} and above. At low strain rates the material showed either slight strain softening or almost ideally plastic behavior. At higher strain rates the strain hardening rate showed an increase with increasing strain rate. The material was found to be well deformable in torsion, exhibiting shear strains over 300% without failure.

The tests were also monitored using digital cameras to facilitate the calculation of strains on the surface of the specimen during deformation. During the tests, deformation localized very rapidly and a shear band formed across the gage section of the specimen. At low strain rates, however, the development of the shear band was slower and the band nucleated and grew from one side of the specimen and only then propagated through the gage section. At higher strain rates, the formation of the shear band was much faster and it extended over the whole gage section almost immediately after yielding.

REFERENCES

1. May J. Höppel H., Göken M., Strain rate sensitivity of ultrafine-grained aluminum processed by severe plastic deformation. Scripta Materialia, 53, pp. 189-194, 2005.
2. El-Danaf E. Mechanical properties and microstructure evolution of 1050 aluminum severely processed by ECAP to 16 passes. Materials Science and Engineering A, 487, pp 189-200, 2008.
3. El-Danaf E., Soliman M. Almajid A., El-Rayes M., Enhancement of mechanical properties and grain size refinement of commercial purity aluminum 1050 processed by ECAP. Materials Science and Engineering A, 458, pp 226-234, 2007.
4. Kokkonen J. Kuokkala V.-T., Lech Olejnik, Andrzej Rosochowski, Dynamic behavior of ECAP processed aluminum at room and sub-zero temperatures. In the proceedings of the annual SEM conference, Orlando Fl, 2008.
5. Rosochowski A., Olejnik L. Numerical and Physical modeling of plastic deformation in 2-turn equal angular extrusion. Journal of Materials Processing Technology, 125-126, pp. 309-316, 2002.
6. Olejnik L. Rosochowski A., Methods of fabrication metals from nano-technology. Bulletin of the Polish Academy of Sciences, Technical Sciences, 53, pp. 413-423, 2005.
7. Gilat A., Torsional Kolsky bar testing. ASM Handbook, 8, Materials Park, Ohio, USA, 2000.
8. Kokkonen J., Kuokkala V.-T., Seidt J., Walker A., Gilat A., Olejnik L., Rosochowski A. High strain rate deformation analysis of UFG aluminum sheet samples. In the proceedings of the annual SEM conference, Albuquerque NM, 2009.
9. Kuokkala V.-T., Kokkonen J., Song B., Chen W., Olejnik L., Rosochowski A., Dynamic responce of severe plastic deformation processed 1070 aluminum at various temperatures. In the proceedings of the Dymat Technical Meeting, Bourges, France, 2008.
10. Valiev R., Langdon T. Principles of equal-channel angular pressing as a processing tool for grain refinement. Progress in Materials Science, 51, pp 881-981, 2006.
11. Kokkonen J., Kuokkala V.-T., Isakov M., Dynamic behavior of UFG aluminum at a wide range of strain rates and temperatures in compression and tension. Journal de Physique IV, 1, pp. 647-653, 2009.
12. Sivaraman A., Chakkingal U., Investigations on workability of commercial purity aluminum processed by equal channel angular pressing. Journal of Materials Processing Technology, 202, pp. 543-548, 2008.

Compression Behavior of Near-UFG AZ31 Mg-Alloy at High Strain Rates

Mikko Hokka[1,2], Jeremy Seidt[2], Thomas Matrka[2], Amos Gilat[2], Veli-Tapani Kuokkala[1], Juha Nykänen[1], Sören Müller[3]

[1]Tampere University of Technology
P.O.B. 589, 33101 Tampere, Finland
mikko.hokka@tut.fi
[2]The Ohio State University, Department of Mechanical Engineering
[3]Technische Universität Berlin, Extrusion Research and Development Center

ABSTRACT

The superior specific strength of magnesium alloys makes them very attractive for several applications, especially in transportation, aviation, and space industries. Usually the properties of most metals, including magnesium alloys, can be enhanced by reducing the average grain size, which leads to increasing strength without decreasing the ductility of the material too much. One of the methods used today to decrease the grain size is the severe plastic deformation (spd), where the grain size is decreased by applying a very high shear strain under high hydrostatic pressure, leading to the accumulation of dislocations and eventually forming new smaller grains. Usually the amount of material that can be processed at one time is very limited, making most of the severe plastic deformation techniques less suitable for industrial production. One of the interesting techniques that allows larger batch sizes to be processed at one time is called reciprocating extrusion. In this work, the compression properties of the reciprocating extrusion processed standard magnesium alloy AZ31 were studied in a wide range of strain rates. The results show that the strength of AZ31 is significantly higher after reciprocating extrusion as compared to squeeze cast AZ31, and at the same level as for the hot rolled and ECAP processed AZ31. The compression tests were also monitored using digital cameras, and the surface strain distributions on the specimen were calculated using digital image correlation. The strains on the surfaces of the specimens were fairly homogeneous and no significant barreling was observed. The failure of the specimens occurred at a 45 degree angle in all tests, preceded by a rapid formation of a shear band.

INTRODUCTION

Magnesium alloys are one of the lightest constructional metals that are used for special applications in the aerospace and transportation industries, mainly due to their high specific strength and stiffness. Most magnesium alloys are used as castings, but also forged components are manufactured for mechanically more demanding applications. Generally magnesium alloys have moderate strength and limited formability due to their hexagonal crystal structure. The strength of most alloys can, however, be improved by increasing the alloying, by using heat treatments, or by reducing the grain size of the metal. The latter can be done, for example, by alloying, by thermomechanical treatments, or by subjecting the material to severe plastic deformation. Severe plastic deformation (spd) basically increases the dislocation density of the material until the dense dislocation walls become high angle grain boundaries and the average grain size of the material is significantly reduced. For metals with good formability, such as aluminum and copper, the severe plastic deformation processing can usually be done at room temperature, but for metals with limited formability, such as magnesium alloys, the processing is usually carried out at elevated temperatures that limits the achievable grain sizes.

Crystalline metals can be distinguished into coarse grained materials with grain sizes larger than 1 μm, ultrafine grained (UFG) materials with grain sizes between 1 μm and 0.1 μm, and nanocrystalline materials with grain sizes less than 0.1 μm. Most metals respond positively to severe plastic deformation processing and the grain sizes can be reduced to ultrafine or even nanocrystal levels. Grain refinement by severe plastic deformation has received considerable attention in the past decade due to its strength enhancing capabilities. However, magnesium alloys

have not been the most studied material, and more effort has gone to studying other more deformable metals such as aluminum, copper, and titanium. The magnesium alloys offer great weight reduction potential for the transportation and aviation industries, where heavier materials may be replaced with these alloys. The magnesium alloys, however, have some drawbacks, e.g., lower ductility and strong textural effects, which have hindered their implementation in the past.

One of the aims of the severe plastic deformation processing is to increase the strength of the material without expensive alloying and heat treatments, and without decreasing the ductility too much. However, according to the literature, increasing the strength of magnesium alloys is not as straightforward as for some other commonly used construction metals. Zúberová et al. [4] studied the compression behavior of the magnesium alloy AZ31 with different grain sizes. They found that the yield strength of the equal-channel angular pressed (ECAP) AZ31 was significantly higher than that of the squeeze cast AZ31 but not much higher than the strength of the hot rolled AZ31. The fracture strength was actually higher for the hot rolled material. At higher temperatures the yield strength of the ECAP processed AZ31 decreased very rapidly, and at 200 °C the yield strength of the hot rolled material exceeded the yield strength of the ECAP processed material. Kang et al. [2] studied AZ31 magnesium alloy and were able to decrease the grain size of the material down to less than 3 µm by warm ECAP, but the strength of the material decreased with decreasing grain size, whereas the micro hardness and elongation increased with decreasing grain size. Li et al. [3] were able to decrease the grain size of a ZK60 magnesium alloy to about 0.8 µm by ECAP at 473 K. However, this particular alloy is an age hardening alloy, and the ECAP processing under high hydrostatic stress changed the morphology of the precipitates and the strength of the material actually decreased by over 200 MPa. Also, due to their hexagonal structure, magnesium alloys can show a distinctively different behavior in tension and in compression, and the strength properties can be generally very anisotropic. Müller et al. [1] studied the strength differential effect (SDE) in magnesium alloys and found that the SDE is significantly reduced when the grain size of the material is reduced.

In this work, the compression behavior of the reciprocating extrusion processed AZ31 magnesium alloy was studied in a wide range of strain rates using a conventional hydraulic materials testing machine and a Hopkinson Split Bar device. Usually the strain is measured using extensometers at low strain rates and calculated from the displacements of the ends of the pressure bars in the Hopkinson Spit Bar methods. In this study, the strain in the specimen is measured directly from the surface of the specimen using high speed photography and digital image correlation (DIC). DIC enables measuring of the strain with the same method at low and high strain rates, thus improving the comparison of the results obtained at different strain rate regimes.

EXPERIMENTAL

The material studied in this work was a standard magnesium alloy AZ31, which was SPD processed using the reciprocating extrusion. The material was SPD processed with and without prior extrusion, and both grades were studied. The reciprocating extrusion processing was performed by extruding the billet five times back and forth through the extrusion (kneeding) die, which is basically a narrower collar in the extrusion channel (see Fig. 1). The inner diameter of the extrusion die was 30 mm, while the diameter of the collar was 24 mm. Back pressure was applied to force the billet back into its original thickness after passing the collar, and the process was repeated several times before the billet was extruded to a round bar with a 10 mm diameter. The temperature of the die and the specimen was 300 °C, and after the final extrusion the material was air cooled. The microstructures of both grades were very similar, consisting mainly of very small grains and a few larger grains with an average grain size between 6-8 micrometers. The alloy processed in the extruded state had a more equiaxed grain structure, whereas the microstructure of the alloy processed without prior deformation contained more deformed and elongated grains. The material was prepared at the Technische Universität Berlin.
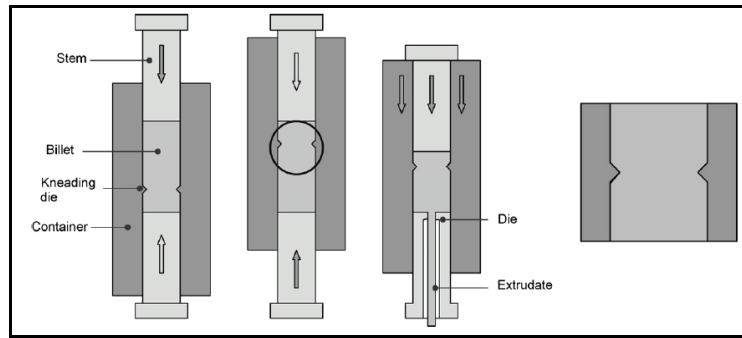
Figure 1: Schematics of the reciprocating extrusion device used to process the AZ31 alloy [after 1].

The materials were tested in compression at various strain rates. The tests were performed using a servohydraulic materials testing machine at low rates ($\dot{\varepsilon}$ <1 s^{-1}) and a Hopkinson Split Bar device at high rates ($\dot{\varepsilon}$ >500 s^{-1}). The conventional Hopkinson Split bar equipment that was used in this study has high strength titanium bars with ½ inch diameter. The stress in the specimen was measured using strain gages bonded on the surface of the transmitted bar.

The compression tests were monitored by two digital cameras looking at the specimen at different angles. At low strain rates, two Point Gray Research Grasshopper cameras with 2 megapixel resolution were used to obtain the image pairs, and at strain rates of 1 s^{-1} and above, two Photron Fastcam SA1.1 high speed cameras were used. The specimens and short sections of the bars or anvils were painted with a base coat, over which a high contrast speckle pattern was applied. For low rate experiments, a white base coat with black speckles were used, whereas at high strain rates the colors were reversed due to the increased need of illumination at higher frame rates, which lead to excess glare when using the white base coat. Spatial Lagrange strains in the specimen were calculated from the displacements on the surface of the specimen by tracking the movement of small image subsets. Average engineering strain over the surface of the specimen was calculated from the spatial Lagrange strains using Equation 1, where E_{11} is the Lagrange strain in the axial direction of the specimen. For a good overview of the digital image correlation techniques with examples see, e.g., ref. [6].

$$\varepsilon_E = \frac{\sum_{i=1}^{N} \sqrt{1 + 2E_{11}^i} - 1}{N} \tag{1}$$

RESULTS AND DISCUSSION

Figure 2 shows the compression true stress vs. true strain curves measured at room temperature at different strain rates. The fracture strain in the tests varies between 0.15 and 0.22. The yield strength of the AZ31, which was cast and SPD processed (Fig 2b) is slightly higher than that of the AZ31, which was extruded before SPD processing (Fig. 2a). At low strain rates, the strength of both materials continuously increases after the yield point. At high strain rates, however, the strain hardening rate in the beginning of the test is significantly lower but then increases rapidly after about 3% of strain. Such high strain hardening rates are typical for magnesium alloys, and the concave shape of the curve is normally attributed to the mechanical twinning [5], which is enhanced at higher strain rates and leads to an increasing strain hardening rate with increasing strain rate.
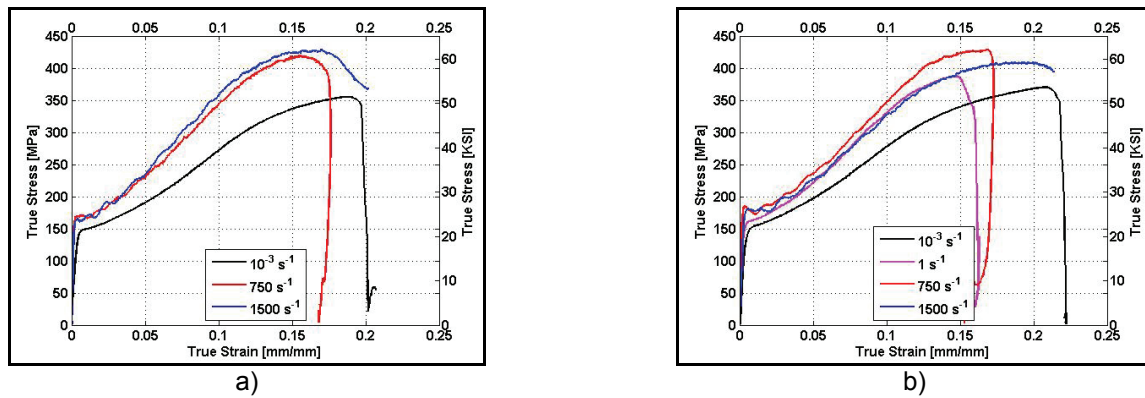
a)   b)

Figure 2: True stress vs. true strain curves for the studied AZ31 alloy: a) cast, extruded and SPD processed and b) cast and SPD processed material.

The yield strength of both materials clearly increases with strain rate, which can be seen even better in Figure 3a, which shows the yield strength, flow stress at 10% of plastic strain, and the fracture strength as a function of logarithmic strain rate. From the figure it is, however, clear that the strain rate sensitivities for both grades of AZ31 are not very high. For the yield strength, the increase is only from about 150 MPa at the strain rate of 10^{-3} s^{-1} to 175 MPa at 1000 s^{-1}, and for the fracture strength from about 360 MPa to ca. 400 MPa.

In Figure 3b, the results of this work are compared with the results of Zúberová et al. [4], who studied the compression behavior of AZ31 alloy in squeeze cast, hot rolled, and ECAP processed states. The yield strength of the AZ31 processed with the reciprocating extrusion is about 60 MPa higher (or 50%) than that of the squeeze cast AZ31, whereas the strength of the hot rolled material lies just below the ECAP processed and reciprocating extrusion processed materials. The squeeze cast material has a very coarse microstructure compared to all other grades of the same material. However, it is interesting to notice that ECAP processing does not provide any significant increase in the yield strength compared to hot rolling or reciprocating extrusion processing. Also, Müller at al. [1] studied the reciprocating extrusion processed AZ31, and they measured yield strengths exceeding 200 MPa for the same alloy as studied in this work. However, the problem with the reciprocating extrusion is the gradient microstructure and increasing grain size towards the center of the bar axis. In this study, the specimens were machined from the extruded10 mm bars so that and the outer layers of the bars were removed by turning. The outer regions are most likely the most deformed areas during the reciprocating extrusion and therefore have the smallest grain sizes and highest strength. Removing these regions to fabricate the compression specimens will most likely influence the measured strength values.
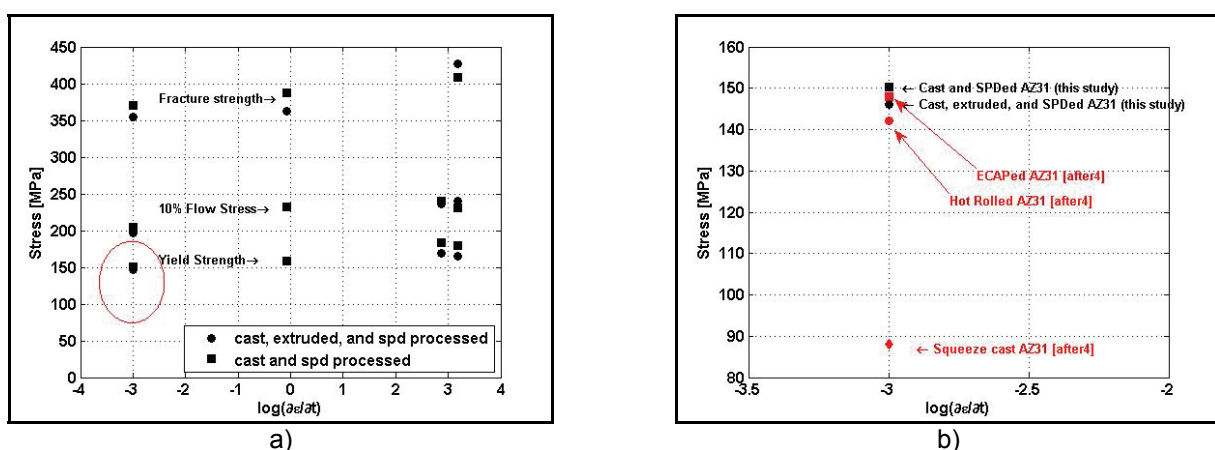

a)   b)

Figure 3: Results of the compression tests at a wide range of strain rates, a) yield strength, flow stress at 10% of plastic strain, and fracture strength, and b) comparison of the results of this study to the ones presented by Zúberová et al. [4].

The strains on the surfaces of the specimens were calculated from the image pairs acquired with the two digital cameras. The difference between the maximum and minimum axial strains was of the order of 5 to 8 %, as shown in Figure 4, where the strain distributions on the surface of the specimen along the compression axis are shown together with average strains (dashed lines) for different stages of deformation. The strain distributions appeared to be somewhat asymmetric with respect to position in all tests, but the amount of strain increased quite uniformly with deformation. The degree of asymmetry was also different in each test for reasons that are not completely understood. The evolution of strain with time was very similar for both materials and independent of strain rate. The distribution of strains remains fairly uniform until the localization of strain and the formation of the shear band at a 45 degree angle with respect to the loading axis. The shear band forms very rapidly just before the final fracture. In all tests, the maximum compressive strains were found somewhere near the middle of the gage section, not at either end of the specimen. The overall deformation was fairly uniform and the specimens did not barrel much during the deformation, which is probably due to the low maximum strains and adequate lubrication of the specimen and bar interfaces.

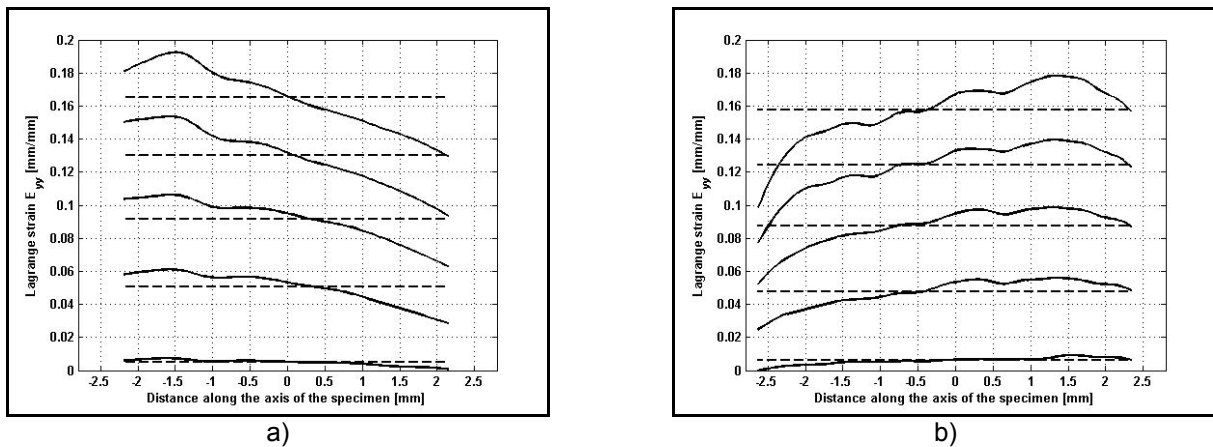a)   b)

Figure 4: The axial strain along the gage section of the specimen for the a) cast, extruded and SPD processed AZ31, and b) cast and SPD processed AZ31.

Figure 5 shows the last frame before the fracture, overlaid with the Lagrange strain on the surface in the transverse direction (Fig. 5a) and in the axial direction (Fig. 5b) for the cast and SPD processed AZ31 tested at the strain rate of 1000 s^{-1}. The specimen fractured no more than 10 µs (~0.015 in strain) after these images were obtained. In both images, the formation of the shear band is very clearly seen and the strain localization is very strong. In the transverse direction, the Lagrange strain in the shear band exceeds 0.3, whereas the strain elsewhere in the gage area varies from 0.12 to 0.18. In the axial direction, the maximum Lagrange strains are around 0.24, and the strain elsewhere in the specimen is less than 0.2. The shear strain component in the xy-plane was very low.
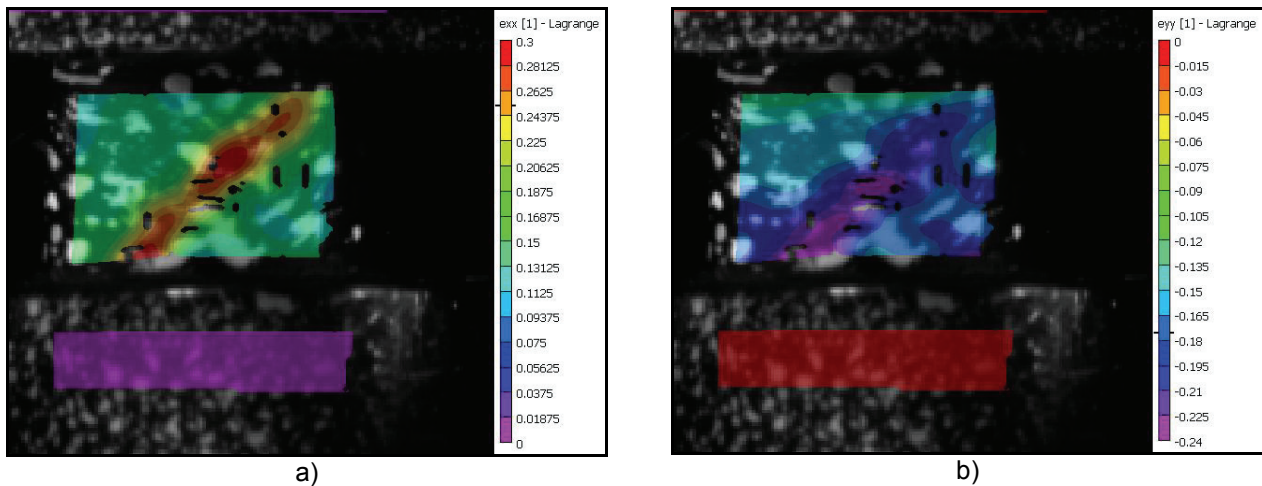
a)   b)

Figure 5: Last frame before fracture for the cast and SPD processed AZ31 alloy at a strain rate of 1000 s^{-1}, a) Lagrange ε_{xx} (transverse strains) and b) Lagrange ε_{yy} (axial strains).

SUMMARY

The mechanical behavior of a reciprocating extrusion processed AZ31 magnesium alloy was studied in compression at a wide range of strain rates. The tests were monitored using digital cameras, and from the acquired image pairs the strains on the surface of the specimens were calculated using digital image correlation. This method enables non-contact measurement of strains directly from the specimen at a very wide strain rate range, where typically several techniques are needed to measure the strain. Also, the DIC technique was shown to be able to capture the formation of a shear band even at very high strain rates.

The results of the mechanical tests show that the strength of the SPD processed AZ31 increases with strain rate and that the fracture strength increases more than the yield strength or the flow stress at low strains. The strain hardening rate of AZ31 also increases strongly with increasing strain rate and the stress strain curves show an upward concave appearance, which are both typical for twinning and slip controlled deformation due to the increased incidence of twinning at high strain rates. The yield strengths of the studied SPD processed AZ31 are significantly higher than those of the squeeze cast AZ31 but comparable to the yield strengths of the hot rolled and ECAP processed AZ31 [4].

The final failure of the specimen occurs by a 45 degree shear fracture along a shear band that develops very rapidly just before the fracture. After the formation of the shear band, most of the strain localizes into the narrow region around the band, which rapidly leads to the final failure of the specimen.

ACKNOWLEDGEMENTS

REFERENCES

1. K. Müller, S. Müller, Severe plastic deformation of the magnesium alloy AZ31, Journal of Materials Processing Technology, 187-188, 2007.
2. S. H. Kang, Y. S. Lee, J. H. Lee, Effect of grain refinement of magnesium alloy AZ31 by severe plastic deformation on material characteristics. Journal of Materials Processing Technology, 201, 2008.
3. B. Li, S. Joshi, K. Azevedo, E. Ma, K.T. Ramesh, R.B. Figueiredo, T.G. Langdon, Dynamic testing at high strain rates of an ultrafine-grained magnesium alloy processed by ECAP. Materials Science and Engineering A, 517, 2009.

4. Z. Zúberová, Y. Estrin, T. T. Lamark, M. Janecek, R. J. Hellmig, M. Krieger, Effect of equal channel angular pressing on the deformation behavior of magnesium alloy AZ31 under uniaxial compression. Journal of Materials Processing, 184, 2007.
5. J. Jiang, A. Godfrey, W. Liu, Q. Liu, Microtexture evolution via deformation twinning and slip during compression of magnesium alloy AZ31. Materials Science and Engineering A, 483-484, 2008.
6. M. Sutton, J. Orteu, H. Schreier, Image Correlation for Shape, Motion and Deformation Measurements. Springer Science, 2009.

Characterization of the mechanical behavior of ultrafine-grained metals using digital image correlation

M. Hokka[1,2,a], J. Seidt[2], T. Matrka[2], A. Gilat[2], V.-T. Kuokkala[1], J. Kokkonen[1] and S. Müller[3]

[1]Tampere University of Technology, Department of Materials Science, POB 589, Tampere, Finland
[2]The Ohio State University, Department of Mechanical Engineering, 201 West 19th Avenue, Columbus OH, 43210 USA
[3]Technische Universität Berlin, Extrusion Research and Development Center, Gustav-Meyer-Allee 25, D-13355 Berlin, Germany

Abstract. Nanocrystalline and ultrafine-grained materials show many very interesting properties compared to the conventional coarse-grained materials. For example, their strength values are usually much higher but, on the other hand, their ductility and deformability can be significantly lowered by the grain size refinement processes. One of the methods used to refine the grain size of metals is severe plastic deformation (SPD), which usually produces highly oriented structures that are strong but may deform non-homogeneously. In this paper, the deformation behavior of severe plastic deformation processed AZ31 magnesium alloy and commercially pure 1070 aluminum were characterized in compression and torsion using mechanical testing and high speed photography with digital image correlation. The results show that the AZ31 magnesium alloy deforms fairly uniformly in compression until fracture and the strains calculated from the movements of the ends of the anvils and the Lagrange strain on the surface of the specimen describe the overall deformation quite well. For the 1070 UFG aluminum, the shear deformation localizes very rapidly and the average strains measured from the surface or calculated from the displacements of the bars underestimate the true strain in the shear bands significantly. Also, the deformation in the torsion tests was not uniform shear but substantial strains were also measured in the axial direction. These strains were most likely due to small experimental errors, such as slight misalignment of the bars and the specimen in the test.

1 Introduction

The mechanical properties of most materials are strongly affected by strain rate. Usually the strength of material increases with increasing strain rate, especially at strain rates around 10^3 s^{-1}, where a rapid increase in strength is often observed. In practice, high strain rates in the range of 10^3 s^{-1} to 10^4 s^{-1} occur in many industrial applications and high speed material forming methods, such as dynamic loading of structures and cold heading, as well as in many events of practical importance such as automotive crashes and various defense and aerospace applications. At quasi-static and intermediate

---

[a] e-mail : mikko.hokka@tut.fi

strain rates ($<\sim$500 s^{-1}), the deformation behavior of crystalline materials such as coarse-grained metals is readily explained by the thermally activated dislocation motion. At higher strain rates ($>\sim$1000 s^{-1}), the dislocation drag mechanisms start to control the deformation behavior, and usually the strength of the material increases much faster than in the thermally activated region due to the change in the deformation and transient hardening mechanisms. However, when the crystal sizes are decreased to nanometer scale, the movement of dislocations becomes more and more difficult and new phenomena may take place. At the moment, the strain rate dependent deformation and strain hardening mechanisms of nanocrystalline metals are not yet properly understood, despite the quite extensive research that has been done on these materials over the past decade.

Bulk nanocrystalline (nc) metals have significantly improved strength properties and usually lower deformability and ductility compared to the coarse-grained metals. These materials can be produced using several techniques, but the two main competing technologies are compaction and sintering of nanopowders and severe plastic deformation (SPD) of bulk metals. However, only SPD techniques enable production of impurity and porosity free bulk metals from basically any metal, which cannot be done with conventional powder metallurgical techniques. In addition, severe plastic deformation does not require atomization of the metal as the nanocrystallization is performed in bulk form, which is environmentally more friendly and less hazardous since there is no need to handle the nanoparticle powders. In principle, any coarse-grained bulk metal may be plastically deformed in such a way that its grain size is reduced to submicroscopic level, but so far the most commonly studied nanocrystalline bulk metals are copper, aluminum and its alloys, titanium and its alloys, and tantalum. Ultrafine-grained (ufg) materials have similar properties as the nanocrystalline metals, i.e., very high strength, generally low ductility due to tensile or shear instability, low strain hardening capability, high fatigue strength, and altered strain rate sensitivity compared to coarse-grained materials [1]. Usually materials with grain size below 100 nm are referred to as nanocrystalline and those with grain size between 100 nm and 1 μm as ultrafine-grained. The potential applicability of both nanocrystalline and ultrafine-grained materials is wide, including aerospace applications, transportation, health care equipment and components, defense applications, and even implant technology due to the high purity of the materials.

1.1 Digital image correlation

Digital image correlation (DIC) can be used to measure 3D surface displacement fields of the specimen during dynamic or static loading. Typically two digital cameras viewing the specimen at different angles are used to acquire pairs of images of the specimen. The displacements are then calculated by dividing the images into smaller subsets or facets and by matching the facets in each image pairs to track their movement in subsequent images. Theoretically, the accuracy of the image subset matching can be even as high as 1/200 of a pixel [7]. The strains on the surface of the specimen can therefore be determined with a very high spatial resolution even with relatively poor pixel resolution of the image.

The digital image correlation has been found very useful in the characterization of strain distributions in compression and tension experiments [2-4]. In high strain rate tension experiments, in particular, the strains calculated based on the relative motions of the ends of the specimen can give erroneous results due to the localization of strain after necking, but also because of the yielding of the rounded fillet regions of the specimens and the uncertainties in the true gage length determination of the specimen.

Due to the large plastic strains involved in the SPD processing, many ultrafine-grained metals have a very strong texture. Also, some SPD techniques such as high pressure torsion or reciprocating extrusion produce gradient structures, where some regions have much higher strains while other regions are deformed significantly less. This of course leads to different microstructures and grain sizes throughout the cross section of the material, and most likely also the mechanical properties vary along the cross section. Therefore, due to these gradient structures accurate determination of mechanical properties and analyzing the mechanical behavior of these materials can be very difficult

using conventional material testing methods. Also, while conducting mechanical testing at a very wide range of strain rates, the average strain in the specimen is usually measured using several different techniques that may lead to problems when comparing the properties in different strain rate regimes. The digital image correlation can be used virtually at any strain rate provided that the frame rates of the cameras are sufficient. In this paper, the mechanical properties of a reciprocating extrusion processed AZ31 magnesium alloy were tested in compression and ECAP processed 1070 commercially pure (99.7-wt%) aluminum in torsion. The tests were monitored with two digital cameras and the strains were calculated using the digital image correlation technique. Special emphasis was placed on how the digital image correlation can be effectively used to analyze the development of strains during the test.

2 Materials and experiments

The materials studied in this work were ultrafine-grained AA1070 (99.7 wt-% Al) commercial purity aluminum and near-UFG AZ31 magnesium alloy. Torsion tests at a wide range of strain rates were performed on the UFG aluminum, whereas compression tests were performed on the near-UFG AZ31 magnesium alloy. Some torsion tests were also performed on the standard AA7075 aluminum alloy for comparison.

The grain size of the 1070 aluminum was refined by Equal Channel Angular Pressing by passing the billet four times through a 2-turn 90° channel die at room temperature, leading to a total accumulated shear strain of about 9.4. The average grain size after the ECA –pressing was estimated to be roughly 750 nm based on transmission electron micrographs [5]. The aluminum was produced at the Institute of Materials Processing Technology at Warsaw University of Technology. The technique and equipment used for the processing are described in more details in refs. [9-10]

The original size of the billets was 26*26*120 mm^3, from which the torsion specimens were manufactured. First the billets were dissected into four rectangular blocks of 12*12*120 mm^3 and then machined into thin walled tube specimens. The gage length of the specimens was 5.08 mm (0.2 in) or 2.54 mm (0.1 in), the mean gage diameter 9.27 mm (0.365 in), and the wall thickness 0.38 mm (0.015 in) and 0.76 mm (0.03 in) for the 7075 aluminum alloy and ultrafine grained 1070 aluminum, respectively.

The AZ31 magnesium alloy was processed by reciprocating extrusion at 300 °C. A schematic picture of the reciprocating extrusion tool is shown in Figure 1. A more detailed description of the processing apparatus can be found in ref. [6]. The 30 mm diameter billet was first extruded back and forth through the kneeding die with a 26 mm diameter collar in the middle of the extrusion channel. After five passes through the die, the billet was extruded into a round bar with a 10 mm diameter and then cooled in air. The material was processed both in the as-cast and as-cast and extruded conditions, and the compression behavior of both alloys was studied in a wide range of strain rates. The microstructures for the cast and reciprocating extrusion processed AZ31 was very close to that of the cast, extruded and reciprocating extrusion processed AZ31. The average grain sizes for both grades were around 6-8 micrometers, and their microstructures consisted of very small grains surrounding larger diameter less-deformed grains. The small grains were equiaxed for the AZ31 extruded prior to the grain size refinement. More elongated and deformed grains were found in the AZ31 without prior extrusion. The magnesium alloys were prepared at the Technische Universität Berlin.
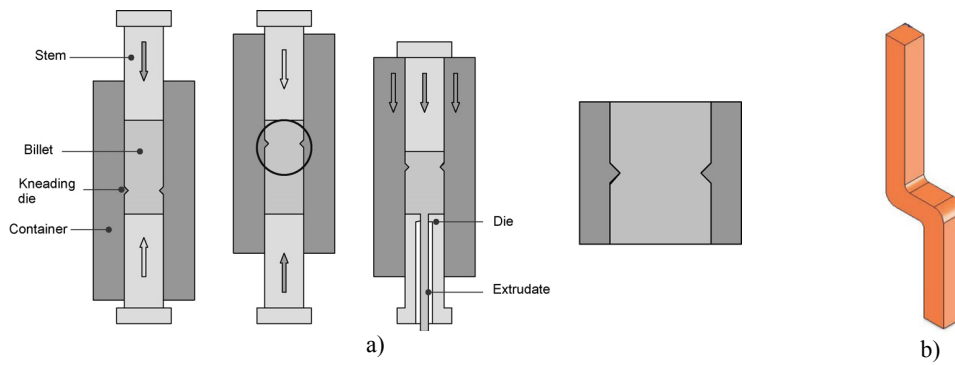
Fig. 1. Schematics of the grain size refinement procedures used for the tested materials, a) the reciprocating extrusion used for the AZ31 magnesium alloy [after 6], and b) the ECAP die used for the 1070 aluminum.

Mechanical testing at low strain rates was performed using a servohydraulic materials testing machine equipped with both axial and angular actuators and load cells, whereas the high strain rate testing was done using Split Hopkinson Pressure Bar devices.

The compression Split Hopkinson Pressure Bar consisted of two 12.7 mm (0.5 in) titanium bars, between which the specimen was sandwiched. The SHPB test is performed by impacting a striker bar on the free end of the incident bar, producing a compressive stress pulse that propagates in the incident bar towards the specimen. As the pulse reaches the bar-specimen interface, part of the pulse is reflected back as a wave of tension while part of the incident wave is transmitted through the specimen into the transmitted bar. The three stress pulses, incident, reflected, and transmitted, are measured using resistive strain gages bonded on the surfaces of the bars, amplified and finally recorded on a digital oscilloscope. The stress, strain, and strain rate in the specimen can then be easily calculated from the stress pulses using Matlab based calculation routines.

The torsion Split Hopkinson Pressure Bar device is somewhat more complicated than the compression equipment. The torsional stress is first stored in the incident bar by a hydraulic pulley and a clamp-release system. The torsion stress pulse is generated simply by releasing the stored torque by breaking the clamp pin by a second hydraulic press. The bar stresses are measured by three strain gage stations and the pulses are calculated from the measured signals by applying the appropriate time shifts [8].

2.1 Strain Measurements

Measuring strain at a wide range of strain rates usually requires several different measurement techniques to cover each strain rate regime. At low strain rates, the strain is usually measured directly from the specimen using extensometers, or calculated from the motion of the anvils from the LVDT transducer signals. At high strain rates, on the other hand, the strains are usually calculated from the time resolved strain signals measured from the stress bars with strain gages. With digital image correlation, the strains can be measured using the same method at a very wide range of strain rates, and the maximum strain rate is only limited by the maximum frame rate, resolution, and optical properties of the digital cameras. In this study, two Grasshopper (Point Gray Research) 2 megapixel cameras were used in the low strain rate tests at the maximum frame rate of 19 s^{-1}. Two Photron Fastcam SA1.1 high speed cameras were, in turn, used at higher strain rates operating at frame rates between 1000 and 120.000 s^{-1}.

In the compression tests, the Lagrange strains were calculated from the images recorded directly from the surface of the specimen. The spatial Lagrange strains were then converted into average engineering strains using Equation 1, where E_{11} is the Lagrange strain in the axial direction of the specimen.

$$\varepsilon_E = \frac{\sum_{i=1}^{N}\sqrt{1+2E_{11}^i}-1}{N} \qquad (1)$$

In the torsion tests, the strain measurements were complicated by the very high degrees of strain and the problems in maintaining a good contrast pattern on the surface of the specimen. First, a black base coat with hand painted white coarse dots were used for maximum contrast, but the paint chipped off from the surface after 30-40% of strain and the DIC signal was lost. A white Krylon base coat and spray painted black contrast patterns were found to have better adhesion to the surface, but the lower contrast lead to slightly lower spatial accuracy of the measurements.

To overcome the problem of losing the contrast pattern at high strains, the ends of the specimen outside the gage section were also painted and the displacements of the ends of the gage section were calculated from the images. From these displacements, the rotation or the twist angle of the specimen was calculated, and finally the average strains in the specimen were calculated using Equation 2, where r_s and l_s are the average radius and length of the gage section of the specimen, θ is the angle of twist, and $\overline{a}$ and $\overline{b}$ are the vectors from the centerline of the specimen to the surface at the opposite ends of the gage section.

$$\gamma = \frac{r_s\theta}{l_s} = \frac{r_s}{l_s}\arccos\left(\frac{\overline{a}\bullet\overline{b}}{\|a\|*\|b\|}\right) \qquad (2)$$

3 Results and discussion

In Figure 2a, compressive stress-strain curves for the cast, extruded and SPD processed near-UFG AZ31 alloy measured at the strain rate of 10^{-3} s^{-1} are plotted using both the strains measured directly from the specimen and the strains calculated from the displacements of the anvils of the materials testing machine. The difference between the curves is quite small at low strains, but at higher strains there is an increasing shift between the curves, indicating that the strains measured directly from the specimen are much smaller than those calculated from the displacements of the anvils. This is typical for a compression test, and the difference is mainly due to the barreling of the specimen during compression. The different compressive strains measured from the anvil displacements with DIC or directly from the surface of the specimen are well comparable for this type of a material, which deforms fairly uniformly and fractures at a fairly low strain. If the strains were much higher, the strains would most likely differ more due to the increasing barreling at higher strains.

In the dynamic torsion test, the shear strain can be calculated either from the stress pulses in the bars, from the Lagrange shear strain ($\gamma=2*\varepsilon_{xy}$) measured directly from the surface of the specimen, or from the displacement of the ends of the specimen using Eq. 2. Figure 2b shows the comparison of the shear stress-shear strain curves obtained with strains determined with the three above mentioned methods for the UFG 1070 aluminum at the strain rate of 1000 s^{-1}. The Lagrange strain could be calculated only to about 50% strain, where the paint on the surface of the gage section chips off. As seen in the figure, at higher strains the shear strain calculated from the stress waves is about 8% higher than the strain calculated from the displacements of the ends of the specimen.
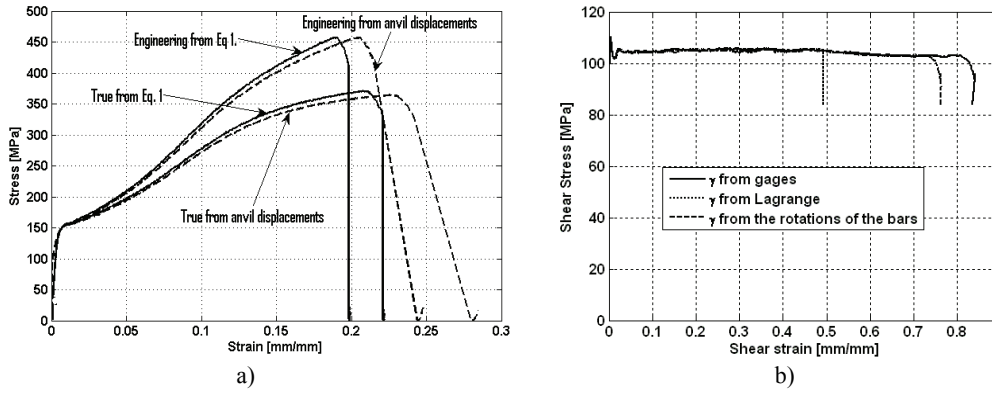
a)   b)

Fig. 2. Stress-strain curves obtained with different strain determination methods for a) cast, extruded and SPD processed AZ31 in compression at the strain rate of 10^{-3} s^{-1}, and b) UFG 1070 aluminum in torsion at the strain rate of 1000 s^{-1}.

The strains measured and calculated from the torsion specimens are better shown in Figure 3, which shows the transverse and axial strain components, ε_{xx}, ε_{yy}, and the three different shear strains measured with digital image correlation and using the stress waves in the bar. Figure 3a shows the strains for the 7075-T6 aluminum alloy at the strain rate of 480 s^{-1}, and Figure 3b for the UFG 1070 aluminum at the strain rate of 1000 s^{-1}. For both materials it is clear that the deformation is not uniform shear, as assumed by the one dimensional wave propagation that is used in calculating the specimen strain from the stress pulses measured from the pressure bars. The specimen undergoes deformation also in other directions, especially in the direction of the axis of the specimen (ε_{yy}), whereas the transverse strain component ε_{xx} is very small. The shear strain calculated from the stress pulses increases quite linearly, whereas the strain calculated from the displacements of the ends of the bars shows somewhat less linear behavior. The average shear strain measured directly from the surface of the specimen over the gage section is clearly higher than the average shear strain calculated from the rotations of the bars. The strains ε_{xx} and ε_{yy} are most likely caused by a combination of several small experimental errors, including slight misalignment of the bars, bending of the bars near the specimen, eccentric positioning of the specimen, and eccentric machining of the tubular specimen.
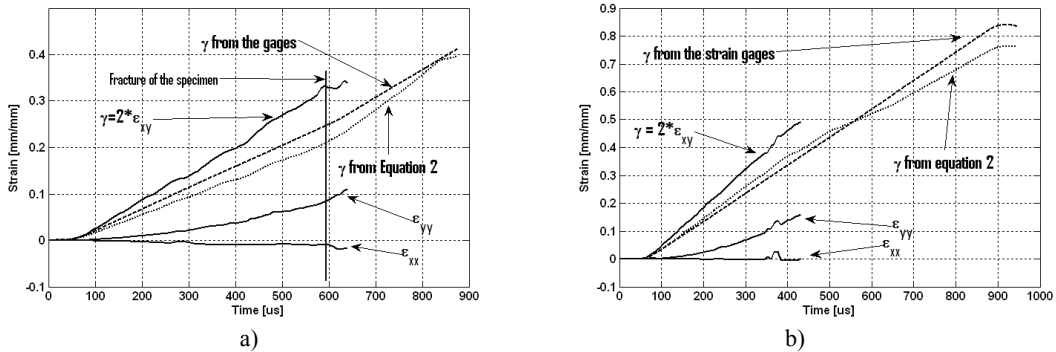

a)   b)

Fig. 3. Lagrange strains measured from the surface of the specimen (ε_{xx}, ε_{yy}) and the shear strains calculated from the Lagrange strain, displacement of the ends of the specimen, and from the stress pulses in the bars for a) the 7075-T6 aluminum alloy and b) the UFG 1070 aluminum.

Figure 4 shows the waterfall plots (strain as a function of position and time) for both a compression test of AZ31 (Fig.4a.) and a torsion test of UFG AA1070 (Fig.4b.). In the compression test of AZ31,

the strain is somewhat asymmetric with respect to position but increases quite uniformly with time. In different tests, however, the degree of asymmetry varied quite much for reasons that are not completely understood. The average strain (dashed lines in Figure 4a) represent fairly well the overall deformation of the specimen, especially at low strains, which is typical for compression tests [2]. In the compression tests of AZ31, the strain localized and shear bands were formed just before the final fracture. In the torsion tests of UFG aluminum, strain localizes very rapidly after yielding and most of the deformation occurs in a very narrow region roughly in the middle of the gage section. A fully developed shear band can be seen in Fig 4c. Therefore, in a torsion test the average strain over the whole gage section is significantly lower than the local strains in the shear band. As seen in Figure 4b, the maximum strain at the ends of the specimen is around 5% at one end and 25% at the other end, whereas in the shear band it is around 45%. The average shear strain calculated over the whole gage section of the specimen from the Lagrange strain ($\gamma=2*\varepsilon_{xy}$) is significantly higher than the other average shear strains, i.e., shear strain calculated from the stress pulses and from the displacements of the ends of the specimen, but it still is much lower than the shear strains in the shear band. Therefore, the "true" shear strain should be calculated only from the localized region instead of using an average over the whole gage section of the specimen.
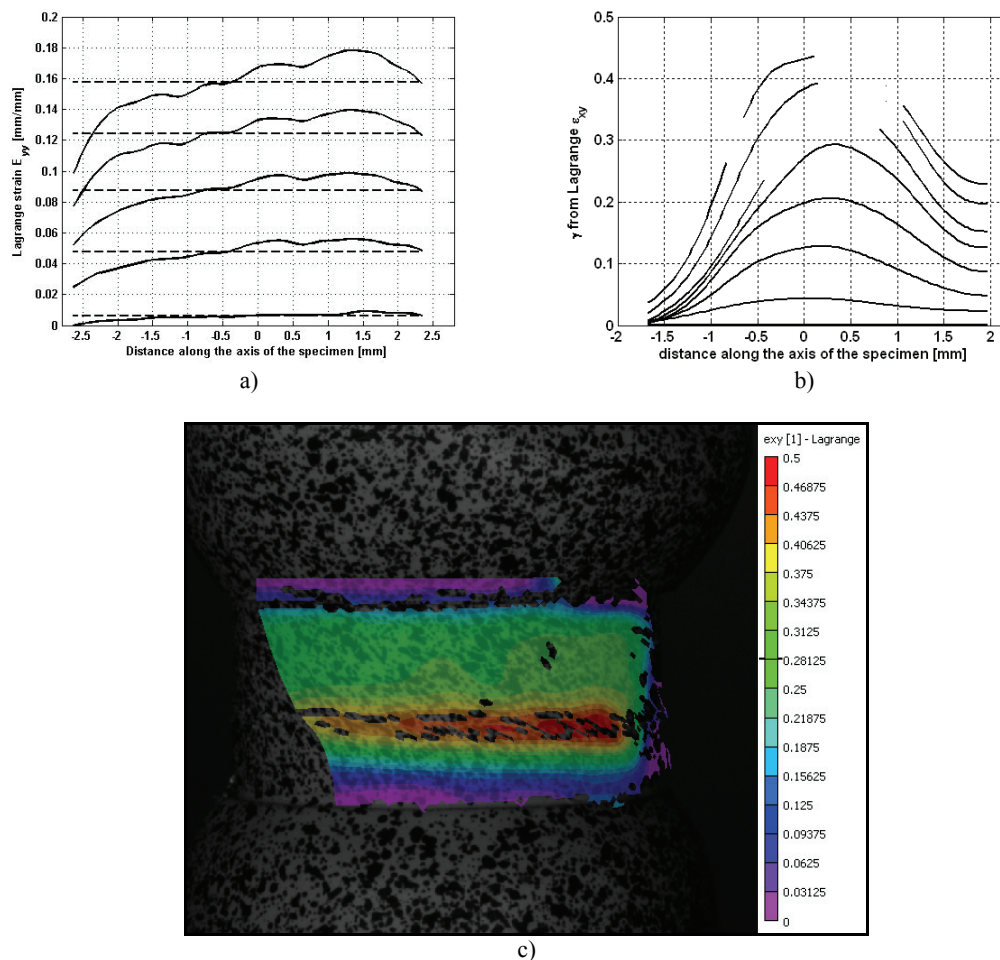

a)

b)

c)

Fig. 4. Waterfall plots for a) AZ31 in compression and b) ultrafine-grained 1070 aluminum in torsion, and c) a fully developed shear band in a torsion test of ultrafine-grained 1070 at the strain rate of $1.6 \ 10^{-4} \ s^{-1}$.

3 Summary

Mechanical testing was performed on reciprocating extrusion processed near-ultrafine-grained AZ31 magnesium alloy, ECAP processed ultrafine-grained commercially pure AA 1070 aluminum, and standard 7075-T6 aluminum alloy. Compression tests were performed on the AZ31 alloy and torsion tests on the UFG aluminum and 7075 aluminum alloy. The tests were monitored using digital cameras, and the strain distributions on the specimen surfaces were calculated using the digital image correlation technique. In the compression tests of AZ31, the strains in the specimen were relatively homogeneously distributed and uniform, and no localization of strain was observed until the final 45º shear fracture of the specimen that was preceded by the formation of a shear band with very high local strains. The behavior of the ultrafine-grained aluminum in the torsion tests was more complicated, and the strains localized very rapidly already in the early stages of the test. In general, the shear band that is formed during the deformation has much higher strains than the surrounding areas, and the average strain measured from the displacements of the ends of the bars do not describe the material's true behavior correctly. Also, the deformation in the torsion tests was found not to be uniform shear, but also significant axial strains were observed during the tests. These axial strains were obviously due to slight experimental errors such as the slight misalignment of the bars and the specimen. Strain measured from the rotational displacements of the ends of the specimen seem to be more accurate than the strain obtained from the signals of the strain gages glued in the stress bars, which do not take into account the possible eccentric motions of the ends of the bars.

Acknowledgements

References

1. R. Valiev, T. Langdon, Progress in Materials Science. **51**, (2006)
2. A. Gilat, T. Schmidt, A. Walker, Experimental Mechanics, **49**, (2009)
3. A. Gilat, T. Schmidt, J. Tyson, *Society for Experimental Mechanics*, (2006)
4. A. Gilat, A. Walker, J. Seidt, *Society for Experimental Mechanics*, (2008)
5. J. Kokkonen, V.-T. Kuokkala, L. Olejnik, A. Rosochowski, *Society for Experimental Mechanics*, (2008)
6. K. Müller, S. Müller, Journal of Materials Processing Technology, **178-188**, (2007)
7. M. Sutton, J.-J. Orteu, H. Schreier, *Image Correlation for Shape, Motion and Deformation Measurements* (Springer Science, New York, NY, USA, 2009)
8. A. Gilat, *ASM Handbook, Volume 8, Mechanical Testing and Evaluation* (ASM International, Materials Park, OH, USA, 2000)
9. A Rosochowski, L. Olejnik, Journal of Materials Processing Technology, **125-126**, (2002)
10. L. Olejnik, A. Rosochowski, Bulletin of the Polish Academy of Sciences, **53**, (2005).
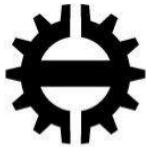
TAMPEREEN TEKNILLINEN YLIOPISTO
Automaatio-, kone- ja materiaalitekniikan tiedekunta

OKKO NISKANEN, 201667
Metallien ECAP ja HESP prosessointi
Kandidaatintyö

Tarkastaja: Yliassistentti Mikko Hokka
Jätetty tarkastettavaksi: 12.6.2009

TAMPEREEN TEKNILLINEN YLIOPISTO
Materiaalitekniikan koulutusohjelma
NISKANEN, OKKO: Metallien ECAP ja HESP prosessointi
Kandidaatintyö, 28 sivua
Kesäkuu 2009
Pääaine: Yleinen materiaalioppi
Tarkastaja: Yliassistentti Mikko Hokka
Avainsanat: ECAP, HESP

Tässä työssä esitellään kaksi SPD (Severe Plastic Deformation) metallien muokkausmenetelmää – ECAP (Equal Channel Angular Pressing) ja HESP (High Energy Shot Peening).

ECAP prosessista käydään läpi vaihtoehtoja erimuotoisten kappaleiden muokkaukseen ja esitellään jatkuvaan prosessointiin sopivia ECAP menetelmiä. Lisäksi esitellään prosessiin kriittisesti liittyvät parametrit ja tutkitaan vaihtoehtoja ECAP laitteiston rakentamiselle.

HESP prosessista käydään läpi materiaalissa tapahtuvat muutokset eri kiderakenteen metalleilla, esitellään menetelmään vaadittava laitteisto sekä perehdytään prosessin kannalta tärkeimpiin parametreihin.

Lopuksi esitetään yhteenveto ECAP ja HESP prosesseista sekä pohditaan menetelmien soveltuvuutta metallien jalostamiseen.

Alkusanat

Tämä kandidaatintyö lähti liikkeelle MOL-2200 Materiaalien mekaaninen käyttäytyminen-kurssilta, jossa kurssin vastaava, yliassistentti Mikko Hokka tarjosi opiskelijoille kolmea kandidaatintyötä liittyen kurssin sisältöön. Työt ovat osa TEKES:n tutkimusprojektia, jossa mukana on suomalaisia teollisuusyrityksiä, esimerkiksi OVAKO, Metso ja Rautaruukki sekä valtiollisia instituutteja, kuten VTT ja TKK. Aiheet liittyivät SPD (Sever Plastic Deformation) menetelmiin, joiden avulla materiaaliin voidaan saada ultrahieno raekoko ja sitä kautta parannettua mekaanisia ominaisuuksia. Tässä työssä menetelmistä on esitelty ECAP (Equal Channel Angular Process) ja HESP (High Energy Shot Peening).

Työn ohjaajana on toiminut yliassistentti Hokka ja hänen roolinsa työn oikeansuuntaisessa edistymisessä sekä tekijän tieteellisen kirjoittamisen kehittymisessä on ollut merkittävä. Kiitokset hänelle. Työn aihe on ollut vaativa ja edellyttänyt perehtymistä kursseilla käsiteltyjen asioiden ulkopuolelta.

Sisällys

1. Johdanto

Viimeisen parin vuosikymmenen aikana SPD (Severe Plastic Deformation) menetelmät ovat herättäneet materiaalitieteiljöiden mielenkiinnon metallien prosessoinnissa. Näillä menetelmillä materiaaliin saadaan keskimäärin nano- tai mikrometrin kokoluokkaa oleva raekoko, jolloin mekaaniset ominaisuudet parantuvat huomattavasti. SPD menetelmien lujittava vaikutus perustuu hyvin suureen muodonmuutokseen ilman, että kappaleen dimensiot muuttuvat. Tässä työssä SPD-menetelmistä esitellään ECAP (Equal Channel Angular Pressing) ja HESP (High Energy Shot Peening) eli korkeaenerginen kuulapuhallus.

HESP on jo osana teollista tuotantoa, mutta ECAP menetelmää ei ole vielä onnistuttu jalkauttamaan osaksi kannattavaa metallinjalostusta. Esteenä ovat olleet korkeat kustannukset, mutta tällä hetkellä huomio keskittyy niiden alentamiseen. Saavutettavat mekaaniset ominaisuudet ovat tavoittelemisen arvoisia. Myös suomalaiset metallinjalostajat ovat osaltaan heränneet SPD menetelmien mahdollisuuksiin ja ovat mukana tukemassa TEKES:n tutkimusprojektia, joka keskittyy mikrorakeisten materiaalien joustavaan valmistukseen. Myös tämä työ on saanut alkunsa tuosta projektista. Tähän mennessä suomenkielistä tekstiä ECAP menetelmästä ei ole ollut saatavilla.

Työ on jaettu selkeästi kahteen aihealueeseen – ECAP ja HESP. ECAP osuudessa esitellään laitteiston hyödyntäminen poikkileikkaukseltaan erilaisille kappaleille, jatkuva ECAP prosessointi, työstöön vaikuttavat parametrit sekä kokeelliset tekijät. HESP menetlmistä laitteiston ja etujen lisäksi perehdytään materiaalin mikrorakenteessa tapahtuviin muutoksiin. Lopuksi työssä vedetään yhteen ECAP ja HESP prosessien eri ominaisuudet sekä niihin vaikuttavat parametrit.

2. ECAP

ECAP (Equal-Channel Angular Pressing) on SPD prosessointimenetelmä, jolla pystytään valmistamaan nanokiteisiä ja ultrahienoraerakenteisia metallimateriaaleja. Siinä työstettävä kappale painetaan kanavan läpi, jonka keskivaiheilla on nollasta poikkeava kulma, minkä läpäistessä kappaleeseen kohdisutuu voimakas leikkausmyötymä. ECAP on tällä hetkellä pääasiassa helposti muokattavien metallien, kuten alumiinin ja kuparin muokkausmenetelmä mutta tutkijat ovat viime aikoina raportoineet myös vaikeammin muokattavien metallien, kuten titaanin ja magnesiumin ECAP prosessoinneista [1].

Monikiteisten materiaalien mekaanisiin ominaisuuksiin vaikuttavat monet mikro – ja makrorakenteen tekijät. Yksi merkittävimmistä on raekoko, jonka vaikutusta myötölujuuteen (σ_y) kuvataan yleensä Hall-Petch-yhtälöllä [2]

$$\sigma_y = \sigma_0 + k_y d^{-\frac{1}{2}} \tag{1}$$

jossa σ_y on materiaalin myötölujuus, σ_0 on dislokaatioiden liikuttamiseen tarvittava jännitys eli myötölujuus ilman raerajoja, k_y on lujittamisvakio ja d on rakeen halkaisija. Yhtälöstä (1) seuraa, että rakeen halkaisijan pieneneminen johtaa myötölujuuden kasvuun, mikä puolestaan tekee monikiteisen materiaalin raekoon pienentämisen houkuttelevaksi materiaalien muokkausvaihtoehdoksi.

Vaihtoehtoja lujittamiselle on monia, mutta ECAP on erityisen mielenkiintoinen monestakin syystä. Ensinnäkin, ECAP prosessia voidaan soveltaa suhteellisen isoihin aihioihin, jolloin sitä voidaan käyttää monipuolisesti rakennemateriaaleihin. Toiseksi, ECAP-laitteisto on yksinkertainen ja on jo valmiina muottia lukuunottamatta useissa laboratorioissa. Kolmanneksi, ECAP prosessilla voidaan muokata puhtaiden metallien useita eri metalliseoksia, metallien välisiä yhdisteitä, erkaumakarkaistuja metalleja sekä metalli-matriisikomposiitteja. Neljänneksi, kappaleista saadaan riittävän homogeenisia edellyttäen, että käytettävä jännitys on tarpeeksi suuri. Viidenneksi, menetelmällä on potentiaalia kehittyä kaupalliseksi metallien muokkausmenetelmäksi [3].

2.1 ECAP – prosessit

2.1.1 ECAP sauvojen ja tankojen muokkauksessa

ECAP prosessin perusperiaate on esitetty kuvassa 2.1. Syöttö – ja poistoaukkoja kutsutaan kanaviksi, jotka ECAP laitteessa ovat kohdakkain. Mäntä painaa aihion muotin läpi, jossa on tässä tapauksessa 90° kulma.
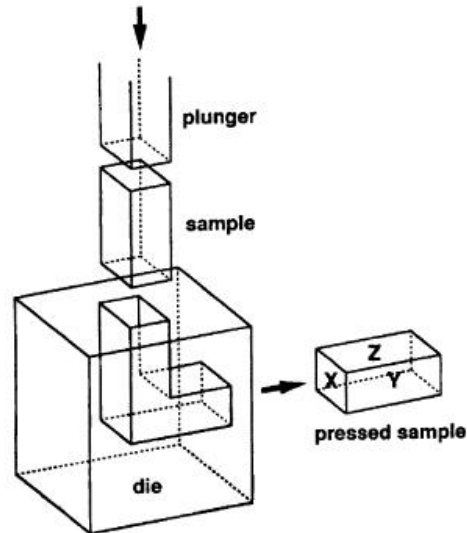
Kuva 2.1 *Mäntä (plunger) painaa aihion (sample) ECAP laitteiston läpi [4].*

Raekoon pienenemisestä aiheutuva lujittuminen tapahtuu, kun metalli pakotetaan muotin läpi suurella jännityksellä useita kertoja, jolloin materiaaliin kumuloituu jopa useiden tuhansien prosenttien suuruinen myötymä [4]. Laboratoriokokeet suoritetaan yleensä halkaisijaltaan 10–25 mm:n kokoisilla näytteillä, jotka voivat olla poikkileikkaukseltaan erimuotoisia, esimerkiksi pyöreitä tai neliötankoja. Kuvassa 2.1 läpipainetun kappaleen tasoja on merkitty kirjaimilla X, Y ja Z. Virtaussuuntaa vastaan kohtisuorassa oleva taso on X ja sitä sanotaan poikittaiseksi – tasoksi, Y on virtaustaso ja Z pitkittäissuuntainen taso.

Raekoon pienenemisen mahdollistaa leikkausmyötymä, joka seuraa kun aihio painetaan muotin läpi. Kuvassa 2.2 on havainnollistettu leikkausmyötymää materiaalissa. Materiaali myötää 45° kulmassa tulosuuntaan nähden. Kuvan 2.2 kappaleen osat 1 ja 2 kuvastavat leikkausjännityksen aiheuttamaa myötymää materiaalissa.
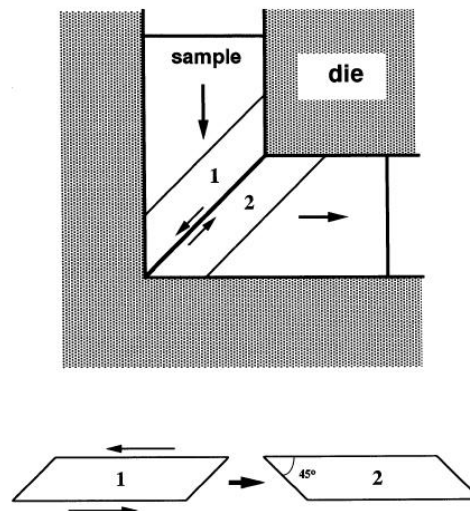

Kuva 2.2 *Aihioon kohdistuva leikkausmyötymä, kun se painetaan muotin läpi [5].*

On huomioitavaa, että metallin poikkileikkaus ei muutu ECAP prosessoinnin aikana, mikä selkeimmin erottaa sen muista tavanomaisista metallien muokkausmenetelmistä, esimerkiksi ekstruusiosta. Sen ansiosta samaa kappaletta voidaan painaa useaan kertaan muotin läpi, mikä aktivoi joka kerta eri liukusysteemejä. Tämä johtaa voimakkaaseen muokkauslujittumiseen [2]. Prosessin toisto voidaan tehdä siten, että jokaisen läpäisyn jälkeen käännetään kappaletta 90°. Tämä on helpointa ja käytännöllisintä toteuttaa poikkileikkaukseltaan neliön tai ympyrän muotoisilla kappaleilla [6]. Eri prosessointireittejä käsitellään tarkemmin luvussa 2.2.2.

2.1.2 ECAP levyjen muokkauksessa

ECAP prosessia voidaan käyttää myös levymäisten rakenteiden lujittamiseen. Kun tutkitaan ECAP prosessin vaikutusta levymäisen kappalen lujuuteen, on huomioitava, että nyt mahdollisia painamistapoja on kaksi. Kappale voidaan painaa muotin läpi joko pystysuorassa tai vaakasuorassa. Tällöin otetaan avuksi karteesinen koordinaatisto, jonka käyttöä on havainnollistettu kuvassa 2.3 X -, Y -ja Z – tasot ovat samat kuin tankojen ja sauvojen tapauksessa.
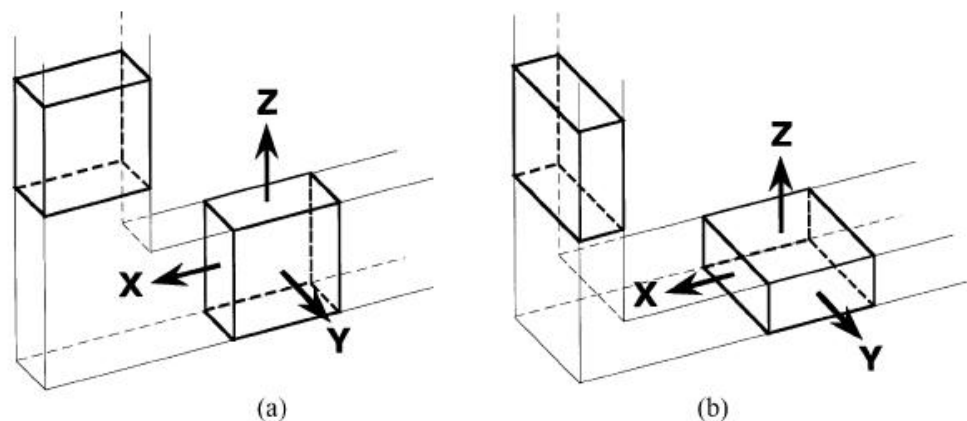
Kuva 2.3 *Pystysuora a) ja vaakasuora b) painallus [7].*

Koordinaatiston käyttö helpottaa prosessointireittien määrittämisessä. Tarkastellaan lähemmin vaakasuoraa reittiä B_{CZ}, jossa levyä käännetään Z-akselin ympäri ensin myötäpäivään ja sen jälkeen vielä X-akselin ympäri eli A-reittiä. Koko reittiä merkitään B_{CZ}:lla. Kuva 2.4 havainnollistaa kyseistä reittiä.
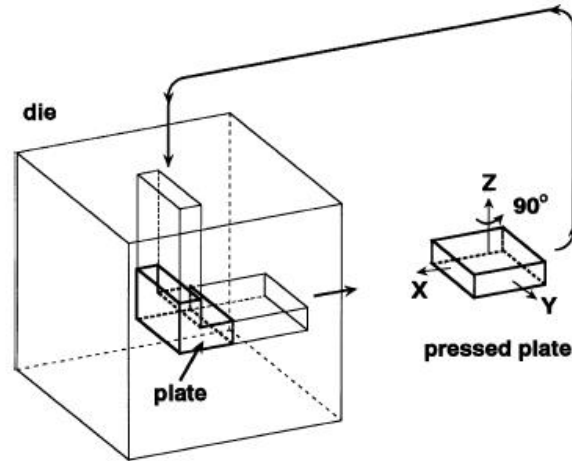
Kuva 2.4 *Muokkausreitti* B_{CZ} *levymäisten materiaalien muokkauksessa [7].*

Kamachi et al. [7] tutkivat 99,99 % alumiinilevyä neljän painalluksen jälkeen. Raekoko neljän painalluksen jälkeen oli 0,9 μm mutta 20–30% rakeista oli venyneitä, kun taas loput olivat aksiaalisesti orientoituneita. Venyneet rakeet eivät kuitenkaan ilmeisesti vaikuta kovuuteen tai jännitys-myötymä-käyttäytymiseen huoneenlämpötilassa yhtä vahvasti kuin aksiaalisesti orientoituneet rakeet [7].

2.1.3 RD –, sivuekstruusio – sekä MP–ECAP

Tavanomainen ECAP prosessointi vie paljon aikaa ja työvoimaa, koska usean painalluksen suorittaminen vaatii, että kappale työnnetään uudelleen laitteistoon. Työvoiman tarvetta on pyritty vähentämään eri menetelmillä. RD-ECAP (Rotary Die– ECAP) menetelmässä muottia käännetään siten, että kappale voidaan puristaa uudelleen muotin läpi. Kuvassa 2.5 on sekamaattinen esitys RD–ECAP:n toiminnasta.
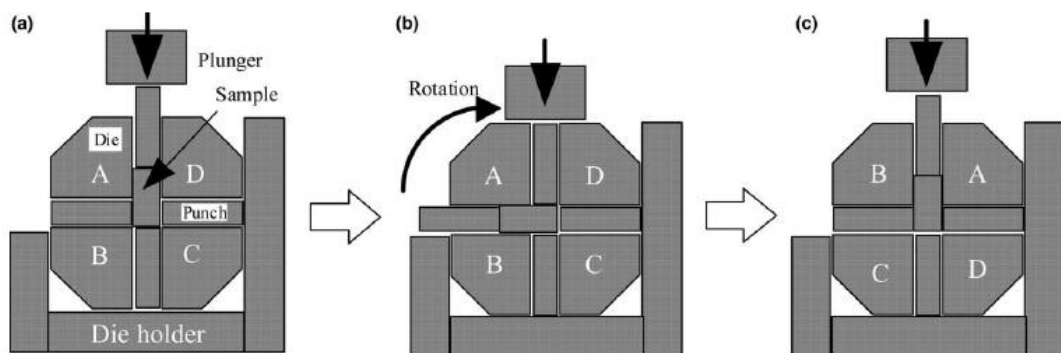
**Kuva 2.5** *Pyörivällä muotilla toteutettu ECAP eli RD-ECAP alkutilassa (a), yhden painalluksen jälkeen (b) ja muotin 90° pyöräytyksen jälkeen (c) [8].*

RD–ECAP laitteessa on kolme vartta, joita painetaan männällä. Jokaisen painalluksen jälkeen muottia käännetään 90° vastapäivään, jonka jälkeen voidaan suorittaa uusi painallus. RD-ECAP prosessin merkittävin etu on sen yksinkertaisuus. Ma et al. [8]

keskittyivät piillä seostetun alumiininäytteiden prosessointiin ja sen vaikutukseen materiaalin iskusitkeyteen. Kappaletta voidaan painaa jopa 32 kertaa peräkkäin muotin läpi, kun lämpötila T = 350 °C. Huomionarvoista on, että RD–ECAP prosessoinnissa itse kappale ei pyörähdä ollenkaan, jolloin tavanomaisen ECAP prosessin eri prosessireittimahdollisuuksia ei voida kuvan 2.5 laitteistolla hyödyntää. Saman tutkimuksen mukaan iskusitkeys näytteillä on parhaimmillaan 10-kertaistunut.

Toinen menetelmä, joka pyrkii nopeuttamaan prosessia ja vähentämään työvoiman tarvetta on niin sanottu sivuekstruusio–ECAP. Se on samantyylinen kuin RD–ECAP mutta tässä tapauksessa laitteistossa on neljä mäntää, joiden avulla kappaletta painetaan. Painetta kappaleeseen tuodaan vuoroin ylhäältä, vuoroin sivusta. Kuva 2.6 havainnollistaa sivuekstruusio–ECAP:n toimintaa.
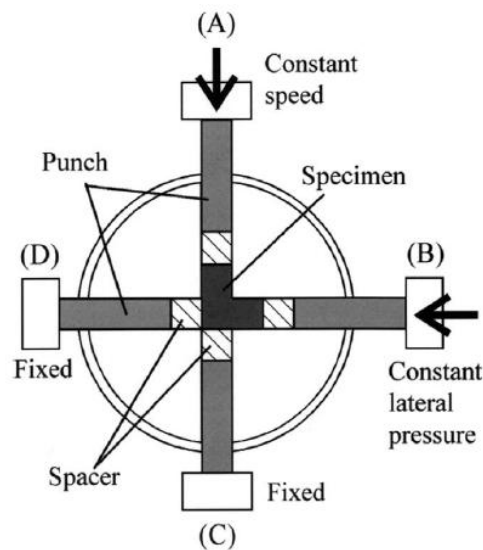
Kuva 2.6 *Sivuekstruusio-ECAP laitteisto. Painalluksissa toistuu sama reitti, joka saavutetaan tavanomaisella ECAP prosesoinnilla kääntämällä kappaletta 180° sen y-akselin ympäri [9].*

Azhusima ja Aoki onnistuivat toistamaan sivuekstruusio–ECAP painalluksen kymmenen kertaa erittäin matalahiilisellä teräksellä (0,0015 % C) [9]. Raekoon dimensioiksi saatiin 0,5μm x 0,2μm. Tällöin kovuus kolminkertaistui ja myötölujuus nousi yli 1000 MPa.

Vaihtoehtoinen menetelmä painallusten järkevälle toistamiselle on rakentaa ECAP laitteisto, jossa yhdellä läpimenolla materiaali muokkautuu useassa kohdassa. MP (multi pass)-ECAP on esitetty kuvassa 2.7.
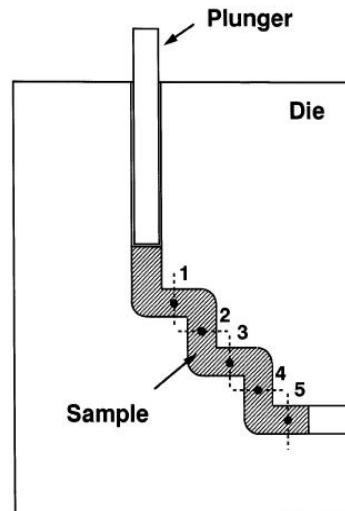
Kuva 2.7 *ECAP-laitteisto, jossa kappale muokkautuu läpäisyn aikana useassa eri kohdassa [10].*

Huolellinen tarkastelu osoittaa, että menetelmä on itse asiassa sama kuin kappaleessa 2.1 käsitellyllä tavanomaisella ECAP:lla, jossa kappaletta käännetään painallusten välissä 180° sen y-akselin ympäri. Nakashima et al. [5] tutkivat puhtaan alumiinin mikrorakenteen kehittymistä MP-ECAP prosessoinnin aikana. He totesivat, että mikrorakenne kehittyy samalla tavalla, kun vertailtiin tavanomaisen ECAP prosessin ja MP-ECAP prosessin jälkeistä mikrorakennetta kunkin läpäisyn jälkeen. Kuvasta 2.8 nähdään, että puhtaalla alumiinilla kovuus kasvaa läpäisyjen funktiona samalla tavalla, oli menetelmä sitten tavanomainen ECAP tai usean läpäisyn ECAP. Jälkimmäisen etuna on kuitenkin lyhyempi prosessointiaika.
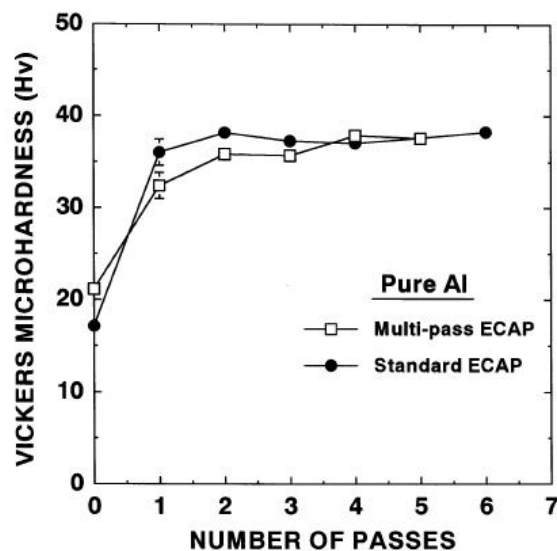
Kuva 2.8 *Vickers kovuus MP-ECAP ja tavanomaisen ECAP prosessoitujen materiaalien välillä [5].*

2.1.4 Yhdensuuntaisten kanavien ECAP

Yhdensuuntaisten kanavien ECAP-laitteistolla on saatu lupaavia tutkimustuloksia aivan viime aikoina [10]. Menetelmän etuna on sen yksinkertaisuus ja nopeus, sillä yhden painalluksen aikana kappale muokkautuu kahdessa eri kohdassa. Tällöin ultrahienoraerakenne saadaan pienemmällä painallusmäärällä. Kuvasta 2.9 nähdään, että laitteisto koostuu kahdesta muokkauskohdasta, jotka ovat yhdensuuntaisia. Parametrit, jotka vaikuttavat eniten metallin virtaukseen ja leikkausjäljen homogeenisyyteen ovat kanavien välinen etäisyys K ja kulma Φ, joka muodostuu kanavien välille. Raab [10] tutki parametrien vaikutuksia 2-D FEM (*2*-dimensional finite element method) simuloinnilla ECAP:n aikana. Hän osoitti, että homogeenisin myötymäjakauma saadaan kappaleeseen, kun $\Phi=100°$ ja $K \approx d_c$, joka on kanavan halkaisija. Simulaation antamat tulokset on vahvistettu kokeellisesti hilamenetelmällä.
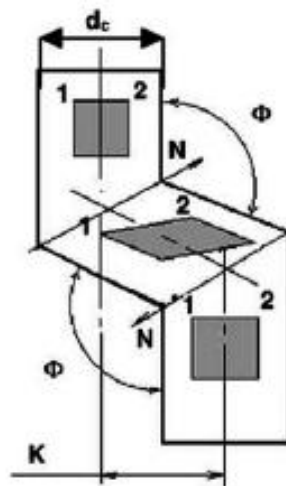
Kuva 2.9 *Kaavioesitys kahden yhdensuuntaisen kanavan ECAP prosessista, jossa N on leikkaussuunta, K on kanavien välinen etäisyys ja Φ on kulma, joka muodostuu kanavien välille [10].*

Yhdensuuntaisten kanavien ECAP prosessin tutkimuksessa on saatu merkittäviä parannuksia myös kuparin ja titaanin mikrorakenteeseen. Raab et al. [11] havaitsivat, että neljän painalluksen jälkeen molempien metallien mikrorakenne vastaa kahdeksaa painallusta tavanomaisella ECAP prosessoinnilla. Tutkimus suoritettiin 500 °C lämpötilassa ja mikrorakenne analysoitiin läpivalaisumikroskoopilla. Tämän lisäksi ultrahienoraerakenne oli tasaisesti jakautunut kappaleen pituudelle, mikä helpottaa materiaalin käyttöä ECAP prosessoinnin jälkeen.

2.1.5 Jatkuva ECAP prosessointi

Edellä esitetyt ECAP prosessit tarvitsevat työvoimaa siirtämään kappaleita muottiin ja sieltä pois. Jotta automaatioastetta saataisiin nostettua, tulisi näistä välivaiheista päästä

eroon tai ainakin niiden kesto tulisi minimoida. Jatkuvalla ECAP prosessoinnilla on potentiaalia vastata kaupallisesti merkittävän ECAP prosessoinnin asettamiin haasteisiin. Läpimurtomenetelmää ei vielä kuitenkaan ole löytynyt. Ongelmana jatkuvassa ECAP prosessoinnissa on ollut sen soveltuvuus vain tietyille materiaaleille ja pienet eräkoot [3]. Jatkuvan ECAP prosessin kehittämistä tutkitaan tällä hetkellä paljon.

ECAP–Conform on ECAP prosessin ja conform-ekstruusion yhdistelmä, jossa kappale painuu ECAP muotin läpi liikuteltavan muotin keskiosan avulla. Muottia on muokattu siten, että prosessointi voidaan toistaa. Tuloksena saadaan ultrahienorakeisia rakenteita. ECAP–Conform laitteisto on esitetty kuvassa 2.10.
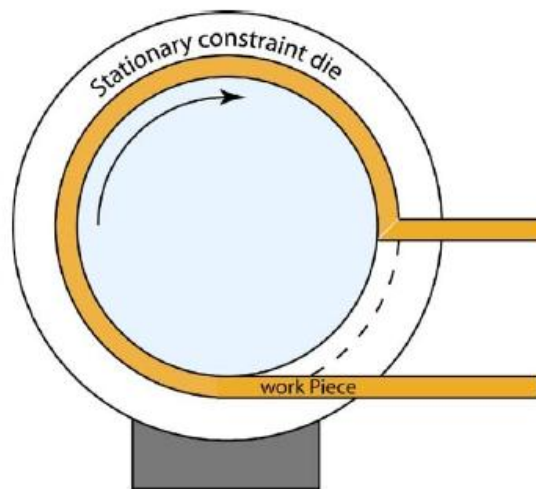
Kuva 2.10 *ECAP–Conform laitteisto. Ulkokehällä on paikallaan pysyvä muotti, jonka sisäkehällä kappale liikkuu [12].*

Laitteiston keskiosa on liikkuva ja se on uritettu keskeltä. Työstettävä kappaleella on kolme kosketuspintaa liikkuvan osan kanssa ja yksi kosketuspinta paikallaan olevan ulkokehän kanssa. Näin ollen se liikkuu kitkavoimien ansiosta laitteiston keskiosan mukana. Laitteiston lopussa on ECAP laitteistolle tyypillinen kulma, jonka johdosta raekokoa saadaan pienennettyä. Raab et al. [12] tutkivat 99,95 % karkearakeista (5-7 µm) alumiiinilankaa ECAP–confrom prosessoinnin jälkeen. Kappaleen halkaisija oli 3,4 mm ja pituus yli metrin. Koe suoritettiin huoneenlämpötilassa ja lankaa pyöräytettiin 180° jokaisen läpäisyn jälkeen. Läpäisyjä oli neljä. Kuvassa 2.11 nähdään näytteen mikrorakenne neljän läpäisyn jälkeen ja taulukossa 2.1 on havainnollistettu mekaanisten ominaisuuksien kehitystä kunkin läpäisyn jälkeen.
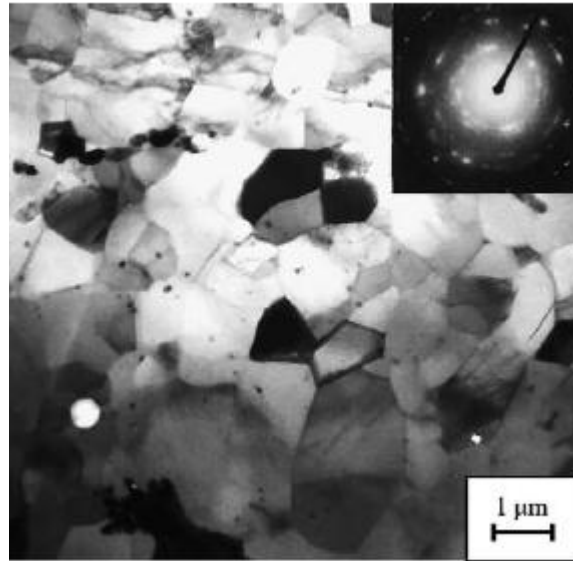
Kuva 2.11 *99,95% alumiinin mikrorakenne neljän läpäisyn jälkeen ECAP-conform prosessilla [12].*

Kuten kuvasta 2.11 käy ilmi, on mikrorakenne pienentynyt alkuperäisestä (5-7 µm) alle mikrometriin. Tosin lievää epähomogeenisuutta on havaittavissa. Taulukosta 2.1 puolestaan nähdään, että myötölujuus ja murtolujuus kasvavat huomattavasti ECAP-Conform käsittelyn jälkeen mutta lujuusarvot eivät juuri parane läpäisyjen lisääntyessä.

Taulukko 2.1 *Alumiininäytteen myötölujuus (YS), murtolujuus (UTS) ja murtovenymä (δ) kunkin painalluksen jälkeen [12].*

Painallus	YS (MPa)	UTS (MPa)	δ (%)
Toimitustila	47	71	28
Ensimmäinen	130	160	13
Toinen	140	170	12
Kolmas	130	160	14
Neljäs	140	180	14

ECAP-Conform prosessin ongelmina ovat olleet poikkileikkauksen muuttuminen läpäisyn aikana ja plastinen muodonmuutos ennen ECAP muotin läpäisyä [12].

Uusi jatkuvan prosessoinnin ECAP menetelmä on CFAE (Continuous Frictional Angular Extrusion) [13]. Se on mukautettu ECAP–conform prosessista ja paikkaa osittain sen aukkoja. CFAE menetelmässä on minimoitu kosketuspinta pyörivän keskikohdan kanssa, jolloin plastista muodonmuutosta ei juuri tapahdu ennen varsinaista muokkausta. Näin ollen poikkipinta-ala ei muutu, mikä helpottaa läpäisyjen toistettavuutta. Kuvassa 2.12 on skemaattinen esitys CFAE menetelmästä
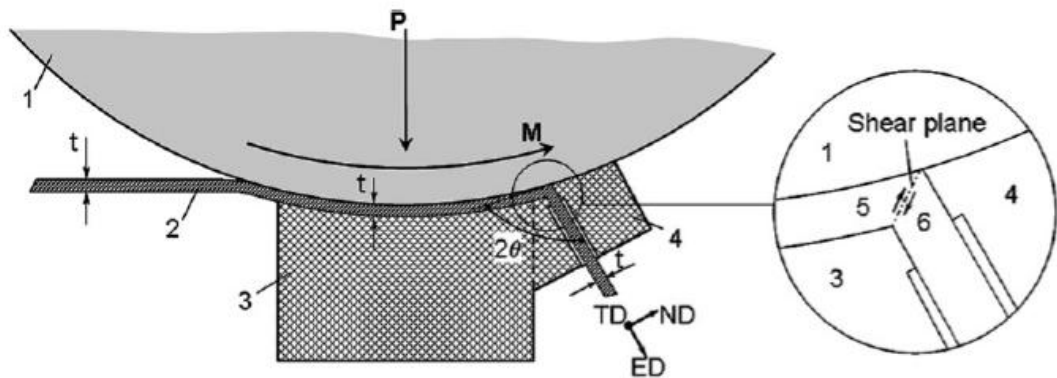
Kuva 2.11 *CFAE-laitteisto. 1) Pyörivä rulla, 2) Työstettävä kappale, 3) Kiinteä tuki kappalelle, 4) Muotti, 5) Ensimmäinen ekstruusiokanava 6) Toinen ekstruusiokanava, t = kappaleen paksuus, ED = Ekstruusion suunta, ND = Normaalin suunta, TD = Poikittainen suunta [13].*

2.1.6 ECAP laitteiston konstruiointi

Kuten tähän mennessä esitellyistä ECAP menetelmistä voi päätellä, ECAP laitteisto ei ole mekaaniselta rakenteeltaan kovinkaan monimutkainen. Tavanomaisen ECAP laitteiston rakentaminen onnistuu kahdesta halkaistusta harkosta, jotka on kiillotettu sisäpinnalta hyvin. Halkaistut harkot pultataan yhteen, mutta läpäisyjen jälkeen tulee pultteja kiristää. Kitkan vähentämiseksi laitteiston sisäseinämällä käytetään yleensä molybdeenidisulfidia. Laitteistoon voidaan tehdä myös liikkuvat muotin seinät [14]. Tällöin kappaleen läpäistessä muotin, liikkuu sisäänpäin mennessä sisäänmenoseinä ja poistuessa ulostuloseinä. Näin ollen kitka saadaan minimoitua.

Toinen vaihtoehto muotin rakentamiselle on tehdä kokonaan kiinteä muotti. Tässä tapauksessa täytyy huomioida, että kappale saadaan muotista pois vain työntämällä uusi kappale tilalle, jolloin kanavaan jää aina painalluksen jälkeen kappale [3]. Monimutkaisemmat ja vaikeammin työstettävä kappaleet vaativat laitteistolta erikoisjärjestelyjä, esimerkiksi jotta painava voima saadaan tarpeeksi suureksi. Tämä asettaa haasteen, jotta ECAP menetelmiä voidaan hyödyntää kaupallisesti [3].

2.2 ECAP prosessiparametrit

ECAP prosessin luonnetta voidaan kuvata eri parametreilla. Tärkeimpiä ovat leikkausmyötymä, joka aiheutuu leikkausjännityksestä, eri prosessointireittien kombinaatiot sekä eri prosessointireiteissä aktivoituvat liukusysteemit. Nämä vaikuttavat UFG-materiaalin lopulliseen mikrorakenteen laatuun [3].

2.2.1 Myötymä

Materiaali myötää voimakkaasti ECAP prosessoinnin aikana. Iwahasi et al. [15] ovat kehittäneet menetelmän, jolla myötymän suuruutta voidaan arvioida eri ECAP laitteistoille.
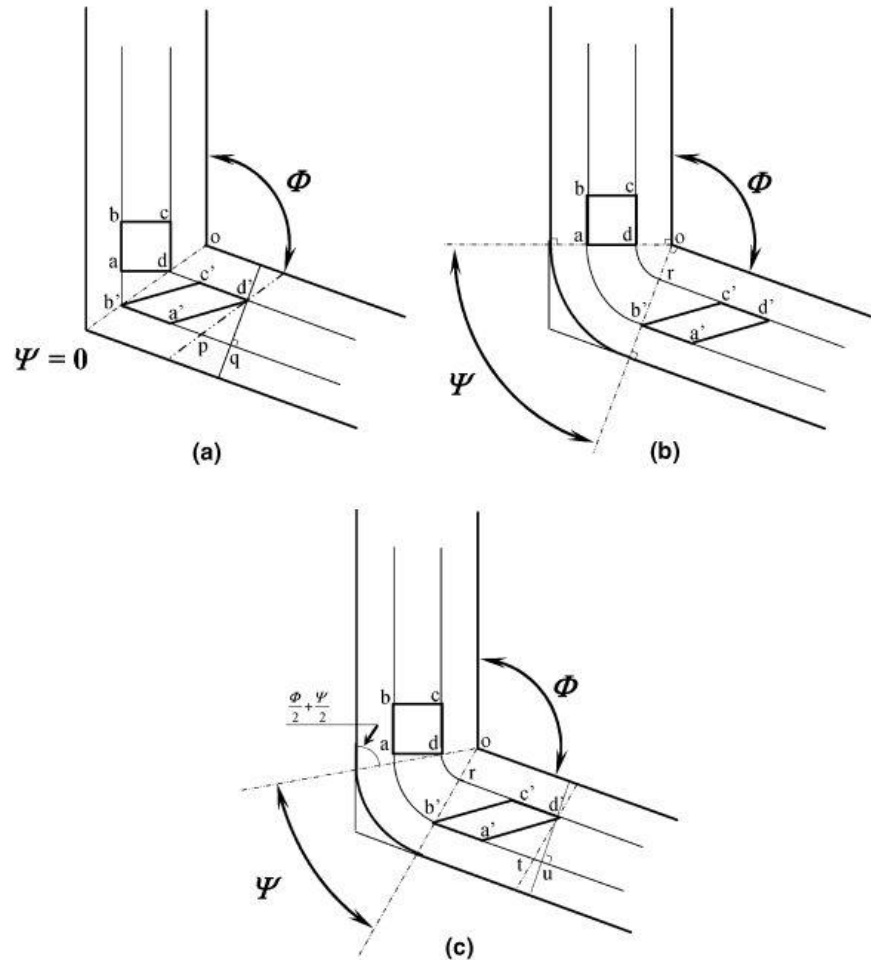
Kuva 2.12 Myötymän suuruuden arvioimiseen käytettäviä tapauksia. Kanavien välinen kulma on Φ ja ulkokaaren kaarevuuskulma Ψ. a) Ψ = 0, b) Ψ = π − Φ ja c) 0 < Ψ < Φ − π [15].

Kuvassa 2.12 on esitetty kolme erillistä tapausta, joissa kussakin pieni neliön muotoinen pala (abcd) metalliaihiosta läpäisee ECAP laitteiston. Palasen dimensiot muuttuvat läpäisyn aikana ja näistä erillisestä tapauksista voidaan johtaa myötymälle yleinen yhtälö [15]

$$\varepsilon_N = \frac{N}{\sqrt{3}}\left[2\cot\left(\frac{\Phi}{2}+\frac{\Psi}{2}\right) + \Psi\,\mathrm{cosec}\left(\frac{\Phi}{2}+\frac{\Psi}{2}\right)\right] \tag{2}$$

jossa Φ on kanavien välinen kulma, Ψ on ulkokaaren kaarevuuskulma ja N on läpäisyjen lukumäärä. Arvio olettaa, että kappale ja muotti on voideltu, jolloin kitka

voidaan jättää huomiotta. Yhtälö (2) on todettu tarkaksi myös kokeellisesti värjätyn plastisiinin [16] ja puhtaan alumiinin avulla [17]. Kulmien Ψ ja Φ vaikutusta myötymään ensimmäisen läpäisyn (N=1) jälkeen on kuvattu kuvassa 2.13.
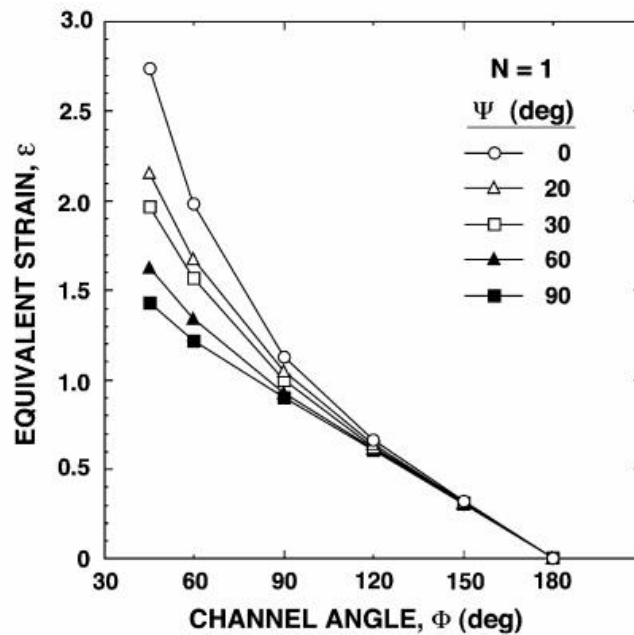
Kuva 2.13 *Kanavakulman Φ ja kaarevuuskulman Ψ vaikutus materiaalin myötymään yhden ECAP painalluksen jälkeen [18].*

Kuvasta 2.13 voidaan vetää joitakin johtopäätöksiä. Todella suuri myötymä saadaan aikaan, kun sekä Ψ ja Φ ovat pieniä. Ulkokaaren kaarevuuskulmalla on pieni vaikutus myötymään, kun kanavien välinen kulma on yli 90°. Tavanomaisella ECAP prosessilla, jolla kanavien välinen kulma on yleensä 90°, ekvivalentti myötymä on noin 1 ja ulkokaaren kaarevuuskulma ei juuri siihen vaikuta.

2.2.2 Eri prosessointireitit ja niissä aktivoituvat liukusysteemit

Materiaalin eri liukusysteemien aktivoituminen riippuu siitä, miten päin aihio työnnetään ECAP laitteistoon. Kääntämällä aihiota painallusten välillä saadaan aktivoitua eri liukusysteemejä ja näin ollen vaikutetaan mikrorakenteen muodostumiseen. Kuvassa 2.14 on vedettynä yhteen neljä perustapaa toistaa kappaleen painallus, jotka kukin aktivoivat eri liukusysteemejä [19].
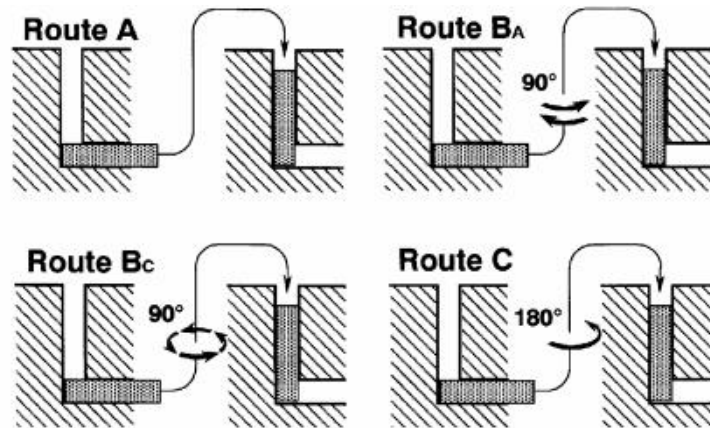
Kuva 2.13 *Neljä perustapaa toistaa kappaleen painallus [19].*

Reitissä A kappaletta ei käännetä lainkaan, reitissä B_A kappaletta käännetään 90°
vuoronperään eri suuntiin, reitissä B_c 90° samaan suuntaan ja reitissä C 180°
painallusten välissä. Reittejä voi yhdistää mutta käytännössä materiaalin mekaaniset
ominaisuudet eivät siitä merkittävästi parane [20]. Reiteillä A, B_A, B_C ja C saadaan
aktivoitua muokkaamisen kannalta oleellisimmat liukusysteemit.
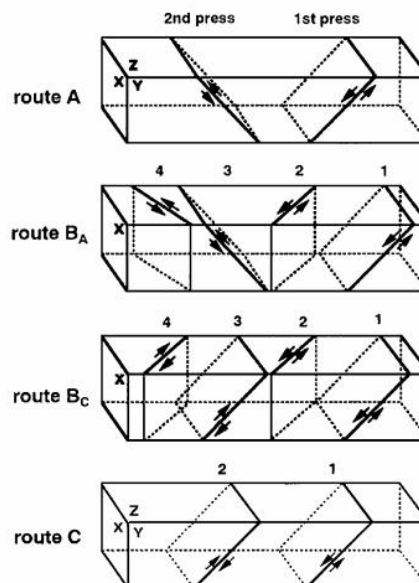
Kuva 2.14 *Reittien A, B_A, B_C, ja C aktivoimat liukusysteemit. Numerot 1-4 kuvaavat
painalluksien järjestystä [19].*

Kuvassa 2.14 on esitettynä kunkin reitin aktivoimat liukusysteemit. Kuten kuvasta
huomataan, kappaleita käännetään painallusten välissä. Reitit voidaan jaotella sen
mukaan, kumoutuuko painalluksen aiheuttama liukuminen reitin myöhemmässä
vaiheessa vai aktivoiko kääntäminen uusia liukusysteemejä. Reitissä C liukuminen
kumoutuu joka toisella painalluksella ja reitissä B_C ensimmäisen painalluksen

liukuminen kumoutuu kolmannella painalluksella ja toisen neljännellä. Reitissä B_A liukuminen kumuloituu samoille tasoille, samoin reitissä A.

2.3 ECAP menetelmään vaikuttavat kokeelliset tekijät

ECAP laitteistoon ja työstöolosuhteisiin liittyy useita kokeellisia tekijöitä, jotka vaikuttavat työstettyjen materiaalien mekaanisiin ominaisuuksiin.

2.3.1 Kanavien välinen kulma $Φ$

Tärkein yksittäinen laitteiston ominaisuus on kanavien välinen kulma $Φ$ eli kanavakulma, koska se vaikuttaa myötymään kaikista voimakkaimmin, kuten kappaleessa 2.2.1 todettiin. Nakashima et al. [21] tutkivat kanavakulman vaikutusta puhtaaseen alumiinin ECAP painalluksissa. Tutkimuksessa käytettiin neljää eri ECAP laitteistoa, joiden kanavakulmat olivat 90°, 112,5°, 135° ja 157.5°. Kuvassa 2.15 on esitetty ECAP muotit kyseisillä kanavakulmilla.
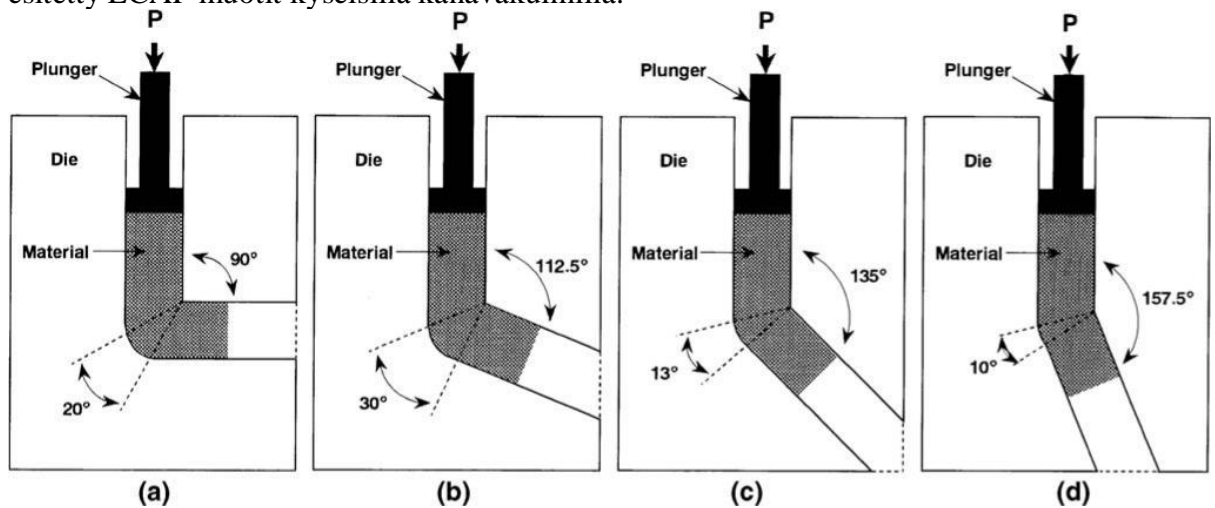
Kuva 2.15 *Muottien kanavakulmat. a)* $Φ = 90°$ *b)* $Φ = 112,5°$ *c)* $Φ = 135°$ *d)* $Φ = 157,5°$ *[21].*

Tutkimus tehtiin siten, että kumulatiivinen myötymä kussakin tapauksessa oli noin 4. Tämä saatiin aikaiseksi yhtälön (2) avulla painamalla kappaletta useammin kulman kasvaessa. Kun myötymä on samaa suuruusluokkaa, ovat tulokset vertailukelpoisia keskenään. Puhtaalle alumiinille raekoko on hienoin ja tasa-akselisin, kun kappale altistuu mahdollisimman suurelle myötymälle, eli tässä tapauksessa kun $Φ = 90°$. Onkin tärkeää huomata, että kokonaismyötymä ei niinkään ole tärkeä, vaan yksittäisen painalluksen aiheuttama mahdollisimman suuri myötymä materiaalissa. Yhtälön (2) mukaan kanavakulma kannattaisi valita mahdollisimman pieneksi, jotta yksittäisen painalluksen aiheuttama myötymä materiaalissa olisi mahdollisimman suuri. Tämä on mahdollista ja Furunon et al. [18] mukaan raekoko pienenee hiukan enemmän puhtaalla

alumiinilla ja Al-Mg-Sc-seoksella 60º muotilla kuin 90º muotilla. Painamiseen vaadittava voima kuitenkin kasvaa kulman pienentyessä ja tällöin materiaali altistuu säröilylle. 90º muotti on sopiva kompromissi, jolla saavutetaan ultrahieno raekoko, ja materiaali säilyy ehjänä.

2.3.2 Ulkokaaren kaarevuuskulma Ψ

Kuten ECAP prosessia kuvaavien parametrien käsittelyn yhteydessä todettiin, ei ulkokaaren kaarevuuskulmalla Ψ ole kovin suurta merkitystä kappaleen myötymään. Asia on kuitenkin käsittelemisen arvoinen, sillä kiinteään ECAP muottiin tulee aina nollasta poikkeava kaarikulma ja toisaalta kahdesta kappaleesta valmistetun ECAP muotin ulkokulma on 0º [22].

Shan et. al. [23] tutkivat puhtaan alumiinin ECAP prosessointia kiinteällä muotilla, jossa poikkileikkaus on ympyrä ja ulkokaaren kulma 0º sekä kahdesta osasta valmistetulla muotilla, jossa poikkileikkaus on neliö ja jonka ulkokaaren kulma oli 20º. Neljän painalluksen jälkeen kappaleiden poikkileikkausten Vickers kovuus oli lähes identtinen. Kovuusjakaumaa on havainnollistettu kuvassa 2.16.
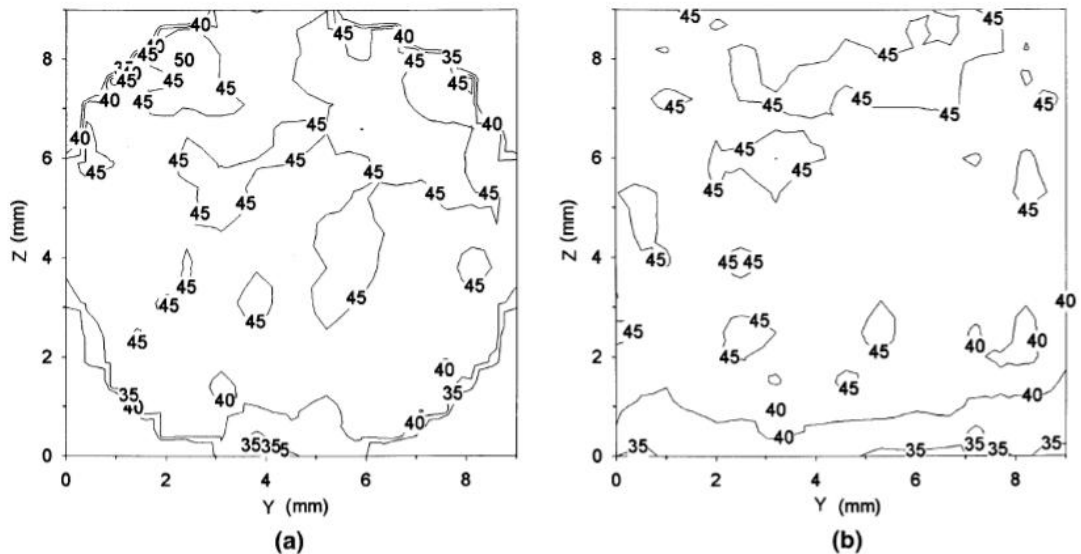
Kuva 2.16 *Puhtaan alumiinin poikkileikkauksen kovuusjakauma neljän painalluksen jälkeen, kun ulkokaaren kulma a) Ψ = 20º ja b) Ψ = 0 º [23].*

Kuten kuvasta 2.16 huomataan, on molemmissa tapauksissa kappaleiden alaosassa lievää epähomogeenisyyttä, joka näkyy myös kovuudessa. Teoriassa tämä voitaisiin välttää, jos ulkokaaren ja sisäkaaren kaarevuuskulmat olisivat yhdensuuntaisia [24]. Eli muotilla olisi kanavakulma Φ ja sekä sisäpuolella että ulkopuolella muottia olisi kaarevuutta, joiden kulmat olisivat yhdensuuntaisia. Kyseistä muottia on kuitenkin vaikea työstää. Ehkä uusilla valamismenetelmillä voidaan hakea ratkaisua asiaan.

2.3.3 Lämpötila

Lämpötila on yksi merkittävimmistä prosessointiparametreista ja sitä voidaan myös säätää suhteellisen helposti. Yamashitan et al. [25] mukaan raekoko kasvaa lämpötilan funktiona puhtaalla alumiinilla, Al-3 % Mg- sekä Al-3 % -0,3 % Sc-seoksilla. Kuva 2.17 havainnollistaa raekoon kasvua lämpötilan kasvaessa.
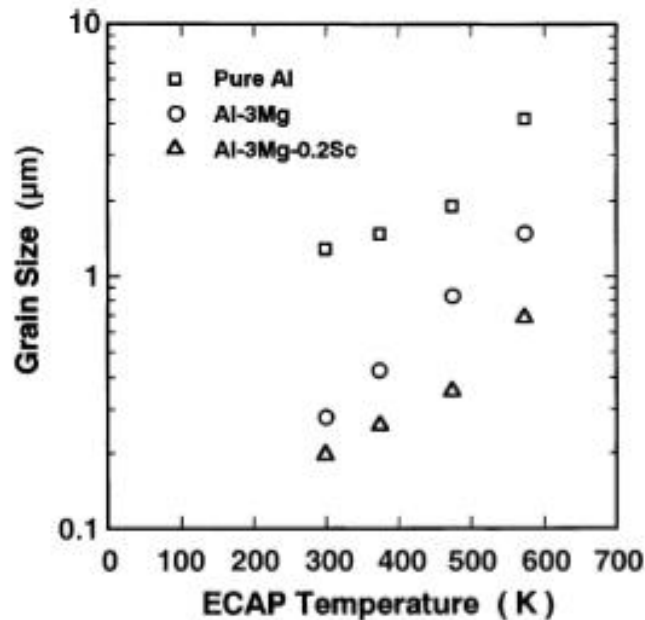
Kuva 2.17 *Lämpötilan vaikutus raekokoon puhtaalla alumiinilla, Al-3 % Mg – sekä Al 3 % Mg-0,2 % Sc – seoksilla [25].*

Raekoon lisäksi materiaalien pienen kulman raerajat lisääntyivät lämpötilan kasvaessa. Selityksenä tälle on dislokaatioiden annihilioituminen rakeiden sisällä sekä niiden vähäisempi absorboituminen soluseinämiin korkeammassa lämpötilassa [25]. Jotta raekoko saadaan mahdollisimman pieneksi ja sitä myöten lujuus suureksi, kannattaa ECAP prosessointi suorittaa alhaisessa lämpötilassa, vaikka materiaalin prosessointi onkin helpompaa korkeassa lämpötilassa.

2.3.4 Painallusnopeus

ECAP prosessointi suoritetaan yleensä voimakkailla hydraulipuristimilla, jotka toimivat 1-20 mm/s painallusnopeuksilla. Berbon et al. [4] tutkivat Al-1%Mg seoksen raekoon kehittymistä, kun painallusnopeus oli 0,01 mm/s – 10 mm/s. Raekokoon painallusnopeudella ei näytä olevan merkittävää vaikutusta mutta hitaammalla nopeudella mikrorakenteesta saadaan tasaisempi.

2.3.5 Vastustava paine

ECAP laitteiston ulostuloaukkoon voidaan kehittää painallusta vastustava paine. Se tuo mukanaan merkittäviä etuja. Yksi niistä on materiaalien huomattavasti parantunut työstettävyys. Esimerkiksi kuparin pintaan tulee säröjä 12–13 työnnön jälkeen ilman vastapainetta mutta jo 300 Mpa:n vastustavan vastustavan paineen avulla toistoja voidaan suorittaa yli 16 [26]. Toinen merkittävä etu on yhtenäinen materiaalivirta kanavan läpi. Kanavan ulkokaarelle myötymäkohdassa saattaa muodostua niin sanottuja kuolleita alueita, joissa myötymä jää vajaaksi. Samoin muodonmuutosalue keskellä kanavaa on yleensä viuhkamainen, eikä yhtenäinen [14]. Vastustavan paineen avulla kuollutta aluetta ei muodostu ja muodonmuutos keskittyy pienemmälle alueelle.

Vastustava paine voidaan toteuttaa kitkan avulla ulostuloaukossa [27] tai vastustamalla työntöä toisen männän avulla [28]. Työntöä vastustava mäntä herättää enemmän lupauksia, sillä sitä voidaan ohjata tietokoneella, jolloin materiaalivirrasta saadaan kontrolloidumpi. Kuvassa 2.18 on ECAP laitteisto, jossa vastustava paine on toteutettu työntöä vastustavalla männällä.
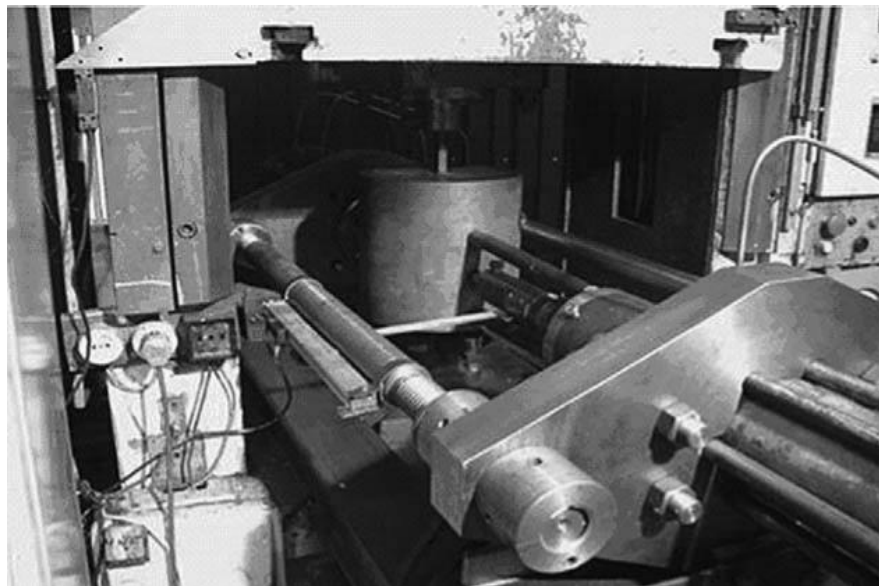
Kuva 2.18 *ECAP laitteisto, jossa on työntöä vastustaa toinen mäntä [28].*

3. HESP

HESP (High Energy Shot Peening) eli korkeaenerginen kuulapuhallus on toinen SPD menetelmä, jolla saadaan aikaan ultrahieno raekoko. Merkittävänä erona ECAP

prosessointiin on se, että HESP menetelmässä ultrahieno rakenne muodostuu materiaalin pinnalle, kun se ECAP menetelmällä muodostuu koko kappaleeseen. Raekokoa pienentävä myötymä saadaan HESP menetelmässä pienillä (~ 5 mm halkaisijaltaan) kuulilla, jotka ammutaan paineilman avulla työstettävän materiaalin pintaan. Seurauksena materiaalin pintaan kohdistuu puristusvoima, jota bulkkiosa pyrkii työntämällä vastustamaan. Koska muodonmuutos on nopea, jää pintaan jäännösjännitys, johon HESP menetelmän käyttökelpoisuus perustuu [29]. Tässä kappaleessa tarkastellaan HESP laitteistoa, sen aiheuttamia muutoksia mikrorakenteessa sekä menetelmän merkittävimpiä etuja ja sovellusalueita.

3.1 Muutokset materiaalissa

Materiaalitieteen kannalta mielenkiinto kohdistuu työstettävän materiaalin pintarakenteeseen ja erityisesti siinä eri kerroksissa tapahtuviin muutoksiin mikrorakenteessa [29–31]. Tutkimustuloksia on perinteisesti raportoitu pkk- ja tkk-metalleilla [30–31], joilla on korkea pinousvikaenergia, mutta aivan viime aikoina myös hcp-metallien, HESP prosessointi on herättänyt lupauksia [29].

3.1.1 Teräkselle

HESP menetelmässä materiaalin pintaan kohdistuu suuri myötönopeus. Umemoto et al. [30] tutkivat nanokiteisyyden muodostumista pudottamalla ferriittisen ja sferoidiittisen teräksen pintaan pallon, johon on kiinnitetty paino. Pudotuksia toistettiin enimmillään 50 kertaa ja mikrorakenne kuvattiin pyyhkäisyelektronimikroskoopilla sopivin väliajoin. Materiaalin myötönopeus oli keskimäärin 10 000 1/s, joten menetelmä sopii hyvin HESP menetelmän arvioimiseen. Kuvassa 3.4 on skemaattinen esitys koejärjestelyistä.
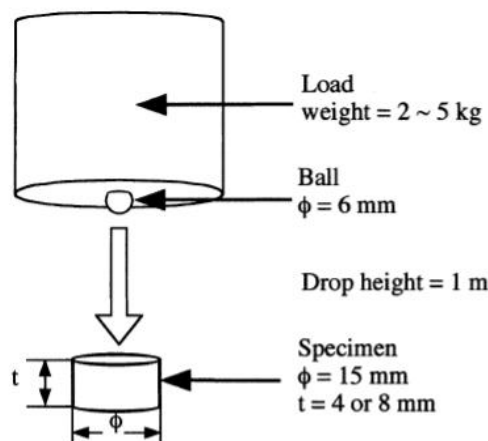
Kuva 3.4 *Skemaattinen esitys pallonpudottamiskokeesta [30].*

Pallonpudotuskokeen tuloksena molempien terästen pintaan muodostui kovempi alue. Myös useiden kymmenien mikrometrien päähän pinnasta muodostui samanlainen mikrorakenne ja tämä johtuu, siitä että jännitys saattaa olla suurimmillaan juuri niillä alueilla johtuen pallon ja pinnan kitkasta törmäyksessä. Kuvan 3.5 tummat alueet ovat muokkautuneet testissä eniten.
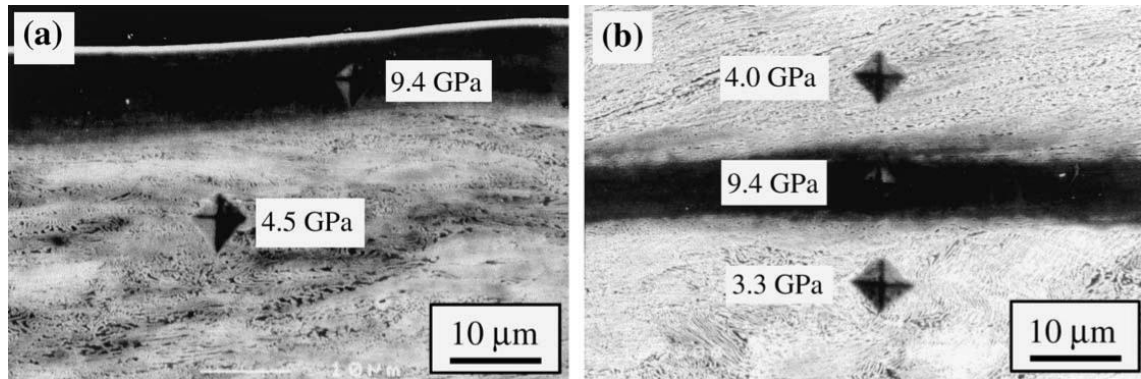
Kuva 3.5 *Ferriittisen teräksen mikrorakenne pallonpudotustestissä a) 50 pudotuksen jälkeen 3 kg:n painolla b) 10 pudotuksen jälkeen 5 kg:n painolla.*

Tulokset olivat samanlaisia sferoidiittiselle teräkselle. Materiaalin kohdistunutta myötönopeutta arvioitiin putoavan pallon liike-energian avulla. Myös energian muuttumista törmäyksessä lämmöksi arvioitiin. Paikallisesti lämpötila saattaa nousta yli 1000 °C, jolloin teräs austenoituisi ja jäähtyessään muuttuisi martensiittiseksi. Martensiittimuutos vaatii lisäselvitystä.

Korkealla myötönopeudella on yhteys nanokiteisyyden muodostumiseen teräksillä [32]. Kun myötönopeus materiaalissa kasvaa, dislokaatiotiheys kasvaa ja dislokaatiosolujen koko pienenee sekä epäsäännöllisesti järjestäytyneiden solujen osuus kasvaa. Solut muuttuvat jyvämäisiksi, kun dislokaatiotiheys ylittää kriittisen arvon. Nanokokoisen mikrorakenteen muodostuminen edellyttää suurta myötönopeutta [30].

3.1.2 Magnesiumille

Hcp-metalleilla plastinen muodonmuutos eroaa pkk – ja tkk-metalleista, koska kaksostuminen on dislokaatioiden liukumisen ohella merkittävä tekijä muodonmuutoksessa. Magnesiumin lujuusominaisuuksien parantaminen on esimerkiksi autoteollisuuden tavoitteena, sillä sen pieni tiheys, kierrätettävyys ja vaimennusominaisuudet ovat erinomaisia. Hou Li-Feng et al. tutkivat AZ91D-magnesiumin mikrorakenteen kehitystä, kun sitä työstetään HESP menetelmällä [29]. Tulosten mittaamiseen käytettiin röntgendiffraktiota, läpäisyelektronimikroskooppia sekä korkean resoluution läpäisyelektronimikroskooppia (HRTEM).

TEM-kuvien perusteella, mikrorakenne muuttuu hienorakeisemmaksi tultaessa kohti materiaalin pintaa ja on pienimmillään pinnassa 40 nm. Muodonmuutosmekanismi on

alhaisella myötymällä eli noin 20 μm:n etäisyydellä pinnasta dislokaatioiden liukumista. Lähempänä pinnassa, jossa myötymä siis on suurempi, dislokaatiotiheys on kasvanut ja kuulapuhalluksen aiheuttama vaihteleva jännitys yhdessä lämpötilän nousun kanssa käynnistää dynaamisen rekristallaation. Sen seurauksena rakenteesee tulee mikro – ja nanometrin kokoisia rakeita. Muodonmuutosmekanismia on havainnollistettu kuvassa 3.2.
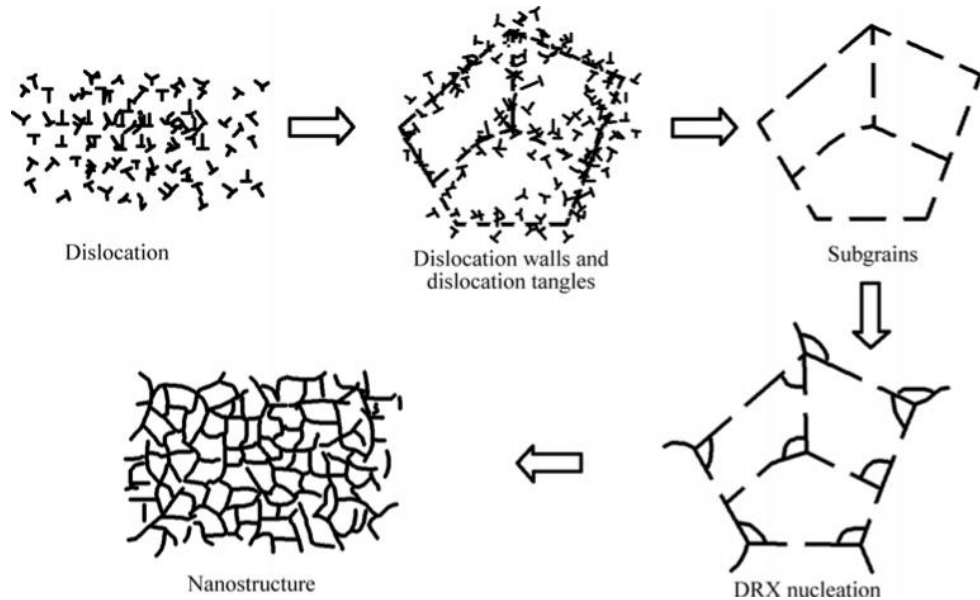
Kuva 3.2 *Skemaattinen esitys AZ91D-magnesiumseoksen rekristallaatiosta HESP menetelmässä. DRX tarkoittaa dynaamista rekrystallaatiota [29].*

AZ91D-magnesiumin kovuus parani huomattavasti HESP käsittelyn jälkeen. Kuvassa 3.3 on esitetty kovuus eri etäisyyksillä materiaalin pinnasta.
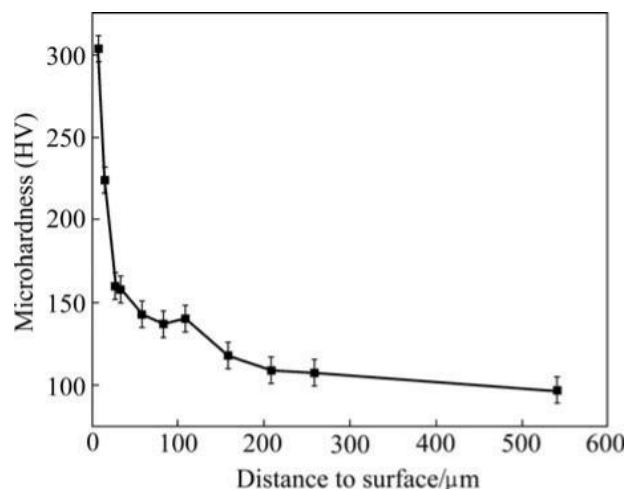
Kuva 3.3 *AZ91D-magnesiumin kovuus mitattuna eri etäisyyksillä materiaalin pinnasta [29].*

3.2 HESP laitteisto

HESP laitteiston peruskomponentit ovat korkeaenerginen puhalluslaite, kuulien kierrätyslaite ja liikutuslaitteisto [32]. Kuulat puhalletaan paineilman avulla, jolla niille saadaan tarpeeksi korkea liike-energia. Paineilma, johon kuulat eli puhallusmedia on johdettu, ammutaan käsiteltävän kappaleen pintaan suuttimen läpi. Kuulina käytetään teräs-, rauta-, lasi- tai keraamisia kuulia. Rautakuulat valmistetaan valamalla, kun taas teräskuulat katkaistaan ohuesta teräslangasta noin halkaisijan mittaisiksi paloiksi. Palojen kulmat pyöristetään, jotta kappaleista tulee kuulan muotoisia. Teräskuulien etuna on pitkä kestoikä, puhalluksen laatu ja puhalluskaluston kesto. Huonona puolena on korkea hinta. Rauta – ja lasikuulat ovat halvempia mutta rautakuulat kuluttavat kalustoa. Lasikuulia käytetään, kun käsitellään materiaalia, jonka ei haluta reagoivan median kanssa, esimerkiksi titaania ja ruostumatonta terästä. Keraamiset kuulat ovat zirkoniumoksidin ja piioksidin seosta. Niiden etuna on hyvä kierrätettävyys, mutta korkea hinta rajoittaa niiden käyttöä. Kuulien kierrätys tapahtuu erottelemalla halkaisijaltaan alimittaiset kuulat ja särkyneet kuulat hyvien kuulien joukosta. Kuulia lisätään kuulasäiliöön sen pinnankorkeutta tarkkailemalla.

3.3. HESP prosessiparametrit

HESP prosessiin vaikuttavia parametreja ovat kuulasuihkun peitto, kuulien koko ja kovuus, puhalluksen nopeus, puhalluskulma pintaan nähden sekä puhallusaika. Nämä parametrit vaikuttavat puhalluksen intensiteettiin, joka puolestaa vaikuttaa työstettävään kappaleen pintaan saatavaan puristusvoimaan. Puhallusaikaa käsiteltiin jo kappaleessa 3.1.1. Tässä kappaleessa käsitellään kuulasuihkun peitto, kuulien koko ja kovuus sekä kuulien energia.

3.3.1 Kuulasuihkun peitto

Puhalluksen peitolla tarkoitetaan suihkun osumapinta-alan suhdetta kappaleen koko pinta-alaan. Jotta materiaalin mekaaniset ominaisuudet paranenisivat merkittävästi, on peitto pyrittävä saamaan mahdollisimman kattavaksi. Peittoa voidaan mitata visuaalisella tarkastelulla tutkimalla muutoksia faasirakenteessa tai mittaamalla pinnan jäännösjännityksiä esimerkiksi röntgendiffraktiolla [32]. Käytännössä 98 % peittoa pidetään maksimina, sillä sitä suurempaa peittoa on vaikea mitata.

3.3.2 Kuulien koko ja kovuus

Suuri kuulakoko kasvattaa puhalluksen intensiteettiä mutta pienentää peittoa. HESP menetelmissä kuulakoko vaihtelee 1 -8 mm:n välillä [29; 31; 34]. Yleensä valitaan pienin kuulakoko, jolla saavutetaan haluttu intensiteetti. Myös normaalia suurempaa kuulakokoa voidaan käyttää, jolloin intensiteetti kasvaa ja tunkeuma on syvempi. Kuulien kokoa rajoittaa pinnan ja puhallussuunnan välinen kulma. Kuulan säteen tulee olla pienempi, kuin puhallettavan kulman pyöristyssäteen, jotta pinnan puhallus olisi mahdollista. Kuulien kovuus on tyypillisesti teräskuulilla Rockwell asteikolla 40–50. Kovuus ei vaikuta puhalluksen intensiteettiin, mikäli se on korkeampi kuin työstettävän materiaalin kovuus. Pehmeämpi media puolestaan laskee intensiteettiä [33].

3.3 HESP prosessoinnin edut

HESP prosessoinnin merkittävin etu on väsymiskestävyyden paraneminen. Väsymismurtuma alkaa usein materiaalin pinnasta [2], joten väsymisen kannalta ominaisuuksien parantaminen saadaan keskitettyä juuri oikeaan paikkaan. Myös muut mekaaniset ominaisuudet paranevat. Kuten kappaleessa 3.1.2 todettiin, HESP käsittelyn jälkeen magnesiumin kovuus nousi merkittävästi. Muita etuja HESP käsittelyllä ovat [29; 33]:

- Estää jännityskorroosiota.
- Parantaa voiteluominaisuuksia.
- Mahdollistaa kevyempien metallien käytön.
- Pintaan tulee yhdenmukainen tekstuuri, jolloin pintakäsittelyominaisuudet ja ulkonäkö paranee.
- Tukkii pinnan huokoisuuden.
- Suhteellisen taloudellinen ja käytännöllinen.
- Sopii isoillekin kappaleille.

HESP käsittelyllä on vain vähän huonoja puolia. Suurin niistä, joka koskee kaikkia raekoon pienentämiseen perustuvia lujittamismenetelmiä, on materiaalien pääseminen korkeissa lämpötiloissa [33]. Myös koneistus saattaa aiheuttaa raekoon kasvua työstettävän alueen läheisyydessä. Kappaleen muoto asettaa joitakin rajoituksia [33]. Terävät kulmat tulee suojata käsittelyn ajaksi. Monipuolisella liikuttelulaitteistolla saadaan kuitenkin lähes jokaiseen pintaan kohtisuoraan tuleva suihku.

HESP prosessia käytetään jo nyt paljon lentokone – ja autoteollisuudessa, jossa materiaalien hyvä väsymiskestävyys on etu [33]. Lisäksi sillä voidaan vahivstaa jo käytössä olleita kappaleita tuomalla puristusjännitys uudestaan kappaleen pintaan.

Menetelmän laajennus kevyempien metallien prosessointiin on mielenkiintoinen vaihtoehto perinteisille metalleille.

4. Yhteenveto

Raekoon pienentäminen ultrahieno – ja nanokokoiseksi on erittäin houkutteleva vaihtoehto metallien prosessoinnille, sillä sen lujittava vaikutus on erinomainen. SPD-menetelmät ovat kehittyneet vilkkaan tutkimustyön ansiosta paljon. Prosesseista on saatu kappaletta vähän kuluttavia sekä kappaleita voidaan työstää eri poikkileikkauksilla.

ECAP prosessin kohdalla perusmenetelmä on poikkileikkaukseltaan neliön tai ympyrän muotoisten aihioiden muokkaus. Tätä voidaan laajentaa levyjen muokkaukseen. Tällöin materiaalin kohdistuva myötymä riippuu painallusten määrästä, kanavakulmasta sekä ulkokaaren kaarevuuskulmasta yhtälön 2.2 mukaisesti. Ulkokaaren kaarevuuskulma vaikuttaa eriyisesti raekoon tasalaatuisuuteen. Menetelmät ovat kuitenkin hitaita ja automaatioasteen nostamiseksi on kehitetty RD-ECAP, MP-ECAP ja sivuekstruusio-ECAP sekä jatkuvatoimisia ECAP prosesseja, kuten ECAP-Conform ja CFAE. Myös näissä menetelmissä samat parametrit määräävät myötymän suuruuden. Ongelmana erityisesti jatkuvan ECAP-prosessoinnin osalta on tähän asti ollut materiaalin säröily muokkauksen aikana. Muokkausta voidaan helpottaa laitteistoon liittyvillä kokeellisilla tekijöillä. Työntöä vastustavalla paineella muodonmuutosaluetta saadaan yhtenäisemmäksi ja materiaalivirrasta tasainen. Myös lämpötilaa voidaan pienentää, jolloin raekoko pienenee mutta tässä tapauksessa työstettävyys saattaa kärsiä.

HESP on erinomainen menetelmä väsymiskestävyyden parantamiseksi. Kriittisimmät parametrit ovat kuulien koko ja kuulasuihkun peitto. Kuulien koko määräytyy intensiteetin mukaan. Yleensä valitaan pienin kuulakoko, jolla saavutetaan haluttu intensiteetti suihkulle mutta myös normaalia suurempaa kuulakokoa voidaan käyttää kasvattamaan tunkeumaa. Suihkun peitto tulisi olla mahdollisimman suuri, sillä pintaan jäävät säröt laskevat väsymiskestävyyttä. HESP laitteistoon kuuluu puhalluslaite, kuulien keräyslaite sekä suihkun ja kappaleen liikuttelulaitteisto. Monipuolisen liikuttelulaitteiston avulla voidaan työstää monia geometrisia muotoja. Kuulien keräyslaitteen avulla saadaan käyttökelpoiset kuulat kierrätettyä, mikä vähentää käyttökustannuksia. HESP menetelmän ansiosta myös keveiden metallien käyttö lujuutta vaativissa sovelluksissa on mahdollista.

5. Lähteet

[1] Balasundar I,Sudhakara Rao M, Raghu T 2008. Equal channel angular pressing die to extrude a variety of materials. Materials and Design 30, 4, pp. 904-908.

[2] Courtney, Thomas H. Mechanical behavior of materials. 1990. 710 p.

[3] Valiev RZ , Langdon TG. 2006. Principles of equal-channel angular pressing as a processing tool for grain refinement. Progress in material science 51, 7, pp. 881-981 .

[4] Berbon PB, Furukawa M, Horita Z, Nemoto M, Langdon TG. 1999. Influence of pressing speed on microstructural development in equal-channel angular pressing Metallurgical and Materials Transactions A 30, 8, pp. 1989-1997.

[5] Nakashima K, Horita Z, Nemoto M, Langdon TG. 2000. Development of a multi-pass facility for equal-channel angular pressing to high total strains. Materials Science and Engineering A 281, 82, pp.82-87.

[6] Furukawa M, Iwahashi Y, Horita Z, Nemoto M, Langdon TG. 1998. The shearing characteristics associated with equal-channel angular pressing. Materials Science and Engineering A 257, 2, pp. 215-366.

[7] Kamachi M, Furukawa M, Horita Z, Langdon TG. 2003. Equal-channel angular pressing using plate samples. Materials Science and Engineering A 361, 1-2, pp. 258-266.

[8] Ma A ,Suzuki K, Nishida Y, Saito N, Shigematsu I, Takagi M, Iwata H,Watazu A, Imura T. 2005. Impact toughness of an ingot hypereutectic Al–23 mass% Si alloy improved by rotary-die equal-channel angular pressing. Materials Science and Engineering A 399, 1-2, 15, pp. 181-189

[9] Azushima A, Aoki K. 2002. Properties of ultrafine-grained steel by repeated shear deformation of side extrusion process. Materials Science and Engineering A 337, 1-2, pp. 45-49

[10] Raab GI. 2005. Plastic flow at equal channel angular processing in parallel channels. Materials Science and Engineering A 410-411, 1-2, pp. 230-233.

[11] Pat. RU 2181314 Raab GI, Valiev RZ, Kulyasov GV, Polozovsky VA. 2002.

[12] Raab GJ, Valiev RZ, Lowe TC, Zhu YT. 2004. Continuous processing of ultrafine grained Al by ECAP–Conform. Materials Science and Engineering A 382, 1-2, pp. 30-34.

[13] Huanga Y, Prangnell PB. 2007. Continuous frictional angular extrusion and its application in the production of ultrafine-grained sheet metals. Scripta Materialia 56, 5, pp. 333–336.

[14] Semiatin SL, DeLo DP, Shell EB. 2000. The effect of material properties and tooling design on deformation and fracture during equal channel angular extrusion. Acta Materialia 48, 8, pp. 1841-1851

[15] Iwahashi Y, Wang J, Horita Z, Nemoto M, Langdon TG. 1996. Principle of equal-channel angular pressing for the processing of ultra-fine grained materials. Scripta Materialia 35, 2, pp. 143-146

[16] Wu Y, Baker I.1997. An experimental study of equal channel angular extrusion. Scripta Materialia 37, 4, pp. 437-442

[17] Shan A, Moon IG, Ko HS, Park JW. 1999. Direct observation of shear deformation during equal channel angular pressing of pure aluminium. Scripta Materialia 41, 4, pp. 353-357

[18] Furuno K, Akamatsu H, Oh-ishi K, Furukawa M, Horita Z, Langdon TG. 2004. Microstructural development in equal-channel angular pressing using a 60° die. Acta Materialia 52, 9, pp. 2497-2507

[19] Horita Z, Furukawa M, Nemoto M, Langdon TG. 2000. Development of fine grained structures using severe plastic deformation. Material science and technology 16, 11-12, pp. 1239-1245

[20] Lee S, Langdon TG. 2000. Influence of Equal-Channel Angular Pressing on the Superplastic Properties of Commercial Aluminum Alloys. Materials Research Society Symposium Proceedings 601, p. 359

[21] Nakashima K, Horita Z, Nemoto M, Langdon TG. 1996. Influence of channel angle on the development of ultrafine grains in equal-channel angular pressing. Acta materialia 46, 5. pp. 1589-1599.

[22] Semiatin SL, DeLo DP, Shell EB. 2000. The effect of material properties and tooling design on deformation and fracture during equal channel angular extrusion Acta Materialia 48, 8, pp. 1841-1851.

[23] Xu C, Langdon TG. In: Jin Z, Beaudoin A, Bieler TA, Radhakrishnan B, editors. Hot deformation of aluminum alloys III. Warrendale (PA): The Minerals, Metals and Materials Society (2003). p. 373.

[24] Luis Perez CJ. Scripta Mater 2004. On the correct selection of the channel die in ECAP processes. Scripta Materialia 50, 3, pp. 387-393

[25] Yamashita A, Yamaguchi D, Horita Z, Langdon TG. 2000. Influence of pressing temperature on microstructural development in equal-channel angular pressing. Materials Science and Engineering A 287, 1, pp. 100-106

[26] Valiev RZ, Alexandrov IV, Lowe TC, Zhu YT. 2002. Paradox of strength and ductility in metals processed by severe plastic deformation. Journal of materials research 17, 5, pp. 5-8

[27] Raab GI, Krasilnikov NA, Valiev RZ. Fizika i Tekhnika Vysokikh Davleniy Physics and Engineering of High Pressures 10(2000)4 p. 73

[28] Krasilnikov NA. Russian Metall 3(2005)35.

[29] Li-feng HOU, Ying-hui WEI, Bao-sheng LIU, Bing-she XU. 2008. Microstructure evolution of AZ91D induced by high energy shot peening. Transactions of Nonferrous Metals Society of China 18, 5, pp. 1053-1057

[30] Unemoto M., Huang B., Tsuchiya K., Suzuki N. 2002. Formation of nanocrystalline structure in steels by ball drop test. Scripta Materialia 46, 5, pp. 383-388.

[31] G. Liu, S. C. Wang, X. F. Lou, J. Lu, K. Lu. 2001. Low carbon steel with nanostructured surface layer induced by high-energy shot peening. Scripta Materialia 44, 8-9, pp. 1791-1795

[32] Lee W.S., Lam H.F. 1996. The deformation behaviour and microstructure evolution of high-strength alloy steel at high rate of strain. Journal of Materials Process Technology 57, 4-5, pp. 233-240

[33] Lyman, T., Boyer, H. E., Unterweiser, P. M, Hontas, J. P, Mehlman, L. R, Carnes, W. J., Lawton, H. Metals Handbook, 8th Edition, Vol 2. American Society for Metals. Metals Park, Ohio, USA. 1964. pp. 398-405.

[34] T. Wang, J. Yu, R. Dong. 2006. Surface nanocrystallization induced by shot peening and its effect on corrosion resistance of 1Cr18Ni9Ti stainless steel. Surface and Coatings Technology 200, 16-17, pp. 4777-4781

High Strain Rate Torsion Properties of Ultrafine-Grained Aluminum

M. Hokka · J. Kokkonen · J. Seidt · T. Matrka · A. Gilat · V.-T. Kuokkala

Abstract Mechanical properties of most metallic materials can be improved by reducing their grain size. One of the methods used to reduce the grain size even to the nanometer level is the severe plastic deformation processing. Equal Channel Angular Pressing (ECAP) is one of the most promising severe plastic deformation processes for the nanocrystallization of ductile metals. Nanocrystalline and ultrafine grained metals usually have significantly higher strength properties but lower tensile ductility compared to the coarse grained metals. In this work, the torsion properties of ECAP processed ultrafine grained pure 1070 aluminum were studied in a wide range of strain rates using both servohydraulic materials testing machines and Hopkinson Split Bar techniques. The material exhibits extremely high ductility in torsion and the specimens did not fail even after 300% of strain. Pronounced yield point behavior was observed at strain rates 500 s^{-1} and higher, whereas at lower strain rates the yielding was continuous. The material showed slight strain softening at the strain rate of 10^{-4} s^{-1}, almost ideally plastic behavior at strain rates between 10^{-3} s^{-1} and 500 s^{-1}, and slight but increasing strain hardening at strain rates higher than that. The tests were monitored using digital cameras, and the strain distributions on the surface of the specimens were calculated using digital image correlation. The strain in the specimen localized very rapidly after yielding at all strain rates, and the localization lead to the development of a shear band. At high strain rates the shear band developed faster than at low strain rates.

Introduction

Metallic materials can be distinguished into coarse grained, fine grained, ultrafine grained, and nanocrystalline depending on the average grain size. If the average grain size is larger than 1 μm, the material is either fine grained or coarse grained, the transition between these two being somewhere around 10 μm. Between 100 nm and 1 μm, the material is called ultrafine grained, and when the grain size is less than 100 nm, it is classified as a nanocrystalline material. Nanocrystalline and ultrafine grain size metals have many excellent properties compared to the coarse grained materials with the same chemical composition. For example, most metals with grain sizes in the nanocrystalline range show excellent strength, hardness, and fatigue properties as well as improved wear and corrosion resistance, in some cases combined with increased toughness even at low temperatures. Potential applicability of these materials is also wide, including aerospace applications, transportation, health care equipment and components, defense applications, and even implant technology due to the possibility of the high purity materials (i.e., even pure metals can exhibit substantial strength values when the grain size is small enough).

There are basically two main techniques to produce metals with grain sizes less than one micrometer; consol-

M. Hokka (✉) · J. Kokkonen · V.-T. Kuokkala (SEM member)
Department of Materials Science,
Tampere University of Technology,
P.O.B. 589, 33101 Tampere, Finland
e-mail: mikko.hokka@tut.fi

M. Hokka · J. Seidt (SEM member) · T. Matrka (SEM member) ·
A. Gilat (SEM member)
Department of Mechanical Engineering,
The Ohio State University,
Columbus, OH, USA

idating and sintering of metal powders, and severe plastic deformation. Sintering of metal powders, however, often produces porous microstructures with higher impurity content. Severe plastic deformation, on the other hand, can be used to produce nanocrystalline or ultrafine grain size metals from virtually any metal by simply applying extreme plastic strains on the existing coarse grained bulk material. One of the severe plastic deformation processes that have been successfully used to produce nanocrystalline and ultrafine grained materials is the Equal Channel Angular Pressing (ECAP). In the traditional ECAP, the material billet is pressed several times through the channels in the ECAP die. The ECAP die consists of input and output channels, which meet at an angle usually close to 90°. The material undergoes simple shear as the billet is pushed through the die and the strain accumulates during consecutive passes. Eventually, the high plastic shear strains will lead to refined microstructure and texture. Different kind of microstructures and textures can be manufactured by using different processing "routes", in which the billet is rotated between consecutive passes. In route C, the billet is rotated 180° between passes, while in route B_a the billet is rotated 90° between passes changing the direction of rotation from clockwise to counter-clockwise for each consecutive pass. In route Bc, the billet is rotated 90° in the same direction between passes. In route A, the billet is not rotated at all and each pass accumulates shear strain in the same direction. Route Bc has been found to produce the most equiaxed grain structure with the highest ratio of high-angle boundaries [1]. For a good review of the ECAP processes, see for example ref. [2].

The mechanical properties and behavior of most materials are strongly affected by the applied strain rate, temperature, and type of loading. For coarse grained metals, the strength usually increases with increasing strain rate, especially at strain rates around 10^3 s^{-1}, where a rapid increase in strength is often observed. At quasi-static and intermediate strain rates ($<\sim$500 s^{-1}), the deformation behavior of crystalline materials, such as coarse grained metals, is readily explained by the thermally activated dislocation motion. At higher strain rates ($>\sim$1,000 s^{-1}), the dislocation drag mechanisms start to control the deformation behavior, and usually the strength of the material increases dramatically as the mechanism changes. However, when the crystal size is decreased to nanometer scale, the movement of dislocations becomes increasingly difficult. At the moment, however, the strain rate dependent deformation and hardening mechanisms of nanocrystalline metals are not properly understood yet. May et al. [3] studied the strain rate sensitivity of coarse grained and ECAP processed ultrafine grained aluminum (AA1050) and found that the strain rate sensitivity in compression for the ultrafine grained grade was about 3.5 times higher than that

for the coarse grained material. The effect was even more clear at elevated temperatures, where the strain rate sensitivity factor, $m = \log(\sigma)/\log(\dot{\varepsilon})$, was as high as 0.25, which is ten times higher than that for the same coarse grained material. Also the strain hardening rate, $\theta = d\sigma/d\varepsilon$, is different for the ultrafine grained metals when compared to large grained metals. Kokkonen et al. [4] performed tension and compression tests at various strain rates and temperatures for ECAP processed AA1070 and found that the strain softening observed at low strain rates changes to strain hardening at high strain rates and/or low temperatures. The strain softening in ECAP processed aluminum at low strain rates has generally been attributed to dynamic recovery, which is reduced at low temperatures [1, 5].

Some materials such as the ECAP processed metals can show fairly poor ductility in tension, which is due to the low strain hardening capability and plastic instability of the material that occurs rapidly after the yielding. However, the material can still flow significantly in tension after the necking and the fracture strains can be fairly high. Therefore, the formability of ultrafine grained materials can still be very good as was shown by Sirivaraman and Chakkingal [6], who studied the deformability of ultrafine grained commercial purity aluminum by upsetting tests. Also, the instability and fracture that are observed in tension do not necessarily occur in the same way in shear, and the torsion deformation can continue to much higher strains before the final fracture of the material. Therefore, the torsion behavior often describes the overall formability of the material better than the results of a simple tension test, which are influenced also by the geometrical effects of the specimen. In this work, the torsion properties and behavior of ECAP processed 1070 aluminum were studied at a wide range of strain rates. In the tests, also high speed digital imaging and digital image correlation were used to obtain the strain distributions in the specimens.

Materials and Experiments

The material studied in this work was pure AA1070 (99.7 wt-% Al) aluminum. The material was processed at the Warsaw University of Technology by forcing 25*25*115 mm^3 billets through a two-turn ECAP die four times and rotating the billet 90° between the passes. The channels in the two-turn die make two 90° turns, so one pass effectively corresponds to two passes in a single turn die following the route C, and when the billets are rotated 90° between the passes, the route becomes C + B$_c$. The total accumulated strain after the ECAP processing was equivalent to about 9.4, leading to the average grain size around 750 nm. The grain size was determined from

transmission electron micrographs in a previous study [4]. The die construction, numerical simulations used for the optimization of the design, and the actual ECAP processing are presented in more details in refs. [7, 8]. In addition to the ultrafine grained AA1070 aluminum, some tests were also performed on a standard AA7075-T6 aluminum alloy for comparison.

The behavior of the studied ufg aluminum at different strain rates and temperatures has been previously characterized in tension and in compression [4, 9, 10]. In this study, the material properties were characterized in torsion using both a servohydraulic materials testing machine and a torsion Split Hopkinson Pressure Bar (SHPB) device with a pre-torque clamp-release system. The device used in this work is described in details in ref. [11].The SHPB device consists of 7/8 inch diameter aluminum alloy incident and transmitted bars, between which the thin-walled tube specimen is glued. The incident torsion pulse is generated by releasing a pre-stored torsion load from the free end of the incident bar. The pre-torque is applied by a hydraulic pulley and stored by clamping the incident bar at a suitable distance from the pulley. The clamp is held by a brittle(ish) aluminum pin, which can be rapidly broken by a second hydraulic press. When the pin is broken, the torsion pulse is released to propagate in the bar towards both the specimen and the pre-torque pulley. As the wave reaches the pulley, it is reflected back as a torsion wave with equal magnitude but opposite sign, which cancels the original pulse creating an incident pulse with a length equal to twice the distance from the clamp to the hydraulic pulley. As the incident wave reaches the specimen, part of it is reflected back as a wave of torsion with a sign opposite to the incident wave, and part of the incident wave is transmitted through the specimen into the transmitted bar deforming the specimen at a high rate. The time resolved load and strain history of the specimen can be calculated from the incident, reflected, and transmitted shear stress pulses using equations (1–3). In the current experimental setup, the stress pulses in the bars are measured at three strain gage stations, and the reflected stress pulse is calculated by applying appropriate time shifts to the measured signals. A more detailed description of the method can be found in ref [11]. Calculation of the stress, strain, and strain rate in the specimen can be done using all three stress pulses ('three wave' stress, strain, and strain rate), or the stress can be calculated from the transmitted pulse and strain and strain rate from the reflected pulse only ('one wave' stress, strain, and strain rate). In this study, the shear stresses were calculated using the transmitted wave only assuming stress equilibrium in the specimen, which is not necessarily the case in high strain rate tests. In the current work, however, the torques measured on the front and back sides of the specimens were identical from the very beginning of loading and therefore the use of the 'one wave' equations is well justified. Figure 1 shows schematically the high strain rate test setup, measured signals, and the incident, reflected and transmitted torques calculated from the measured signals.

$$\tau = \frac{T_c}{2\pi r_s^2 t_s} \tag{1}$$

$$\dot{\gamma} = \frac{r_s}{l_s}\left[\frac{1}{\rho Jc}\left[T_a(t-t_a) + T_a(t-t_a+2t_b) - T_b(t+t_b) - T_c(t+t_c)\right]\right] \tag{2}$$

$$\gamma = \int \dot{\gamma}\,dt \tag{3}$$

In equations (1–3), T_i is the torque in the bar measured with the strain gages at gage stations A, B and C, r_s, t_s, and l_s are the average radius, wall thickness, and gage length of the specimen, and ρ, J, and c, are the density, polar moment of inertia, and torsional wave speed of the stress bar. The time shifts $t_a=L_a/c$, $t_b=L_b/c$, and $t_c=L_c/c$ are the times required for the elastic wave to propagate the distance L_i from the specimen to the gage station A, B, and C, respectively.

The high rate torsion tests were monitored using two Photron Fastcam SA1.1 high speed cameras, whereas two Point Gray Research Grasshopper cameras with 2 megapixel resolution were used to monitor the low rate experiments. The cameras were viewing the specimen at different angles and synchronized to take images at the same time. VIC 3D image correlation software was used to calculate the full field strain distributions on the surface of the specimens as well as the displacements of the grip sections of the specimen, from which the average shear strain can also be calculated. The cameras were acquiring images at the frame rate of 125.000 s^{-1} in the high rate experiments and at frame rates between 0.1..19 s^{-1} in the low rate experiments, yielding about 150–400 image pairs for each test, which was found to be enough for construction of good quality stress-strain curves and for monitoring the shear band formation.

The thin walled torsion specimens were machined from rectangular bars for the ultrafine grained aluminum and from a standard 0.5 inch diameter round bar for the 7075-T6 aluminum alloy. The gage length of the specimens was 5.08 mm (0.2 in), the outer diameter 9.65 mm (0.38 in), and the wall thickness 0.38 mm (0.015 in) for the 7075 alloy. The dimensions were the same for the ultrafine grained specimens except for the wall thickness that was increased to 0.76 mm (0.03 in). Also specimens with the gage length of 2.54 mm (0.1 in) were used to achieve higher strain rates. The specimens were further
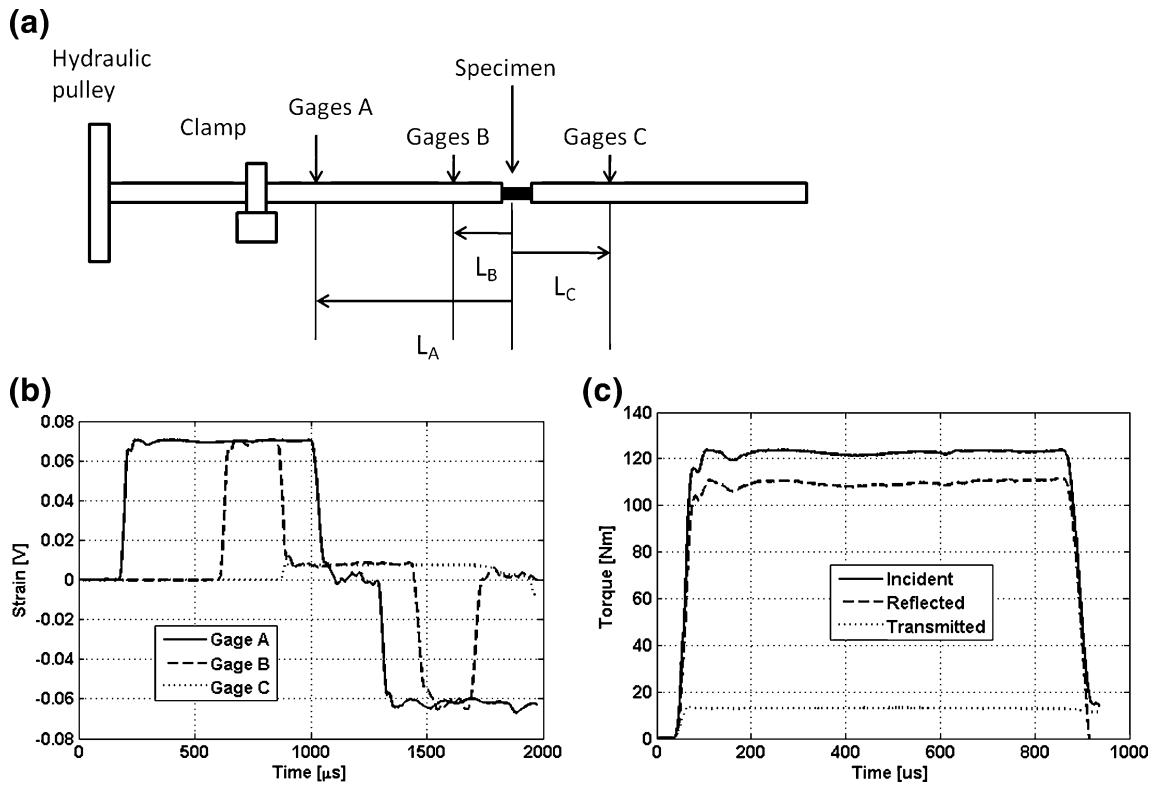
(a)

(b)

(c)

Fig. 1 (a) Schematic presentation of the test equipment, (b) example of measured signals, and (c) example of the stress pulses calculated from the measured signals

connected to aluminum adaptors, and the whole specimen adaptor assembly was glued to the ends of the stress bars of the Hopkinson Bar device or fixed to the hydraulic clamps of the servohydraulic materials testing machine. The adaptor has a negligible effect on the results, because the acoustic impedances of the bars and adaptors are essentially the same. The glue used for the high strain rate experiments was Loctite 480 cyanoacrylate based "superglue", but higher strength epoxy glue was required for the low strain rate tests due to the creep of the cyanoacrylate glue at longer test times. The effect of the glue on the mechanical properties measured in the tests is negligible as it only holds the specimen adaptor assembly together and firmly attached to the bars. Furthermore, the glue was not allowed to spread on the gage section of the specimen. The contrast pattern for photography was first applied by painting the gage section of the specimens and the adaptors with black base color, over which white speckles were hand painted for maximum contrast. However, it was soon noticed that the hand painted dots were too thick and broke off from the surface at fairly low strains. Even though white base color and spray painted black contrast pattern were found to have better adhesion to the surface, they still broke off at shear strains around

60%–90%. Therefore, the average strain on the specimen was finally calculated from the 3D displacements of the ends of the bars using equation (4)

$$\gamma = \frac{r_s \theta}{l_s} = \frac{r_s}{l_s} \arccos\left(\frac{\overline{a} \bullet \overline{b}}{\|a\| * \|b\|} \right) \qquad (4)$$

where r_s and l_s are the average radius and gage length of the specimen, θ is the angle of twist between the opposite ends of the specimen, and $\overline{a}$ and $\overline{b}$ are vectors from the centerline to the surface of the specimen at the opposite ends of the gage section. The optically measured strains and the shear stresses obtained from the stress bars were correlated using the incident stress pulse as a trigger signal for the optical measurement system.

Results and Discussion

Figure 2(a) shows the shear stress *vs.* shear strain curves at different strain rates for the ultrafine grained 1070 aluminum and Fig. 2(b) the corresponding curves for the 7075-T6 aluminum alloy. Different strain rates were achieved by varying the specimen gage length and the amplitude of the incident loading pulse. The strength
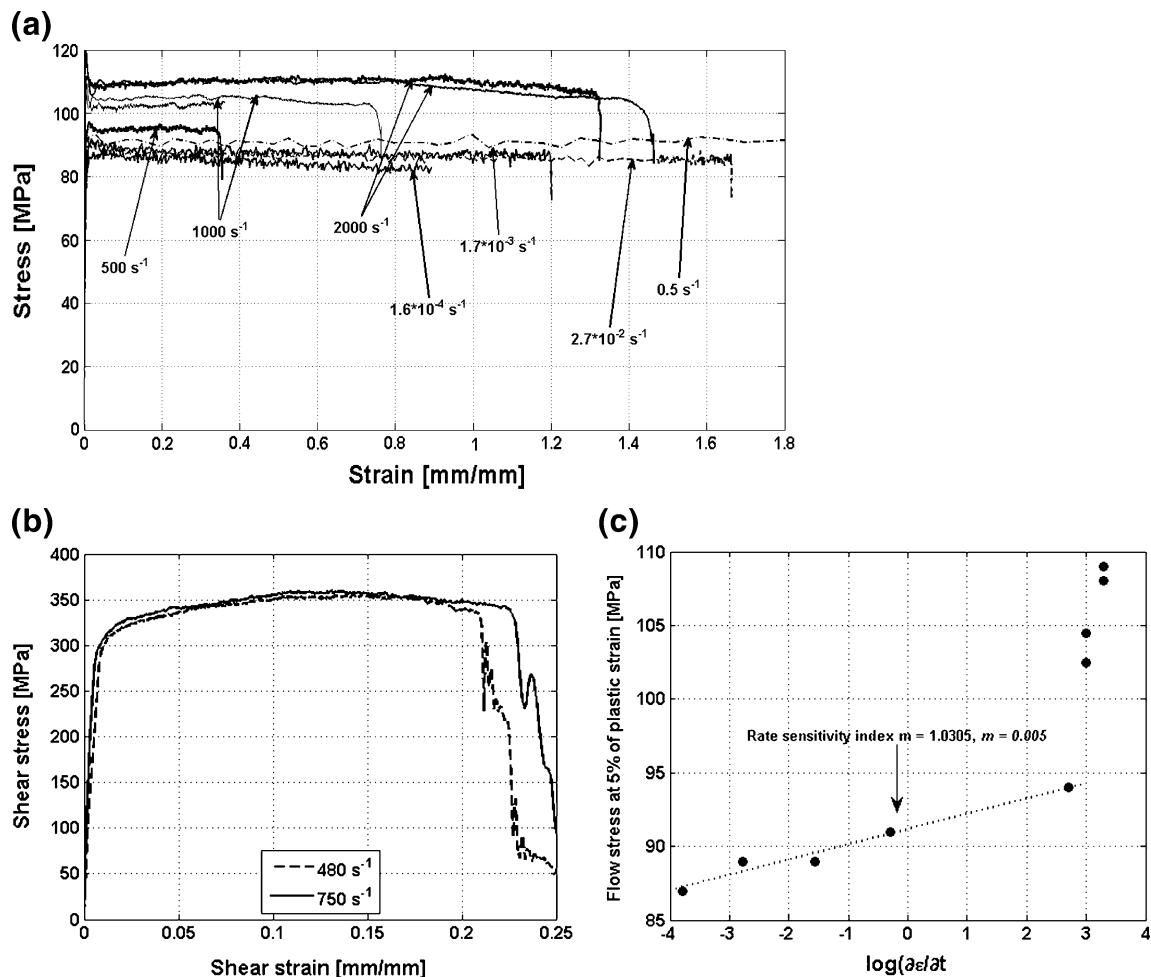
(a)

(b)

(c)

Fig. 2 Results from the torsion tests: (**a**) stress strain curves for the ultrafine grained pure 1070 aluminum, (**b**) stress strain curves for the 7075-T6 aluminum alloy, and (**c**) flow stress at 5% of plastic strain for the ultrafine grained aluminum as a function of logarithmic strain rate

levels for the 7075 alloy are naturally significantly higher than those measured for the ultrafine grained 1070 pure aluminum. However, the maximum strains are rather low for the 7075 aluminum alloy, whereas none of the ultrafine grained 1070 specimens failed in any of the tests, and shear strains of more than 300% were measured without fracture. At strain rates ~10^{-4} s^{-1}, the ultrafine grained material clearly softens with increasing strain, but when the strain rate is increased by a factor of ten, the strain softening is already reduced significantly. At strain rates from 10^{-3} s^{-1} to 10^{-2} s^{-1} the ultrafine grained material still softens in the beginning of the test, but above 20% of strain the material is almost ideally plastic. At the strain rate 0.5 s^{-1}, the behavior of the material is virtually ideally plastic without the previously seen softening in the beginning of the test. At higher strain rates, the yielding of the specimen is clearly different from that observed at low strain rates. At the strain rate of 500 s^{-1}, the yield point is clearly pronounced, and at the strain rate of

2,000 s^{-1}, the peak is already more than 10 MPa higher than the subsequent flow stress after a few percent of plastic strain. Also, the material slightly hardens with strain at the strain rate of 2,000 s^{-1} and shows a maximum flow stress at around 80%–100% of shear strain, after which the strength slightly decreases. The observed behavior resembles the behavior found for this material also in compression [4]. The strain softening at very low strain rates is most likely due to dynamic recovery, which is significantly reduced at higher strain rates and lower temperatures [1, 5], leading to slightly increasing strain hardening of the material. The pronounced yielding behavior, on the other hand, is most likely explained by the insufficiency of mobile dislocations in the initially heavily deformed material, leading to the observed increasing yield peak with increasing strain rates. It should, however, be noted that in the stress strain plots presented in Fig. 2 the strains are average values measured over the whole gage section. For the ultrafine grained

aluminum, the strain tends to localize very rapidly, and therefore the average strain does not represent the true behavior of the material quite correctly. This is also one of the reasons why digital image correlation was used in this study.

Figure 2(c) shows the flow stress at 5% of plastic strain for the ultrafine grained 1070 aluminum. In the low strain rate region, the flow stress steadily increases from 87 MPa to 94 MPa, and the absolute strain rate sensitivity factor, $m = \Delta\sigma/\Delta\log(\dot{\varepsilon})$, and the relative strain rate sensitivity factor, $m = \Delta\log(\sigma)/\Delta\log(\dot{\varepsilon})$, have values of 1.0305 MPa and 0.005, respectively. The values measured in this study for torsion are somewhat lower than those presented by Kokkonen et al. [12] and Kuokkala et al. [10] in compression and tension for the nominally same ultrafine grained 1070 aluminum. However, the differences are small and can most likely be explained by slight differences in the grain size refinement processes between individual billets, leading to slightly different microstructures, such as grain size distribution, texture, and length-to-width ratio of the grains.

Figure 3 shows the image correlation results for a torsion test of an ultrafine grained 1070 aluminum sample at the strain rate of $1.6 \ 10^{-4} \ \mathrm{s}^{-1}$. At the very early stages of the test [Fig. 3(a)], both ends of the specimen are nearly undeformed and the yielding starts rather uniformly in the middle of the gage section but then rapidly localizes to the right side of the gage section. The maximum strain is around 6% of Lagrange shear strain $(\varepsilon_{xy} = 1/2 * \gamma)$, whereas most of the gage section is still at around 2%–3% of Lagrange strain. In Fig. 3(b), the localization is more clearly visible, showing a maximum Lagrange shear strain of 10%, while the surrounding regions still remain at around 6%–7%. However, the shear band does not extend over the whole gage section until at much higher strains. Figure 3(c) shows the fully developed shear band in the middle of the gage section with a maximum Lagrange shear strain around 50%, while the surrounding areas remain closer to 35%. The behavior does not change much in the other low rate experiments, which can be seen in Fig. 4, where similar pictures taken from a test performed at the strain rate of $0.5 \ \mathrm{s}^{-1}$ are shown. The yielding starts this time from the
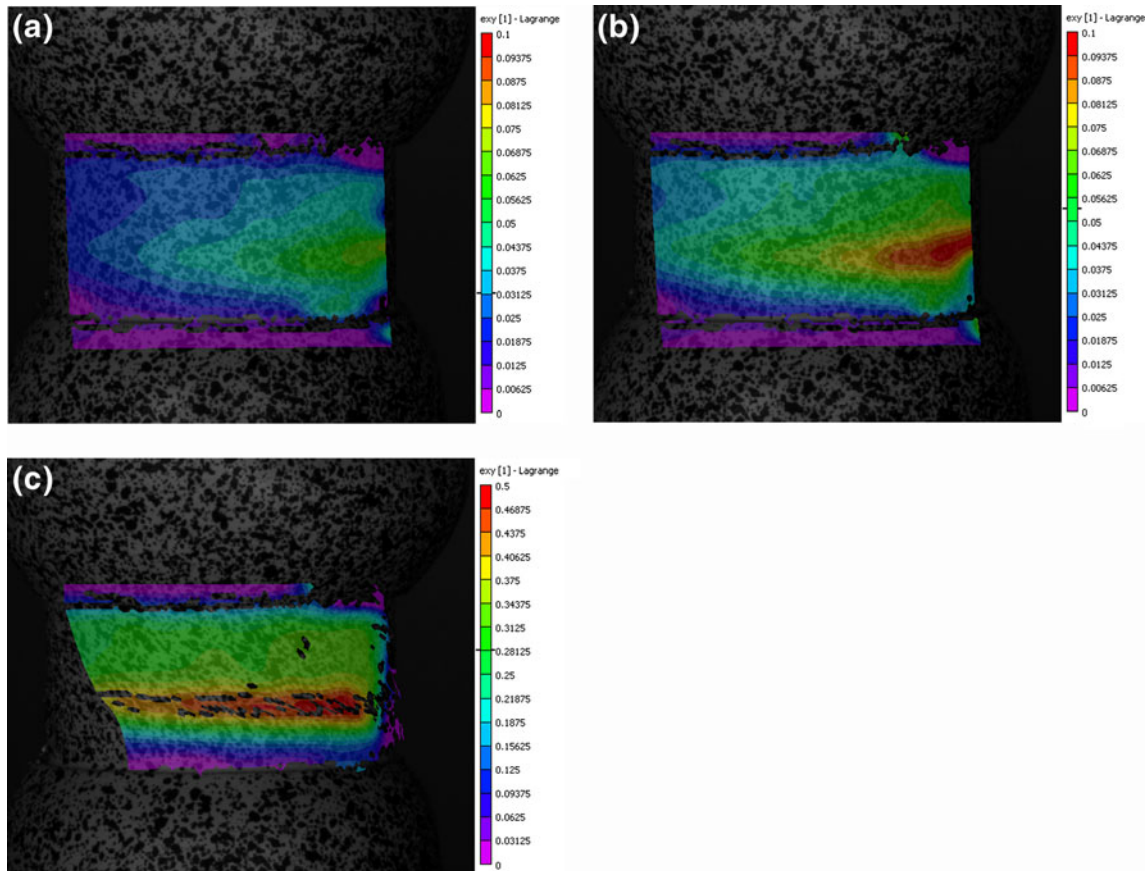

Fig. 3 Localization of strain in a torsion test at the strain rate of $1.6 \ 10^{-4} \ \mathrm{s}^{-1}$: (**a**) strains just after yielding ($\varepsilon_{ave} \sim 2\%$), (**b**) a developing shear band ($\varepsilon_{ave} \sim 15\%$), and (**c**) a fully developed shear band ($\varepsilon_{ave} \sim 30\%$)
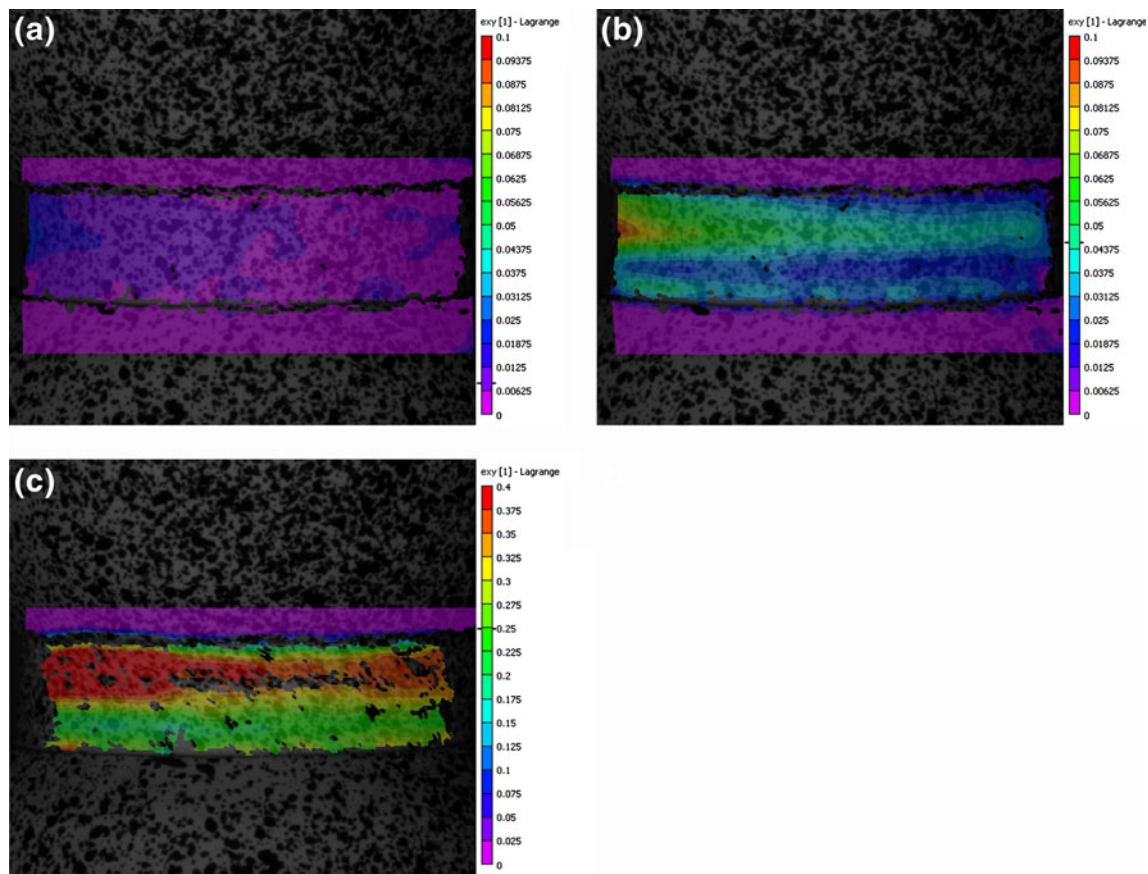
Fig. 4 Localization of strain in a torsion test at the strain rate of 0.5 s^{-1}: (**a**) strains just after yielding ($\varepsilon_{ave} \sim 2\%$), (**b**) a developing shear band ($\varepsilon_{ave} \sim 15\%$), and (**c**) a fully developed shear band ($\varepsilon_{ave} \sim 30\%$)

left hand side and localizes rapidly only after a few percent of strain. The shear band develops, and in Fig. 4 (b) it already extends across the whole gage section but still shows a clear maximum on the left hand side with strains up to 10%. The right hand side is still at only 5% of strain, and the regions outside the shear band at around 2%–3%. At later stages, the shear band develops further and the strain increases more rapidly within the shear band, while other regions experience much less strain. Figure 4(c) shows a fully developed shear band with twice as much strain compared to the surrounding regions.

The development of the shear band clearly changes when the strain rate is further increased. Figure 5 shows the development of a shear band at the strain rate of 1,000 s^{-1}. Also at this strain rate the strain localizes already after the first few percent of Lagrange shear strain, but the localization zone is much narrower and extends through the gage section already at very low strains. Figure 5(a) shows the early stages of the test, where the strain has already localized and the shear band extends through the entire gage section. The strain in the localized region is around 3%–4%, whereas in the

surrounding regions it is only 0%–2%. The shear band develops fast and the localization continues throughout the test, as shown in Fig. 5(b) and (c). This type of behavior was observed in all high strain rate tests. It should be noted, however, that despite the localization of strain and the development of the shear band, the strain also increases in the surrounding regions throughout the test at all strain rates. This means that the material in the shear band must show some strain hardening at all strain rates and that it is high enough to compensate for the thermal softening taking place in the shear band, which at high strain rates and high strains can be quite significant.

The more rapid development of the shear band at high strain rates could simply be explained by the adiabatic heating and consequent thermal softening of the material. However, the shear band extends through the gage section almost immediately after yielding, and therefore the thermal softening alone cannot contribute enough to the development of the shear band. The faster development of the shear band is most likely related to the different yield behavior of the material at higher strain rates. The pronounced yielding of utrafine grained metals is usually explained by the lack
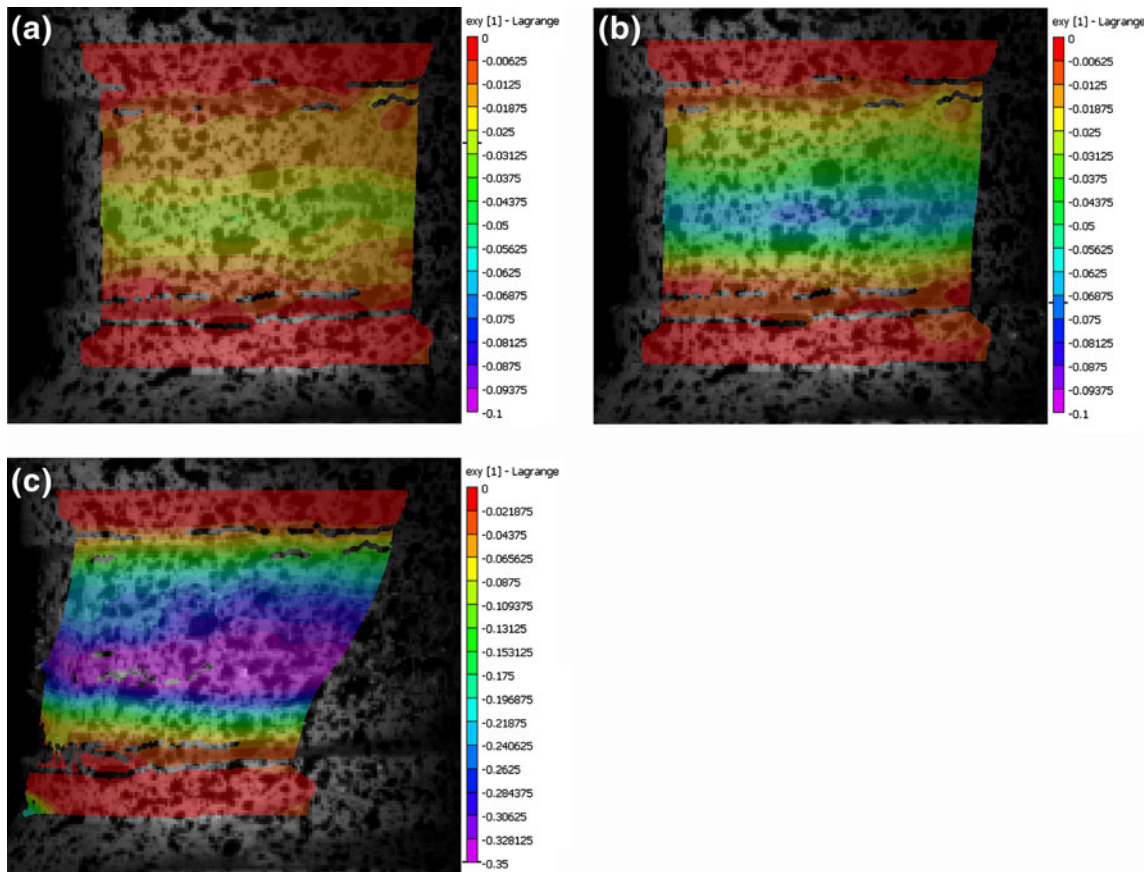
Fig. 5 Localization of strain in a torsion test at the strain rate of 1,000 s^{-1}: (**a**) strains just after yielding ($\varepsilon_{ave}\sim$2%), (**b**) a developing shear band ($\varepsilon_{ave}\sim$15%), and (**c**) a fully developed shear band ($\varepsilon_{ave}\sim$30%). Notice the opposite direction of rotation compared to Figs. 2 and 3

of mobile dislocations that causes the remaining free dislocation to move faster in the beginning of the test [3], thus requiring a higher stress. Therefore it is possible that the avalanche of gliding dislocations that follows the break-up of pinned dislocations causes faster localization of strain due to the very high local deformation rates and consequent thermal softening.

From the digital image correlation results it is very clear that the average strain calculated from the displacements of the ends of the bars does not represent the behavior of the material very well, as strain localizes very rapidly already during the first few percent of deformation. The maximum strain in the shear band can be more than twice as high as in the surrounding regions of the gage section. However, the problems with the adhesion of the contrast pattern currently limits the usable range of digital image correlation to about 60%–100% of shear strain.

Summary

The behavior and properties of pure 1070 aluminum were characterized in a wide range of strain rates in torsion. Thin-walled tube specimens were machined from ECAP processed 1070 aluminum and tested using a conventional servohydraulic materials testing machine at low strain rates and the Hopkinson Split Bar technique at high strain rates. A pronounced yielding behavior was observed at strain rates 500 s^{-1} and above. At low strain rates the material showed either slight strain softening or almost ideally plastic behavior. At higher strain rates the strain hardening rate showed an increase with increasing strain rate. The material was found to be well deformable in torsion, exhibiting shear strains over 300% without failure.

The tests were also monitored using digital cameras to facilitate the calculation of local strains on the surface of the specimen during deformation. During the tests, deformation localized very rapidly and a shear band formed across the gage section of the specimen. At low strain rates, however, the development of the shear band was slower and the band nucleated and grew from one side of the specimen and only then propagated through the gage section. At higher strain rates, the formation of the shear band was much faster and the band extended over the whole gage section almost immediately after yielding.

References

1. El-Danaf E, Soliman M, Almajid A, El-Rayes M (2007) Enhancement of mechanical properties and grain size refinement of commercial purity aluminum 1050 processed by ECAP. Mater Sci Eng A 458:226–234
2. Valiev R, Langdon T (2006) Principles of equal-channel angular pressing as a processing tool for grain refinement. Prog Mater Sci 51:881–981
3. May J, Höppel H, Göken M (2005) Strain rate sensitivity of ultrafine-grained aluminum processed by severe plastic deformation. Scr Mater 53:189–194
4. Kokkonen J, Kuokkala V-T, Olejnik L, Rosochowski A (2008) Dynamic behavior of ECAP processed aluminum at room and sub-zero temperatures. In: The Proceedings of the Annual SEM Conference, Orlando FL
5. El-Danaf E (2008) Mechanical properties and microstructure evolution of 1050 aluminum severely processed by ECAP to 16 passes. Mater Sci Eng A 487:189–200
6. Sivaraman A, Chakkingal U (2008) Investigations on workability of commercial purity aluminum processed by equal channel angular pressing. J Mater Process Technol 202:543–548
7. Rosochowski A, Olejnik L (2002) Numerical and physical modeling of plastic deformation in 2-turn equal angular extrusion. J Mater Process Technol 125–126:309–316
8. Olejnik L, Rosochowski A (2005) Methods of fabrication metals from nano-technology. Bull Pol Acad Sci Tech Sci 53:413–423
9. Kokkonen J, Kuokkala V-T, Seidt J, Walker A, Gilat A, Olejnik L, Rosochowski A (2009) High strain rate deformation analysis of UFG aluminum sheet samples. In: The Proceedings of the Annual SEM Conference, Albuquerque NM
10. Kuokkala V-T, Kokkonen J, Song B, Chen W, Olejnik L, Rosochowski A (2008) Dynamic responce of severe plastic deformation processed 1070 aluminum at various temperatures. In: The Proceedings of the Dymat Technical Meeting, Bourges, France
11. Gilat A (2000) Torsional Kolsky bar testing. ASM Handbook, 8, Materials Park, Ohio, USA
12. Kokkonen J, Kuokkala V-T, Isakov M (2009) Dynamic behavior of UFG aluminum at a wide range of strain rates and temperatures in compression and tension. J Phys IV 1:647–653

TAMPEREEN TEKNILLINEN YLIOPISTO

MIMMI VIHERKOSKI
METALLIEN SPD-PROSESSOINTI, MIKRORAKENTEET JA OMINAISUUDET
Kandidaatintyö

Tarkastaja: yliassistentti Mikko Hokka

Tarkastaja ja aihe hyväksytty

TIIVISTELMÄ

Metallin raekoon ja lujuuden välinen yhteys ilmaistaan tyypillisesti Hall-Petch -yhtälöllä, joka osoittaa, että metallin lujuus useimmiten kasvaa raekokoa pienentämällä. Perinteisessä metallurgiassa metallien raekokoa pienennetään termomekaanisilla käsittelyillä, joilla saavutettavat raekoot ovat tyypillisesti muutamia mikrometrejä. Lujempien materiaalien valmistamiseksi on kehitetty plastiseen muodonmuutokseen pohjautuvia SPD-menetelmiä (severe plastic deformation), joilla saadaan tuotettua UFG-metalleja (ultrafine-grained), joiden keskimääräinen raekoko on alle 1 µm.

Yksi tyypillisimmistä SPD-menetelmistä on metallien extruusiota muistuttava ECAP-menetelmä (equal channel angular pressing), jossa metallikappale puristetaan ECAP-muotin läpi. Prosessoinnin aikana kappaleeseen kohdistuu erittäin suuria jännityksiä, jotka johtavat suuriin plastisiin muodonmuutoksiin, joiden vaikutuksesta prosessoidun kappaleen raekoko pienenee ja dislokaatiotiheys kasvaa. Käytännössä tämä johtaa materiaalin lujittumiseen. Materiaalin lujittuessa sen muovattavuus kuitenkin pienenee.

Kappaleen lopulliseen mikrorakenteeseen ja sitä kautta sen ominaisuuksiin on mahdollista vaikuttaa prosessiparametreja muuttamalla. Tässä työssä on tutkittu kirjallisuudessa esitettyjen havaintojen pohjalta prosessointireitin, muotin kanavakulman, muotin ulkopinnan kaarevuuskulman, puristusnopeuden, lämpötilan ja kokonaismyötymän vaikutuksia ECAP-prosessoitujen metallien ominaisuuksiin. Kokonaismyötymä vastaa 90° kanavakulmaisessa muotissa suurin piirtein läpäisyjen lukumäärää.

Prosessiparametreista prosessointireitti, muotin kanavakulma ja kokonaismyötymä vaikuttavat selvästi eniten syntyvään mikrorakenteeseen ja lopullisiin ominaisuuksiin.

ALKUSANAT

Tämä kandidaatintyö on tehty osana tekniikan kandidaatin tutkintoa Tampereen teknillisen yliopiston materiaalitekniikan laitokselle. Työssä ohjaajanani toimi yliassistentti Mikko Hokka. Haluan kiittää häntä kärsivällisyydestä sekä korvaamattomasta avusta tämän pitkän kirjoitusprosessin aikana. Lisäksi haluaisin kiittää vanhempiani minun tukemisestani ja kannustamisestani. Omistan tämän työn edesmenneelle isälleni.

Tampereella 20.11.2009

Mimmi Viherkoski

SISÄLLYS

LYHENTEET JA TERMIT

d	Rakeen halkaisija
k_y	(Myötämisen) vakio Hall-Petch -yhtälössä
N	Läpäisyjen lukumäärä
ε_N	Kokonaismyötymä
ψ	ECAP-muotin ulkopinnan kaarevuuskulma
Φ	ECAP-muotin kanavakulma
σ_0	Vakio Hall-Petch -yhtälössä
σ_y	Myötölujuus
ARB	Accumulative roll bonding
C2S2	Continuous confined strip shearing
DCAP	Dissimilar channel angular pressing
ECAP	Equal channel angular pressing
ECAR	Equal channel angular rolling
HPT	High pressure torsion
SPD	Severe plastic deformation
UFG	Ultrafine grain size

1.   JOHDANTO

Metallimateriaalien mekaanisiin ominaisuuksiin vaikuttaa hyvin monta tekijää, joista raekoko on yksi tärkeimmistä [1]. Raekokoa pienentämällä voidaan kasvattaa metallin lujuutta. Raekoon ja metallin lujuuden välistä yhteyttä kuvastaa Hall-Petchin yhtälö (1) [1].

$$\sigma_y = \sigma_0 + \frac{k}{\sqrt{d}} \qquad\qquad (1)$$

Yhtälössä σ_y on myötölujuus, σ_0 ja k vakioita sekä d raekoon halkaisija.

Perinteisen metallurgian termomekaanisilla menetelmillä tuotettujen metallien raekoot ovat tyypillisesti muutamien mikrometrien luokkaa [2]. Pyrkimys yhä lujempien metallien tuottamiseen on johtanut uusien raekokoa pienentävien menetelmien kehittämiseen. SPD-menetelmillä on mahdollista valmistaa materiaaleja, joiden keskimääräiset raekoot ovat jopa nanometritasolla [1]. Näistä materiaaleista käytetään nimitystä UFG (ultrafine-grained) eli ultrahienoraemateriaali.

UFG-rakenteen aikaansaamiseksi tulee materiaalissa tapahtua tiettyjä muutoksia. Materiaalin dislokaatiotiheys kasvaa ja raekoko pienenee, kun kappaleeseen kohdistetaan erittäin suuri plastinen muodonmuutos [1]. Suurin lujuus saavutetaan, kun raerajat ovat suuren kulman raerajoja, jolloin hilatasojen välinen orientaatio on suuri [1]. Pienen raekoon lisäksi tavoitellaan myös homogeenista mikrorakennetta, joka pystytään saavuttamaan sopivilla prosessointiparametrien valinnoilla.

Lukuisista tieteellisistä ja teknologisista syistä johtuen SPD-menetelmiä ei vielä ole otettu teollisuudessa laajalti käyttöön [3]. Teollisuudessa ei useista tutkimuksista huolimatta edelleenkään tiedetä tarpeeksi UFG-materiaaleista, niiden eduista ja ongelmista. Lisäksi teollisuudelle ei pystytä tuottamaan sopivan kokoisia UFG-näytekappaleita kokeiltavaksi, eikä vielä ole selvää mikä SPD-menetelmistä olisi sopivin teollisuuden käytettäväksi.

Muutamia käytännön sovelluksia kuitenkin on. Esimerkiksi lentokone- ja autoteollisuudessa käytetään ECAP-prosessoituja titaanipultteja [3]. Azushima et al. [3] mukaan myös sputterointitauluja valmistetaan UFG-metalleista. Lisäksi ECAP-prosessoiduista metalleista titaania hyödynnetään biolääketieteessä implanttimateriaalina [4]. Latysh et al. [4] mukaan ECAP-prosessoitu titaani on riittävän lujaa korvatakseen hieman myrkyllisiä atomeja sisältävän perinteisen Ti-6Al-4V -seoksen käytön implanttimateriaalina.

2. SPD-MENETELMÄT

Perinteisessä metallurgiassa on käytetty termomekaanisia käsittelyjä sekä seostamista raekoon pienentämiseksi [2]. Termomekaanisella käsittelyllä tarkoitetaan materiaalin muovaamista korotetussa lämpötilassa tiettyjen ominaisuuksien aikaansaamiseksi. Tyypillisesti termomekaanisilla käsittelyillä pyritään hienontamaan syntyvää mikrorakennetta ja erityisesti pienentämään raekokoa, jolloin materiaalin lujuus kasvaa ilman materiaalin merkittävää sitkeyden alenemista tai haurastumista. Esimerkkejä termomekaanisista käsittelyistä ovat muun muassa erilaiset kuumavalssaustekniikat [5]. Metallirakenteeseen lisätään usein seosaineiksi titaania ja niobia. Näitä aineita kutsutaan mikroseosaineiksi ja niitä käytetään hillitsemään rakeenkasvua [6].

Karkearakeiset materiaalit on mahdollista muuntaa ultrahienorakeisiksi UFG-materiaaleiksi kohdistamalla todella suuri plastinen muodonmuutos näihin kappaleisiin. Perinteiset termomekaaniset käsittelyt ovat tässä suhteessa ongelmallisia, sillä niiden aiheuttama kokonaismyötymä on rajallinen. Lisäksi käsittelyissä käytetään usein liian alhaista lämpötilaa, jolloin työstettävyys jää vähäisemmäksi ja aikaansaatu muodonmuutos riittämättömäksi UFG-mikrorakenteen muodostumiselle [2]. Näistä syistä on kehitelty uusia menetelmiä, SPD-menetelmiä, joissa edellä mainittuja ongelmia ei esiinny.

SPD-menetelmissä työkappaleeseen kohdistetaan erittäin suuri jännitys ja muodonmuutos, jonka seurauksena kappaleen raekoko pienenee merkittävästi. SPD-menetelmien käytön tavoitteena on valmistaa monikiteisiä materiaaleja tai kappaleita, joiden raekoko on alle 1 μm [1]. SPD-prosesseissa tällainen UFG-mikrorakenne saadaan aikaan ilman ulkoisten dimensioiden muuttumista. Menetelmien etuna voidaan pitää myös lopullista rakennetta, joka käsittelyn jälkeen on erittäin tiivis. Lisäksi SPD-menetelmiä käyttämällä on mahdollista tiivistää kiinteitä kappaleita erilaisista jauheista.

2.1. Yleistä SPD-menetelmistä

SPD-menetelmiä käytetään raekoon pienentämiseksi jopa nanometritasolle. Tämä tulos saavutetaan kohdistamalla työkappaleeseen riittävän suuri plastinen muodonmuutos, jotta materiaalissa olevien dislokaatioiden esiintymistiheyttä voitaisiin kasvattaa. Lisäksi näiden dislokaatioiden on järjestäydyttävä uudelleen, jotta saataisiin suuri joukko raerajoja.

UFG-materiaalien valmistukseen on olemassa kaksi erityyppistä lähestymistapaa [1]. "Bottom-up" -menetelmässä UFG-materiaaleja valmistetaan tiivistämällä nanopartikkelijauheista makroskooppisia kappaleita, jotka sintrataan korotetussa lämpötilassa. Nämä menetelmät soveltuvat ainoastaan melko pienten kappaleiden

valmistukseen, ja valmiit kappaleet sisältävät lähes aina huokoisuutta ja pieniä pitoisuuksia epäpuhtauksia. "Top-down" -menetelmässä isorakeinen bulkkikappale altistetaan suurelle jännitykselle tai äkkikuormitukselle. Tämän menetelmän ehdoton etu on mahdollisuus soveltaa sitä laajaan joukkoon metalliseoksia.

2.2. Equal Channel Angular Pressing (ECAP)

Perinteisen ECAP-menetelmän esitteli ensimmäisen kerran tohtori Vladimir Segal työtovereineen Minskin tutkimuslaitoksella vuonna 1977 [1,3]. Tämän jälkeen on kehitetty useita edistyneempiä samantyyppisiä menetelmiä.

2.2.1. Yleistä

ECAP-laitteisto koostuu muotista, jonka sisällä on ontto, poikkileikkauspinnoiltaan yhtä suuri kanava, joka kaartuu kuvan 1 mukaisesti. Kuvassa 1 kulma Φ on kahden kanavan välinen kulma ja kulma ψ kuvaa kanavien risteyskohdan kaarevuutta.
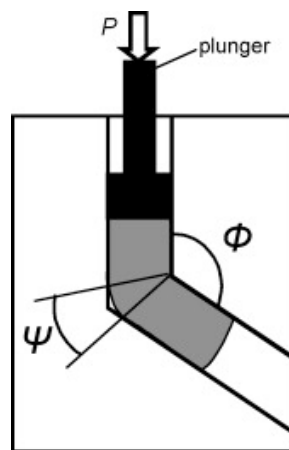
Kuva 1. *ECAP-menetelmä kaavamaisesti esitettynä* [3].

Perinteisessä ECAP-menetelmässä muokattava tanko, levy tai palkki työstetään aluksi kanavaan sopivaksi. Tämän jälkeen kappale puristetaan kanavan läpi paineella P käyttäen apuna mäntää (plunger). Menetelmän käyttö ei muuta työkappaleen ulkoisia poikkileikkauspintoja, toisin kuin perinteisten termomekaanisten menetelmien käyttö, joita käytettäessä jokaisen läpimenokerran jälkeen työkappaleen ulkomitat ovat muuttuneet. ECAP-menetelmää voidaan käyttää periaatteessa myös suurille bulkkikappaleille, sillä ainoastaan muotin ja kanavan koko rajoittavat työstettävän kappaleen mittoja. [1] Käytännössä materiaalin muodonmuutoskyky, muut mekaaniset ominaisuudet ja perusominaisuudet, kuten kiderakenne ja pinousvikaenergia, vaikuttavat merkittävästi ECAP-menetelmän soveltuvuuteen ja syntyviin mikrorakenteisiin sekä saattavat usein rajoittaa käytettävää kappalekokoa.

Perinteiseen ECAP-menetelmään liittyy neljä erilaista prosessointireittiä, joita sovelletaan, kun kappale puristetaan toistuvasti muotin läpi [2]. Reittiä A käytettäessä

työkappale puristetaan joka kerta täsmälleen samalla tavalla, ilman rotaatiota käsittelykertojen välillä. Kun käytetään reittiä B_A, kappaletta käännetään 90° vuoroittaisiin suuntiin käsittelykertojen välillä. Reitti B_C on hyvin samankaltainen reitin B_A kanssa, sillä erotuksella, että tätä reittiä käytettäessä 90° rotaatio toteutetaan aina vastapäivään. 180° rotaatio käsittelykertojen välillä tehdään, kun käytetään reittiä C. Lisäksi on kehitetty edellä mainittujen reittien yhdistelmiä, joista tutkituimpia ovat yhdistelmäreitit B_A-A ja B_C-A. Käytetyllä prosessointireitillä on suuri vaikutus muodostuvaan mikrorakenteeseen, esimerkiksi saavutettuun raekokoon ja syntyvään tekstuuriin [7].

2.2.2. ECAP-sovelluksia

Perinteisen ECAP-prosessin lisäksi on kehitetty lukuisia muita ECAP-menetelmiä. Moni menetelmä on kehitetty paikkaamaan perinteisen ECAP-menetelmän puutteita, esimerkiksi heikkoa automatisoitavuutta.

Azushima [3] kehitti ECAP-menetelmän (repetetive side extrusion process with back pressure), jossa kappale työnnetään nelisakaraiseen onttoon muottiin, jonka kaksi sakaraa ovat kiinteitä. Kaksi muuta sakaraa ovat liikkuvia ja työntävät vuorotellen paineen vaikutuksesta kappaletta edestakaisin keskellä muottia. Tämän menetelmän etuna on sen automatisoitavuus, sillä koko prosessi on ohjattavissa tietokoneella. Toinen samantyyppinen on ECAP-menetelmä, jossa käytetyn muotin kanavassa on kaksi tai useampi kulma (multiple turn ECAP) [1,3]. Tällöin prosessissa saavutettava muodonmuutos kasvaa ja ECAP-menetelmän tehokkuus kasvaa. Tämänkin menetelmän ohjaus on automatisoitavissa.

Hiljattain on kehitetty myös valssaukseen perustuvia ECAP-menetelmiä, joita ovat muun muassa C2S2- (continuous confined strip shearing), DCAP- (dissimilar channel angular pressing) ja ECAR- (equal channel angular rolling) menetelmät [1]. Menetelmissä ohut metalliliuska syötetään kahden rullan väliin (guide roll, feeding roll) ja puristetaan ulos kahden muotin välisestä ohuesta kanavasta (outlet channel). Näillä menetelmillä voidaan valmistaa ohutta levyä jatkuvalla tuotannolla.
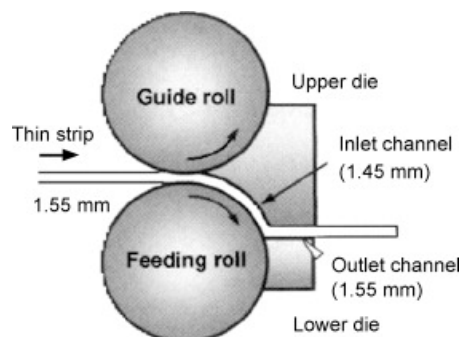

Kuva 2. *DCAP-menetelmä* [1].

DCAP-menetelmä eroaa muista ECAP-menetelmistä, sillä siinä käytetty kanava ei ole kauttaaltaan tasapaksu [1].

2.3.   Accumulative Roll Bonding (ARB)

ECAP-menetelmä on SPD-menetelmistä käytetyin ja sovelletuin [8]. ECAP-menetelmien lisäksi on kuitenkin kehitetty muita erilaisia SPD-menetelmiä, joiden tarkoituksena on myös valmistaa materiaaleja, jotka ovat mikrorakenteeltaan hienorakeisia. Näitä prosesseja on kehitetty, sillä ECAP-menetelmien haittapuolia ovat niissä käytetyt valmistuskustannuksiltaan kalliit koneet, joita tarvitaan tuottamaan suuria kuormia [8]. Lisäksi kappaleiden valmistuksessa käytettävät muotit ovat usein kalliita tehdä. Myös ECAP-menetelmien tuottavuus on melko alhainen.
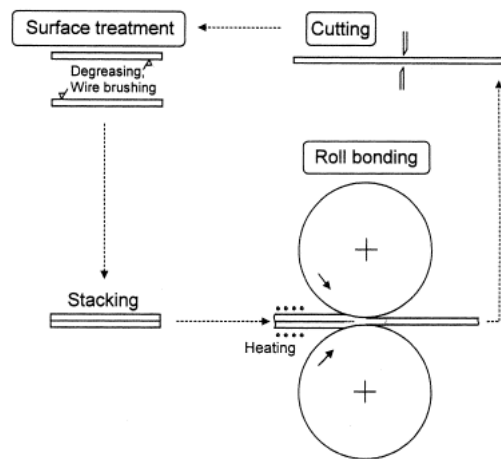
Kuva 3. *ARB-prosessi* [8].

Eräs uudemmista kehitetyistä menetelmistä on ARB (kuva 3), joka on kehitetty korvikkeeksi juuri ECAP-menetelmille [3]. ARB-prosessi aloitetaan kahden ohuen levyn pintakäsittelyllä, jotta näiden sidoslujuusominaisuudet paranisivat. Sitten nämä levyt pinotaan täsmällisesti. Tämän jälkeen pinotut levyt lämmitetään ja liitetään yhteen valssaamalla. Lopuksi yhteen liitetty levykappale halkaistaan kahteen yhtä pitkään osaan ja toistetaan koko prosessi alusta.

ARB-menetelmiä käytettäessä lämpötilan merkitys on erittäin suuri. Mikäli käsittely suoritetaan liian alhaisessa lämpötilassa, saattaa tuloksena olla riittämättömät sitkeys- ja liitoslujuusominaisuudet [8]. Korotettu lämpötila on siis oleellista käsittelyn onnistumiseksi, mutta lämpötila ei kuitenkaan saa nousta yli rekristallaatiolämpötilan, sillä näin korkeissa lämpötiloissa käsittelyn vaikutus kumoutuu. Homologisen lämpötilan ollessa alle 0.5 on mahdollista aikaansaada hyvä ja puhdas liitos siten, että materiaalin paksuus vähenee yli 50 %.

ECAP-menetelmien tapaan oleellista ARB-prosessoinnissa on toistettavuus [3]. Ensimmäisellä valssauskerralla saatava mikrorakenne ei vielä ole riittävän

homogeeninen. Useimmiten tarvitaan muutama, noin viisi läpivalssauskertaa ennen kuin saadaan tarpeeksi homogeeninen mikrorakenne, josta erottuvat ohuet ja pitkulaiset rakeet.

2.4. High Pressure Torsion (HPT)

Kun HPT-menetelmiä kehitettiin, syntyi aluksi menetelmä, jossa pieneen renkaaseen kohdistettiin voimia jokaisesta suunnasta (ring tension device) [3]. Näin luotiin hydrostaattista painetta vastaava tila. Myöhemmin on kehitetty omat menetelmät sekä levymäisille että bulkkikappaleille.

Levymäisen kappaleen muokkaukseen käytetyssä disc-HPT -menetelmässä ohut levymäinen kappale puristetaan kovalla paineella muottiin [3]. Mäntä aiheuttaa vääntömomentin, joka kohdistuu muottiin, jonka kanssa levyllä on kitkaa. Levymäisen kappaleen muokkauksen haittapuolena on epähomogeeninen mikrorakenne, joka muodostuu käsittelyn aikana. Lisäksi menetelmää voidaan soveltaa ainoastaan erittäin ohuille ja tasapintaisille levyille.

Bulkkimaisille kappaleille on kehitetty oma HPT-menetelmänsä, joka toimii samalla periaatteella kuin disc-HPT [3]. Bulkkikappale asetetaan sopivan muotin sisään, ja muottiin kohdistetaan kova paine ja rotaatioliike. Muotin ja bulkkikappaleen välinen kitka aiheuttaa vääntöä itse kappaleessa, jolloin sen mikrorakenne muuttuu. Tätä menetelmää kutsutaan nimellä bulk-HPT.

3. MIKRORAKENNE JA MEKAANISET OMINAISUUDET

Perinteisillä termomekaanisilla menetelmillä pystytään tuottamaan hienorakeisia metallimateriaaleja, joiden minimiraekoot tyypillisesti ovat muutamien mikrometrien tasolla. SPD-menetelmillä prosessoidut materiaalit ovat niin sanottuja ultrahienorakeisia UFG-materiaaleja, joiden keskimääräinen raekoko on alle mikrometrin.

Lopullinen mikrorakenne riippuu muun muassa käytetystä menetelmästä, useista prosessiparametreista sekä materiaalin koostumuksesta. Puhtaille metalleille ja metalliseoksille SPD-prosessoinnin vaikutukset eroavat toisistaan. Tässä työssä keskitytään SPD-prosessoinnin aikaansaamiin mikrorakenteisiin ja mekaanisiin ominaisuuksiin puhtaissa metalleissa.

Yleisesti puhtailla metalleilla ECAP-prosessoinnin jälkeinen keskimääräinen raekoko vaihtelee välillä 200 – 300 nm [9]. Parempia tuloksia saadaan HPT-menetelmällä, jolloin keskimääräiset raekoot ovat luokkaa 50 – 150 nm. Raekoon ja mikrorakenteen muodostumiseen vaikuttavat kuitenkin useat eri tekijät, joita seuraavaksi käsitellään yksitellen.

Kun SPD-prosessointi muokkaa työstettävän kappaleen mikrorakennetta, samalla muuttuvat myös kappaleen mekaaniset ominaisuudet. Ultrahienoraemateriaaleilla erittäin suuret lujuudet ovat tyypillisiä. Usein lujuuden kasvun myötä ongelmaksi muodostuvat alhainen muokkauslujittumiskyky ja muovattavuus. Hehkuttamalla materiaalia muovattavuutta voidaan kuitenkin hieman parantaa [3].

3.1. Prosessointireitin vaikutus mikrorakenteeseen ECAP-prosessissa

ECAP-prosessoinnissa prosessointireitin valinnalla, eli sillä miten työstettävää kappaletta käännetään puristuskertojen välillä, on merkittävä vaikutus työstettävän kappaleen lopulliseen mikrorakenteeseen ja erityisesti materiaalin leikkausominaisuuksiin [7]. Kappaletta voidaan työstää ECAP-menetelmällä neljää yleistä eri reittiä käyttäen (ks. kappale 2.2.1.). Näiden neljän reitin lisäksi on olemassa reittejä, jotka ovat yhdistelmiä yleisistä reiteistä. Myös tarvittavien läpäisyjen määrä vaihtelee eri reittien välillä.

Mikrorakenteen muuttuminen ECAP-prosessoinnissa aiheutuu kappaleeseen kohdistetusta suuresta jännityksestä ja leikkausmuodonmuutoksesta [7]. Eri prosessointireittejä käyttämällä on mahdollista tuottaa erilaisia leikkaustasoja ja leikkaussuuntia. Furukawa et al. [7] mallinsivat kuutta eri reittiä prosessin optimoimiseksi. Mallinnuksessa käytettiin ECAP-muottina yksinkertaista muottia, jonka kanavakulma $\Phi = 90°$ ja ulkopinnan kaarevuuskulma $\psi = 0°$. Tutkimuksen tulokset pätevät ainoastaan ideaalisessa kitkattomassa ympäristössä. Todellisissa olosuhteissa, joissa on kitkaa ja kaarevuuskulman ollessa nolla, saattaa työstössä esiintyä vaikeuksia, sillä kahden kanavan risteyksessä oleva ulkokulma jää usein helposti täyttymättä.

Leikkautumista voidaan havainnollistaa kuutiolla, jonka sivuja eli leikkaustasoja merkitään kirjaimin X, Y ja Z. Furukawan tutkimuksen [7] mukaan reiteillä A ja B_A sekä reiteillä C ja B_C tasojen leikkautuminen on samankaltaista. Prosessointireitti A:lla työstettäessä muuttuvat leikkaustasot X ja Y jatkuvasti, mutta taso Z säilyy muuttumattomana. Reitti B_A muuttaa jokaista leikkaustasoa. Työstettäessä reitillä C palautuu leikkaustasojen kuutiomainen muoto joka toisen läpäisyn jälkeen, reitillä B_C vastaava vaikutus on joka neljännellä läpäisyllä.

Tavoitteena ECAP-prosessoinnissa on kohdistaa kappaleeseen suuret leikkausvoimat, jotka muokkaavat leikkaustasoja [7]. Optimitilanteessa näiden tasojen tulisi palautua takaisin kuutiomaisiksi, jotta leikkautumisprosessi voisi alkaa jälleen alusta.

Kuva 4. *Eri prosessointireittien aiheuttamat leikkausmyötymät tasoilla X, Y ja Z* [7].

Kuvasta 4 nähdään, että reitti B_C-A on mitä todennäköisimmin optimaalisin, sillä siinä tapahtuu jokaisella tasolla suuria leikkausmuutoksia ja jokaisen leikkaustason kuutiomainen muoto palautuu joka kahdeksannen läpäisyn jälkeen. Tällöin muodostuu mahdollisimman tasainen mikrorakenne, jossa rakeet ovat hyvin erilaisesti suuntautuneita.

Valiev et al. [1] mukaan prosessointi tavallisia prosessointireittejä käyttäen kasvattaa alumiinin myötö- ja vetomurtolujuutta, eivätkä monimutkaisemmat reittiyhdistelmät merkittävästi paranna mekaanisia ominaisuuksia tavallisiin prosessointireitteihin verrattuna. Lujuuksien kasvaessa vastaavasti muovattavuus vähenee. Tarkemmin asiaa ovat tutkineet Furukawa et al. [7]. He havaitsivat tutkimuksessaan, että reittien B_C ja C käytöllä voidaan tuottaa hienompia mikrorakenteita kuin reittien A ja B_A käytöllä. Myös Rebhi et al. [10] vertailivat reittien B_C ja C vaikutuksia puhtausasteeltaan 99.1 % alumiiniin. Heidän tutkimuksissaan selvisi, että toipuminen reitillä C työstettäessä on tehokkaampaa. Tämä johtuu siitä, että työstettäessä materiaalia ECAP-prosessissa kyseisellä reitillä muodostuu rakenne, jossa dislokaatiotiheys on suurempi. Samanlaisiin tuloksiin ovat päätyneet Iwahashi et al. [11,12] ja Oh-ishi et al. [13], joiden mukaan alumiinin raekoon pienentäminen onnistuu parhaiten käyttämällä reittiä B_C ja huonoiten käyttämällä reittiä A.

3.2.   ECAP-muotin kulmien vaikutus

Kanavakulmalla Φ tarkoitetaan kahden kanavan väliin jäävää kulmaa. Kulman suuruus vaikuttaa muodostuvaan mikrorakenteeseen ja sitä kautta mekaanisiin ominaisuuksiin. Kanavakulma on mikrorakenteeseen vaikuttavista tekijöistä tärkein, sillä se määrittelee kappaleeseen kohdistuvan kokonaismyötymän jokaisella läpäisyllä [1]. Kokonaismyötymä kasvaa kanavakulman pienentyessä.

Nakashima et al. [14] tutkivat kanavakulman vaikutusta ECAP-prosessoidun alumiinin ominaisuuksiin neljää erilaista kanavakulmaa käyttäen. Muottien kanavakulmat olivat 90°, 112.5°, 135° ja 157.5°. Kaikki näytteet prosessoitiin samaan kokonaismyötymään. TEM-kuvista (kuva 5) voidaan havaita, että tasainen ultrahienorakeinen mikrorakenne on helpointa saavuttaa kanavakulman ollessa 90°.

Kuvista (kuva 5) nähdään myös, että kun kanavakulmaa kasvatetaan, kasvavat myös mikrorakenteen vaihtelut. Nakashiman [14] mukaan kanavakulma 90° olisi optimaalinen.
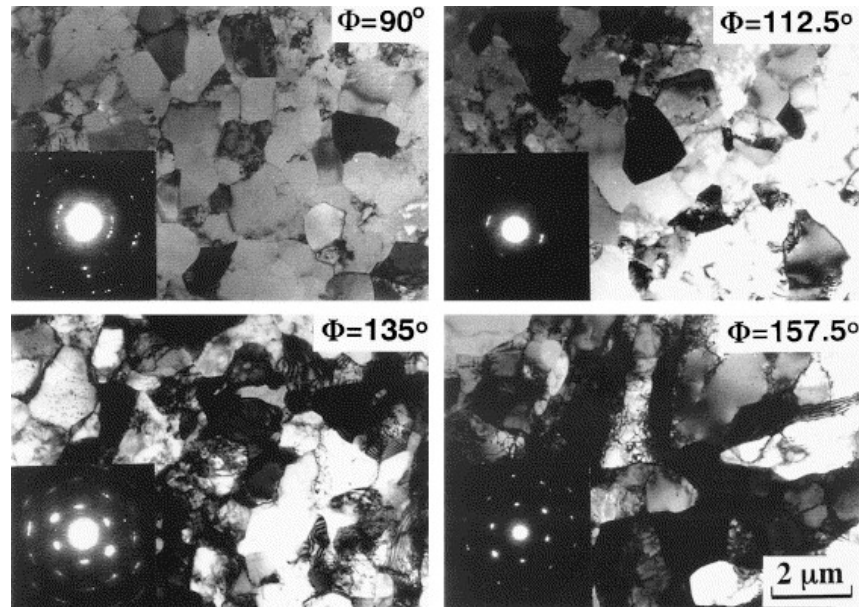
Kuva 5. *Alumiinin mikrorakenteet eri kanavakulmilla tehdyn ECAP-prosessoinnin jälkeen* [1].

Vaikka parhaimmat tulokset saataisiin kanavakulman ollessa 90°, on joskus järkevämpää käyttää suurempia kanavakulmia [1]. Erityisesti todella kovia ja vaikeasti työstettäviä materiaaleja prosessoitaessa kannattaa suuremman kanavakulman käyttämistä harkita, sillä tällöin voidaan välttää mahdollista kappaleessa tapahtuvaa työstöstä johtuvaa halkeilua. Lisäksi on tärkeää muistaa, että mitä suurempi kanavakulma, sitä vähemmän voimaa tarvitaan kappaleen puristamiseen muotin läpi.

Furuno et al. [15] tutkivat ECAP-prosessointia alle 90 asteen kanavakulmilla. Tutkimuksessa käytettiin kanavakulmaa 60° ja mikrorakenteita verrattiin 90° kanavakulman läpi puristettujen kappaleiden mikrorakenteisiin. Pienentämällä kanavakulmaa voidaan tuottaa mikrorakenteita, joissa keskimääräiset raekoot ovat hieman pienempiä kuin suuremmilla kanavakulmilla työstetyissä kappaleissa. Kanavakulman ollessa alle 90° tarvitaan kuitenkin todella suuria puristuspaineita, jotta kappaleeseen ei muodostuisi halkeamia. Käytännössä puristuspaineiden kasvattaminen on kuitenkin hankalaa, joten 90° kanavakulmaa pidetään optimaalisena ECAP-muotille [1].

Kanavan ulkopinnan kaarevuuskulma on ECAP-muotissa kanavien välille muodostuva ulkokulma ψ [1]. Tällä kulmalla on vähäisempi vaikutus muodostuvaan mikrorakenteeseen kuin esimerkiksi kanavakulmalla Φ. Valiev et al. [1] tutkivat kaarevuuskulman vaikutuksia puhtaan alumiinin mikrorakenteeseen mittaamalla mikrokovuuksia kaarevuuskulmilla $\psi = 0°$ ja $\psi = 20°$ työstetyissä kappaleissa ja

havaitsivat, että työstetyissä kappaleissa esiintyi pieniä epähomogeenisia alueita riippumatta muotin kaarevuuskulmasta. Lisäksi Valiev et al. [1] havaitsivat, että käytettäessä muottia jonka kaarevuuskulma on $\psi = 0°$, jää muotin ulkokulmaan usein niin sanottu kuollut alue (dead zone). Tämä alue jää kokonaan tyhjäksi puristettavasta materiaalista, ja tällöin materiaali ei koske muotin seinämään. On kuitenkin vaikeaa valmistaa muottia, jonka molemmat ulkokulmat olisivat kaarevia. Tämän takia päädytäänkin usein valmistamaan muotti, jonka kanavakulma $\Phi = 90°$ ja ulkopinnan kaarevuuskulma $\psi = 20°$.

3.3. Puristusnopeuden vaikutus

Tyypillisesti puristusnopeudet ECAP-prosessoinnissa vaihtelevat välillä 1 – 20 mm/s [1]. Berbon et al. [16] tutkivat puristusnopeuden vaikutusta syntyvään mikrorakenteeseen. Varsinaisesti puristusnopeudella ei ole vaikutusta esimerkiksi raekokoon. Kuitenkin alhaisilla puristusnopeuksilla jää enemmän aikaa toipumiselle ja on täten mahdollista saavuttaa tasaisempi mikrorakenne. Kuvasta 6 nähdään, että puristusnopeudella ei juuri ole vaikutusta alumiiniseoksen myötölujuuteen, mutta läpäisyjen kasvaessa myötölujuus tasaantuu kolmen läpäisyn jälkeen.
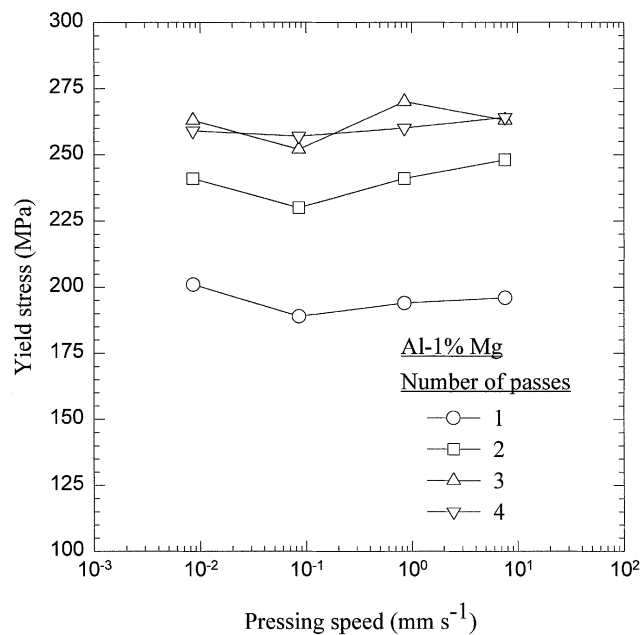

Kuva 6. *Alumiiniseoksen myötölujuudet eri puristusnopeuksilla ja läpäisykerroilla* [16].

3.4. Lämpötilan vaikutus

Lämpötilan vaikutukset ECAP-prosessoinnissa voidaan jakaa kahteen eri ryhmään: puristuslämpötilan sekä kappaleen sisäisten lämpötilamuutosten aiheuttamiin vaikutuksiin [1]. Puristuslämpötilaan on kohtalaisen helppo vaikuttaa ja sen vaikutus syntyviin mikrorakenteisiin on suuri.

Yamashita et al. [17] tutkivat ECAP-prosessoinnin vaikutusta prosessoitavan kappaleen mikrorakenteeseen huoneenlämpötilassa ja korotetuissa lämpötiloissa 373 K, 473 K ja 573 K. Tutkimuksessa koekappaleiden ECAP-prosessointi suoritettiin ahjossa. Käytetyn ECAP-muotin kanava- ja ulkopinnan kaarevuuskulmat valittiin siten, että myötymä läpäisykertaa kohden vastaisi arvoa yksi. Lopullisia mikrorakenteita analysoitiin TEM-kuvien avulla.

Tutkimuksessa selvisi, että puristuslämpötilan nostaminen kasvattaa keskimääräistä raekokoa [17]. Hall-Petch -yhtälöstä (1) voidaan päätellä, että mahdollisimman lujan rakenteen aikaansaamiseksi tulisi puristuslämpötila täten pitää alhaisena. Kuvassa 7 on esitetty puhtaan alumiinin (99.99 %) mikrorakenteet huoneenlämpötilassa sekä korotetuissa (373 K, 473 K, 573 K) lämpötiloissa.
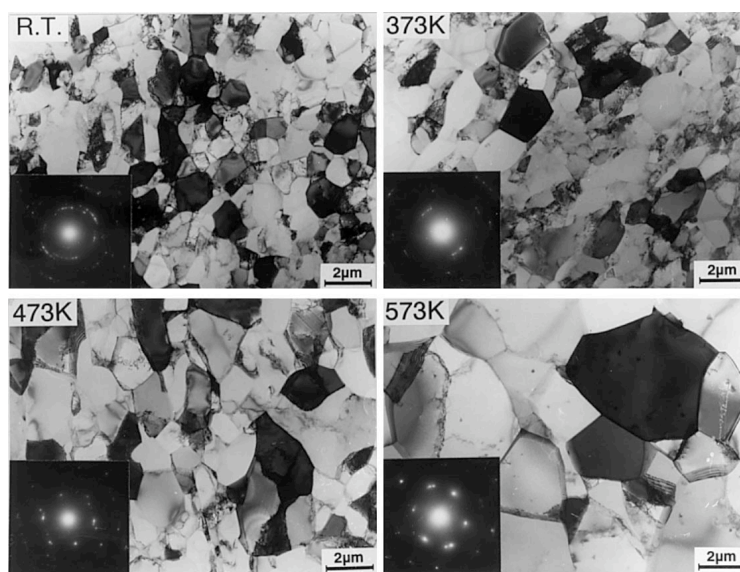
Kuva 7. *Puhtaan alumiinin mikrorakenne ECAP-prosessoinnin jälkeen eri puristuslämpötiloilla* [17].

Huoneenlämpötilassa puristetun puhtaan alumiinin raekoko on selkeästi 573 K lämpötilassa puristetun puhtaan alumiinin raekokoa pienempi. Yamashita et al. [17] mukaan alhaisissa lämpötiloissa puristetun alumiinin rakeet erottuvat toisistaan suuren kulman raerajoilla, kun taas korkeimmissa lämpötiloissa raerajojen misorientaatiokulma pienenee nopeamman toipumisen ja dislokaatioiden annihilaation takia. Joskus ECAP-prosessointi alhaisissa lämpötiloissa saattaa osoittautua mahdottomaksi paineen riittämättömyyden takia [1]. Näin käy etenkin kovien materiaalien kohdalla.

Puristuslämpötilan lisäksi työstettävään kappaleeseen vaikuttavat myös sen sisäiset lämpötilamuutokset [1]. Adiabaattinen nousu lämpötilassa tapahtuu, kun ECAP-prosessoinnissa leikkaustasolle kohdistuvat jännitykset aiheuttavat kappaleessa myötymistä ja suuri osa mekaanisesta energiasta muuttuu lämmöksi. Jos puristusnopeus on tarpeeksi korkea, ei lämpöenergia ehdi johtua kappaleesta pois ja kappaleen lämpötila nousee, mikä voi laskea materiaalin lujuutta. Kappaleen lämpötilan noustessa

tapahtuu myös tasapainorakenteessa muutoksia [18]. Tämä voidaan estää, jos kappale puristetaan ECAP-muotin läpi tarpeeksi alhaisella nopeudella (noin 0.18 mm/s). Tällöin puristetun kappaleen lujuus ei laske merkittävästi. Kuitenkin liian alhaisella puristusnopeudella puristettaessa, tulee ongelmaksi materiaalin liian nopea toipuminen [18], mikä voi johtaa dislokaatiotiheyden pienenemiseen.

3.5. Kokonaismyötymän vaikutus

Kokonaismyötymää voidaan helpoiten kasvattaa lisäämällä läpäisyjen määrää [1]. Tämä voidaan tehdä joko yksinkertaisesti puristamalla kappale useamman kerran ECAP-muotin läpi tai vaihtoehtoisesti käyttämällä erilaisia ECAP-menetelmiä (ks. kappale 2.2.2.). Jokaisella läpäisyllä kappaleen myötymään vaikuttaa ECAP-muotin kaksi kulmaa, joista suurempi merkitys on kanavakulmalla Φ.

Furukawa et al. [19] esittävät kokonaismyötymän ε_N laskemiseksi kaksi seuraavanlaista yhtälöä,

$$\varepsilon_N = \frac{N}{\sqrt{3}}\left[2\cot\left(\frac{\Phi}{2}+\frac{\Psi}{2}\right)\right]+\Phi\cos ec\left(\frac{\Phi}{2}+\frac{\Psi}{2}\right) \qquad (2)$$

$$\varepsilon_N = \frac{N}{\sqrt{3}}\left[2\cot\left(\frac{\Phi+\Psi}{2}\right)+\Psi\right] \qquad (3)$$

joissa N on läpäisyjen lukumäärä, Φ muotin kanavakulma ja ψ ulkopinnan kaarevuuskulma. Yhtälöistä 2 ja 3 voidaan päätellä, että suurin vaikutus kokonaismyötymään on juuri läpäisyjen lukumäärällä. Yhtälöt antavat hieman eriävät arvot kokonaismyötymälle kanavakulman ollessa alle 90° [19]. Ulkopinnan kaarevuuskulman suuruudella ei ole vastaavanlaista vaikutusta lopputulokseen.

El-Danaf et al. [20] tutkivat ECAP-prosessoinnin vaikutuksia puhtaan alumiinin (seos 1050) mikrorakenteeseen ja mekaanisiin ominaisuuksiin. ECAP-prosessointi suoritettiin käyttäen reittejä B_C ja C muotin kanavakulman ollessa 90°. Koska kokonaismyötymä on suoraan verrannollinen läpäisyjen määrään, on seuraavassa kuvassa 8 esitetty alumiiniseoksen 1050 Vickers-kovuudet eri läpäisyjen jälkeen.
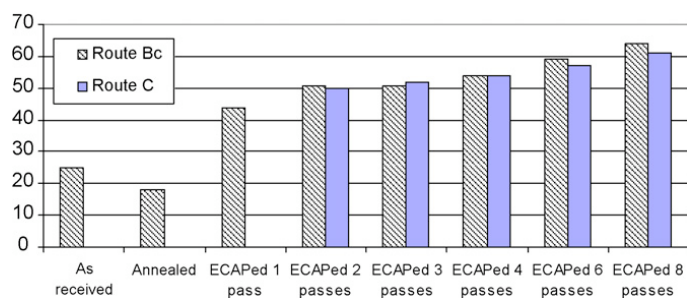
Kuva 8. *Alumiiniseoksen 1050 Vickers-kovuudet ECAP-prosessoinnin jälkeen* [20].

Kuvasta 8 nähdään, että Vickers-kovuudet kasvavat läpäisyjen eli kokonaismyötymän kasvamisen myötä, tosin kasvu ei ole kovinkaan suurta.

Samassa tutkimuksessa [20] tehtiin ECAP-prosessoiduille alumiinikappaleille puristuskokeita, joiden tuloksista muodostettiin jännitys-venymäkäyrät.
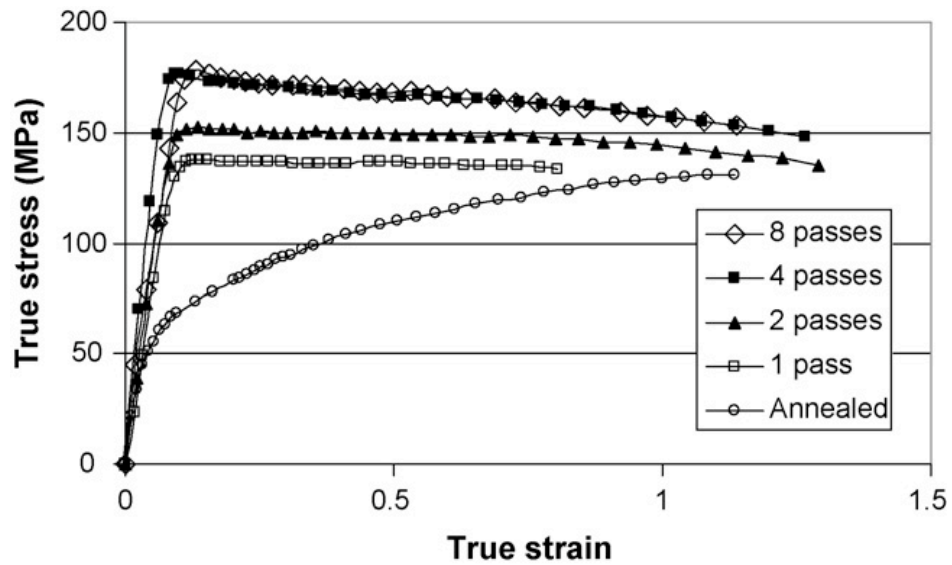
Kuva 9. *Jännitys-venymäkäyrä B_C reitillä ECAP-prosessoidulle alumiinille (seos 1050) eri läpäisyillä* [20].

Kuvan 9 jännitys-venymäkäyrästä voidaan päätellä myötölujuuden kasvavan läpäisykertojen kasvaessa. Tämä tarkoittaa käytännössä sitä, että myötölujuus kasvaa kokonaismyötymän kasvaessa. Sama kasvusuhde pätee myös murtolujuudelle.

4.   YHTEENVETO

Tässä työssä käsiteltiin erilaisia SPD-menetelmiä ja SPD-prosessoinnin vaikutusta prosessoitavan kappaleen mikrorakenteeseen sekä ominaisuuksiin. SPD-menetelmistä eniten tutkittu on ECAP-menetelmä, jossa työstettävä kappale puristetaan männän avulla muotin läpi. ARB on SPD-menetelmä, jossa katkaistuja levyjä liitetään yhteen valssaamalla korotetussa lämpötilassa. Valssauksen jälkeen levy katkaistaan uudelleen, levyjen pinnat puhdistetaan ja prosessi alkaa alusta, kunnes saavutetaan haluttu mikrorakenne. HPT-menetelmässä työstettävä kappale asetetaan muottiin, johon kohdistetaan suuri paine. Tämän jälkeen kappaletta väännetään joko mäntää tai kappaleen ja muotin välistä kitkaa apuna käyttäen.

SPD-prosessoinnilla voidaan muuttaa metallin mikrorakennetta ja täten myös sen ominaisuuksia. Haluttu tulos aikaansaadaan kontrolloimalla prosessiparametreja, joista tässä työssä käsiteltiin kuutta tärkeintä. Prosessointireitillä, muotin kanavakulmalla ja kokonaismyötymällä eli läpäisyjen lukumäärällä on suurin vaikutus muodostuvaan mikrorakenteeseen.

Lukuisten tutkimusten [7,11,12,13] perusteella prosessointireiteistä tehokkaimmaksi havaittiin reitti B_C, jossa kappaletta käännetään aina 90° läpäisyjen välillä. Kanavakulmalla Φ todettiin olevan suuri vaikutus muodostuvaan mikrorakenteeseen siten, että pienempiä kulmia käytettäessä saavutettiin myös pienempirakeinen mikrorakenne. Ulkopinnan kaarevuuskulmalla ψ ei todettu olevan juurikaan vaikutusta muodostuvaan mikrorakenteeseen. Helpomman prosessoinnin takia kuitenkin käytetään useimmiten kulmaa 20°.

Työssä todettiin, että puristusnopeudella ei ole lähes lainkaan vaikutusta muodostuvaan mikrorakenteeseen. Sitä vastoin prosessointilämpötila vaikuttaa saavutettavaan raekokoon. Prosessointilämpötila tulisi pitää mahdollisimman alhaisena pienirakeisen mikrorakenteen aikaansaamiseksi. Kokonaismyötymän havaittiin kasvattavan sekä materiaalin kovuutta että lujuutta.

LÄHTEET

[1]   Valiev, R.Z., Langdon, T.G. Principles of equal-channel angular pressing as a processing tool for grain refinement. Progress in Materials Science 51 (2006), pp. 881-981

[2]   Langdon, T.G. The principles of grain refinement in equal-channel angular pressing. Materials Science and Engineering A 462 (2007), pp. 3-11

[3]   Azushima, A., Kopp, R., Korhonen, A., Yang, D.Y., Micari, F., Lahoti, G.D., Groche, P., Yanagimoto, J., Tsuji, N., Rosochowski, A., Yanagida, A. Severe plastic deformation (SPD) processes for metals. CIRP Annals - Manufacturing Technology 57 (2008), pp. 716-735

[4]   Latysh, V., Krallics, Gy., Alexandrov, I., Fodor, A. Application of bulk nanostructured materials in medicine. Current Applied Physics 6 (2006), pp. 262-266

[5]   Callister, William D. Jr. Materials science and engineering, an introduction. Kuudes painos, Yhdysvallat 2003, John Wiley & Sons. 820 p.

[6]   ASM Materials Information, Metals Handbook [WWW]. Mechanical properties of carbon and alloy steels, effects of alloying elements. [Viitattu 10.12.2008]. Saatavissa: http://products.asminternational.org/hbk/index.jsp

[7]   Furukawa, M., Iwahashi, Y., Horita, Z., Nemoto, M., Langdon, T.G. The shearing characteristics associated with equal-channel angular pressing. Materials Science and Engineering A257 (1998), pp. 328-332

[8]   Saito, Y., Utsonomiya, H., Tsuji, N., Sakai, T. Novel ultra-high straining process for bulk materials - development of the accumulative roll-bonding (ARB) process. Acta Materialia 47 (1999) 2, pp. 579-583

[9]   Valiev, R.Z., Alexandrov, I.V. Nanostructured materials from severe plastic deformation. NanoStructured Materials 12 (1999), pp. 35-40

[10]   Rebhi, A., Makhlouf, T., Njah, N., Champion, Y., Couzinié, J-P. Characterization of aluminum processed by equal channel angular extrusion: Effect of processing route. Materials Characterization XX (2009), pp. XXX-XXX

[11]   Iwahashi, Y., Horita, Z., Nemoto, M., Langdon, T.G. The process of grain refinement in equal-channel angular pressing. Acta Materialia 46 (1998) 9, pp. 3317-3331

[12]   Iwahashi, Y., Horita, Z., Nemoto, M., Langdon, T.G. An investigation of microstructural evolution during equal-channel angular pressing. Acta Materialia 45 (1997) 11, pp. 4733-4741

[13]   Oh-Ishi, K., Horita, Z., Furukawa, M., Nemoto, M., Langdon, T.G. Optimizing the rotation conditions for grain refinement in equal-channel angular pressing. Metallurgical and Materials Transactions A: Chemistry and Materials Science 29 (1998) 7, pp. 2011-2013

[14]   Nakashima, K., Horita, Z., Nemoto, M., Langdon, T.G. Influence of channel angel on the development of ultrafine grains in equal-channel angular pressing. Acta Materialia 46 (1998) 5, pp. 1589-1599

[15]   Furuno, K., Akamatsu, H., Oh-ishi, K., Furukawa, M., Horita, Z., Langdon, T.G. Microstructural development in equal-channel angular pressing using a 60° die. Acta Materialia 52 (2004) 9, pp. 2497-2507

[16]   Berbon, P.B., Furukawa, M., Horita, Z., Nemoto, M., Langdon, T.G. Influence of pressing speed on microstructural development in equal-channel angular pressing. Metallurgical and Materials Transactions A: Physical Metallurgy and Materials Science 30 (1999) 8, pp. 1989-1997

[17]   Yamashita, A., Yamaguchi, D., Horita, Z., Langdon, T.G. Influence of pressing temperature on microstructural development in equal-channel angular pressing. Materials Science and Engineering A287 (2000), pp. 100-106

[18]   Yamaguchi, D., Horita, Z., Nemoto, M., Langdon, T.G. Significance of adiabatic heating in equal-channel angular pressing. Scripta Materialia 41 (1999) 8, pp. 791-796

[19]   Furukawa, M., Horita, Z., Nemoto, M., Langdon, T.G. Processing of metals by equal-channel angular pressing. Journal of Material Science 36 (2001), pp. 2835-1843

[20]   El-Danaf, E.A., Soliman, M.S., Almajid, A.A., El-Rayes, M.M. Enhancement of mechanical properties and grain size refinement of commercial purity aluminum 1050 processed by ECAP. Materials Science and Engineering A458 (2007), pp. 226-234

TAMPEREEN TEKNILLINEN YLIOPISTO

Ville Viberg
Mechanical Properties of Austenitic Manganese Steel
Report 27.5.2011

1. INTRODUCTION

Austenitic manganese steels are also known as Hadfield steels after inventor Sir Robert Hadfield. High manganese content and proper heat treatment enables the formation of metastable austenite in room temperatures. Hadfield steels are ductile due to austenitic microstructure and have large work hardening capacity. That is why Hadfield steels are commonly used in many wear applications, especially in high impact wear. [1]

Despite over hundred years have passed from the invention of the Hadfield steel it is still excellent choice to the certain wear applications. Typical applications for Hadfield steels are rock crusher cones and jaws and railroad crossings. Poor machinability and weldability hinder the use of Hadfield steels [2]. Wear of Hadfield steel may be intensive in applications where it is exposed only to mild abrasive wear without impacts. [3]

1.1. Composition

The main alloying elements of traditional Hadfield steels are manganese and carbon. Manganese content varies from 10 % to 14 % and carbon from 1.0 % to 1.4 %. Highest strength and elongation values are achieved when manganese content is approximately 14 %. When manganese content is increased from 14 %, work hardening capacity increases and fracture elongation decreases. Mn/C proportion defines the basic mechanical properties of manganese steel. Higher carbon content increases strength of Hadfield steels. Typically, maximum carbon content is 1.4 % because higher carbon content leads to the formation of grain boundary carbides which make structure brittle [4]

Mechanical properties of austenitic manganese steel could be modified with different alloying elements. Chromium is added to the steel typically from 1 to 2 % to increase strength and hardness. Also molybdenum could be used for the same reason as chromium. [5]

1.2. Work Hardening

High toughness and large work hardening capacity are the main reasons why austenitic manganese steels are used in many wear applications. Hardness of typical as-cast austenitic manganese steels are 200-280 HV. Working, especially high energy impacts, increases hardness and it can increase up to 900 HV. [6]

Mechanism of unusual strain hardening behaviour of Hadfield steels is complicated and could not be explained with only one mechanism. Work-hardening in standard Hadfield steels is mainly caused by deformation twinning. Formation of hcp (hexagonal close packing) martensite is also one work-hardening method. High vanadium content increases formation of ε-martensite. [7] Efstathiou [8] et al. represents that deformation mechanisms in Hadfield steels include interactions between interstitial atoms and dislocations, between dislocations and twins and between twinning systems.

2. EXPERIMENTAL PROSEDURE

The mechanical properties of samples were tested with differed tensile and compression tests. Low strain rate (0.001-1 1/s) tests were conducted on a servo hydraulic Instron 8800 testing machine and high strain rate (1500-4000 1/s) on a Hopkinson Split Bar (HSB).

Test samples were taken from bigger (500 kg) part which was cast and heat treaded. Samples were then cut from bigger part by Muototerä Oy using water cutting and wire-cutting. Chemical analysis of cast part is represented in Table 1. Composition is measured with emission spectrometer.

Table 1 *Chemical composition of tested austenitic steel.*

Element	C	Si	Mn	P	S	Cu	Cr	Ni	Mo	Al	V	Fe
wt %	1.15	0.51	16.53	0.06	0.01	0.09	1.83	0.23	0.13	0.04	0.02	bal.

Manganese content of the test samples is 3 % higher than in traditional manganese steels. In consequence of higher manganese content, tensile strength is slightly lower but work-hardening capacity higher than in traditional Hadfield steels.

2.1. Tensile tests

The same kinds of samples were used in all tensile tests. Geometry of tensile test samples is represented in Figure 1. Test sample geometry was selected so that they are suitable for HSB testing. Thickness of the tensile samples must be 2 mm to fit in notches of the bars and the shorter the sample the higher strain rates.
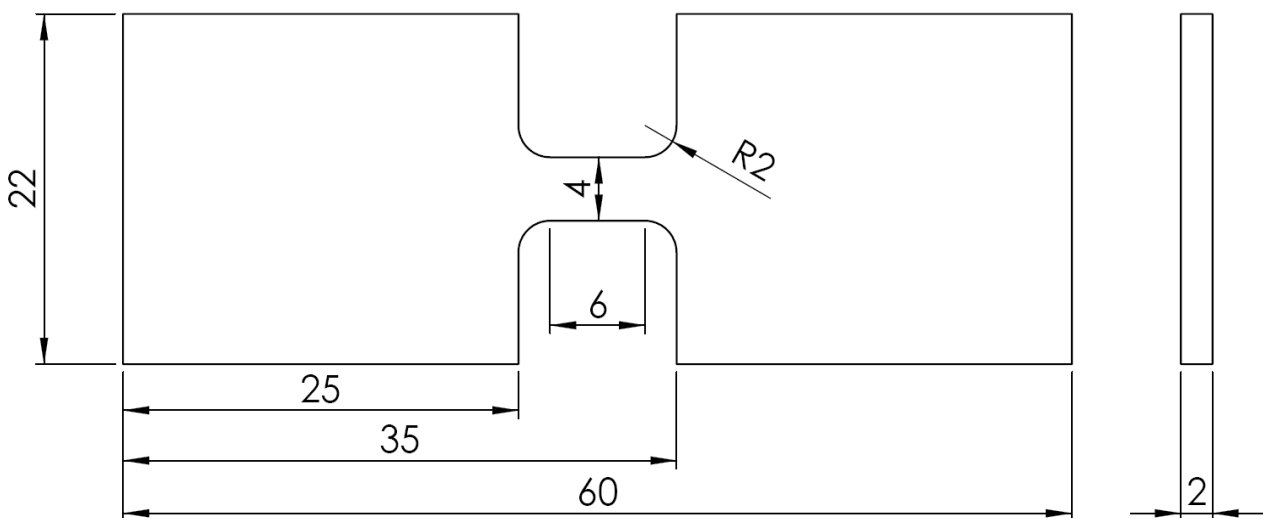

Figure 1 *Geometry of tensile test sample. All dimensions in millimetres.*

Low strain rate tensile tests were performed with four different strain rates. Used strain rates were 0.001, 0.01, 0.1 and 1 1/s and desired strain rates were attained using crosshead speeds from 0.006 to 6 mm/s. All tensile tests were continued until the specimen was broken. During tensile tests, load data was collected from the load cell and elongation of narrowed area was measured by extensometer with 6 mm gauge length. Extensometer was attached to the sample as tight as possible to prevent slipping of the extensometer blades.

Tensile Hopkinson Split Bar (THSB) were used in high strain rate tensile tests. The main parts of the THSB are presented in Figure 2.
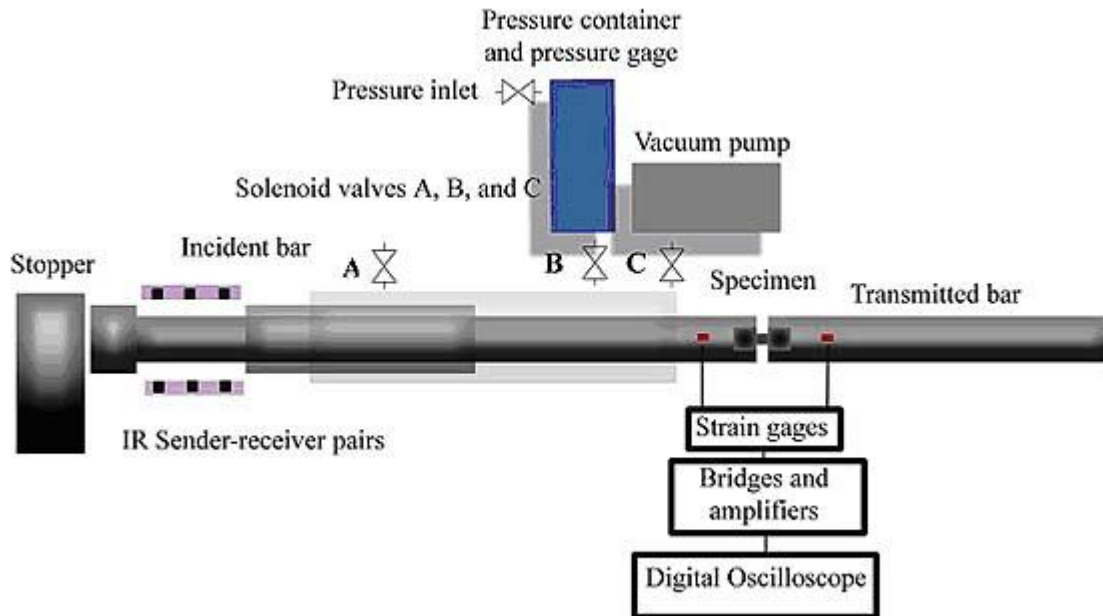

Figure 2 *Tensile Hopkinson Split Bar [9].*

The striker creates a stress wave in the incident bar. When wave reaches the sample part of the stress wave is reflected back as a pulse of tension, while the remaining part is transmitted through the specimen to the transmitted bar. Three stress pulses, incident, reflected, and transmitted, are recorded at strain gage stations Stress, strain, and strain rate in the specimen can be calculated from the measured pulses.

In THSB tests sample must be attached to the bars. In this study samples were glued in to the notches on the bars. In THSB tests 1600 mm striker and 6.35 bar pressure were used. With those parameters, approximately 1500 1/s strain rates were attained.

2.2. Compression tests

Small cylindrical samples with the height of 6 mm and 8 mm in diameter were used in all compression tests. Before testing the top and bottom surfaces of the samples were straightened and polished to minimize barreling effect and sliding of the sample. Also lubricant was used between the sample and the compression head.

Low strain rate compression tests were performed with the servo hydraulic testing machine using compression heads with cemented carbide tips. Loads in compression tests were measured

with the load cell and elongations with the extensometer attached to the sides of compression heads. Two different kinds of compression tests were performed. First samples were compressed 1.8 mm using different strain rates to attain 30 % strain. Then samples were compressed with different strains using constant strain rate 0.01 1/s. In 30 % strain compression tests the same strain rates (0.001-1.0 1/s) were used as in tensile tests.

High strain rate compression tests were performed with Hopkinson Slit Bar (HSB). The main components of the HSB are presented in Figure 3. Compression HBS works the same principles as tensile HSB.
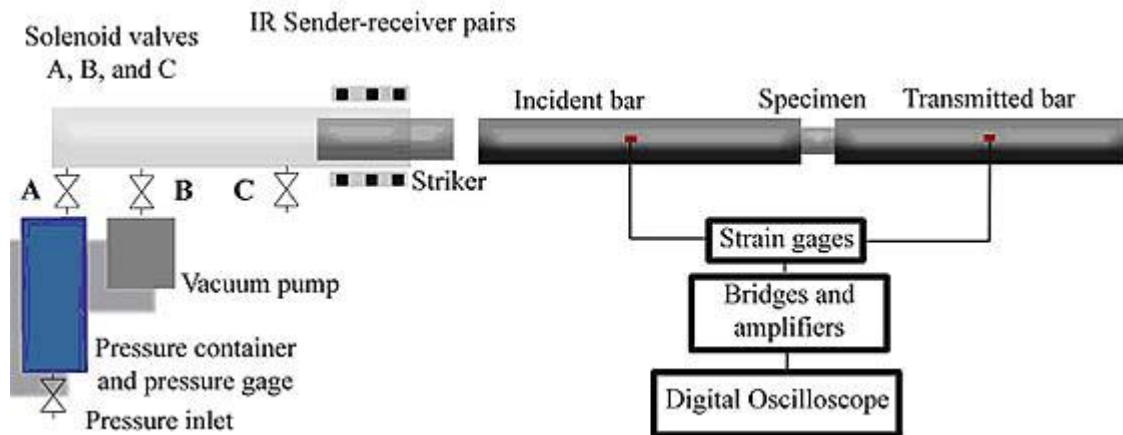

Figure 3 *Compression Hopkinson Split Bar [9].*

Two different kinds of strikers and pressures were used in the high strain rate compression tests of this study. In 4000 1/s strain rate tests, 200 mm in length maraging steel striker and pressure of 5 bar were used. Longer striker (400 mm) made from 4030 stainless steel and lower pressure (2.2 bar) were used to attain enough strain with the strain rate of 1500 1/s.

3.   RESULTS AND DISCUSSION

The results are divided into three sections which correspond to different test methods. The first section will present results from compression tests, the second from tensile test and the third from hardness measurements. In the results of compression and tensile tests stress-strain curves are presented firs and then there are some discussion about graphs.

3.1.   Results of compression tests

Both engineer and true stress-strain curves of compression tests are presented in this chapter. The true stress-strain curves from high strain rate test (1500 & 4000 1/s) are smoothed with some kind of approximation. Therefore there is less noise in true stress-strain curves.
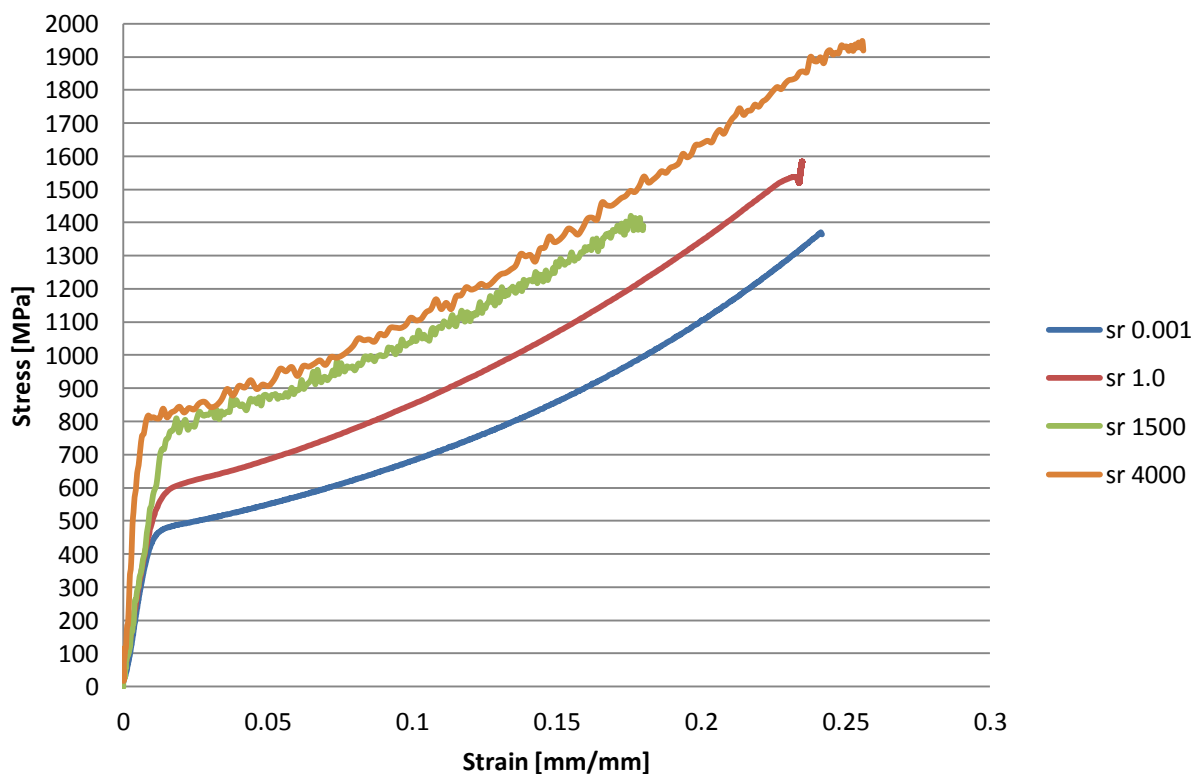

Figure 4 *Compression stress-strain curves with different strain rates.*

As perceived from Figure 4 the compressive yield strength of the tested manganese steels range between 450 and 800 MPa depending on the strain rate. Strains of the high strain rate test are not identical to strains of the low strain rate samples, but close enough so that results could be compared. Strain rate dependence of compressive yield strength of tested steels is positive, so that yield strength is higher in high strain rate tests
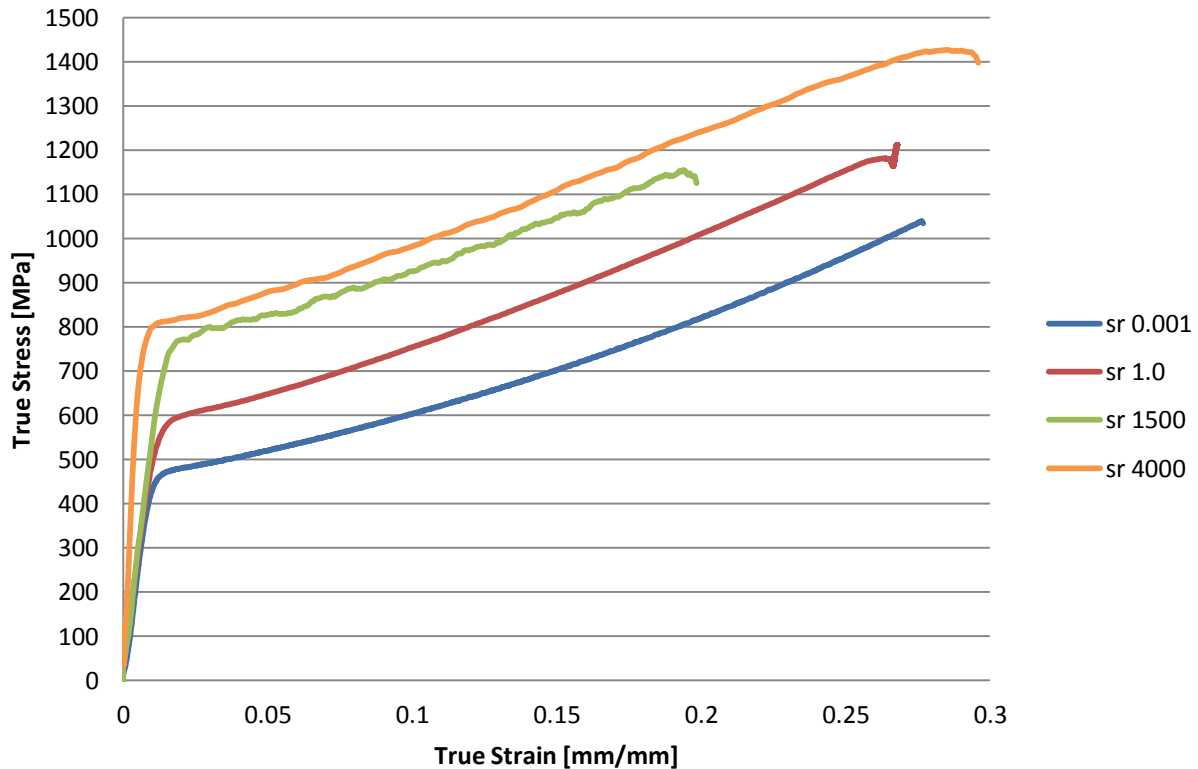
Figure 5 *Compression true stress-true strain curves with different strain rates.*

Slope of the true stress-true strain curves after the yield point is almost the same in all different strain rates. It shows that there are not significant changes in work hardening mechanism when strain rate changes. Slightly different slope in elastic part of 4000 1/s strain rate curve is result from the calculation errors of HSB pulses, so it can be forgotten.

Formation of martensite during the compression tests were studied from microstructure images and with strong magnet. No evidence of martensite was found from the microstructure images. Also samples were almost nonmagnetic after compression tests. Slight magnetism may ensue from oxide layer on the sample or very small amounts of martensite formed during compression.

3.2.   Results of tensile tests

Both engineer and true stress-strain curves of tensile tests are presented in this chapter. The true stress-strain curves from high strain rate test are again smoothed with some kind of approximation. When looking results of the tensile tests, must be remembered that tests have been made to quite small specimens produced from cast steel. Casts have always some defects and if there is defect in tensile test specimen, it can have great effect to the results. High strain rate (1500 1/s) stress-strain curves of different samples are presented in Figure 6.
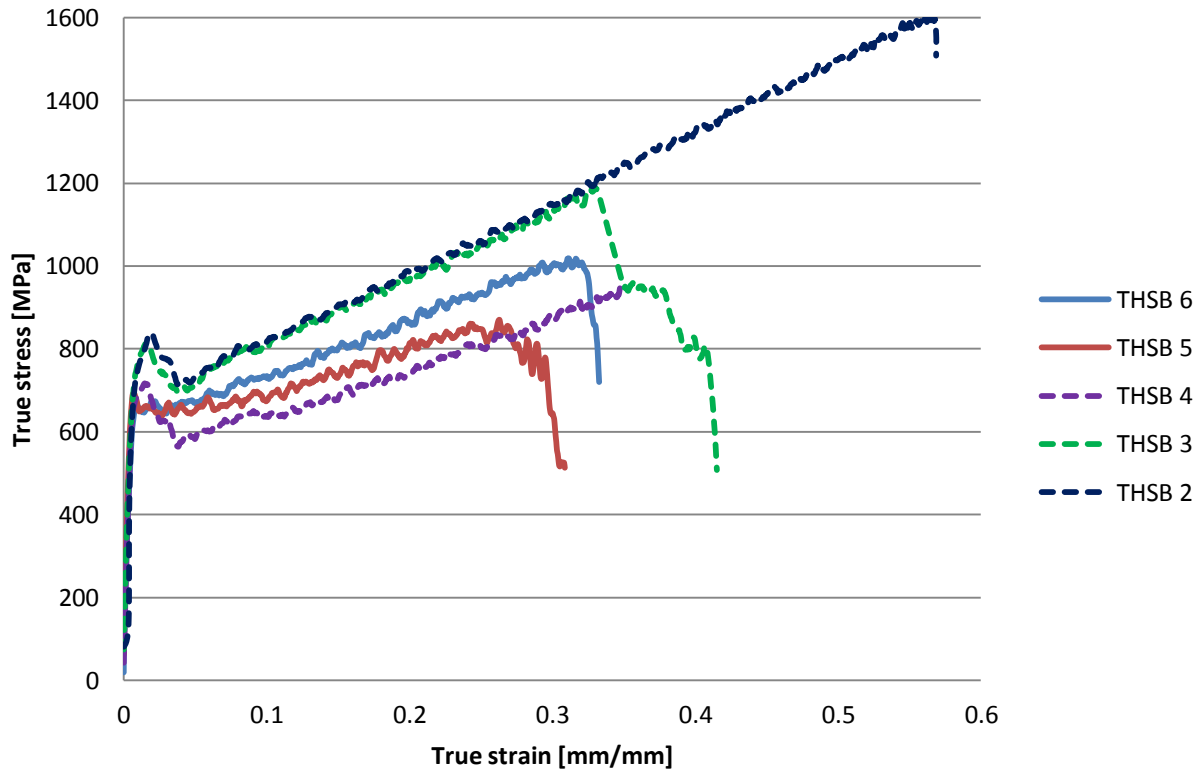
Figure 6 *Tensile HBS tests using strain rate 1500 1/s. Tests 4-2 are done with different bars.*

As the curves in Figure 6 show, there are big differences, especially in strain, between different samples. Tests THSB 2-4 are done using transmitted bar having hole which could be used to fix the sample. Tests 5 and 6 are performed using bars with no holes. We notice that yield limit in the samples 2-4 is caused by holes in the bars, not by properties of the sample. Strains of the low strain rate tests are from 0.4 to 0.7. That's why THSB 2 test is compared to low strain rate tests in figures below.
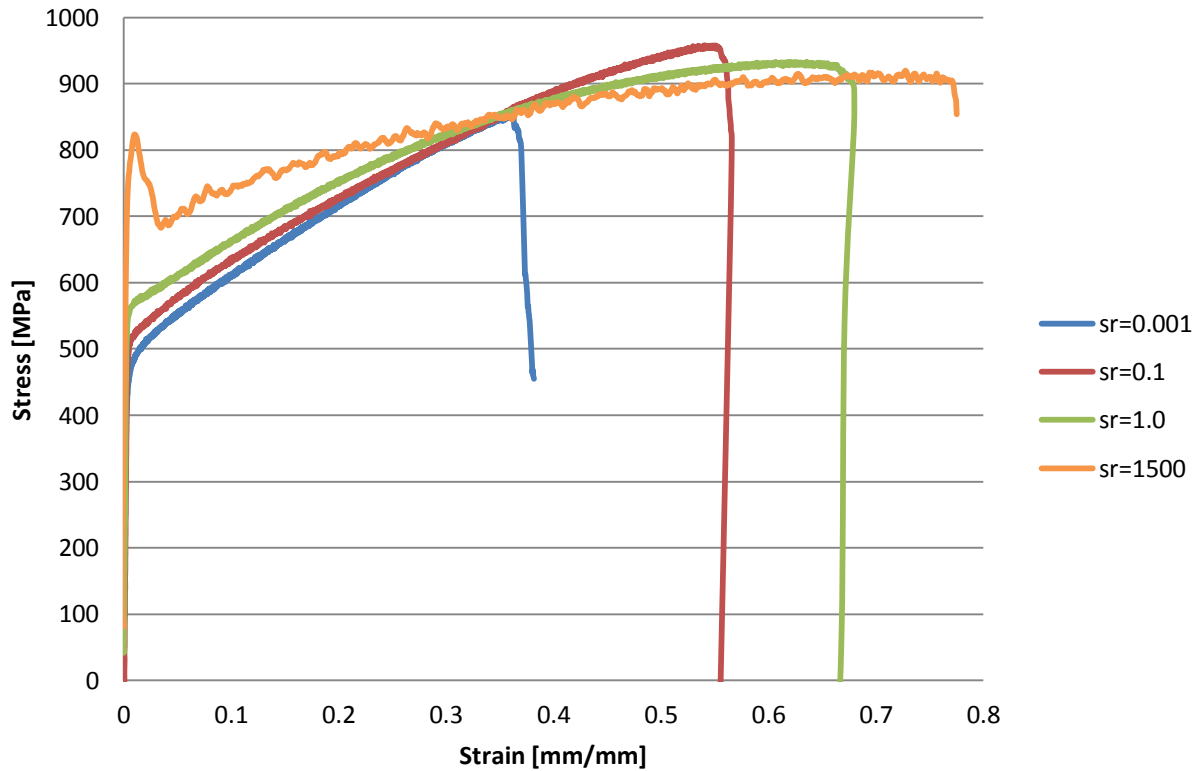
Figure 7 *Tensile stress-strain curves with different strain rates.*
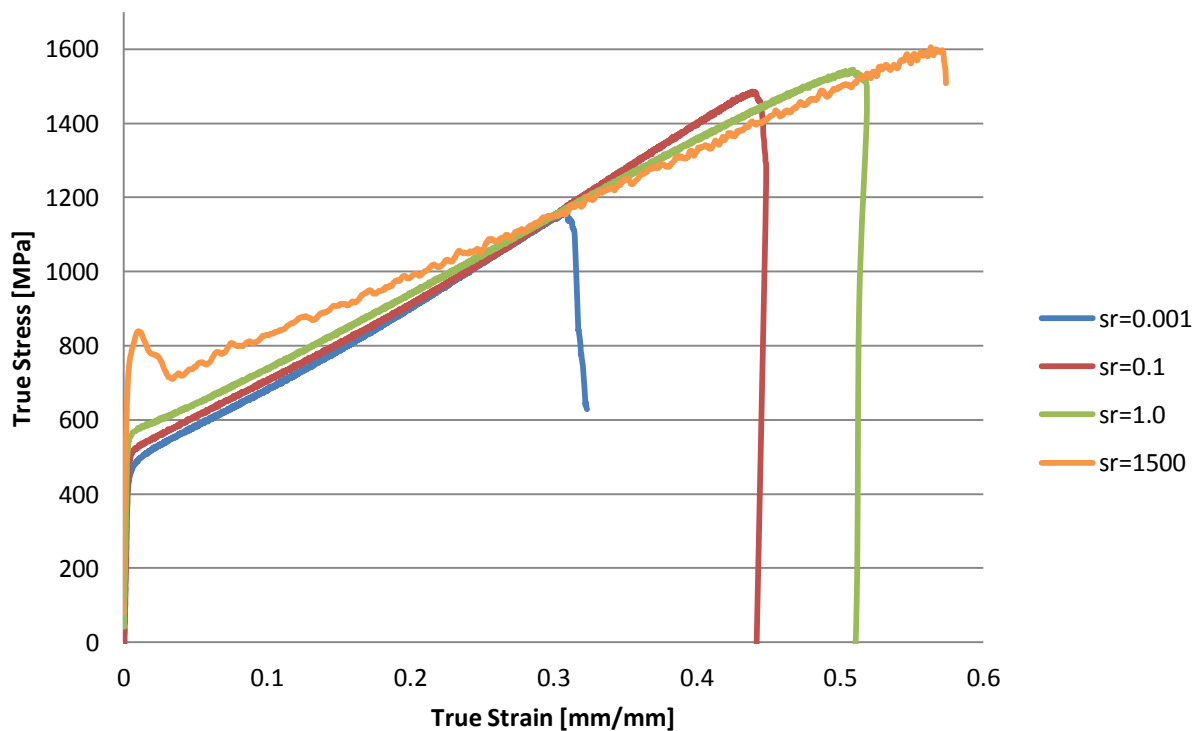

Figure 8 *Tensile true stress-true strain curves with different strain rates.*

Ultimate tensile strain and strength increases with higher strain rates. On the other hand work hardening rate decreases with higher strain rates. Adiabatic heating of the specimen may be one

reason to the different work hardening rate. As noted earlier peak in the yield point of the high strain rate (1500 1/s) tests is caused by sample fixation hole in the transmitted bar, so peak should be forgotten.

Microstructure images are taken from some samples after mechanical tests. Samples are etched with 4% nitric acid in ethanol to reveal grain boundaries and twins. Microstructures in Figure 9 are taken from one of the tested THSB samples.
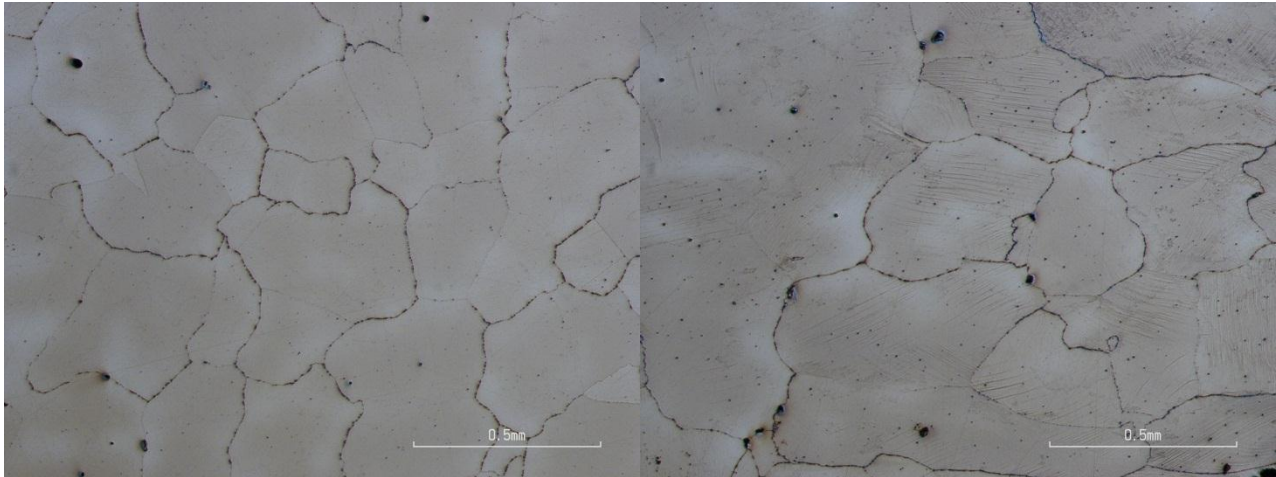

Figure 9 *Microstructure of tensile test sample. Undeformed area on the left and deformed area on the right.*

Grain size measured from microstructure images varies from 200 to 500 µm. Figure on the left side is taken from undeformed area of the TSHB sample. Microstructure is fully austenitic and there are only small carbides on the grain boundaries. No twins could be seen in left side images. Right side figure is taken from deformed area, near of the fracture surface. Deformation twins could be seen as parallel lines on different grains.

3.3.   Results of hardness tests

Hardness values measured from compression samples are introduced in this chapter. First hardness values are measured with Matzuzawa micro hardness tester using 200 g test load. Hardness values have been measured from the cross-section of compression samples. Measurements have been taken from different distances from the edges of the sample. There was no clear difference in hardness values taken from the surface and from the centre of the specimen. Average hardness values have been measured using Duramin-A300 hardness tester and 5 kg test load. Ten points are measured from different places of the sample. Hardness of compression samples with different amount of strain is presented in Figure 10. All of the samples in Figure 10 have been tested with the same strain rate 0.01 1/s.
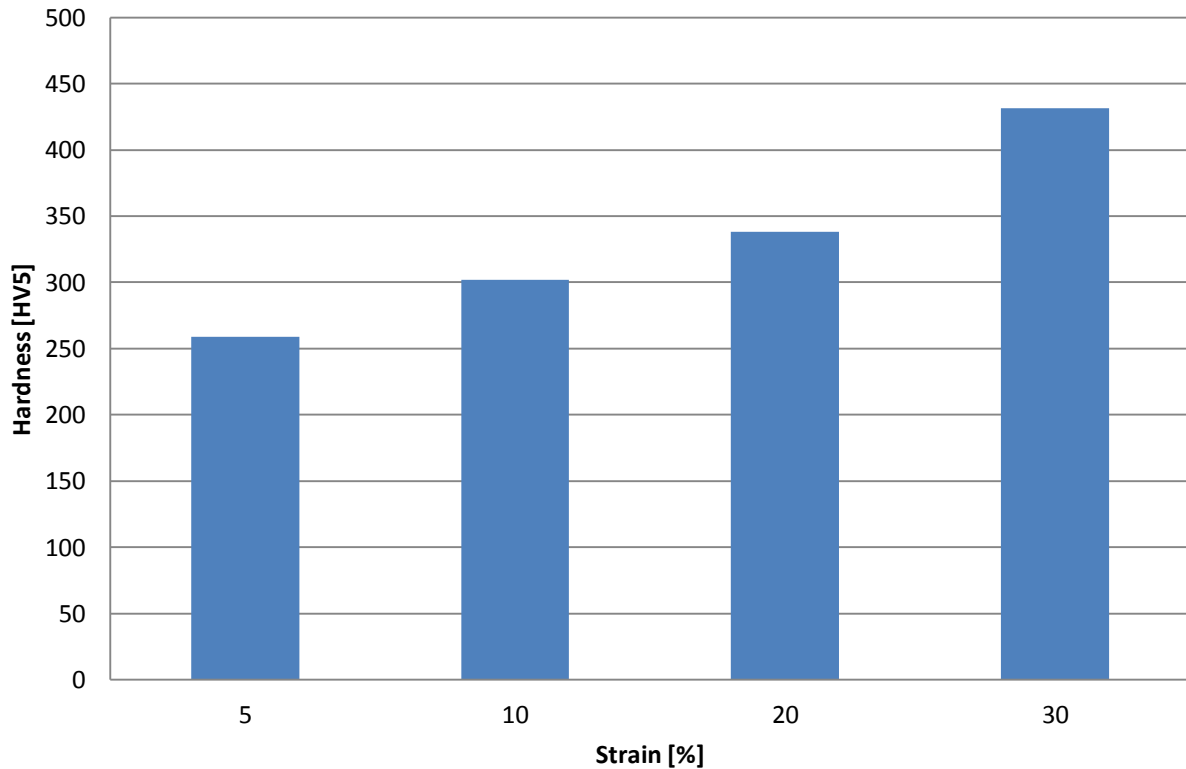
Figure 10 *Average hardness of compression samples with different strains.*

Hardness of the compression samples rises when amount of plastic deformation grows due work hardening. Microstructures of compression samples with different strains are presented in Figure 11.
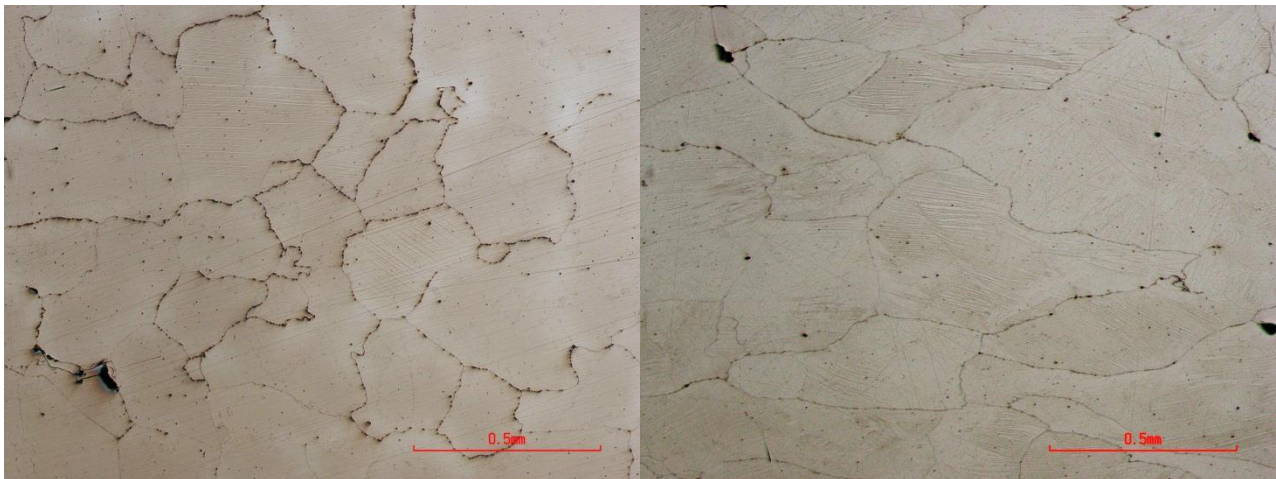

Figure 11 *Compression samples. Strain of the left sample 10% and right 30%.*

On the left picture, there are visible deformation twins only in few grains. Sample on the right, which has been compressed to 30 % strain, there are visible twins in almost every grain. Hardness difference of 10 % and 30 % samples is about 100 HV. Deformation twinning is the main reason for higher hardness. No signs of martensite are discovered from the compression samples.

Hardness of samples compressed with different strain rates are presented in Figure 12. All the samples have been compressed about 30 %.
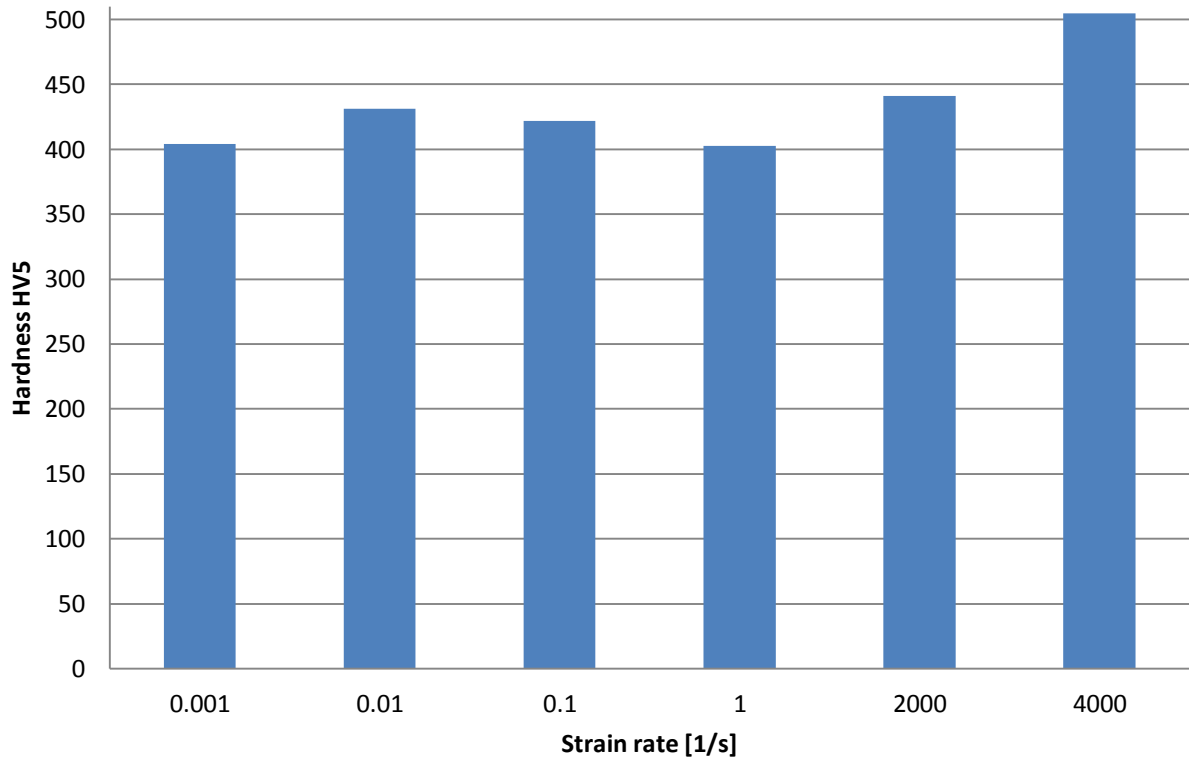
Figure 12 *Average hardness of compression samples with different strain rates.*

It seems that there are not dependence between strain rate and hardness on low strain rates (<1 1/s). At high strain rates, especially at 4000 1/s, hardness is clearly higher than in other samples. Main reason for higher hardness in the high strain rate samples is greater amount of deformation twinning.

4.   CONCLUSIONS

The main conclusions that can be drawn from this study are:
1. Deformation twinning is the primary mechanism for the work-hardening of 17 % manganese steel regardless of the strain rate. Number of twins rises when amount of forming or strain rate increases.
2. Hardness rises when amount of plastic deformation rises. At low strain rates (0.001-1 1/s) strain rate doesn't have much effect to the hardness. But in higher strain rates (1500 & 4000 1/s) hardness rises when strain rate rises.
3. Significant traces of martensite were not found in the tested specimens.

The wear resistance of manganese steel with different working history will be tested in the future. At least some scratching test with pin-on-disk tribometer will be done.

5. REFERENCES

[1] Lindroos, V., Sulonen, M. & Vesitinen, M., *Uudistettu Miekk-ojan metallioppi*. Keuruu: Otava, 1986.

[2] Mendez, J., Ghoreshy, M., Mackay, W.B.F., Smith, T.J.N., Smith, R.W., "Weldability of austenitic manganese steel," *Journal of Materials Processing Technology*, vol. 153-154, no. 1-3, pp. 596-602, November 2004.

[3] Materiaalivalinta, *Kulumista kestävät metallit ja pinnoitteet.* Helsinki: Metalliteollisuuden keskusliiton julkaisu 1/86, 1986.

[4] ASM Metals handbook. Vol. 3, *Properties and selection stainless steels, tool materials and special-purpose metals.*: Metals Park, OH : American Society for Metals, 1980.

[5] Rintamäki, J., *Mangaaniteräksen raekoon hienontaminen seostusta hyväksi käyttäen*, Diplomityö ed. Tampere: TTKK, 1999.

[6] ASM Metals Handbook, *Wear-Resistant Austenitic Manganese Steels*.

[7] Sant, S. B. & Smith, R. W., "A study in the work-hardening behaviour of austenitic manganese steels," *JOURNAL OF MATERIALS SCIENCE*, vol. 22, pp. 1808-1814, 1987.

[8] Efstathiou, C. & Sehitoglu, H., "Strain hardening and heterogeneous deformation," *Acta Materialia*, vol. 58, pp. 1479–1488, 2010.

[9] (2011, March) TUT - Laboratory of Materials Characterization. [Online]. http://www.tut.fi/index.cfm?MainSel=12870&Sel=13652&Show=18694&Siteid=142

TAMPERE UNIVERSITY OF TECHNOLOGY
Degree Programme in
Materials Engineering

PASI HAKONEN

RECRYSTALLIZATION AND THERMAL STABILITY OF ECAP PROCESSED ALUMINUM

Bachelor of Science thesis

Supervisor: Senior Assistant Mikko Hokka

TIIVISTELMÄ

Tämä työ käsittelee kaupallisesti puhtaan alumiinin käsittelyä Severe Plastic Deformation –prosesseilla, keskittyen Equal Channel Angular Pressing -prosessiin ja tämän vaikutukseen alumiinin rekristallaatioon. Muutokset rekristallisaatio-olosuhteissa vaikuttavat alumiinin käyttölämpötilaan ja siten saattavat rajoittaa materiaalin käytettävyyttä.

Tässä tutkimuksessa mitattiin 5 minuutin ja 30 minuutin lämpökäsittelyjen aiheuttamaa rekristallaatiota ECAP-prosessoiduissa alumiininäytteissä eri lämpötiloissa.

Viiden minuutin lämpökäsittelyssä materiaalissa esiintyi rekristallaation aiheuttamia muutoksia kovuudessa $250\ °C$ lämpötilassa ja 30 minuutin hehkutuksella jo lämpötiloilla 150 - 200 °C. Tutkimuksen tulokset soveltuvat lähinnä vain kaupallisesti puhtaalle alumiinille ja tutkimuksessa käytetylle ECAP –prosessille ja niiden hyödynnettävyys muiden materiaalien ja menetelmien kanssa on rajallinen.

Tulosten tärkein sovellusalue onkin avustaa tulevien tutkimusten suunnittelussa ja rekristallaation vaikutusten arvioinnissa koejärjestelyiden yhteydessä, sillä nämä voivat aiheuttaa muutoksia testien tuloksiin.

ABSTRACT

This thesis discusses processing of commercially pure aluminum with Severe Plastic Deformation process and concentrates more closely on the effects of Equal Channel Angular Pressing process on the recrystallization of aluminum. Aluminum alloy (1070) processed with ECAP was annealed in varying temperatures for different holding times. The progress of recrystallization was determined by measuring the changes in microhardness of the samples.

The results show that commercially pure SPD aluminum withstands temperatures of around 250 centigrade for short periods of time without noticeable recrystallization, while longer holding is limited to about 150 - 200 centigrade in order to avoid recrystallization in the material. Alloying elements and varying treatments may alter this and the results obtained in this study are closely tied with the material in question.

The main application of these results is in the planning of future research of the material and evaluating the effects of recrystallization in tests conducted in elevated temperatures.

TABLE OF CONTENTS

ABRREVIATIONS AND NOTATION

DRX   Discontinuous dynamic recrystallization

EBSD   Electron Backscattered Diffraction

ECAE, ECAP   Equal Channel Angular Extrusion or Equal Channel
                                 Angular Pressing

SPD   Severe Plastic Deformation

LM   Reversed Leica light microscope

φ   The angle of the die channel

1.   INTRODUCTION

With new technologies come new requirements for materials. Ever increasing need for strength and hardness forces manufacturers to seek new materials and to improve existing ones. The traditional way to improve metal materials is using alloying and different heat treatments.

SPD (Severe Plastic Deformation) process is a method that achieves similar effects to complex heat treatments with the use of physical force. The process aims to alter the microstructure of the material by deforming and minimizing grain size. An important fact to know with the SPD process, as with all treatments, is the temperature range where the processed materials are usable afterwards. This is partly limited by the recrystallization process where the microstructure of the material starts to reform and the mechanical properties can drop significantly.

The effect of SPD process to a materials usable temperature range can be determined by measuring the change in mechanical properties of the material under different annealing treatments. This thesis describes such research performed on Equal Channel Angular Pressing (ECAP) processed commercially pure aluminum.

2. SPD PROCESS

The microstructure of aluminum affects greatly the mechanical properties of the material. One of the affecting features is the material's grain size. Small grain size improves the toughness and hardness of aluminum. One of the traditional ways to minimize grain size has been utilizing cold working followed by annealing. Complex heat treatments can require long periods of time and specific conditions to work properly, which of course, increase the production costs of more advanced materials. The SPD process aims to provide a cheaper and faster alternative [1]. Another clear difference between SPD processes and more traditional methods to induce high degrees of strain is that the cross sections of processed samples remain the same in SPD processes [2]. SPD process is also shown to affect properties like Curie and Debye temperatures [1].

2.1. ECAP

Equal Channel Angular Pressing is an SPD process where the sample billet is forced through a channel in a die. The ECAP process was originally invented by Segal in Russia in the 1970's. The process is still under research and commercial usage is very limited even today [3]. Still, research by Lowe and Zhu [4] shows that the interest in SPD processes is clearly increasing and articles written and patents applied and accepted of the subject are on the rise.

Figure 1 describes the general principle of ECAP and shows the key parts of the process. The punch pushes the billets through the die and the turns in the die channel. Turns in the channel induce severe shear strain in to the material and deform the microstructure. ECAP treatment usually consists of passing the billet through the die several times and different microstructures can be achieved by turning the billet between passes. More advanced dies have several turns in the channel and they induce greater strain on the material on a single pass thus reducing the process time [3].
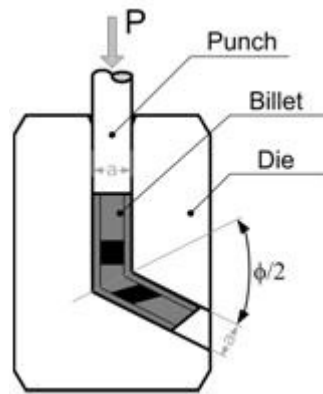
Figure 1 Schematics of ECAP [3]

Another goal of increasing the amount of turns in the channel is to limit the non-uniform deformation of the outer dimensions of the billet. With only a single turn in the channel the ends of the billet deform less than the core regions and the billet size reduces from the original shape as the number of passes increases. Most of this material loss is due to the fact that the deformed end of a billet after passing a single turn die cannot be used as it is and needs to be cut out before the next pass through the die. Figure 2 shows the comparison between billets passed through single turn and two turn channel dies [3]. A clear downside in the ECAP process is the limitations on shape and dimensions of the billet. A continuous process is hard to accomplish and changing the dimensions of the resulting billet requires the change of die.

Processing of stronger and harder materials require more advanced materials to be used in the die. One way to ease the deformation process is to raise the surrounding temperature. The change of processed material affects the process in many ways and every material requires its own process parameters to obtain the best result [5].
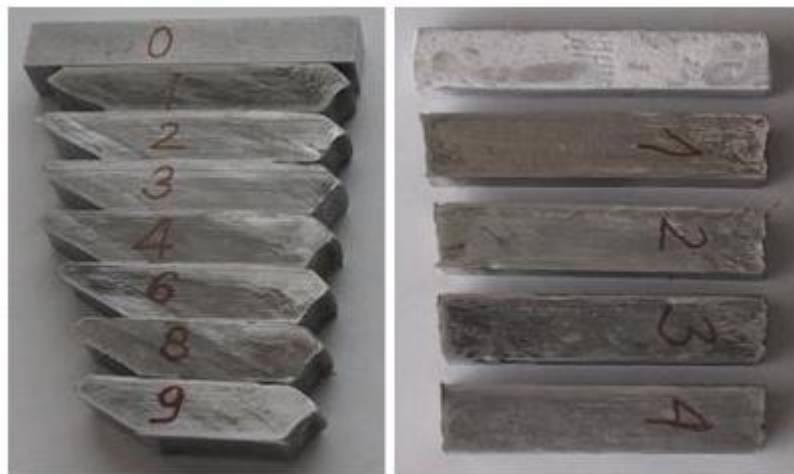
Figure 2 ECAP billets passed through single turn and two turn channels [3]

2.2.   Effects of ECAP on the microstructure

The effect of the SPD processing on the microstructure of an AA1200 aluminum alloy is shown in Figure 3. The method used to process the samples of Figure 3 was single turn ECAP with a circular channel. The billets were rotated 180 degrees along the channel axis between passes. The figure clearly shows how the grain size of the original AA1200 aluminum decreases significantly with successive passes [6]. The decrease in grain size increases the strength and hardness of aluminum [7].

The effect of SPD on mechanical properties is evident already from the first pass. The first pass doubled the yield strength and ultimate tensile strength of commercial purity aluminum. The increase in mechanical properties is weaker during the following passes. The major initial improvement is due to work hardening and the following improvements come from grain refinement [8].
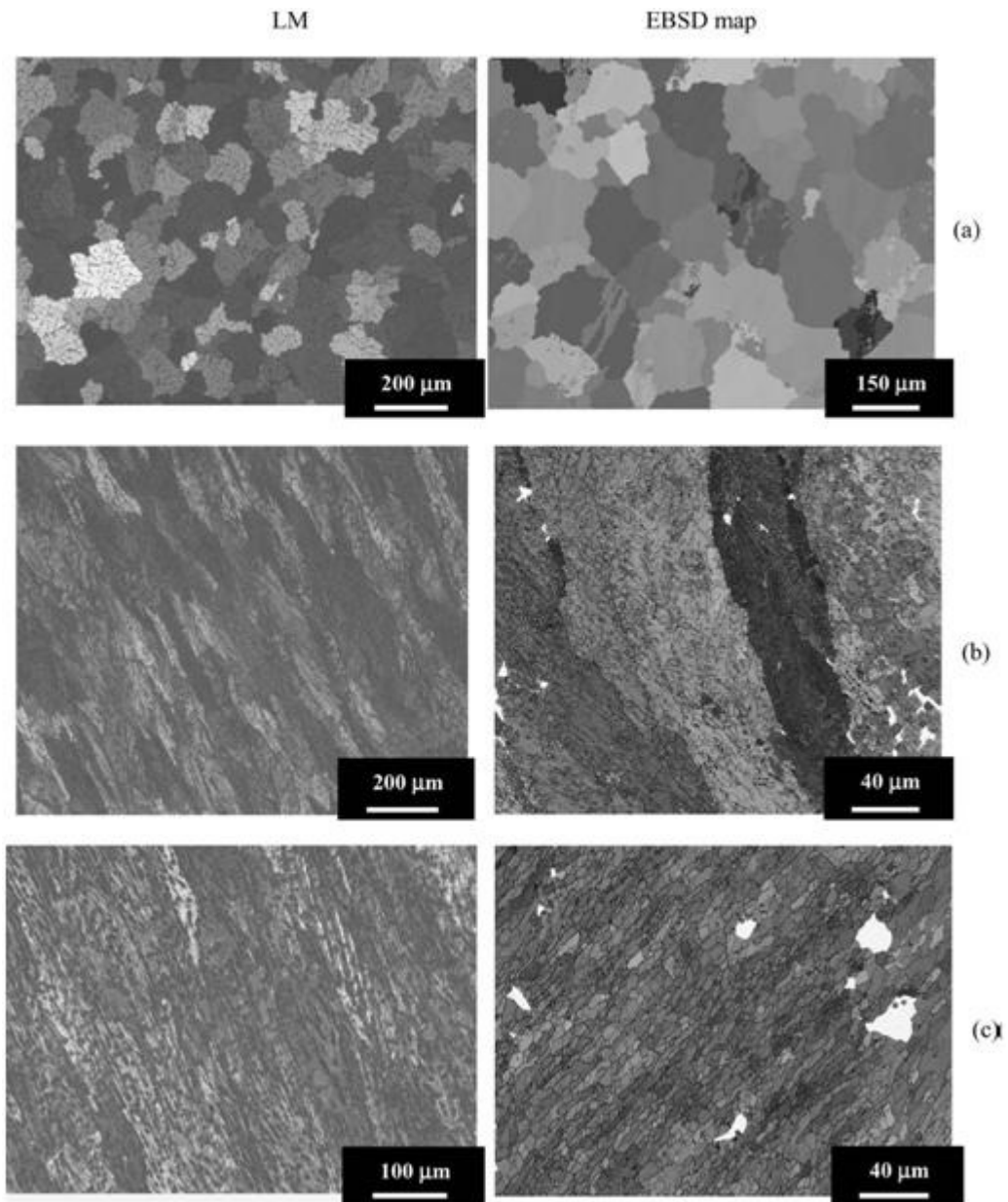
Figure 3 LM micrographs and EBSD maps of 1200 aluminum as a) not deformed, b) after one pass, and c) after 5 passes [6].

2.3.   Downsides of ECAP

There are several limiting factors in the usage of ECAP as a commercial process. First, with a single turn ECAP the utilization of material can be as poor as 65% and so a significant amount of material is wasted. This can be countered with use of multiple turns in the channel and proper channel design that enables significantly higher material utilization [3].

Second limiting factor is the dimensions of the billets. Significant increase of processing forces are needed with increasing billet dimensions. This further increases the strength requirements of the die. The aluminum billets used in the research had a cross section

of 26mm x 26mm and required 300 kN of press force. If the cross section was to be increased or harder material was used, the need for force and therefore the properties needed from the die material would increase significantly [3].

From this is seen that the third limiting factor is the materials that can be processed with ECAP. The bulk of materials processed with ECAP are softer metals like aluminum, magnesium and different alloys. Harder materials impose problems on the die design. The final restricting factor is how to achieve continuous production. Short billets are useful for research purposes but commercial applications would require the ability to process longer bars and preferably with different varying cross sections [3].

3.   RECRYSTALLIZATION

Recrystallization of material is a process where new grain structure forms in a deformed material. Recrystallization is closely related and easily mixed with recovery and grain growth processes. In both recovery and recrystallization the deformed grains aim to minimize internal energy by moving dislocations and forming new, often smaller grains. Grain growth on the other hand is a process that continues the work done by recrystallization and recovery [9].

The difference between recovery and recrystallization is tied with the migration of high angle grain boundaries. In recovery, high angle grain boundaries are static while in recrystallization the boundaries migrate. High angle grain boundaries have misalignment angle between the adjacent grains higher than 10-15 degrees [9].

When the internal energy of the grains is minimized and the only driving force left is the energy bound in the grain boundaries, grain growth begins. Material with small grains have more grain boundaries than similar material with larger grains and the energy bound to grain boundaries lessens when the amount of boundaries decrease. Smaller grains grow larger and this causes often a drop in strength properties [7, 9].

Recrystallization itself can be categorized by several factors. In continuous recrystallization grains evolve from older grains and grain boundaries move longer distances, while in discontinuous recrystallization new grains nucleate with no long range motion of boundaries [9]. Recrystallization that occurs during deformation of material is known as dynamic recrystallization (DRX) and requires higher initial strain to activate. Traditional recrystallization, known as static recrystallization, occurs usually after treatments or during annealing and can be prevented with treatments like quenching [10]. Recrystallization usually shows as a drop in hardness and strength and as an increase in ductility. This can be considered either a beneficial effect used as a part of heat treatment or a negative effect that degrades the material properties [7].

3.1.   Effects of ECAP on recrystallization conditions

The static recovery process begins when temperature climbs enough to allow dislocations to move [7]. The dislocations move toward grain boundaries and if two opposite dislocations meet, they annihilate each other out. The process continues with the grains forming into small spherical shapes. As most of the energy tied in dislocations is freed in the grain reformation, grains begin to grow in size with time [7]. The loss of dislocations allows new dislocations to move more freely through the material, which is shown as a drop in hardness and yield strength.

Figure 4 shows the drop in hardness caused by the recrystallization and decrease in dislocation density of ECAP samples in annealing. The samples were commercial purity aluminum and they were annealed for 2 hours in different temperatures. The figure shows how recrystallization is strongly tied to the temperature and how a certain critical temperature is required to activate recrystallization. A shift of mere 50 degrees in temperatures causes a great difference in hardness in a two hour annealing [11]. Recrystallization affects other properties as well and material properties in general restore to values prior to cold working. While hardness decreases and the material becomes weaker, the ductility of the material increases. Also electrical properties are affected to some degree [7].
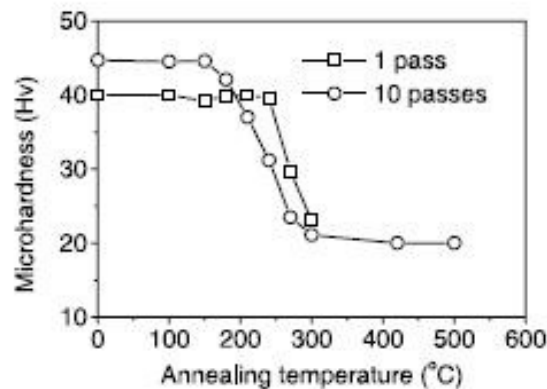

Figure 4 Changes in hardness as recrystallization progresses [11].

The temperature where a material is fully recrystallized after an hour of annealing is called the material's recrystallization temperature. The recrystallization temperature of aluminum is largely dependent on several factors. The degree of cold working, alloying elements and fabrication method all have significant effects and the recrystallization temperature of aluminum can vary from 100°C all the way to 500°C [12]. A notable fact is that recrystallization requires a certain degree of cold working and grain deformation before the process can occur. Increasing the recrystallization temperature is one way to avoid its effects, but when the materials have to endure elevated temperatures for only a limited time the recrystallization rate also affects the situation. Increase in recrystallization rate is affected by the temperature and alloying elements [7].

The purity of material and the amount of alloying elements has a clear impact on the microstructure. The difference is evident when comparing between a commercial purity aluminum (99% aluminum) and high purity aluminum (99,998 % aluminum) grain sizes after ECAE process. The high purity aluminum reached a grain size of 20μm with static recrystallization while commercially pure aluminum managed to reach grain size of 1.5μm with dynamic recovery [13].

4. EXPERIMENTAL

To obtain data on the operational temperature range of the aluminum, several samples were fabricated from ECAP processed aluminum and annealed at different temperatures for varying times.

4.1. Measuring the effects of recrystallization

The progress of recrystallization can be observed as a change in material properties. Small grain size and a great amount of dislocations usually provide a stronger and harder material. Recrystallization can be seen as a drop in these properties. Therefore the easiest way to measure recrystallization is by watching closely the drop in hardness when a sample is heated. During the research the change in hardness was observed by measuring the Vickers microhardness of the samples before and after annealing treatments. The recrystallization process can be considered to end as the drop in hardness reaches a plateau and increasing annealing temperature or time has no further effects on results.

4.2. Sample material

The tests were run on a commercially pure (99,7% Al) aluminum 1070 that was processed with ECAP in which the die channel had 2 turns and the sample billet was turned 90 degrees between passes. The billet was passed through the die 4 times and the final dimensions of the billet were 26mm X 26mm X 120mm. The process achieved plastic strain of approximately 940% in the billet.

Proper sized test samples were produced by cutting a part of the ECAP billet in to 15 samples. One surface of the samples was ground with silicon carbide abrasive. Hardness tests were performed on all the samples after the polishing to establish the initial hardness of the material. Some difficulties were experienced as the microhardness of the samples was not homogenous and varying measurement location affected the results. The hardness measurements shown in the results are the average of three separate hardness measurements.

4.3. Heat treatments

Half of the samples were annealed at varying temperatures for 30 minutes and the other half for approximately 5 minutes. To determine the change in hardness in shorter annealing times the heating rate of the material posed some problems. To obtain 5

minutes of annealing in the target temperature the sample has to be first allowed some time to obtain the desired temperature. To determine the time required to reach a temperature close enough for annealing, a single sample was sacrificed for the examination of heating rate of the samples within the oven. With examining the heating rate of the sample it was decided that to achieve a 5 minute annealing in the appropriate temperature the sample would be inserted in the oven for 7 and half minutes. The first two and half minutes were required for the sample to reach the target temperature within ten centigrade.

After the annealing the samples were removed from the furnace without quenching. All the samples were left to cool down gradually in room temperature. After reaching the surrounding temperature the samples were tested for changes in the microhardness.

4.4.   Results and discussion

The results of hardness tests are shown in Figure 5. The shorter annealing time of 7.5 minutes produces steeper decrease in hardness around the 250 centigrade area. Thus the sample is capable of withstanding greater temperatures for a short period of time without noticeable recrystallization. When subjected to longer annealing times the operation temperature range is more limited. The first signs of recrystallization can be seen between 150 and 200 centigrade with the 30 minute annealing time. The results also show that even short holding times are enough for the recrystallization process when the temperature increases sufficiently.
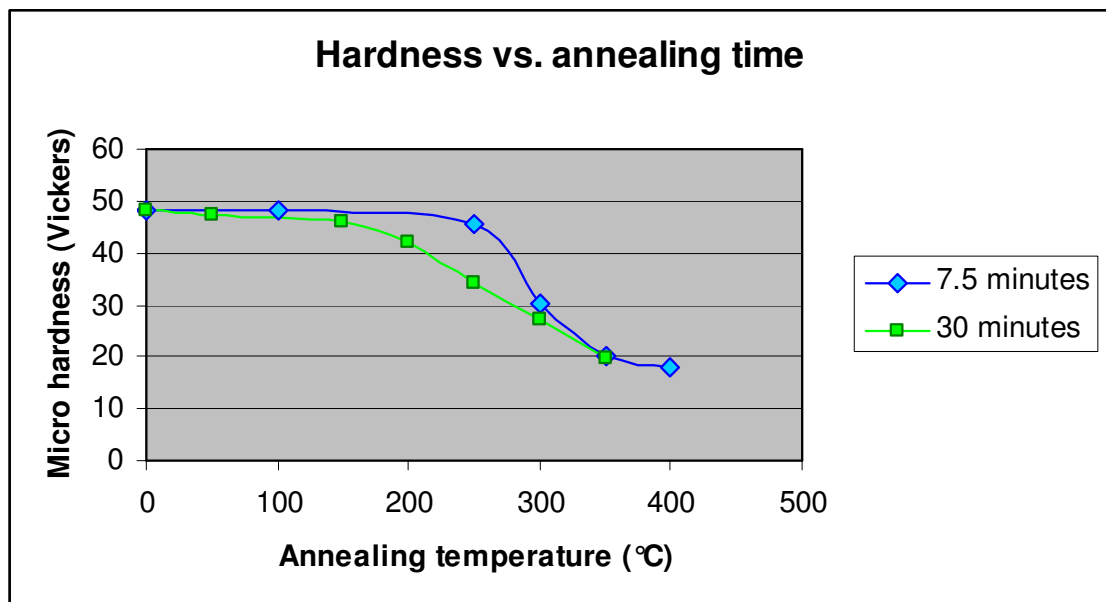

Figure 5 Changes in the microhardness of the aluminum versus annealing temperature under 7.5 and 30 min annealing times

When compared to the results found in the literature the results are consistent. Even with a 2 hour annealing and 10 ECAP passes the recrystallization temperature is located near 300 centigrade [11]. This indicates that the changes in the usable temperature range

induced by ECAP small. Some variance may occur in the recrystallization behavior, but the minor changes in composition are more likely to change the recrystallization temperatures rather than the processing by ECAP. Expansion of the usable temperature range will require alternative methods, such as increasing alloying [7, 11].

The results presented in this thesis are quite similar to results found in other studies. Aluminum alloys processed with ECAP tend to begin the recrystallization around 200-250 centigrade. Though this gives a broad estimate, there is still variation between alloys and results [8, 11, 14, 15].

The results also indicate that any testing, mechanical or other, taking longer than 5-10 minutes should be performed at temperature below 200 centigrade when the recrystallization and change in the material properties should be avoided. Shorter tests can be performed at temperatures up to 250 centigrade with minimal recrystallization and change in the mechanical properties. These results are somewhat limited to the particular material and process, but should still prove useful for further research.

5. CONCLUSIONS

SPD is a process still under development that can be used to alter and enhance mechanical properties of mainly metallic materials. Recrystallization limits the usable temperature range of several cold worked materials. This is often experienced as a decrease in mechanical properties related to recrystallization process. ECAP and other SPD processes affect the recrystallization behavior by changing the activation temperature. Aluminum and its alloys processed with ECAP generally experience recrystallization around 250 centigrade.

The studied 1070 aluminum alloy (99.7% Al) began experiencing recrystallization and decrease in hardness around 250 centigrade under short annealing of 7.5 minutes. Longer annealing of 30 minutes initiated the recrystallization in noticeable amounts between 150 and 200 centigrade.

REFERENCES

1. *Principle of Equal-channel Angular Pressing for the Processing of Ultra-fine Grained Materials.* **Iwahashi, Yoshinori, et al.** 2, July 15, 1996, Scripta Materialia, Vol. 35, pp. 143-146. Available at: [http://www.sciencedirect.com/]. Cited: 16.3.2009.

2. *Processing by equal-channel angular pressing: Applications to grain boundary engineering.* **Furukawa, Minoru and Horita, Zenji, Langdon Terence G.** 40, 2005, Journal of materials science, pp. 909-917. Available at: [http://www.springerlink.com/]. Cited: 7.4.2009.

3. *Scaled-up ECAP with enhanced productivity.* **Olejnik, Lech and Rosochowski, Andrzej.** 2008. International Metal Forming.

4. *Commercialization of Nanostructured Metals Produced by Severe Plastic Deformation Processing.* **Lowe, Terry C and Zhu, Yuntian T.** 5, 2003, Advanced Engineering Materials, Vol. 5, pp. 373-378. Available at: [http://www3.interscience.wiley.com]. Cited 28.5.2009.

5. *The use of severe plastic deformation techniques in grain refinement.* **Lowe, Terry C and Valiev, Ruslan Z.** 10, s.l. : Springer Boston, October 2004, JOM Journal of the Minerals, Vol. 56, pp. 64-68.

6. *Thermal stability study on two aluminum alloys processed with equal channel angular pressing.* **Cabibbo, M, Evangelista, E. and Latini, V.** 2004, Journal of materials science, Vol. 39, pp. 5659-5667. Avalaible at: [http://www.springerlink.com]. Cited: 10.4.2009.

7. **Callister, William D. jr.** *Recovery, recrystallization, and grain growth.* 6th Edition. s.l. : John Wiley & Sons, Inc, 2003. pp. 180-190. 0-471-22471-5.

8. *Effect of equal channel angular pressing on microstructure and mechanical properties of commercial purity aluminum.* **Manna, R., Mukhopadhyay, N.K. and Sastry, G.V.S.** 2008, Metallurgical and materials transactions A, Vol. 39, pp. 1525 - 1534. Avalable at: [http://www.springerlink.com]. Cited: 7.5.2009.

9. *Current issues in recrystallization: a review.* **Doherty, R. D, et al.** 1997, Materials Science and Engineering A, Vol. 238, pp. 219-274. Available at: [http://www.sciencedirect.com]. Cited: 9.6.2009.

10. **García Fernández, Víctor Gerardo.** *Constitutive relations to model the hot flow of commercial purity copper.* 2004. pp. 127-202. Available at: [http://www.tdx.cat/TDX-0104105-092144/]. Cited: 9.6.2009. B-6809-2005/84-689-0578-X.

11. *EBSP study of annealing behavior of aluminum deformed by equal channel angular processing.* **Cao, W. Q., et al.** 2003, Materials Science and Engineering A, Vol. 360, pp. 420-425. Available at: [http://www.elsevier.com/locate/msea]. Cited: 12.4.2009.

12. **Hatch, John E.** *Aluminum: properties and physical metallurgy.* 2nd Edition. s.l. : ASM International, 1984. pp. 105-133. Available at: [http://books.google.fi]. Cited: 7.5.2009. 0871701766.

13. *Strain-Path Effects on the Evolution of Microstructure and Texture during the Severe-Plastic Deformation of Aluminum.* **Salem, A. A, et al.** 9, s.l. : Springer Boston, 2006, Metallurgical and Materials Transactions A, Vol. 37, pp. 2879-2891. Available at: [http://www.springerlink.com/]. Cited: 9.7.2009. 1073-5623 (Print) 1543-1940 (Online).

14. *Annealing of Al–Si alloys after equal-channel angular pressing.* **Szczygiel, Przemyslaw, Roven, Hans Jorgen and Reiso, Oddvin.** 1-2, October 15, 2008, Materials Science and Engineering: A, Vol. 493, pp. 202-206. Available at: [http://www.sciencedirect.com/]. Cited: 17.5.2009.

15. *Equal-channel angular pressing of commercial aluminum alloys: Grain refinement, thermal stability and tensile properties .* **Horita, Zenji, et al.** 3, March 2000, Metallurgical and Materials Transactions A, Vol. 31, pp. 691-701. Available at: [http://www.springerlink.com/]. Cited: 26.6.2009.

Digital Image Correlation in Mechanical Materials Testing

Mikko Hokka, Amos Gilat, and Veli-Tapani Kuokkala

Abstract. Mechanical testing of materials involves measurement of stress, strain, and strain rate and typically several different techniques are used to determine strain and stress at different strain rate and temperature regimes. The techniques usually include LVDT transducers, extensometers, and strain gages. Comparison of the strains measured using these different techniques can sometimes be difficult, especially if different specimen geometries are used at different strain rate regimes. Digital image correlation combined with high speed digital cameras is an extremely effective tool that can be used to measure strains directly from the surface of the specimen by following the displacements of the high contrast speckle pattern applied on the surface of the specimen. The technique is not restricted by strain rates rather than by the technical performance of the cameras. The spatial 3D displacements and strain distributions on the surface of the specimen can be calculated from the image pairs with a very high spatial resolution even with moderate pixel resolutions of the images. This paper describes the digital image correlation procedures and shows how the technique can be used in practice to analyze tension, compression, and torsion tests at a wide range of strain rates.

Keywords: Digital Image Correlation, Mechanical Testing, Hopkinson Split Bar, High Strain Rates

Introduction

Understanding the material behavior and knowing the material properties is critical for all engineering purposes. Design of structures and building of constitutive models to simulate the behavior of structures requires reliable material data. Also, the material and structural behavior of components and structures usually has to be characterized in a wide range of conditions for a safe and well predictable operation of machines and constructions. Therefore, material testing has been an important part of mechanical engineering for centuries and a myriad of testing methods and techniques exist for different purposes. Often the material behavior and properties must be known also at different temperatures and loading rates in compression, tension, and torsion. In addition to these, knowing also the fatigue, corrosion, and fracture behavior of materials is important.

The material behavior at different temperatures, strain rates and loading conditions can vary significantly. The strength of most crystalline metals increases with increasing strain rate and decreasing temperature. Also the ductility, strain hardening rate, and fracture toughness are usually affected by strain rate and temperature. At low and intermediate strain rates (<500 s^{-1}) the strength typically increases linearly with respect to the logarithm of strain rate. The material behavior is explained at these conditions by the

thermally activated dislocation motion. At higher temperatures the dislocations have more thermal energy to overcome the glide obstacles on the glide planes and at lower strain rates they have more time to wait for a suitable energy boost with high enough amplitude to help them overcome the obstacles. At higher strain rates the behavior changes significantly and the strength increases more rapidly than predicted by the thermal activation concept. The dislocation motion is now controlled by several drag mechanisms that consume more energy that can only be supplied by the externally applied force. For most metals, the mechanisms change at strain rates around 10^3 s^{-1}, which is seen as an upturn in the strength vs. logarithmic strain rate plot.

Material testing, such as compression, tension, and torsion testing can be carried out at a wide range of strain rates and temperatures. Low rate experiments are typically carried out with servohydraulic materials testing machines that can also be equipped with high and low temperature capabilities. For intermediate strain rates, there are several possibilities such as high velocity hydraulic actuators, drop tower tests, cam-plastometers, and recently developed intermediate strain rate Hopkinson Bar devices [1]. The conventional Hopkinson Bar devices are used to characterize the material behavior at even higher strain rates, whereas explosive driven impact tests are performed to study the in the highest strain rate regime. The techniques used for different temperature and strain rate regimes as well as for different loading conditions are different, and the material properties are measured using several techniques. At low strain rates the force acting on the specimen is usually measured simply with an axial and/or angular load cell that is connected in series with the specimen and the load frame. The strain can be measured using linear variable differential transducers or with an extensometer attached directly to the specimen. At higher strain rates, the load cannot be measured using a simple load cell, because the load is applied by a rapidly increasing stress pulse that reverberates in the load cell causing severe oscillations in the measured signal. Also measurement of strain with an extensometer at high strain rates is practically impossible due to the small size of the specimens and the limited dynamic properties of the extensometer. Therefore, specimen force and strain are usually measured from pressure bars, where the stress pulses can be recorded if the bars are long enough and the reflections of the pulses from the ends of the bars do not overlap with the measurement signal. The stress pulses are usually measured using strain gages bonded on the surfaces of the stress bars, amplified, and then recorded with a digital oscilloscope. The time resolved stress, strain, and strain rate can be calculated from the measured stress pulses. However, the comparison of results obtained at different strain rate regimes can sometimes be difficult, especially if different specimen geometries are used in low and high strain rate tests.

The specimens in high rate testing are limited in size by the need to reach force equilibrium within the first few percent of strain. Therefore, the strain is usually calculated from the displacements of the ends of the specimen or stress bars and assuming a simple shear, uniaxial compression, or tensile state of stress. The stress state in compression usually is close to uniaxial, at least for small or moderate strains, and the strains measured from the displacements of the ends of the push rods are quite accurate [2]. In tension, however, the stress state is more complex especially in the fillet areas of the dog bone shaped specimen. Typically, the specimen yields also in the fillets, and all this contributes to the strain determined from the movements of the ends of the specimen or the stress bars where the specimen is connected. As a consequence, the strains

measured in tension tests can differ significantly from the true strains in the specimen. Previously, the effect of specimen geometry on the tension test results has been studied by several authors. Verleysen and Degrieg [12-14] extensively studied the effect of specimen geometry in tension using rotating drum cameras to measure the axial strain distributions in a high rate test. According to their work, the strains measured before necking from the displacements of the bars tend to overestimate the true strains in the specimen due to the yielding of the fillet areas. Similar findings were presented by Curtze et al. [15]. Also, in both tension and torsion tests the strain typically localizes at some point during the test, which is usually followed by plastic instability, necking, and failure of the specimen. The strain measured from the displacements of the ends of the bars or the specimen does not take into account the locally higher strains in the necking region that can be significantly higher than elsewhere in the specimen. The true stress calculated by assuming uniform reduction of the original cross section of the gage section does not either take into account the locally lower cross sectional area in the localized region. Therefore, the values of both the average strain and average stress can be significant underestimatious of the true strain and true stress in the localized region. TÄHÄN ASTI!

One of the methods that has been developed to overcome these limitations is the Digital Image Correlation (DIC) technique. Digital image correlation enables non-contact measurement of the strains on the surface of the specimen during the test at a very wide range of strain rates. The technique is based on recording a series of images of the specimen during the deformation with digital cameras and calculating the surface displacements from these images. The technique can be used with only one camera (2D) for planar strain analysis, or with two cameras (3D) that allow the determination of the full field strains during the test. The surface strains can be determined with a very high spatial resolution, and the applicable strain rate range is only limited by the image acquisition rate, optical capabilities, and resolution of the digital cameras.

Digital image correlation consists of several steps that include recording the measurement data in the form of digital images, algorithms to analyze the data contained in the images, and automating the procedures. Today, very sophisticated software are available that combine all necessary steps and algorithms for reliable image correlation. The software basically needs to be able to transfer the real coordinates of the specimen's 3D coordinate system to the image plane 2D coordinate system, and to combine the data from the two cameras and form the digital 3D coordinates of the surface of the specimen.(onko tämä parempi? Siis yritän erottaa todellisen ja lasketun koordinaattisysteemin toisistaa, eli "Real"->"2D-image"->"3D-image" tuon 3D koordinaatiston periaatteessa pitäisi olla sama kuin "Real", mutta mutta laskennallinen, ja kuvatasossa eli pixelikoordinaatisto. Tässä lauseessahan on nimenomaan kyse siitä, että softan *pitäisi/pitää* pystyä tuo laskemaan oikein) This is usually done by applying a simple pinhole projection model and by correcting the lens distortions and other experimental errors by calibrating the model with a known target pattern. The most important feature of the digital image correlation software is the pattern recognition capability, which has to work for the reference image pair and for all the consecutive image pairs to enable calculation of the 3D coordinates in the deformed configurations. The pattern recognition cannot usually be done for individual pixels, but instead small groups of pixels or image subsets are used to identify the coordinates in each image pair. In 3D image matching, the same pattern must be recognized from both images in order to

calculate the coordinates of the surface. Therefore, the cameras must be synchronized to take the images at the same moment at time, and also pixel-to-pixel correspondence of the images must be close enough for successful pattern matching. In other words, the cameras must be aligned so that each pixel in both images corresponds to same the spot on the surface of the specimen. The algorithms used for image matching are complex and include subset shape functions that enable matching of the image subsets after deformation and interpolation of coordinates between the subset. The interpolation of coordinates can be done with very high spatial resolution up to 1/200 pixel. For a good overview on digital image correlation, the reader is referred to for example ref. [3]. In this paper, we demonstrate the application of the digital image correlation to the mechanical testing of materials and explain the benefits of the technique with examples from tests performed on ultrafine grained metals.

Experimental techniques

The work presented in this paper was carried out at the Mechanical Engineering Department of The Ohio State University. Mechanical testing was done in tension, compression, and torsion at strain rates ranging from 10^{-4} s^{-1} to 2000 s^{-1}. The studied materials were severe plastic deformation processed ultrafine grained (UFG) 1070 commercially pure (99.7 wt-% Al) aluminum and near UFG AZ31 magnesium alloy. The tests were monitored using two digital cameras, and the strains on the surface of the specimen were then calculated using the digital image correlation.

Digital Image Correlation

At low strain rates (<1 s^{-1}), two Point Gray Research Grasshopper two megapixel cameras were used to obtain the image pairs. The cameras were operated at frame rates from 0.067 s^{-1} to 19 s^{-1} depending on the strain rate, yielding an average of 200-400 image pairs per test. At strain rates of 1 s^{-1} and above, two Photron Fastcam SA1.1 high speed cameras were used in the compression and torsion tests, and Photron APX RS high speed cameras in the tension tests. The frame rates for the high strain rate tests were selected so that the total number of image pairs was in the same range as for the low rate experiments. With the high speed cameras, the resolution of the images changes from 1 megapixel at the frame rate of 10.000 s^{-1} to 192*144 pixels at the frame rate of 120.000 s^{-1}.

The quality of the speckle pattern must be very good and the contrast should be maximized for maximum spatial resolution. Also, when using the 3D image correlation, recognition of the same pattern in both images is much easier with high quality high contrast patterns. The contrast pattern must be random to avoid correspondence and aperture problems that occur if one image subset can be matched to several locations in the following images. Also, the size of one contrast dot or speckle has to be larger than a single pixel in the image, and therefore the size of the dots must be adjusted when changing the pixel resolution of the cameras.

In the tension tests discussed in this paper, the contrast pattern was simply applied using a black permanent marker over white base coat, whereas in the torsion and

compression tests, the black contrast pattern was spray painted over the white background. At low strain and frame rates, the high resolution of the images allowed using of fine pattern, which is easier to apply. Also the lighting at low strain rates can be simply applied by using regular spot lights that are aligned so that no excess glare from the specimen to the cameras occur and the lighting is even over the whole surface of the specimen.

At higher strain rates, the shutter time becomes shorter and the need for light increases. Therefore, two to four high intensity fiber optic lights were used to illuminate the specimen in the high rate experiments. The fiber optic lights produce a very high intensity light radiation, and the possibility of excess glare increases significantly. Also, the resolution of the cameras degreases quickly at higher frame rates. Therefore, the contrast patterns in the high strain rate compression and tension tests were hand painted either by using a black permanent marker over white base coat (tension) or with a white paint using a single bristle over a black non-glossy satin paint. The black base coat with white pattern gave the highest contrast of all patterns, the black base coat also removed all glare. However, the pattern did not stay on the surface very well at high strains due to the high layer thickness of paint, and in the torsion tests the contrast pattern chipped off from the surface at strains higher than 30-40 percent. Therefore, in the torsion tests the black pattern was spray painted over white base coat, which had much higher adhesion to the surface, allowing testing up to 50-80 percent of strain. Figure 1 shows examples of the contrast patterns used in the tests at different strain rates.
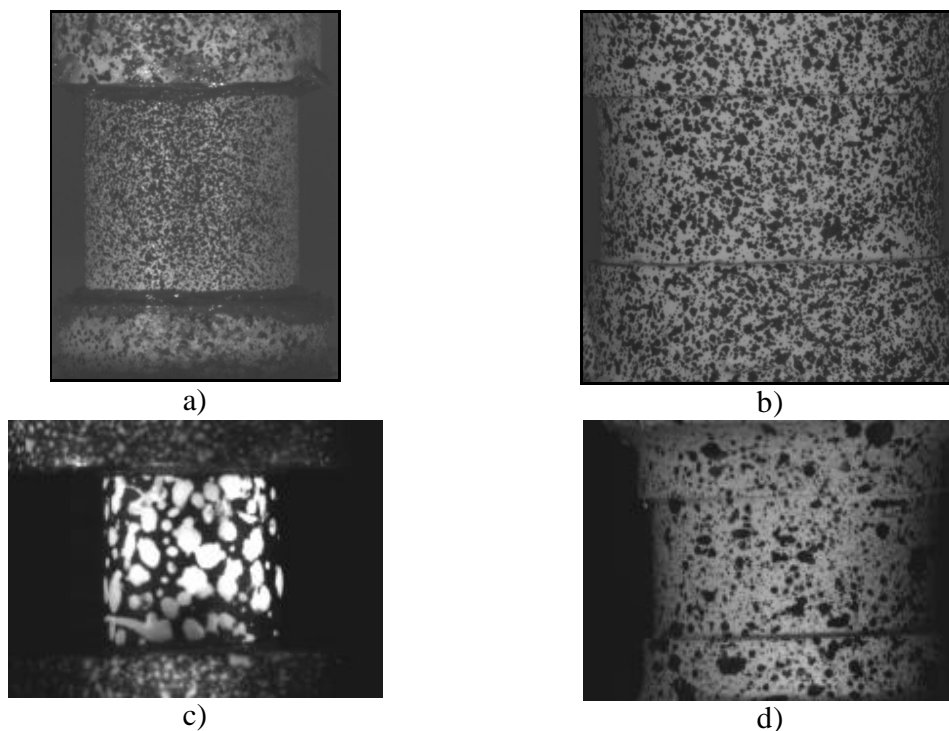

Figure 1. Examples of speckle patterns used at different strain rates; a) low rate compression tests, b) low rate torsion tests, c) high rate compression tests, and d) high rate torsion tests.

The strains in the specimens were calculated from the image correlation results. In the compression tests, the average engineering strain was calculated from the spatial Lagrange strains measured from the surface of the specimen using Equation 1, where E^i are the spatial Lagrange strains in the tangential direction of the specimen surface. In the torsion tests, the strains on the specimen were calculated from the rotational displacements of the ends of the specimen using Equation 2, where θ is the angle of twist between the ends of the specimen and $\bar{a}$ and $\bar{b}$ the vectors from the center axis of the specimen to the surface of the grip section. In the torsion tests the strain was also calculated from the Lagrange surface strains using the relation $\gamma=\frac{1}{2}\varepsilon_{xy}$. Technical strain was used in the tension tests, which was calculated from the elongation of an infinitesimal line element using Equation 3, where l is the length of the line in the undeformed configuration and l+dl is the corresponding length in the deformed configuration.

$$\varepsilon_E = \frac{\sum_{i=1}^{N}\sqrt{1+2E_{11}^i}-1}{N}$$
(1)

$$\gamma = \frac{r_s\theta}{l_s} = \frac{r_s}{l_s}\arccos\left(\frac{\bar{a}\bullet\bar{b}}{\|a\|*\|b\|}\right)$$
(2)

$$\varepsilon^T = \lim_{l\to 0}\left(\frac{l+dl}{l}\right)-1$$
(3)

Hopkinson Split Bar Techniques

The low rate testing was done with a conventional materials testing machine and the high rate tests using the Hopkinson Split Bar techniques. In compression the Hopkinson equipment is fairly simple, consisting basically of two half inch high strength titanium alloy pressure bars. The small cylindrical specimen is sandwiched between the bars. A third bar, the striker bar, is impacted at the free end of the incident bar creating a compressive stress pulse that propagates in the incident bar towards the specimen. As the stress pulse reaches the specimen, part of it is reflected back as a wave of tension and part is transmitted through the specimen into the transmitted bar. As the wave travels through the specimen, the specimen undergoes dynamic elasto-plastic deformation at a high rate. The displacements of the ends of the bars and the time resolved force history of the bars can be calculated from the three stress pulses; incident, reflected, and transmitted that are measured with strain gages bonded on the surfaces of the bars, amplified, and recorded on a digital oscilloscope. From these signals, the strain, strain rate, and stress in the specimen can be calculated as a function of time using equations 4-6. In Equations 4-6, C_0 is the longitudinal wave velocity in the bar, L_s is the gage length of the specimen, A_b is the diameter of the stress bar E is the Young's modulus of the stress bar, A_s the cross sectional area of the specimen, and the strains ε_r and ε_t are the reflected and transmitted

strain pulses measured with strain gages. A schematic picture of a compression Hopkinson Bar device is shown in Figure 2.

$$\dot{\varepsilon} = \frac{2C_0 \varepsilon_r(t)}{L_s} \tag{4}$$

$$\varepsilon(t) = \frac{2C_0}{L_s} \int_0^t \varepsilon_r(t)\, dt \tag{5}$$
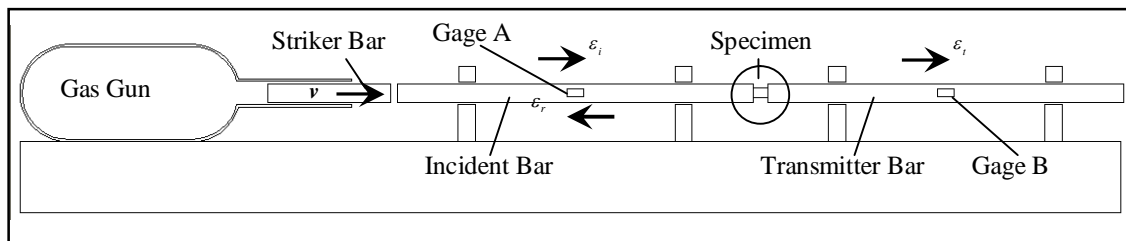
$$\sigma(t) = \frac{A_b\, E \varepsilon_t(t)}{A_s} \tag{6}$$

Figure 2. Schematic picture of a compression Hopkinson Split Bar device.

The tension and torsion Hopkinson Split Bar devices are more complex than the compression bar. The incident tension or torsion pulse cannot be created simply by impacting the striker bar at the free end of the incident bar. Also, the specimen has to be properly fixed to the ends of the bars. There are several methods that can be used to create the incident tension pulse, such as impacting a tubular striker at a flange machined to the free end of the incident bar. Both mechanical fixing and gluing are used to fix the specimen to the bars. In this work, both the tension and torsion incident pulses were created by first clamping the incident bar at a suitable position and storing the load into it by a hydraulic pulley, and then suddenly releasing the stored load/torque by breaking the brittle clamp pin with a second hydraulic press. The specimen was fixed to the stress bars by gluing it to special adaptors, which were then further glued to the ends of the stress bars. A schematic picture of the torsion setup is shown in Figure 3, and a general overview of the tension and torsion devices is shown in Figure 4.
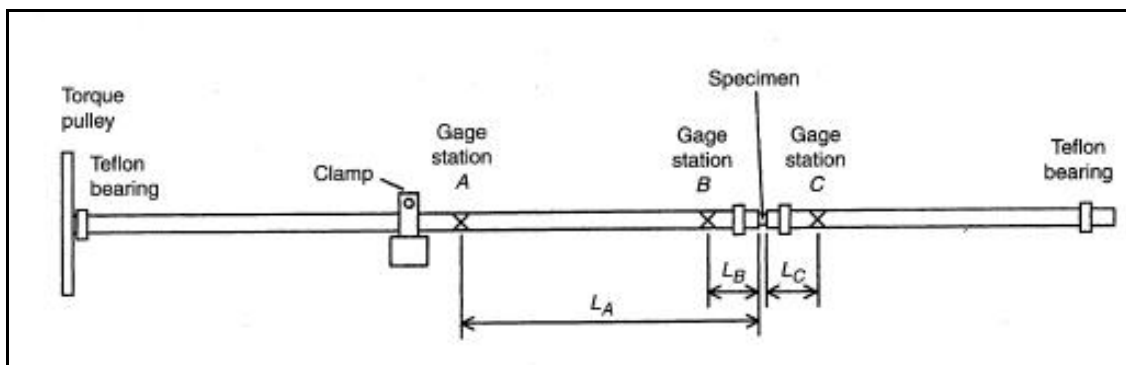
Figure 3. A schematic picture of a torsion Split Hopkinson Pressure bar device [after 4].
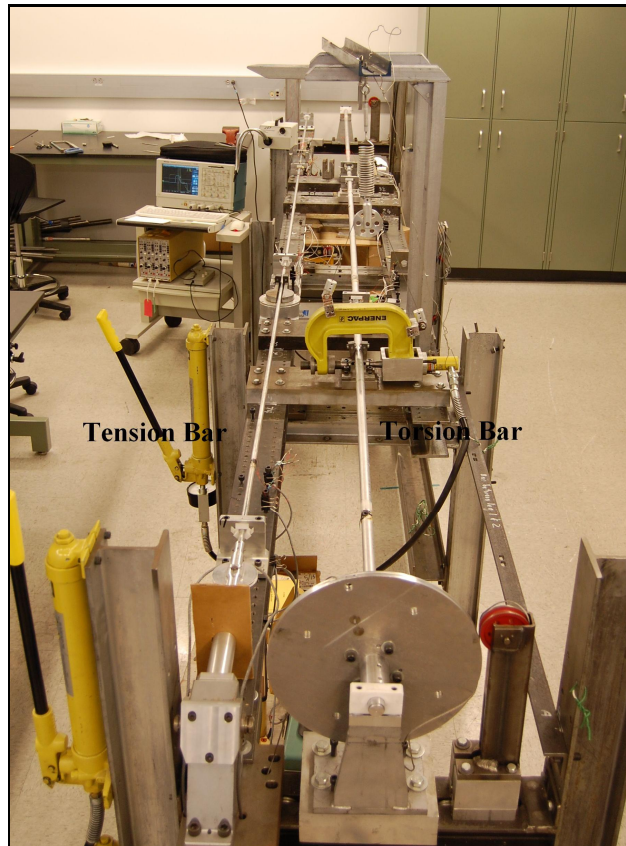

Figure 4. Tension and torsion bar setups at the Department of Mechanical Engineering of The Ohio State University.

In these setups, the incident bar has two strain gage stations, and the reflected pulse is calculated from the measured pulses by applying appropriate time shifts [4]. The strain rate in the tension and torsion tests was calculated using Equations 7 and 8, and the strain simply by integrating the strain rate over time. Shear stress is calculated using Equation 9. In Equations 7-9, c is the shear wave speed in the bar, L_s is the gage length of the specimen, r_s and r_b are the radii of the specimen and the stress bar, t_s is the average wall thickness of the torsion specimen, and the strains ε and γ are the strain gage signals measured at strain gage stations a, b and c. T_s is the transmitted torque, and the time shifts t_a, t_b and t_c are the distances in time that the pulse travels from the respective strain gage station to the specimen or from the specimen to the strain gage station, i.e., $t_a = L_a/c$ etc.

$$\dot{\varepsilon} = \frac{c}{L_s}\left[\varepsilon_a(t-t_a) + \varepsilon_a(t-t_a-2t_b) - \varepsilon_b(t-t_b) - \varepsilon_c(t-t_c)\right] \quad (7)$$

$$\dot{\gamma} = \frac{c}{L_s}\frac{r_s}{r_b}\left[\gamma_a(t-t_a) + \gamma_a(t-t_a-2t_b) - \gamma_b(t-t_b) - \gamma_c(t-t_c)\right] \quad (8)$$

$$\tau = \frac{T_t}{2\pi r_s^2 t_s} \quad (9)$$

Materials

The results shown in this paper are from tests performed on an ECAP processed ultrafine grained 1070 (99.7-wt% Al) aluminum and a reciprocating extrusion processed near ultrafine grained AZ31 magnesium alloy. Tension and torsion tests were performed for the ultrafine grained 1070 aluminum alloy and compression tests for the near UFG AZ31 magnesium alloy. Also a few torsion tests were performed on a standard 7075-T6 aluminum alloy for comparison. For a full description of the materials, tests and discussions of the results, see refs. [5-11]

Discussion and examples of the results

Materials testing at very high strain rates is complicated by several scientific and practical challenges. One of the most difficult tasks to conduct at high rates is accurate measurement of strain, which is usually done by assuming that the stress state is uniaxial and the deformation is limited inside a well defined gage length. In most cases neither of these is exactly true and especially the strains measured in high rate tension and torsion tests can be markedly erroneous. Also, in tension tests the true strain and true stress can only be calculated until necking of the specimen. The following Chapter demonstrates with examples how digital image correlation can be used to overcome these problems.

Tension testing

In the high rate tension tests, the strain calculated from the stress pulses measured on the bars is based on the assumption that the specimen only yields inside the gage section and that the deformation is uniform until the final fracture of the specimen. Therefore, any kind of localization of strain is not taken into account, and the strain after necking can contain significant errors. Figure 5 shows typical dog bone specimens used in the tensile tests. For the UFG 1070 aluminum, the gage length was only 6 mm, the width 4 mm, and thickness 2 mm. The black horizontal lines plotted in Figure 5 are the lines along which the waterfall plots shown in Figure 6 are plotted. The red diamond shows the location of maximum axial strain.
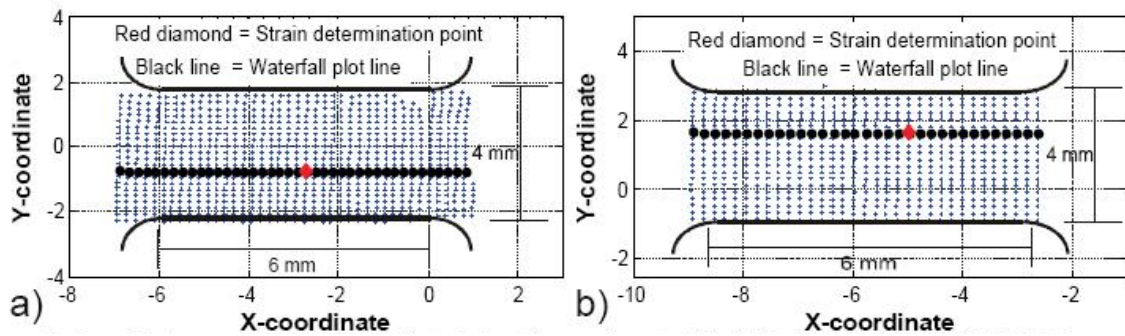
Figure 5. Coordinate maps for the tension specimens and locations of the maximum strain and the paths along which the waterfall plots in Figure 6 were plotted, a) a specimen tested at an average strain rate of 1500 s^{-1} and b) a specimen tested at an average strain rate of 350 s^{-1} [after 10].

Figure 6 shows the waterfall plots determined from the tension tests performed at strain rates 1500 s^{-1} and 350 s^{-1} for the UFG 1070 aluminum. The strain localization starts very rapidly after the initial yielding at both strain rates. This is consistent with the engineering stress strain curves typically measured for the nanocrystalline and ultrafine grained metals. The localization continues throughout the tests, and the maximum strains are located in the necking region. From the waterfall plots it is clear that also the shoulder regions of the specimens yield and axial strain between 3 and 8 percent can be observed for both specimens. The inhomogeneous deformation gradually leads to increasing stress triaxiality instead of the assumed one dimensional stress state. Also, the strains, stresses, and strain rates are much higher in the necking region than the average values measured for the whole cross section and gage length. Therefore, the stress strain curves calculated from the average values do not represent the material behavior correctly after necking.
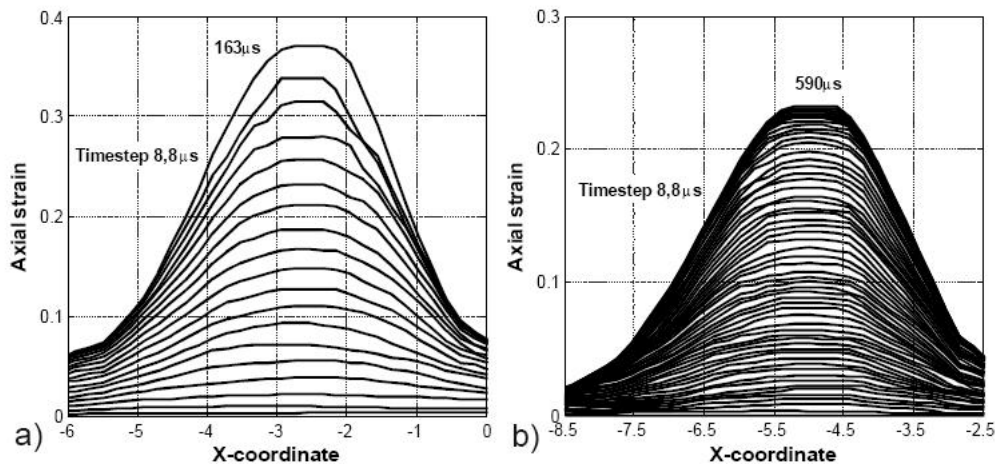

Figure 6. Axial strains along the gage length at 8.8 microsecond time intervals a) for a specimen tested at an average strain rate of 1500 s^{-1}, and b) for a specimen tested at an average strain rate of 350 s^{-1} [after 10].

The true stress in the tensile test can be calculated with the commonly used equations only until the necking starts. However, with DIC the true cross sectional area of the

specimen also in the necking region can be calculated either by assuming constant volume, i.e., dV=0, or by measuring the actual strain in the specimen also in the Z-direction and then assuming that the relative strain rate is the same in the Z-direction as in the axial and transverse directions. Figure 7 shows a comparison of the different stress strain curves that can be obtained from the tension test. The gray solid line is the original Hopkinson Split Bar data, where the engineering stress and strain are calculated from the bar stresses. The dashed black line represents the engineering stress strain curve, where the strain is determined with DIC. The strain used in the plot is determined from the point shown in Fig. 5a. The solid and dotted black lines are the true stress – true strain curves, where the cross sectional area of the specimen is determined from the actual strain measurement and by assuming constant volume. From the plot it is clear that the true stress - true strain curves are at significantly higher stress levels than the engineering curves simply due to the rapidly reducing cross sectional area. In addition, the true stress – true strain curves show a clearly positive strain hardening rate, which is not obvious from the engineering values. However, it should be noted that the stress triaxiality gradually increases after the necking, and in the present analysis this is not taken into account. However, at least for moderate levels of necking the stresses calculated in the described manner may be assumed to represent the real true stresses in the neck area quite well.
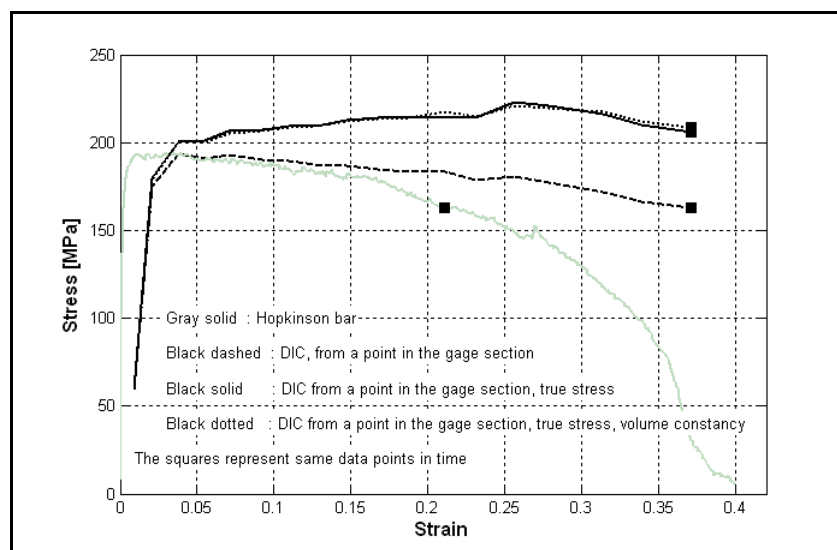

Figure 7. Stress-strain curves with different strain and stress determination for the ultrafine grained 1070 aluminum at the strain rate of 1500 s^{-1} [after 10].

Torsion testing

The strains determined in the torsion tests are shown in Figure 8. The shear strain calculated from the Lagrange shear strain ($\gamma=2*\varepsilon_{xy}$) shows higher values than the shear strain calculated from the displacements of the ends of the bars (Eq.2) and from the strain gage signals for both 7075-T6 (Fig. 8a) and UFG 1070 (Fig. 8b). The shear strains obtained from the displacements of the ends of the bars (Eq.2) and from the stress pulses measured from the bars are closer to one another. The difference between the strains can

be simply explained by the localization of strain, which is not taken into account in the average strains calculated from the stress pulses or obtained with Eq. 2 for the whole gage section. The average Lagrange strain, on the other hand, is calculated directly from the gage section and includes also the high strains in the shear band. However, even the Lagrange strain does not correspond to the maximum strain in the localized shear band which is still higher than the spatial average strain in the gage section. The average shear strains in the specimen calculated from the rotational displacements of the ends of the bars (Eq.2) and from the stress pulses differ mainly due to the eccentric motion of the bars and the specimen and due to the axial and transverse strains that are not taken into account by the one dimensional theory of wave motion that is applied in the calculation the specimen strain from the stress pulses in the bars. The Lagrange strains in the axial (ε_{yy}) and the transverse (ε_{xx}) directions are clearly non-zero, i.e., the deformation is not simple shear. These nonshear strain components are due to the eccentric rotation of the specimen caused by small experimental errors, such as misalignment of the bars, and the specimen and bending of the bars near the specimen.

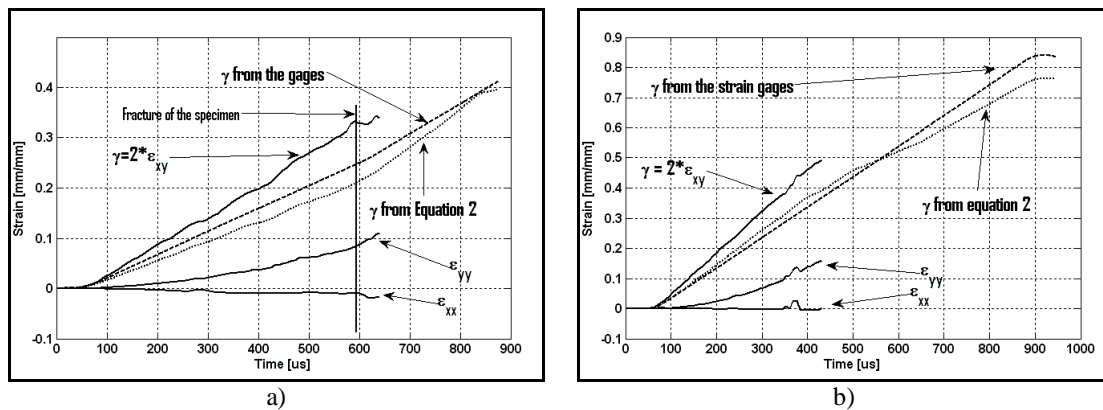a)   b)

Figure 8. Strains measured during a dynamic torsion test for a) the 7075-T6 aluminum alloy and b) UFG 1070 aluminum [After 7].

The shear stress - shear strain curves obtained with different strain determinations are shown in Figure 9. The specimens did not fail during the tests and therefore the decrease of stress at the end of the test does not represent failure but only marks the end of the experiment. The strain calculated from the spatial Lagrange strains show the highest values, but the pattern chips off at around 50 percent and the signal is lost. The strains measured with strain gages are slightly higher than the average strains calculated from the displacements of the ends of the bars using Equation 2. As seen in Figure 9, at higher deformations the shear strain calculated from the stress waves is about 8% higher than the strain calculated from the displacements of the ends of the specimen. The stress, however, does not depend on the strain or its localization in the torsion tests unless there is a significant axial strain component that leads to changes in the wall thickness of the specimen during the experiment.
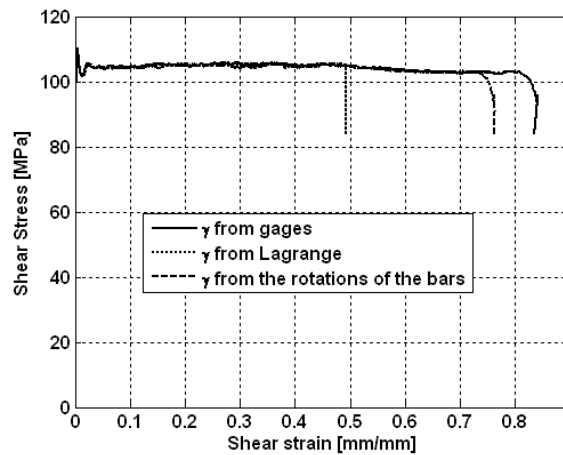
Figure 9. The stress - strain curves obtained with different shear strain determinations for the ultrafine grained 1070 aluminum tested at the strain rate of 1000 s^{-1} [after 7].

Figure 10 shows the localization of shear in the torsion tests. Figure 10a is a waterfall plot of the shear strain calculated from the Lagrange shear strain ($\gamma = 2 * \varepsilon_{xy}$) along the gage length of the specimen. The localization of strain starts very rapidly after yielding and continues throughout the test. The maximum strain at the time when the contrast pattern chips off from the specimen surface is already more than 45 percent, while the right hand side of the specimen shows only about 22% of strain and the left hand side as little as 5 % of strain. Figure 10b shows a fully developed shear band after a significant amount of strain. The maximum strains in the shear band are around 50 percent, and the width of the shear band is of the order of one millimeter. The strain immediately outside the shear band is roughly half of that, and the ends of the gage section are almost nondeformed.
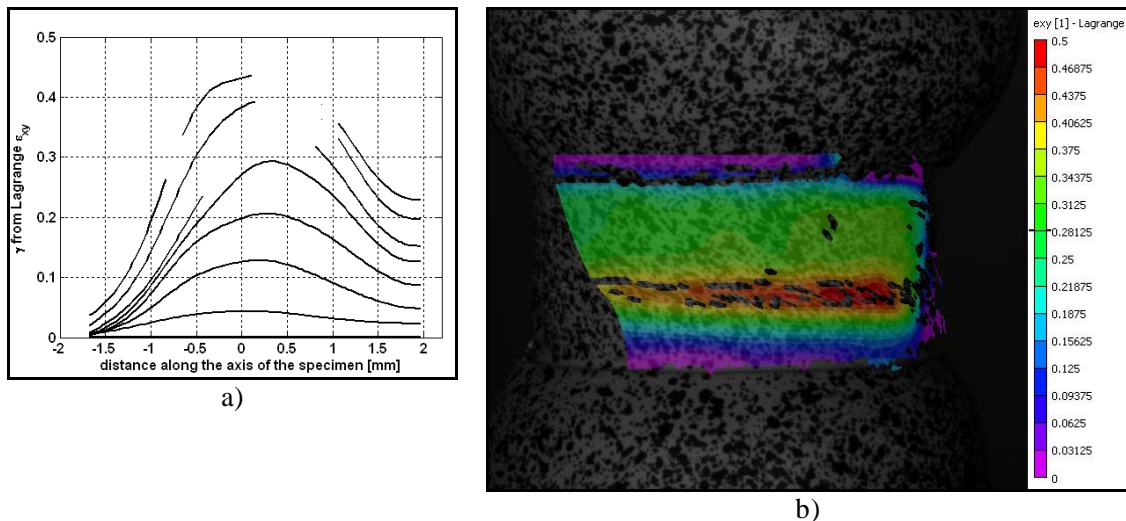

Figure 10. Shear band formation in the torsion test of UFG 1070 aluminum a) waterfall plot along the gage section of the specimen [after 7] and b) fully developed shear band in the middle of the gage length [after 8].

Compression testing

The stress - strain curves obtained from the compression tests using different strain determinations are compared in Figure 11. The average strains calculated from the displacements of the anvils are very close to those determined from the surface of the specimen using Equation 1, both strains being determined using digital image correlation technique. In the beginning of the test the strains are almost identical, but at larger deformations the strains measured from the anvil displacements show slightly higher values. This is typical for compression tests, where the small differences can be explained by the slight barrelling of the specimen and therefore lower tangential strains on the surface of the specimen. However, for a material such as the near ultrafine grained AZ31, for which the fracture strains and the barrelling of the specimen are very low, the average strains measured from the displacements of the anvils are very close to those measured from the surface of the specimen.
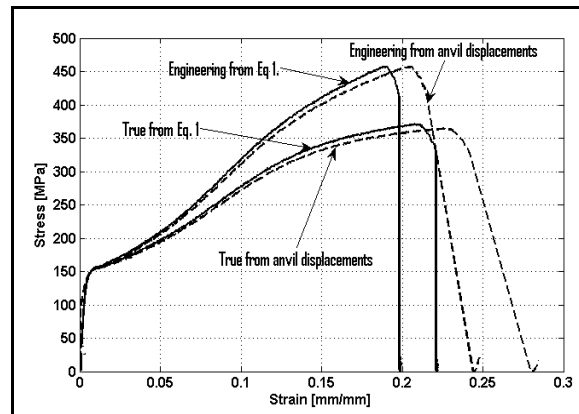

Figure 11. Stress strain curves obtained with different strain determinations for the cast, extruded, and SPD processed AZ31 in compression at the strain rate of 10^{-3} s^{-1} [after 9].

Waterfall plots from a compression test on the near UFG AZ31 magnesium alloy are shown in Figure 12a. The spatial Lagrange strain distributions along the axis of the specimen are more even when compared to the torsion and tension tests. The strains are somewhat asymmetric with respect to position but still increase quite uniformly with time. The largest difference between the maximum and minimum strains is around 7 percent. Strain localization in the specimen does not occur until just before the final fracture. The last image before the fracture is shown in Figures 12b and 12c, where the Lagrange strains in axial and transverse directions are shown over the gage section of the specimen. The fracture occurs at a 45 degree angle along the formed shear band.
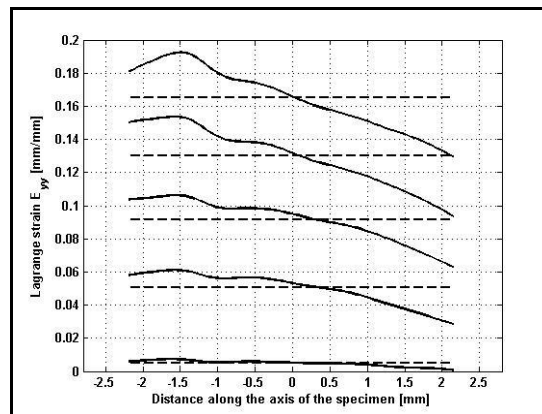
a)
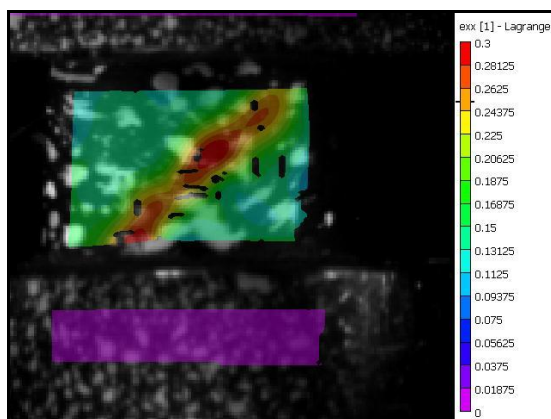
b)
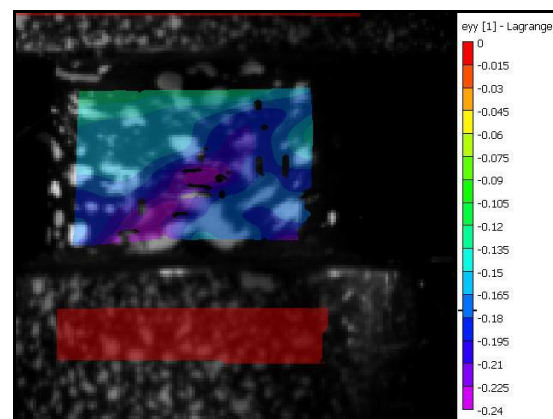
c)

Figure 12: Strain distributions and localizations in the compression test: a) axial strains along the gage section and the average strains (dashed lines) in the specimen for the cast, extruded, and SPD processed AZ31, and the last frame before fracture at a strain rate of 1000 s^{-1}, b) Lagrange ε_{xx} (transverse strains) and c) Lagrange ε_{yy} (axial strains) [after 9].

Summary

Digital image correlation is a very effective non-contact method for accurate strain measurements. Combined with high speed digital cameras, the technique can be used to measure 3D surface displacements and strains even at high rates of deformation. In this paper, we have described how the DIC can be applied to materials testing in a wide range of strain rates in tension, torsion, and compression. In tension tests with the Hopkinson Split Bar method, the DIC yields more accurate strain data from the gage section than the strains calculated from the displacements of the ends of the bars. The strains measured with DIC can also be used to calculate the local true stresses and strains even after necking.

A in Hopkinson Split Bar torsion tests pure 1070 aluminum shows almost immediate localization of strain, the local strains measured on the surface of the specimen are

significantly higher than the average strains measured from the rotational displacements of the pressure bars. The average torsional strains in the specimen were calculated both from the displacements measured from the grip sections of the specimens using DIC and from the stress waves measured from the pressure bars. The small differences in the two strains can be explained by small experimental errors mostly due to the misalignment of the specimen and the bars and to the eccentric positioning of the specimen.

The strains in the compression tests were found to be more uniform than in the tension and torsion tests. The fracture of AZ31 magnesium alloy specimens was preceded by a formation of a shear band in a 45 degree angle with respect to the loading direction. Also the rapid formation of the shear band could be recorded with digital image correlation.

References

[1]   A. Gilat, T. Matrka, A new compressive intermediate strain rate testing apparatus, submitted to the, SEM annual conference, Indianapolis, 2010.

[2]   A. Gilat, T. Schmidt, A. Walker, Full field strain measurements in compression and tension Split Hopkinson Bar experiments, *Experimental Mechanics*, 49:291-302, 2009.

[3]   M. Sutton, J.-J. Orteu, H. Schreier, *Image Correlation for Shape, Motion, and Deformation Measurements.* Springer Science, New York, 2009.

[4]   A. Gilat, Torsional Kolsky bar testing. ASM handbook, 8, Mechanical Testing and Evaluation, ASM International, Materials Park, OH, USA, 2000.

[5]   A. Rosochowski, L. Oljenik, Numerical and physical modeling of plastic deformation in 2-turn equal channel angular extrusion. *Journal of Materials Processing Technology,* 125-126:309-316, 2002.

[6]   L. Oljenik, A. Rosochowski, Methods of fabricating metals from nano-technology *Bulleting of the Polish Academy of Sciences,* 53:413-423, 2005.

[7]   M. Hokka, J. Seidt, T. Matrka, A. Gilat, V.-T. Kuokkala, J. Kokkonen, S. Müller, Characterization of the mechanical behavior of ultrafine grained metals using digital image correlation, *Submitted to the ICEM14 international conference on experimental mechanics*, Poitiers, France, 2010.

[8]   M. Hokka, J. Kokkonen, J. Seidt, T. Matrka, A. Gilat, V.-T. Kuokkala, Dynamic torsion properties of Ultrafine Grained Aluminum, *Submitted to the SEM annual conference,* Indianapolis, IN, USA, 2010.

[9]   M. Hokka, J. Seidt, T. Matrka, A. Gilat, V.-T. Kuokkala, J. Nykänen, S. Müller, Compression behavior of near-UFG AZ31 Mg-Alloy at high strain rates, *Submitted to the SEM annual conference,* Indianapolis, IN, USA, 2010.

[10] J. Kokkonen, V.-T. Kuokkala, J. Seidt, A. Walker, A. Gilat, L. Oljenik, A. Roshochowski, High strain rate deformation analysis of UFG aluminum sheet samples, *In the proceedings of the Annual SEM conference*, Albuquerque, NM, USA, 2009.

[11] J. Kokkonen, V.-T. Kuokkala, Lech Olejnik, A. Rosochowski, Dynamic behavior of ECAP processed aluminum at room and sub-zer temperatures, *In the proceedings of the Annual SEM conference*, Orlando, FL, USA, 2008.

[12] P. Verleysen, J. Degrieck, Optical measurements of the specimen deformation at high strain rate, *Experimental Mechanics,* 44, 2004.

[13] P. Verleysen, J. Degrieck, Experimental investigation of the deformation of Hopkinson Bar specimens, *International Journal of Impact Engineering,* 30, 2004.

[14] P. Verleysen, J. Degrieck, Measurement of the evolution of the axial strain distribution in Hopkinson specimens. *Journal de Physique IV,* 110, 1993.

[15] S. Curtze, M. Hokka, V.-T. Kuokkala, T. Vuoristo, Experimental analysis on the influence of the specimen geometry on the tensile Hopkinson Split Bar test result of steel sheet, *In the proceedings of the MS&T conference,* Cincinnati, OH, USA, 2006.

Mikko Hokka, Veli-Tapani Kuokkala
Tampere University of Technology, Department of Materials Science
POB 589, 33101 Tampere
mikko.hokka@tut.fi

Amos Gilat, Mikko Hokka
The Ohio State University, Department of Mechanical Engineering
209 W 19th Avenue, Columbus, OH 43210, U.S.A.
gilat.1@osu.edu

Review

Nanocrystalline and Ultrafine Grain Size Steels by Severe Plastic Deformation - Sheet Steels and Surface Nanocrystallization

Dr. Mikko Hokka

Tampere University of Technology – Department of Material Science
POB 589, 33101 Tampere, Finland
mikko.hokka@tut.fi
The Ohio State University – Department of Mechanical Engineering
201 West 19th Avenue, Columbus OH, 43210, USA

Abstract

Nanocrystalline (nc) and ultra-fine grain size (ufg) metals have been found to have many excellent properties compared to their large grained counterparts. For example, most metals with grain sizes in the nanocrystalline range show excellent strength, hardness, and fatigue properties [28-33], and improved friction, wear, and corrosion properties [52, 53, 71] combined with increased toughness even at low temperatures [45]. The development of severe plastic deformation (SPD) processing for grain size refinement of metals begun already in early 80's, according to the literature however, not many serious attempts to produce nanocrystalline and ultrafine grained bulk metals has been reported until recent years. Between 1990 and August 1999 there were only 24 publications concerning severe plastic deformation of iron and iron based alloys [62] and by December 2002 there were 160 publications [19]. Since then the number of reported studies and registered patents towards commercialization of continuous production of severe plastic deformation processed steels and other metals has been steadily increasing.

There are some major barriers that are impeding the commercialization of SPD processed steels and metals in general, which are all mainly due to the immaturity of the technology. The main problems are the lack of extensive knowledge of processing ultrafine grained metals and consequent lack of any large scale production of bulk metals as well as poor standardization of the processing, properties, and characterization of nanocrystalline and ultrafine grained metals. Also, the conventional characterization methods such as optical microscopy are ineffective in characterizing nanocrystalline metals and usually transmission electron microscopy is needed to resolve the individual grains and their underlying structures. This of course makes characterization of the material structures more complicated and not many industrial producers have direct access to such advanced characterization techniques. The present literature survey was undertaken to address the presented problems and also to gather information concerning severe plastic deformation processing of steels aiming at continuous production at a larger scale.

SPD of steels - processes, structures, and properties

Several scientists have processed iron based alloys with SPD, mainly low carbon and stainless steels have been studied. Examples of SPD methods for steels include equal channel angular pressing (ECAP), high pressure torsion (HPT), and conform extrusion for producing bars and rods, whereas continuous confined strip shearing (C2S2), dissimilar-channel angular rolling (DCAR), conshearing, accumulative roll bonding, and repeated cold rolling and folding for processing of sheet metals. For a good overview of processing, microstructure, and mechanical properties of ultrafine grained bcc steels see ref. [21] and for an overview of severe plastic deformation techniques in general the reader is referred to refs. [35, 42].

Processes for strips and plates

Continuous SPD processing of strips and sheets can, in principle, be done by dissimilar-channel angular rolling and conshearing, but so far no attempts with steel or iron based alloys have been reported in the literature. Both methods have been used for processing of aluminum and aluminum alloys [1-3] with good results. Utsunomiya et al. [1] processed AA1100 aluminum alloy with consearing process and were able to increase the strength to about 170 MPa after 6 passes while still maintaining a fracture elongation of 23%. However, the following Chapter presents only methods that are clearly aimed at continuous production of steel strips or plates.

Frictional angular extrusion and single roll drive ECAP

Similar method to conshearing is the frictional angular extrusion [43]. In this method, the continuous shearing is generated by pushing the steel strip through an equal-channel angular die. The sheet is pushed through the die by a single frictional roll, which presses the sheet against a work piece supporter that provides enough normal loads for the frictional drive. A schematic picture of the technique is shown in Figure 1. The frictional angular extrusion can be used to process large volumes of various forms of material. Yan et al. [43] processed interstitial steel sheet with frictional angular extrusion, the sheet specimen dimensions in their study were 2 mm*20-50 mm* 1000 mm. The grain size was efficiently refined from the initial size of about 40 µm to 0.83 µm just after 2 passes. After 8 passes the equivalent strain was around 5.3 yielding grain size of about 0.25 µm.
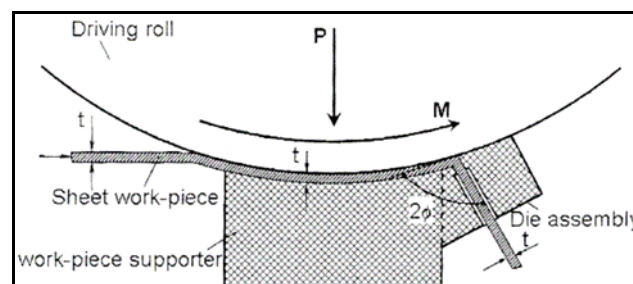

Figure 1. Schematic diagram of the frictional angular extrusion setup [43].

Single roll drive equal channel angular process [63] can be used for continuous processing of square rods, billets as well as strips, sheets and plates. It is also very similar technique to consearing and frictional angular extrusion. The equipment consists of fixed die, movable die, guide rolls, and drive roll. The fixed dies restrict the width of the sheet, whereas the movable die presses the sheet against the drive roll, which drives the sheet by frictional force between the drive roll and the sheet. The surface of the drive roll can be mechanically roughened to increase the friction. Figure 2 presents the principles of operation for this technique.
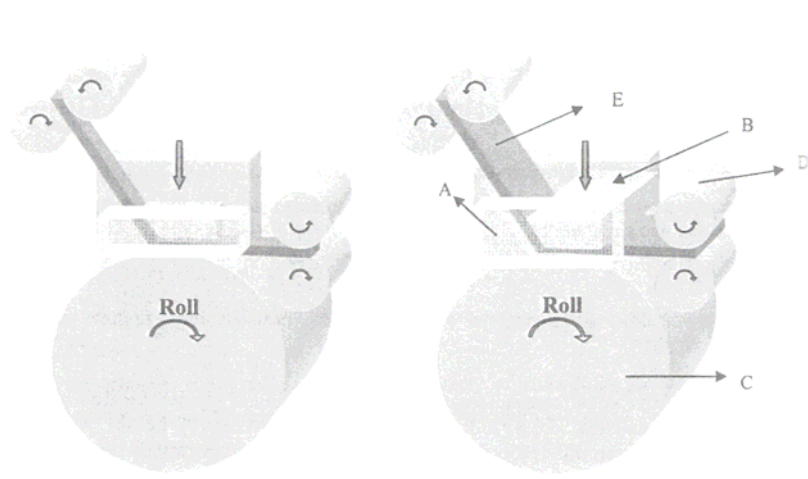

Figure 2. Sketch of the single roll drive equal channel angular process for a) processing billets and b) processing sheets [63].

Accumulative roll bonding

Accumulative roll bonding (ARB) and repeated cold rolling and folding are SPD processed used to deform metals sheets, but they are not readily continuous. In ARB, the rolled material is cut into shorter slabs, stacked, and then rolled again to original thickness and length. In between the rolling sequences, the surfaces need to be degreased and wire brushed to improve the bonding between the strips. The strips are heated to elevated temperature prior to roll bonding; however, the temperatures are to be kept within cold rolling range, because too high temperatures will lead to scaling, recrystallization, and grain growth. Figure 3 illustrates the principles of the accumulative roll bonding process. See ref. [12-13] for more detailed description of the method, and ref. [14-15] for a detailed analysis.
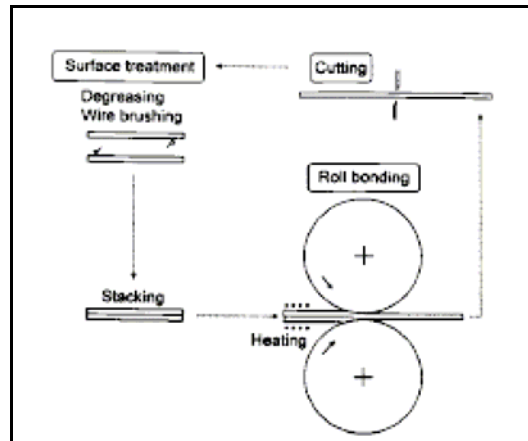
Figure 3: Schematic illustration showing the principles of the accumulative roll bonding process.

The frictional conditions between the rolls and the sheet can have significant effects on the structure that forms during accumulative roll bonding process. The absence of lubrication will lead to a high redundant shear strain near the surface of the sheet and an inhomogeneous strain distribution through the thickness of the sheet [14-15]. However, after the first rolling sequence, the sheet is cut and the surface layers become the middle section of the sheet after the next rolling sequence. Therefore, the shear strain distribution becomes more even as the processing continues. Kamikawa et al. [15] performed a detailed study on the effect of the lubrication conditions on the strain distributions through the thickness of the sheet. If the rolling was conducted under properly lubricated conditions, the equivalent strain distribution was very even after the first rolling sequence. This was very close to a plane strain condition with uniform compression strain through the thickness of the sheet. Without any lubrication, the equivalent strain has a clear maximum at around $t/t_0 \sim 0.4$ with significantly higher equivalent strain than with proper lubrication. Therefore, under lubricated conditions, the strain distribution is uniform, but the achievable strains are much lower. Also the structure was found to be quite different after one ARB cycle under fully lubricated conditions when compared to the non-lubricated conditions. Both average misorientation angle between the grains and the fraction of high angle grain boundaries were higher for non-lubricated ARB processed steel. However, again the distribution of high angle grain boundary fraction varied significantly along the thickness profile from about 20% in the center line to 60% at the surface, while the steel deformed under lubricated conditions had constant 15% of high angle grain boundaries through the thickness. After five cycles, however, both well lubricated and non-lubricated steels showed ultrafine grained structure with high fraction of high angle grain boundaries. The texture in the steel processed under lubricated conditions was a typical sharp sheet texture with extremely elongated grains, whereas the steel processed without lubrication showed more equiaxed pancake shaped grains and complicated texture distribution depending on the thickness location.

Edge cracking of the steel sheet can sometimes occur after several cycles. Tsuji et al. [12, 68] reported edge cracking to occur after several cycles for titanium alloyed interstitial free steel, but were successful in processing sheets up to 7 cycles. However, after seven cycles 99.2% of the volume of the steel sheet was already filled with ultra-fine grains. The sheets were rolled to 50% reduction per cycle at 773K followed by water quenching. The UTS of the processed steel increased from around 250 MPa to about 870 MPa, while total elongation dropped from 55% to only few percent.

Adequate bonding of the sheets must be obtained during the rolling sequence. The wire brushing and degreasing must be performed between each rolling cycle, but also the oxidation of the surfaces of the layers must be avoided during the heating of the sheets. The oxidation can lead to poor bonding, but it can be avoided by welding the edges together before heating of the plates. According to Salvatori [18], good bonding between the strips needs a minimum amount of strain, which depends on the rolling temperature. For a commercial plain low-C steel, for holding at 615 °C for 2 minutes prior to rolling requires minimum of 40% of reduction for good bonding between the strips. Also according to Jiang et al. [27] the bond strength increases with both rolling temperature and also with the rolling reduction per single pass.

Repeated cold rolling and folding

Repeated cold rolling and folding (RCR) is a method very similar to the accumulative roll bonding, but without the intermediate brushing operation. RCR process is performed by repeatedly rolling the sheet metal with intermediate folding. RCR is performed without lubrication allowing higher strains to be achieved and at lower rolling rates than ABR to avoid frictional heating of the sheet. RCR can basically be repeated infinitely and the reachable grain sizes are really low. Dinda et al. [16-17] and Wilde [11] processed nickel, zirconium, and titanium using RCR and reached grain sizes of 80 ± 40 nm for Zr and Ti and around 10 nm for nickel after 80 RCR cycles.

Processes for bars, rods, and profiles

Severe torsion straining process

The severe torsion straining process (Fig 4) [22-24] is a technique for processing of rods and bars. In this technique, the bar is continuously rotated from one end while the other end is fixed. The deformation is localized by a powerful induction heating coil, which moves from one end of the bar towards the other end. Both sides of the heated zone are cooled by water sprays keeping the heated zone narrow and effectively localizing the deformation to the warm area. The main process parameters that affect the microstructure are processing temperature and the ratio of rotation and axial movement of the bar respect to the heater. Too low temperature will easily lead to failure of the bar, whereas high temperatures will cancel the accumulated strain. The ratio of rotation and movement of the bar must also be kept within certain limits due to possible fracture of the bar at too

high rotation speeds and too low accumulated torsion strains at low rotation speed. Kawasaki et al. [22] processed S45C steel with severe torsion straining at 650 °C, 10 rpm, and 200 mm/min. They were able to reduce the grain size of the 12 mm diameter steel bar from about 15 μm to ~2 μm. However, the processing produces slightly inhomogeneous structure and the grain size varies across the cross-section and from 2 μm at close to the surface to around 4 μm at the centerline of the bar. The yield strength of the steel increased from about 350 MPa to 520 MPa, UTS increased from 540 MPa to 750 MPa, while the uniform elongation dropped only from about 24% to 19%.
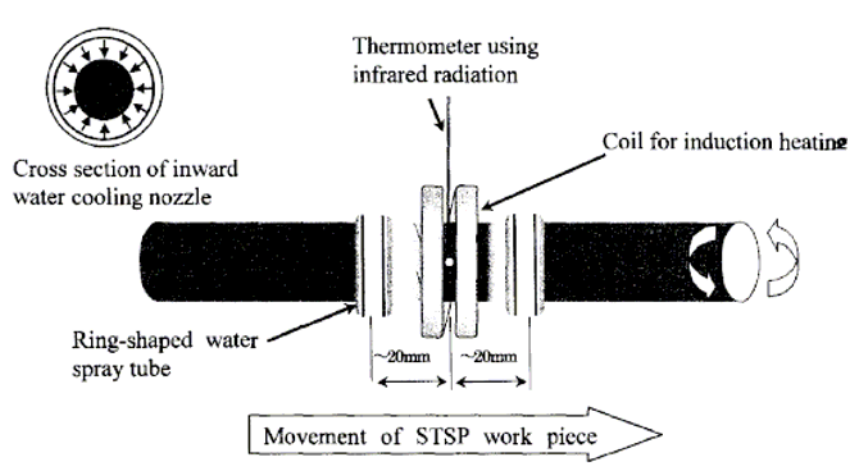

Figure 4. Schematic presentation of the severe torsion straining process for steels [24].

Linear flow splitting

One of the severe plastic deformation processes potentially suitable for large scale production is called linear flow splitting [25-26]. This technique is actually a cold forming method, which is used to produce profiles for branched sheet metal structures. A distinctive feature of this process is that it is actually intended for production of sheet metal profiles and not just a bulk UFG metals for further forming. Processing by linear flow splitting consists of a blunt angled splitting roll and two supporting rolls (Fig. 5 and 6). The forming of the sheet occurs by passing several forming steps, where the splitting roll drives into the edge of the sheet by incremental steps. The severe plastic strain is introduced in the most deformed zones, i.e., flange surfaces and the splitting center, leading to an ultrafine grained structure at these locations. However, processing by linear flow splitting always leads to microstructural gradients, and therefore also the properties of the finished profile will not be the very different on the flanges when compared to the non-processed section of the profile. Bruder et al. [26] measured grain sizes and hardness profiles of the processed flanges and found that for HSLA steel, the grain size varied from about 0.2 μm at the surface to 1.2 μm at depth of 800 μm. Also the hardness of the steel dropped from 350 HV0.5 on the surface to about 250 HV0.5 at the depth of 800 μm. However, the method is fast and continuous and can be readily used to produce flanged profiles, where the strength of the flanges is very high.
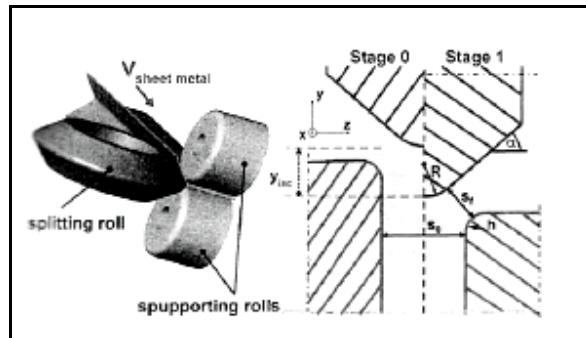
Figure 5. Process principle and geometrical characteristics of the linear flow splitting process [25].
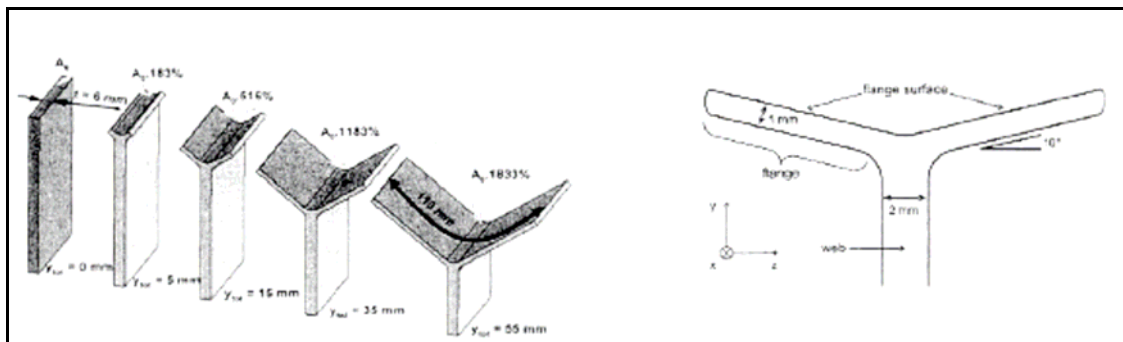

Figure 6. Surface increase during linear flow splitting and the profile scheme [25].

Equal-channel angular pressing

The ECAP processing is basically very simple; the material is pushed through channels, which meet each other in an angle. The billet undergoes simple shear deformation while it is extruded through the channels. The magnitude of the shear strain depends on the geometry of the die channels, mainly on the angle between the two channels, but also on the angle of curvature where the two channels meet. Figure 7 shows the principles of the technique. For specific description of the technique the reader is referred to ref. [35]
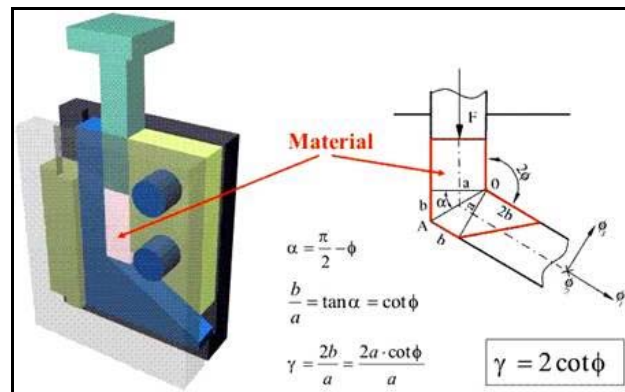
Figure 7. Schematic pictures of Equal Channel Angular Pressing tool and material flow in the channel.

Even though equal channel angular pressing is one of the most effective SPD techniques to refine grain sizes of various metals, applying the technique for continuous production nanocrystalline and ultrafine grained steels can be rather difficult. ECAP has been applied to processing of steels by several scientists [28-34] and the results are promising. However, also some modifications of the ECAP technique have been proposed, which are better suited for continuous processing even at the industrial scale. Most of the ECAP experiments on steels have been performed with interstitial steels [33], plain low carbon steels [28, 30-32], and dual phase steels [28-29, 34].

The microstructural evolution during ECAP processing has been studied by Fukuda et al. [36] and Shin et al. [37]. During the first pass through the die, the grains extend parallel to the channel and the grain boundaries are mainly low angle boundaries. The bands of elongated grains are separated from each other by about 0.3 μm and the dislocation density within the grains is fairly low. After the second pass the grains become less elongated and the misorientation between the grains increases. After four passes through the die, the grains are equiaxed with an average size between 0.2 μm and 0.3 μm, and the grain boundaries were mainly high angle boundaries. The microstructural development, however, depends on the processing route i.e., how the billet is rotated between passes.

ECAP processing of steels is complicated by increasing pressing forces required to push the rods through the ECAP die. Also, the deformability of steels is generally lower than that of for example pure aluminum and copper. Therefore, ECAP processing of steels is usually conducted at elevated temperatures. The effect of temperature on the microstructure and mechanical properties was studied by Shin et al. [31]. They ECAPed low carbon steels with different compositions at different temperatures between 350 °C and 600 °C and the results clearly show that the strength of the steel decreases with increasing processing temperatures, while the ductility clearly increases with increasing temperature. After four passes through the die and effective strain of about ~4, the strength of the steel processed at 600 °C increased only from ~300 MPa to 450 MPa, whereas the strength of the steel processed at 350 °C was 920 MPa after the ECA pressing. This effect, however, seems also to depend strongly on the chemical composition of the steel, and a steel with minor vanadium and niobium additions was

much less temperature sensitive and the strength levels were much higher; the strength of the steel processed at 600 °C increased from 370 MPa to 630 MPa and the strength of the steel processed at 300 °C was around 950 MPa. In addition to the strength, the processing temperature has also a significant effect on the ductility and strain hardening behavior of the steel. The steels processed at temperatures between 400 °C to 600 °C showed clearly higher uniform elongations and strain hardened during the tensile test. However, the steel processed at the lowest temperature of 300 °C had practically no uniform strain and necked right after the yield point. The effect of temperature on the mechanical properties can be explained through the structure of the material, which for the steel processed at lowest temperature was clearly an UFG structure with an average grain size of ~0.3 µm. As the temperature increases, the grain size increases and coarser grains with low angle boundaries and lower dislocation densities are introduced to the material due to rapid recovery processes.

Son et al. [29] and Shin et al. [34] ECAPed dual phase steels at 500 °C and passed the bar four times through the ECAP die yielding a total strain of ~4, which was enough to saturate the structure of the steel bars. After the ECAP processing, the specimens were annealed at 730 °C for 10 minutes followed by water quenching. The grain size dropped from of ~30 µm to 0.2-0.5 µm during the ECAP treatment, but increased during the intercritical annealing to about 1 µm. It is clear from their tensile test data that the strength of the ECAP processed and annealed DP steel is much higher than that of the coarse grained DP steel. Also, the intercritical annealing clearly improved the strain hardening rate of the UFG-DP steel and the shape of the stress-strain curves were similar with the coarse grained DP steels.

Wang et al. [64] studied the mechanical properties of low carbon steels after ECAP processing. They were able to refine the grain size to 0.2-03 µm after 10 passes at room temperature through the ECAP die. Also Azushima and Aoki [65, 66] reached similar structures and properties after 10 ECAP cycles with repetitive side-extrusion. The corresponding tensile strength was just above 1200 MPa [64], while the tensile ductility remained very low. After annealing for 1 hour just below the recrystallization temperature at 773 K, the structure was equiaxed grains with average grain size between 0.3 to 0.4 µm and tensile strength still above 1100 MPa and clearly increased tensile ductility. If the annealing temperature was higher than the recrystallization temperature the strength properties drop to around 500 MPa and elongation values increase significantly.

According to Yanagida et al., the formability of steels decreases only very little during the ECAP treatment compared to for example cold rolling and swaging. This means that the shear strain imposed by the ECAP processing is less harmful to formability than uniaxial deformation such as compression caused by rolling. Similar findings were also reported by Wang et al. [64] who studied the formability of ECAP processed steels by cold rolling the ECAP processed steel specimens up to 95% reduction in several steps without failure of the specimen.

The biggest problem with ECAP processing is the need to repeat the processing several times for each billet. Therefore, the processes are actually quite far from being continuous or fully automated. Some improved versions have been presented, where the die consists of several turns, usually two to three [38-39], which reduces the need for manual operations. The schematic picture of a multi-turn die is shown on Figure 8. The idea of the multi-turn die is very simple, with a three-turn die, one pass through the die produces roughly three times more strain than in a conventional single turn die. Nakashima [39] et al. found the evolution of the microstructure and properties die to be similar for an aluminum alloy pressed through the five turn die (Fig. 5) and multiple times through a single pass die.
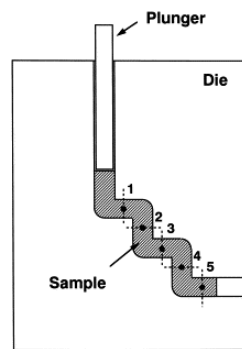

Figure 8. Schematics of a multi-turn ECAP die with five turns. One pass through the die produces a strain close to ~5 [39].

Also, an incremental ECAP [40-41] (Fig 9.) processing method has been proposed, where the pressing of the billet occurs in small increments by a reciprocating part of a die, which is synchronized with the incremental feeding of the billet. This modification is clearly aimed at continuous production as the length of the billet is no longer limited by the size of ECAP die. The feeding of the billet occurs during the withdrawal of the reciprocating punch (part C in Fig. 9), and can therefore be done with very low force. The deformation of the billet occurs as the punch moves towards the billet at an angle pushing the material forward into the exit channel. If the deformation occurs in small steps the deformation is simple uniform shear. This technique, however, has been only applied to processing aluminum and no results of any attempts on processing of steels have been reported.
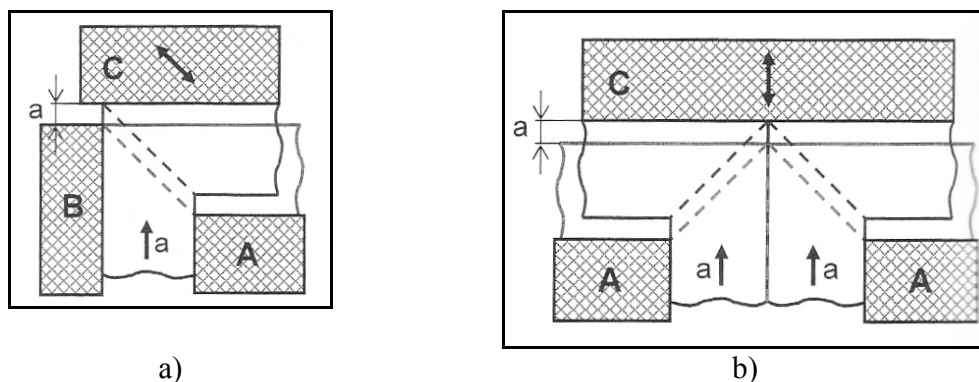

a)   b)

Figure 9. Schematic presentation of the incremental ECAP for single billet a) and double billet b) [42].

High pressure torsion

High pressure torsion (HPT) was one of the first techniques used to fabricate nanocrystalline and ultrafine grained metals. This technique basically uses torsion strain applied under high isostatic pressure to refine the grain size of the metal. A schematic picture of the technique is shown in Figure 10. Usually, the specimens are only very thin small diameter disks, but also some techniques for bulk specimens have been developed. HPT has some distinctive benefits over other SPD techniques including continuous variation of strain and extremely high achievable strains. The drawbacks are the small sample size, uneven microstructure along the radius of the disk, and high pressing forces up 4000 kN even for such small specimens [46]. A bulk high pressure torsion technique was presented by Sakai et al. [47]. They simply replaced the disk specimen with a cylindrical specimen with 8.5 mm length. This specimen was then pressed with anvils having a truncated cone shape. The specimen was deformed to the shape of the die and before applying the heavy torsion strain on the specimen. However, the microstructure of the aluminum alloy specimen varied from center to the edges significantly even after several turns.
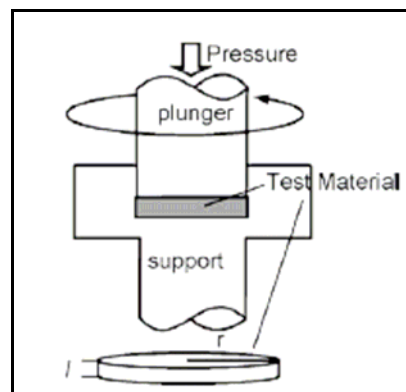

Figure 10. Schematic presentation of the high pressure torsion technique [42].

Surface nanocrystallization

In many cases, material failures occur only on the surfaces, such as, fatigue fracture, wear damages, and corrosion. These failures can be very sensitive to the structure, quality, and properties of the surface of the metal. Therefore, optimizing the properties near the surface can significantly increase the lifetime of the component. In case of stronger and or thicker steel plates, bulk nanocrystallization of the whole metal block might be very difficult and cost inefficient. In such cases, it might be sufficient to nanocrystallize only the surface layer to improve, for example, corrosion and wear resistance. Traditionally, surface treatments have been obtained by various coatings. One of the disadvantages of

these processes is the bonding of the coating to the bulk metal and possible porosity, which are critical in most applications. The surface severe plastic deformation processes can produce a layer of nano or ultrafine grain sizes on the surface of the metal, which can greatly enhance the overall performance of the component.

The surface nanocrystallization or the surface mechanical attrition treatment (SMAT) can be basically any mechanical treatment, where severe plastic deformation induces changes on the surface of the bulk metal by repeated dynamic impacts with high velocity steel or ceramic balls. The balls can be impacted on the treated surface by any suitable method depending on the treated area and the needed size and velocity of the balls. Commonly, the balls are impacted by compressed air [52], centrifugal-force in-impeller [20], or a vibrating chamber [48-51], which can be vibrated by electric drive or by an ultrasonic generator (ultrasonic shot peening). These three types of shot peening are presented schematically in Figure 11.

The shot peening conditions, e.g., impact velocity, energy per shot, coverage, hardness of the balls, hardness of the material etc. all have an effect on the shot peening outcome. Todaka et al. [20] studied the effects of shot peening condition on the formation of the nanocrystalline structure on martensitic steel plates. Their results indicate that increasing the coverage increases the depth of the nanocrystalline layer, but the effect tends to saturate at higher coverages. The most effective way to increase the depth of the nanocrystalline layer is to increase the energy of a single shot by increasing the mass or impact velocity of the balls. By increasing the kinetic energy of the impacts the deformation occurs not only near the surface layer, but also in the inner regions of the material. Also, the depth of the nanocrystallized zone depends on the initial hardness of the material and the hardness of the balls. If the hardness of the metal is too high, the deformation will necessarily occur only near the surface and the thickness of the nanocrystalline layer will decrease. Also, Todaka et al. [20], found that there is no nanocrystallized layer formed if the hardness of the balls is less than the initial hardness of the steel. Also Umemoto et al. [54-55] studied the effect of strain rate and strain imposed by the impacting balls by performing single impact tests with a drop-tower type device, where the impact energy can be adjusted by changing both impact velocity and mass. Their conclusions were that the nanocrystallization in steel initiates already after few impacts if the impacts produce high strain at a high strain rate around 10^4 s^{-1}. The surface structures and hardness produced after few impacts, each producing high strains at high strain rates, were comparable that of a ball milled surface.
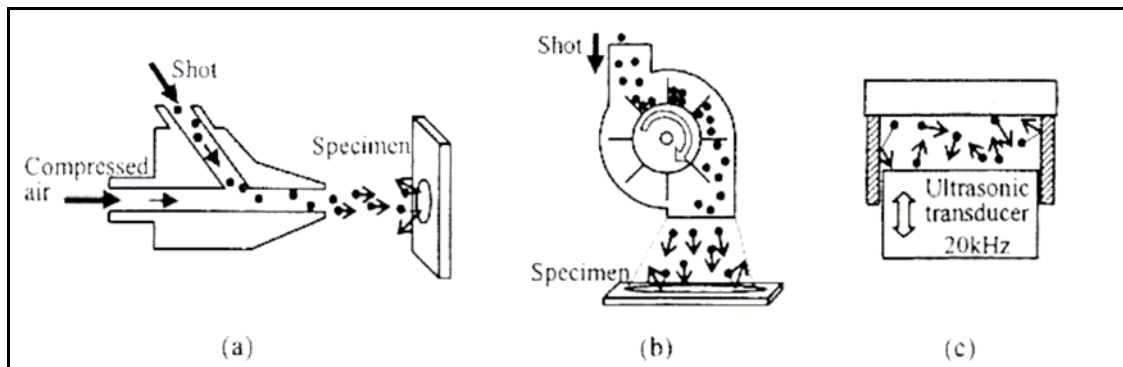
Figure 11. Schematic illustration showing the equipments for a) air blast shot peening, b) centrifugal force in-impeller shot peening, and c) vibrating chamber shot peening [20].

Friction and wear properties can be significantly improved by surface nanocrystallization treatments. Yan et al. [52] studied a Hatfield steel where they induced a nanocrystalline surface by blasting steel balls with compressed air on the surface of the steel. After obtaining a nanocrystalline layer, they performed wear tests on the specimens and found that the two-body abrasion resistance of the metal was increased by 70% compared to the coarse grained material when the abrasive particles were not too hard. With very hard particles, the wear resistance was not improved by the surface treatment. Also, the resistance to impact wear was increased at low impact velocities, but the treatment did not improve the behavior too much at high impact energies due to microcracking of the surface. Also, excessive shot peening was found to be detrimental to wear resistance due to microcracks that form beneath the surface during excessive blasting. Similar findings were presented by Ba et al. [53] who studied quenched and tempered steel. The nanocrystalline layer obtained by supersonic shot peening decreased both friction coefficient and volume loss by abrasive wear. Also the sliding wear properties depend on the grain size. According to Zhou et al. [72] the wear resistance of AISI52100 steel increases with decreasing surface grain size and has a maximum at 32 nm. Smaller grain sizes than this lead to decreasing wear resistance due to decreasing plasticity of the steel. The optimum wear resistance at 32 nm grain size is achieved by a good combination of high strength and hardness and moderate toughness.

Villegas et al. [56] and Dai et al. [57-58] presented a method for nanocrystallization of metal surfaces using WC-Co balls encapsulated in a cylindrical container. The ends of the container, or the specimens, were repeatedly hit by the balls when the container was shacked in all three dimensions. With method, they were able to produce deformed layer in nickel alloy (Hastelloy) up to 600 μm deep having a nanocrystalline structure of tens of micrometers deep. TEM studies clearly revealed deformation twinning even in the grains several tens of micrometers below the surface. The role of deformation twinning in the refinement the grain size was significant and likely is so for other medium stacking fault energy FCC metals.

An approach for using incremental metal forming technique called spin extrusion was introduced by Neugebauer et al [59-61]. This method allows creating an altered structure

in the surface region, while keeping the core section unchanged. The technique can be described as partial roll forming under compressive loading and it is used to manufacture axis symmetrical hollow components out of solid bars. A solid bar is deformed by rolls on the outer surface and by a rotating shaping mandrel simultaneously applying compressive load on the center axis of the bar. The material flows off the direction of feed of the mandrel and is extruded by the rolls over the mandrel forming a tubular hollow component with severely deformed structure. Figure 12 shows the principles of spin extrusion.
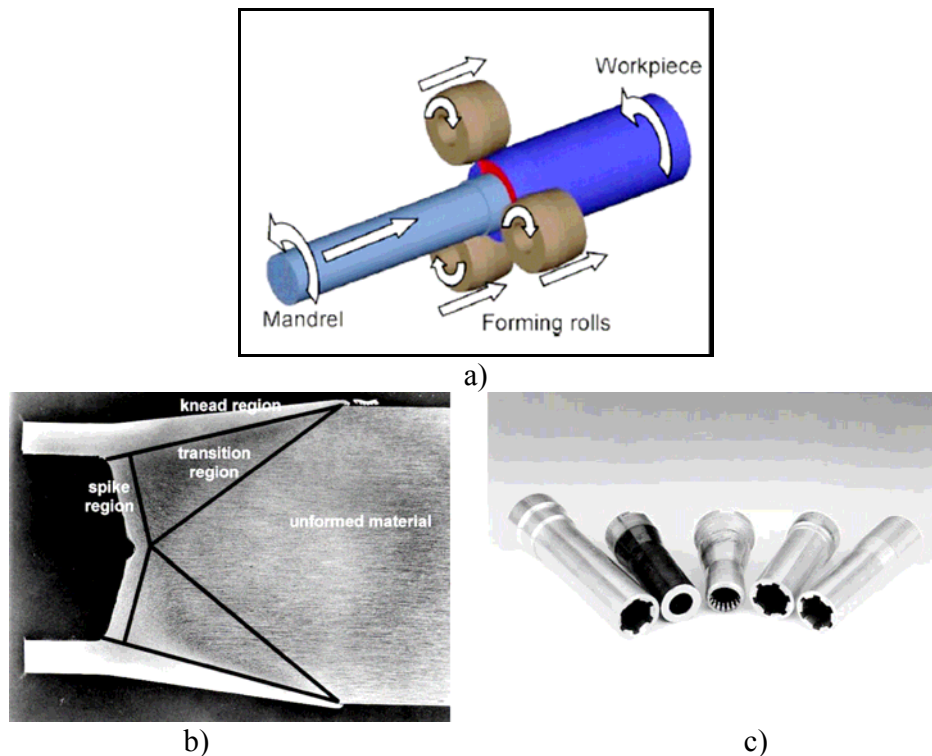

a)

b)   c)

Figure 12. a) principles of spin extrusion, b)deformation regions of the spin extruded metal and c) shafts produced by spin extrusion [60].

Summary

The main reason for processing metals by severe plastic deformation is to improve their overall performance. In the case of steels, the most interesting properties that are improved compared to the coarse grained steels include strength, fatigue, corrosion, wear, and toughness. Therefore, there are various applications where nanocrystalline metals can significantly improve the performance of the components. Markets exist in nearly all sectors, where higher strength-to-weight ratios, fatigue life, and wear resistance are critical. At the moment, there are only few publications addressing fabrication of components from nanocrystalline metals. SPD processed commercial pure titanium has been used to fabricate dental implants for front teeth [73-74]. The nanocrystalline

titanium has several benefits over other titanium alloys, which are usually alloyed with allergenic elements, such as aluminum and vanadium.

Currently the price of the SPD processed metals is still very high due to the lack of continuous mass production. Current cost to produce 5-20 mm diameter SPD processed nanocrystalline titanium is about 50-150 $ / kg [75]. This is comparable to conventional batch forming techniques such as high reduction drawing of a wire, but not with any continuous high volume production methods. Scaling up the capabilities is the key to lowering the costs for more competitive prices. Horita et al. [76] ECAPped aluminum billets with 40 mm diameter and Zhu et al. [75] were able to process titanium bars with diameter of 50 mm. According to Horita et al. [76] the properties and structure of the ECAP processed material is independent of the billet size, therefore, making it possible to scale the process even up to industrial scale.

Because steel is the most useful structural metal, refining its grain size to the ultra fine grain sizes is greatly desired. A vide range of microstructures and consequent material properties can be achieved by severe plastic deformation processing depending on the material and the structure prior to processing. Also, the properties can be further modified by heat treatments after applying the severe deformation. Grain refinement is the only strengthening method, which increases the strength without drastic embrittlement of the steel. In practice, small grain sizes can be achieved by advanced thermomechanical treatments or by severe plastic deformation. Good results can be achieved by both methods; however, the advanced thermomechanical treatments can only reach grain sizes around 1 μm or slightly below, whereas the severe plastic deformation processing can refine the grain size to the nanometer range [69]. The benefits of grain refinement by severe plastic deformation include reduced need for expensive alloying and heat treatments, such as quenching and tempering. In this literature review the most commonly used severe plastic deformation processes for processing of sheet steels and surface treatments of steel plates was presented and their applicability to continuous processing is discussed. Also, the material properties achievable with these methods are presented with some of the challenges related to each method. Even though equal channel angular pressing is so far the most effective method to produce nanocrystalline and ultrafine grained steels, the applicability of this method to continuous production is somewhat limited. Recently, however, some improvements have been made to improve the processing rate by scaling up the billet sizes. Also, an incremental ECAP processing has been introduced with a capability to process two billets at the same time. ECAP facilities with several turns also increase the processing rate by ECAP. SPD processes clearly aimed at continuous production of sheet steels include the continuous confined shearing, frictional angular extrusion, and single roll drive equal channel angular processing, which all are have inbuilt continuous production capability. Other processes for sheets steels are accumulative roll bonding and repeated cold rolling and folding, which are utilize cold (or warm) rolling to bond several layers of steel together by severe plastic deformation. Linear flow splitting is a continuous forming method aimed at producing profiles by cold rolling. The nanocrystalline structure forms on the surfaces of the flanges near the splitting centre, creating a gradient structure.

The surface nanocrystallization by severe plastic deformation is usually carried out by high energy shot peening. The most important parameters in HESP are the velocity of the balls and the coverage of the blasting. The strain imposed by the impacting balls alone is not the most important factor in determining change of the crystal structure, but also the s rate at which the strain occurred has a strong influence on the structure and depth of the deformed layer. The nanocrystallized surface layer helps to reduce friction and wear of the steel.

References

[1] H. Utsunomiya, K. Hatsuda, T. Sakai and Y. Saito, Continuous grain refinement of aluminum strip by conshearing. Materials Science and Engineering A Volume 372, Issues 1-2, 15 May 2004, Pages 199-206. doi:10.1016/j.msea.2003.12.014

[2] J. -C. Lee, H. -K. Seok and J. -Y. Suh, Microstructural evolutions of the Al strip prepared by cold rolling and continuous equal channel angular pressing. Acta Materialia Volume 50, Issue 16, 20 September 2002, Pages 4005-4019. doi:10.1016/S1359-6454(02)00200-8

[3] Jae-Chul Lee, Hyun-Kwang Seok, Jun-Hyun Han and Young-Hoon Chung, Controlling the textures of the metal strips via the continuous confined strip shearing(C2S2) process. Materials Research Bulletin Volume 36, Issues 5-6, March-April 2001, Pages 997-1004. doi:10.1016/S0025-5408(01)00557-8

[4] A.L.M. Costa, A.C.C. Reis, L. Kestens, M.S. Andrade, Ultra grain refinement and hardening of IF-steel during accumulative roll-bonding, *Materials Science and Engineering: A*, *Volume 406, Issues 1-2*, *15 October 2005*, *Pages ,79-285*. doi:10.1016/j.msea.2005.06.058

[5] N. Kamikawa, N. Tsuji, Y. Minamino, Microstructure and texture through thickness of ultralow carbon IF steel sheet severely deformed by accumulative roll-bonding. *Science and Technology of Advanced Materials*, *Volume 5, Issues 1-2, January-March 2004*, *Pages 163-172*. doi:10.1016/j.stam.2003.10.018

[6] N. Kamikawa, T. Sakai, N. Tsuji, Effect of redundant shear strain on microstructure and texture evolution during accumulative roll-bonding in ultralow carbon IF steel. *Acta Materialia*, *Volume 55, Issue 17*, *October 2007*, *Pages 5873-5888* N. Kamikawa, T. Sakai, N. Tsuji. doi:10.1016/j.actamat.2007.07.002

[7] N. Tsuji, Y. Saito, H. Utsunomiya, S. Tanigawa, Ultra-fine grained bulk steel produced by accumulative roll-bonding (ARB) process. *Scripta Materialia*, *Volume 40, Issue 7, 5 March 1999*, *Pages 795-800*. doi:10.1016/S1359-6462(99)00015-9

[8] G. Krallics, J. G. Lenard, An examination of the accumulative roll-bonding process. *Journal of Materials Processing Technology*, *Volume 152, Issue 2, 20 October 2004*, *Pages 154-161*. doi:10.1016/j.jmatprotec.2004.03.015

[9] Cheng Lu, Kiet Tieu, David Wexler, Significant enhancement of bond strength in the accumulative roll bonding process using nano-sized SiO_2 particles. *Journal of Materials Processing Technology*, *Volume 209, Issue 10, 1 June 2009*, *Pages 4830-4834*. doi:10.1016/j.jmatprotec.2009.01.003 .

[10] Tao N., Lu J., Lu K., <u>Surface nanocrystallization by surface mechanical attrition treatment</u>. *Materials Science Forum Volume 579, 2008, Pages 91-108.*

[11] Wilde G., <u>Synthesis of bulk nanocrystalline materials and bulk metallic glasses by repeated cold rolling and folding (RCR)</u>. *Materials Science Forum, Volume 579, 2008, Pages 10-134.*

[12] N. Tsuji, Y. Saito, H. Utsunomiya, S. Tanigawa, <u>Ultra-fine grained bulk steel produced by accumulative roll-bonding (ARB) process</u>. *Scripta Materialia, Volume 40, Issue 7, 5 March 1999, Pages 795-800.* <u>doi:10.1016/S1359-6462(99)00015-9</u>.

[13] Y. Saito, H. Utsunomiya, N. Tsuji, T. Sakai, <u>Novel ultra-high straining process for bulk materials—development of the accumulative roll-bonding (ARB) process</u>. *Acta Materialia, Volume 47, Issue 2, 15 January 1999, Pages 579-58.* <u>doi:10.1016/S1359-6454(98)00365-6</u>

[14] N. Kamikawa, T. Sakai, N. Tsuji, <u>Effect of redundant shear strain on microstructure and texture evolution during accumulative roll-bonding in ultralow carbon IF steel</u>. *Acta Materialia, Volume 55, Issue 17, October 2007, Pages 5873-588.* <u>doi:10.1016/j.actamat.2007.07.002</u>

[15] N. Kamikawa, T. Sakai, N. Tsuji, <u>Effect of redundant shear strain on microstructure and texture evolution during accumulative roll-bonding in ultralow carbon IF steel</u>. *Acta Materialia, Volume 55, Issue 17, October 2007, Pages 5873-588.* <u>doi:10.1016/j.actamat.2007.07.002</u>

[16] G.P. Dinda, H. Rösner, G. Wilde, <u>Synthesis of bulk nanostructured materials by repeated cold-rolling</u>. *Materials Science and Engineering: A, Volumes 410-411, 25 November 2005, Pages 328-33.* <u>doi:10.1016/j.msea.2005.08.091</u>

[17] G.P. Dinda, H. Rösner, G. Wilde, <u>Synthesis of bulk nanostructured Ni, Ti and Zr by repeated cold-rolling</u>. *Scripta Materialia, Volume 52, Issue 7, April 2005, Pages 577-582.* <u>doi:10.1016/j.scriptamat.2004.11.034</u> .

[18] I. Salvatori, <u>Ultra grain refinement of low C steels by accumulative roll bonding.</u> Materials Science Forums, Vols. 503-504, 2006, pp. 311-316.

[19] Terry Lowe, <u>Outlook for manufacturing materials by severe plastic deformation</u>. Materials science forum, Vols. 503-504 (2006), pp. 355-362.

[20] Todaka Y., Umemoto M., Watanabe Y., Tsuchiya K., <u>Formation of nanocrystalline structure by shot peening</u>. Materials science forum, Vols. 503-504 (2006), pp. 669-674.

[21] R. Song, D. Ponge, D. Raabe, J.G. Speer, D.K. Matlock, <u>Overview of processing, microstructure and mechanical properties of ultrafine grained bcc steels</u>. *Materials Science and Engineering: A, Volume 441, Issues 1-2, 15 December 2006, Pages 1-17.* <u>doi:10.1016/j.msea.2006.08.095</u>.

[22] Kawasaki Y., Neishi K., Miyahara Y., Nakamura K., Kaneko K., Nakagaki M., Horita Z., <u>Application of severe torsion straining process for grain refinement of steels.</u> Materials science forum, Vols. 503-504 (2006), pp. 943-948.

[23] Miayhara Y., Emi N., Neishi K., Nakamura K., Kaneko K., Nakagaki M., Horita Z. <u>Microstructures and mechanical properties of Mg alloy after severe torsion straining process.</u> Materials science forum, Vols. 503-504 (2006), pp. 949-954.

[24] Nakamura K., Neishi K., Kaneko K., Nakagaki M., Horita Z., <u>Continuous grain refinement using severe torsion straining process</u>. Materials science forum, Vols. 503-504 (2006), pp. 385-390.

[25] Müller C., Bohn T., Bruder E., Groche P., <u>UFG-microstrucure by linear flow splitting.</u> Vols. Materials science forum, Vols. 584-586 (2008), pp. 68-73.

[26] Bruder E., Bohn T., Müller C., Properties of UFG HSLA steel profiles produced by linear flow splitting. Materials science forum, Vols. 584-586 (2008), pp. 661-666.

[27] Jiang L., Pérez-Prado M., Ruano O., Kassne M., <u>Bond strength of ultrafine grained Zr fabricated by accumulative roll bonding.</u> Materials science forum, Vols. 584-586 (2008), pp. 243-248.

[28] Dong Hyuk Shin, Kyung-Tae Park, <u>Ultrafine grained steels processed by equal channel angular pressing</u>. *Materials Science and Engineering: A, Volumes 410-411, 25 November 2005, Pages 299-30.* doi:10.1016/j.msea.2005.08.025

[29] Young Il Son, Young Kook Lee, Kyung-Tae Park, Chong Soo Lee, Dong Hyuk Shin. <u>Ultrafine grained ferrite–martensite dual phase steels fabricated via equal channel angular pressing: Microstructure and tensile properties</u>. *Acta Materialia, Volume 53, Issue 11, June 2005, Pages 3125-3134.* doi:10.1016/j.actamat.2005.02.015.

[30] Ho-Kyung Kim, Myung-Il Choi, Chin-Sung Chung, Dong Hyuk Shin. <u>Fatigue properties of ultrafine grained low carbon steel produced by equal channel angular pressing</u>. *Materials Science and Engineering A, Volume 340, Issues 1-2, 15 January 2003, Pages 243-250.* doi:10.1016/S0921-5093(02)00178-8

[31] Dong Hyuk Shin, Jong-Jin Pak, Young Kuk Kim, Kyung-Tae Park, Yong-Seog Kim. <u>Effect of pressing temperature on microstructure and tensile behavior of low carbon steels processed by equal channel angular pressing</u>. *Materials Science and Engineering A, Volume 323, Issues 1-2, 31 January 2002, Pages 409-415.* doi:10.1016/S0921-5093(01)01395-8

[32] Botvina L., Tyuyin M., Levin V., Demina Y., Panteleev I., Dobatkin S., <u>Specific features of static and fatigue fracture of the 0.09%C-0.08%Mo-0.03%Nb-0.06%V steel with ultrafine-grained structure</u>. *Materials science forum, Vols. 584-586 (2008), pp. 281-286.*

[33] Niendorf T., Marten T., Maier H., Karaman I., <u>The effect of texture on the fatigue properties of ultrafine grained interstitial free steel.</u> *Materials science forum, Vols. 584-586 (2008), pp. 864-869.*

[34] Shin D., Kim W., Ahn J., Park K., Kim Y., <u>Ultrafine grained dual phase steel fabricated by equal channel angular pressing.</u> *Materials science forum, Vols. 503-504 (2006), pp. 447-454.*

[35] Ruslan Z. Valiev, Terence G. Langdon, <u>Principles of equal-channel angular pressing as a processing tool for grain refinement</u>. *Progress in Materials Science, Volume 51, Issue 7, September 2006, Pages 881-981.* doi:10.1016/j.pmatsci.2006.02.003 .

[36] Y. Fukuda, K. Oh-ishi, Z. Horita, T. G. Langdon. <u>Processing of a low-carbon steel by equal-channel angular pressing</u>. *Acta Materialia, Volume 50, Issue 6, 2 April 2002, Pages 1359-1368.* doi:10.1016/S1359-6454(01)00441-4.

[37] Dong Hyuk Shin, Byung Cheol Kim, Yong-Seog Kim, Kyung-Tae Park, <u>Microstructural evolution in a commercial low carbon steel by equal channel angular pressing</u>. *Acta Materialia, Volume 48, Issue 9, 29 May 2000, Pages 2247-2255.* doi:10.1016/S1359-6454(00)00028-8 .

[38] A. Rosochowski, L. Olejnik, <u>Numerical and physical modelling of plastic deformation in 2-turn equal channel angular extrusion</u>. *Journal of Materials Processing Technology, volumes 125-126, 2002, Pp. 309-316.* doi:10.1016/S0924-0136(02)00339-4

[**39**] Kiyotaka Nakashima, Zenji Horita, Minoru Nemoto, Terence G. Langdon, Development of a multi-pass facility for equal-channel angular pressing to high total strains. *Materials Science and Engineering A, Volume 281, Issues 1-2, 2000, Pp. 82-87.* doi:10.1016/S0921-5093(99)00744-3

[**40**] Olejnik L., Rosochowski A., Richert M., Incremental ECAP of plates. *Materials Science Forum, Vols. 584-586 (2008), pp. 108-113.*

[**41**] Rosochowski A., Olejnik L., Richert M., Double billet incremental ECAP. *Materials Science Forum, Vols. 584-586 (2008), pp. 139-144.*

[**42**] A. Azushima, R. Kopp, A. Korhonen, D.Y. Yang, F. Micari, G.D. Lahoti, P. Groche, J. Yanagimoto, N. Tsuji, A. Rosochowski, A. Yanagida Severe plastic deformation (SPD) processes for metals. *CIRP Annals - Manufacturing Technology, Volume 57, Issue 2, 2008, Pages 716-735.* doi:10.1016/j.cirp.2008.09.005

[**43**] Yan B. Dove S., Jin L., Shen J., Huang Y., Jiao S., Microstructure evolution during continuous frictional angular extrusion of interstitial free steel. *Materials Science Forum, Vols. 584-586 (2008), pp. 631-636.*

[**44**] Y. Huang, P.B. Prangnell, Continuous frictional angular extrusion and its application in the production of ultrafine-grained sheet metals. *Scripta Materialia, Volume 56, Issue 5, March 2007, Pages 333-336.* doi:10.1016/j.scriptamat.2006.11.011

[**45**] Tanaka M., Fujimoto N., Yokote T., Higashida K., Fracture toughness enhanced by severe plastic deformation in low carbon steels. *Materials Science Forum, Vols. 584-586 (2008), pp. 637-642.*

[**46**] Pippan R., Scheriau S., Hohenwarter A., Hafok M., Advantages and limitations of HPT: a review. *Materials Science Forum, Vols. 584-586 (2008), pp. 16-21.*

[**47**] Sakai G., Nakamura K., Horita Z., Langdon T., Application of high pressure torsion to bulk samples. *Materials Science Forums, Vols. 503-504 (2006), pp. 391-396.*

[**48**] Dema Ba, Shining Ma, Changqing Li, Fanjun Meng, Surface nanostructure formation mechanism of 45 steel induced by supersonic fine particles pombarding. *Journal of University of Science and Technology Beijing, Mineral, Metallurgy, Material, Volume 15, Issue 5, October 2008, Pages 561-567.* doi:10.1016/S1005-8850(08)60105-X

[**49**] N. R. Tao, M. L. Sui, J. Lu, K. Lu, Surface nanocrystallization of iron induced by ultrasonic shot peening. *Nanostructured Materials, Volume 11, Issue 4, June 1999, Pages 433-440.* doi:10.1016/S0965-9773(99)00324-4

[**50**] N. R. Tao, Z. B. Wang, W. P. Tong, M. L. Sui, J. Lu, K. Lu, An investigation of surface nanocrystallization mechanism in Fe induced by surface mechanical attrition treatment. *Acta Materialia, Volume 50, Issue 18, 28 October 2002, Pages 4603-4616.* doi:10.1016/S1359-6454(02)00310-5

[**51**] G. Liu, S. C. Wang, X. F. Lou, J. Lu, K. Lu. Low carbon steel with nanostructured surface layer induced by high-energy shot peening. *Scripta Materialia, Volume 44, Issues 8-9, 18 May 2001, Pages 1791-1795.* doi:10.1016/S1359-6462(01)00738-2

[**52**] Weilin Yan, Liang Fang, Zhanguang Zheng, Kun Sun, Yunhua Xu. Effect of surface nanocrystallization on abrasive wear properties in Hadfield steel. *Tribology International, Volume 42, Issue 5, May 2009, Pages 634-641.* doi:10.1016/j.triboint.2008.08.012

[**53**] D.M. Ba, S.N. Ma, F.J. Meng, C.Q. Li, Friction and wear behaviors of nanocrystalline surface layer of chrome–silicon alloy steel. *Surface and Coatings*

Technology, *Volume 202, Issue 2, 25 November 2007, Pages 254-260.* doi:10.1016/j.surfcoat.2007.05.033

[54] M. Umemoto, B. Huang, K. Tsuchiya, N. Suzuki, Formation of nanocrystalline structure in steels by ball drop test. *Scripta Materialia, Volume 46, Issue 5, 11 March 2002, Pages 383-388.* doi:10.1016/S1359-6462(01)01258-1

[55] M. Umemoto, K. Todaka, K. Tsuchiya, Formation of nanocrystalline structure in carbon steels by ball drop and particle impact techniques. *Materials Science and Engineering A, Volumes 375-377, 15 July 2004, Pages 899-904.* doi:10.1016/j.msea.2003.10.198

[56] Juan C. Villegas, Kun Dai, Leon L. Shaw, Peter K. Liaw. Nanocrystallization of a nickel alloy subjected to surface severe plastic deformation. *Materials Science and Engineering: A, Volumes 410-411, 25 November 2005, Pages 257-260.* doi:10.1016/j.msea.2005.08.087

[57] K. Dai, L. Shaw, Comparison between shot peening and surface nanocrystallization and hardening processes. *Materials Science and Engineering: A, Volume 463, Issues 1-2, 15 August 2007, Pages 46-53.* doi:10.1016/j.msea.2006.07.159

[58] K. Dai, J. Villegas, Z. Stone, L. Shaw, Finite element modeling of the surface roughness of 5052 Al alloy subjected to a surface severe plastic deformation process. *Acta Materialia, Volume 52, Issue 20, 1 December 2004, Pages 5771-5782.* doi:10.1016/j.actamat.2004.08.031

[59] R. Neugebauer, R. Glass, M. Hoffmann, Spin Extrusion – A New Partial Forming Technology based on 7 NC-Axes Machining. *CIRP Annals - Manufacturing Technology, Volume 54, Issue 1, 2005, Pages 241-244.* doi:10.1016/S0007-8506(07)60093-6

[60] R. Neugebauer, M. Kolbe, R. Glass, New warm forming processes to produce hollow shafts. *Journal of Materials Processing Technology, Volume 119, Issues 1-3, 20 December 2001, Pages 277-282.* doi:10.1016/S0924-0136(01)00939-6

[61] Reimund Neugebauer, Roland Glass, Matthias Kolbe, Michael Hoffman, Optimisation of processing routes for cross rolling and spin extrusion. *Journal of Materials Processing Technology, Volumes 125-126, 9 September 2002, Pages 856-862.* doi:10.1016/S0924-0136(02)00392-8

[62] T. Lowe, Y. Zhu, S. Semiatin, D. Berg, Overview and outlook for materials processed by severe plastic deformation. Proceedings of the NATO Advanced Research Workshop on *Investigations and applications of severe plastic deformation*, Moscow, Russia, 1999, pp. 347-356. Published by Kluwer Academic Publishers, Netherlands, 2000.

[63] Chen B., Lin D., Zeng X., Lu C., Single roll drive equal channel angular process – a potential severe plastic deformation (SPD) process for industrial application. *Materials Science Forum, Vols. 503-504 (2006), pp.557-560.*

[64] Jing Tao Wang, Cheng Xu, Zhong Ze Du, Guo Zhong Qu, Terence G. Langdon, Microstructure and properties of a low-carbon steel processed by equal-channel angular pressing. *Materials Science and Engineering: A, Volumes 410-411, 25 November 2005, Pages 312-315.* doi:10.1016/j.msea.2005.08.111

[65] Akira Azushima, Koshiro Aoki, Properties of ultrafine-grained steel by repeated shear deformation of side extrusion process. *Materials Science and Engineering A,*

Volume 337, Issues 1-2, 25 November 2002, Pages 45-49. doi:10.1016/S0921-5093(02)00005-9

[66] A. Azushima, K. Aoki, Mechanical Properties of Ultrafine Grained Steel Produced by Repetitive Cold Side Extrusion. *CIRP Annals - Manufacturing Technology, Volume 51, Issue 1, 2002, Pages 227-230.* doi:10.1016/S0007-8506(07)61505-4

[67] A. Yanagida, K. Joko, A. Azushima, Formability of steels subjected to cold ECAE process. *Journal of Materials Processing Technology, Volume 201, Issues 1-3, 26 May 2008, Pages 390-394.* doi:10.1016/j.jmatprotec.2007.11.199

[68] N. Tsuji, Y. Ito, Y. Saito, Y. Minamino. Strength and ductility of ultrafine grained aluminum and iron produced by ARB and annealing. *Scripta Materialia, Volume 47, Issue 12, 9 December 2002, Pages 893-899.* doi:10.1016/S1359-6462(02)00282-8

[69] B. Q. Han, S. Yue, Processing of ultrafine ferrite steels. *Journal of Materials Processing Technology, Volume 136, Issues 1-3, 10 May 2003, Pages 100-104.* doi:10.1016/S0924-0136(02)01014-2

[70] Azdiar A. Gazder, Wenquan Cao, Christopher H.J. Davies, Elena V. Pereloma. An EBSD investigation of interstitial-free steel subjected to equal channel angular extrusion. *Materials Science and Engineering: A, Volume 497, Issues 1-2, 15 December 2008, Pages 341-352.* doi:10.1016/j.msea.2008.07.030

[71] Branislav Hadzima, Miloš Janeček, Yuri Estrin, Hyoung Seop Kim, Microstructure and corrosion properties of ultrafine-grained interstitial free steel. *Materials Science and Engineering: A, Volume 462, Issues 1-2, 25 July 2007, Pages 243-247.* doi:10.1016/j.msea.2005.11.081

[72] L. Zhou, G. Liu, Z. Han, K. Lu, Grain size effect on wear resistance of a nanostructured AISI52100 steel. *Scripta Materialia, Volume 58, Issue 6, March 2008, Pages 445-448.* doi:10.1016/j.scriptamat.2007.10.034

[73] http://www.oeaw.ac.at/esi/english/research/facilities/spd/ECAP.html. Referred August 12, 2009.

[74] V. Latysh, Gy. Krallics, I. Alexandrov, A. Fodor, Application of bulk nanostructured materials in medicine. *Current Applied Physics, Volume 6, Issue 2, February 2006, Pages 262-266.* doi:10.1016/j.cap.2005.07.053

[75] Valiev R., Semenova I., Jakushina E., Latysh V., Rack H., Lowe T., Petruzelka J., Dluhos L., Hrusak D., Sochova J., Nanostructured SPD processed titanium for medical implants. Materials Science Forum, Vols. 584-586 (2008), pp. 49-54.

[76] Yuntian T. Zhu, Terry C. Lowe, Terence G. Langdon , Performance and applications of nanostructured materials produced by severe plastic deformation. *Scripta Materialia, Volume 51, Issue 8, October 2004, Pages 825-830.* doi:10.1016/j.scriptamat.2004.05.006